Structural characterization of vasopressin V2 receptor in complex with Gs and bêta-arrestin1 proteins by cryo-electron microscopy

Julien Bous

THÈSE POUR OBTENIR LE GRADE DE DOCTEUR
DE L'UNIVERSITÉ DE MONTPELLIER

En Biologie Santé

École Doctorale Sciences Chimiques et Biologiques pour la Santé (CBS2)

Unités de recherche:

1. Centre de Biologie Structurale de Montpellier (CBS) CNRS UMR5048-INSERM U1054
2. Institut de Génomique Fonctionnelle (IGF) CNRS UMR5203-INSERM U1191

Structural characterization of vasopressin V2 receptor in complex with Gs and βarrestin1 proteins by cryo-electron microscopy

Présentée par Julien Bous

Le 27 Septembre 2021

Sous la direction de Bernard Mouillac et Patrick Bron

Devant le jury composé de

Dr. Christopher G. Tate, FRS; MRC Investigator and Programme Leader, MRC Laboratory of Molecular Biology, Cambridge	Examinateur
Dr. Jean-Louis Banères, DR2, Institut des Biomolécules Max Mousseron, Montpellier	Président
Dr. Michel Bouvier, Professeur, Faculté de Médecine, Directeur de l'IRIC, Université de Montréal	Rapporteur
Dr Ralf Jockers, DR1, Institut Cochin , Paris	Rapporteur
Dr Patrick Bron, DR2, Centre de Biologie Structurale, Montpellier	Directeur de Thèse
Dr Bernard Mouillac, DR2, Institut de Génomique Fonctionnelle, Montpellier	Directeur de Thèse

UNIVERSITÉ DE MONTPELLIER

Acknowledgements

First of all, I would like to thank Bernard Mouillac and Patrick Bron for allowing me to fulfill this thesis in their laboratories. Bernard Mouillac for its unconditional support, human qualities, wise pieces of advice and critically reading the manuscript of this thesis. Patrick Bron for its guidance in electron microscopy, advice, trust in my capacities to run this exciting project, and for carefully reading this manuscript.

A load of grateful thanks to Hélène Orcel and Joséphine Lai-Kee-Him for sharing their valuable experience, their technical and moral support in any circumstances.

I would also like to thank Stefano Trapani for many instructive scientific discussions and its valuable help and support.

I would like to thank all the members of Bron and Granier-Mouillac groups, former and present, for the friendly and warm atmosphere, which made working in their respective departments a great pleasure. My special thanks go to Christopher Chevillard for his precious friendship. Thanks to Aurélien Fouillen for his help and support and friendship.

I would like to thank all members of my thesis jury Chris Tate, Jean-Louis Banères, Michel Bouvier, Ralph Jocker, Patrick Bron, and Bernard Mouillac for kindly agreeing to participate in the defense of this thesis.

I would also like to thank my former and present office colleagues, other PhD Students, and Postdocs for their kindness.

I would like to thank my family for their support.

The last thanks go to Elise, who supported me throughout this adventure with a lot of patience and commitment no matter how hard it was.

This research fellowship was atributed by the Doctoral school grant: CBS2 Doctoral School (Chemical & Biological Sciences for the Health) and funded by the Ministry of Higher Education. The project was also funded by the "Agence nationale de la recherche" (ANR) and Fondation pour la Recherche Médicale (FRM).

Résumé

L'arginine-vasopressine (AVP) est l'hormone antidiurétique et régule une fonction vitale de notre organisme: l'équilibre hydrique. Elle agit au niveau du rein, plus précisément à la membrane plasmique des cellules principales du tubule collecteur, segment distal du néphron. C'est par son interaction avec son récepteur spécifique de type 2 (V2R), protéine membranaire de la famille des récepteurs couplés aux protéines G (RCPGs), que cette hormone peptidique active une voie de signalisation cellulaire, dépendante de la protéine Gs, qui conduit à une relocalisation des canaux à eau, les aquaporines 2. Cette relocalisation vers la membrane du pôle apical des cellules principales, permet la réabsorption de l'eau de l'urine vers le sang. Le couplage du V2R à la protéine Gs mais aussi à la β-arrestine1 (βarr1), partenaires de signalisation privilégiés, constituent des étapes clés de la régulation du récepteur. Le couplage à l'arrestine entraîne l'activation de la voie de signalisation MAP kinases et la désensibilisation du V2R. Au cours de cette thèse, j'ai produit et purifié les complexes fonctionnels AVP-V2R-Gs-Nb35 et AVP-V2R- βarr1-ScFv30 pour étudier leur structure tridimensionnelle par cryo-microscopie électronique (Cryo-EM).

Complexe AVP-V2R-Gs-Nb35

Concernant le complexe AVP-V2R-Gs-Nb35, le V2R et la protéine G ont été produites en cellules d'insecte, le Nb35 a été produit en bactéries. Les différentes protéines recombinantes ont ensuite été purifiées à travers une série de chromatographies d'affinité et de chromatographies d'exclusion de taille puis associées pour former le complexe. Le complexe à été purifié à son tour et déposé sur des grilles pour une analyse des particules isolées par Cryo-EM.

Trois états conformationnels différents du complexe, appelés état relâché (L), serré-1 (T1) et serré-2 (T2) ont été identifiés. Les cartes de densité générées pour chaque état affichent une résolution moyenne de 4.2 Å, 4.5 Å et 4.7 Å, avec respectivement une distribution de 16, 48 et 36 %. La résolution locale varie de 3.2 à 6.4 Å. Les cartes de densité diffèrent principalement au niveau de l'interface d'interaction entre le récepteur et la protéine G. Cette dynamique est confirmée par une analyse de variabilité des particules réalisée lors du traitement des données.

Afin de reconstruire un modèle tridimensionnel (3D) consistant malgré une résolution limitée des cartes de densité, nous avons conçu une stratégie hybride originale basée sur une

combinaison des cartes de cryo-EM, de simulations numériques de dynamique moléculaire (MDS) et de résonance magnétique nucléaire (RMN) expérimentale de différence de transfert de saturation (STD). Seules les cartes des sous états L et T1 ont la qualité suffisante pour construire un modèle atomique. Les modèles définitifs ont ensuite été analysés par comparaison avec d'autres structures de récepteurs de la Classe A des RCPGs. Les complexes AVP-V2R-Gs-Nb35 ont notamment été comparés à la structure inactive du récepteur à l'oxytocine (OTR) qui possède 47% d'identité de séquence avec V2R. D'autre part, les modèles que nous avons obtenus ont été comparés aux deux structures AVP-V2R-chimère miniGsGi-Nb35-ScFv16 publiées de façon concomitante à notre travail.

Liaison de l'AVP au V2R

Le positionnement de l'AVP dans les structures des complexes de signalisation est en accord avec les données de pharmacologie moléculaire accumulées depuis plus de vingt cinq ans. La poche de liaison est une cavité au centre des 7 hélices transmembranaires du V2R. Le fond est principalement composé de résidus hydrophobes tandis que l'entrée est plus hydrophile. Ceci est cohérent avec la double polarité de l'AVP. Celle-ci est composée de résidus hydrophobes (Cys1,Tyr2, Phe3, Cys6) qui sont orientés vers le fond de la poche et de résidus polaires (Gln4, Asn5 et le tripeptide C-terminal Pro7-Arg8-Gly9NH_2) qui interagissent avec l'entrée du site de liaison.

Conformation active du V2R

Comme attendu pour un RCPG lié à un partenaire de signalisation, le V2R présente toutes les caractéristiques des RCPGs adoptant une conformation active. Cela correspond à un large déplacement du domaine transmembranaire 6 vers l'extérieur, un déplacement du domaine transmembranaire 7 vers l'intérieur ainsi qu'à un réarrangement de certains motifs conservés pour les RCPGs de classe A. En comparant le V2R lié à l'AVP avec la structure inactive de l'OTR lié à un antagoniste non peptidique (le retosiban), on peut observer que le site de liaison de l'agoniste et de l'antagoniste se superposent partiellement mais que l'antagoniste se positionne plus profondément dans la poche de liaison. La différence de positionnement et de contact des deux ligands induit de larges réarrangements conformationnels à l'origine de l'activation du récepteur ou de son inactivation.

Interface V2R-Gs

Les cartes cryo-EM du complexe ternaire établissent clairement les détails structurels du couplage V2R-Gs. L'interface est similaire à celle caractérisée pour d'autres complexes GPCR-

protéine G. Les conformations L et T1 ont une architecture classique comprenant l'engagement de l'hélice α5 C-terminale de la sous-unité αs de la protéine G au centre des 7 hélices transmembranaires du V2R. Cependant, il existe des différences intéressantes par rapport à d'autres structures de complexes GPCR-protéine G, en particulier par rapport aux structures des complexes AVP-V2R-chimère miniGsGi-Nb35-ScFv16. Pour les deux structures L et T, le V2R établit de nombreux contacts directs avec la sous-unité β de la protéine G. Dans l'état T, les résidus de la boucle ICL1 L62-A63-R64-R65-G66 interagissent avec G β R52, D312-N313 et D333-F335. Dans l'état L, les résidus de la boucle ICL1 R65-G66-R67-R68 interagissent avec Gβ R52, D312 et D333. Ces contacts entre V2R et Gβ sont beaucoup plus nombreux que dans les autres complexes de GPCR de classe A, ainsi que dans les complexes AVP-V2R-chimère miniGsGi-Nb35-ScFv16. De plus, dans la conformation T, il existe aussi des contacts supplémentaires entre V2R et l'hélice N-terminale de la sous unité Gαs, résultant en une interaction plus compacte que celle communément observée pour les RCPGs de classe A.

Liens entre informations structurales et données pharmacologiques/cliniques

Cette étude va plus loin que la simple description d'une structure d'un récepteur ou d'un complexe de signalisation. En effet, de nombreuses mutations du récepteur sont responsables de deux maladies génétiques rares présentant un tableau clinique inversé: 1/ le diabète insipide néphrogénique congénital (DINc) dû à des mutations «perte de fonction» associées à une incapacité des patients à concentrer leurs urines, 2/ le syndrome néphrogénique d'antidiurèse inappropriée (SNADI) lié à des mutations constitutivement actives qui provoquent une intoxication à l'eau et une hyponatrémie. Les structures du V2R permettent de proposer des hypothèses afin d'expliquer l'effet de certaines de ces mutations sur une base structurale, par exemple pourquoi les mutants de l'acide aminé arginine 137 en leucine ou cystéine (R137L ou R137C) provoquent une activation constitutive du V2R et donc la maladie SNADI.

Complexe AVP-V2R-βarr1-ScFv30

Comme précédemment, le V2R et a été produit en cellules d'insecte Sf9. Une version de l'arrestine avec le domaine C-terminal tronqué pour favoriser son interaction avec le V2R à été produite en bactéries. Le ScFv30 qui stabilise le complexe a été produit dans le milieu extracellulaire d'une culture de cellules d'insecte Schneider S2. Les différentes protéines recombinantes ont ensuite été purifiées séparément puis mixées pour former le complexe. Le complexe AVP-V2R-βarr1-ScFv30 a à son tour été purifié puis déposé sur des grilles pour une analyse de particules isolées par Cryo-EM.

La forte dynamique de ce système ne nous a cependant pas permis d'atteindre la haute résolution. Mais les données structurales que nous avons obtenues peuvent être interprétées à l'échelle des structures secondaires. Notre nouvelle structure fournit des informations précieuses pour comprendre la spécificité de couplage de la βarr1 aux RCPGs de manière générale. A ce jour, seules quelques structures de RCPGs en complexe avec une arrestine ont été publiées, ce qui limite pour l'instant l'établissement un consensus.

Liaison de l'AVP au V2R

L'AVP adopte globalement la même position dans la poche de liaison du V2R que dans les structures actives du V2R couplé à la protéine Gs. Cependant, la résolution limitée (résolution moyenne de 4.7Å) ne permet pas d'analyser les contacts entre les résidus de la poche de liaison et de l'AVP et de discriminer des différences fines.

Conformation active du V2R

Le récepteur adopte une conformation active similaire à celle du V2R couplé à la protéines Gs avec comme caractéristiques apparentes le large déplacement du TM6 vers l'extérieur et le déplacement du TM7 vers l'intérieur. Le récepteur engage la βarr1 à travers une partie de son extrémité C-terminale (résidus 356–368), son cœur transmembranaire, la boucle ICL1 et l'extrémité des boucles ICL2 et ICL3. Des analyses complémentaires de spectrométrie de masse confirment la phosphorylation de la majorité des sérines et des thréonines localisées dans la région C-terminale du V2R. Il est connu que l'état de phosphorylation de ces résidus joue un rôle essentiel dans la capacité de recrutement du V2R vis-à-vis de la βarr1.

Interface V2R-βarr1

Le couplage de βarr1 à V2R est significativement différent par rapport à celui observé dans les structures des complexes RCPG-arrestine récemment publiées. L'interface est intermédiaire entre les deux tendances d'architectures générales reportées à ce jour. En effet, l'arrestine diffère d'une rotation d'environ 80°-90° parallèlement au plan membranaire entre les complexes récepteur β1 adrénergique (**β_1**AR)-βarr1, récepteur muscarinique 2 (M2R)-βarr1 et rhodopsine-Arr1, et les complexes de récepteurs à la neurotensine (NTSR1)-βarr1. La βarr1 couplée à V2R, quand à elle, diffère d'une rotation d'environ 30° parallèlement au plan membranaire, en comparaison avec le complexe β_1AR-βarr1. La βarr1 affiche une conformation active comme prévu dans ce contexte avec une rotation d'approximativement 13° du lobe C par rapport au lobe N, si on la compare à ses conformations inactives. Dans la structure V2R–βarr1, le lobe C de l'arrestine est fortement incliné vers la membrane. Cette forte inclinaison peut être attribuée à l'interaction des boucles 344 et 164 de l'arrestine situées en périphérie du lobe C

avec la micelle de détergents qui présente une forte courbure par rapport à une membrane plane. L'analogue du phospholipide phosphatidylinositol 4,5-bisphosphate ($PtdIns_{(4,5)}P_2$) utilisé pour stabiliser le complexe durant sa purification pourrait également avoir une influence sur l'orientation de l'arrestine. En effet il semble interagir avec le V2R et l'arrestine au niveau du lobe C, ce qui pourrait potentiellement amplifier l'orientation atypique de l'arrestine. De plus, le seul complexe qui partage cette spécificité à ce jour est le NTSR1-βarr1 dont la structure a été également résolue en détergeant et en présence du même analogue du $PtdIns_{(4,5)}P_2$. Par analogie, la carte de densité établie lors de nos travaux présente une extension de densité qui pourrait correspondre à l'analogue du $PtdIns_{(4,5)}P_2$.

Ce détail est d'un grand intérêt car le $PtdIns_{(4,5)}P_2$ joue un rôle central dans la formation des vésicules de clathrine et pourrait ainsi être impliqué dans la dynamique de recrutement des complexes RCPG-arrestine vers les vésicules de clathrine (VCs) et/ou la formation synergique des VCs incluant les complexes RCPG-Arrestine. Ce processus est méconnu et doit être étudié plus en détail pour être mieux compris.

Discussion

Les structures de plusieurs conformations actives du V2R représentent des outils essentiels pour mieux comprendre les mécanismes moléculaires mis en jeu lors de son activation par l'AVP et pour avoir une idée plus précise de sa fonction. Elles constituent une base de réflexion pour comprendre certaines mutations du récepteur responsables de deux maladies génétiques rares et une base structurale rationnelle pour le développement de nouvelles molécules thérapeutiques par des approches de «drug design». Par exemple, ces données permettent d'avancer des hypothèses pour expliquer pourquoi les mutants de l'acide aminé arginine 137 en leucine ou cystéine (R137L ou R137C) et le mutant de l'isoleucine 130 en asparagine provoquent une activation constitutive du V2R, et donc un syndrome néphrogénique d'antidiurèse inappropriée. Dans un contexte plus large, la structure du V2R-βarr1 apporte des informations utiles pour comprendre la spécificité de couplage entre les RCPGs et les arrestines, informations limitées aujourd'hui à quelques structures dont il est difficile de tirer des règles générales. De ce point de vue, les différences importantes avec ce que l'on observe pour d'autres RCPGs illustrent une large plasticité du potentiel de liaison des arrestines avec cette famille de récepteurs membranaires.

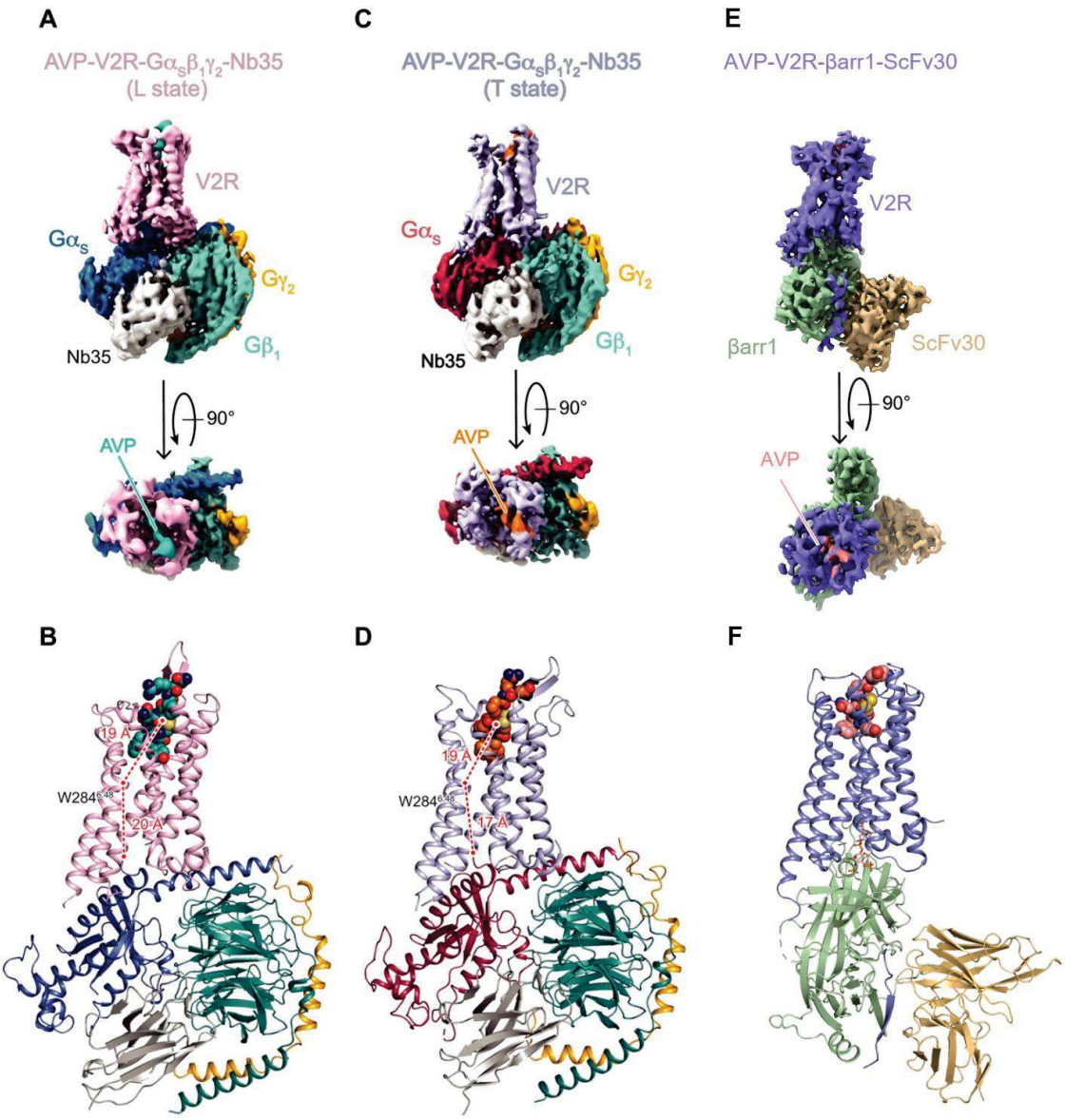

Structures of AVP-V2R-Gs-Nb35 complexes in L and T conformations and of the AVP-V2R-βarr1-ScFv30 complex. (A) Orthogonal views of the cryo-EM density maps of the L state of the AVP-V2R-Gs-Nb35 complex and (B) corresponding model as cartoon representation. The distances between $W284^{6.48}$ (at its Cα carbon) and the AVP center of mass (COM) and between $W284^{6.48}$ and the C-terminal end of α5 helix of Gs are shown. (C and D) Corresponding maps and model for the T state. (E and F) Corresponding maps and model for the AVP-V2R-βarr1-ScFv30 complex.

Abstract

The arginine-vasopressin (AVP) V2 receptor (V2R) is a G protein-coupled receptor that controls body water homeostasis. It is involved in many water balance and urine disorders. Point mutations of its gene are directly responsible for two rare genetic diseases. As such, it is a key therapeutic target. Despite important progress in understanding the molecular basis of its function, it remained for a long time refractory to structure determination. This work is thus focused on the determination of the three-dimensional (3D) V2R structure in complex with its canonical signaling partners Gs protein or β-arrestin1 (βarr1) by cryo-electron microscopy (Cryo-EM). The comparison of the two active states of the V2R at an atomic level is an important step toward the understanding of the molecular mechanisms involved in its activity.

We first successfully determined the AVP-V2R-Gs complex structure by using a combination of single particle analysis (SPA) Cryo-EM, experimental NMR, and molecular dynamic simulations. This structural biology hybrid approach allowed to solve molecular details of AVP binding to V2R and of the interface of the receptor with the Gs protein signaling partner. The structure is in agreement with molecular pharmacology data accumulated over 25 years. The binding pocket is a deep cleft in the center of the seven-helix bundle. The bottom of the orthosteric crevice is mainly composed of hydrophobic residues while the entrance is more hydrophilic. This is consistent with the dual polarity of AVP with the hydrophobic residues (cys1, Tyr2, Phe3, Cys6) oriented toward the bottom of the pocket and polar residues (Gln4, Asn5, and the C-terminal tripeptide Pro7-Arg8-Gly9NH2) interacting with the entrance of the pocket. The active V2R displays hallmarks of receptor activation such as a large outward movement of the transmembrane domain (TM) 6 and inward movement of the TM7 and a break of the Ionic lock involving helices TM3 and TM6 (D/ERY motif). The coupling between the receptor and its Gs signaling partner is significantly tighter compared to what is observed for other class A GPCRs and interestingly, strongly dynamic, allowing us to characterize three conformational sub-states. This study goes further than a simple description of a receptor or a signaling protein complex structure. Indeed, 3D models were interpreted to understand the structural consequences of V2R mutations responsible for two rare genetic diseases. Congenital Nephrogenic Diabetes Insipidus (cNDI) is associated with V2R loss-of-function mutations whereas Nephrogenic Syndrome of Inappropriate Antidiuresis (NSIAD) is associated with V2R constitutively active mutations.

Abstract

To be able to purify the AVP-V2R-βarr1-ScFv30 complex, we used a truncated version of βArr1(ΔCT) in which the C-terminus is deleted. The complex was then successfully investigated by SPA Cryo-EM. Since there are only a few structures of GPCRs in complex with arrestins, our new structure provides valuable insights of information to understand the coupling specificity of arrestins to GPCRs, and more specifically the coupling of βarr1 to V2R. The AVP displays the same overall position in the binding pocket as in the AVP-V2R-Gs complex, with respect to the limited resolution. The V2R adopts an active conformation similar to the one observed in complex with the Gs protein. The coupling is significantly different compared to the recently published structures. The βarr1 pose is intermediate between the ones reported for the β1-adrenergic receptor (β_1AR-βarr1), the muscarinic M2 receptor (M2R)-βarr1 , and to the rhodopsin-Arr1 which adopt a similar overall conformation, and the ones reported for the neurotensin receptor 1 (NTSR1)-βarr1. Nonetheless, βarr1 coupled to V2R comparatively to βarr1 coupled to β_1AR differs by a rotation of approximately 30° parallel to the membrane plane, and displays a strong tilt relatively to the membrane plane. The βarr1 displays an active conformation as expected in this context. In the V2R–βarr1(ΔCT) structure, arrestin is strongly tilted towards the membrane. The strong tilt may be attributed to the interaction of the C-edge with the detergent micelle, as well as to the presence of the phosphatidylinositol-4,5-bisphosphate ($PtdIns_{(4,5)}P_2$) analog used to stabilize the complex during purification. It is of great interest since the $PtdIns_{(4,5)}P_2$ plays a pivotal role in clathrin-coated vesicles (CCVs) formation and might thus be involved in the dynamic of GPCR-Arr complexes recruitment to CCVs or in synergic formation of CCVs with these complexes. This process remains to be clearly established. The V2R coupled to its two canonical signalisation partners shares the same overall architecture and a common overall AVP position in the binding site. The arrestin finger loop seems to occupy a similar position to the α5-helix of the Ras domain of the Gs α subunit into the V2R core but the helices display a different orientation. Structural differences at the atomic level might exist but a AVP-V2R-βarr structure with an improved resolution will be necessary to identify such differences.

Table of contents

Table of contents

Figures

Figures

Abbreviations

2D: two-dimensional
3D: three-dimensional
$A_{2A}R$: adenosine A2A receptor
ADPKD: autosomal dominant polycystic kidney disease
AQP: aquaporin
ARPKD: autosomal recessive polycystic kidney disease
Arr: arrestin
AT1AR: Angiotensin II receptor type 1
AVP: arginine-vasopressin
BRET: Bioluminescence Resonance Energy Transfer
BRIL: cytochrome b562RIL
cAMP: Cyclic adenosine monophosphate
CCD: charge coupled device
CCV: clathrin-coated vesicles
CDMD: correlation-driven molecular dynamics
CG: coarse-grained
CHS: cholesteryl hemisuccinate
CMOS: complementary metal-oxide-semiconductor
cNDI: Congenital Nephrogenic Diabetes Insipidus
CRD: cysteine-rich domain
CRE: cAMP-responsive element
Cryo-EM: cryo-electron microscopy
Cter: C-terminal domain
CTF: contrast transfer function
CTR: Calcitonin receptor
CV: column volume
dDAVP: desmopressine
DDM: *n*-dodecyl-β-d-maltopyranoside
DQE: detective quantum efficiency
ECD: extracellular domain
ECL: extracellular loop
EM: electron microscopy
ENaC: epithelial sodium channel
ERK: extracellular signal regulated kinase
FEG: Field emission gun
FSC: Fourier shell correlation
FT: Fourier transform
FT^{-1}: inverse Fourier transform
FZD: Frizzled
GDP: guanosine diphosphate
GEF: guanine nucleotide exchange factors
GIF: Gatan image filter
GLP1R: glucagon-like peptide-1 receptor
GPCR: G protein-coupled receptors
GRK: GPCR kinases
GTP: guanosine triphosphate

Abbreviations

HEK: human embryonic kidney cells
HRV3C: Human Rhinovirus 3C protease
ICL: intracellular loop
IDP: Intrinsically disordered protein
IGFR: insulin-like growth factor receptor
LMNG: Lauryl Maltose Neopentyl Glycol
LVP: lysine-vasopressin
M2R: muscarinic M2 receptor
MQ1: mambaquaretin toxin
MWCO: molecular weight cutoff
NCS: Na^+/Cl^- Symporter
NCX1: Sodium/calcium exchanger
NMR: Nuclear magnetic resonance
NS-EM: negative stain electron microscopy
NSIAD: Nephrogenic Syndrome of Inappropriate antidiuresis
NTSR1: neurotensin receptor 1
OT: oxytocin
OTR: oxytocin receptor
PAM: positive allosteric modulator
PKA: protein kinase A
$PtdIns_{(4,5)}P_2$: phosphatidylinositol-4,5-bisphosphate
PTH: parathyroid hormone
PTHR1: parathyroid hormone receptor 1
RMSD: root-mean-square deviation
SGD: stochastic gradient descent
SIADH: syndrome of inappropriate antidiuretic hormone secretion
SMO: Smoothened
SNR: signal-to-noise ratio
SPA: single particle analysis
SPR: single-particle reconstruction
STD: saturation transfer difference
T4L:T4 lysozyme
TE: three-element
TEM: Transmission electron microscopy
TM: transmembrane domain
TRPM6: transient receptor potential cation channel subfamily M member 6
TRPV5: transient receptor potential channel subfamily V
TVP: tolvaptan
V1aR: vasopressin 1a receptor
V1bR: vasopressin 1b receptor
V2R: vasopressin 2 receptor
VFT: Venus flytrap
β_1AR: β1-adrenergic receptor
β_2AR: β2-adrenergic receptor
βarr1: βarrestin1
ΔCT: C-terminus deleted

1 Introduction

1.1 A short history of vasopressin type 2 receptor discovery

1.1.1 Early vasopressin investigations

The first study referring to the arginine-vasopressin (AVP) was published in 1895 by Oliver and Schafer (Schafer 1895) with the characterization of the hypertensive effect induced by intravenous injections of an extract of the pituitary glands in different animals. After this first discovery, other biological effects of neurohypophysial extracts were also characterized. For instance, the antidiuretic activity of posterior pituitary extracts in humans was reported by Von Der Velden in 1913. It is the first experiment studying the involvement of the V2R activation, although at this time receptors for vasopressin were not discovered. Further, a study on the physiology of water in frog demonstrated the role of neurohypophysial hormones in osmoregulation in 1921 (Brunn 1921). The first quantitative antidiuretic assays were carried out in dogs with bladder fistulae (Kestranek, Pick, and Moliter 1925) and in human subjects (Bijlsma, Burn, and Gaddum 1928). In 1952, the minimal dose of post-pituitary extract necessary to induce an antidiuretic effect was investigated in dogs (Dicker et al. 1952). Concomitantly in the early fifties, the discovery of the chemical structure of two important neurophysiological hormones oxytocin (OT) (Du Vigneau, Ressler, and Trippet 1953) and arginine-vasopressin (Du Vigneaud, Lawler, and Pofenoe 1953; Chauvet 1954) (Figure 1-1) as well as their chemical synthesis (du Vigneaud, Gish, and Katsoyannis 1954; du Vigneaud et al. 1954), were important steps to the characterization of the AVP-OT receptors. OT and AVP are two cyclic nonapeptides with a strong identity (Figure 1-1). They differ only by two amino acids: (i) the third amino acid is a phenylalanine in AVP and an isoleucine in oxytocin, (ii) the positively-charged arginine at position 8 in AVP is replaced by a hydrophobic aliphatic leucine in OT. The two hormones are produced in separate populations of magnocellular neurons of the paraventricular and supraoptic nuclei in the hypothalamus. By binding to the carrier proteins neurophysins, they are transported along the supraoptic hypophyseal tract to the axonal terminals of magnocellular neurons in the posterior pituitary and released into the systemic circulation from the neurohypophysis (Figure 1-1) (Arima et al. 1998; Legros 2010).

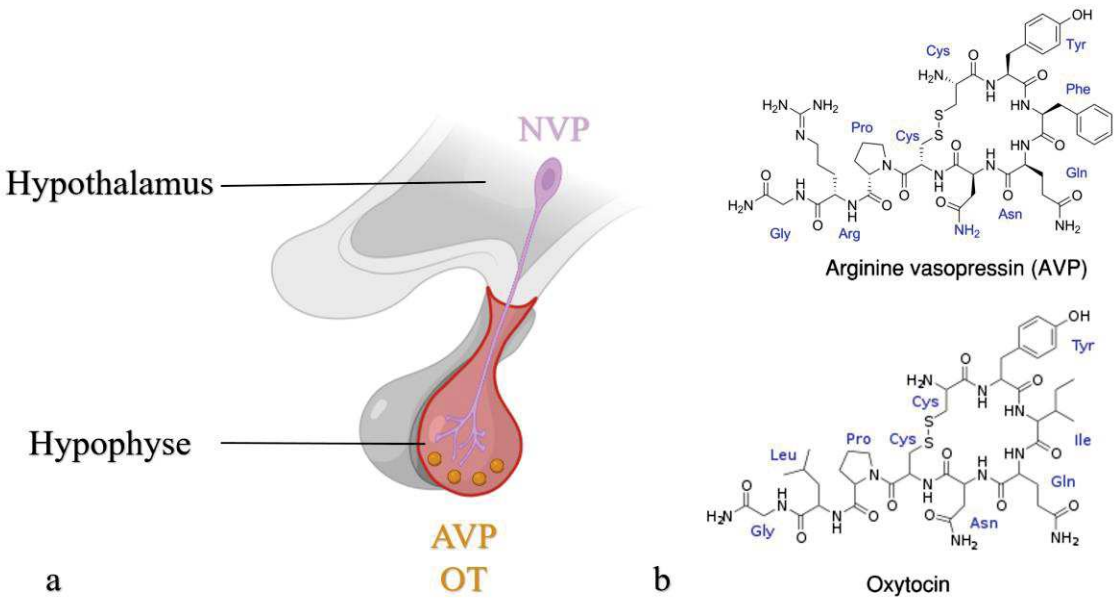

Figure 1-1 Oxytocin and Vasopressin
a) Oxytocin and vasopressin are produced in the Paraventricular Nucleus (NVP) of the hypothalamus and released from the post hypophyse. b) Structures of the two neurohypophysial hormones (https://en.wikipedia.org)

1.1.2 Development of vasopressin analogs and demonstration of a vasopressin-induced release of cAMP

The major discovery of AVP/OT hormones was followed by the development of new analogues. More potent antidiuretic, oxytocic and vasopressor ligands were identified as well as antagonists able to block specific properties of the neurohypophysial hormones. Those new molecules proved to be valuable tools and led to important progress in the field (see for review, M. Manning et al. 2012; Maurice Manning et al. 2008; Farah, Herken, and Welch 1968). An extensive list of vasopressin/oxytocin analogues and their respective pressor and antidiuretic effects are nicely reviewed here (Farah, Herken, and Welch 1968). It has been demonstrated that structural modifications of AVP can affect vasopressor and antidiuretic activities in a clearly differential manner, for example regarding the $Phe^{2}Lys^{8}$-vasopressin (Octapressin®). The pressor activity of this analogue, by the intravenous route, is about five times higher in man than in the rat, and its antidiuretic activity in man is thirteen times weaker than that of lysine-vasopressin (LVP) in man (Guhl 1961). At the opposite, the antidiuretic activity of $thialysine^{8}$vasopressin is almost four times higher than the vasopressor activity (Berde and Boissonnas 1968). In 1963, Serge Jard demonstrated competitive inhibition of lysine- or

arginine-vasotocin in the frog by various analogues, including oxytocin, and introduced the notion of receptors for neurohypophysial hormones (F. Morel and Jard 1963).

The first radioactive AVP analogue was synthetized in 1959 (Schoessler 1959). [^{3}H]-LVP was synthetized using purified LVP from beef and hog pituitary powder. The authors demonstrated [^{3}H]-LVP renal localization on anesthetized rats. Tritium activity was measured in the kidneys. A competition with free cysteine allowed to partially unbind the radioactive molecules. Based on these results, the authors hypothesized that LVP is attached to its receptor site through a disulfide bound. This theory was comforted by a second study (I. Schwartz et al. 1960). However, this first interpretation at the molecular level was later refuted by the use of a cyclic vasopressin analogue without disulfide group but which is still able to bind and induce bladder permeability in the toad (L. Schwartz, Rasmussen, and Rudinger 1964).

In parallel, Orloff and Handler (Orloff and Handler 1962) established that the neurohypophysial hormone AVP could produce a specific action on epithelial cells of toad bladder, allowing the release of cyclic adenosine monophosphate (cAMP) in those cells. The effect of AVP is mimicked by the addition of exogenous cAMP. The addition of theophylline, an inhibitor of cAMP phosphodiesterase, also affected and allowed permeabilization of a toad bladder and salt transport (Handler et al. 1965). These findings validated the role of cAMP as a second messenger as theorized by Sutherland and coworkers (Sutherland and Rall 1960; Robison, Butcher, and Sutherland 1967)

Based on the work of Orloff and Handler, Brown hypothesized and demonstrated that AVP achieves its antidiuretic action through the synthesis of cAMP (Brown et al. 1963). Other works confirmed this demonstration (Chase and Aurbach 1968). In 1971, Dousa and coworkers developed an in-vitro bioassay system to evaluate the antidiuretic activity of neurohypophysial hormones from several mammals and demonstrated the second messenger role of cAMP in this function (Dousa et al. 1971).

In the early seventies, tritiation of oxytocin and vasopressin based on the catalytic substitution of peptide-bound iodine with tritium followed by a new affinity chromatography purification led to the development of powerful new tools which became commercially available (Flouret et al. 1977; Pradelles et al. 1972). The labeled AVP allowed the characterization of vasopressin-specific binding sites in different tissues and a direct correlation between site occupation by AVP and cAMP accumulation (J. Bockaert et al. 1973).

For instance, interesting results were reported on the specific binding of [3H]-LVP to pig kidney plasma membranes (Bockaert et al. 1973). Several characteristics of the system were evoked. It has been shown that cAMP response is not linear as a function of the dose of [3H]-LVP and that the tritiated hormone incubation time has an important role in activation level. This first study highlights a complex mechanism of activation. Bockaert and coworkers made several hypotheses to explain this phenomenon: cooperativity, receptor population heterogeneity, and receptor dimerization were evoked.

Other complementary characterizations on bovine (Hechter, Terada, Spitsberg, et al. 1978; Hechter, Terada, Nakahara, et al. 1978), rat (Butlen et al. 1978; Rajerison et al. 1974), and human (Guillon et al. 1982) kidneys confirmed this study and showed: i) the presence of a unique population of receptors and no cooperativity in binding, ii) a dissociation constant for vasopressin binding much higher (K_D= 20-30 nM) than the circulatory hormone concentration (physiological vasopressin concentrations are 0.5–5 pg/ml corresponding approximatively to 4-7 pM) (Cowley et al. 1981). This suggests a large pool of receptors acting as a reserve and an amplification system between receptor hormone binding and antidiuretic effect. Those are important criteria to mediate vasopressin action, in order to provide a rapid regulation of kidney function.

The use of LLC-PKl, a pig kidney cell line allowed to recapitulate vasopressin effect in kidney and to discriminate Bockaert's hypotheses. This cell line responds to vasopressin stimulation by increasing intracellular cAMP content similarly to the main cells of the collecting duct (Roy and Ausiello, 1981).

The concentration of LVP for 50% receptor's occupancy is in agreement with precedent values determined on pig, rat and bovine kidney membranes (Roy and Ausiello, 1981). Binding kinetics of AVP as well as characterization of the cAMP response, in these cells, allowed the authors to demonstrate that neither negative cooperativity nor receptor distinct populations can properly describe the system (Roy and Ausiello, 1981). Nevertheless, the authors were able to best describe the experimental data with dimeric receptor model theory. More recently, the first results using Bioluminescence Resonance Energy Transfer (BRET) technology demonstrated the presence of V2R dimers in transfected human embryonic kidney 293T cells (Terrillon et al. 2003; Terrillon, Barberis, and Bouvier 2004).

1.1.3 Classification of the Different Vasopressin Receptor Subtypes

The first assumptions of different AVP receptor subtypes with specific tropisms and actions result from the use of different vasopressin analogues (Farah, Herken, and Welch 1968). Indeed, unlike AVP, specific analogues display just one of the two pharmacological properties of the AVP, the pressor effect or the antidiuretic effect. Furthermore, those two responses have been proven to be linked to different activation pathways. On this basis, at least two types of AVP receptors could be distinguished: the renal type is also known as the antidiuretic receptor and the vascular type also named the pressor receptor. Moreover, it was also shown that AVP promotes glycogenolysis in isolated rat hepatocytes, which is not mediated by cAMP second messenger (Kirk and Hems 1974; Hems and Whitton 1973), as it was the case with glucagon. In 1977, Keppens and coworkers showed that AVP-induced glycogenolysis is linked to an increase of intracellular calcium concentration (Keppens, Vandenheede, and De Wulf 1977) and stimulation of inorganic phosphate incorporation into phosphatidylinositol (J. Kirk, Verrinder, and Hems 1977). Based on precedent studies on the stimulation of phosphatidylinositol metabolism by several hormones within cells of various tropism (nervous, secretory, smooth muscle), vasopressin primarily interacts with a subtype of receptor that is functionally similar to the α1-adrenergic receptor and the H1-Histamic receptor (Michell, Kirk, and Billah 1979). It induces the metabolism of phosphatidylinositol and the mobilization of intracellular calcium. This receptor subtype was named vasopressin 1 receptor (V1R) by opposition to the one displaying a renal tropism and which is responsible for the antidiuretic effect of AVP (linked to a cAMP production). The renal receptor subtype of AVP was then defined as V2R. Based on pharmacological studies, the V1 receptor category was subdivided later into V1a receptors (vascular and hepatic type) and V1b receptors (located in corticotropic cells of the anterior pituitary) (Michell, Kirk, and Billah 1979; Jard et al. 1986).

Currently, it is well established that the V1a and V1b subtypes are coupled to stimulation of phospholipase C and generation of inositol triphosphate as a second messenger (Berridge and Irvine 1984). As already explained above the V2 receptor subtype is coupled to adenylyl cyclase activation and production of cAMP.

Since the V2R discovery, the pharmacology and functioning of the antidiuretic effect activated by V2 have been carefully studied. In 1992, OPC-31260 (Mozavaptan) (Yamamura et al. 1992), the first specific non-peptide V2 antagonist was characterized. It is a first step in the development of non-peptide V2 antagonists for therapeutic purposes (hyponatremia). The following year, the first specific V2R receptor peptide antagonist was reported as d(CH2)5[D-

Ile2, Ile4]AVP in a review characterizing several new antagonists of the AVP/OT receptor family (Manning and Sawyer 1993).

The human AVPR2 gene located on chromosome region Xq28 and encoding the V2 was cloned in 1992 for the first time, the gene was used to clone a complementary library of human kidney genes and identified as belonging to the family of 7-transmembrane domain proteins, based on its sequence and hydrophobic properties (Birnbaumer et al 1992).

1.2 AVP Antidiuretic Effect

1.2.1 Nephron architecture (Figure 1-2)

The mammalian nephron is the structural and functional unit of the kidney. There are approximately 1.2 million nephrons by kidney. It is a tubular system allowing a gradual primary urine concentration before entrance into the collecting duct. (Figure 1-2)

It is constituted by:

-The renal corpuscle is composed of the glomerulus and the Bowman capsule.

-The proximal convoluted tubule

-The limb of Henle is composed of the descending and the ascending segment. It drains urine into the distal convoluted tubule.

-The distal convoluted tubule

-The collecting tubule: It flows into the collecting duct

First, the plasma is filtered in the glomerulus at a rate of approximatively 120ml/min (170 l/jour) into the surrounding Bowman capsule. Glomerular ultrafiltration is a movement of water across capillaries which is governed by Starling forces. The fluid motion occurs because of a gradient of hydrostatic pressure in the glomerular capillary network (Figure 1-2). Primary urine is composed of water, electrolytes, nutriments, amino acids, and other small molecules.

Then the primary urine goes through the distinct segments of the nephron and its composition is gradually modified by secretion/reabsorption mechanisms, specific to each segment. 85% of the primary urine is automatically reabsorbed and 15% is mediated by the AVP/V2R

antidiuretic system. This regulation allows maintaining the body water balance. This represents between 1 and 1.5 urine liter every day.

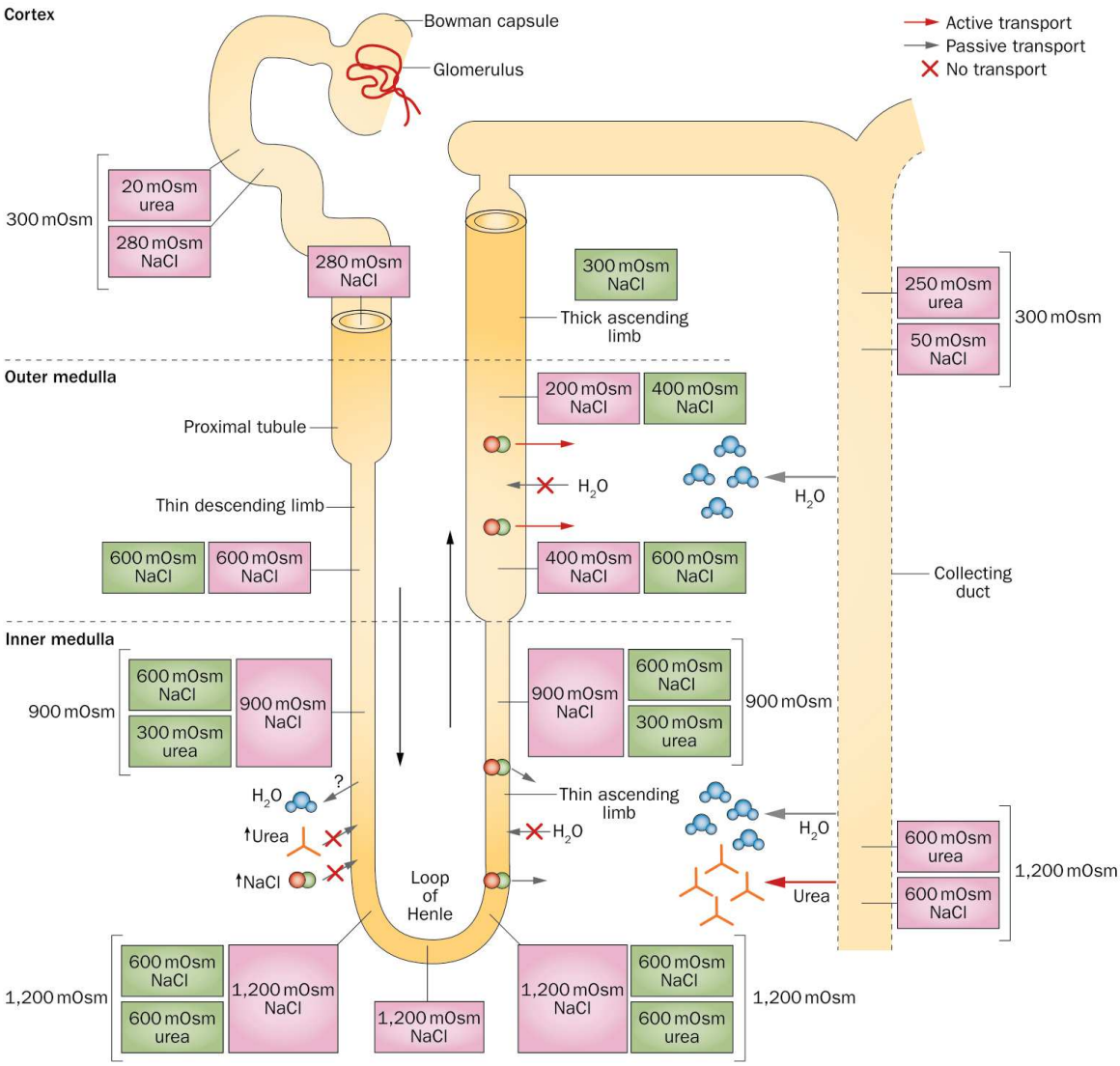

Figure 1-2 The renal concentration and dilution mechanism
The loop of Henle forms a counter-current multiplier system Nature Reviews | Nephrology that concentrates the urine. Urine is isotonic when it enters the loop of Henle and hypotonic when it exits into the collecting duct. The concentration gradient generated in the loop of Henle is driven by the active reabsorption of NaCl in the thick ascending limb by the transporter solute carrier family 12 members 1. The mechanism of concentration in the thin descending limb is not completely resolved, but likely involves passive water efflux and/or NaCl influx. The final concentration of urine occurs in the collecting duct and depends on the availability of aquaporin 2 water channels. The approximate osmolalities of the tubular fluid (pink boxes) and interstitial fluid (green boxes) are indicated (Bockenhauer and Bichet 2015)

1.2.2 Mechanism of urine production

1.2.2.1 Glomerular filtration

The glomerular filtration occurs within the renal corpuscle composed of the glomerulus and the Bowman capsule (Figure 1-3 A). This complex filter produces 170l of primary urine by day. This urine contains electrolytes and waste products, glucose lipids, and amino acids. This primary urine is further concentrated in the following segments of the nephron (Richard Kitching and Hutton 2016).

1.2.2.1.1 The glomerulus is a complex filter composed of the following elements (Figure 1-3)

-The afferent arteriole which feeds the glomerula in blood.

-The fenestrated capillaries where the fenestration pores allow particles less than 50-100 nm diameter to go to the next layer.

-The glomerular basement membrane is composed of 3 sublayers. It filters negatively charged proteins but is a barrier to plasma albumin which is also negatively charged (Miner 2012)

-The lamina rara externa is composed by Heparin negatively charged sulfate sublayer

- The lamina densa is composed of type4 collagen and laminin

-The lamina rara interna is composed of Heparin negatively charged sulfate sublayer

-The efferent arteriole which expel the blood out of the glomerula

1.2.2.1.2 The Bowman capsule is composed of the following elements (Figure 1-3)

-The podocytes and the slit diaphragm which is composed of nephrin and filters particles bigger than 9nm

-The mesangial cells phagocyte all the proteins which unevenly end up stuck in the slit diaphragm.

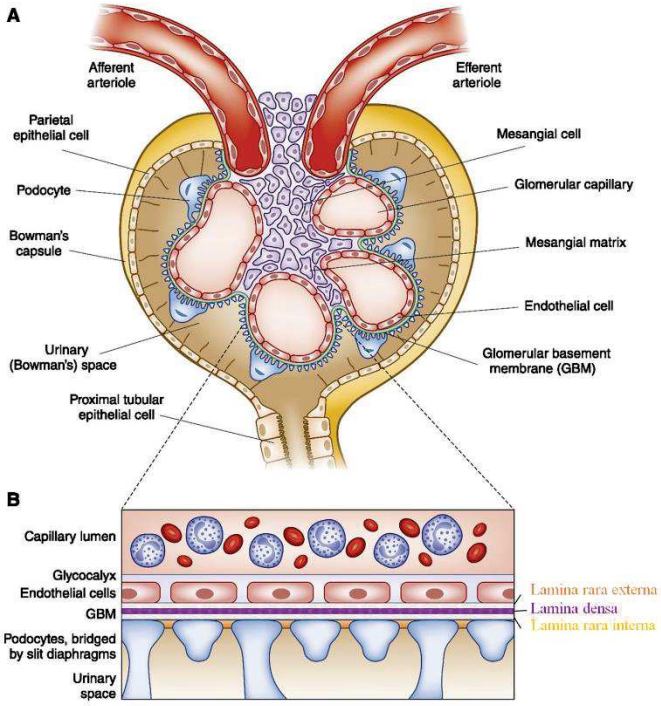

Figure 1-3 Renal corpuscle
Basic structure of the glomerulus and the glomerular filtration barrier. (A) Each glomerulus is composed of an afferent arteriole, which supplies the glomerular capillaries, and an efferent arteriole, into which they drain. Mesangial cells and mesangial matrix provide structural support for the glomerular capillaries, lined by specialized fenestrated endothelium, and then the glomerular basement membrane. On the urinary side of the glomerular basement membrane are podocytes, with foot processes that wrap around the glomerular capillaries. The urinary space is lined by a cup-like layer of parietal epithelial cells which adhere to the basement membrane of Bowman's capsule. (B) The glomerular filtration barrier is a specialized molecular sieve, with properties that aid filtration of small solutes from the blood to the urine, while limiting the passage of macromolecules such as albumin. Adapted from (Richard Kitching and Hutton 2016).

1.2.2.2 Proximal convoluted tubule

In the proximal tubule, approximately 60% to 70% of the primary urine as well as NaCl, HCO_3^- and other solutes like glucose, lactate, amino-acids or important anions like phosphate and citrate are reabsorbed.

1.2.2.2.1 Tubular reabsorption

The reabsorption of ions and small molecules occurs through Na^+-dependent active co-transporters located on the apical side of the proximal tubule cells. The process is driven by the basolateral $3Na^+/2K^+$-ATPase pumps, which create an inward negative membrane potential and a Na^+ gradient. The water is reabsorbed by osmosis accordingly to the Na^+ gradient. This mechanism is called "obligatory water reabsorption" (Figure 1-4). (*Renal Physiology* 2010)

Other ions like K^+, Mg^{2+}or Cl^- are reabsorbed by paracellular transport (Figure 1-4) and Cl^- can be reabsorbed through K^+/Cl^- cotransporters.

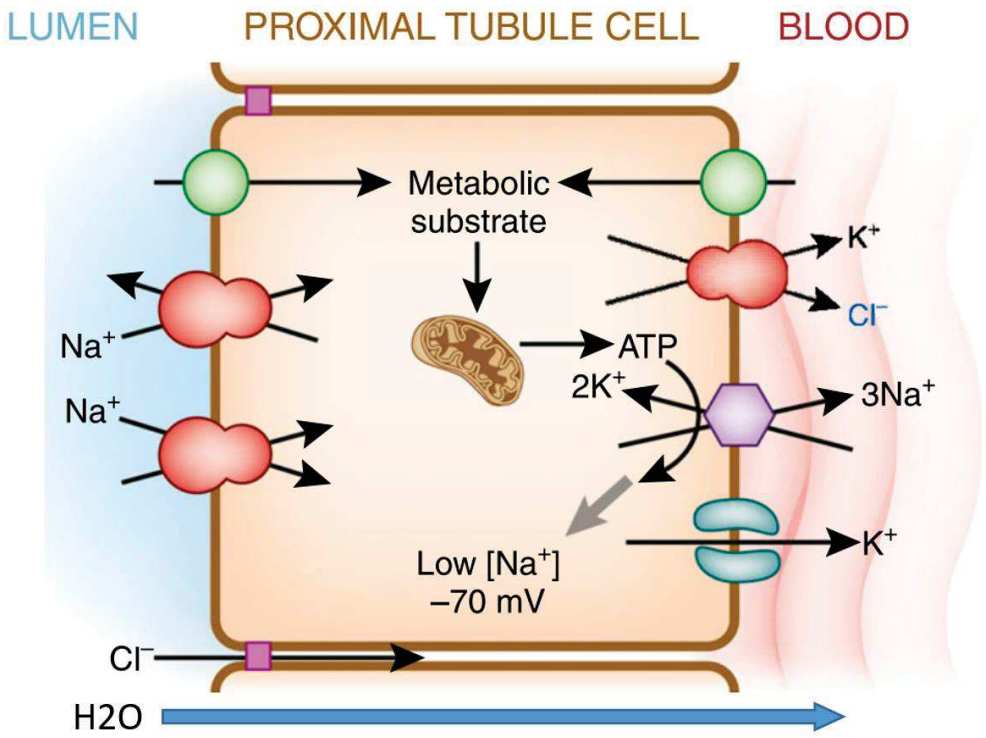

Figure 1-4 Obligatory water reabsorption
Generic scheme of the proximal tubule cell. The primary energy currency is organic metabolic substrates that enter the proximal tubule and are catabolized to produce ATP, which serves as the secondary energy currency. Some transporters are directly coupled to ATP hydrolyses (enthalpic transport), such as the H1-ATPase and Na1/K1-ATPase. The latter represents the main workhorse of the proximal tubule responsible for the majority of the cellular ATP consumption. The Na1/K1-ATPase converts the energy stored in ATP into low cellular [Na1] and high cellular [K1]. The presence of K1 conductance allows the [K1] gradient to increase the negative interior potential. The low cell [Na1] and negative voltage serve as the tertiary energy currencies that drive multiple secondary active apical transporters to achieve uphill movement of solutes coupled to downhill movement of Na1 (entropic transport). The transported solutes move in the same (symport or cotransport) or opposite (antiport, exchanger, or countertransport) direction as Na1. Movement of solute can also proceed via paracellular routes driven by electrochemical forces (*Renal Physiology* 2010)

1.2.2.2.2 Tubular secretion

HPO_4^{2-} and other molecules such as drugs or uric acid can be excreted into the proximal convoluted tubule directly from the blood by active transport.

1.2.2.3 Loop of Henle

1.2.2.3.1 Countercurrent multiplication

The generation of a gradient of increasing osmolality along the medulla occurs in the descending segment of the loop of Henle. Indeed, the osmolality rises gradually from 300mosm in the proximal tubule to 1200mOsm in the inner medulla. This occurs because of the countercurrent multiplication mechanism. The solutes released by the active transporters $Na^+/K^+/2Cl^-$ cotransporter located in the large segment of the ascending limb, increase the inner medulla osmolality (Figure 1-5 b). The water is passively reabsorbed from the descending limb to the medulla interstitium by osmosis through type-1 aquaporins. It results in an increase of osmolality in the descending loop and a gradual decrease of osmolality in the ascending loop (Figure 1-5 a). The countercurrent multiplication mechanism is maintained by the exchanges in solute and water between the renal medulla and the *vasa recta*, a branch of the afferent arteria located in the medulla (Hogg and Kokko 1979).

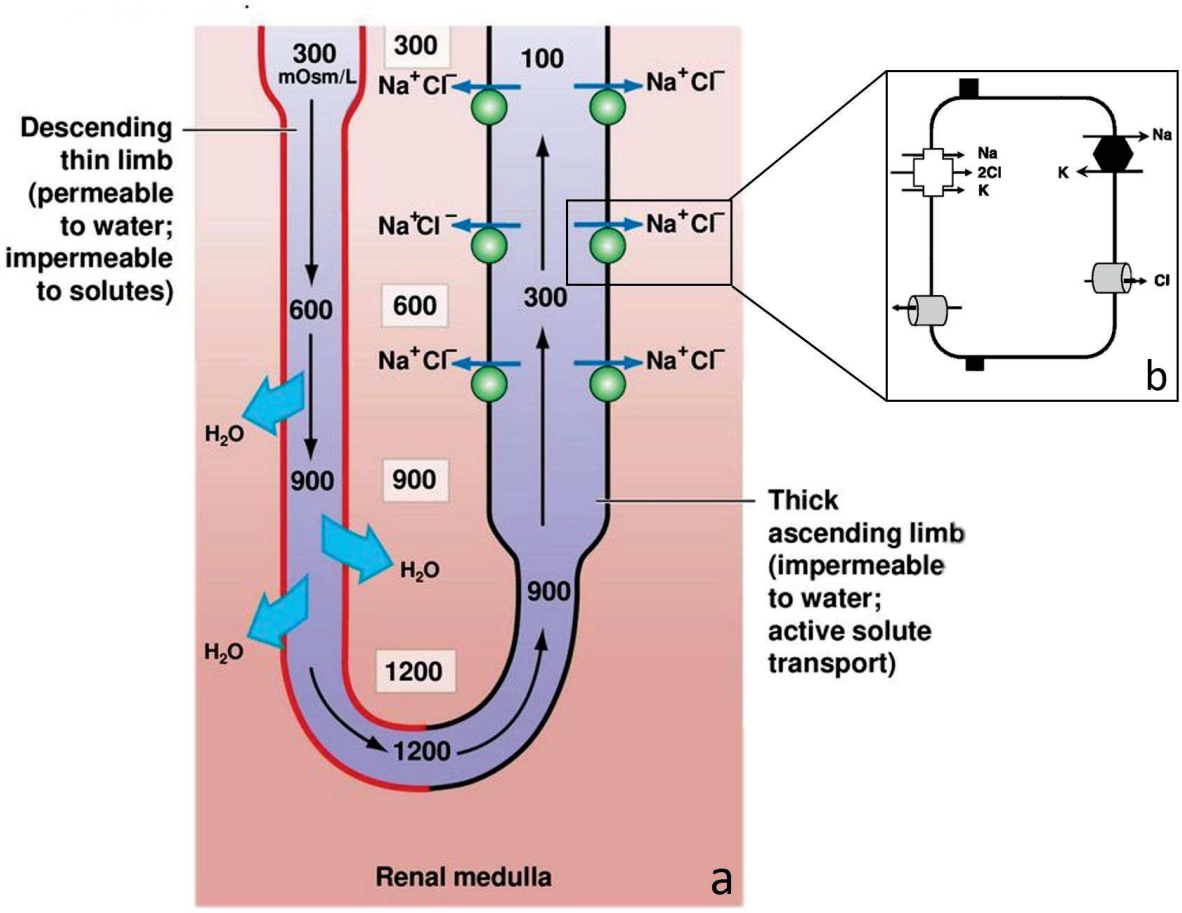

Figure 1-5 Loop of Henle and countercurrent multiplication
a) Diagram of a single loop of Henle, illustrating how classic countercurrent multiplication could produce the osmotic gradient in the outer medulla b). Active transporters $Na^+/K^+/2Cl^=$ cotransporter located in the large segment of the ascending limb, to increase the inner medulla osmolality (https://slideplayer.com/slide/14610145/90/images/118/Figure+2613b+Countercurrent+Multiplication+and+Urine+Concentration..jpg)

1.2.2.4 Distal convoluted tubule

The distal convoluted tubule is the nephron segment that lies directly in the continuity of the loop of Henle. Although short in length, the distal convoluted tubule plays a critical role in sodium, potassium, and divalent cation homeostasis.

1.2.2.4.1 Mechanism of Na^+ reabsorption

The distal convoluted tubule reabsorbs 5 to 10% of the filtered sodium load. Na^+ is extruded from the lumen to the cells by Na^+/Cl^- Symporter (NCC) and epithelial sodium channel (ENaC), located on the apical side of the cells. NCC and EnaC channels are therapeutic targets for thiazides and amilorides, two molecule families used medicinally for their diuretic properties (Velazquez and Wright 1986; Ellison, Velazquez, and Wright 1987). Na^+/K^+-ATPase located on the basolateral side of the distal convoluted tubule cells generate a Na^+ motion from the

filtrate to the blood (Figure 1-6 A). K^+ plays an important role in Na^+ reabsorption through the Na1-K1-ATPase. The basolateral potassium channel allows intracellular K^+ to be reabsorbed into the blood. This mechanism called "pump leak coupling" maximizes the sodium absorptive capacity (Schultz 1981; Reichold et al. 2010). In the late distal convoluted tubule aldosterone also play a role in Na^+/K^+ reabsorption/excretion modulation, by stimulating transporters synthesis within cells, to maintain blood homeostasis (Meneton, Loffing, and Warnock 2004).

1.2.2.4.2 Mechanism of Cl^- reabsorption

Chloride can be passively transported transcellularly and returns to the plasma, it is also reabsorbed in cells through NCC channels (Figure 1-6 A). Cl^- exits from the cells to the plasma across the chloride channel ClC-Kb and potassium chloride cotransporter 4 (Gillen et al. 1996; Kieferle et al. 1994).

1.2.2.4.3 Mechanism of Ca^{2+} and Mg^{2+} reabsorption

Ca^{2+} reabsorption is achieved by the action of parathyroid hormone (PTH) through PTH receptor 1 (PTHR1)-associated signal transduction (Lau and Bourdeau 1995) (Figure 1-6 B). Indeed, PTHR1-induced G protein activation induces cAMP synthesis, which activates the protein kinase A (PKA). PKA, in turn, activates transient receptor potential channel subfamily V member (TRPV5) responsible for the calcium reabsorption from the lumen to the cells (De Groot et al. 2009). Calcium can either bind calmodulin proteins in the cell or be excreted in the blood through Na^+ mediated secondary active transport (NCX1) or calcium ATPase (Figure 1-6 B) . Another divalent cation, Mg^{2+}, is reabsorbed through a transient receptor potential cation channel subfamily M member (TRPM6). Currently, how Mg^{2+} travels from the cells to the blood is unknown (Meneton, Loffing, and Warnock 2004; Subramanya and Ellison 2014).

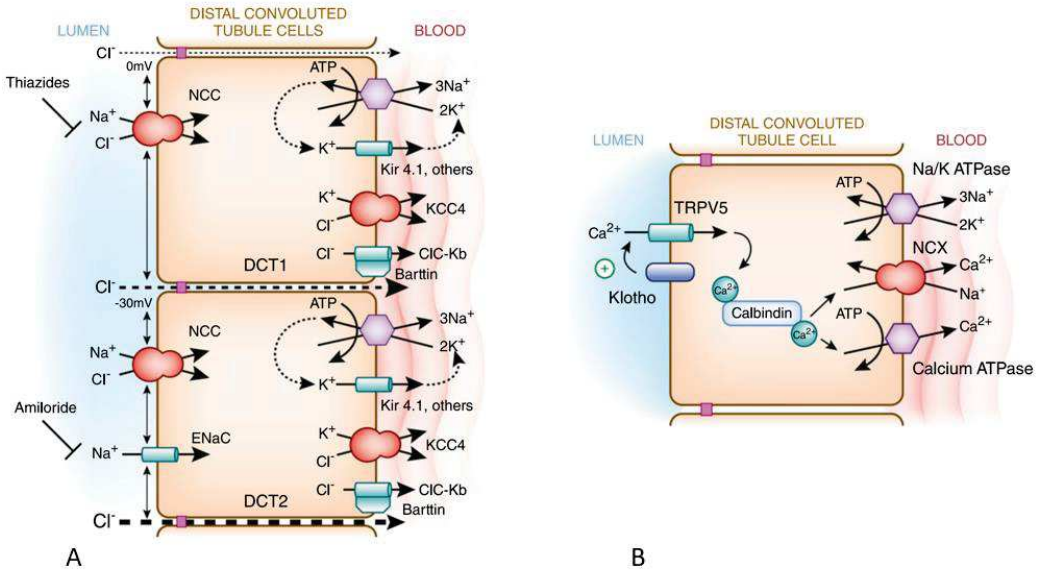

Figure 1-6 Distal convoluted tubule solute exchanges
A) Main solutes exchanges in the distal convoluted tubule cells. B). Ca^{2+} transports in the distal convoluted tubule cells (*Renal Physiology* 2010)

1.2.2.5 Collecting duct

1.2.2.5.1 Acid-Base Regulation and excretory effect

Type A and type B intercalated cells play a major role in proton and bicarbonate secretion in the collecting duct and play a pivotal role in the process of renal net acid excretion. Type A intercalated cells secrete protons via an apical H^+ ATPase and reabsorb bicarbonate by a band 3-like $Cl^-/HCO3^-$ exchanger, AE1, located in the basolateral plasma membrane. Type B intercalated cells secrete bicarbonate by an apical $Cl^-/HCO3^-$exchanger. They express H^+ ATPase in the basolateral plasma membrane and vesicles throughout the cytoplasm (Figure 1-7) (Kim et al. 1999).

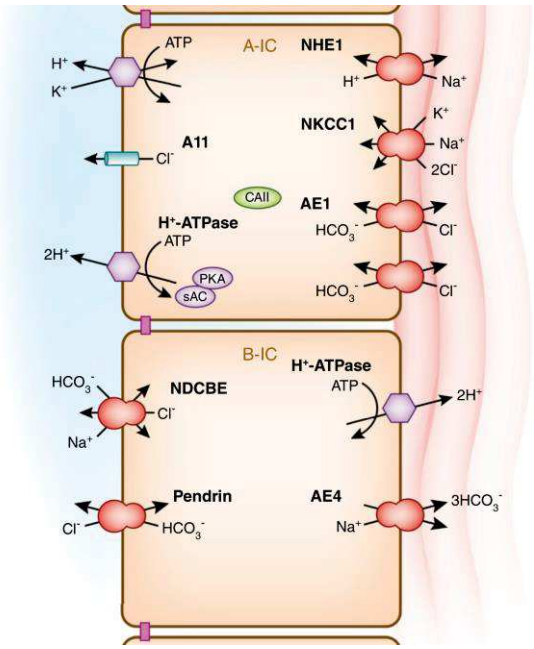

Figure 1-7 Intercalated A and B cells
Acid-Base Regulation and excretory effect within the Intercalated A and B cells (*Renal Physiology* 2010)

1.2.2.6 Collecting duct: Vasopressin 2 receptor and antidiuretic effect

V2 receptors are found on the basolateral surface of the main cells of the collecting tubules. They are stimulated by the AVP hormone to induce an antidiuretic effect, i.e. water reabsorption from the urine to the blood. AVP is produced in the pituitary gland by different types of stimulus. The two main stimuli are hyperosmolality and effective circulating volume depletion. In both cases, the angiotensin 2 induces the release of AVP to increase blood pressure or restore osmolality (Fitzsimons 2021).

The binding of vasopressin to the cell surface V2 receptors initiates an intracellular cascade, it activates the Gs stimulatory protein, which will then activate the adenyl-cyclase and generates cAMP.

cAMP mediates upregulation of aquaporin 2 (AQP2) transcription via cAMP-responsive element (CRE) through a cAMP/Epac/ERK pathway, which increases AQP2 expression, as demonstrated on mpkCCDc14 cells, which endogenously express AQP2 (Nishimoto et al. 1999; Umenishi et al. 2006). Interestingly these results suggest that AQP2 upregulation involves a PKA-independent pathway. The clear upregulation pathway remains to be determined.

Moreover, cAMP activates the PKA which, in turn, causes the steady state distribution of the AQP2 water channel to shift from cytoplasmic vesicles to the plasma membrane of collecting duct principal cells (Fushimi, Sasaki, and Marumo 1997; Sasaki and Noda 2007). Translocation occurs in parallel with the vasopressin-stimulated phosphorylation of S256 on the cytoplasmic C-terminus of AQP2 (Nishimoto et al. 1999; Nejsum et al. 2005; Fushimi, Sasaki, and Marumo 1997). Other sites of phosphorylation, such as S261, are recruited in absence of AVP and might have an opposite role in AQP2 trafficking (Hoffert et al. 2007). When AQP2 reaches the apical membrane it allows water reabsorption from the lumen of the collecting duct to the cytoplasm, and water crosses the basolateral membrane of the main cells throw the AQP-3 and AQP-4 (Figure 1-8).

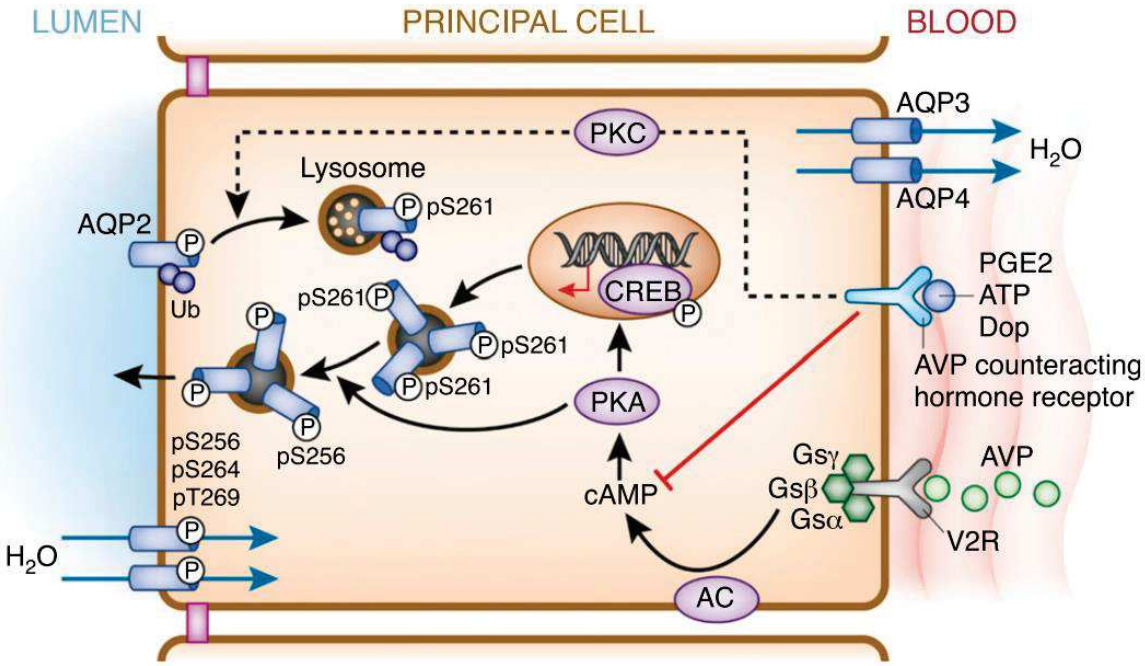

Figure 1-8 Antidiuretic effect
AVP mediated antidiuretic effect involving V2R activation and Gs protein signal transduction (*Renal Physiology* 2010)

1.2.2.7 Non-canonical pathways associated to V2R activation

1.2.2.7.1 β–arrestin dependent pathways, implication in cell multiplication

β-arrestins (βarr) regulate GPCR signal transduction through desensitization and endocytosis (DeWire et al. 2007). Additionally to this fundamental role, βarr are also GPCR signalization partners (DeWire et al. 2007).

For the V2R, both G protein-dependent and βarrestin-dependent mechanisms have been shown to play an important role in the AVP-stimulated ERK1/2 (Charest et al. 2007; Umenishi et al. 2006) but contradictory results are observed according to the cellular context.

In immortalized mouse cortical collecting duct cell line mpkCCDC14, a study suggests that AVP stimulation activated ERK pathway through Gαs signaling (Umenishi et al. 2006) while in human embryonic kidney cells (HEK293) Gαs signaling is proposed to inhibit the MAPK pathway through stimulation of cAMP production (Charest et al. 2007). More specifically, they proposed that V2R stimulation leads to a dual regulation of ERK1/2 involving a Gαs-dependent inhibition and a G protein-independent βarrestin-mediated activation of the MAPK (Charest et al. 2007).

More recent findings demonstrate that stimulation of the V2R in cultured cells or directly in rat kidney medullar collecting ducts led to the activation of ERK1/2. This mechanism is dependent on the metalloproteinase-mediated shedding of a factor activating the insulin-like growth factor receptor (IGFR). This process was found to be both Src- and β-arrestin–dependent (Oligny-Longpré et al. 2012). Moreover, sustained elevated levels of circulating AVP stimulate the proliferation of kidney tubular ells via the activation of V2R (G. Alonso et al. 2009).

Taken together, these results suggest that an AVP-stimulated V2R signaling has the potency to transactivate IGFR via a βarrestin-dependent mechanism leading to the proliferation of kidney tubular cells.

1.2.2.7.2 V2R coupling to Gq

V2R can activate or engage Gq proteins in addition to the canonical Gs coupling. This coupling was proposed to induce the mobilization of intracellular calcium through the action of phospholipase C and inositol phosphate production (Zhu et al. 1994; Ecelbarger et al. 1996; Heydenreich et al. 2021). In this context, no clear physiological outcome was associate to this pathway.

1.3 V2R-associated diseases

1.3.1 Introduction

The V2R is a major therapeutic target. Its malfunction is involved in several water balance (hyponatremia consecutive to congestive heart failure, hypertension, hepatic cirrhosis,

syndrome of inappropriate antidiuretic hormone secretion (SIADH)), and urine disorders (incontinence, nocturia). Inactivating and constitutively active mutations in the V2R sequence are responsible for two rare genetic diseases: (i) the congenital Nephrogenic Diabetes Insipidus (cNDI) characterized by excessive urine voiding, (ii) the nephrogenic syndrome of inappropriate antidiuresis (NSIAD) characterized by excessive water loading and hyponatremia. V2R is also a target for treating autosomal dominant polycystic kidney disease (ADPKD or PKD), the most frequent Mendelian inherited disorder affecting millions of people worldwide.

1.3.2 Congenital Nephrogenic diabetes insipidus

cNDI has been reported as X-linked nephrogenic diabetes insipidus for the first time in 1945 (Forssman 1945). It can be inherited or acquired and it is characterized by an inability to concentrate urine despite normal or elevated plasma concentrations of the antidiuretic hormone AVP (Morello and Bichet 2001). Clinical symptoms of the disease are polyuria, with hyposthenuria, and polydipsia. The main strategy for treating cDNI patients consists of a sufficient water supply to replace the urinary water loss, but this can seriously impact the quality of life due to excessive drinking and urine voiding. Some diuretics, like hydrochlorothiazide, amiloride, or the cyclooxygenase inhibitor indomethacin, have been proven effective to reduce urine output by up to 50% (Bichet and Bockenhauer 2016). However, diuretics may affect the potassium and sodium balance in patients, and therefore this treatment requires tight monitoring of serum electrolytes and osmolality.

In 1992, following the cloning of the V2R gene, a direct link between cNDI “gene” and V2R was demonstrated. Several teams investigated mutations leading to cNDI phenotypes (Walter Rosenthal, Anita Seibold, Anaid Antaramian, Michèle Lonergan, Marie-Francoise Arthus, Geoffrey N. Hendy 1992; Lolait, S. J., O’Carroll, A. M., McBride, O. W., Konig, M., Morel, A., & Brownstein 1992; Pan, Y., Metzenberg, A., Das, S., Jing, B., & Gitschier, n.d.; van den-Ouweland et al. 1992) and identified two different genes responsible for cNDI, the gene coding for V2R and the gene coding for aquaporin2. V2R mutations are found in 90% of cNDI cases (Bichet 1996). More than 250 loss-of-function cNDI V2R mutations (Figure 1-9) have since then been reported (Bichet and Bockenhauer 2016; Makita et al. 2020; Spanakis, Milord, and Gragnoli 2008). The mutations have been classified in three categories in 1995 (Tsukaguchi et al. 1995): (i) type 1 receptors reach the cell surface but have impaired binding or coupling, they are unable to induce a normal cAMP stimulation. (ii) type 2 V2R have defective intracellular

transport and accumulate in the endoplasmic reticulum, (iii) type 3 receptors are ineffectively transcribed. Type-2 mutations are involved in 70% of cNDI cases. In such cases, pharmacochaperones (Morello, Salahpour, et al. 2000; Morello, Bouvier, et al. 2000) are a promising therapeutic perspective (Bernier et al. 2006; Bockenhauer and Bichet 2015). Both agonist (Jean-Alphonse et al. 2009) and antagonist pharmacochaperones constitute a potential treatment since they can increase membrane expression of type-2 mutant receptors (Makita et al. 2020).

1.3.3 Nephrogenic syndrome of inappropriate antidiuresis

Activating mutations of V2R cause X-linked nephrogenic syndrome of inappropriate antidiuresis (NSIAD). Unlike cNDI, NSIAD induces an inability to excrete water in urine. It results in urine overconcentration and loss of water balance in the body because of water retention. The clinical symptoms resulting are hyponatremia, hypoosmolality, and natriuresis. It was first described in 2005 in two infant male cases with severe hyponatremia despite a low AVP blood level. NSIAD is a very rare disease with 30 cases reported to date. Four mutations in AVPR2 gene have been identified to induce NSIAD to date, I130N, R137L/C, F229V (Figure 1-9). From a therapeutic point of view, nonpeptide antagonists of the vaptan family, Tolvaptan (OPC-41061) (Yoshitaka Yamamura et al. 1992) and Satavaptan (SR121463) (Serradeil-Le Gal et al. 1996) can inhibit cAMP accumulation for F229V and I130N mutants but not for R137L/C mutants (Decaux et al. 2007;(Tenenbaum et al. 2009; Carpentier et al. 2012). Moreover, a patient carrying the R137L mutation was found to be insensitive to either of these drugs administrated during a phase III clinical trial (Decaux et al. 2007).

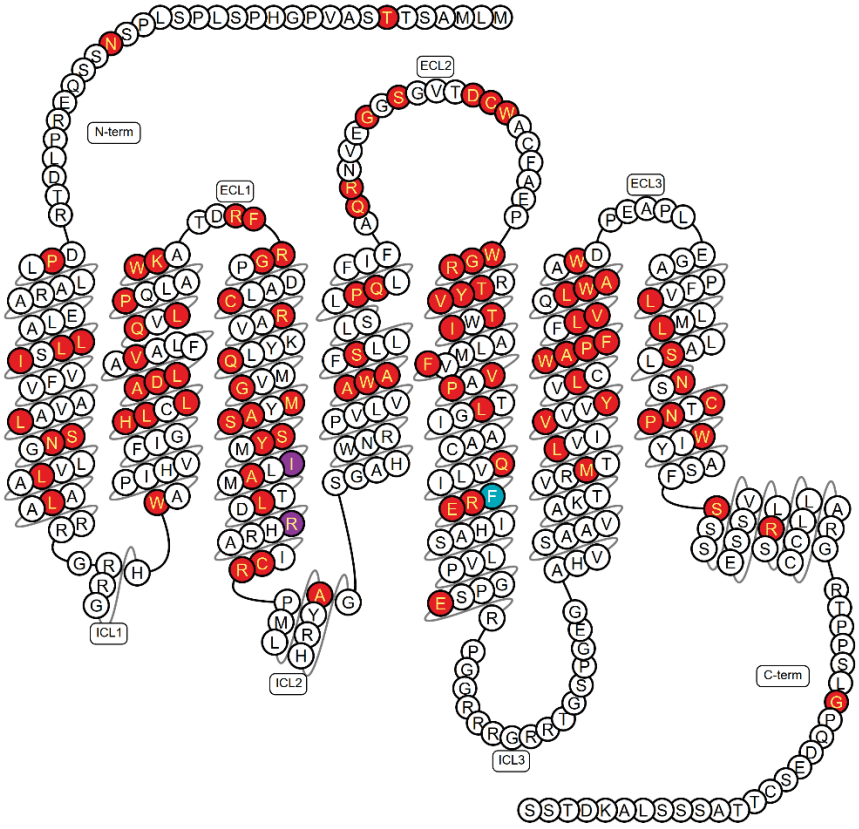

Figure 1-9 V2R Snake plot: mutants associated to cDNI and NSIAD
Red: mutated residues associated to a V2R loss of function. Blue: mutated residues associated to a V2R gain of function. Purple: Mutated residues associated to either a loss or a gain of function.

1.3.4 Polycystic kidney disease

Autosomal dominant polycystic kidney disease (ADPKD) and autosomal recessive polycystic kidney disease (ARPKD) are genetic human disorders and the most common polycystic liver diseases. ADPK is mostly presents in adults, whereas ARPKD is a rarer and often more severe form of polycystic kidney disease that usually presents perinatally or in early childhood (Bergmann et al. 2019). PKDs are characterized by progressive formation of bilateral renal cysts, liver cysts, and an increased risk of intracranial aneurysms (Figure 1-10).

ADPKD is the most common monogenic cause of end-stage kidney disease. Its prevalence is reported to be between 1 in 400 and 1 in 1,000 live births, based on two early clinical studies (Dalgaard 1957; G Iglesias et al. 1983). It represents more than 10 million people worldwide. More recent studies highlight a strong geographical heterogeneity. For example, the prevalence is 1 in 2,459 in the UK study (Davies et al. 1991), 1 in 1,111 in the French study (P. Simon et al. 1996), and 1 in 542 for the Seychelles (Yersin et al. 1997).

ADPKDs can be subdivided into two main families: i) mutations in PKD1 (chromosome 16p13.3) are responsible for 80% of cases of ADPKD, ii) mutations in PKD2 (chromosome 4q22.1) represent 15% of ADPKD cases, iii) genetically unresolved mutations or rare mutations in other loci represent 5–10% of ADPKD cases. PKD1 and PKD2 genes code for Polycystin 1 (PC1) and Polycystin 2 (PC2) proteins. PC1 acts as a mechanosensitive receptor in primary cilia, it can also mediate cell adhesion (Streets et al. 2009; Nauli et al. 2003). One of its fundamental functions is to regulate PC2 trafficking, channel assembly, and activity (Giamarchi et al. 2010; Pharmacol 2000). PC2 is involved in ion transport (Pharmacol 2000) and can affect Ca^{2+} signaling. ADPKD is accompanied by abnormal levels of two intracellular messengers, cAMP and Ca^{2+}. cAMP is the key driver of cyst growth and expansion (M. Grant et al. 1992; Shumate et al. 2017; J J Grantham 1 , R Mangoo-Karim, M E Uchic, M Grant, W A Shumate, C H Park 1989; Grantham et al. 1989). There are two essential cAMP-dependent components to cyst growth: cell proliferation (Grantham et al. 1989) and cAMP-mediated chloride secretion (Shumate et al. 2017). Blocking AVP effects on the kidney via the V2R and lowering circulating AVP concentration are effective treatments to mediate the cAMP concentration in the main cells of the collecting duct.

In 1999, treatment with V2R antagonist mozavaptan (OPC-31260) (Y. Yamamura et al. 1992) was reported to protect kidneys against the development of cysts in cpk mice, a model of rapidly progressive autosomal recessive polycystic kidney disease (ARPKD) (Gattone et al. 1999). Further investigations on different models of PKD (PCK rats and *Pkd2*$^{WS25/-}$ mice, two models of ADPKD, and *pcy* mouse, a model of adolescent nephronophthisis) (Gattone et al. 2003; V. E. Torres et al. 2004) were carried out. In all studies, cAMP kidney levels, which are dramatically increased in untreated animals, have been significantly reduced by the use of OPC-31260. Tolvaptan (OPC-41061), due to its more potent and selective antagonist effect as compared to OPC-31260, is best suited as a candidate to reduce V2R activity and thus cAMP concentrations in the main cells of the collecting duct (X. Wang et al. 2005; Y Yamamura et al. 1998). Three clinical trials were performed with tolvaptan in ADPKD patients (V. Torres et al. 2016; V. E. Torres et al. 2018; 2012). Very recently, a long-term phase 3 safety study has further characterized tolvaptan as a safe drug to treat ADPKD thanks to a careful hepatic monitoring every three months (V. E. Torres et al. 2021).

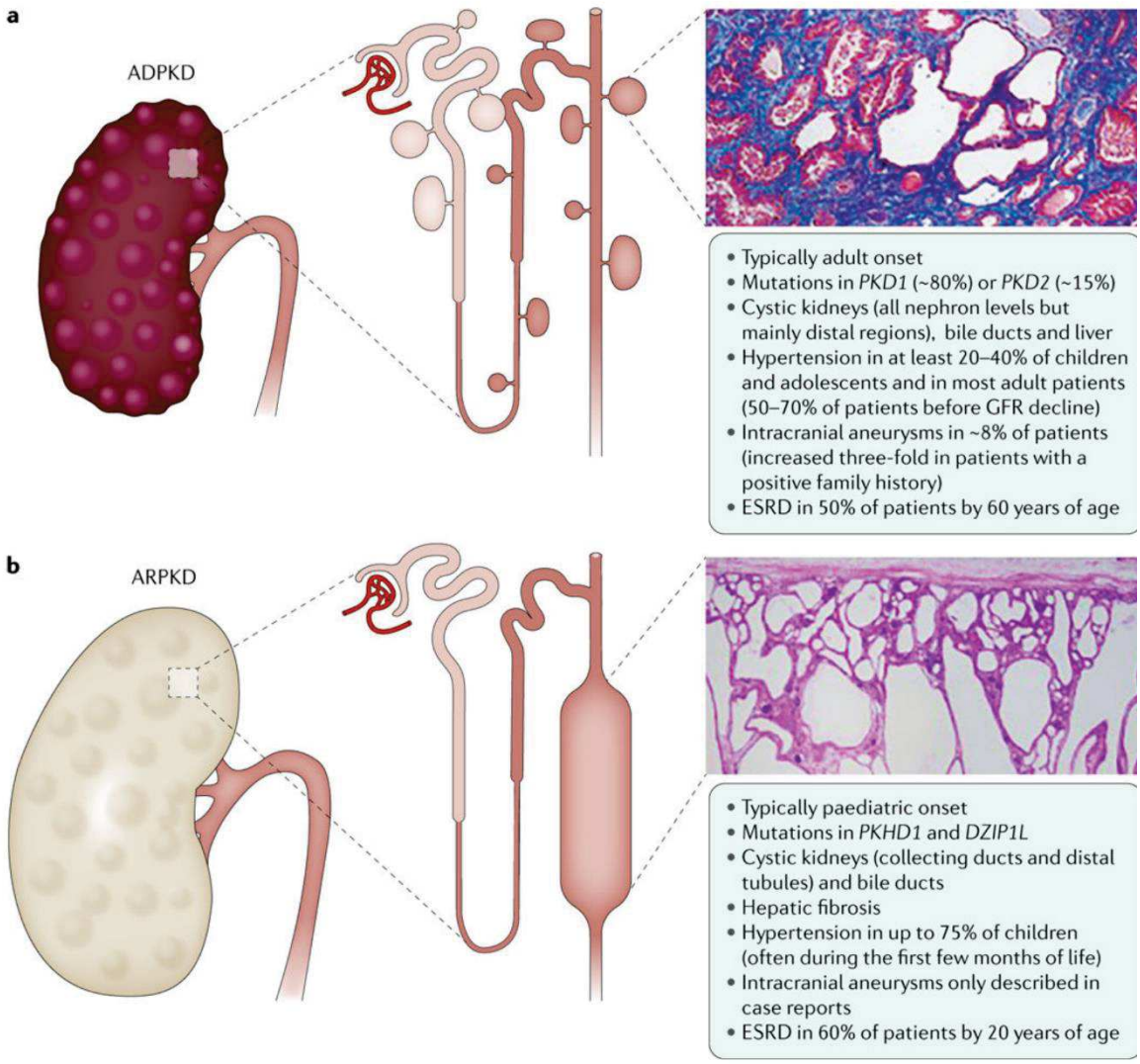

Figure 1-10 Renal and extrarenal manifestations in polycystic kidney disease
(Bergmann et al. 2019)

1.3.5 Therapeutic molecules on the market

Currently, there are two molecules commonly used to treat V2-associated diseases, the antagonist tolvaptan used for the treatment of hyponatremia or ADPKD and the agonist desmopressin used mainly to treat central DI or nocturia.

1.3.5.1 Tolvaptan to treat hyponatremia or ADPKD

The tolvaptan is a selective V2R antagonist with a half-life between 6-8 hours. It binds to the V2R and its competition with AVP prevents the antidiuretic effect. Indirectly, it can limit the water reabsorption from the urine to the body and prevent hypervolemic and euvolemic hyponatremia (serum sodium levels less than 134 mEq/L). Strong hypernatremia (sodium level less than 120 mEq/l) is a medical emergency.

The tolvaptan is sold under the trade name Samsca (https://www.samsca.com/) to treat the hyponatremia consecutive to congestive heart failure, SIADH, or hepatic cirrhosis. As it was observed in many trials (Garcha and Khanna 2011), tolvaptan has a critical effect on hyponatremia consecutive to heart failure, nonetheless, it has no effect on mortality directly induced by heart failure. Its ability to regulate the serum sodium level is more striking in SIADH, where it prevents V2R activation by competing with AVP. It is less efficient to modulate the sodium concentration in case of hepatic cirrhosis.

The tolvaptan is also used under the brand name JINARC (https://www.otsuka-europe.com) to prevent or at least delay cyst apparition and growth in ADPKD as previously described.

Tolvaptan is highly selective to V2R but was shown to promote adverse effects, particularly liver injury (elevation of transaminase activity), and aquaretic problems were common. Its use has to be strictly managed (V. Torres et al. 2016; V. E. Torres et al. 2012; 2018).

1.3.5.2 Desmopressin to treat central DI and water balance disorders

The Desmopressin (1-deamino-8-D-arginine-vasopressin) ((Zaoral, Kolc, and Sorm 1967) sold under the name of minirin, minirinmelt or OCTIM (https://www.ferring.com) is a synthetic analogue of vasopressin. It is used to treat bed wetting and night urination or central DI, where it plays a role as a substitute for AVP.

Desmopressin is also the first-line treatment for bleeding disorders. It is used for the therapeutic control of bleeding and bleeding prophylaxis in connection with minor surgical procedures in patients with mild hemophilia A and von Willebrand's disease (type I) (see "Notice MINIRIN®" 2011)

Potential side effects of dDAVP are hyponatremia, headache, and nausea. Furthermore, it can increase blood pressure through its potential activation of other AVP receptor subtypes, V1aR and V1bR since it is not highly selective to V2R. (see "Notice MINIRIN®" 2011)

1.3.5.3 Conclusions

Currently, despite an extensive knowledge of V2R biology and a large array of V2R pharmacological tools, just a few therapeutic options are available on the market. Moreover, there is no therapeutic solution to treat cDNI or NSIAD to date. There is a need for new therapeutic molecules targeting V2R (Figure 1-11).

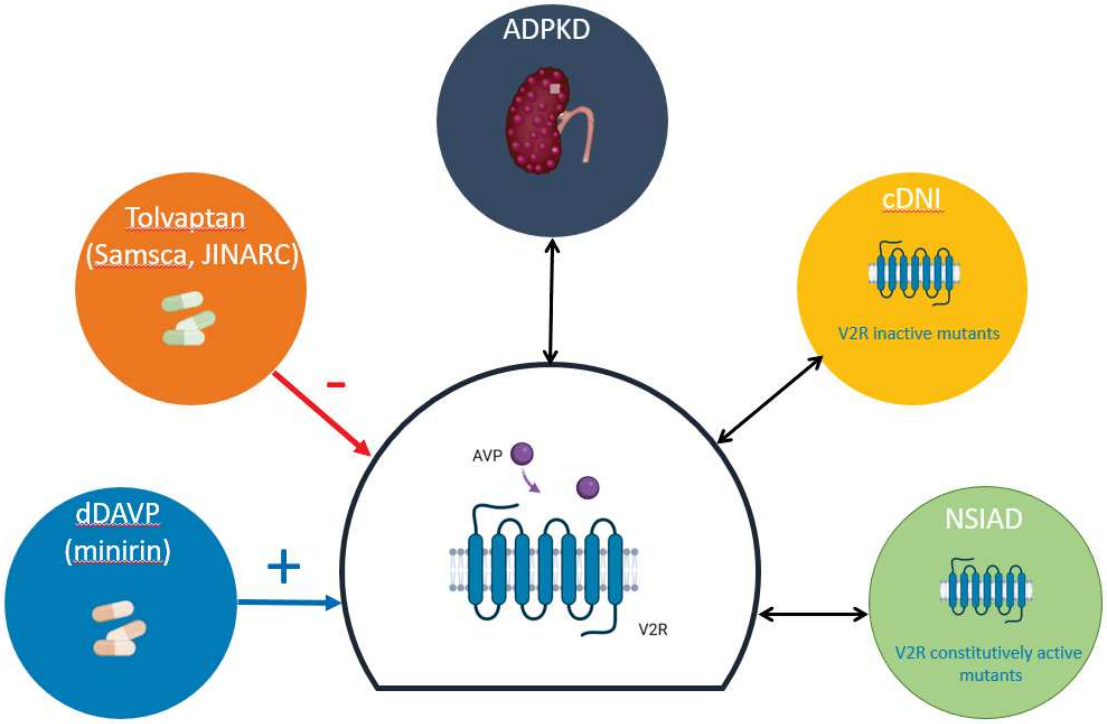

Figure 1-11 V2R associated diseases and associated drugs

1.4 Molecular pharmacology of Vasopressin Oxytocin receptors

From a pharmacological point of view, neurohypophysial hormone receptors are unique concerning the huge amount of pharmacological data accumulated and the number and variety of molecular probes (M. Manning et al. 2012). From the cloning of the different AVP/OT receptors (A. Morel et al. 1992; Sugimoto et al. 1994; Kimura et al. 1992), molecular pharmacology of this receptor family was more focused on the definition of AVP/OT binding sites.

AVP/OT receptors were studied experimentally using a combination of molecular modeling, site-directed mutagenesis, photolabelling with ligand structure-activity relationships. Because of their high sequence identity, and their common AVP affinity, molecular knowledge that can be inferred from a single receptor type may be applied to other receptors of the whole family (Figure 1-12).

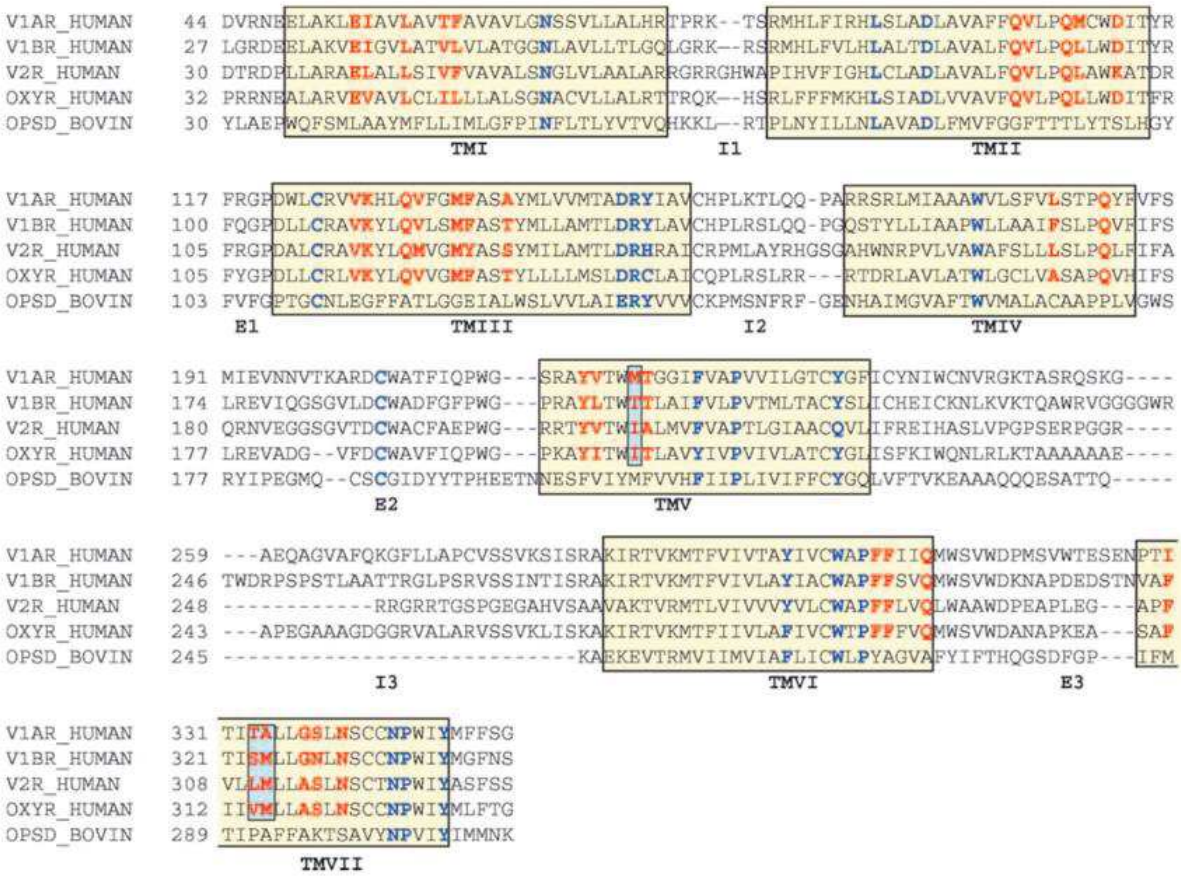

Figure 1-12 Alignment of the vasopressin/oxytocin receptors to that of bovine rhodopsin
The amino acid sequence of the human AVP/OTreceptor subtypes, $V_{1a}R$ (V1AR_HUMAN), $V_{1b}R$ (V1BR_HUMAN), V_2R(V2R_HUMAN), and OTR (OXYR_HUMAN) are compared with that of the bovine rhodopsin (OPSD_BOVIN) (Kimura et al. 1992)

1.4.1 Initial and subsequent models for AVP/OT receptors

A molecular dynamic simulation study validated with site-directed mutagenesis of hypothetical key residues (Mouillac et al. 1995) proposed the first overview of AVP binding to V1aR with an exhaustive list of molecular contacts. The three-dimensional (3D) model of V1a was built based on the structure of the bacteriorhodopsin and the relative position of the TMs was determined by comparison with bovine rhodopsin low-resolution map (Schertler, Villa, and Henderson 1993). The model displays a binding pocket as a deep cleft in the center of the helix bundle with a depth of 15-20Å. The bottom is mainly composed of hydrophobic residues while the entrance is more hydrophilic. This is consistent with the dual polarity of the AVP with the hydrophobic residues (cys1, Tyr2, Phe3, Cys6) oriented toward the bottom of the pocket and polar residues (Gln4, Asn5, and the C-terminal tripeptide Pro7-Arg8-Gly9NH_2), interacting with the top of the pocket. This is a rational ab initio assumption for AVP binding hypothesis.

The hypothesized key binding residues were mutated by substitution with alanine to validate the model (Figure 1-13).

Mutations of Q104 (Q92 in V2R), Q108 (Q96), K128 (K116), Q132 (Q119) led to a loss in AVP binding affinity of respectively 6-fold, 290-fold, 60-fold, and 40-fold. Nonetheless, those mutations did not significantly change affinity for different classes of antagonists, the non-peptide SR49059, and the linear and cyclic peptides HO-LVA and d(CH_2)5-[Tyr(Me)2]AVP respectively.

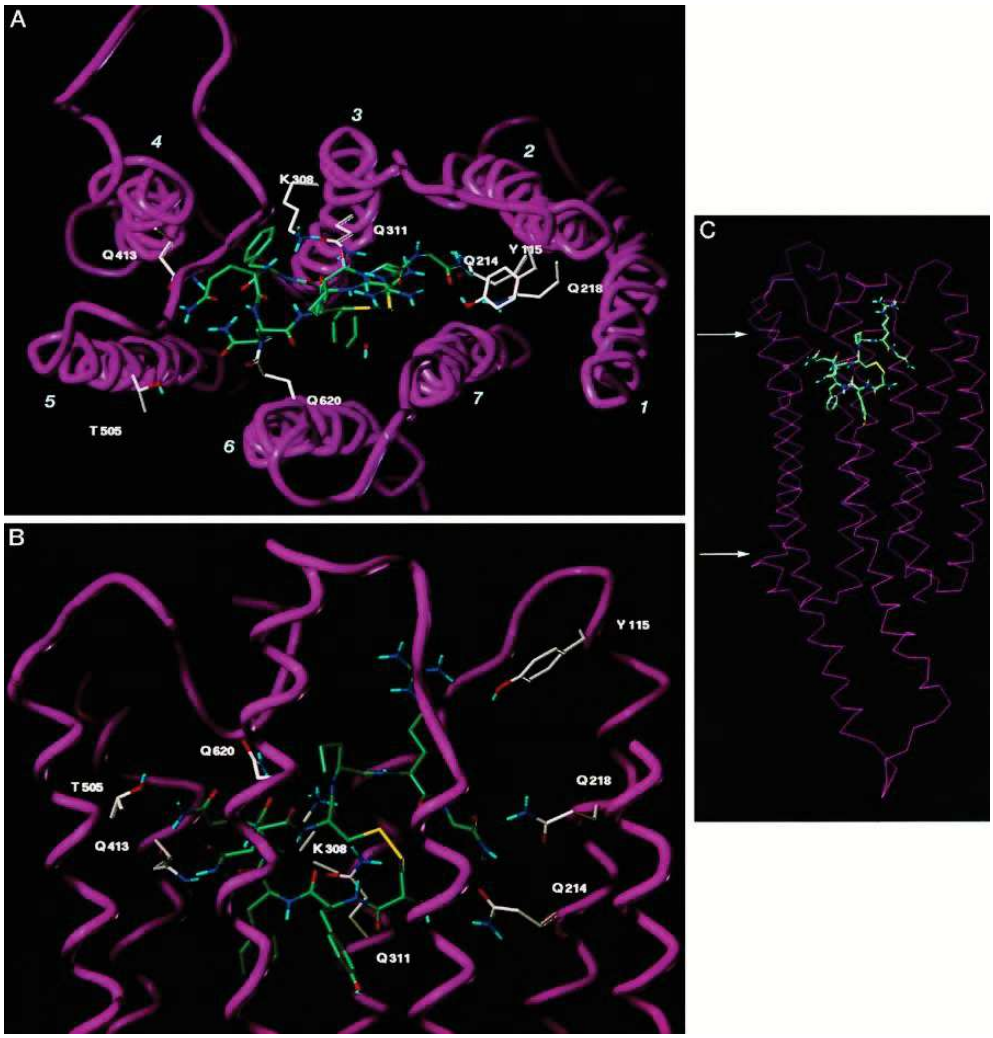

Figure 1-13 Vasopressin docked into the rat V1a vasopressin receptor
A), view of the complex from the extracellular surface of the receptor, in a direction perpendicular to the membrane. B and C), side views from a direction parallel to the cell membrane surface. B) shows in detail the interactions between the receptor and the hormone. C) shows that the binding pocket for the neuropeptide is localized in the upper part (first third)of the transmembrane regions. (Mouillac et al. 1995)

On the opposite, Q185A (Q174 in V2R) mutant displayed a 100-fold drop in affinity for the antagonist d(CH_2)5[Tyr(Me)2]AVP and 10-fold for both other antagonists investigated. This

mutant also displayed a strong loss in affinity for AVP (1220-fold). The last substitution Q310A (Q290) induced a weak decrease in affinity for AVP of 8-fold.

Q104 (Q92 in V2R), Q108 (Q96) were proposed to interact with the Cter AVP glycinamide.

Results from this paper suggested different binding sites for agonists and antagonists ligands. However, since AVP displays an equivalent affinity for the different receptor subtypes and because most of the binding pocket residues are conserved throughout the receptor family, the AVP binding mode was proposed to be common to all AVP/OT receptors. Indeed, molecular modeling of OT into the human OTR confirmed an equivalent position for AVP/OT hormones into the different receptor subtypes (Bice Chini et al. 1996). In addition in this study, authors investigated the mechanism that regulates the efficacy of agonists in this receptor family and presented evidence at a molecular level that AVP a full agonist of vasopressin receptors acts as a partial agonist on the OTR.

Another study using molecular modeling combined with side-directed mutagenesis investigated the binding of AVP and a nonpeptide antagonist specific to V1aR, OPC-21268 (Imaizumi et al. 1992). Interestingly, this antagonist displays a greater affinity for the rat V1a than for the human V1a. Point mutations were carried out to define residues mediating this interspecies specificity (Thibonnier et al. 2000) This work confirmed that agonist and antagonist binding, as well as peptide versus non-peptide compounds, were distinct (Mouillac et al., 1995). However AVP and OPC-21268 partially superimpose, the non-peptide antagonist being able to interact more deeply within the transmembrane region (Figure 1-14).

The authors proposed a list of hypothetical contacts between V1aR and AVP confirming those proposed in the initial AVP-V1a receptor model.

The AVP C-terminal tripeptide was proposed to be in the vicinity of the TM1 and the extracellular loop (ECL)1 with a more specific contact between the Arg8 and D112. Trp111 forms van der Waals contacts with the hydrophobic part of Arg8. The bottom of the pocket is composed of a hydrophobic cluster (Met135, Phe136, Phe179, Phe307, Ile330) which interacts with the hydrophobic AVP side. Hydrogen bonds were proposed between Q4 and Q185, N5 and K128 as well as between Y2 and Ser213. The study was consistent with the fact that the amino acid residues which are important for peptide agonist binding are not critical determinants in the binding of non-peptide antagonists (Figure 1-14; Figure 1-18)

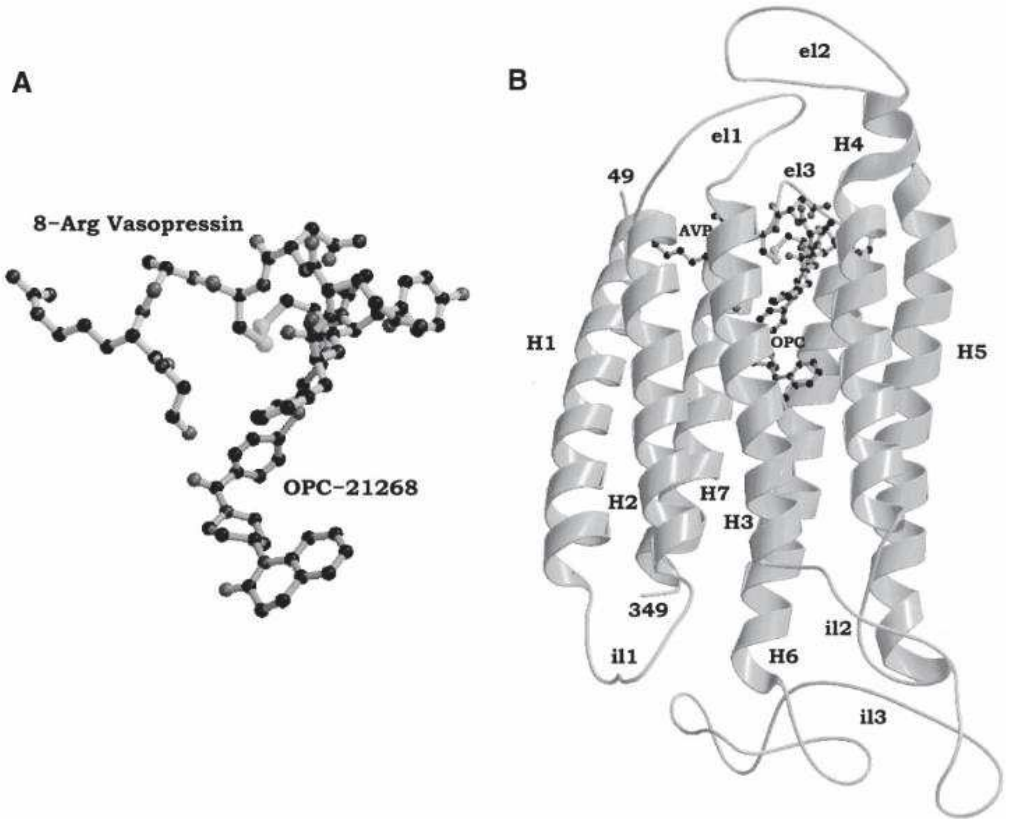

Figure 1-14 Superposition of the models of AVP and the nonpeptide antagonist OPC-21268 as bound to the human V1 R
AVP and OPC-21268 in ball-and-stick representation (A) and with the receptor shown in ribbons (B). The loops are labeled il1, il2, and il3 for the intracellular loops and el1, el2, and el3 for the extracellular loops. The different binding modes of agonist and antagonist are clearly shown. (Thibonnier et al. 2000)

More recently, AVP binding to V1a and V1b receptors was investigated by molecular dynamic simulations combined with site-directed mutagenesis (Rodrigo et al. 2007). In this study, the authors took advantage of a new high-resolution structure of bovine rhodopsin (Palczewski et al. 2000) to get a more accurate ab-initio model than those obtained by homology with bacteriorhodopsin in precedent studies (Mouillac et al., 1995; Thibonnier et al. 2000). They compared the molecular features of the two models. AVP binding mode obtained for V1aR and V1bR (Figure 1-18), are similar to earlier binding modes, but different molecular contacts were proposed. They unambiguously demonstrated that arginine-8, a very important residue for ligand binding, interacts with a set of negatively charged amino acids $E54^{1.35}$, $D112^{2.65}$ (Ballesteros-Weinstein nomenclature (Ballesteros and Weinstein 1994)) at V1a and V1b receptor subtypes, not with extracellular loop 1 as proposed earlier (Mouillac et al. 1995). Moreover, a rational explanation to the V1b-selective binding of agonist d[Cha4]AVP was

proposed and confirmed by site-directed mutagenesis of two amino acids (V169$^{4.61}$ and P196$^{5.35}$) of the V1b receptor.

Molecular models of V2R were not constructed in the different studies detailed above, but as proposed, conclusions regarding AVP binding in V1aR, V1bR, and OTR can be extrapolated to V2R.

In 2015, a computational work investigated the human V2R natural hormone binding site. An ab initio approach was chosen to model the receptor protein with I-TASSER. 5 models were built and the best of them, based on C-score, TM-score, and root-mean-square deviation (RMSD) were selected. The 3D structure of AVP was extracted from the crystal structure of the trypsin-vasopressin complex (PDB ID: 1YF4-chain B) (Ibrahim and Pattabhi 2005) (Sebti et al. 2015). The study selected hypothetical key residues for binding: Trp 293, Trp 296, Asp 297, Ala 300, and Pro 301, all located in ECL3. Those residues were artificially mutated in silico and their effect was assessed in terms of energy state of the ligand-receptor complexes. Based on the mutation/docking predictions, the authors found that some mutants such as W293D and A300E possess positively inducing effects in ligand binding and some of them such as A300R present negatively inducing effect in ligand binding. Based on previous models of AVP docked into V1aR, V1bR, or OTR, it is surprising that none of the residues located in TMs domains or in other extracellular loops that were proposed to interact with AVP (Mouillac et al., 1995; Thibonnier et al. 2000) were identified using this particular modeling approach.

1.4.2 Photolabeling of AVP/OT receptors: application to agonist and antagonist binding sites

Both agonist and antagonist binding sites for AVP/OT receptors were probed using radiolabeled photoactivatable versions of AVP and different classes of antagonists. The first structural investigation was performed using a purified V2R from bovine kidneys and a photoactivable analogue of 1-deamino[8-lysine]vasopressin containing a photoreactive aryl-azido group at the side chain of Lys8. This analogue displays an affinity in a nanomolar range (Kojro et al. 1993). This study provided the first insight into the interaction of specific regions of V2R with an agonist analogue of AVP. After radiolabeling and purification of the bovine V2R, isolation of potential interacting regions was carried out. Edman degradation discriminated one fragment encompassing residues 101-110 in the first extracellular loop (ECL1) of the receptor. R106 was covalently bound as well as T102. These results indicated that this extracellular domain is involved in peptide agonist binding of the V2R. Moreover, in proximity to the labeled amino

acids are three aspartic residues (D100, D103, and D109;(Figure 1-15)) which could initiate binding by ion-ion interaction with the positively charged side chain at position 8 of the photoreactive ligand or the natural hormone.

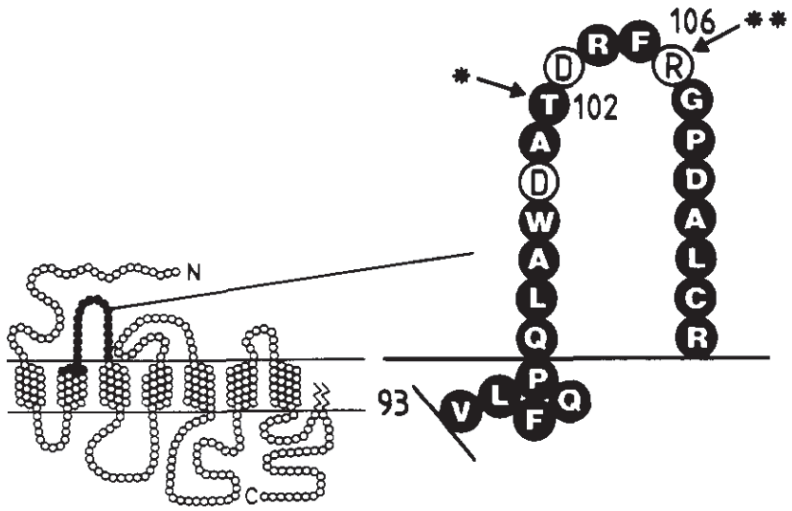

Figure 1-15 The second extracellular domain of the bovine V2 receptor
Radioactively labeled amino acids identified by Edman degradation as hormone contact sites are marked with asterisks. Residues which are conserved in V2 receptors are shown in white letters on a black background. Furthermore, the endogenous proteinase cleavage site between residues corresponding to Q92 and V93 in the human V2 receptor is indicated (Kojro et al. 1993).

Later, based on those precedent results, site-directed mutagenesis was used by the same authors, to investigate the role of specific amino acids located in the ECL1 in the binding of dDAVP (desmopressin), a V2R-specific analogue of AVP (Ufer et al. 1995). They targeted the residue at position 103 in the bovine V2R and at position 102 in the porcine V2R. It's an aspartic acid residue for bovine V2R (D103) whereas it is substituted with a tyrosine (Y102) in the porcine V2.

dDAVP possesses a high affinity for bovine, rat, and human V2R, and a 15-fold lower affinity for porcine V2R. Interestingly, both V1a receptors and porcine V2 receptor all display a Y residue at this position in ECL1, and V1a receptor also displays a lower affinity for dDAVP.The authors demonstrated that bovine V2R D103Y induced a loss in dDAVP affinity about 40-fold as compared to the wild-type. Interestingly this drop in affinity was not measured for the natural agonist AVP. This suggested D103 is a key residue for peptidic agonist specificity. Results also suggested that D103 is not a key residue for the binding of AVP but it might nonetheless be in the vicinity of the C-terminal tripeptide.

Similar investigations for the V1aR Y115 corresponding to D103 in the V2R showed evidence that this tyrosine is a key residue for determining agonist selectivity in the VlaR and corroborated the precedent studies (B. Chini et al. 1995).

The first structural investigation of the OTR binding sites was carried out using site-directed mutagenesis (point mutations and construction of chimeric OTR/V2R receptors) combined with the development of a radioiodinated photoreactive oxytocin antagonist (Postina, Kojro, and Fahrenholz 1996). Indeed, the introduction of a photoreactive 4-azidophenylamidino group at Orn8 of OT antagonist d(CH_2)5[Tyr(Me)2,-Thr4,Orn8,Tyr9]vasotocin (Postina, Kojro, and Fahrenholz 1996) and radioiodination at Tyr9 were performed. By transfer of domains from the G protein-coupled OT receptor into the related V2 AVP receptor, chimeric "gain in function" V2/OT receptors (Figure 1-16) were produced that were able to bind either OT receptor agonists or the competitive peptide antagonist with high affinity. The binding site for the radiolabeled photoreactive OT antagonist was found to be formed by transmembrane helices 1, 2, and 7 with a major contribution to binding affinity by the upper part of helix 7. In contrast, OT binding and selectivity were found in the first three extracellular receptor domains (N-terminus, ECL1 and ECL2). These results provided evidence for the existence of separate domains and different conformations of a peptide hormone receptor involved in binding and selectivity for agonists and peptide antagonists (Postina, Kojro, and Fahrenholz 1996). The ECL1 is particularly important in this selectivity as described before (Kojro et al. 1993; B. Chini et al. 1995; Ufer et al. 1995). The possibility of a gate function of the ECL1 was proposed as previously described for opioid receptors (Metzger and Ferguson 1995).

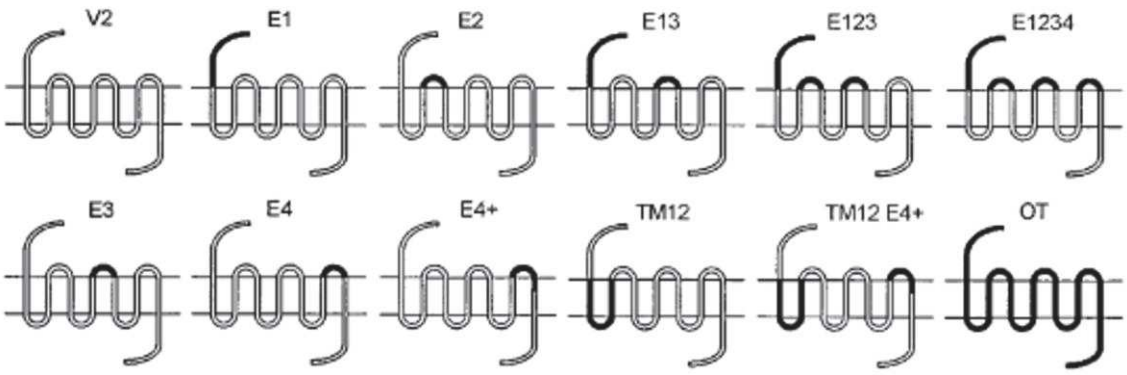

Figure 1-16 schematic representation of chimera investigated
Schematic representation of the investigated wild-type and chimeric receptors. The V2 vasopressin receptor is indicated by an open line and the OT receptor sequences by a black line. (Postina, Kojro, and Fahrenholz 1996)

A structural investigation of the V1aR antagonist binding sites was carried out using a combination of site-directed mutagenesis and photolabeling, using a radiolabeled peptidic linear photoactivatable antagonist [^{125}I]3-N_3-Phpa-LVA (Phalipou et al. 1997). The authors clearly demonstrated that the antagonist created a covalent bound with V1aR in a region including transmembrane domain VII (residues N327-K370). This region is close to a cluster of aromatic residues in TM6 (less than 4Å) that are conserved in Class A GPCRs. Point mutations of these residues (W304A, F307V, and F308L) were introduced in the V1aR. The affinity (Kd) of wild-type and mutant (W304A, F308L) V1aR remained unchanged for both AVP and 3-N_3-Phpa-LVA, while the substitution of F307 with a valine resulted in a 1700-fold reduction in antagonist affinity and only a 4-fold reduction in AVP binding. Based on this finding, the authors proposed a potential interaction between the hydrophobic NH_2 terminus of the peptide antagonist and the aromatic cluster of transmembrane helix VI. The same authors synthesized and characterized another linear peptide antagonist selective for the V1aR vasopressin receptor, [^{125}I][Lys(3-N3 Phpa)8]HO-LVA (Phalipou et al. 1999). They used it as a tool to further study V1aR antagonist binding sites (Figure 1-17). A region of interest was identified, Asp112–Pro120. Based on the present experimental result and on previous photoaffinity labeling data obtained with [125I]3N3Phpa-LVA, 3D models of the antagonist-bound receptors were constructed and then verified by site-directed mutagenesis studies. The two linear peptides were proposed to adopt a pseudocyclic conformation similar to cyclic agonists like AVP. Those antagonist binding positions significantly overlapped with the natural hormone vasopressin binding pocket even if they involved different contacts. Indeed, as

confirmed from the mutagenesis results, aromatic/aromatic contacts represent the most important interactions for antagonists, whereas hydrogen bonds with conserved hydrophilic receptor residues were proposed to represent the most crucial interactions for agonists like AVP (Mouillac et al. 1995; B. Chini et al. 1995).

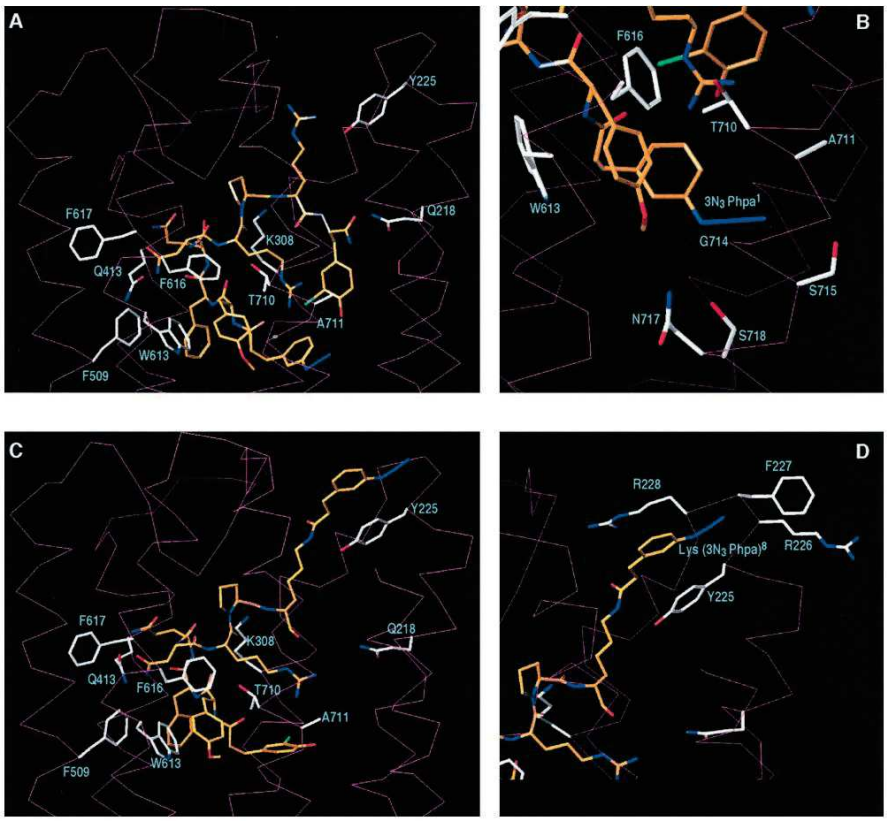

Figure 1-17 Docking of two linear peptide photoactivable antagonists in the three-dimensional model of the human V1aR
Panels A and B show the interaction between the receptor and [125I]3N3Phpa-LVA. Panels C and D show the interaction between the receptor and [125I][Lys(3N3 Phpa)8]HO-LVA (Phalipou et al. 1999).

Later, the development, characterization, and use of a new photosensitive radioiodinated human OTR/V1aR antagonist ([Tyr(Me)2,Thr4,Orn8,Phe(3^{125}I,4N3)-$NH_2$9]vasotocin) was done (Breton et al. 2001). The photoaffinity labeling experiments allowed the identification of a covalently labeled region in the OTR transmembrane domain III consisting of the residues L114-V115- K116. Using the same photoreactive ligand, analysis of contact sites in the V1aR led to the identification of the homologous region consisting of the residues V126-V127-K128. Interestingly residue K116 has been shown to play a pivotal role in the binding of agonists (Mouillac et al. 1995; Cotte et al. 2000), two different classes of peptide antagonists such as linear peptides (Phalipou et al. 1997; 1999) or the cyclic peptide d$(CH_2)_5$[Tyr(Me)2]AVP and also the nonpeptide compound SR 49059 (Cotte et al. 2000). Another approach was used to

define the human V1aR nonpeptide antagonist binding site. A sulfydryl-reactive version of the V1aR-selective SR49059 (containing an isothiocyanate reactive moiety) (Serradeil-Le Gal et al. 1993) was used in combination with the introduction of cysteine residue into the V1aR to create a site-directed irreversible covalent labeling (Tahtaoui et al. 2003). The F225, located in TM5, was demonstrated to directly participate in the binding of the V1a-selective nonpeptide antagonist SR49059.

All these data together suggested that members of AVP/OT receptor family share the same orthosteric ligand binding mode. Cyclic agonists, cyclic and linear peptidic antagonists, as well as nonpeptidic antagonists, bind within a common pocket but with different contacts. In particular, it seems that antagonists favor hydrophobic/aromatic interactions deep in the binding pocket. This variability in binding combined with a variation of key residues within the orthosteric pocket in the family may explain subtype specificity and agonist/antagonist intrinsic properties.

1.4.3 Receptor subtype and species selectivity

Most of the studies described above were focused on the definition of agonist and antagonist binding sites of V1aR and OTR. To improve the knowledge of the functional architecture of the V2R and in particular of its binding sites, different studies were conducted. First, differences among mammalian species in ligand binding were taken into advantage to search for the rat versus human selectivity determinants of the V2R. Indeed although many peptides V2R antagonists were shown to be highly potent in the rat, most of them were found to be ineffective in humans (Kinter, Huffman, and Stassen 1988).

In the late nineties, a series of cyclic peptides antagonist displaying species selectivity for the rat and human V2R were used in combination with site-directed mutagenesis to determine key residues involved in such a phenomenon (Cotte et al. 1998). Human and rat V2R share 88% sequence identity and divergent residues may represent potential major determinants responsible for the binding of these species selective AVP antagonists. Among them, residues 202 and 304 were demonstrated to fully control the species selectivity of the discriminating antagonists in an independent and additive manner. A third residue (position 100) is necessary to observe an equivalent phenomenon for the discriminating agonists (dDAVP). The substitution of these three residues does not modify the affinity of the nonselective agonists and antagonists. These results were in agreement with previous data describing 3D models of AVP V1aR and OTR (Mouillac et al. 1995; Chini et al. 1995).

Whereas arginine vasopressin binds to its receptor subtypes V1aR, V1bR, and V2R with an equal affinity of approximately 2 nM, many nonpeptide antagonists interact differently with AVP receptor subtypes. This is true for instance for SR49059 and OPC21268 which are specific for V1aR, for OPC41061 (tolvaptan), OPC31260, and SR121463 which are all specific to V2R, and finally for SSR149415 which is selective to V1bR.

Thibonnier and his collaborators used molecular dynamic simulations coupled to site-directed mutagenesis to investigate the binding sites of these nonpeptide antagonists and particularly those for the human V2R (Macion-Dazard et al. 2006). Site-directed mutagenesis at six non-conservative selected amino acid positions, K100D, A110W, M120V, L175Y, R202S, and F307I, predicted to be involved in antagonist binding differences between V2R and V1R, was performed.

All those residues are located in the putative binding pocket. None of the six mutations affected AVP affinity in agreement with in silico AVP docking on V2R. However, the affinity for six nonpeptide receptor antagonists was altered to varying degrees, resulting in differences up to 6000 fold.

Molecular modeling revealed that the binding sites for AVP and the nonpeptide antagonists are partially overlapping. Whereas AVP binds on the extracellular surface of V2R, the nonpeptide antagonists penetrate deeper into the transmembrane region of the receptor, in particular OPC21268. The mutagenesis data pointed to significant differences in the shape of the V1aR and V2R antagonist binding pockets. The most important factor determining the specificity of nonpeptide antagonists seems to be the shape of the binding pocket of the receptor (Macion-Dazard et al. 2006).

AVP	V1a (Mouillac 1995)	V1a (Thibonnier 2000)	V1a (Rodrigo 2007)	V1b (Rodrigo 2007)	V2 (Sebti 2015)	V2 (Bellucci 2020)	Numbering^b
Cys1	Gln 104			Gln 87			2.57
	Trp 304						6.48
	Ser 338		Ser 338	Asn 328			7.43
			Asn 340	Asn330			7.45
			Ala334	Ala324			7.39
			Leu335	Leu325			7.40
			Asn340				7.45
						Phe 307	7.35
Tyr2	Gln 185						4.60
	Trp 304		Trp304	Trp294			6.48
	Phe 307		Phe307	Phe297		Phe 287	6.51
	Cys 303						6.47
			Gln 131	Gln 114		Gln 119	3.32
			Ala334	Met324			7.39
			Ile310				6.54
			Thr333	Ser323		Leu 310	7.38
Phe3	Met 135		Met135	Met118			3.36
	Phe 225						5.47
	Trp 304		Trp304	Trp294			6.48
		Ile 330					7.35
		Phe179					4.54
		Phe 307	Phe307	Phe297			6.51
			Val132	Val115			3.33
			Phe136	Phe119			3.37
			Met220				5.42
			Gln131				3.32
						Phe 91	2.56
Gln4	Lys 128		Lys128				3.29
	Gln 131						3.32
	Gln 185	Gln 185	Gln 185	Gln168		Gln 174	4.60
	Thr 221						5.43
			Tyr186				4.61
				Arg175			E2
Asn5	Gln 311		Gln311	Gln301		Gln 291	6.55
		Lys128					3.29
			Gln131	Gln114			3.32
				Lys111			3.29
Cys6	Lys 128						3.29
	Gln 131						3.32
			Ala334	Met324			7.39
			Leu335				7.40
Pro7	Lys 128		Lys128	Lys111			3.29
			Trp204	Trp187			E2
			Cys203	Cys186			E2
Arg8	Glu 326						7.31
	Tyr 214						2.67
	Asn 327						7.32
	Gln 131						3.32
		Asp112	Asp112	Asp95			2.65
		Trp 111					2.64
			Asp202	Asp185			E2
			Glu54	Glu37			1.35
				Gln91			2.61
						Glu 40	N-term
Gly9	Gln 104						2.57
	Gln 108						2.61
	Thr 331						7.36
		Ile 54					1.36
			Lys128	Lys111			3.29
Not Specified					Trp 293		6.57
					Trp 296		6.60
					Asp 297		6.61
					Pro301		6.65

OPC21268	SR121463B	SR49059	SSR149415	OPC21268	OPC41061	OPC31260	Numbering^b
(Thibonnier 2000)	(Macion-Dazard 2005)						
Ala 343 (V1a rat)							7.42
Asp 330 (V1a rat)							7.29
Val 226 (V1a rat)							5.46
Val 316 (V1a rat)							6.54
Trp 175 (V1a rat)							4.50
Phe 179 (V1a rat)							4.54
Phe 313 (V1a rat)							6.51
Trp 310 (V1a rat)							6.48
	Lys 100 (V2)						2.65
	Met 120 (V2)	Met 120 (V2)	Met 120 (V2)		Met 120 (V2)	Met 120 (V2)	3.33
	Leu 175 (V2)	Leu 175 (V2)	Leu 175 (V2)		Leu 175 (V2)		4.61
	Phe 307 (V2)	Phe 307 (V2)	Phe 307 (V2)	Phe 307 (V2)	Phe 307 (V2)	Phe 307 (V2)	7.35
		Arg 202 (V2)					5.35

Figure 1-18 AVP/OT receptor residues predicted to be involved in the binding of AVP and antagonists

1.4.4 Involvement of the V2R intracellular loop 3 in coupling and signaling

To better understand what are the determinants of AVP receptors responsible for coupling to G proteins, Wess and his collaborators took advantage of the differential G protein binding

profiles of V1aR and V2R. Indeed, the AVP receptors family is unique since the V1aR, for example, is preferentially linked to Gq/11 class (inositol phosphate pathway), whereas the V2R is selectively coupled to Gs (cAMP pathway) (J. Liu and Wess 1996). To elucidate the structural basis underlying this functional heterogeneity, they have systematically exchanged different intracellular domains between these two receptors (Figure 1-19). Transient expression of the resulting hybrid receptors showed that all mutant receptors containing V1aR sequence in the second intracellular loop (ICL2) were able to activate the phosphatidylinositol pathway with high efficiency. On the other hand, only those hybrid receptors containing V2R in the third intracellular loop (ICL3) were capable of efficiently stimulating cAMP production. These data strongly suggested that ICL3 of V2R plays a key role in the recognition and activation of Gs proteins.

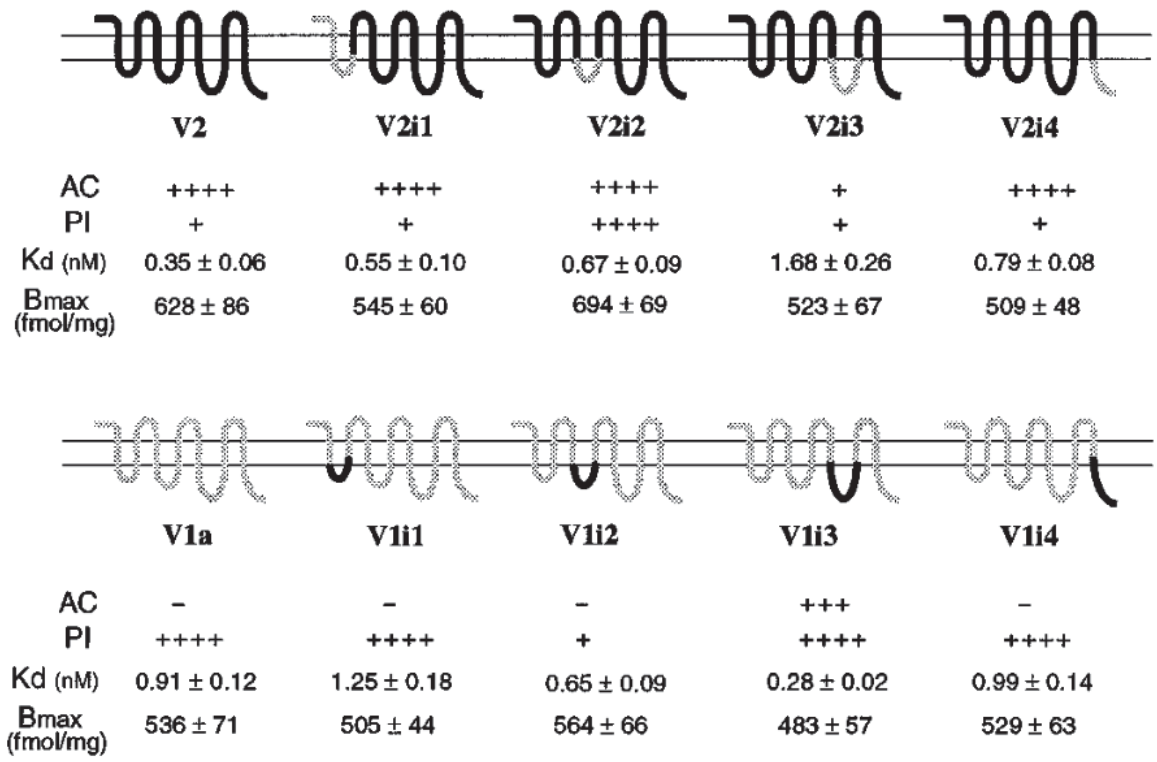

Figure 1-19 Structure, ligand binding properties, and functional profile of wild type and mutant V1a/V2 vasopressin receptors
[3H]AVP saturation binding studies were carried out as described under "Experimental Procedures." Kd and Bmaxvalues are given as means S.E. of three independent experiments, each performed in duplicate. The functional properties of the various receptors are summarized underneath the receptor structures. (J. Liu and Wess 1996)

To go further, the same research team determined the molecular basis of V2R/Gs coupling selectivity through the identification of residues that are crucial in this interaction. As in their previous study (J. Liu and Wess 1996), the same strategy based on constructing chimeric

receptors was performed. To explore the structural basis underlying the ability of the V2 receptor to selectively recognize Gs, they systematically substituted distinct V2R segments (or single amino acids) into the V1aR and studied whether the resulting hybrid receptors gained the ability to mediate hormone-dependent cAMP production (Erlenbach and Wess 1998). A detailed mutational analysis of the V2R ICL3 showed that two polar residues, Gln225 and Glu231, play key roles in Gs recognition. In addition, a short sequence at the N terminus of the cytoplasmic tail was found to make an important contribution. Moreover, the efficiency of V2 receptor/Gs coupling can be modulated by the length of the central portion of ICL3 rather than the specific amino acid sequence within this domain (Erlenbach and Wess 1998).

Interestingly, the role of V2R ICL3 is not limited to Gs coupling. Others investigations unrevealed its involvement in the formation of non-canonical signalization complexes. A proteomic approach combining pull-down assays using a cyclic peptide mimicking the ICL3 of V2R as a bait and mass spectrometry analyses of proteins isolated from either rat or human kidney tissues or the HEK 293 cell line, was developed to identify the multifunctional protein GC1q-R as a novel V2R interacting protein (Granier et al. 2008). The GC1q-R appears to interact with the arginine domain (RRRGRR) of V2R ICL3. GC1q-R is a small acidic protein which is known to inhibit the hemolytic activity of C1q (a family implicated in the complement cascade signaling). It is believed to be a multifunctional and multicompartmental protein involved in inflammation and infection processes, ribosome biogenesis, protein synthesis in mitochondria, regulation of apoptosis, transcriptional regulation, and pre-mRNA splicing (Ghebrehiwet et al. 2021). At the cell surface, it is thought to act as an endothelial receptor for plasma proteins of the complement and kallikrein-kinin cascades. (http://au. expasy.org/uniprot/Q07021) . Also, it has been demonstrated to interact with other GPCRs such as α1B-adrenergic receptors (Xu et al. 1999). Its role in the regulation of V2R function is not well understood but the authors hypothesized that GC1q-R may be part of the endoplasmic reticulum control-quality system and proposed its potential involvement in the sequestration of V2R in this subcellular compartment. The group of Déméné and collaborators further analyzed and characterized V2R/GC1q-R interactions (Bellot et al. 2009). Nuclear magnetic resonance (NMR) solution structure of the V2 ICL3 under a cyclized form was determined in the presence or not of GC1q-R. GC1q-R binding promoted the folding of the otherwise flexible ICL3 short peptide into a left-twisted α-helical hairpin (Figure 1-20a). The hairpin solvent-exposed surface is mainly composed of positively charged residues (RRRGRR) (Figure 1-20c). Upper in the loop, hydrophilic residues side chains were proposed to interact with the membrane lipids

chains (Figure 1-20c). Interestingly, the V2R ICL3 loop can adopt a less flexible conformation in contact with GC1q-R. This intrinsically disordered protein (IDP) behavior might allow ICL3 to interact with a large variety of protein partners by modulating its three-dimensional conformations.

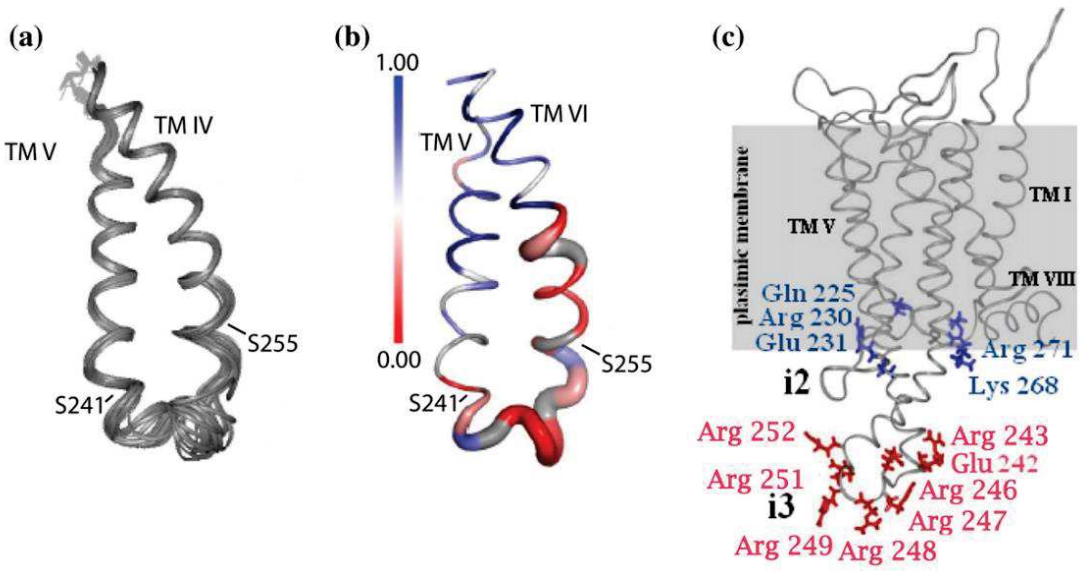

Figure 1-20 Structure of the V2 intracellular loop i3_cyc is either isolated or integrated into the whole receptor. Superposition of the 20 best structures of i3_cyc
(a) Superposition was done using the backbone atoms of segments Gln225-Glu242 and Gly254-Thr273. (b) Mean minimized structure of the backbone of i3_cyc. The width of the backbone line is proportional to the flexibility as calculated by the RCI method.43 Color of the backbone depends on the intensity of attenuation factor in the presence of Gd(DTPA-BMA): red corresponds to the most exposed residues and blue corresponds to the most protected residues. (c) Model of the V2 receptor constructed with the bovine structure (PDB code: 1GZM) and the NMR- derived structure of i3_cyc as templates. The side chains of strongly polar and charged amino acids of the i3 loop are represented. Roman numerals refer to TM domains. For clarity, the first 25 and last 25 amino acids of the receptor are not represented since they were generated in extended conformations as they were constraint free. (Bellot et al. 2009)

1.4.5 Oxytocin receptor structure

During the frame of my Ph.D., the crystal structure of the inactive OTR in complex with a selective nonpeptidic antagonist developed as an oral drug for the prevention of preterm labor, retosiban, was recently published (Waltenspühl et al. 2020). It is the first elucidated 3D structure for a member of the AVP/OT receptor family (PDB ID:6TPK). It gives valuable structural informations, particularly about the global architecture of this inactive GPCR. Overall, OTR displays the canonical GPCR topology consisting of a seven-transmembrane helical bundle, three extracellular loops (ECLs), three intracellular loops (ICLs), and a C-

terminal amphipathic helix 8. Similar to other class A peptide GPCRs, the ECL2 of OTR forms an extended β-hairpin structure that is anchored to the extracellular tip of helix3 by the conserved disulfide bridge between C112$^{3.25}$ (Ballesteros-Weinstein nomenclature) and C187 of ECL2. It also gives valuable informations about the orthosteric binding pocket. In comparison to other peptidergic GPCRs, the antagonist-bound OTR structure displays an enlarged binding pocket, which is exposed to the extracellular solvent. Specific contacts with the co-crystallized antagonist retosiban are mediated through both polar and hydrophobic interacting residues that are located on opposing hemispheres of the binding cavity (Figure 1-21). Furthermore, the large size of the extracellular binding pocket of OTR is consistent with the necessity to accommodate cyclic peptides like OT and AVP, a feature that is shared within the closely related vasopressin receptors. Moreover, identification of an extrahelical cholesterol molecule, bound between helices IV and V, provides a structural rationale for its allosteric effect and critical influence on OTR function. Finally, the structure in combination with experimental data allows the identification of a conserved neurohypophyseal receptor-specific coordination site for Mg^{2+} that acts as a potent, positive allosteric modulator for agonist binding (Waltenspühl et al. 2020).

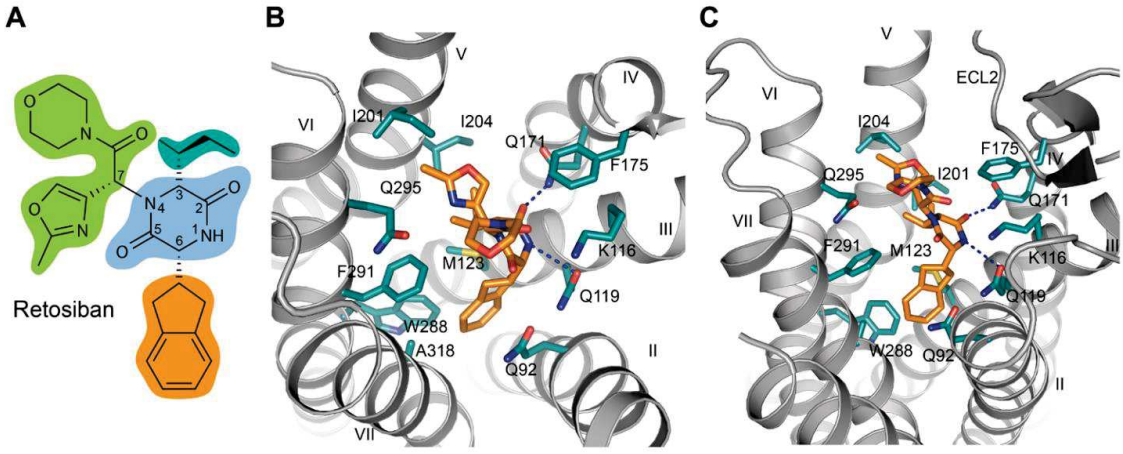

Figure 1-21 The OTR-binding pocket for retosiban.
(A) Chemical structure of retosiban with structural topology highlighted by colored circles (2,5-diketopiperazine core in blue, indanyl group in orange, sec-butyl group in cyan, and oxazol-morpholine amide moiety in green). (B) Detailed interactions of retosiban with OTR as viewed from the extracellular space from a position above helices I and II. The receptor backbone is shown in gray. Retosiban and key interaction residues within 4 Å of the ligand are shown as sticks. Hydrogen bonds are indicated by dashed, blue lines. (C) Interactions of retosiban with OTR as viewed from the membrane plane. (Waltenspühl et al. 2020)

1.4.6 Conclusion

Despite a consistent bundle of information regarding AVP/OT molecular pharmacology, the exact AVP binding mode, as well as receptor regions involved in G protein coupling or arrestin recruitment, are still missing. The molecular contacts proposed in the different dynamic studies don't converge to a clear consensus. The determination of experimental AVP/OT receptor structures in complex with their canonical signaling partners are decisive for a better knowledge of AVP/OT receptor functioning.

1.5 G protein-coupled receptors

1.5.1 Generalities

Cells contain a plethora of membrane proteins with a large range of functions. The G protein-coupled receptors (GPCRs) represent the largest family of membrane proteins in eukaryote organisms. They represent more than 2% of the functional human genome and count more than 800 members in humans. GPCRs have a major therapeutic interest and are targeted by 30% of the currently available drugs (Hopkins and Groom 2002; Fredriksson et al. 2003) They are represented in almost all eukaryote cells (Bissantz, Logean, and Rognan 2004a; Gershengorn and Osman 2001; Bissantz, Logean, and Rognan 2004b; Fredriksson and Schiöth 2005) and fulfill essential roles in signal transduction. These receptors can be activated by a wide range of endogenous hormones, neurotransmitters, growth, and developmental factors or external stimuli such as light, odors, and gustative molecules (Joël Bockaert and Pin 1999). They are named GPCRs because of their ability to interact and activate G proteins.

These receptors can interact with other effectors such as GPCR kinases (GRKs) or arrestins playing for instance a role in GPCR desensitization, and other proteins allowing a large possibility of biological responses (for review (Gurevich and Gurevich 2019)). Multimeric interactions between GPCRs can also play a role in signal response modulation. The biological response can be tuned and adapted to every situation depending of the cellular context. GPCRs and receptor-interacting proteins are differentially expressed in distinct cellular tropisms adding a level of complexity in the possibility of signal modulation.

1.5.2 GPCR Kolakowski Classification

Numerous classification schemes have been proposed over the years based on different criteria such as the nature of the ligand or physiological and structural features. Nonetheless, the standard has been to classify the GPCRs in 6 classes based on their sequence homology. All

GPCRs are represented in this classification, however, some families are not present in humans. It's the Kolakowski classification (Kolakowski 1994; Attwood and Findlay 1994).

1.5.2.1 Class A/1: Rhodopsin-like receptors

It's the largest and the more extensively studied group of receptors, structurally and physiologically. This class includes hormones, neurotransmitters, and light receptors. This represents 80% of all GPCRs. It consists of 286 non-olfactory receptors and 388 olfactory receptors. The receptors belonging to this class display strong sequence heterogeneity and can bind a wide variety of ligands such as chemokines, peptide hormones like AVP or angiotensin as well as small non-peptidic molecules like prostaglandins, biogenic amines. They also have variability in the G protein binding area and can interact with various G proteins. Nonetheless, motifs involved in receptor activation and signal transduction such as the CWxP domain, PIF domain or the ionic lock are conserved (Filipek 2019).

1.5.2.2 Class B/2: Secretin receptor family

Class B (Bortolato et al. 2014) is composed of 21 receptors (IUPHAR) also named the secretin-like family. Those are involved in a broad range of human diseases, such as diabetes, osteoporosis, cancer, neurodegeneration, cardiovascular diseases, headache, and psychiatric disorders (Bortolato et al. 2014). Unlike Class A GPCRs, these receptors include a large extracellular domain. Class B GPCRs usually bind to large hormones (glucagon) or neuropeptides (pituitary adenylate cyclase-activating polypeptide type 1). An adhesion subfamily is also represented in fungi.

1.5.2.3 Class C/3: Metabotropic glutamate/pheromone family

Class C (Møller et al. 2017) is composed of glutamate, calcium, and GABAergic receptors as well as a specific receptor of the vomeronasal organ. This class is characterized by a large N-terminal domain that encompasses the orthosteric pocket. Those receptors have a strong tendency to dimer association. This dimerization is critical for their activity.

1.5.2.4 Class D/4: Fungal mating pheromone receptors

These families include fungal pheromone receptors involved in reproduction and survival (Velazhahan et al. 2021).

1.5.2.5 Class E/5: Cyclic AMP receptors

These receptors targeted by cyclic AMP are not represented in humans (Johnson et al. 1993).

1.5.2.6 Class F/6/ Frizzled/Smoothened

Class F receptors, including the ten Frizzleds (FZD1-10) and Smoothened (SMO) receptors, mediate the effects of WNTs and hedgehog proteins. They are critical in animal development through their central role in the Wnt signal transduction pathway. They regulate numerous processes such as cell polarity, cell proliferation, or embryonic development (Schulte 2020).

1.5.3 GRAFS Classification

The GRAFS classification was first focused on human GPCRs. It sorts GPCRs into five main families, namely glutamate/taste1, rhodopsin, adhesion, frizzled/taste2, and secretin (Fredriksson and Schiöth 2005). In this classification, adhesion and secretin families are splitted into two different groups, it's the main difference with the Kolakowski classification. It presents the advantage to group most of the GPCRs based on phylogenetic criteria while Kolakowski classification does not. The GRAFS system can also be used to classify GPCRs from other species even if it was established on human genome phylogenetic studies.

An updated implementation of the phylogenetic approach is currently used by the gpcrdb website. (https://www.gpcrdb.org/) (Alexander et al. 2019; Kooistra et al. 2021) (Figure 1-22)

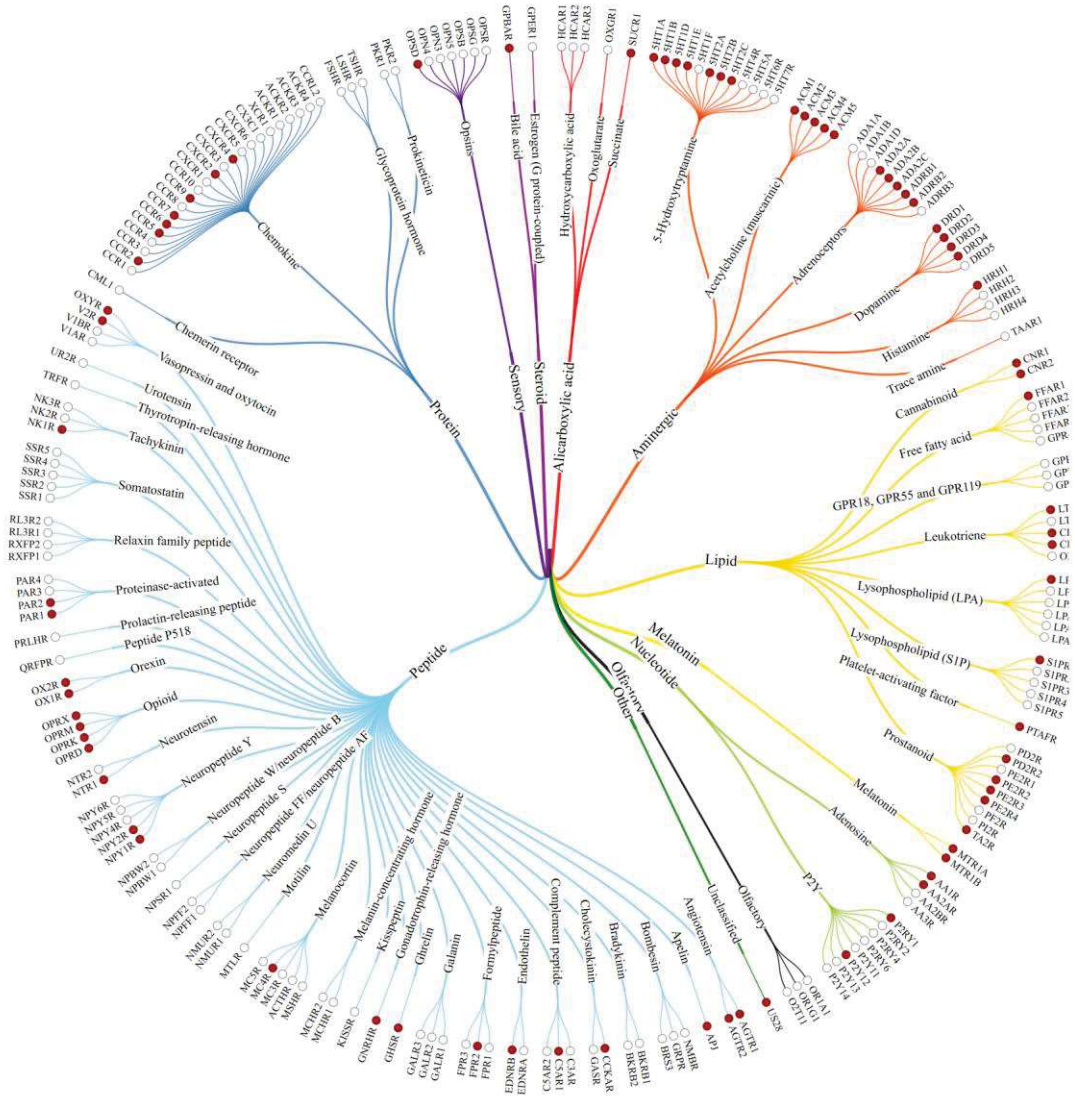

Figure 1-22 Class A GPCRs classification
(https://www.gpcrdb.org) (Katritch, Cherezov, and Stevens 2012)

1.5.4 Canonical G protein-mediated signaling

G Proteins are also known as guanine nucleotide-binding proteins (M. I. Simon, Strathmann, and Gautam 1991). In the inactive state, they form a heterotrimer composed of a Gα subunit bound to guanosine diphosphate (GDP) and the Gβγ subunits, a constitutive dimer. Once bound to the GPCR, G proteins can be activated. Indeed, the receptor binding induces an allosteric conformational change of the G protein, leading to catalyze the GDP release from the Gα subunit. The receptor and G protein without nucleotide form a high-affinity complex until the guanosine triphosphate (GTP) recruitment. Then the binding of GTP to the Gα subunit causes a structural rearrangement of Gα(GTP), Gβγ, and the receptor. This mechanism relies on a GTP

high concentration and a high ratio GTP/GDP in the vicinity of the complex (Oldham and Hamm 2008). Subsequently, the two subunits Gα(GTP) and Gβγ independently disengage from the receptor to associate with a large range of intracellular effectors (Figure 1-23). Various signaling cascades involving adenylyl cyclases, phospholipases, ion channels, tyrosine kinases, MAP kinases, and others are activated (Dorsam and Gutkind 2007). The Gα subunit displays constitutive GTPase activity allowing GTP hydrolysis and regeneration of the inactive heterotrimer. Regulators of G protein signaling can accelerate the process by activating the Gα GTPase activity or slowing it down by impairing the Gαβγ binding to the receptor for regulation and desensitization purposes (Figure 1-23).

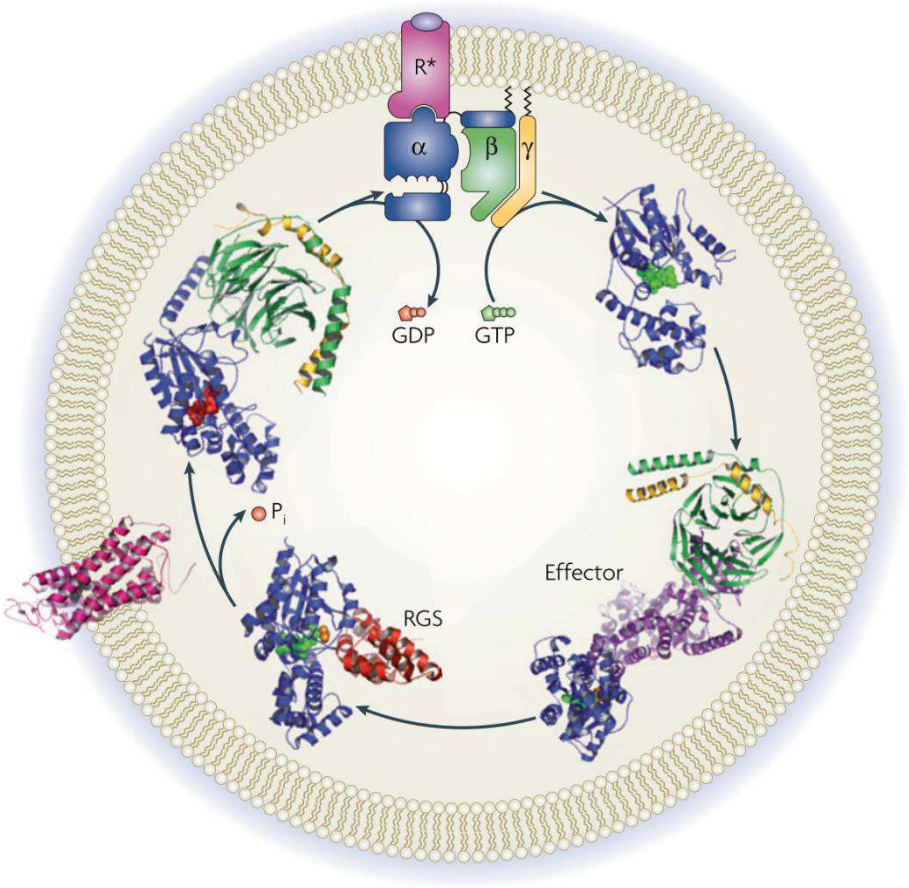

Figure 1-23 The G protein cycle
The receptor–G-protein complex remains the only Nature Reviews | Molecular Cell Biology major G protein conformation for which atomic-scale structural information is unavailable. In the resting state, G proteins are heterotrimers of GDP-bound α- (blue), β- (green) and γ- (yellow) subunits ($G\alpha_{t/I}$ β_1 γ_1; Protein Data Bank (PDB ID 1GOT). On binding of an extracellular stimulus (light purple), receptors (pink) (such as bovine rhodopsin; PDB ID 1F88) undergo a conformational change that permits G protein binding and catalyzes GDP release from Gα. Once GDP is released, a stable, high-affinity complex is formed between the activated receptor (R*) and G protein. Binding of GTP (green) to Gα destabilizes this complex, allowing both subunits, Gα(GTP) ($G\alpha_t$ (GTPγS); PDB ID 1TND22) and Gβγ, to interact with downstream effector proteins (purple) ($G\alpha_{i/q}$(GDP·AlF_4)·GRK2·$G\beta_1$- γ_2; PDB ID 2BCJ). The signal is terminated on hydrolysis of GTP to GDP by Gα, which may be catalyzed by regulator of G protein signaling (RGS) proteins (dark red) ($G\alpha_{t/i}$(GDP·AlF_4)·RGS9; PDB ID 1FQK). (Oldham and Hamm 2008)

1.5.4.1 Gα diversity

Sixteen genes are encoding 23 Gα proteins divided into four classes (Figure 1-24), grouped by similarity of function and identity of sequence (M. I. Simon, Strathmann, and Gautam 1991). Each class possesses specific signalization targets. For example, Gs family activates the adenylyl cyclase/cAMP signalization pathway whereas Gi family inhibits adenylyl cyclase/cAMP (García Reyes 1983). The members of Gq family activate the phospholipase C β which catalyzes the phosphatidylinositol-4,5-diphosphate ($PtdIns_{(4,5)}P_2$) in inositol-1,4,5-triphosphate ($Ins_{(1,4,5)}P_3$) and diacylglycerol (Morris and Scarlata 1997). The $G_{12/13}$ family

regulates RhoA small GTPases activation through RhoGEF guanine nucleotide exchange factors. This signalization pathway is critical for the actin skeleton reorganization, cell adhesion, and migration (Siehler 2009; Suzuki, Hajicek, and Kozasa 2009).

1.5.4.2 Gβγ diversity

The main role of the Gβγ constitutive dimer is to inactivate the Gα through reformation of the heterotrimeric G protein complex (Oldham and Hamm 2008). This is critical to Gα signal regulation and Gα-GPCR binding. Nonetheless, Gβγ proteins are also involved in various activation pathways. Gβγ are now known to interact with a wide range of effectors, for example, phospholipases, adenylyl cyclases, G protein-coupled receptor kinases, and ion channels like GIRK1 (Ford et al. 1998; Sierra-Fonseca et al. 2021). In humans, there are 5 Gβ subunits and 12 Gγ subtypes (Figure 1-24). The Gγ subunit shows wider sequence diversity than Gβ suggesting an important role in generating functional diversity (Downes and Gautam 1999) and allowing a large number of potential combinations. Also, every Gα protein might be able to combine with different Gβγ dimers. Each combination might potentially activate various effectors and work exclusively or synergistically with the Gα subunit (Clapham and Neer 1997). Nonetheless, several studies highlighted preferences of distinct Gβγ combinations for specific GPCRs and Gα subtypes (Robishaw 2012).

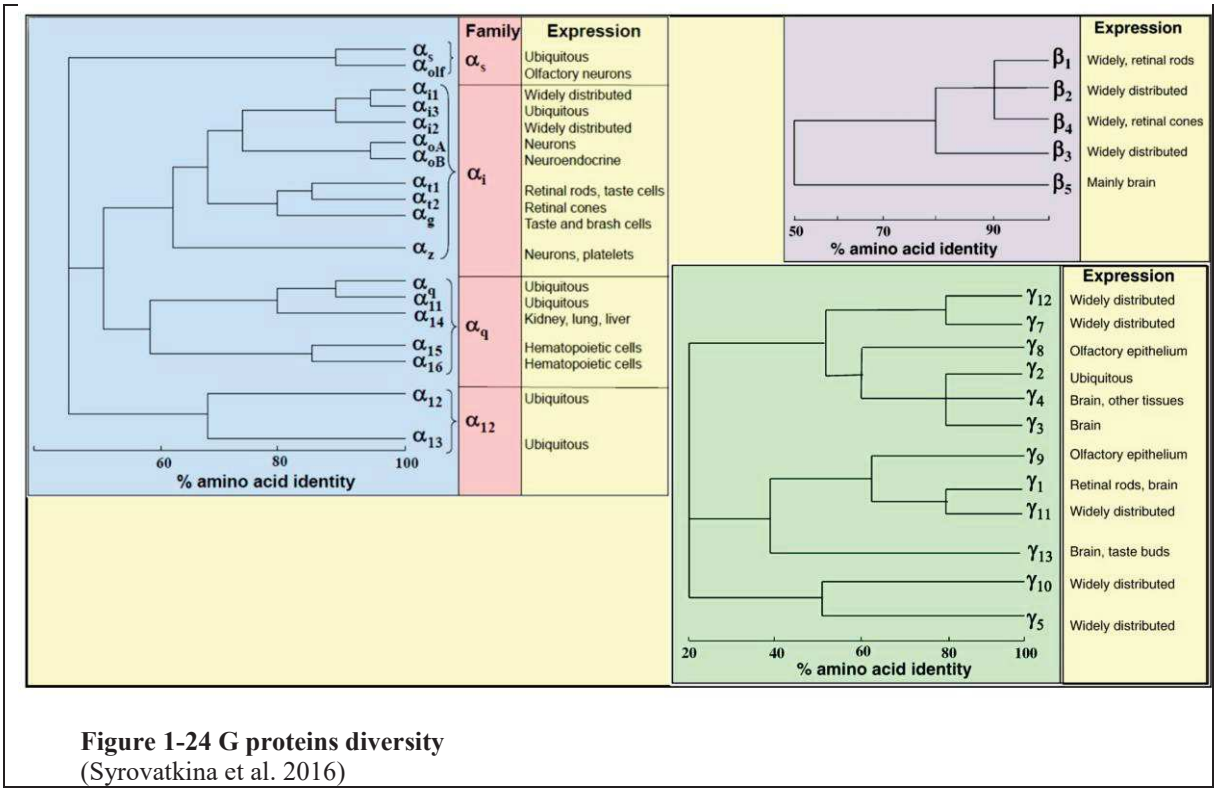

Figure 1-24 G proteins diversity
(Syrovatkina et al. 2016)

1.5.4.3 GRKs regulation

GRK activity was first discovered upon rhodopsin light activation (Kuhn 1974; Kühn and Dreyer 1972; kuhn 1978). Later, another receptor kinase was discovered, which specifically phosphorylated activated β2-adrenergic receptor (β_2AR) as well as light-activated rhodopsin (Robertson 1986; J. L. Benovic et al. 1986). These results suggested that there is a family of GRKs likely targeting different GPCRs (Jeffrey L Benovic et al. 1989). G protein-coupled receptor kinases phosphorylate activated G protein-coupled receptors, which promotes the binding of arrestins to receptors. GRKs phosphorylate serine and threonine residues in the C-terminal as well as in the ICLs of GPCRs acting as binding sites for arrestins. Arrestin binding to phosphorylated active receptor C-terminal domain prevents receptor stimulation of heterotrimeric G protein transducer proteins (Gurevich and Gurevich 2019).

1.5.4.4 Arrestin generalities

The arrestin proteins are key regulators of GPCRs (DeWire et al. 2007; Lohse et al. 1984). Their role has been first unraveled in visual systems through investigations on the interaction between rhodopsin and arrestin1 (Wilden, Hall, and Kuhn 1986), and on the β_2AR with non-visual β-arrestins (Lohse et al. 1984).

There are 4 arrestin subtypes in humans: two are visual arrestins (arrestin1 and arrestin4) which bind the phosphorylated form of rhodopsin, the two others are named arrestin2 and arrestin3 (βarrestin1 and βarrestin2, respectively) and interact with phosphorylated non-visual GPCRs. Arrestins don't display catalytic activity, they act as scaffold proteins to allow desensitization and internalization of GPCRs. Nonetheless their role is not limited to arrest G protein signaling pathways since they can also activate other cellular responses on their own.

1.5.4.5 Desensitization and Internalization

The βarrestins hinder G protein signal transduction in two ways, occurring in two steps: (i) desensitization, where a receptor becomes refractory to continued stimuli; this is induced by the interaction of βarr with the cytoplasmic face of the receptor which prevents G protein recruitment by competition (ii) internalization, where the receptor is physically removed from the cell surface by endocytosis. The arrestins act as multiprotein scaffolds essential for the recruitment of proteins involved in clathrin-mediated internalization, for example: (i) AP2 binding, which occurs on the β2 appendage domain with the motif [D/E]xxFxx[F/L]xxxR in β-arrestins, (ii) Clathrin binding through the clathrin-binding site in β-arrestin, named the clathrin binding box or Lϕxϕ[D/E] motif, (iii) and phosphoinositide molecules through the

phosphoinositides binding site (Xufan, Soo Kang, and Benovic 2014). Those components allow the formation of clathrin-coated pits (CCPs), and further endocytosis (DeWire et al. 2007; Spillmann et al. 2020).

GPCRs can be classified into two groups, Class A and Class B, in terms of arrestin binding. First, some receptors such as β2AR display a low affinity to arrestins resulting in transient binding. For these Class A receptors, the arrestins are released following clathrin-mediated internalization. This allows fast receptor recycling after internalization. On the opposite, Class B receptors like Angiotensin II receptor type 1 (AT1AR) and V2R display a much stronger and long-term binding with arrestins. Thereby, arrestins are not released after internalization and remain bound within endocytic vesicles. Consequently, the dynamics of recycling to the plasma membrane is slower for Class B than for Class A receptors (DeWire et al. 2007).

1.6 GPCRs structural investigations

1.6.1 X-ray crystallography and first GPCR structures

Because of their membrane protein features, GPCRs stayed for a long time reluctant to crystallogenesis and thereby refractory to structural determination.

The first GPCR ever structurally characterized at high resolution was the visual bovine rhodopsin (Okada et al. 2000; Palczewski et al. 2000). This GPCR responsible for the absorption of photons in retinal rod photoreceptor cells was more suited for crystallogenesis than others because of its stability and its high concentration in rod outer segment membranes. Crystals were obtained with the hanging drop vapor diffusion method. Crystals yielded X-ray diffraction to 2.8 Å resolution. The phasing informations were obtained employing multi-wavelength anomalous diffraction method. This scientific breakthrough emphasized structural differences between GPCRs and bacteriorhodopsin (Schertler, Villa, and Henderson 1993), especially in terms of the arrangement of the seven TMs. Rhodopsin structure disclosed larger and more organized extramembrane regions than that of bacteriorhodopsin. It displays also an eighth helix parallel to the membrane plane which is a common feature in most GPCRs. The ECL2 and N-terminal regions make a couple of beta hairpins (Figure 1-25)). Since then, more than 400 structures have been elucidated by X-ray crystallography covering a large variety of different GPCR families. This was made possible by technologic developments, notably in X-ray diffraction methodological improvement on small crystals, synchrotron beamlines quality, and software improvements. Some of the most striking improvements are relative to the

molecular biology and crystallogenesis developments mandatory to get suited samples for structural investigation, as detailed below.

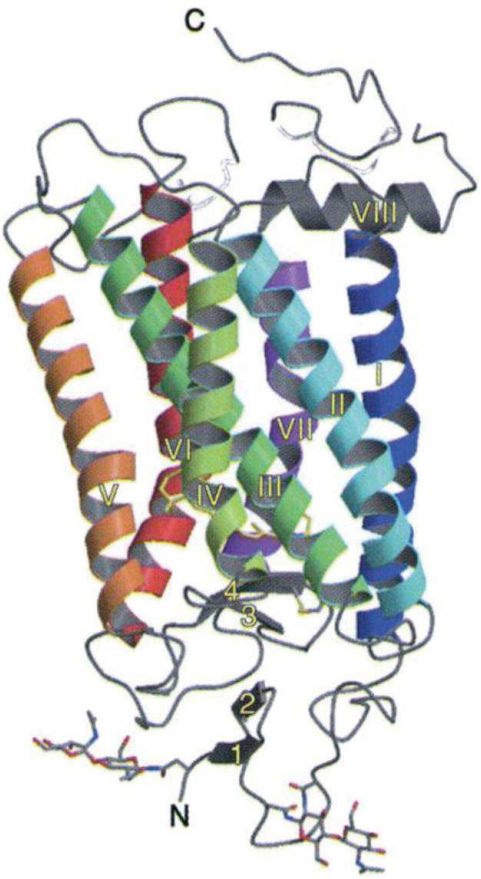

Figure 1-25 Ribbon drawings of rhodopsin
Parallel to the plane of the membrane, on the bottom side, the ECL2 and N-terminal regions make a couple of beta hairpins

1.6.1.1 Lipidic cubic phase

The lipidic cubic phase crystallogenesis (Landau and Rosenbusch 1996) is more suited to membrane proteins than vapor diffusion. It's a crystallization technique in which the receptor is placed in special conditions with monoacylglycerol and lipids. The cubic phase acts as a storage and supplies the proteins to feed growing crystals (Figure 1-26).

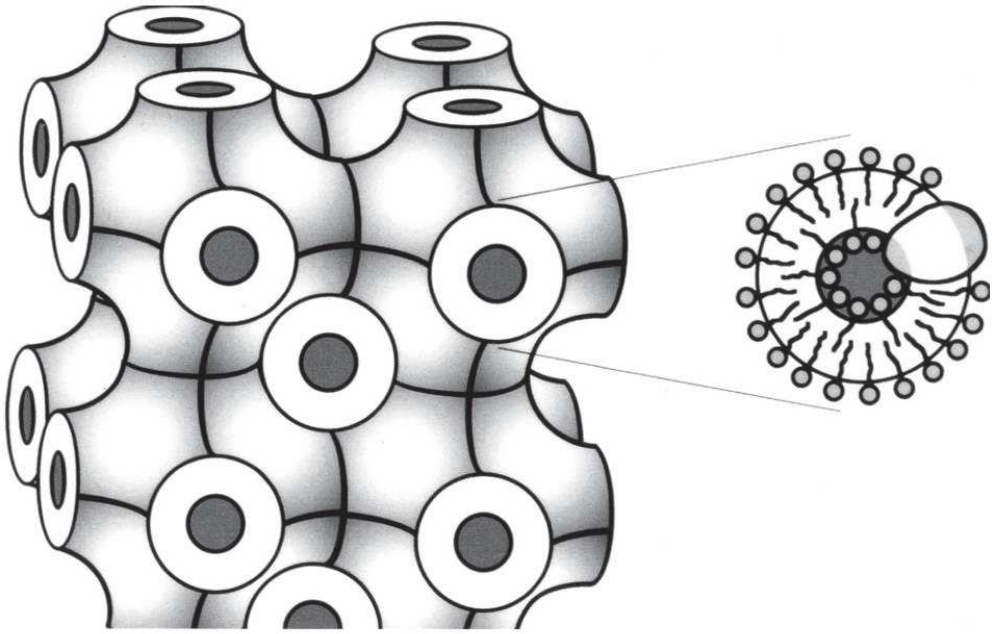

Figure 1-26 Schematic model of a bicontinuous cubic phase
bicontinuous cubic phase is composed of monoolein, water, and a membrane protein. The matrix consists of two compartments, a membrane system with an infinite three-dimensional periodic minimal surface (Left), interpenetrated by a system of continuous aqueous channels (shown in black). The enlarged section (Right) shows the curved lipid bilayer (with an inserted membrane protein molecule) enveloping a water conduit. In a cubic phase consisting of 60–70% monoolein or monopalmitolein and water, hydrophobic proteins diffuse laterally in the bilayer, while water-soluble components diffuse freely through the intercommuni- cating aqueous channel system. (Landau and Rosenbusch 1996)

1.6.1.2 Protein engineering

Other improvements in protein engineering have proven to be critical, such as the addition of protein modules like T4L or BRIL. This method consists of substituting a flexible loop, for example, the third intracellular loop, with a stable soluble protein like T4L. This soluble protein facilitates the formation of crystal lattice contacts, allowing the determination of structures at high resolution (E. Chun et al. 2013) (Figure 1-27). Another improvement is thermostabilization in which the receptor is subjected to an alanine scanning mutagenesis to identify mutations that increase thermostability. The mutations of interest are then combined to generate a more stable mutated version of the receptor of interest (Tate 2012; Serrano-Vega et al. 2008; Lebon et al. 2011; White et al. 2012). This method is compatible with conventional vapor diffusion crystallization of GPCRs in a detergent micelle. Indeed, the thermostability of membrane proteins is often strongly correlated with the stability of short-chain detergents, which favor crystallization by exposing hydrophilic loops to form lattice contacts (E. Chun et al. 2013).

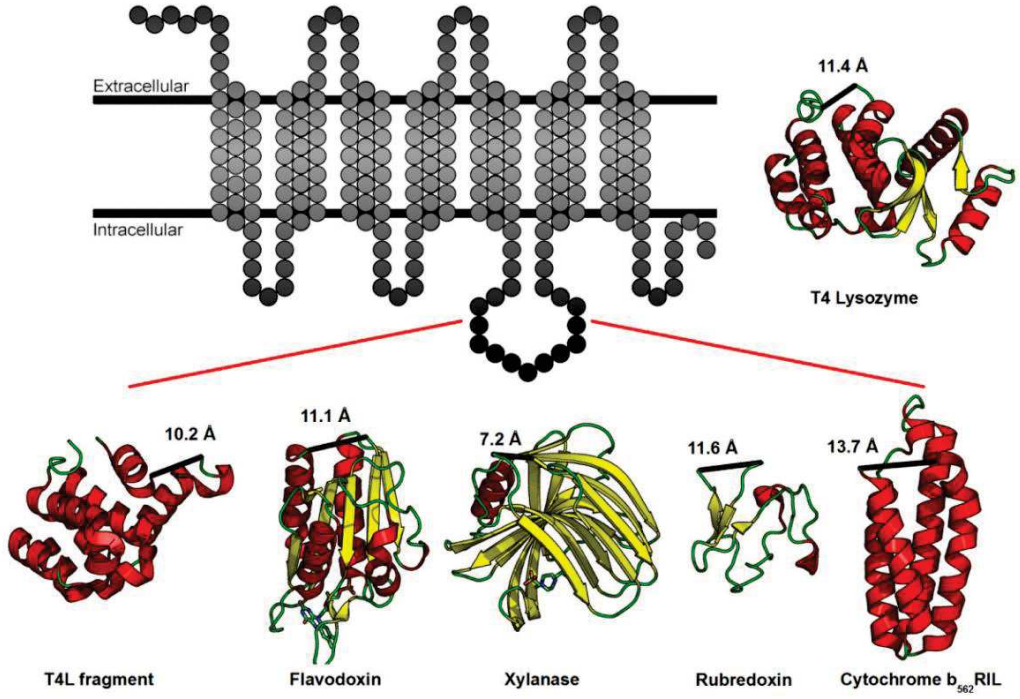

Figure 1-27 fusion domains selected for fusion into the third intracellular loop of A2AAR and β2AR
Five fusion domains selected for fusion into the third intracellular loop of A2AAR and β2AR
Figure illustrating the insertion of five new domains into the ICL3 of a prototypical GPCR, represented as a transmembrane snakeplot. The five domains are a C-terminal fragment of T4L (PDB ID 2O7A, MW 15.9 kD), flavodoxin (PDB ID 1I1O, MW 14.9 kD), xylanase (PDB ID 2B45, MW 19.1 kD), rubredoxin (PDB ID 1FHM, MW 5.5 kD), and cytochrome b562RIL (PDB ID 1M6T, MW 10.9). (E. Chun et al. 2013)

The production and purification were also improved by the use of baculovirus expression systems in insect cells and by the development of new detergents dedicated to membrane protein purification such as maltose neopentyl glycol. (H. Alonso and Roujeinikova 2012).

1.6.1.3 Nanobodies

Nanobodies appeared to be another useful tool for the stabilization of GPCRs during crystallogenesis. They are composed of a single domain isolated from the Vhh domain from *Camelidae* heavy-chain-only antibodies. Specific nanobodies directed again GPCRs-G-protein binding site have the ability to mimic signalization partners and thereby stabilize transient active states of GPCRs (Figure 1-28) (Manglik, Kobilka, and Steyaert 2017). Because of their small size and rigidity, they are suited to fit the GPCRs extra/intracellular cavities. They stabilize GPCR agonist binding likewise G proteins. The β_2AR has been crystallized both with nanobody and Gs protein (Søren G.F. Rasmussen et al. 2011). The structure stabilized with a nanobody is similar to the one elucidated directly in complex with the G protein. Both are

displaying the same activation pattern characterized by an outward movement of the TM6 as compared to the corresponding inactive form of β_2AR. They also share a common configuration of the highly conserved activation motifs (E/DRY and NPxxY) (Sŏren G.F. Rasmussen et al. 2011; Søren G.F. Rasmussen et al. 2011). They differ mostly on the intracellular side of the TMs 5 and 6, with a 3Å outward difference of the TM6. Nanobodies were also used to stabilized GPCRs indirectly by interacting with G proteins or arrestins in the context of GPCR complexes.

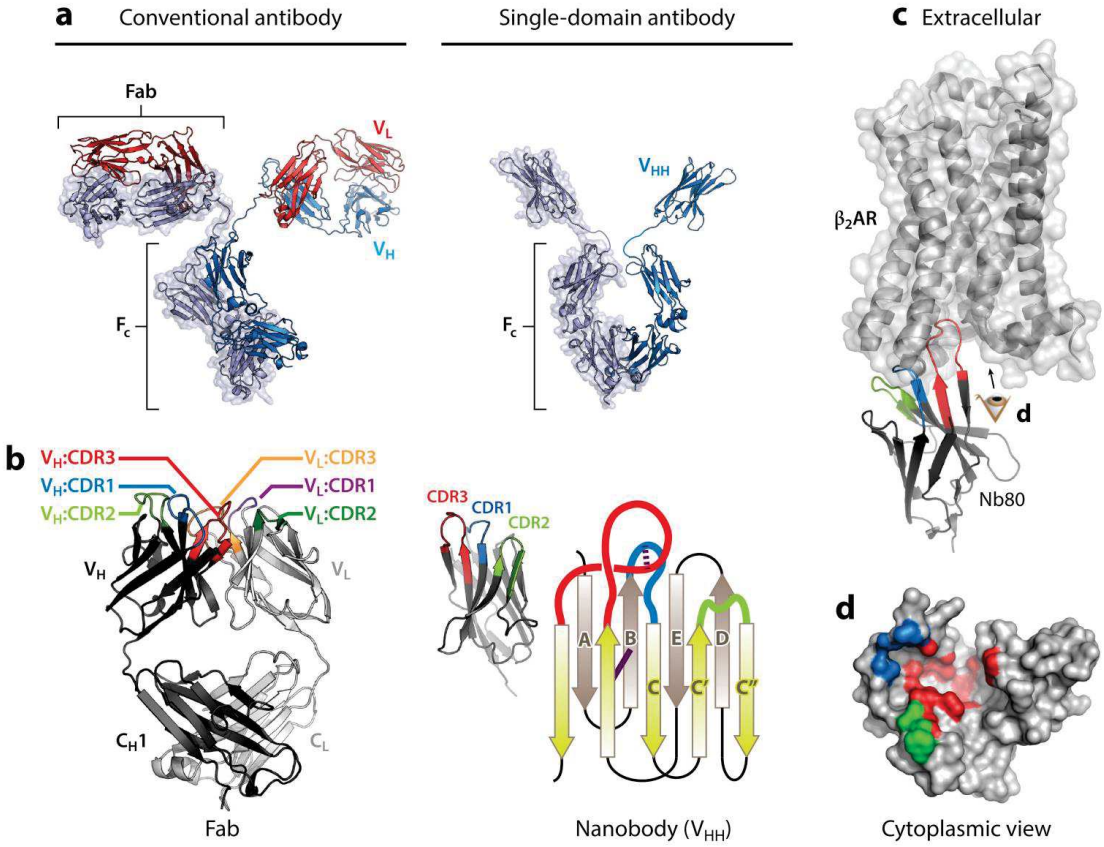

Figure 1-28 Nanobody structure and function and comparison to conventional antibodies
(a) Comparison of conventional antibodies to camelid single-domain antibodies. Conventional antibodies are heterotetrameric molecules consisting of two heavy chains (VH) and two light chains (VL) with a conserved domain called the crystallizable fragment (Fc). Variable loops responsible for antigen binding are within the distal tips of the Fab domain. Camelid single-chain antibodies contain a single immunoglobulin domain (VHH) that binds antigens individually. (b) Comparison of the minimal binding domain of conventional antibodies (Fab) and single-domain antibodies (VHH or nanobody). The antigen-binding region of a Fab is composed of six complementarity-determining regions (CDRs), with three in each VH and VL. Correct VH/VL pairing is required for antigen binding. In contrast, nanobodies contain three CDRs, and the single immunoglobulin fold is sufficient for antigen binding. The nanobody immunoglobulin fold is built from a pair of antiparallel βsheets with a conserved disulfide bond (solid purple line). The CDRs originate from loops between individual strands. Many nanobodies contain an extra interloop disulfide bond that restricts the flexibility ofCDR1 and CDR3 (dotted purple line). (c) The prolate structure of the nanobody forms a convex paratope surface, which allows it to access antigenic cavities. In the β2-adrenergic receptor·Nanobody80 (β2AR·Nb80) complex shown here [Protein Data Bank (PDB) ID: 3P0G], CDR3 ofNb80 inserts into the cytoplasmic surface of active β2AR, with additional interactions made by CDR1 and CDR2. The resulting β_2AR epitope recognized by Nb80, viewed from the cytoplasmic surface (eye symbol), is displayed in panel d. Note that each CDR binds different regions of the complex three-dimensional epitope that is discontinuous in β_2AR sequence (Manglik, Kobilka, and Steyaert 2017)

1.6.2 Advances of CryoEM in GPCR structural biology

Major evolutions in the field of electron microscopy allowed to get the first GPCR-G protein complex structure by Cryo-EM in 2017 (Y. L. Liang et al. 2017). Since then, many structures

of GPCR active states were investigated by Cryo-EM. It is due to gradual technological advances on all plans: (i) for sample preparation, new grid supports with less induced beam motion, new freezing technologies, (ii) new electron microscopes, cold FEG guns, new energy filters, improved acquisition efficiency, and new detectors, fasters and with better sensibility, (iii) new algorithms, better motion estimation and correction, better optical aberration correction within processing, increased computational capabilities. Currently, more than 100 GPCR active state structures are listed in the GPCRDB for 34 different receptors coupled with a G protein signaling partners (García-Nafría and Tate 2019a; Danev et al. 2020; Maeda et al. 2019; Xing et al. 2020) and 4 structures of active GPCRs coupled to arrestins for three different receptors (Y. Lee, Warne, Pandey, et al. 2020; W. Huang et al. 2020; Staus et al. 2020a; Yin, Li, Jin, Yin, Waal, et al. 2019). This huge information is critical and allows in combination with knowledge about inactive state structures to draw potential activation mechanisms. For the most studied receptors, structural information deduced from different conformations (active, inactive, in complex with signalization partners or not, with agonists, biased agonists, or antagonists) provides a better understanding and a rational base for new drug development.

1.6.3 GPCR Structural features

From a structural point of view, despite the broad diversity of their sequence and their activating ligand, these receptors display a common topology. Indeed they share a 7 Transmembrane helix (TM) bundle and an eighth helix, parallel to the membrane plane. Those TM are linked by three extracellular loops (ECLs) and three intracellular loops (ICLs). Most of the receptors contain a TM3–ECL2 disulfide bridge that contributes to receptor stability. Nonetheless specific structural features exist among classes, and specific motifs of residues critical for activation are conserved in each class. Based on this fact, numbering methods were established for each class, using a two digit definition. The first one corresponds to the TM number and the second to the position relative to the most conserved residue which is assigned the number 50. Such a nomenclature was defined for class A (Ballesteros and Weinstein 1994), class B (Wootten et al. 2013), class C (Pin, Galvez, and Prézeau 2003), and Class F (C. Wang et al. 2014) receptors.

1.6.3.1 Class-specific ligand binding modes

1.6.3.1.1 Class A GPCRs

Class A receptors bind a large variety of ligands such as biogenic amines, opioids, chemokines, nucleotides, signaling lipids, and peptides. Most of these ligands bind in a common area, at the extracellular side of GPCRs, both in the ECLs and at the top of the TM bundle. Conserved or

similar residues from TM3, TM6, and TM7 interact with the ligands in most of the GPCRs, such as residues at positions 3.32, 3.33, 3.36, 6.48, 6.51, and 7.39 (Figure 1-29).

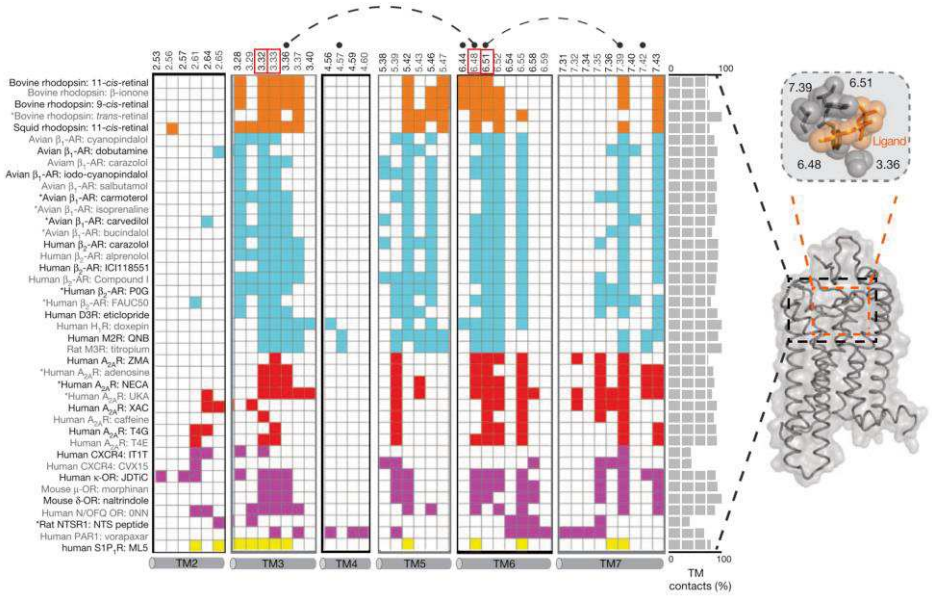

Figure 1-29 Ligand-binding pocket in class A GPCRs
Characterization of ligand-binding pockets of class A GPCRs. Comparison of the TM residues that are present in the ligand-binding pocket is shown as a matrix. Receptor–ligand information is shown as rows, and the Ballesteros–Weinstein numbers ofTM residues that contact the ligand are shown as columns. The TM residues that are present in the consensus inter-TM contact network are marked with black dots and contacts between these residues are shown as dotted lines. Rows marked with an asterisk denote agonist-bound receptor structures. In the matrix, the presence of a contact between the ligand and the TM residue is shown as a colored box, and the absence of a contact is shown as an empty box. The percentage of TM residue contacts made by the ligand is shown as a bar plot on the right of the matrix. (Venkatakrishnan et al. 2013)

Also, two pairs of interacting residues 3.36–6.48 and 6.51–7.39 appear to form the floor of the orthosteric pocket (Figure 1-29) (Venkatakrishnan et al. 2013) Furthermore, the ECL2 may be involved in the ligand entry and potentially play the role of gatekeeper in some cases (T. Liang et al. 2017). To accommodate huge ligand variability, there are strong variations in ECLs and the extracellular side of the TM helices. There are strong fluctuations of the side chain size, shape, and physicochemical properties, notably in the orthosteric pocket. This leads to different binding mechanisms among the rhodopsin-like receptors. GPCRs with small natural ligands like adrenaline or adenosine feature a ligand-binding site deep in the TM bundle. For example, the β2AR binds adrenaline through contacts with the TMs 3, 5, 6, and 7 deep in the TM bundle (Ring et al. 2013), whereas chemokine receptors can bind large ligands (Kufareva et al. 2017) and display different binding mechanisms. CXCR2 for example binds its ligand CXCL8-A mostly through its N-terminal domain which interacts with the core of CXCL8-A. The CXCL8-

A N-terminal domain interacts with the transmembrane bundle (K. Liu et al. 2020). Unlike small neurotransmitters like adrenaline or adenosine with their respective receptors, CXCL8 doesn't dive deep into the helix bundle likely because of its size and its interaction with the N-terminal domain. (K. Liu et al. 2020) (Figure 1-30). In contrast to peptides and small-molecules receptors, the lipid-binding GPCRs display a tight folding on the TM extracellular area. It restricts the ligand access to the orthosteric pocket. This configuration reflects the physic-chemical properties of lipids. Indeed, their amphiphilic nature allows them to access the GPCR core both through the plasma membrane or from the extracellular space. Furthermore, lipids can be actively transported through protein chaperones directly to the location of the GPCR for activation (Audet and Stevens 2019).

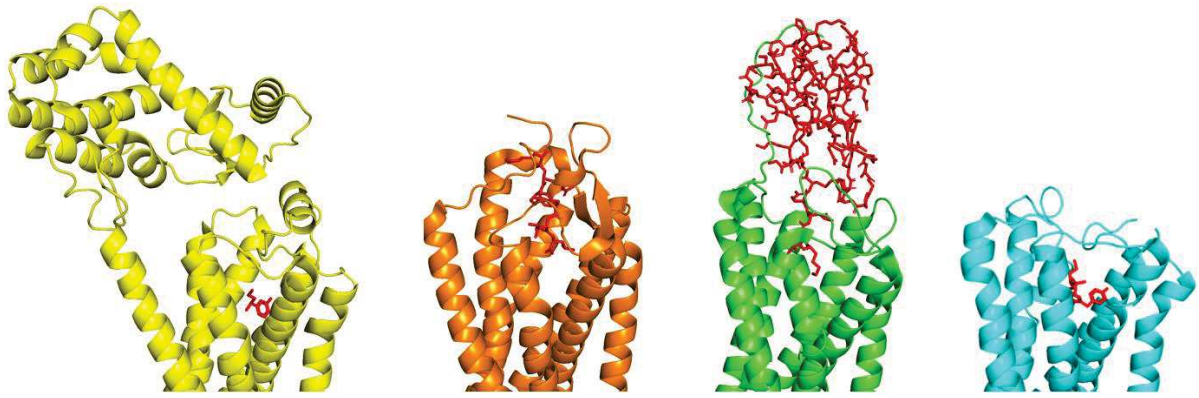

Figure 1-30 Ligands binding in Class A GPCRs
Receptors were aligned in pymol . Ligands are shown in red sticks, receptors are shown in cartoons. β2 adrenergic receptor with adrenalin (PDB 4LDO), NTS1 receptor with neurotensin (PDB 4XES), CXCR2 bound to CXCL8 (PDB 6LFO), and Cannabinoid Receptor 1 coupled to KCA a small antagonist (PDB 6N4B)

Also, different binding modes are represented for a single specific receptor depending on the nature of its ligands. For example, concerning the β_2AR, there are different contacts between an inverse agonist carazolol and agonists such as BI167107 (Søren G.F. Rasmussen et al. 2011), hydroxy benzyl isoproterenol (Ring et al. 2013) (Figure 1-31), or adrenaline.

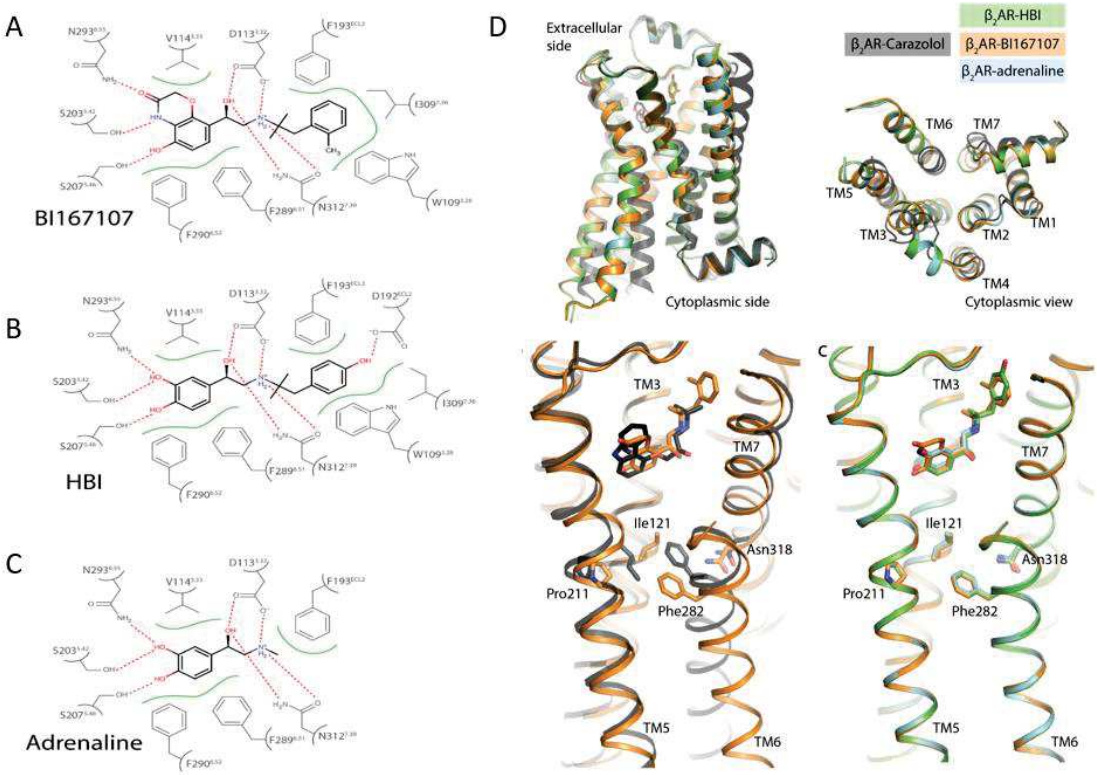

Figure 1-31 Contacts between active β2AR and the three co-crystallized ligands
Contacts between active β_2AR and the three co-crystallized ligands are diagrammed here, with polar contacts shown in red dotted lines and hydrophobic contacts shown as green solid lines. The ligands presented are BI167107 (a), and the catecholimines hydroxybenzyl isoprenaline (HBI, b), and adrenaline (c) The conformation of active β_2AR bound to BI167107, HBI, and adrenaline are nearly identical in the transmembrane segments and cytoplasmic domain Residues that connect the binding pocket to the cytoplasmic domain are reoriented upon activation. These connecting residues adopt highly similar conformations in active β_2AR bound to BI167107, HBI, and adrenaline

In the same idea, ZM-241385 a highly potent antagonist, and the two agonists NECA and adenosine, all interact within the same orthosteric pocket of adenosine A2A receptor ($A_{2A}R$). More precisely, both agonists contact the upper part of the TM 2, 3, 6, and 7. The antagonist doesn't interact with the same pattern of residues. Notably, there is no contact between ZM-241385 and the TM2 (Figure 1-32) (Lebon et al. 2011)

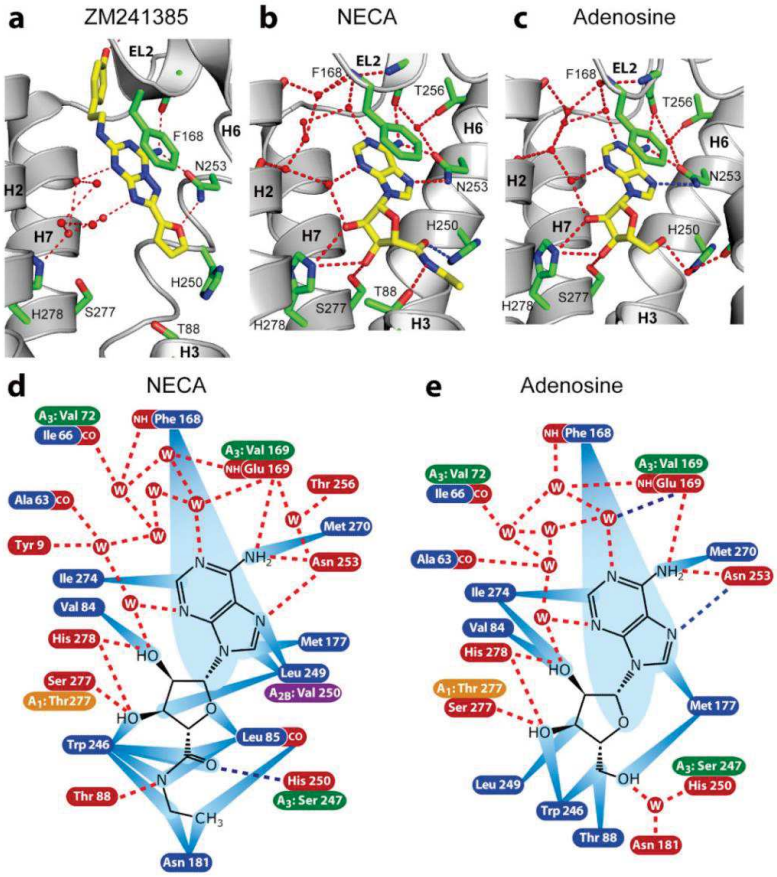

Figure 1-32 Receptor-ligand interactions of human A2AR
Receptor-ligand interactions were compared for the adenosine receptor bound to the inverse agonist ZM241385 and the agonists NECA and adenosine. Structures of the human A2AR in cartoon representation are shown bound to the following ligands: (a) ZM241385 (PDB code 3EML8); (b) NECA; (c) adenosine. (d, e) Polar and non-polar interactions involved in agonist binding to A2AR are shown for NECA (d) and adenosine (e). Amino acid residues within 3.9 Å of the ligands are depicted, with residues highlighted in blue making van der Waals contacts (blue rays) and residues highlighted in red making potential hydrogen bonds with favorable geometry (red dashed lines, as identified by HBPLUS, see Methods Online) or hydrogen bonds with unfavorable geometry (blue dashed lines, donor acceptor distance less than 3.6 Å). Where the amino acid residue differs between the human A2AR and the human A1R, A2BR and A3R, the equivalent residue is shown highlighted in orange, purple or green, respectively. Panels a-c were generated using Pymol (DeLano Scientific Ltd) (Lebon et al. 2011)

1.6.3.1.2 Class B GPCRs

The secretin family receptors bind large α-helical peptides like calcitonin and glucagon. Recently, many active state structures of Class B1 GPCRs were resolved by CryoEM studies (Y. L. Liang et al. 2017; X. Zhang, Belousoff, Zhao, Kooistra, Truong, Ang, Underwood, Egebjerg, Šenel, Stewart, Liang, Glukhova, Venugopal, Christopoulos, Sebastian, et al. 2020; Dong et al. 2020; Y. Liang et al. 2020; Y. L. Liang et al. 2018a; Danev et al. 2020; dal Maso et al. 2019; Kobayashi et al. 2020; dal Maso et al. 2019). These data confirmed the critical role of the N-terminal domain and the GPCR core in both ligand affinity and efficacy (Hilger et al.

2019). In addition, the case of glucagon-like peptide-1 receptor (GLP1R) is particularly interesting. High-resolution GLP1R cryo-EM structures revealed that binding sites for PF-06882961, a nonpeptide agonist, and for the natural agonist GLP-1 substantially overlap, whereas CHU-128, a non-peptide biased agonist, adopts a unique binding mode with a more open receptor confirmation at the extracellular face. Structural differences involving extensive water-mediated hydrogen bond networks could be correlated to functional data to understand how PF 06882961, but not OWL-833, can closely mimic the pharmacological properties of GLP-1 (X. Zhang, Belousoff, Zhao, Kooistra, Truong, Ang, Underwood, Egebjerg, Šenel, Stewart, Liang, Glukhova, Venugopal, Christopoulos, Sebastian, et al. 2020). (Figure 1-33)

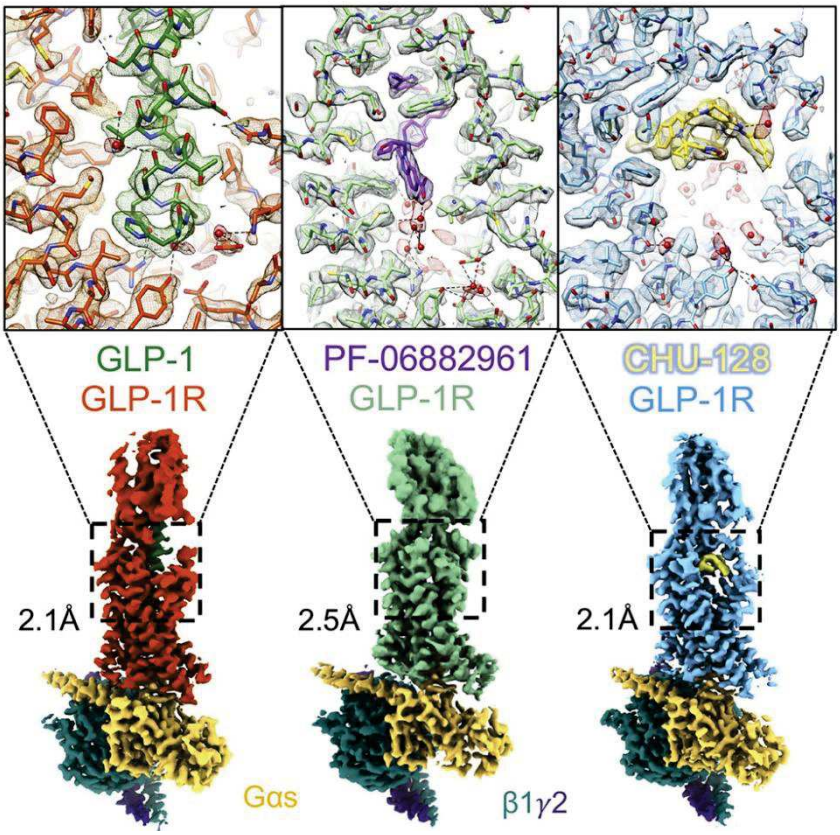

Figure 1-33 Receptor-ligand interactions of GLP1R
GLP1-R bound to GLP1, left bound to PF 06882961 in the middle, and CHU-128 bound on the left; orthogonal views of the cryo-EM maps and backbone models built into the maps in ribbon format. whereas CHU-128, a non-peptide biased agonist, adopts a unique binding mode with a more open receptor conformation at the extracellular face (X. Zhang, Belousoff, Zhao, Kooistra, Truong, Ang, Underwood, Egebjerg, Šenel, Stewart, Liang, Glukhova, Venugopal, Christopoulos, Furness, et al. 2020)

1.6.3.1.3 Class C GPCRs

Unlike other GPCRs, Class C receptors comport an exceptionally large extracellular domain (ECD). This ECD contains a Venus flytrap (VFT) module. It plays the role of orthosteric binding pocket, also there is an allosteric binding pocket in the TM bundle of this class of GPCRs. The VFT is composed of two lobes separated by a cleft where endogenous ligand binds (Figure 1-34) (L. Chun, Zhang, and Liu 2012; Lin et al. 2021). The VFT transiently opens and closes. When the ligand binds the lobe one, it induces the stabilization of a closed form and further interaction between the ligand and the lobe 2.

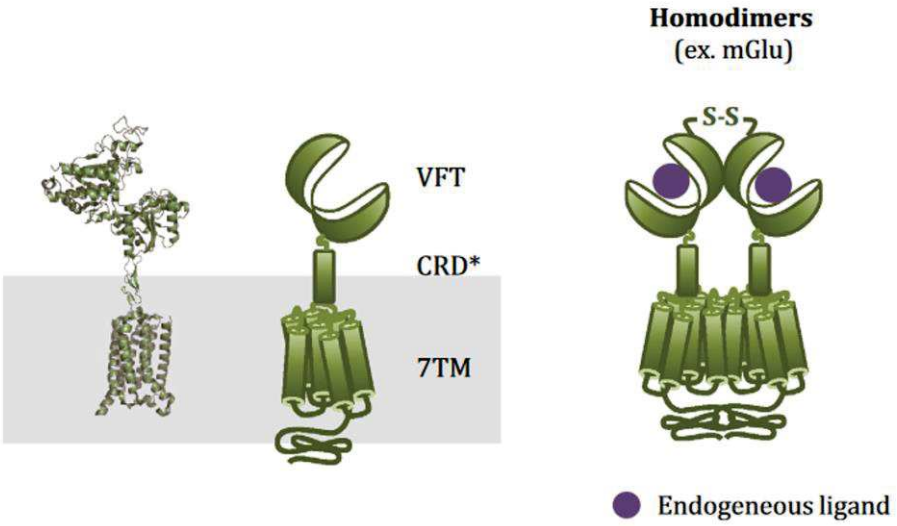

Figure 1-34 Structural model and schematic representation of class C GPCRs
Class C GPCRs are composed of a Venus flytrap (VFT)domain, a cysteine-rich domain (CRD), and a transmembrane(7TM) domain. This class of receptors forms obligatory dimers. (Møller et al. 2017)

1.6.3.1.4 Ste2 ClassD GPCR

There is currently only one active state structure of a class D receptor, the Saccharomyces cerevisiae pheromone receptor Ste2 (Velazhahan et al. 2021). Ste2 has a large orthosteric binding pocket (1,126 $Å^3$) located in the extracellular half of the receptor. The N-terminal part of the ligand resides mainly outside the orthosteric binding pocket but contributes nonetheless to the interaction. The C-terminal part of the ligand dives deeper into the orthosteric pocket (Figure 1-35) (Velazhahan et al. 2021).

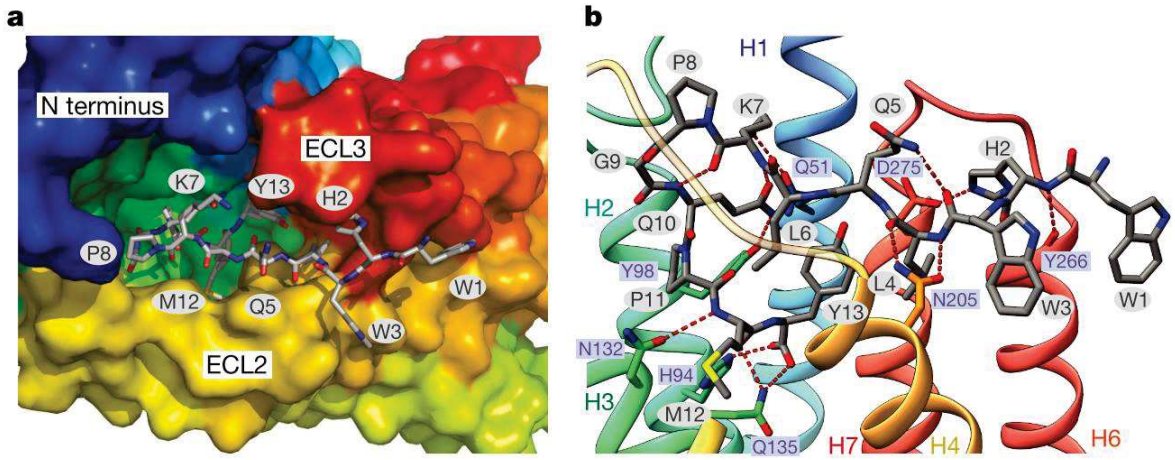

Figure 1-35 Ste2 ClassD GPCR α-Factor-binding site
a, b, View of the orthosteric binding pocket of the Ste2 receptor (Velazhahan et al. 2021)

1.6.3.1.5 Class F GPCRs

It remains unclear how Class F receptors bind their ligands, how ligand binding is translated into receptor activation, and how signal initiation and specification are achieved. Nonetheless, recent structures of SMO-Gi complexes bound to the synthetic SMO agonist (SAG) and to 24(S),25-epoxycholesterol (24(S),25-EC) provide informations on an atypical binding mechanism (Qi et al. 2020). A novel sterol-binding site in the extracellular extension of TM6 was revealed to connect other sites in 7-TMs and cysteine-rich domain (CRD), forming an intramolecular sterol channel from the middle side of 7-TMs to CRD (Figure 1-36). Additional structures of two gain-of-function variants, SMOD384R and SMOG111C/I496C, showed that blocking the channel at its midpoints allows sterols to occupy the binding sites in 7-TMs, thereby activating SMO. These data indicate that sterol transport through the core of SMO is a major regulator of SMO-mediated signaling (Qi et al. 2020).

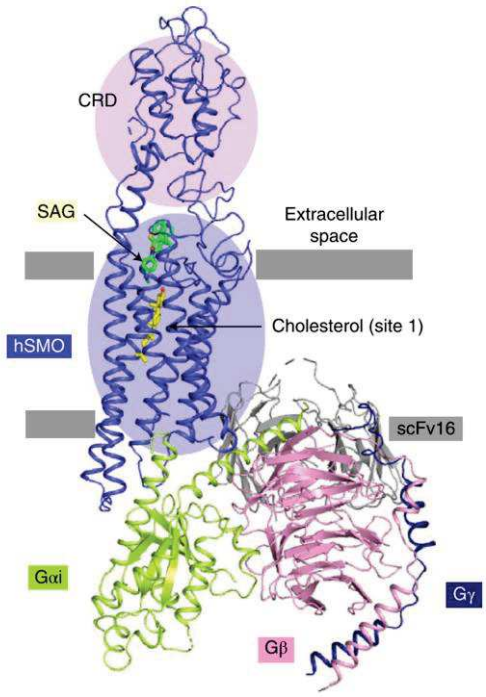

Figure 1-36 Structure of the Smogi-Sag complex
Structure of the Smogi-Sag complex reveals an endogenous sterol in the TM bundle: Ribbon representation of the complex. The CRD and 7-TMs of SMO are indicated by circles. (Qi et al. 2020)

1.6.3.1.6 Allosteric Binding

Interestingly, extensive drug research targeting GPCRs allowed to unravel GPCR allosteric modulators, novel binding sites, or novel action modes. For example, subtype-selective antagonists for muscarinic receptors (MRs) have long been elusive, owing to the highly conserved orthosteric binding site. However, allosteric sites of these receptors are less conserved, motivating the search for allosteric ligands that modulate agonists or antagonists to confer subtype selectivity. Accordingly, a 4.6 million-molecule library was docked against the structure of the prototypical M2R, seeking molecules that specifically stabilized antagonist binding. A positive allosteric modulator (PAM) that potentiated the antagonist N-methyl scopolamine was identified. Structure-based optimization led to compound ’628, which confers subtype selectivity to M2R antagonists. (Figure 1-37) (Korczynska et al. 2018; Yang et al. 2021).

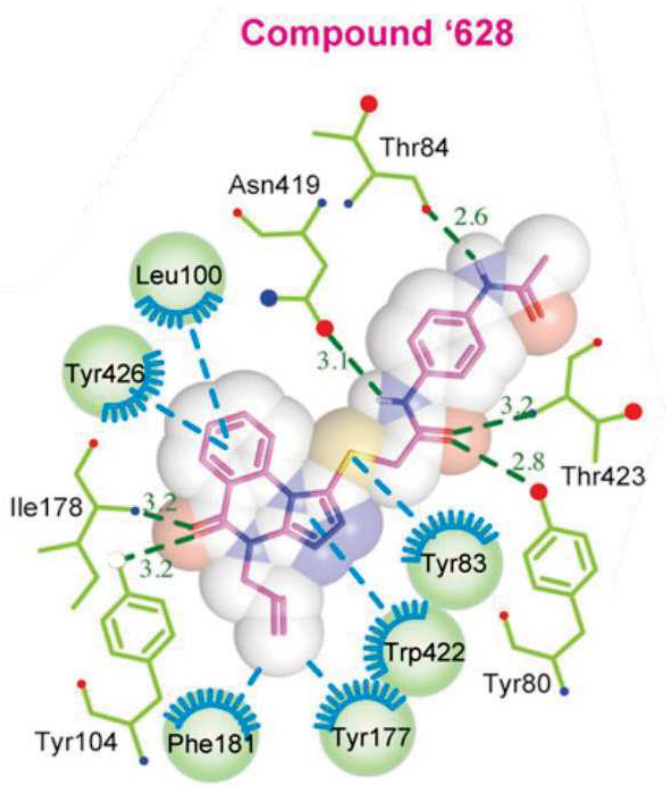

Figure 1-37 representation of the allosteric vestibule with the PAM '628 in the M2 muscarinic receptor
Ligplot representation of the allosteric vestibule with the PAM '628, indicating interactions based on docking pose; hydrogen bonds (green dash) and hydrophobic interactions are indicated (cyan dash). (Korczynska et al. 2018)

1.6.4 Molecular signatures, molecular switches, and common activation mechanisms of GPCRs

Despite the plasticity in binding and the apparent diversity in sequence among GPCRs, many residues and tertiary contacts between TM helices are conserved. A systematic analysis of the different GPCR structures, which includes both active and inactive states, reveals a consensus network of 24 inter-TM contacts mediated by 36 topologically equivalent amino acids (Venkatakrishnan et al. 2013) (Figure 1-38). Among these residues, some are highly conserved such as Asn1.50, Asp2.50, Trp4.50, and Pro7.50 (Ballesteros-Weinstein numbering). Nevertheless, many topologically equivalent positions can tolerate variability in amino acid substitutions(Venkatakrishnan et al. 2013).

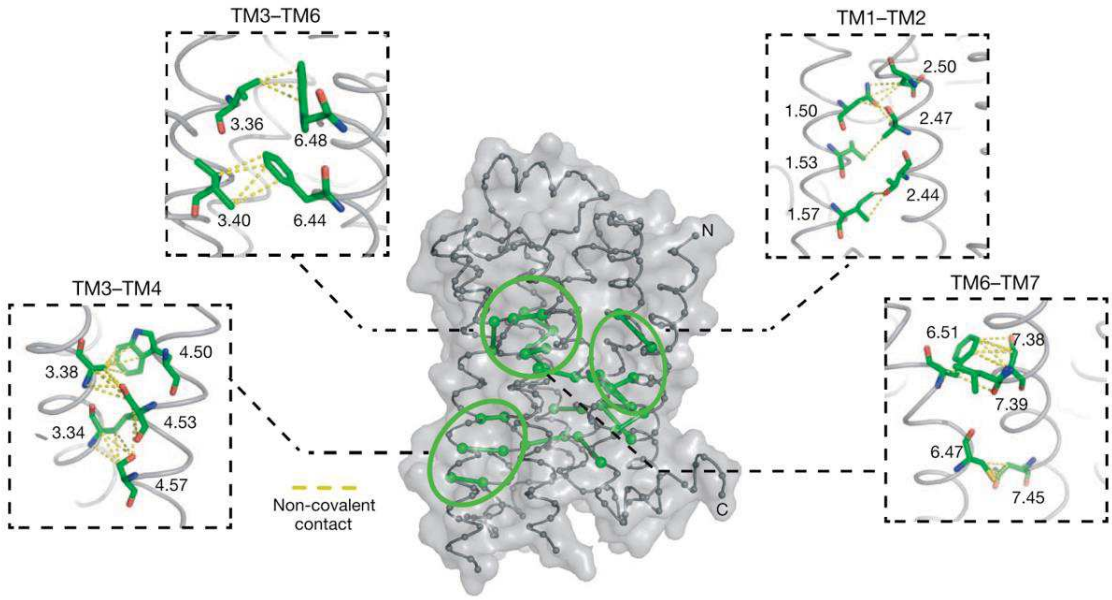

Figure 1-38 Consensus scaffold of non-covalent contacts in GPCRs
Network of 24 inter-helical contacts between 36 topologically equivalent residues is shown on a representative structure of inactive b1-AR. The spatially clustered contacts between the amino acids are shown in the panels; to maintain visual clarity, contacts between TM3 and TM5 are not shown. Here we define that a pair of residues is in contact if the Euclidean distance between any pair of atoms (side-chain and/or main-chain atoms) is within the van der Waal interaction distance (that is, the sum of the van der Waal radii of the atoms plus 0.6A˚). With the availability of more high-resolution structures of other GPCRs, one may converge on a unified subset of inter-helical contacts that is maintained in all GPCRs. (Venkatakrishnan et al. 2013)

Active and inactive GPCR structures are resolved for a reasonable number of receptors to permit to determine canonical conformational changes and modification of conserved motifs involved in activation. First, a typical conformational change upon receptor activation is an outward movement of the intracellular side of the TM6 to create a cavity, necessary to the G protein interaction, and a smaller movement of the TM5 to enlarge this cavity. It is induced by a succession of conformational changes of conserved motifs within the receptor triggered by agonist binding. (Figure 1-39) (Deupi 2014). These conserved motifs are shared by most but not all GPCRs (Filipek 2019). At least, there are four crucial molecular switches.

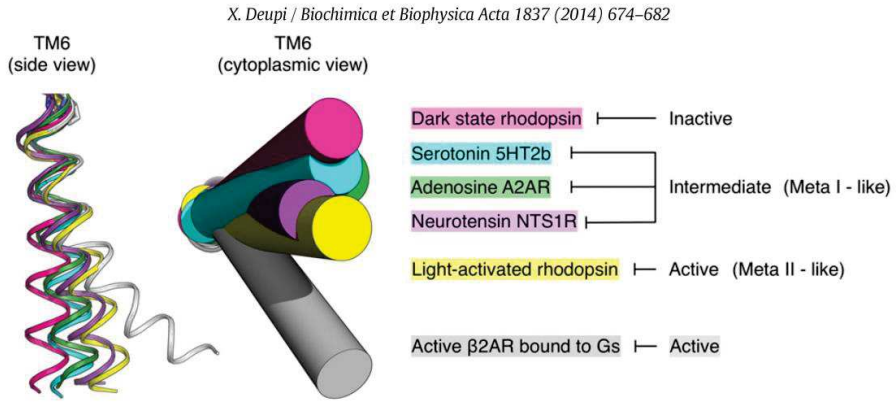

Figure 1-39 The relative orientation of TM6 in variable GPCRs and states
The relative orientation of TM6 in the crystal structures of dark state inactive rhodopsin and agonist-bound GPCRs. In the adenosine A2A and serotonin 5HT2B receptors. (Deupi 2014)

The 3-7 lock is not assigned to any specific sequence. It is located in the vicinity of the ligand pocket and involves an interaction between residues 3.32 and 7.43 through a hydrogen bond (Figure 1-40). Ligand binding induces a temporary break of this hydrogen bond which occurs first in the activation process.

A key residue for GPCR activation is the W6.48 tryptophan toggle switch in the conserved motif CWxP (TM6). Upon agonist binding, a displacement of the toggle switch is triggered. In the active configuration, the side chain of W6.48 is proposed to fluctuate between two positions allowing water diffusion in the receptor core (Yuan et al. 2015). Conformational changes of other microswitches along with the TM helices through a cascade of modifications are observed, involving for instance key residues in positions 6.44 and 7.45 among others (Q. Zhou et al. 2019). One of those key microswitches, the Y7.53 tyrosine toggle switch belongs to the NPxxY motif in TM7. It displays a permanent rotameric change through activation. In an active state, the lateral chain of the Y7.53 has the propensity to form a lock with Y5.58 through a water molecule bridge in several but not all cases. Y5.58 is also hydrogen-bonded with R3.50 of the ionic-lock DRY/ERY motif in the TM3 (Manglik and Kruse 2017).

Activation also breaks this ionic lock, which involves interactions between Glu/Asp3.49-Arg3.50 with 6.30 known to stabilize GPCRs in their inactive state. Conformational changes of this motif allow the outward displacement of the TM6 to accommodate G-protein binding.

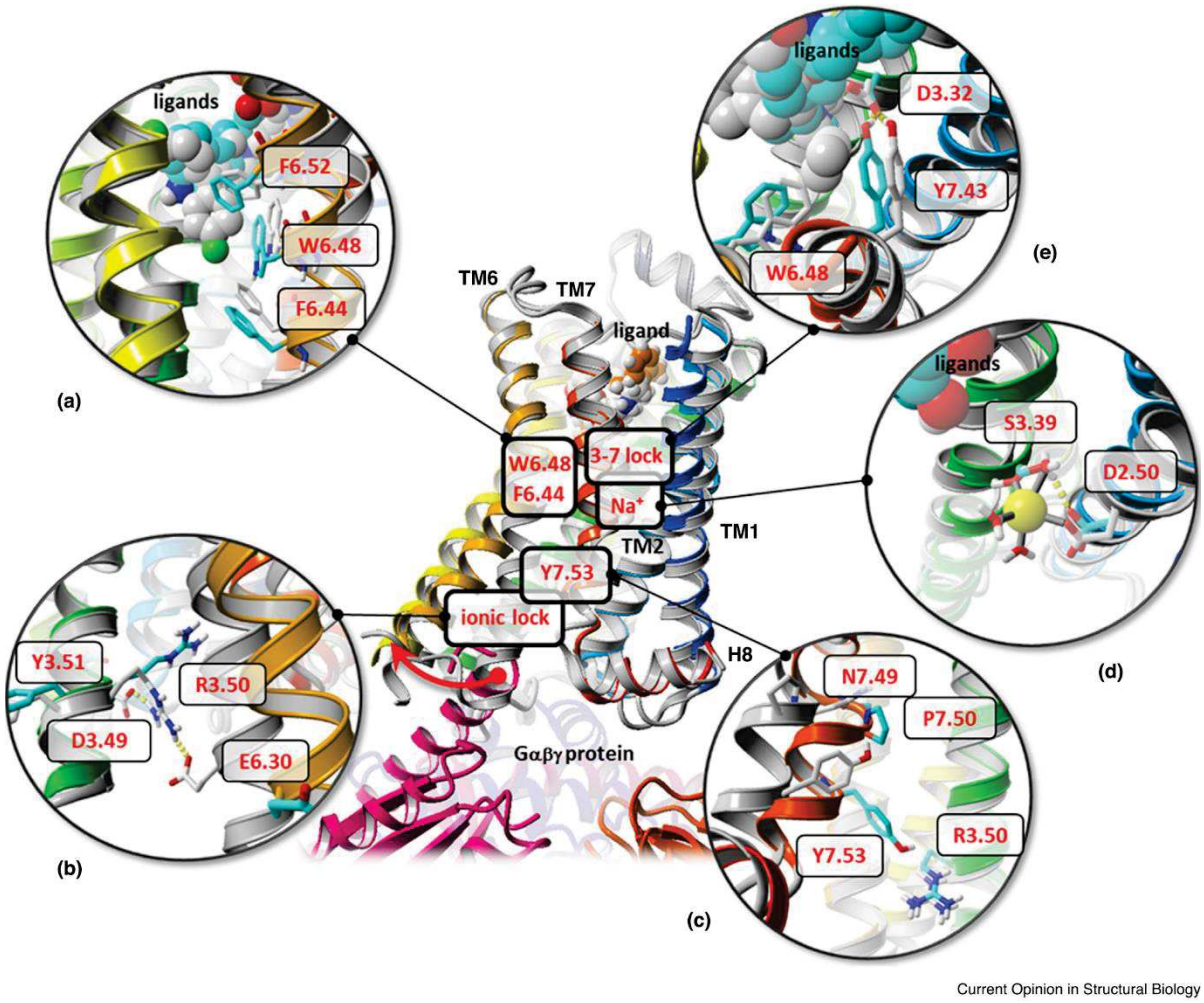

Figure 1-40 Major molecular switches in GPCRs.
(a) W6.48 tryptophan toggle switch and transmission switch in serotonin 5-HT2C receptor (active: 6BQG, agonist ergotamine; inactive: 6BQH, antagonist ritanserin). (b) Ionic lock in DRY motif of rhodopsin (active: 2X72; inactive: 1GZM). (c) Y7.53 tyrosine toggle switch in NPxxY motif of adenosine A2A receptor (active: 2YDO, inactive: 3RFM). (d) Sodium ion binding site in adenosine A2A receptor (active: 3QAK, inactive: 4EIY). (e) 3–7 Lock in opioid receptor mOR (active: 5C1M, inactive: 4DKL). The antagonist is stabilizing the position of Y7.43 so its transient movement is not possible. The inactive receptor–ligand structures are shown in gray while the ligands are shown as van der Waals spheres. The circular panels show the crystal structures with hydrogen atoms added to visualize hydrogen bonds. TM colors: TM1 in blue, TM2 in cyan, TM3 in green, TM4 in yellow–green, TM5 in yellow, TM6 in orange, TM7 in orange–red, and H8 in red. (Filipek 2019)

Interestingly, recent investigations unraveled differences in activation between Class A and Class B GPCRs. Indeed the activation of class B receptors occurs in two steps: the active TM6 adopts a different conformation than in Class A receptors, with a stronger kink and a disruption in helicity on the extracellular side of the TM6. This mechanism involves a high-energy barrier to cross. Thereby ligand binding is not sufficient to induce TM6 outward displacement but will favor an intermediate state. The TM6 activation happens upon G protein binding only, unlike Class A GPCRs. Moreover, TM6 stays in an active conformation after G protein activation and

dissociation. This evidence explains why class B receptors are less efficient than Class A in terms of G protein signaling and their long-term sustained cAMP signaling once activated (Figure 1-41) (Hilger et al. 2021).

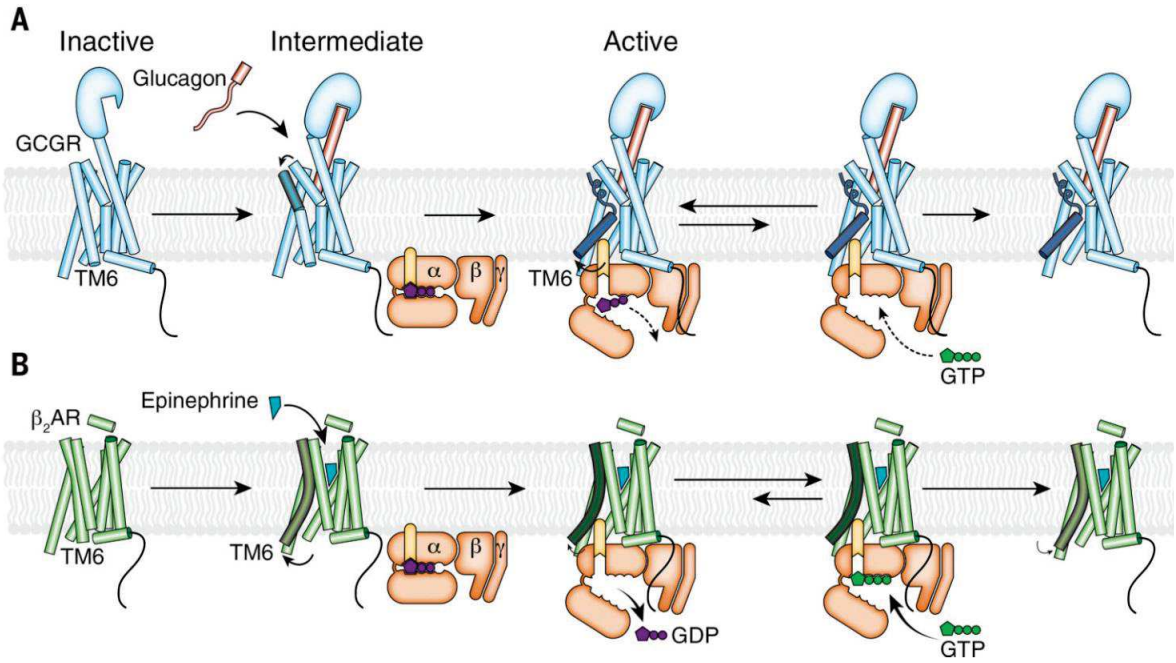

Figure 1-41 Proposed model for GCGR activation and signaling in comparison with β2AR
(A) Glucagon binding to GCGR induces conformational change on the extracellular side of the receptor (ECD, TM1, TM2, TM6, and TM7) without inducing outward movement of TM6 on the intracellular side. Coupling of GDP-bound Gs enables TM6 outward movement. The putative high energy required to produce the kinked and outward-moved TM6 may result in slower rates for the receptor-catalyzed nucleotide release of GCGR in comparison with β_2AR. Another rate-limiting step for GCGR-mediated G protein activation is GTP binding to the nucleotide-free G protein that leads to dissociation of the G protein from the receptor. After disengagement of the G protein, relaxation of TM6 to the inactive state is very slow, which might lead to the previously observed prolonged G protein signaling of GCGR in comparison with β_2AR . (B) β2AR activation by an agonist increases the active state population of the receptor with an outward-moved TM6. Gs coupling to β2AR fully stabilizes the active state and leads to rapid GDP release. The very transient nucleotide-free complex exhibits a high affinity for GTP that readily binds and dissociates the complex. After disengagement of the G protein, β_2AR relaxes back to the more conformational heterogeneous agonist-bound but G protein-free state. (C) Model of the simplified free energy landscapes for GCGR and β_2AR. Shown are the effects of agonist, G protein coupling, and GTP binding to the receptor–G protein complex on the equilibrium between the inactive and active states of the receptors. (Hilger et al. 2021)

Class C GPCRs are obligatory dimers. Ligand binding to the VFT leads to rearrangements of the TMs within the dimer. While in the inactive state two TM bundles are well separated, in ligand-bound structures, there is a TM rearrangement allowing rotation of the two helix bundles and bring them close to each other with a TM6 common interaction interface, as describe for mGlu5R and $GABA_BR$. Furthermore recent $GABA_BR$-Gi investigation demonstrates Class C dimers to be just able to bind one G protein because of steric constraints. G protein binding to

$GABA_BR$ induces new rearrangements of ICL3 and movements of TM3, 4, and 5 (Figure 1-42) (Dutta et al. 2019; Mao et al. 2020).

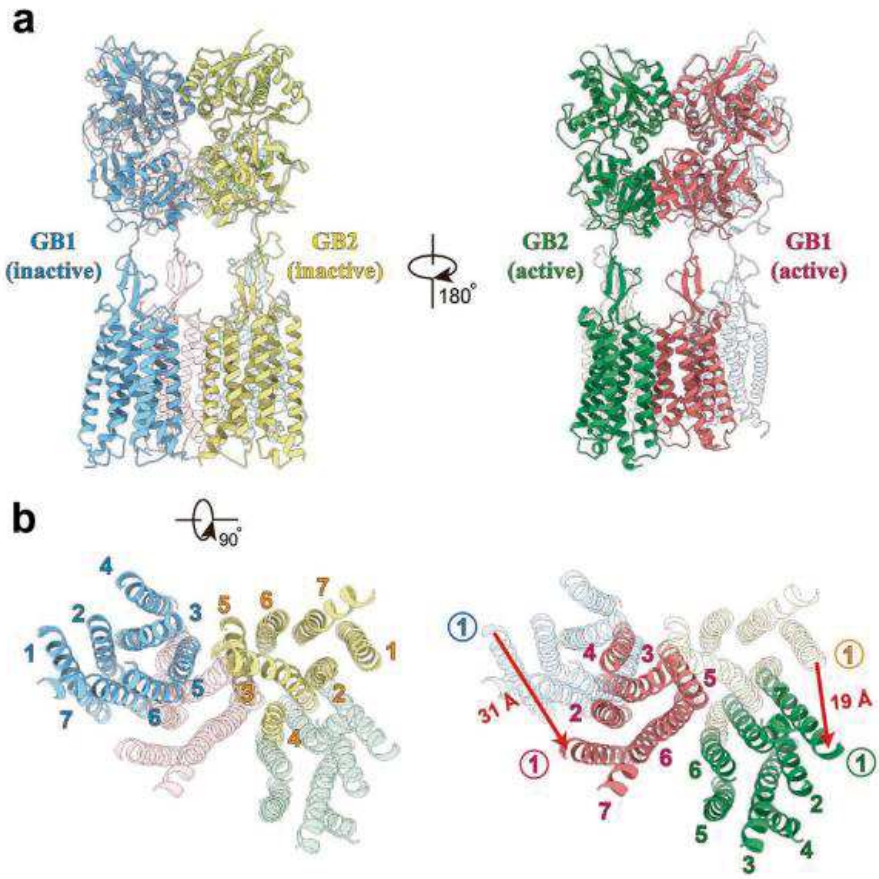

Figure 1-42 Structural comparison of GABAB receptor in inactive and active states
a, b Orthogonal views of the superimposed structures of GABAB receptor in inactive and active states, showing the domain repositioning upon agonist binding-induced activation. Side views (a) and intracellular views (b) of superposed structures are shown, with the active structure in translucent in the left panels and the inactive structure in translucent in the right panels, respectively. VFT domains and loops are omitted for clarity in b. Red arrows indicate the translation direction and distance for GB1 and GB2 (measured at extracellular tips of TM1 helices), respectively. Structures were aligned on the combined domains of GB1 VFT and GB2 lobe 1, the relatively stable parts of the receptor along the activation pathway (Mao et al. 2020)

There is currently only one active state structure of a class D receptor, the Saccharomyces cerevisiae pheromone receptor Ste2 (Velazhahan et al. 2021). This receptor forms a dimer by the N terminus, the transmembrane helices H1, H2, and H7, and the first extracellular loop ECL1. In contrast with class C GPCRs, the dimer binds to two G-proteins Gpa1–Ste4–Ste18. It shares a common TM orientation with mammalian GPCRs with exception of H4. Analogous motifs to the Class A microswitches are found and allow Ste2 activation with similar mechanisms. Also in this structure, G-protein binds more superficially as compared to

monomeric GPCRs. Indeed, the G-protein-binding site is a shallow groove rather than a cleft (Figure 1-43).

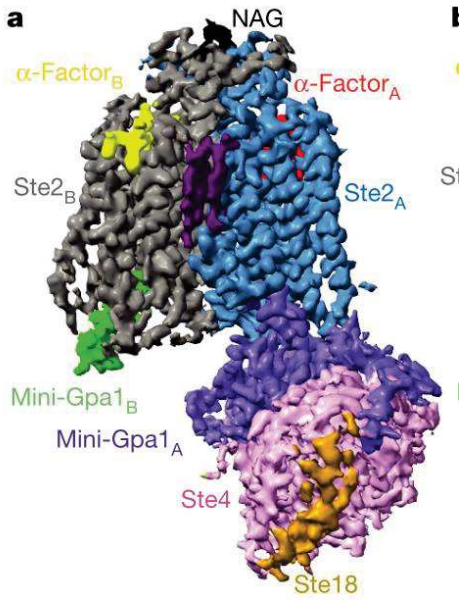

Figure 1-43 overall structure of the Ste2–G-protein heterotrimer complex
The overall structure of the Ste2–G-protein heterotrimer complex is shown as a cryo-EM density map (sharpened with a B factor of -112 Å^2) consisting of a Ste2 dimer (blue, grey), two bound α-factor ligands (red, yellow), two coupled G proteins, six putative CHS molecules (purple) and two N-acetylglucosamine (NAG) molecules (black) (Velazhahan et al. 2021).

Class F GPCR lacks the conserved motifs that are crucial for GPCR-G protein activation in Class A, such as the DR(E)Y or the NPxxY motifs, and a precise activation pattern is still missing. Nonetheless, it was recently demonstrated that FZD5 exhibited a conformational change after the addition of WNT-5A, which is reminiscent of class A and class B GPCR activation. In addition, they performed several live-cell imaging and spectrometric-based approaches, such as dual-color fluorescence recovery after photobleaching (dcFRAP) and resonance energy transfer (RET)–based assays that demonstrated that FZD5 activated Gαq and its downstream effectors upon stimulation with WNT-5A (Wright et al. 2018). Furthermore, the recently published active structure SMO-Gi all display an outward movement of the TM6 relatively to inactive structures (Figure 1-44) and dramatic reorientation of the CRD (P. Huang et al. 2016; Qi et al. 2020). The cholesterol located deep in the catalytic pocket might be critical for receptor activation. More active structures of active complexes are needed to better understand their activation.

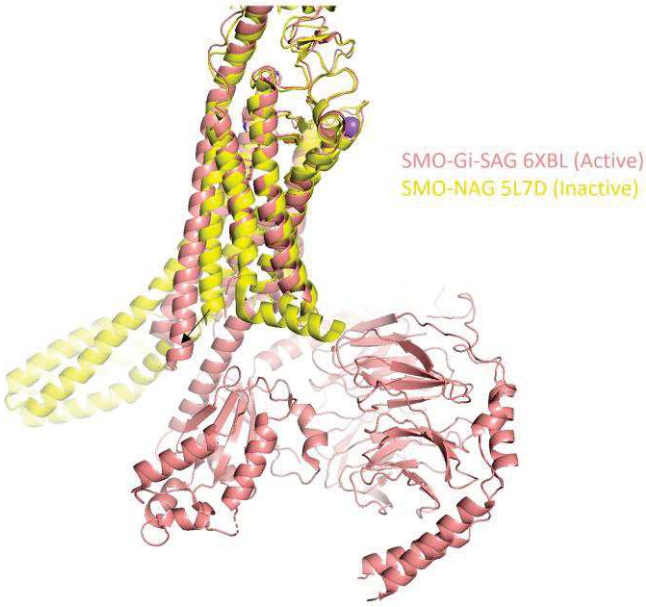

Figure 1-44 Structural comparison of SMO receptor in inactive and active states
SMO-Gi-SAG (PDB: 6XBL) active receptor superposed with the SMO-NAG (PDB: 5L7D) inactive receptor. The active form displays an outward motion of the TM6 to accommodate α5 Gi helix binding.

1.6.5 Biased agonism

Another challenge in GPCR structural biology is to understand the structural modifications mediating activation upon biased agonist binding (Figure 1-45). Indeed, some agonists direct or bias the signaling toward one pathway or another. For instance, the structure of the arrestin-biased drug ergotamine-bound 5-HT_{2B} serotonin receptor (Wacker et al. 2014), revealed how ergotamine stabilizes a distinct receptor conformation in which motifs that are essential for arrestin-biased signaling (e.g., NPxxY) are activated, while others associated with G protein signaling (e.g., DRY or PIF) remain in the inactive state. (Wacker, Stevens, and Roth 2017).

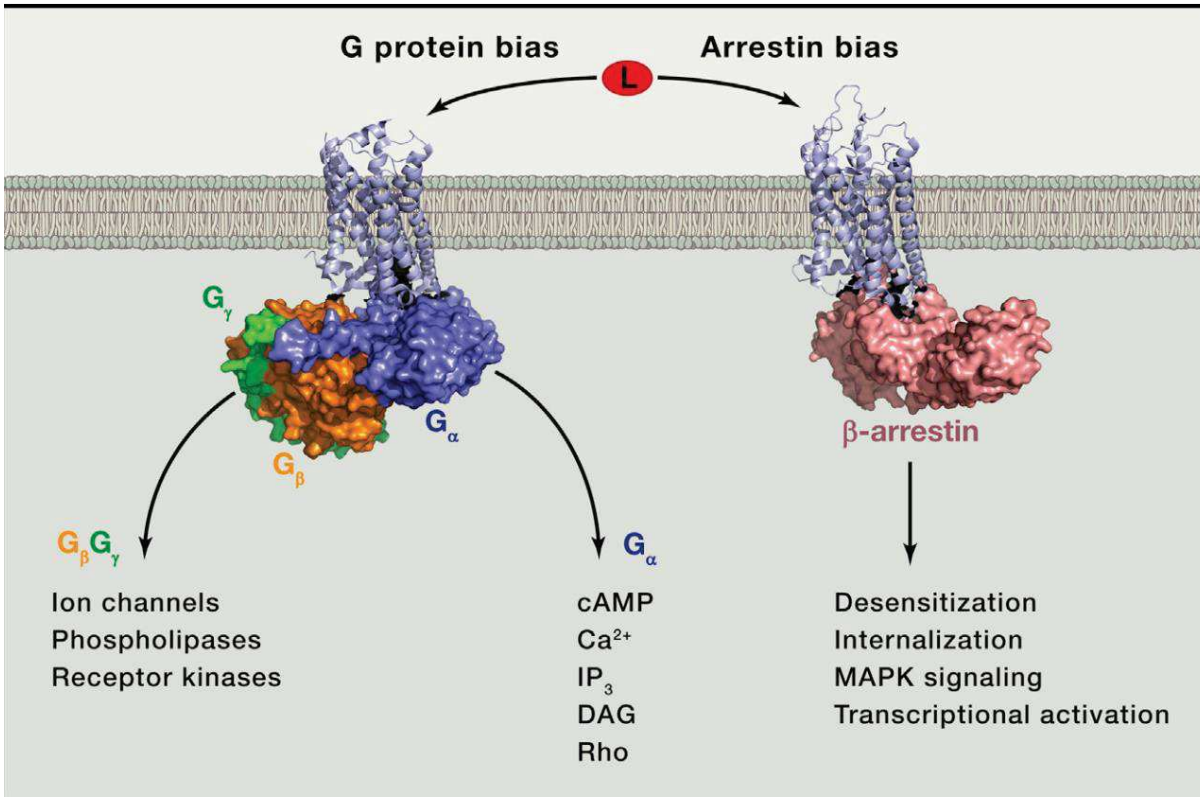

Figure 1-45 GPCRs cannonical activation ans desensitization pathways
Different ligand-stabilized GPCR conformations cause binding and activation of distinct signal transducers, including G proteins and arrestins (Wacker, Stevens, and Roth 2017)

1.6.5.1 GPCR-G Protein complexes

1.6.5.1.1 Generalities

The Gα subunits are composed of two domains: (i) the GTPase domain (Ras-like domain) involved in the binding to GPCRs through the α5 helix (the C-terminal domain of Gα), and GTP hydrolysis, (ii) the helical domain which buries the GTP within its core. The Gα subunits also include three flexible regions, namely switches I, II, and III with the property to become more rigid upon GTP binding.

The Gβ subunit is a β propeller structure containing seven WD-40 repeats. The Gγ subunit interacts tightly with Gβ through a coil-coil interaction along to the N-terminus of Gβ. The Gβγ dimer binds to a hydrophobic pocket accessible in Gα bound to GDP. GTP binding releases this interaction and leads to the dissociation of Gα and Gβγ (Cabrera-Vera et al. 2003) (Figure 1-46).

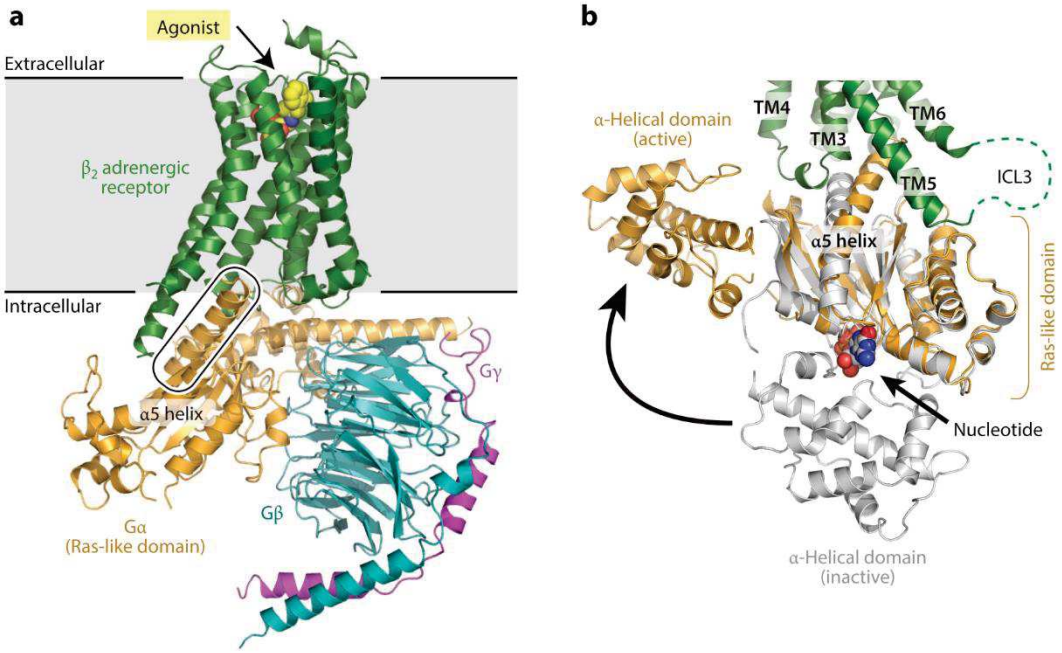

Figure 1-46 Structure of the β2 adrenergic receptor Gs heterotrimer complex
(PDB ID: 3SN6). The G protein α5 helix is the primary site of receptor–G protein interactions and is circled. (b) Conformational changes upon G protein activation are shown, with the GTPγS-bound Gs αsubunit in gray (PDB ID: 1AZT) and its nucleotide-free receptor-coupled conformation in orange. Receptor-catalyzed opening of the interface between the Gs αsubunit Ras-like domain and α-helical domains allows nucleotide exchange. (Erlandson, McMahon, and Kruse 2018)

1.6.5.1.2 Structural features of G proteins in complex with GPCRs

GPCR-G protein complexes show strong conservation in molecular contacts, nonetheless, differences in their interface can be noted between receptors from different families bound to different G proteins. The surface of the interface is variable, from 844 $Å^2$ in the $5HT_{1B}$R-Go complex to 1487 $Å^2$ in the β_2AR-Gs complex (García-Nafría and Tate 2019b). The helix α5, the main component of the interaction with the GPCRs, adopts a common conformation in GPCR-G protein complexes, a wavy hook at its extreme C-terminus. However, the helix α5 displays variation in orientation relative to the receptor in the different structures (Figure 1-47). It results in variability into contacts at the receptor-G protein interface and induces variations in the position of the whole G heterotrimeric regarding the receptor, making it possible or not for the Gβ to contact the receptor.

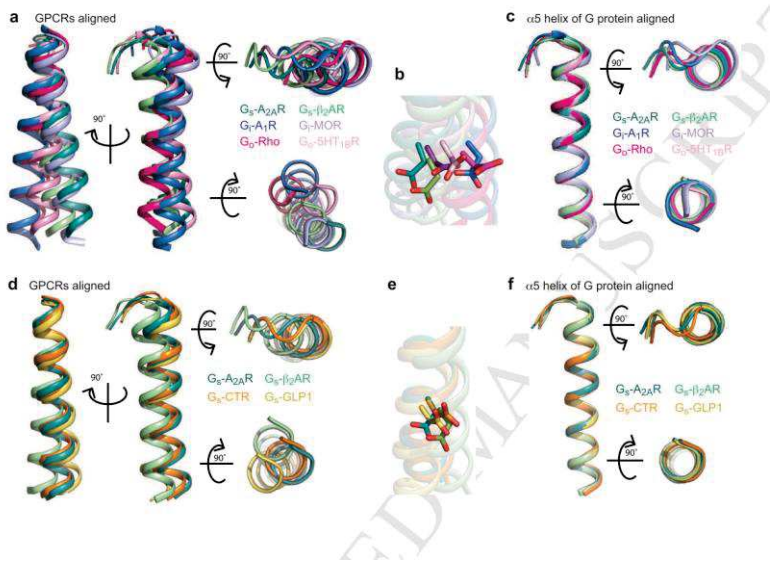

Figure 1-47 Variations in orientation and structure of the α5 helix of the G protein
a, Class A GPCRs coupled to different G proteins were aligned (GESAMT, ccp4 program suite) and the difference in orientation of the α5 helix was depicted. b, The Asp residue DH5.13 is depicted in stick representation using the same alignment as in a. c, The α5 helices were aligned (PyMol) and depicted in the same color scheme as the previous panels. d, Alignment of GPCRs coupled to Gs were aligned (GESAMT, ccp4 program suite) and the α5 helix depicted. e, The Asp residue DH5.13 is depicted in stick representation using the same alignment as in d. f, The α5 helices were aligned (PyMol) and depicted in the same color scheme as d-e. (García-Nafría and Tate 2019b)

The Gβ subunit interaction with GPCRs is also strongly variable among structures. For μOR-Gi, Rho-Gi, and $5HT_{1B}$R-Go complexes, the Gβ subunit doesn't contact the receptor. In contrast, the Gβ subunit strongly interacts with the calcitonin receptor (CTR) in the CTR-Gs complex. This interaction is common in the Gs-coupled structures but not for Gi and Go except for the adenosine A_1 receptor (A1R). The Gγ subunit never interacts with GPCRs. GPCR coupling induces a conformational change in the α-subunit of the G protein. Indeed, The C-terminal domain helix α5 moves by ~6 Å away from the nucleotide-binding site (Sŏren G.F. Rasmussen et al. 2011). This movement leads to the opening of the nucleotide-binding site and the release of the GDP (Figure 1-46).

Crystal and CryoEM GPCR structures have now been reported for receptors in complex with Gs, mini-Gs, Gi, Go, mini-Go, and G11. There are similarities and differences between those signaling complex structures. For most of the GPCR-G protein complexes, the overall assembly and binding mode of GPCRs and G proteins are similar (Figure 1-48). Major interactions between GPCRs and G proteins occur at the cytoplasmic ends of TM3, TM5, and TM6, and the intracellular loops (García-Nafría and Tate 2019b; J. Wang, Hua, and Liu 2020).

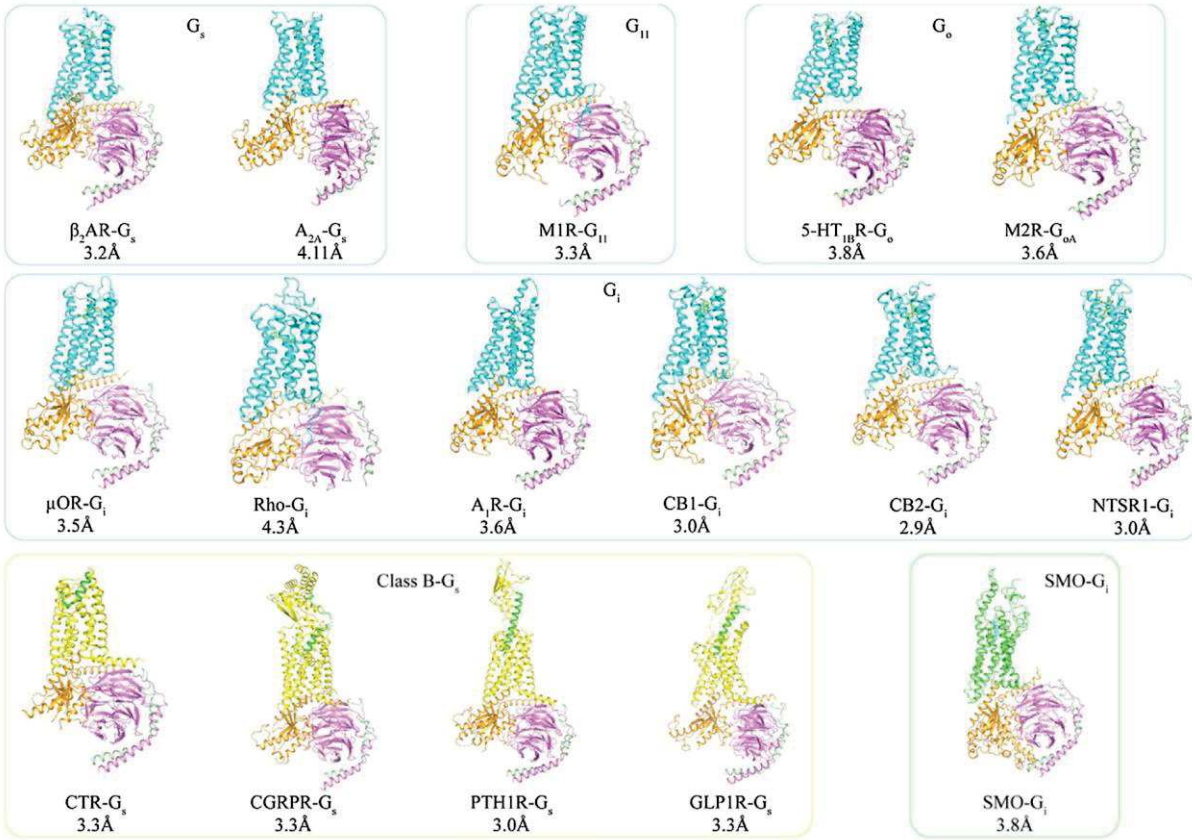

Figure 1-48 Overall architectures of GPCR-G protein/arrestin complexes
The G protein-bound structures include b2AR-Gs (PDB ID 3SN6), A2AR-Gs (PDB ID 6GDG), M1R-G11 (PDB ID 6OIJ), 5-HT1BR-mini-Go (PDB ID 6G79), M2R-GoA (PDB ID 6OIK), m-OR-Gi (PDB ID 6DDE), Rhodopsin (Rho)-Gi (PDB ID 6QNO), A1R-Gi (PDB ID 6D9H), CB1-Gi (PDB ID 6KPG), CB2-Gi (PDB ID 6KPF), NTSR1-Gi (PDB ID 6OS9), CTR-Gs (PDB ID 6NIY), CGRPR-Gs (PDB ID 6E3Y), PTH1R-Gs (PDB ID 6NBF), GLP1R-Gs (PDB ID 6B3J) and SMO-Gi complex (PDB ID 6OT0). The GPCR-arrestin structures include Rho-arrestin 1 (PDB ID 5W0P) and NTSR1-arrestin 2 (PDB ID 6PWC). The receptors for class A, class B, and class F GPCRs are shown as cyan, yellow and green cartoon, respectively. The agonists are shown as green sticks/cartoon in all complex structures. The Ga, Gb, and Gg subunits in G protein are shown as orange, magenta, and green cartoon, respectively. Arrestin 1 and Arrestin 2 are shown as orange cartoon. (J. Wang, Hua, and Liu 2020)

There is low sequence conservation between α-subunits in the regions that make contact with receptors, so this likely plays important role in defining specificity. (García-Nafría and Tate 2019b)

Interestingly, two Gi protein binding modes were reported for the NTSR1. The canonical state and the non-canonical state have been demonstrated to be two steps in the activation mechanism, with the non-canonical state as an intermediate in activation and the canonical state as a fully activated state. The difference between both states is an inward movement of Y7.53 in the NPXXY motif on the intracellular end of TM7, and the Gi heterotrimer rotating by about

45° relative to the receptor. This was only reported for the NTS1 receptor to date (Figure 1-49) (Kato et al. 2019).

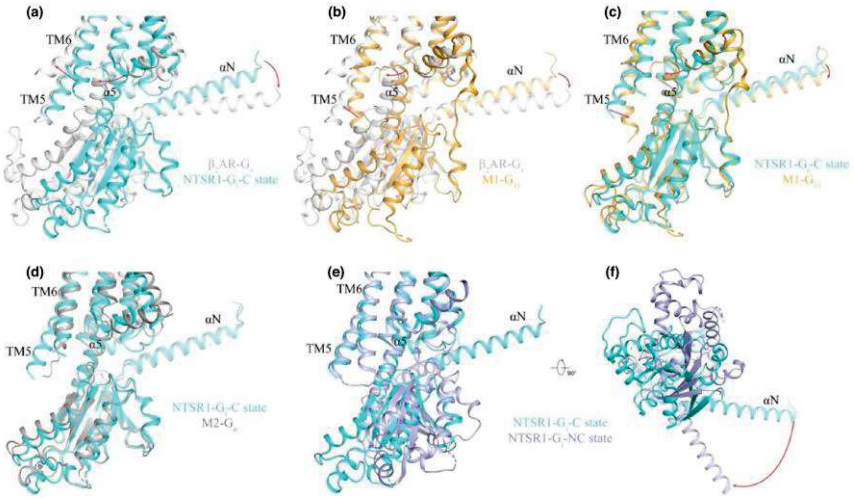

Figure 1-49 Comparison of the interaction interfaces of different G protein subunits among GPCR-G protein complexes
(a–d) Comparison of the receptor- Ga subunit interface between NTSR1-Gi-C state (PDB ID 6OS9) and β_2AR-Gs (PDB ID 3SN6) (a), β_2AR-Gs (PDB ID 3SN6) and M1R-G11 (PDB ID 6OIJ) (b), NTSR1-Gi-C state (PDB ID 6OS9) and M1R-G11 (PDB ID 6OIJ) (c), and NTSR1-Gi-C state (PDB ID 6OS9) and M2R-GoA (PDB ID 6OIK) (d). The NTSR1-Gi-C state is colored as cyan, b2AR-Gs is in light grey, M1R-G11 is in yellow and M2R-GoA is colored dark grey. (e) and (f) Comparison of the NTSR1-Gi-C state and NTSR1-Gi-NC state complexes. The NTSR1-Gi-C state presents a fully active conformational state (canonical, C) and the non-canonical (NC) state of NTSR1 bound to Gi state is a putative intermediate state. The two states are colored as cyan and purple, respectively.

1.6.5.2 GPCR-Arrestin complexes

1.6.5.2.1 Generalities

Structures of the four arrestin subtypes in their unbound state are resolved and display a common global folding (Granzin et al. 1998; Hirsch et al. 1999; Han et al. 2001; Zhan et al. 2011; Sutton et al. 2005).

Arrestins can be divided into two major domains, the N-domain and C-domain (N and C lobes), with each domain primarily consisting of anti-parallel β-sheets connected by short flexible loops, the finger loop (critical in GPCR binding), middle loop, and lariat loop. The N- and C-domains are linked by a flexible region composed of a dozen of amino acids, the hinge domain. The N- and C-termini are not structured and the C-terminus is buried into the N-domain. A polar core of buried salt bridges between N- and C-domains stabilizes the overall structure. (Figure 1-50) (Han et al. 2001; Milano et al. 2002, 2006; Kang et al. 2009; Zhan et al. 2011). Mutations of residues involved in the polar core and C-terminus position are critical for GPCR

binding, highlighting the key role of this region for arrestin functionality (Kovoor et al. 1999a; Celver et al. 2002; Gray-Keller et al. 1997; Gurevich and Gurevich 2013; Wilden, Hall, and Kuhn 1986).

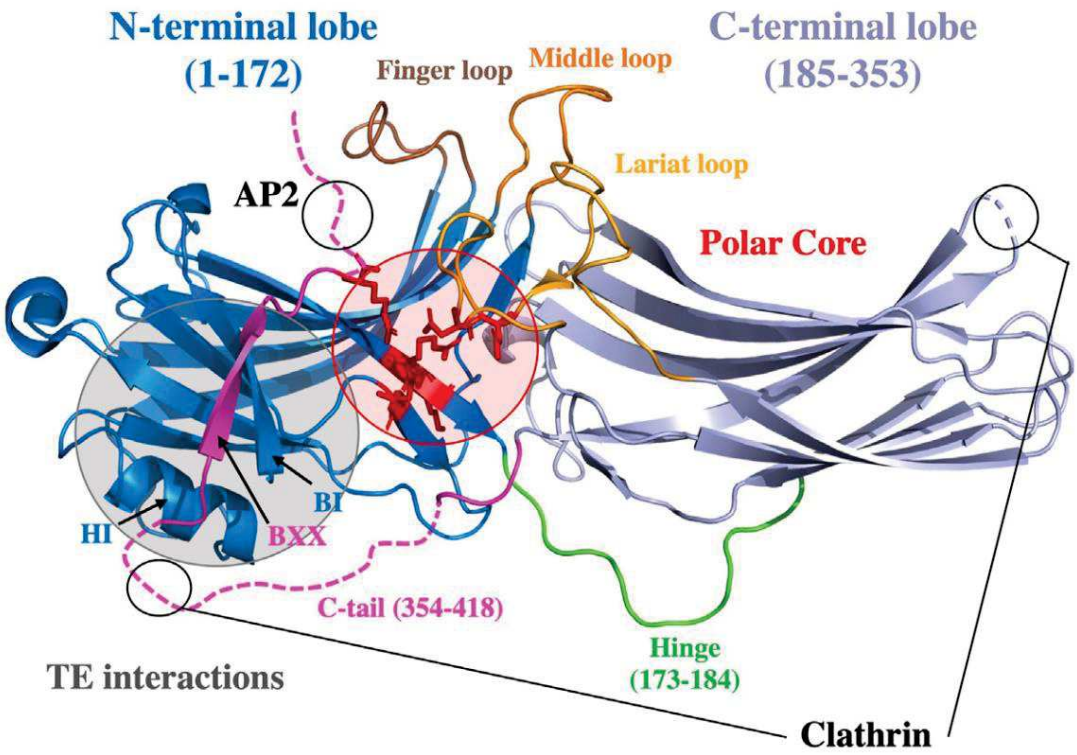

Figure 1-50 Common structural organization of arrestin family
(PDB:1G4M/X-ray structure of arrestin2 inactive state of Ref. 130). Arrestin family shares similar elongated shape and present two concave lobes mostly composed of antiparallel β-sheets: an N-terminal lobe (blue; residues 1–172) and a C-terminal lobe (light blue, residues 185–353), linked by a hinge in green (residues 173–184); flexible loops: finger loop (brown), middle loop (orange) and lariat loop (light orange). The polar core is highlighted by a red circle, mostly composed of charged amino acid (in red, main and side chain of polar core res- idues) and the three-elements (TE) interaction highlighted by a gray circle involving β-strand 1 and 20 (BI and BXX) and α-helix 1 (HI). Arrestin C-tail (pink, residues 354–418) encompasses β-strand 20 (BXX) (which interact with the N-terminal lobe in the "closed" state). Concerning non-visual arrestin isoform, its C-tail contains AP2 bind- ing site (391FARQRLK397; not present in the structure) and one clathrin binding site (376LIELD380; not present in the structure), the second clathrin binding site is localized in a flexible loop of C-terminal lobe (black circles) (Guillien et al. 2020)

1.6.5.2.2 Structural features of arrestins in complex with GPCRs

The arrestins are maintained in their inactive state by two interaction networks: (i) the salt bridges between Asp290/Asp297 (C-Domain) and Arg169 (N-Domain) /Arg393 (C-ter), (ii) the "three-element" (TE) interaction motif involving C-ter βXX strand with β1 strand and H1 helix in the N-domain. The binding of the phosphorylated GPCR C-terminus to the arrestin N-Lobe results in the destabilization of the polar core and in the disruption of the TE interactions. It subsequently releases the arrestin C-terminal domain. The β-arrestin AP2 binding site located

in the C-terminus, until then inaccessible, is thus able to interact with the AP2 β2-appendage domain (Figure 1-51).

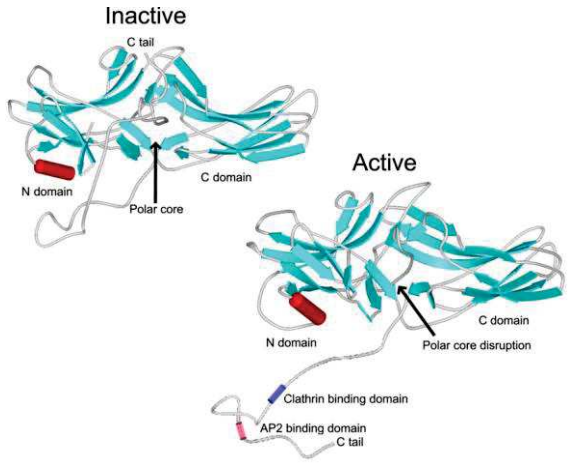

Figure 1-51 Model of Inactive and Active Conformations of b-Arrestin
The inactive conformation of b-arrestin2 displaying an intact polar core at the junction of N and C domains with the C tail in close proximity to the junction. Activation of b-arrestin2 via interaction with the phosphorylated tail of an activated receptor promotes the disruption of the polar core and allows for release of the C tail, exposing both clathrin and AP2-binding domains.(Lefkowitz, Rajagopal, and Whalen 2006)

Recent EM investigations demonstrated that arrestin can bind a GPCR in at least two conformations. In the classic model, the arrestin N-Domain interacts with the receptor C-terminus (hanging conformation) leading to receptor core coupling (core conformation). Moreover, new structural data suggest an interaction of the C domain of β-arrestin with the lipid bilayer. This might stabilize the complex in its core conformation (Figure 1-52) (Y. Lee, Warne, Nehmé, et al. 2020; Staus et al. 2020a; W. Huang et al. 2020).

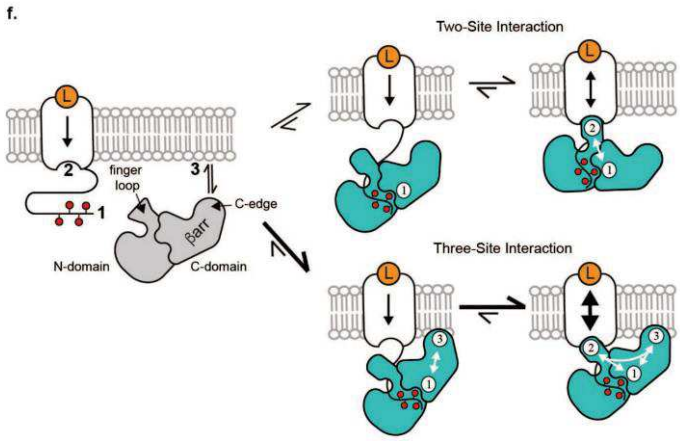

Figure 1-52 Three-site interaction network of GPCR–βarrestin binding
In the classic two-site interaction model, conformational changes in β-arrestin induced by binding to the phosphorylated receptor (1) lead to transmembrane receptor core coupling (2) to sterically block G protein binding. Our findings suggest an expanded model including the interaction of the C domain of β-arrestin with the lipid bilayer (3) because it synergistically enhances the interaction of β-arrestin with the phosphorylated receptor tail/ loops and transmembrane core. Vertical arrows in the receptor represent direction and strength of cooperativity between the extracellular orthosteric ligand-binding and intracellular transducer-binding sites.

Structures of GPCR-arrestin complexes have been resolved for four GPCRs: rhodopsin-Arr1 (X. E. Zhou et al. 2017; Y. Kang et al. 2015), β1ARr-βArr1 (Y. Lee, Warne, Nehmé, et al. 2020), M2R-βArr1 (Staus et al. 2020a), and NTSR1-βArr1 (W. Huang et al. 2020; Yin, Li, Jin, Yin, Waal, et al. 2019).

The overall structures display striking differences. Indeed, the relative binding orientation between arrestin and receptor is strongly variable. NTSR1 and β1AR coupling to βArr1 differs by approximately 80° rotation perpendicularly to the membrane plane, and by a 10° rotation towards the membrane, potentially due to the structures being determined in detergent (Figure 1-53).

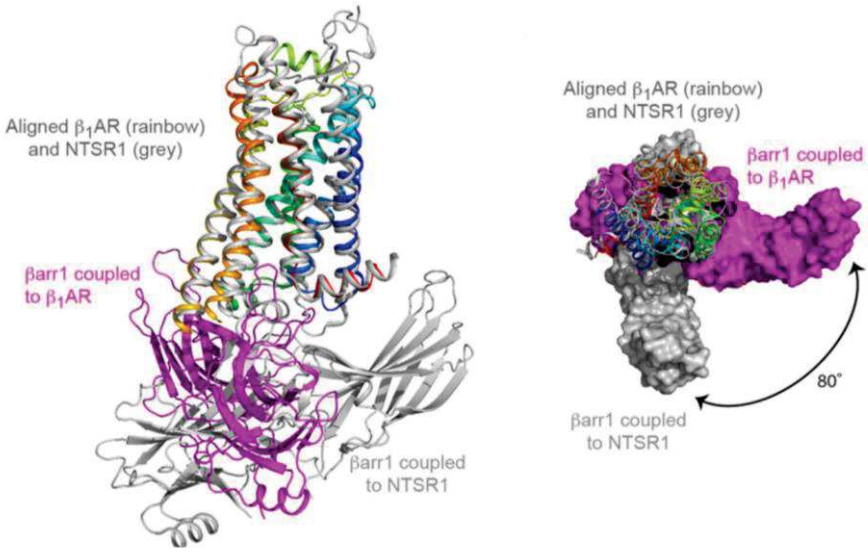

Figure 1-53 Structural comparison of β1AR-βarr1 and NTSR1- β1AR
Superposition of β1AR6P (rainbow cartoon) and NTSR1 (grey cartoon) coupled to βarr1 (magenta) and βarr1 (grey), respectively. (Y. Lee, Warne, Nehmé, et al. 2020)

M2-βArr1 and Rho-Arr1 display the same overall orientation as β1AR-βArr1. Another key difference is the variable conformation of the arrestin finger loop, the main component of the interaction with the GPCRs. Indeed, the Arr1 finger loop arranges in an α-helix and interacts superficially with the rhodopsin, whereas for β1AR-βArr1, the βArr1 finger loop arranges as a β-hairpin which can dive 5Å deeper into the receptor (Y. Lee, Warne, Nehmé, et al. 2020). For M2R-βArr1 and NTSR1-βArr1 complexes, the arrestin finger loop also arranges as an α-helical finger loop, but it displays variability and doesn't superpose with the one in visual arrestin (Arr1) (Figure 1-54).

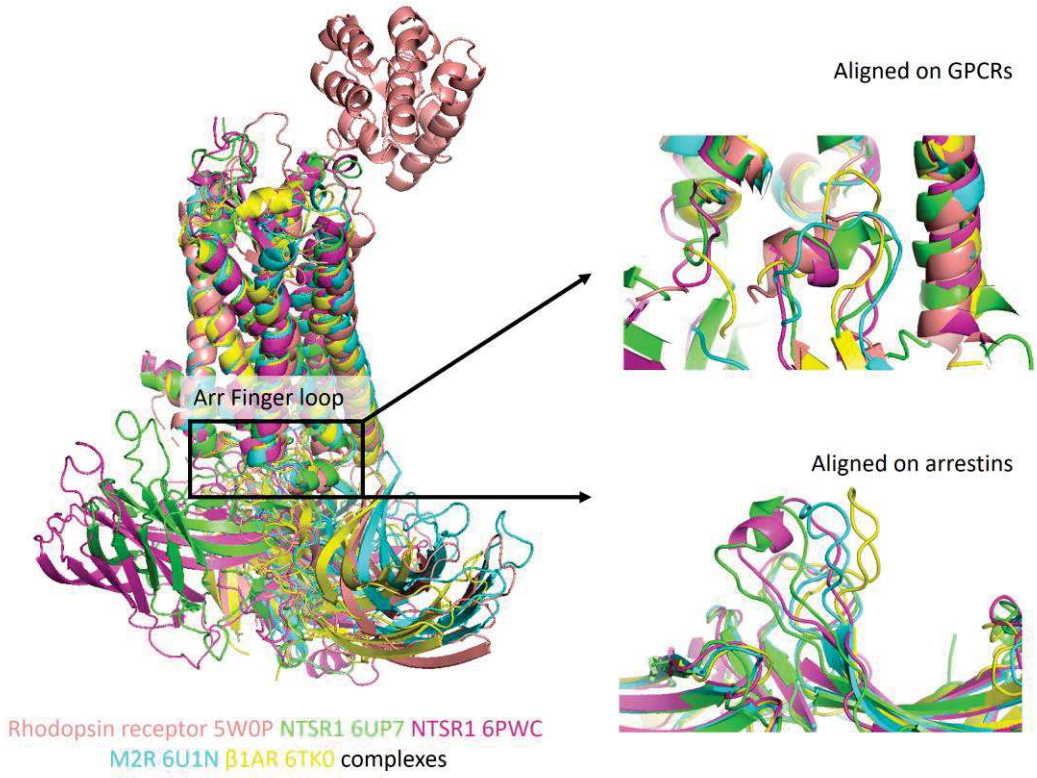

Figure 1-54 Structural comparison of GPCRs-βarr1
Structures of GPCRs-Arrs complexes aligned and inspection of the finger loop variability.

1.6.6 GPCR dynamic properties

CryoEM and X-ray crystallography allowed to dramatically improve our understanding of GPCRs. Nonetheless, these methods highlight discrete highly populated sub-conformations of their conformational landscape and are not suited to investigate dynamic systems. Studies focused on the dynamic aspect of GPCRs demonstrate that the receptors adopt a continuum of conformational states, never observed by crystallography or cryoEM. For example, investigation of β_2AR using fluorescence spectroscopy, fluorine-19 nuclear magnetic resonance , and DEER spectroscopy demonstrated high flexibility (Erlandson, McMahon, and Kruse 2018) (Figure 1-55). Moreover, in agonist saturating concentrations, just a small population of β2AR visits the fully active state. Dynamics have been reported for inactive and active states for several receptors (Sena et al. 2017; Cong, Fiorucci, and Golebiowski 2018; Staus et al. 2016; Ye et al. 2016). This consideration may be taken into account and high-resolution structures alone are not sufficient to describe the complexity of GPCR systems. X-ray crystallography and

cryoEM have to be combined with other techniques to describe a more realistic view of these dynamic proteins.

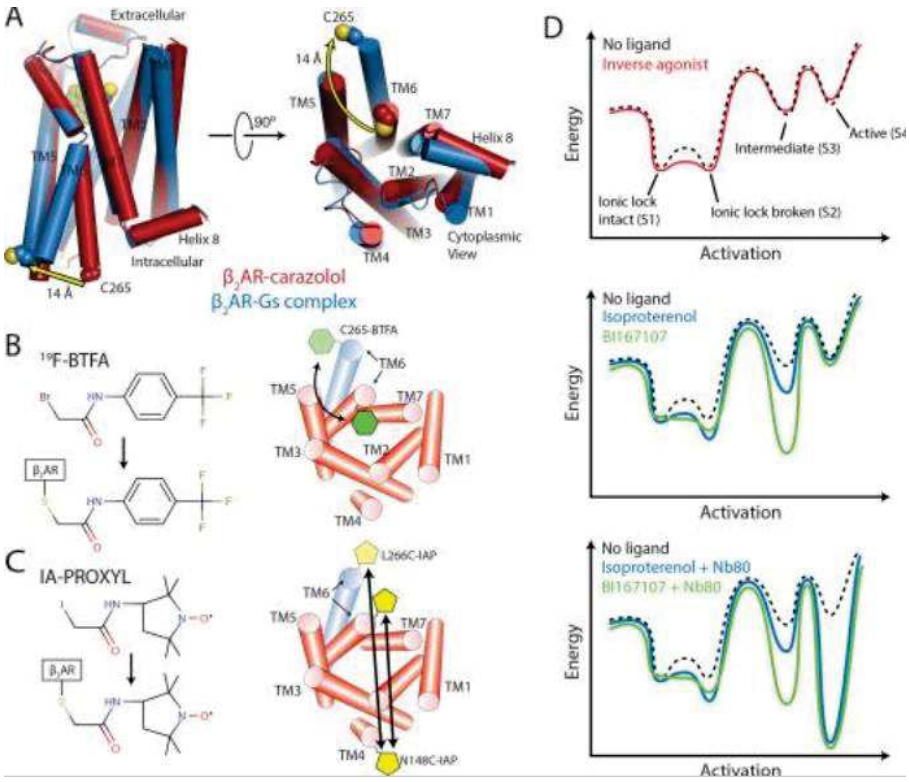

Figure 1-55 Spectroscopic methods for detecting conformational changes of β2AR
(A) Comparison of crystal structures of inactive, carazolol-bound, and active β2AR in complex with agonist BI167107 and Gs. The crystal structures reveal a 14 Å outward displacement of TM6 upon β2AR activation. Cys265, used for 19F-NMR experiments is highlighted in spheres. (B) 19F-NMR studies utilize the fluorine label 2-bromo-4-(trifluoromethyl)acetanilide (19F- BTFA) that reports changes in the chemical environment at the cytoplasmic end of TM6. (C) For DEER spectroscopy, β2AR was labeled at the cytoplasmic ends of TM4 (site N148C-IAP) and TM6 (site L266C-IAP) with the nitroxide label 3-(2-iodoacetamido)-2,2,5,5-tetramethylpyrroline-1-oxyl (IA-PROXYL). (D) Energy landscape of β2AR in the presence of inverse agonists carazolol and ICI-118,551, agonists isoproterenol and BI167107, and agonists with Nb80. (Aashish Manglik et al. 2016)

2 Thesis objectives

My project is focused on the determination of the arginine-vasopressin (AVP) V2 receptor (V2R) structure in complex with its signaling partners G proteins or β-arrestins by cryo-electron microscopy (cryo-EM). The final goal is to understand the V2R function at the molecular scale. The objectives of this work can be divided into sub-sections as below.

AVP-V2R-Gs structure investigation and analysis

V2R governs our body water balance through the control of kidney water reabsorption and is a major therapeutic target widely studied. Despite considerable effort for V2R structural characterization, no structures were available until this study since the receptor remained reluctant to crystallogenesis. The first objective of this work was to take advantage of the Cryo-EM recent advances to elucidate its structure in complex with the natural hormone AVP and its canonical signaling partner Gs protein. It is crucial since the V2R-Gs coupling is responsible for the antidiuretic effect of AVP. The expected outputs resulting from this first study were:

1) to better understand AVP-V2R binding and interpret the new data in a larger context (including data from molecular pharmacology of vasopressin/oxytocin receptors)

2) to characterize a first V2R active state, compare its architecture to that of the inactive OTR structure recently published (Waltenspühl et al. 2020), look at its conformational changes through the modification of activation hallmarks conserved in ClassA GPCRs

3) to interpret on a structural basis V2R missense mutations responsible for two rare genetic diseases, the cDNI where mutations induce a loss of function with an inactive V2R and NSIAD where mutations induce a gain of function with a constitutively active V2R

4) to compare the V2R-Gs interface to that of other GPCR-G protein complexes from classes A and B.

AVP-V2R-βarr1 structure investigation and analysis

The V2R displays a strong affinity for βarr1 and it belongs to class B in terms of arrestin binding. Arrestin-dependent pathways are involved in cellular functions such as MAP kinase activation associated with cell growth and differentiation. This property is strongly dependent on interaction with the C-terminal V2R domain, a key component in arrestin recruitment. By the way, except for the NTSR1-βarr1 complex (W. Huang et al. 2020), all structures of GPCR-βarr1 complexes analyzed by cryo-EM so far, include a GPCR chimera with a V2R-C-terminal domain added to stabilize the complexes (Y. Lee, Warne, Nehmé, et al. 2020; Staus et al. 2020a;

Yin, Li, Jin, Yin, de Waal, et al. 2019). In the light of this information, our second objective, the 3D structure determination of an AVP-V2R-βarr1 complex, was of great interest for both comprehension of V2R activation molecular mechanisms and understanding coupling specificity of arrestins to GPCRs. The specific objectives resulting from this second output were:

1) to compare AVP-V2R binding interactions with those determined in the AVP-V2R-Gs complex active structures

2) to characterize the βarr-specific V2R active conformation and compare it with that in AVP-V2R-Gs complex active structures and with other active structures of class A GPCRs, to discuss the role of V2R C-terminus in the interaction with βarr1 and its pattern of phosphorylation

3) to compare the V2R-βarr1 interface with that of other GPCR-arrestin complexes since there is a strong heterogeneity in coupling among recently published structures

4) to characterize the βarr1 active state and compare it with other active and inactive arrestin structures.

3 Materials and Methods

3.1 Transmission Electron Microscopy: a method of choice to investigate nanoscale objects

3.1.1 Why use electrons? A brief history.

The microscope might be defined as an optical instrument that makes it possible to examine objects or elements invisible or difficult to see with the naked eye. The resolution of a microscope, the ability to distinguish two points close in space, is ultimately limited by the wavelength (λ) of the beam used. Indeed, the relation between resolution and λ is described by the Rayleigh criterion Equation 1 (Rayleigh 1879).

$$r = \frac{0.61\,\lambda}{\mu \sin\beta}$$

Equation 1
λ is the wavelength of the radiation, μ is the refractive index of the medium, β is the semi-angle of collection of the objective, and r is the resolution.

Based on this criterion, the resolution of conventional visible-light microscopes is limited to 200nm. In 1925, Louis de Broglie theorized that the electron had a wave-like behavior, with a wavelength substantially smaller than visible light. Subsequently, two groups independently carried out classic electron-diffraction experiments, which demonstrated their wave-particle duality (Thomson and Reid 1927; Davisson and Germer 1928). Concomitantly, Hans Bush lays the foundations of electronic optics. By calculating the trajectories of electrons in a magnetic field with symmetry of revolution, he showed that they behave in a similar way to light rays in optical systems with symmetry of revolution, thus making it possible to design electronic lenses equivalent to lenses of photonic optics. It didn't take long for the idea of an electron microscope to be proposed. On June 4, 1931, during a conference at the Technical School of Berlin, Hans Bush and his student Ernst Ruska, presented the first images obtained with a two-lens microscope operating at a voltage of a few thousand volts (Figure 3-1) (see for review (Colliex 2008)). On this occasion, they reached a few dozen nanometers in resolution. The fundamental resolution limit of visible-light microscopy was crossed. This was a critical step, for which Ruska received the Nobel Prize in 1986, shortly before his death in 1988.

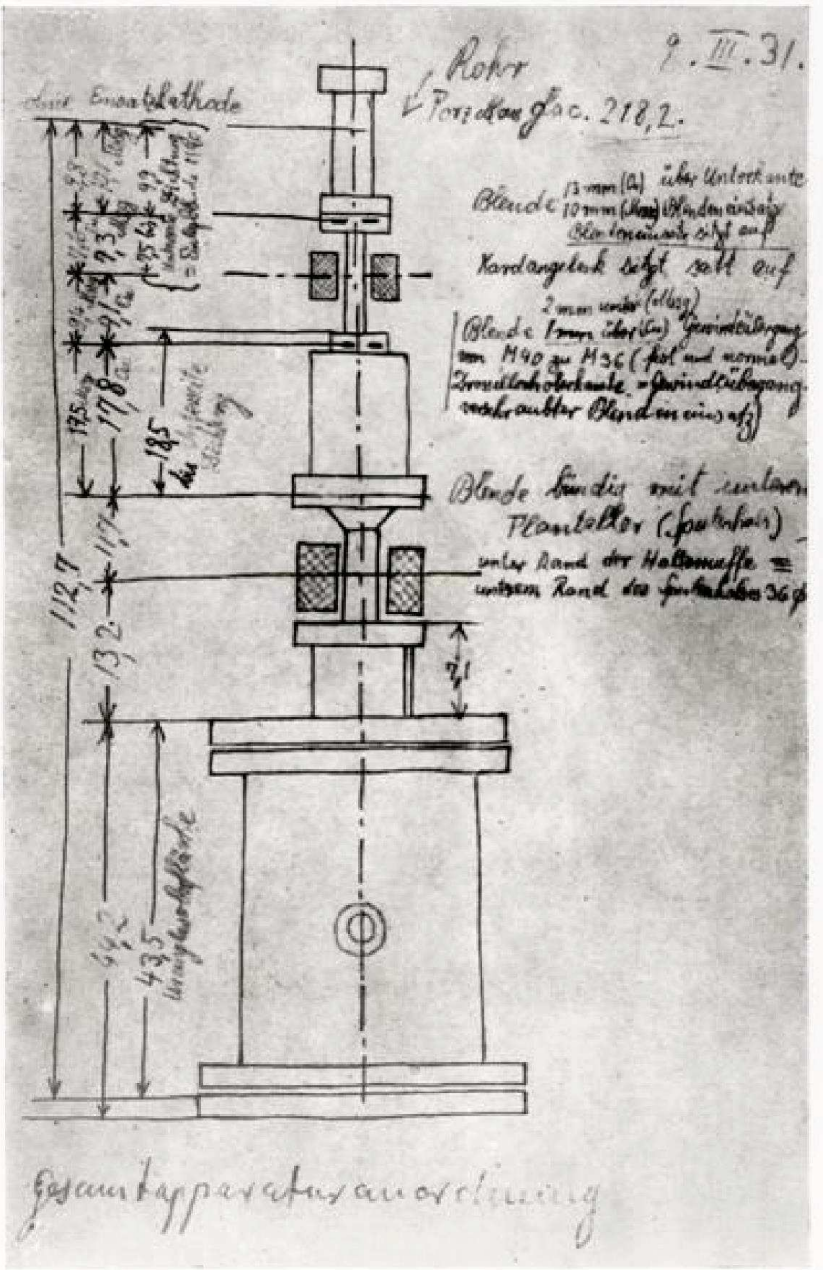

Figure 3-1 Schema of the first electron microscope Ruska (Akademia Leopoldina)

3.1.2 Main components of the electron microscope

3.1.2.1 Overall architecture

The schematic representation of a typical Transmission Electron Microscope is presented in (Figure 3-1). An analogy can be drawn between electron and light microscopes with common overall anatomy whereas the main difference is due to the use of electrons instead of photons as a light source. Thereby, due to electron physical properties, the column has to be under a high vacuum, the physical lenses are replaced by electromagnetic lenses, and the detectors are

specially designed to electrons instead of photons (Figure 3-2). The main components are described in the next sections.

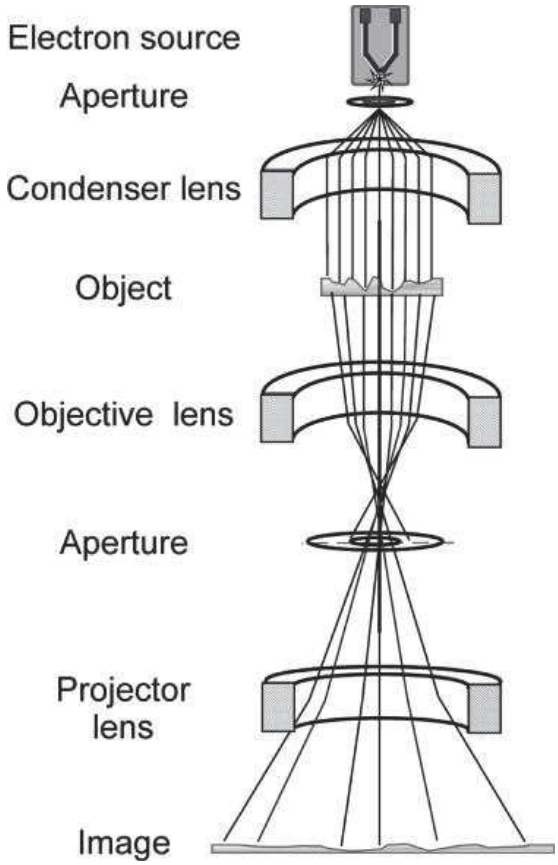

Figure 3-2 Simplified schematic representation of an electron microscope.
(Orlova and Saibil 2011)

3.1.2.2 Electron sources

The electron gun ensures the production of electrons, their acceleration and delivers them to the entrance of the microscope column. It is therefore a complex assembly that must simultaneously fulfill these different functions. It can be represented as an electrostatic lens with several electrodes (Figure 3-3 Figure 3-4

Table).

(https://www.thermofisher.com/blog/microscopy/electron-source-fundamentals/)

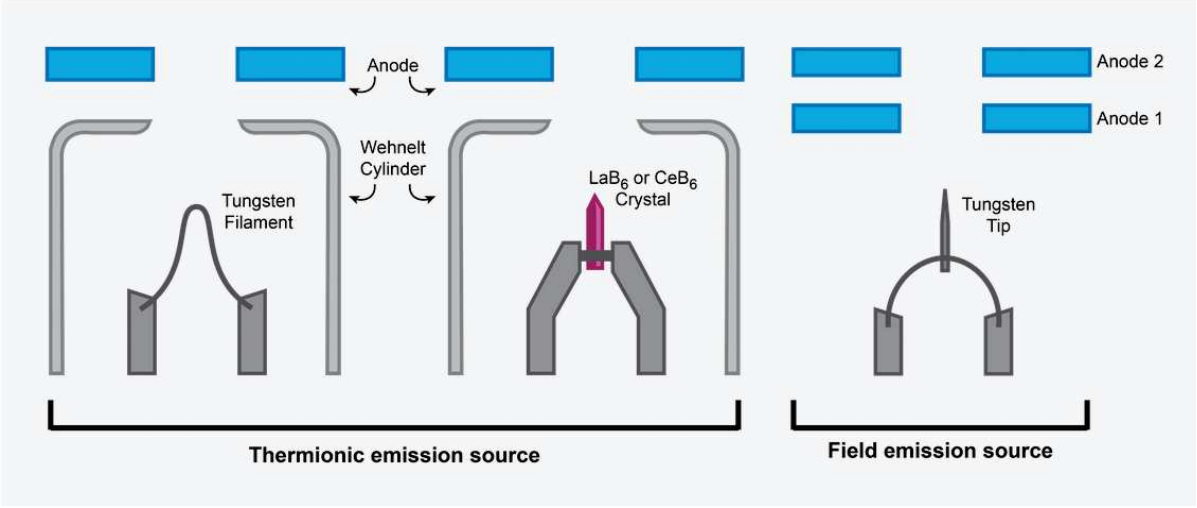

Figure 3-3 Illustration comparing the various electron emission sources
For thermionic sources, the Wehnelt cylinder focuses the electrons as they flow toward the anode. In a field emission source, the first anode accelerates the electrons whereas the second anode focuses them. (https://www.thermofisher.com/blog/microscopy/electron-source-fundamentals/)

There are two main kinds of electron sources: (i) thermionic source, which produces electrons when heated, and (ii) field-emission source (FEG), which produces electrons when an electric potential is applied between it and an anode.

Thermionic sources depend on heat to generate electrons, much like light is produced by incandescent bulbs. When a current is applied to the filament (or crystal), it is gradually heated until its electrons have enough energy to escape from the solid surface. However, the electrons all have to flow in one direction to produce the beam, which is why an anode is placed nearby to attract the electrons and pass them to the column. (Note: here the electron source acts like the cathode, and it is the voltage difference between the anode and the cathode that accelerates the electrons forward.)

Tungsten filament: Tungsten filaments are relatively cheap and easy to maintain; users can easily replace them, eliminating the need for ongoing external maintenance. However, they gradually lose mass due to evaporation and eventually break apart, giving them the shortest lifespan of all sources. Additionally, due to their high operating temperature, they have lower brightness and a wider beam resulting in generally reduced image quality (Figure 3-3 Figure 3-4 Table 1).

LaB6 and CeB6: Lanthanum hexaboride and cerium hexaboride sources are composed of a single crystal of the respective molecule. Just like a tungsten filament, these crystals are heated by an applied current until there is enough energy to emit electrons. Compared to tungsten, lower temperatures are required to emit electrons, resulting in lower beam spread and higher brightness. They are also less volatile than tungsten and therefore have a significantly longer lifetime. However, they also need a higher vacuum, thereby increasing the overall cost of the source (Figure 3-3 Figure 3-4 Table 1).

Electrons field emission guns or (FEGs) use a strong electrostatic field to induce emission of electrons. This field is applied to the sharp tip of a tungsten wire, where the tunnel effect of quantum mechanics allows the release of high energy electrons. The emission area is significantly smaller for a FEG (nanometers) than a thermionic source (micrometers), resulting in higher brightness and, in turn, improved image quality (i.e. say higher spatial resolution and increased signal-to-noise ratio). FEG sources also have the longest longevity, often lasting over a year without replacement. The main disadvantage of FEG sources is the cost; the use of electrostatic fields requires an ultra-vacuum, which makes it more expensive than most thermionic sources. Despite this, the increased resolution, brightness, and lifespan of these sources make them ideal for the widest range of applications (Figure 3-3 Figure 3-4 Table 1).

Schottky FEG vs. cold FEG (CFEG): FEG sources can broadly be divided into Schottky or cold FEGs. As the names might imply, Schottky FEGs are thermally assisted, combining the benefits of thermionic and field emission sources. This is done by coating the tungsten tip in zirconium oxide, which facilitates the thermal emission of electrons when the source is heated. The cold FEGs just recently emerged for biology, they have a longer lifetime, a higher brightness, and a better coherency than the Schottky sources under certain conditions (i.e. lower voltages, where the Schottky emitter has a larger energy spread) (Figure 3-3 Figure 3-4 Table 1).

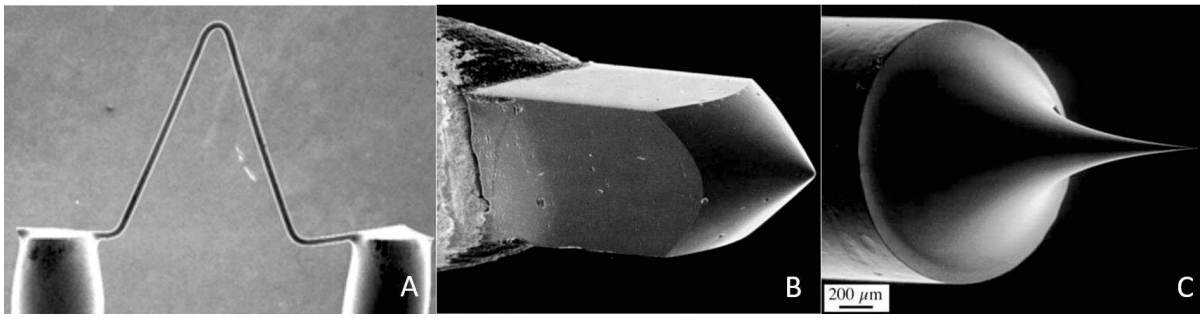

Figure 3-4 Electron light sources
A) V-shaped tungsten filament. B). LaB_6 crystals. C). Field Emission Gun. Adapted from (Williams and Carter 1996)

Table 1 Characteristics of the Principal Electron Sources (Williams and Carter 1996)

	Units	Tungsten	LaB_6	Schottky FEG	Cold FEG
Work function, Φ	eV	4.5	2.4	3.0	4.5
Richardson's constant	A/m^2K^2	6×10^9	4×10^9		
Operating temperature	K	2700	1700	1700	300
Current density (at 100 kV)	A/m^2	5	10^2	10^5	10^6
Crossover size	nm	$> 10^5$	10^4	15	3
Brightness (at 100 kV)	A/m^2sr	10^{10}	5×10^{11}	5×10^{12}	10^{13}
Energy spread (at 100 kV)	eV	3	1.5	0.7	0.3
Emission current stability	%/hr	<1	<1	<1	5
Vacuum	Pa	10^{-2}	10^{-4}	10^{-6}	10^{-9}
Lifetime	hr	100	1000	>5000	>5000

3.1.2.3 Electronic magnetic lenses: principle and operation

Electro-magnetic lenses are the Transmission electron microscopy (TEM)'s equivalent of the glass converging lenses in a visible light microscope. Indeed, due to their negative charge, an electron's trajectory can be bend by an electromagnetic field as described by the Lorentz force Equation 2. The resulting force is always perpendicular to the trajectory of the electron. It always produces work equal to zero and consequently does not modify either the magnitude of the speed or the energy of the electron during the crossing of the field. It just bends its course. Within the magnetic field, the electrons follow a helical trajectory winding on different cylinders, with axes parallel to that of the coil. The electron's deviation depends on their speed (see for review (Williams and Carter 1996)).

$$\vec{F} = -e(\vec{E} + \vec{v} \times \vec{B})$$

Equation 2
When an electron with a charge -e enters a magnetic field with a strength B (Tesla) and an electric field of strength E, it experiences a force F, known as the Lorentz force, which depends on the velocity of the electron v

Electro-magnetic lenses are coils composed of a cylindrically symmetrical core of soft iron (polepiece), with a hole drilled through it (the bore) (Figure 3-5). These lenses are incorporated into different locations into the microscope to drive the electron beam (Figure 3-2). Most lenses in the microscope are weak lenses with large gaps. Either they act to demagnify the source image onto the specimen or they magnify the image or the diffraction plan from the specimen and project it onto the detector.

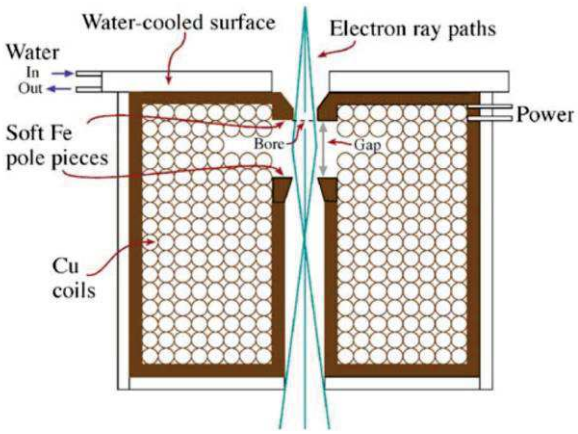

Figure 3-5 Schematic diagram of a magnetic lens
The soft-iron pole- pieces sit in the hole down the middle of the lens and are surrounded by the copper coils through which the current runs to magnetize the polepieces. (Williams and Carter 1996

Electro-magnetic lenses are always coupled to (i) four deflectors before the lens, to orient the beam perpendicularly to the magnetic field, (ii) two stigmators after the lens to compensate asymmetries of the lens and, (iii) an aperture to get rid of not coherent electrons (Figure 3-6).

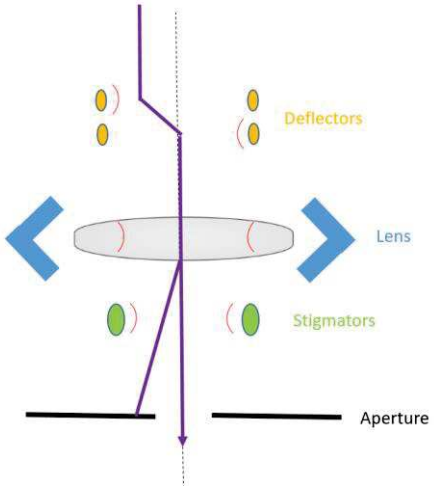

Figure 3-6 schematic representation of an EM lens system.

3.1.2.4 Lenses and energy filters

The relation between electron speed and their trajectory within a magnetic field is used to design energy filters. They are composed of a succession of electro-magnetic lenses with the aim to distribute electrons according to their energy, and a final slit to select electrons with a specific energy. Two types of energy filters exist, post-column with the Gatan Imaging Filter (GIF) or in-column as with the Omega energy filter present in JEOL microscopes (Figure3-7).

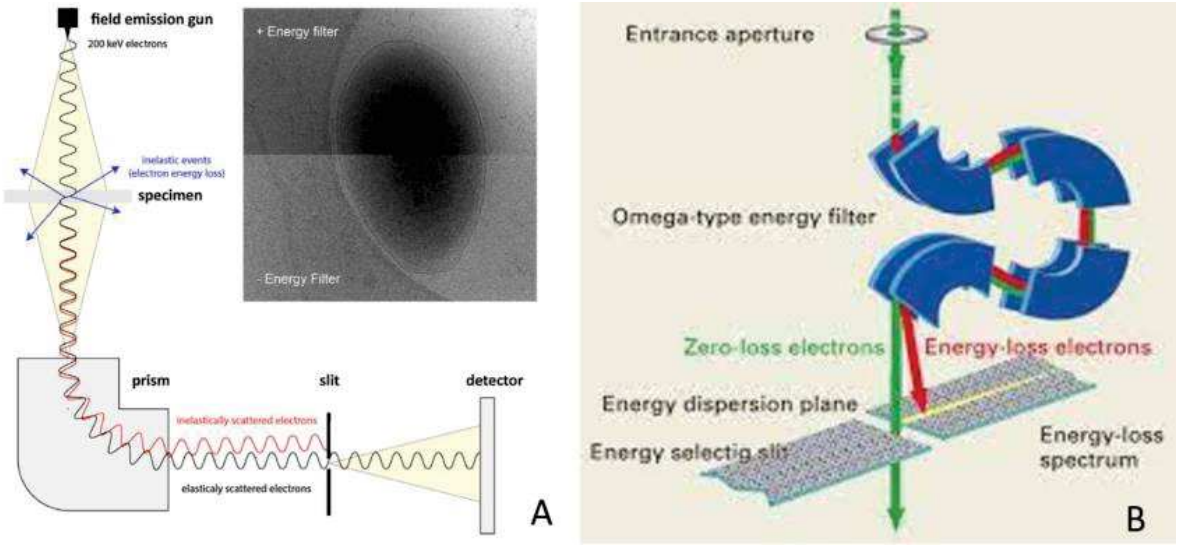

Figure3-7 Energy filters
A Schematic diagram of a GIF Filter and image with and without zero-loss energy filtering
B Schematic diagram of an omega energy filter. (Koning, Koster, and Sharp 2018) (https://embo2017.cryst.bbk.ac.uk/embo2017/course/Lectures/Lecture%2016%20-%20Andy%20Yarwood_p4.pdf)

3.1.2.5 Detectors

Historically, electron microscope images were recorded on photographic film. Although those had very large fields of view, the data collection rate was low and only a few dozen images could be collected in a single session, and each image then had to be digitized for further processing (Baldwin et al. 2018).

The development of charge coupled device (CCD) detectors in the early nineties offered the possibility to perform fast acquisitions of numeric data (Krivanek and Mooney 1993) A scintillator converts incident electrons to a low-light image that can be effectively captured by a CCD detector. The CCD detector is a type of silicon integrated circuit which is fabricated using conventional MOS. The information is converted into a quantity of electric charge. The

device is basically a Shift register; signal charges are stored and transferred in clocked shift register fashion under an array of closely spaced control electrodes (Figure 3-8 A) (Burt 1974).

More recently (2008-2009) complementary metal-oxide-semiconductor (CMOS) sensors were introduced in EM detectors (Booth 2019). They are made up of photodiodes, just like a CCD, the difference between the two types of technology resides in the way they store charge, and transfer it. In CMOS detectors, the charge conversion and read out in digital output are directly done through a charge/voltage converter and amplifier in each pixel (Figure 3-8 B). The benefits of CMOS are their power consumption, much lower than that of CCD sensors, and their reading speed which is significantly faster than a CCD sensor.

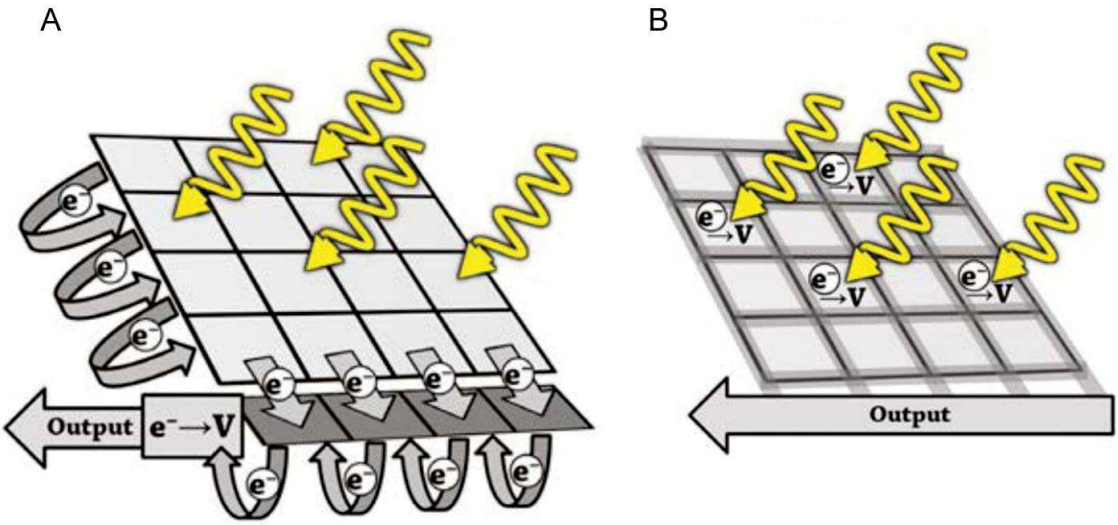

Figure 3-8 CCD and CMOS cheaps
A) Schematic representation of a CCD cheap. B) Schematic representation of a CMOS cheap (Romann Julien 2022)

Nonetheless, the use of scintillators to convert electrons to photons (Figure 3-9) in CCD and CMOS indirect detectors is deleterious for the detective quantum efficiency (DQE). The DQE is a measure of how the signal-to-noise ratio is degraded (i.e., the amount of noise added by the detector) at each spatial frequency during detection. For a perfect detector, the DQE would be 1 at each spatial frequency up to Nyquist, which is the maximum spatial frequency that can be recorded at a given pixel size (McMullan et al. 2009).

In the late 2000s, new generation electron detectors emerged and revolutionized the field of cryo-EM. Unlike detectors precedently developed which required the conversion of electrons

into photons for detection, these detectors named direct electron detectors can directly detect individual electrons (Figure 3-9) (McMullan et al. 2009). The energy deposited in each pixel is read out directly as an analog voltage that is digitized and represents the image after dark-field and bright-field corrections (Figure 3-9).

Because of this, direct detectors have a much higher DQE than both film and CCD (Figure 3-10). Direct detectors are currently available from three companies Gatan, Thermo Fisher, and Direct Electron. All three products are based on similar cheap technology, the electrons directly strike a lightly doped silicon epilayer CMOS supported on a more highly doped silicon substrate, with each frame of the exposure being read out continuously in rolling-shutter mode (McMullan, Faruqi, and Henderson 2016).

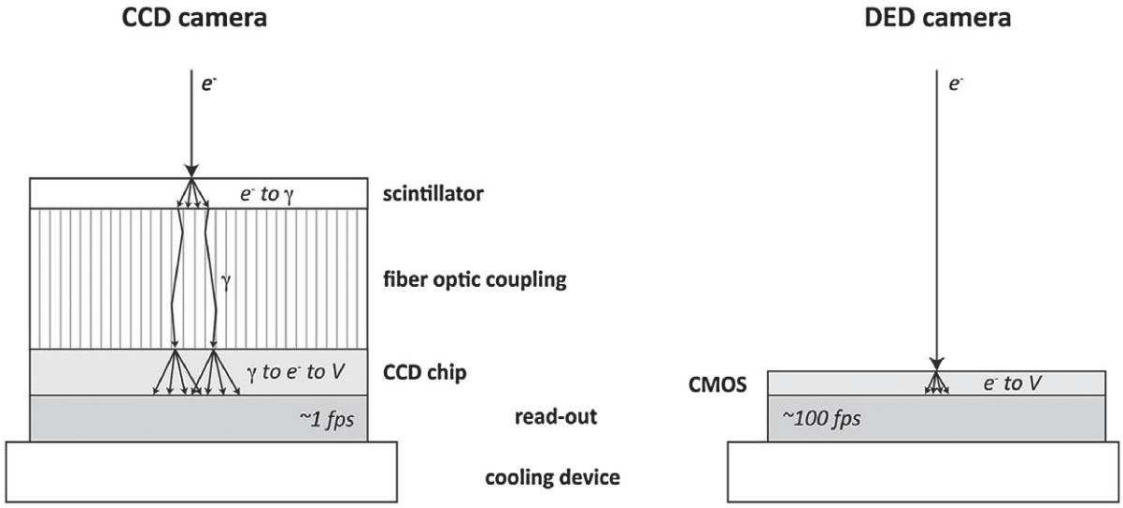

Figure 3-9 Schematic diagram of a CCD detector and a direct detector
(Koning, Koster, and Sharp 2018)

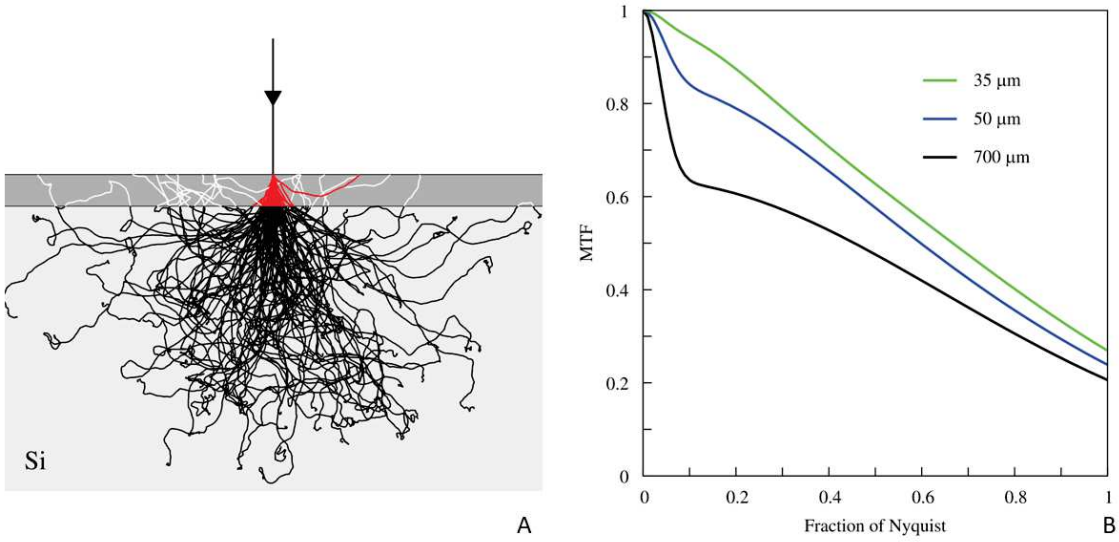

Figure 3-10 electron path in silicon
A. Monte Carlo simulation of 300keV electron tracks in silicon. After back thinning to 35mm, only those parts of the electron tracks highlighted in red would contribute to the recorded signal, which therefore is expected to have a much-improved MTF.
B. The experimentally determined MTF curves for 35mm (dotted line, green), 50mm (dashed line), and 700mm (continuous line, black) thick detectors as a function of spatial frequency between zero and Nyquist frequency are shown.

To date, the last generation of detectors are Gatan K3 (https://www.gatan.com); Falcon 4 (https://www.thermofisher.com), and direct electrons Apollo (https://www.directelectron.com) displaying a much higher frame rate than the first direct detectors developed ten years ago. Also, instead of a single image, these detectors acquire dose fractionated subframe movies to be used for motion correction during cryo-EM image processing.

All those new detectors display high-quality DQE and were proven capable to reach resolutions close to or better than 2Å (Bhella 2019; Kaiming Zhang et al. 2020). The best resolution of a 3D cryo-EM map reached so far is 1.15Å from apoferritin test sample images recorded with a K3 detector (Yip et al. 2020) The resolution obtained with this dataset was initially 1.25 Å but it was recently reprocessed resulting in an improved resolution (https://www.emdataresource.org/EMD-11668). A direct comparison of K3 and Falcon 4 cameras carried out on a 300 kV Titan Krios G3i microscope, in imaging apoferritin sample, gave equivalent results for both detectors (Figure3-11) (Kaiming Zhang et al. 2020). This was confirmed by another publication on the same sample (Danev, Yanagisawa, and Kikkawa 2021), where data shows that there is practically no performance difference between the K3 and the Falcon 4 cameras for a comparable quantity of movies. Both datasets had the same B-

factor (Uniform map B-factor applied to partially restore the fall-off at high resolution) of ~42.8Å2. The average resolution difference between the two cameras of ~0.02Å is negligible and is well within the experimental error. Nonetheless, the K3 has a significantly higher frame and speed acquisition rate than the Falcon4.

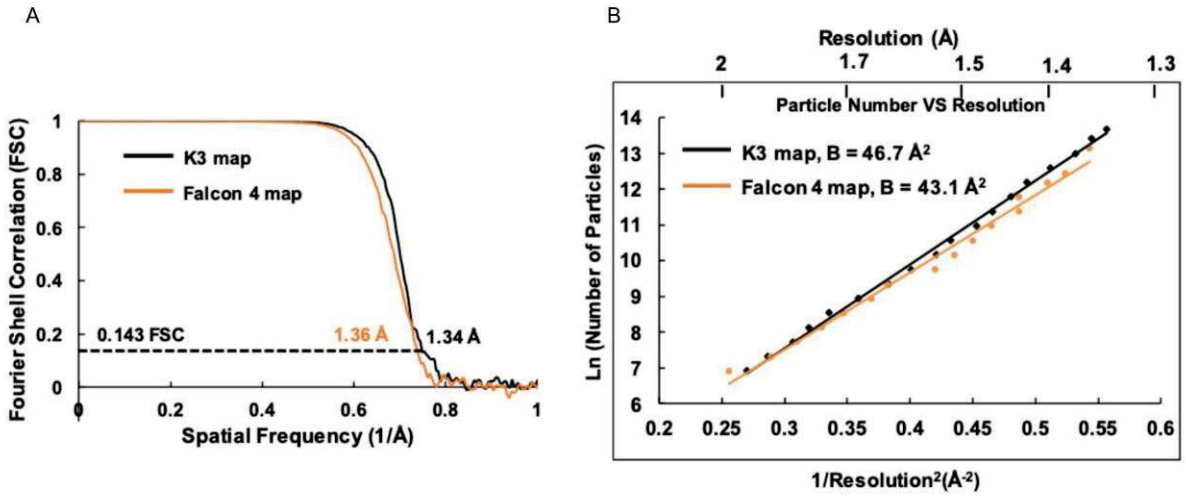

Figure3-11 cryo-EM analysis K3 and Falcon4 detectors comparison
cryo-EM analysis of apoferritin structures at atomic resolution from two datasets collected on K3 and Falcon 4 detectors:
A Gold standard FSC plots for the final 3D reconstructions for the two maps. B Plots of the of projections vs the reciprocal squared resolution. The B-factor was calculated as 2x the linear fitting slope.

These technical features result in the implementation of various acquisition modes on these detectors :

Counting mode Implemented for K3, Falcon4, and Apollo detectors: the individual electron events are identified when they reach the detector. A benefit of counting is that it rejects signal read noise and variability associated with electron scattering, while it dramatically lifts the detector's DQE across all spatial frequencies (Figure 3-12 A). (https://www.gatan.com)

Super-resolution mode Implemented for K3 detectors only: It consists to divide each pixel into four areas and to recognize each electron event by computational analysis and finding the center of the event with sub-pixel precision. This results in a virtual increased number of pixels and an improved DQE (Figure 3-12 B).

Figure 3-12 Detectors imaging modes
A Counting mode process. B Super-resolution mode process. (https://www.gatan.com)

3.1.2.5.1 Detectors and limit of resolution

Also, In practice, a resolution limit of the system is determined by the image pixel size. Indeed, the resolution can't exceed two times the pixel size. Based on the Nyquist–Shannon sampling theorem (Shannon 1949). The image pixel size depends on a combination of the physical pixel size of the detector and the TEM magnification.

3.1.3 Physical rational and image formation

3.1.3.1 Wave properties of electrons and maximal resolution considering rayleigh criterion

Electrons show both particles and wave characteristics, like photons as demonstrated by Young's slits interference patterns. De Broglie's theory of the wave-particle duality allowed to establish the electron optics. The electron particle momentum can be related to its wavelength through Planck's constant. The energy of an electron at rest is

$$E_0 = m_0 c^2$$

Equation 3
Where E_0 is the energy at rest, $m_{0\ is}$ the electron at rest mass, and c is the light speed

The Energie of a moving electron is $E_T = E_c + E_0$. Where E_T is the electron total energy, and E_c the kinetic energy. E_c is determined by the acceleration tension E. $E_c = eE$. Where e is the electron charge. The mass of electrons in motion can then be described.

$$m = \frac{m_0}{\sqrt{1 - \frac{v^2}{c^2}}}$$

Equation 4
m is the mass of an electron in motion; m_0 the mass o

The electron speed can then be described from precedent equations.

$$v = c\frac{\sqrt{2eEm_0c^2 + e^2E^2}}{m_0c^2 + eE}$$

Equation 5

Based on de Broglie ideas, we can relate the particle momentum to its wavelength through Planck's constant

$$\lambda = \frac{h}{p}$$

Equation 6
Where λ is the wavelength, h is the Planck constant, p is the particle momentum ($p = mv$).

In the TEM the momentum is dictated by a potential drop of charge along the column. Inducing electrons acceleration and electron kinetic energy.

$$eV = \frac{m_0v^2}{2}$$

Equation 7
Where eV is the kinetic energy, m_0 is the static electron masse, v is the electron speed

Based on the precedent equations a relation between acceleration tension E and wavelength can be described. Equation 8

$$\lambda = \frac{h}{\sqrt{2m_0eE\left(\frac{1 + eE}{2m_0c^2}\right)}}$$

Equation 8
Where λ is the wavelength, h is the Planck constant, p is the particle momentum ($p = mv$).

The electrons' relative speed and λ can be calculated for TEM commonly used acceleration tensions. (Willaime 1987; Williams and Carter 1996)

E(KV)	v/c	λ (nm)
100	0.548	0.0037
120	0.587	0.00335
200	0.685	0.00251
300	0.828	0.00197

For visible light microscopy, the resolution is limited to approximatively 200nm, based on, the Rayleigh criterion Equation 9 which can be simplified as Equation 10. This limitation is proportional to the λ of visible light photons (for blue light λ is 450-495 nm, and for red light is 620 to 750 nm). In the case of an electron accelerated at 300KV, λ is 0.00197nm, and consequently, the resolution limit is 0.00095nm or 0.0095Å. Unfortunately, TEM is far to be perfect optical system, and other limitations described in the next section impair such high resolution.

$$r = \frac{0.61\,\lambda}{\mu \sin \beta}$$

Equation 9
λ is the wavelength of the radiation, μ the refractive index of the medium, β the semi-angle of collection of the objective and r the resolution

$$r = \frac{\lambda}{2}$$

Equation 10

3.1.3.2 Interaction of Electrons with Matter

Electrons are one type of ionizing radiation, capable to interact with matter. There is a large range of possible interactions between the electrons with the sample depending on the electron energy and sample composition. These interactions represented (Figure 3-13), can be sorted as (i) elastic scattering, where electrons are scattered without energy loss, (ii) inelastic scattering, when energy transfer from incident electrons can ionize atoms in the specimen, inducing X-ray emission, chemical bond rearrangement, and free radicals, or inducing secondary electron scattering. (Orlova and Saibil 2011). Inelastically scattered electrons generate noise and do not contribute to image formation.

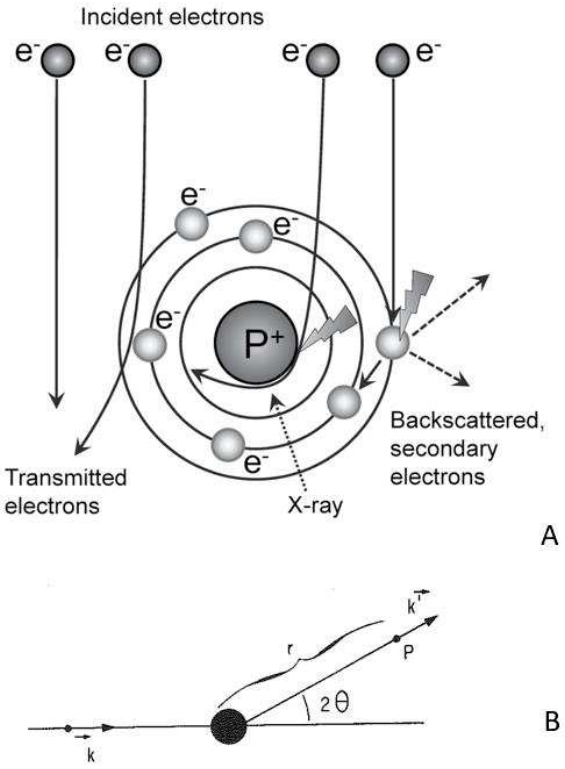

Figure 3-13 Interaction of the electron beam with the sample
(a) Schematic of elastic and inelastic electron scattering. Collision of beam electrons with atomic electrons or nuclei leads to energy loss (inelastic scattering), while deflection by the electron cloud does not change the energy of the electron (elastic scattering). (Orlova and Saibil 2011).
B Electrostatic wave diffusion by an atom, $\vec{k}$ is the wave vector of the incident wave and $\overrightarrow{k^1}$ the wave vector of the scattered wathe.

3.1.3.2.1 Why are we interested in elastic scattering

The electron is a low-mass, negatively charged particle. It can easily be deflected by passing close to other electrons inducing small-angle scattering, or the positive nucleus of an atom (Figure 3-13). These Coulomb (electrostatic) interactions are critical in image formation.

The electron beam can be either considered as a particle or as a plane wave defined by its wave vector $\vec{k}$, with $|k| = 1/\lambda$ the incident wave is scattered by the sample coulomb potential (charges of nucleus and electrons in the sample). The scattered wave is considered as a spherical wave with an amplitude described as $f(\theta)\, Exp^{\frac{(2\pi ik.r)}{r}}$, with r the distance from the spherical wave origin, 2θ the angle with the incident wave and $f(\theta)$ the atomic-scattering factor (is a measure of the scattering amplitude of a wave by an isolated atom) (Willaime 1987). $f(\theta)$ is related to two properties of the scattering atome, The atomic number (Z) correpond to the diffusion by the nucleus and f(x) coresponding to the electronic cloud diffusion (Willaime 1987; Williams and Carter 1996).

$$f(\theta) = \left(\frac{m_0 e^2}{2h^2}\right)(\lambda sin\theta)^2(Z - fx)$$

Interestingly $f(\theta)$ is significantly higher for the electrons than for the photons. Concretely it means that the electrons strongly interact with matter inducing fast sample degradation and involving the necessity to work on thin samples. In the TEM. In reality, if we consider the electrons speed and the beam intensity, each unique electron is produced by the gun, scattered by the sample, and interfere with itself in the microscope independently as a perfect illustration of Young's double-slit experiment to review (Willaime 1987; Williams and Carter 1996).

3.1.3.3 Contrast generation and image formation

The image contrast in TEM that can be defined as a difference in intensity between two adjacent areas, is due to the scattering of the incident beam by the specimen. The contrast can conveniently be decomposed into phase and amplitude contrast (Williams and Carter 1996).

3.1.3.3.1 Amplitude contrast

The amplitude contrast results from variations in mass, thickness, or atom properties, or a combination of the three: the variation in thickness can produce a contrast because the electron interacts with more matter (Figure 3-14).

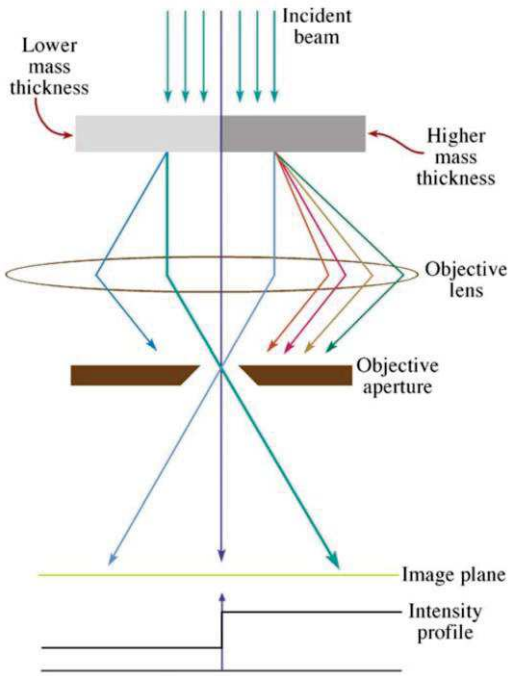

Figure 3-14 Mechanism of mass-thickness contrast in image
Thicker or higher-Z areas of the specimen (darker) will scatter more electrons off-axis than thinner, lower mass (lighter) areas. (Williams and Carter 1996)

3.1.3.3.2 Phase-contrast

The phase contrast is induced by the interference between the elastically scattered wave component and the unscattered wave component. The contrast in cryo-EM is formed predominately by phase contrast (Reimer and Kohl 1997).

3.1.3.3.2.1 Interference of electron waves

To understand the phase-contrast it is necessary to understand wave interference. For the sake of simplicity, we can represent an electron wave by a simple periodic function. (https://courses.physics.illinois.edu)

$$f(x) = A\sin(2\pi sx + \varphi)$$

Equation 11 :
Where A is the amplitude of the wave (intensity (I) $I \propto A^2$), T is the period ($T=1/\lambda$) and φ is the phase.

Supposing we have two sinusoidal waves with the same Amplitude, and period, but variable phase shift: $s_1(x) = A\sin(2\pi Tx + \varphi_1)$ and $s_2(x) = A\sin(2\pi Tx + \varphi_2)$. These wave interferences result in a new wave. The amplitude of this resulting wave is dependant on two parameters the addition of the original amplitudes ($A(s_1)$and $A(s_2)$) and the phase shift $\Delta\varphi = \varphi_1 - \varphi_2$ as described in Equation 12 (Figure 3-15)

$$s_3(x) = s_1(x) + s_2(x) = \underbrace{2A\,\mathbf{s}\cos\left(\frac{\varphi}{2}\right)}_{\text{Amplitude}}\cos\left(2\pi Tx - \frac{\varphi}{2}\right)$$

Equation 12
two periodic waves $s_1(x) = A\sin(2\pi Tx + \varphi_1)$ and $s_2(x) = A\sin(2\pi Tx + \varphi_2)$ interfere, results in a third periodic wave. The amplitude of the resulting wave is $2A\cos(\Delta\varphi)$

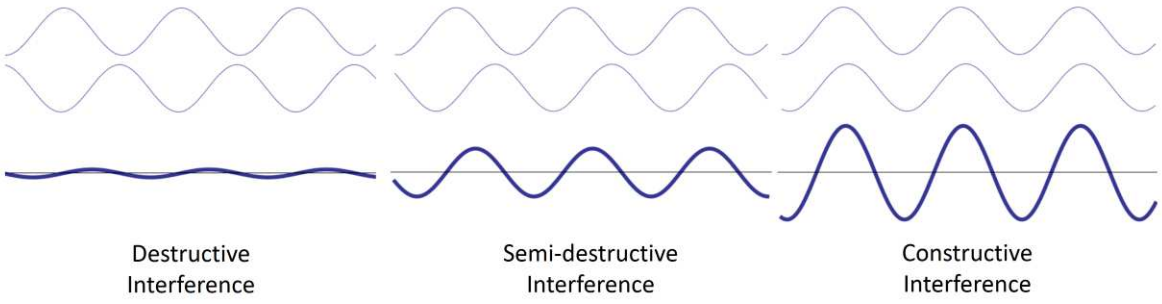

Figure 3-15 Interference of two simple periodic functions
Representation of interference of two simple periodic functions with variable $\Delta\varphi = \varphi_1 - \varphi_2$. Interference can be either constructive or destructive

3.1.3.3.3 Phase-contrast generation

In the TEM, the elastically scattered wave component at different angles is interfering with the unscattered wave component with variable $\Delta\varphi$ (function of their scattering angle (describe in the next section)). Phase-contrast imaging is critical for high-resolution TEM but it appears in most TEM images even at relatively low magnifications. This contrast mechanism can be difficult to interpret because it is very sensitive to many factors like small changes in the thickness, orientation, or scattering factor of the specimen, and variations in the focus or astigmatism of the objective lens. However, it can be exploited to image the atomic structure of thin specimens after image correction in preprocessing (Williams and Carter 1996).

Interestingly, we often distinguish phase and diffraction contrast but it's based on the same phenomenon. In one case with amorphous sample (incoherent elastic scattering) and the other with lattice structure (coherent elastic scattering).

3.1.3.4 Wave propagation and Contrast Transfer Function

3.1.3.4.1 TEMs diffraction and imaging conditions

The microscope can be used either as imaging or as a diffraction instrument. The diffraction plane is the plane in space where unscattered electrons are focalized in one point (Figure 3-16). Since the image plane contains the object's projected image (Figure 3-16). The electrons interfere on the image plane to form a magnified image of the specimen (Saibil 2000).

3.1.3.4.2 Relation between Fourier and direct space

The conversion from the real space to the diffraction space can be described mathematically by the Fourier transform (FT) Equation 13. We are talking about the Fourier space. The back conversion from the Fourier space to the real space is then performed by the inverse Fourier transform ($FT^{=1}$) Equation 14. Real image and Fourier spectra are two different representations of the same signal. One is function of the distance (real space) and the other function of the frequency (Fourier space). Both representations can be interpreted to extract valuable and complementary information.

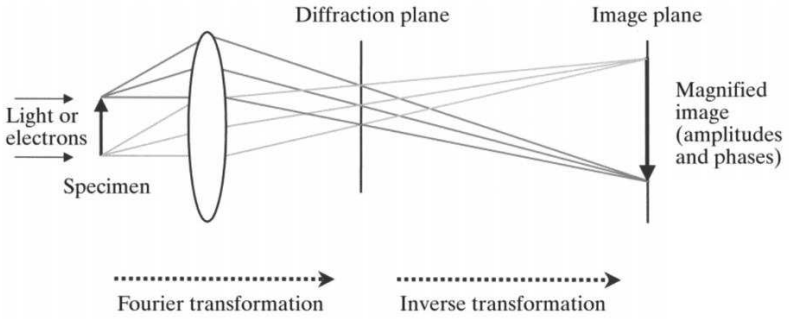

Figure 3-16 The relationship between imaging and diffraction
A simplifed schematic view of imaging and diffraction shows that the waves scattered by the specimen form a Fourier transform, observed as a diffraction pattern. (Saibil 2000)

$$F_{(s)} = \int_{-\infty}^{+\infty} \rho_{(r)} exp^{+i2\pi s.r} d^2r$$

Equation 13
Fourier transform in two dimensions.
F and ρ are two continuous and integrable functions; s is a 2D spatial frequency vector; r a 2D position vector. $exp^{+i2\pi s.r}$ is a complex function composed of a real and imaginary wave function for a specific frequency s. All the frequency components are integrated yielding a 2D representation in the Fourier space

$$\rho_{(r)} = \frac{1}{2\pi}\int_{-\infty}^{+\infty} F_{(s)} exp^{-i2\pi s.r} d^2 s$$

Equation 14
Inverse Fourier transform in two dimensions.
F and $\boldsymbol{\rho}$ are two continuous and integrable functions; s is a 2D spatial frequency vector; $\boldsymbol{r}$ a 2D position vector. $\boldsymbol{exp^{-i2\pi s.r}}$ is a complex function composed of a real and imaginary wave function for a specific position r. All the position components are integrated yielding a 2D image in the real space

3.1.3.4.3 Lens aberrations to consider in image formation

-Astigmatism occurs when the electrons sense a non-uniform magnetic field which has the consequence of imposing a different focal length depending on the azimuthal direction. Concretely this defect arises because the lenses' soft-iron polepieces can't be perfectly cylindrically symmetrical. The soft iron may also have microstructural inhomogeneities which cause local variations in the magnetic field strength (Williams and Carter 1996).

-Spherical aberration (Cs) occurs when the lens field behaves differently for off-axis rays. It is the case in electromagnetic lenses, the further off-axis the electron is, the more strongly it is bent back toward the axis. As a result, a point object is imaged as a disk of finite size (Figure 3-17 A).

- Chromatic Aberration (Cc) is related to the frequency (energy), of the electrons (Equation 2). We've assumed so far that the electrons in the beam are monochromatic, but they aren't really. Consequently, the focal length of each electron is a function of their energy (Figure 3-17 B) (Williams and Carter 1996).

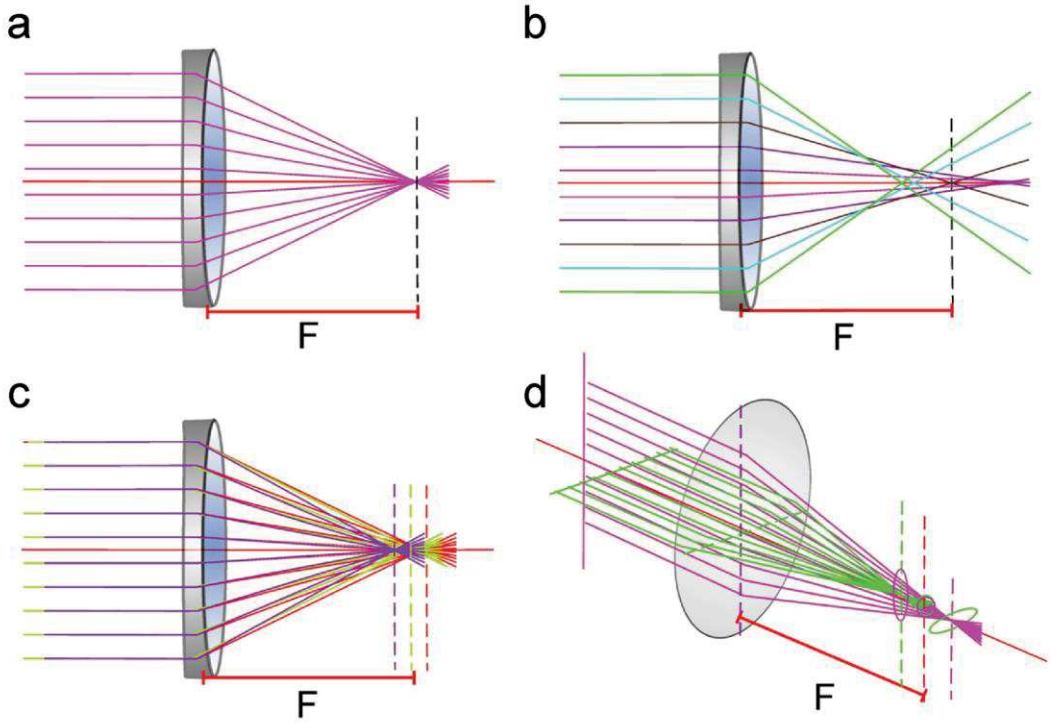

Figure 3-17 Ray diagrams of lens aberrations:
(a) perfect lens, (b) spherical, (c) chromatic, and (d) astigmatic aberration. F is the focal length of the lens. (Orlova and Saibil 2011)

3.1.3.4.4 The contrast transfer function (CTF)

The point spread function which describes the response of an imaging system to a point source or point object in the real space is commonly used in visible-light microscopy. In EM, regarding the specificity of the system the contrast transfer function (CTF) is used instead. The CTF describes the response of an imaging system to a point source or point object in the Fourier space Equation 15 (Thon 1971; Erickson and Klug 1970; Wade 1992). The effects of defocussing and spherical aberration in the electron microscope image are most simply and directly displayed in the Fourier transform of the image.

$$TF(2D\ Image) = TF(Perfect\ projection) * CTF$$

Equation 15

The CTF can be defined by Equation 16

$$CTF\ (\vec{s}) = -\sqrt{1 - A^2}.\sin\big(\gamma(\vec{s})\big) - A.\cos\big(\gamma(\vec{s})\big)$$

$$= -\sin\big(\Delta\varphi + \gamma(\vec{s})\big)$$

Equation 16

Where $\vec{s}$ is the spatial frequency 2D vector; A is the amplitude contrast coefficient; $\gamma(\vec{s})$ is a function of $\vec{s}$ representing the varying phases of the CTF, while $\Delta\varphi$ is a global phase shift contributed by amplitude contrast using empirical values. (Kai Zhang 2016).

In the wave theory of image formation, the effects of spherical aberration and defocussing are attributed to a phase shift introduced by the objective lens, which is a function of the frequency formulated as

$$\gamma(\vec{s}) = \gamma(s,\theta) = -\frac{\pi}{2}C_s\lambda^3 s^4 + \pi\lambda Z(\theta)s^2$$

Equation 17
where s is the modulus of $\vec{s}$, $s = |\vec{s}|$ and $\vec{s} = exp^{i\theta}$; λ is the wavelength of an electron; Cs is the spherical aberration coefficient; $Z(\theta)$ is the defocus in the direction with a varying azimuthal angle θ

The CTF indicates how much each Fourier component contributes to the picture. Each Fourier component is the representation of an elastically scattered electron for a specific angle and its contribution to image contrast can be positive (green Fourier component Figure 3-18), negative (blue Fourier component Figure 3-18), or zero (yellow Fourier component Figure 3-18). As described in Equation 17 and Illustrated (Figure 3-18c) defocus is a key parameter to modify the Fourier component's contribution to the image. Consequently, it is necessary to acquire

images with variable defocus to obtain information for all Fourier components within one dataset.

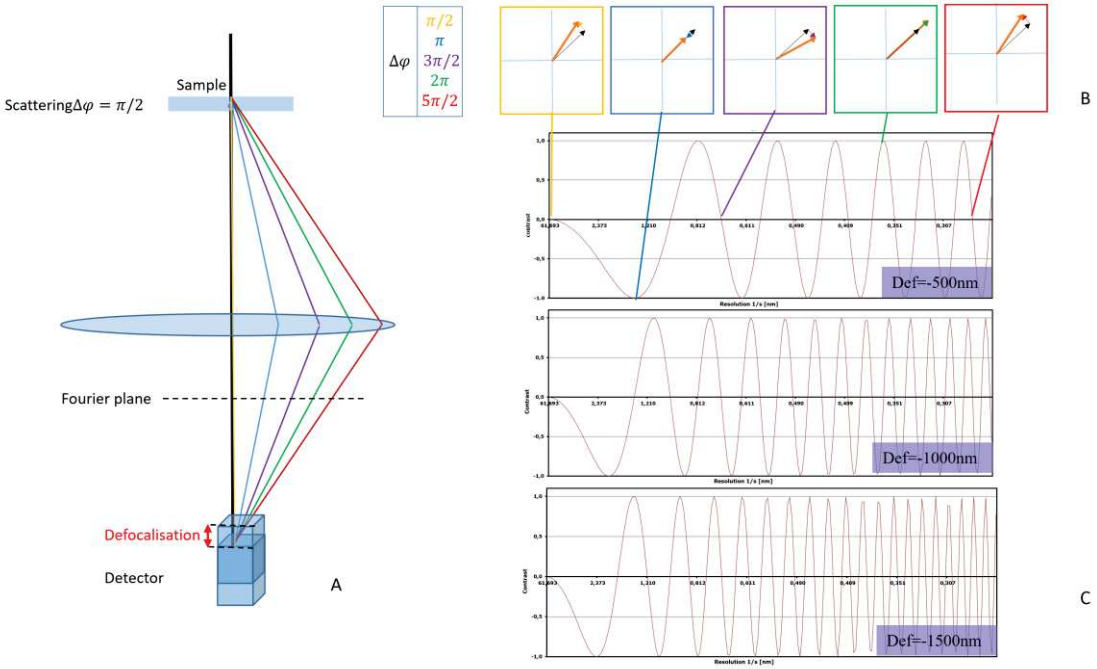

Figure 3-18 Schematic representation of the TEM Fourier components contribution
A Schematic representation of the TEM unscattered wave (black) scattered components to variable angles which produce variable Fourier components (colors).B. Phase shifts relatives to the unscattered component for all Fourier components illustrated in A. C Argand diagram representations of the unscattered component (black), Specific Fourier components illustrated in A (colors) and the result of their interference (orange). D. CTF simulated for variable defocus Amplitude contrast 0.1; Acceleration tension 300kV, Cs 2 mm, FEG gun. (https://www.c-cina.org/stahlberg/research/tools/soft/ctf-simulation/)

3.1.3.4.5 envelope functions of electron microscope

Equation 16 corresponds to a perfect optical system. Unfortunately, the electron is never perfectly coherent and monochromatic, there is also fluctuation in the gun and the lenses, resolution limiting error of the detector and drift. All together these defaults create damping of the high-resolution signal (Penczek et al. 2018). An expansion of the CTF model is given by Equation 16. These can be done by the combination of various Envelope functions Equation 18 described Equation 19 like

$$TF(2D\ Image) = TF(Perfect\ projection) * EF * CTF$$

Equation 18

$$G_{sc}(s) = \exp(-\pi^2\alpha^2(C_s\lambda^2 s^3 - \Delta Z s)^2) \qquad G_{lm}(s) = J_0(\pi\Delta f\lambda s^2)$$

$$G_{tc}(s) = \exp\left(-\frac{\pi^2}{16\ln 2} C_C^2\lambda^2\left(\frac{\Delta E}{E}\right)^2 s^4\right) \qquad G_{tm}(s) = \frac{\sin(\pi s\Delta r)}{\pi s\Delta r}$$

$$G_{ol}(s) = \exp\left(-\frac{\pi^2}{4\ln 2} C_C^2\lambda^2\left(\frac{\Delta I}{I}\right)^2 s^4\right) \qquad G_{au}(s) = \exp(-Bs^2)$$

Equation 19

s, spatial frequency; λ, electron wavelength; C_s, spherical aberration coefficient; C_C, chromatic aberration coefficient; ΔZ, focus, positive for under focus and negative for over-focus; Q, amplitude contrast; α ,semi-illumination angle; E, electron energy; ΔE, electron energy spread; I objective lens current; ΔI, variation of objective lens current; Δf, sample vertical motion amplitude; Δr, sample drift amplitude; B, amplitude decay factor; $G_{sc}(s)$, spatial coherence amplitude decay; $G_{tc}(s)$, voltage temporal coherence amplitude decay; $G_{ol}(s)$, objective lens current stability amplitude decay; $G_{lm}(s)$, sample vertical motion amplitude decay; $G_{tm}(s)$, sample horizontal drift amplitude decay; $G_{au}(s)$, the Gaussian approximation of amplitude decay. (Jiang and Chiu 2001)

Figure 3-19 summarizes the concepts of CTF and envelope function (EF). In A the CTF without EF convolution is an oscillating function without signal damping at high resolution (1/frequency). The Fourier component for which the contrast reaches 1 or -1 contributes maximally to the contrast generation (constructive or destructive interference with the unscattered component Figure 3-15). The Fourier component for which the contrast is close to 0 does not contribute to the signal (semi destructive interference Figure 3-15), the information for these components is lost. In B, C, and D, the CTF is convoluted with the envelope functions with signal damping at high resolution (1/frequency). Higher defocus allows to increase the contribution of low frequencies Fourier components and thus to see the projections but is detrimental for high-resolution information.

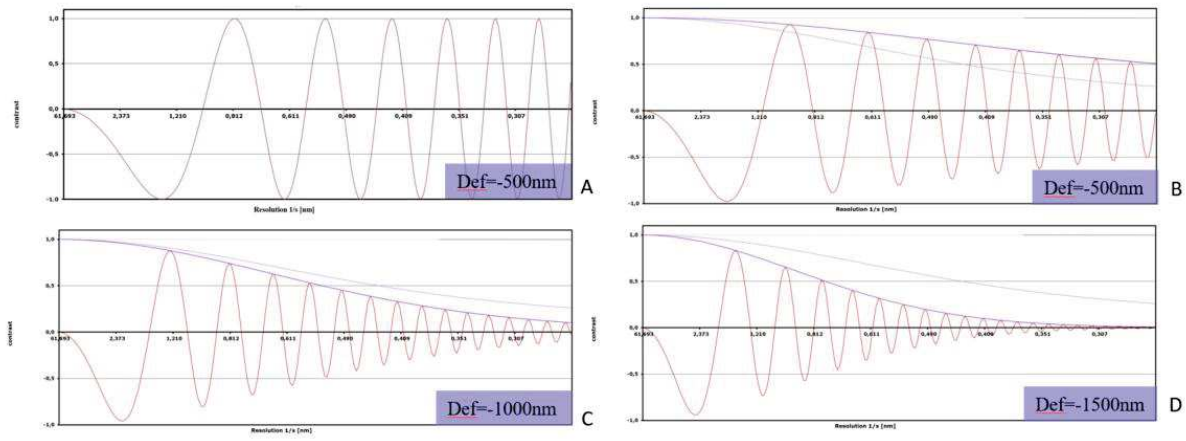

Figure 3-19 CTF simulated for variable defocuses

Amplitude contrast 0.1; Acceleration tension 300kV, FEG gun, Cs 2mm A Theoretical contrast transfer function without envelope functions effects, defocus 500µm. B. C. Theoretical contrast transfer function with envelope functions effects, defocus 500µm (B) 1000 µm (C) 1500 µm (D). (https://www.c-cina.org/stahlberg/research/tools/soft/ctf-simulation/)

3.2 Techniques for preparing organic samples

For observation with TEM, organic matter has specific features linked to its highly deformable nature. It is easy to imagine the damage that can occur when a sample of biological tissue, which contains a very large proportion of water, is introduced into the vacuum environment of an electron microscope. Hopes of seeing living cells have therefore long vanished, even before invoking the destructive role of the electron beam. However, at the cost of many and varied tricks, biologists have been able in recent decades, to observe tissue cells, and molecules such as proteins and nucleic acids. To maintain proteins in a morphological state as close as possible to their natural state, two techniques are commonly used, the negative stain (NS) and the CryoEM.

3.2.1 Negative staining of proteins:

The simplest method to increase contrast and assess the quality of a solution of isolated ~~projections~~ such as proteins or other macromolecules is negative staining. A droplet of the sample suspension is spread onto an EM support film and then embedded with a heavy metal salt solution, typically uranyl acetate (Figure 3-20) (Orlova and Saibil 2011). The method was established in 1959 using phosphotungstic acid as a stain (Brenner and Horne 1959). This method comports two advantages, the sample is protected by the stain and the staining produces a strong inverted contrast of the protein. But it displays major limitations. Indeed we do not directly observe our sample but how the stain surrounds it, then limiting the resolution to about 15 Å.

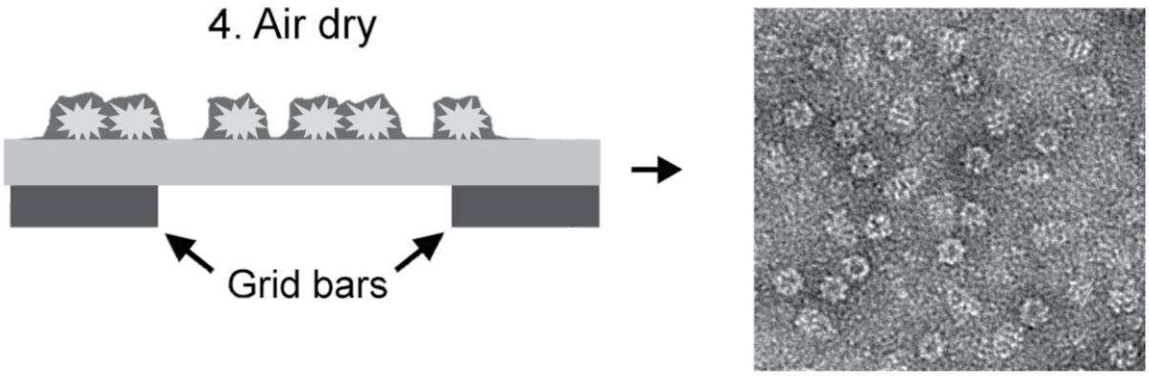

Figure 3-20 Negative stain sample
(a) Schematic view of sample staining, with an example negative stain image. Adapted from (Orlova and Saibil 2011)

3.2.2 Cryo-EM of Isolated proteins

Macromolecules are normally in aqueous solution, and hydration is critical for their structural integrity. Cryo-EM makes it possible to stabilize samples in their native, hydrated state, even under a high vacuum. The method was developed by Dubochet and coworkers at the EMBL of Heidelberg in the 80s (Dubochet et al. 1982; Adrian et al. 1984; J et al. 1988).

Rapid freezing is used to bring the sample to the solid-state without dehydration or ice crystallization. The sample is then maintained at a low temperature (~ -171°C) during transfer and observation in the EM.

The method widely used for freezing aqueous solutions can be described as follow (Figure 3-21 D):

(i) a small volume of sample is deposited on the EM grid, (ii) the excess of sample is removed by blotting, (iii) the grid is immediately plunged into liquid ethane or propane (~ -171°C). Ethane is preferred to nitrogen because of its better thermic transfer capacity.

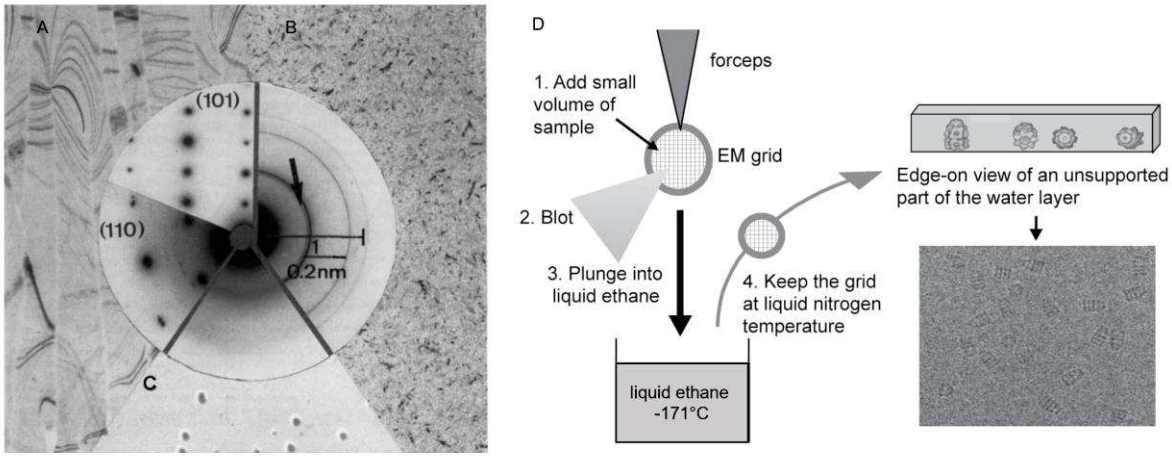

Figure 3-21 Cryo-EM
A Hexagonal ice. B. Cubic ice C. Vitrified ice is necessary for Cryo-EM observations. D. Cryo-EM sample preparation. Schematic representation of particles embedded in ice and Cryo-EM image.

3.2.3 Sample observation in low dose conditions

Because a biological sample is sensitive to electron radiation, it is necessary to image the proteins under low-dose conditions. In those conditions, alignments on the TEM dedicated to biology allow to perform all alignments and focus on one area and then translate the beam, by

beam tilt and beam shift modifications, to a predetermined distance and direction before recording the image of the selected area.

On the Jeol 2200FS a specific sequence acquisition composed of three different modes is used for that purpose:

3.2.3.1 Search mode

An unfocused diffraction mode is used to screen the grid and to find the area of interest. The magnification used is x50,000; the beam is then spread out to maximum and the microscope is set in diffraction mode. In this configuration, a large area of the grid is illuminated with a very low dose to protect the sample.

3.2.3.2 Focus mode

Once the area of interest is localized, an adjacent region is used to determine the focus of the beam allowing to preserve the region of interest. The adjacent area must be located at approximately 2µm from the area of interest. For this mode, The magnification used is x200,000.

3.2.3.3 Imaging mode

In this mode, the area of interest is imaged with the appropriate electron dose (~18e^-/Å) and magnification x50,000. These parameters might be carefully optimized to obtain the best images and are a function of the detector.

3.3 Single-particle analysis

The purpose of single-particle reconstruction (SPR) is to determine the structure of macromolecules from images of individual single-particle projections referred to from now as projections. To process those projections, a template flow chart that aims to obtain a reliable 3D map can be established. It is important to note this is just a general template of the process's general flow path, for the sake of understanding. The flow chart might be adapted accordingly to the sample features (Figure 3-22).

Within the framework of this Ph.D. I mainly used two SPR software: relion and cryosparc. Therefore, I will further describe in detail this software and algorithms used within them. Other software relying on other mathematical rational can also fulfill the same purpose. Indeed, while some software use cross-correlation-based projection-matching algorithms for single-particle analysis (SPA) (Ludtke, Baldwin, and Chiu 1999; Yu, Snapp, and Radermacher 2012), during

projections alignments, relion and cryosparc are based on a statistical approach, the Maximum-likelihood method.

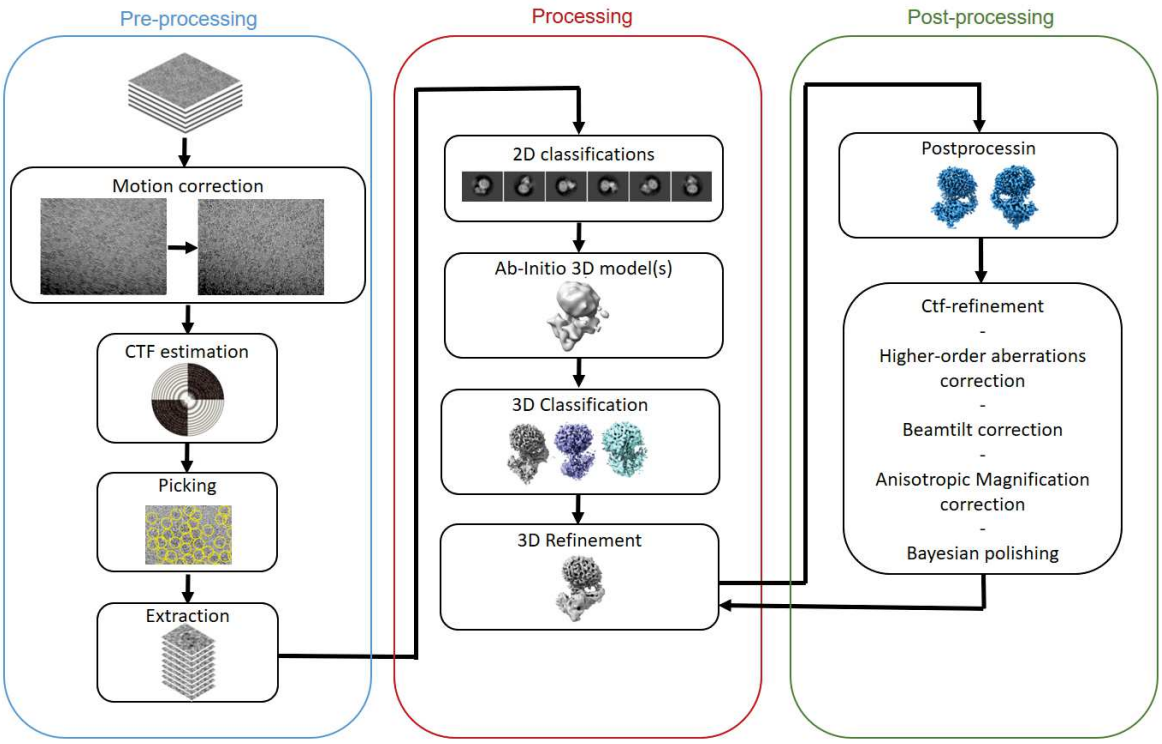

Figure 3-22 A single Cryo-EM image processing workflow template
the workflow is divided into three steps: the pre-processing step where movies are corrected and prepared for processing, the processing step where particles are curated and aligned, and the post-processing step where projections correction is improved based on processing information, and where the map is sharpened to maximize high-resolution components.

3.3.1 Preprocessing

3.3.1.1 Movies Correction

Motion Correction

Direct detectors can record images of frozen-hydrated biological samples as dose-fractionated stacks of subframes (movies). This specificity is used to correct sample motions occurring during beam illumination. Indeed, there are two main causes of motion, (i) a mechanical motion induced by the sample holder stability and, (ii) a motion induced by energy transfer from the beam to the sample during illumination. These motions are deleterious for the image quality (Figure 3-23 A) (Brilot et al. 2012) and can be decomposed into two components,(i) a uniform whole-frame motion and (ii) a nonuniform local motion that varies across the image (Li et al. 2013). The software Motioncorr2 corrects these two components in two steps developed as follows (Figure 3-23 D) (Zheng et al. 2017).

uniform whole-frame motion correction A first operation exploiting redundant information between nonadjacent subframes and allows to align the subframes with each other with a robust subpixel accuracy (Figure 3-23 C) (Zheng et al. 2017).

nonuniform motion correction A second operation correct nonuniform motions. These motions seen in movie stacks are projections of complex 3D sample deformations onto the image plane. A second operation time-varying 2D polynomial function is used to describe these projections. The image is first divided into patches, and motions within each patch are iteratively determined (Figure 3-23 D). The resultant shifts are used to fit the 2D polynomial functions that smoothly vary with time. Each image subframe is subsequently remapped pixel by pixel using the polynomial function (Zheng et al. 2017).

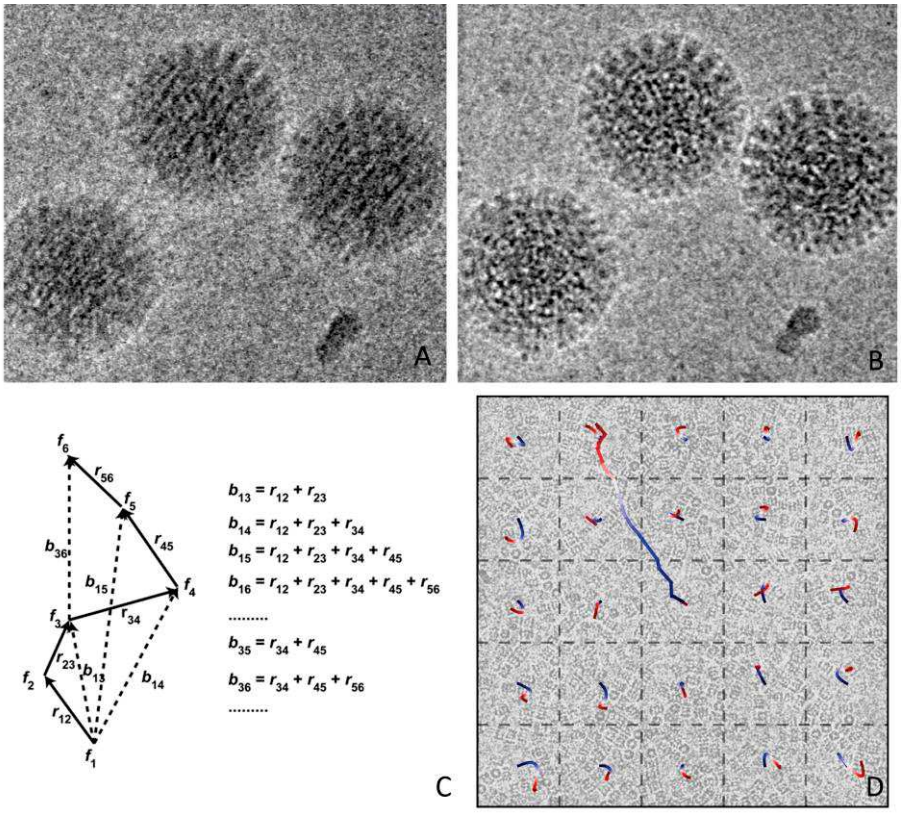

Figure 3-23 Motion correction
A. Average of 60 frames of an area of Movie S1 that experienced significant motion. The projection is blurred and high resolution is lost B. Same area than for A after translational alignment of individual frames.C. image motion during the total exposure can be described as a combination of sequential subframe displacements between every pair of adjacent subframes. D Image of frozen-hydrated archaeal 20S proteasome overlaid with the traces of global motion based upon whole-frame alignment (long trace originated from the center of image) and each patch predicted from the polynomial function. Adapted from A-B (Brilot et al. 2012) C (Li et al. 2013) D (Zheng et al. 2017)

Dose weighting

As already evoked, biological specimens experience radiation damage induced by the electron beam, ultimately limiting the attainable resolution. Indeed the sample is degraded by the beam-induced energy transfer. At the beginning of the illumination corresponding to the first frames, the sample is intact but it will gradually be altered. This results in a loss of information and noise apparition from the high to the low resolution over illumination time. To tackle this limitation movie subframes are dose weighted accordingly to the dose precedently experienced by the sample. An optimal exposure can be defined that maximizes the signal-to-noise ratio in the image and the optimal exposure curve can be used to filter frames based on their exposure. Filtering the frames in this way results in a sum with an increased signal-to-noise ratio (SNR) relative to the unfiltered sum (T. Grant and Grigorieff 2015).

3.3.1.2 CTF Estimation

As precedently discussed the contrast transfer function (CTF) which describes the response of an imaging system, is a function of the objective lens defocus and astigmatism. CTFFIND4 (T. Grant and Grigorieff 2015) and GCTF (Kai Zhang 2016) among others are commonly used to assess the defocus and astigmatism in images. Defocus and astigmatism parameters are estimated by maximizing the cross-correlation of a simulated CTF with the logarithmic amplitude spectra of observed images after background subtraction. They can be represented by two defocus values, $\Delta f1$ and $\Delta f2$, and an angle, α which define an astigmatic CTF (Figure 3-24 A) (Rohou and Grigorieff 2015). Once the CTF parameters are determined correction for the CTF can be done. the CTF correction process can be decomposed into several steps. The simplest correction of the CTF is by ‘‘phase flipping,’’ which corrects the data only for the sign of the CTF, and thus obtain the correct signs of phases in Fourier space. (Figure 3-24 C D).

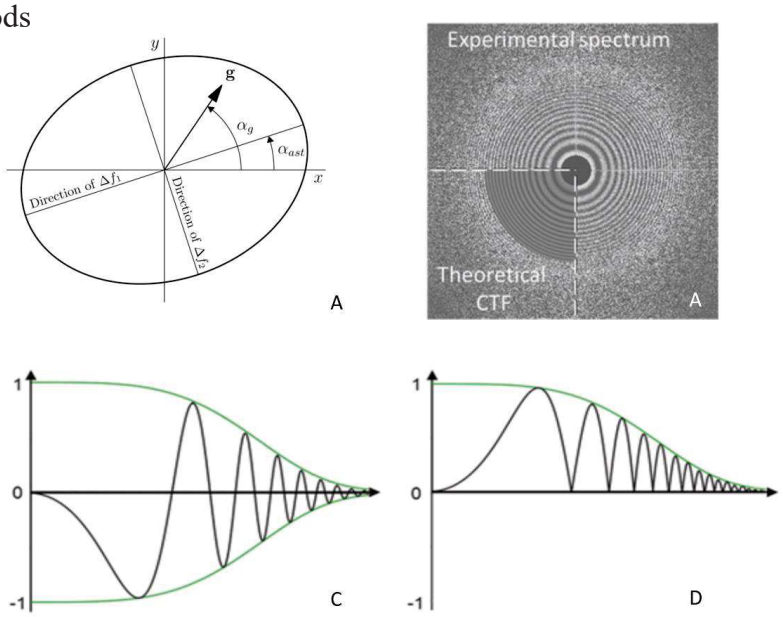

Figure 3-24 CTF estimation
A Two defocus values, Δf1 and Δf2, and an angle, αast define an astigmatic CTF. B Comparison of theoretically calculated CTF (left bottom quadrant) with CTF seen in the experimental spectrum. For an accurate CTF determination, the Thon rings from both image parts should match accurately C Image typical power spectrum before correction. D Phase flipped power spectrum from A (Rohou and Grigorieff 2015) BCD (Costa, Ignatiou, and Orlova 2017)

3.3.1.3 Particle picking

The picking consists to select the projections of interest within each image (Figure 3-25). The coordinates are then saved to be used downstream in the processing workflow.

Various selection strategies have been implemented, from unsupervised picking using Laplacian of Gaussian operators (relion) to reference supervised picking (relion, e2boxer, gautomatch) where a cross-correlation in the Fourier space allows a more efficient but biased picking. Recently, new algorithms have emerged based on machine learning (Topaz, Cryolo, Boxnet (warp)). All these picking strategies had unquestionable success. In the frame of this Ph.D., machine learning approaches were particularly useful to pick more selectively the particles and under-represented orientations.

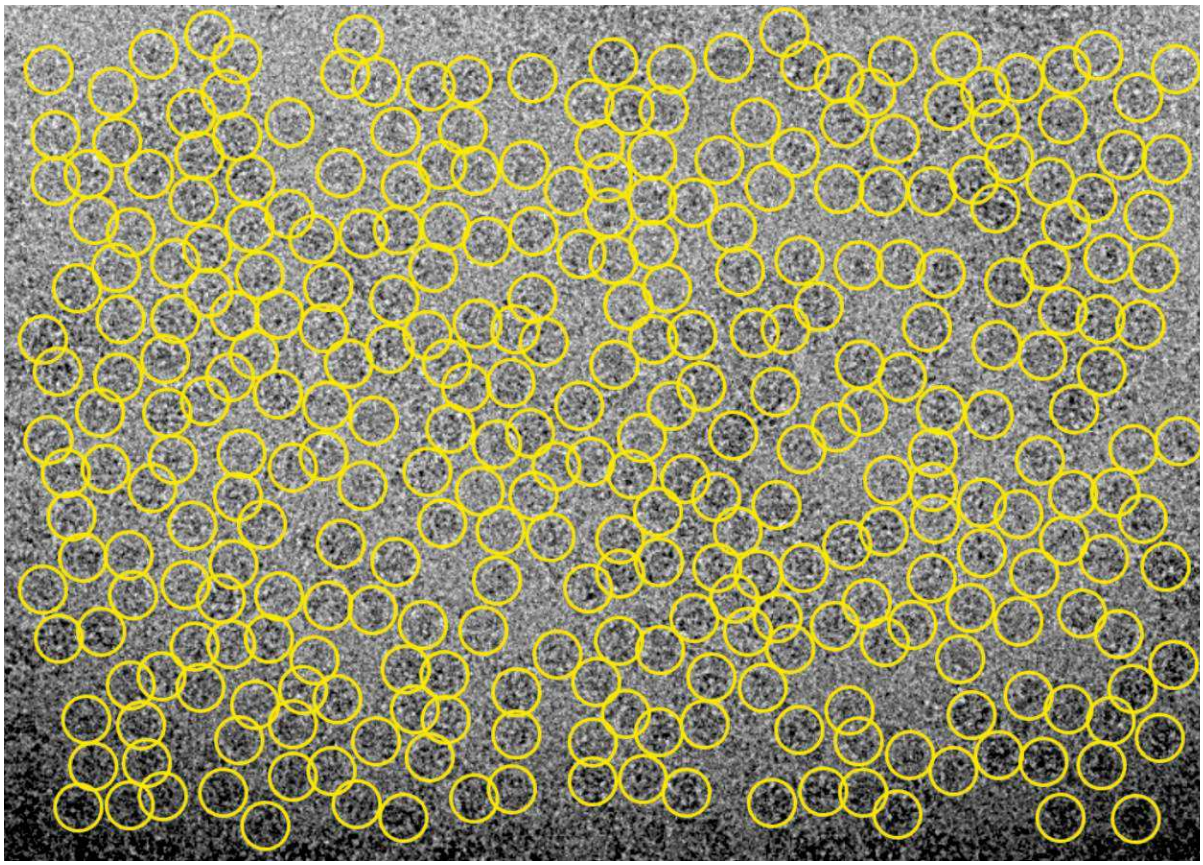

Figure 3-25 AVP-V2R-Arr-ScFv30 automatic picking
Representative image of the AVP-V2R-Arr-ScFv30 sample. The yellow circles represent the projections picked with Boxnet (warp)

3.3.2 Processing

3.3.2.1 Rational

After pre-processing, 2D projections of the sample are extracted for iterative 2D and 3D classifications with the ultimate goal to reconstruct a three-dimensional map of the sample. However, unstained protein molecules in ice yield images with a low signal-to-noise ratio particularly for high frequencies corresponding to high-resolution details at the level of the specimen. Consequently, it is necessary to align and average noisy, low-contrast images of many projections in many orientations recorded under low-dose conditions to extract the high-resolution information. It can be illustrated by a Guinier plot with the natural logarithm of the average structure factor as a function of resolution (Figure 3-26 A). The noise decreases proportionally to the logarithm of the number of projections and it is particularly critical to extract the high-resolution information (Rosenthal and Henderson 2003).

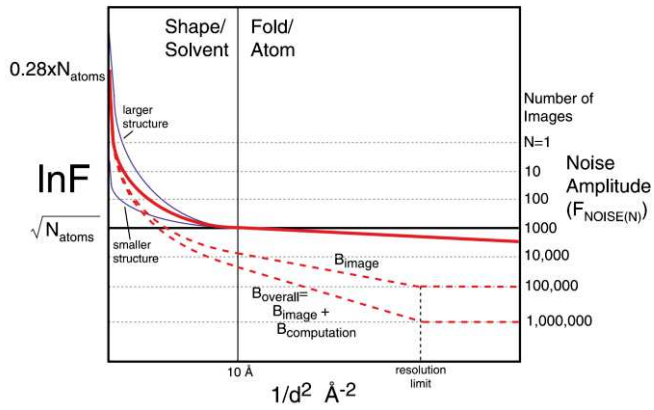

Figure 3-26 Schematic Guinier plot shows the natural logarithm of the spherically averaged structure factor amplitude
(F) for a protein against 1/d2, where d is the resolution (Å). Zero angle scattering is equal to N atoms carbon equivalents of the molecular mass multiplied by the solvent contrast (0.28) and places the scattering on an absolute scale. The protein scattering curve (red line) consists of a low-resolution region (d > 10 Å) determined by molecular shape and solvent contrast, and a high-resolution region (d< 10 Å) which approaches the scattering of randomly placed atoms described by Wilson statistics, which decreases only slightly with resolution and may be approximated by the horizontal line of amplitude $\sqrt{\text{Natoms}}$. The high-resolution region may also have structure corresponding to fold-specific features, including a-helix and b-sheet. The average noise amplitude is $F_{Noise(1)}$ for a single image or $F_{Noise(1)}/\sqrt{N}$ after averaging N images. Low-resolution structure factor amplitudes are also shown for a large structure that might be studied by tomography and a small molecular mass particle which has a low-resolution scattering amplitude below the noise level for one image (blue lines). The experimental contrast loss for structure factors at high resolution due to imperfect images is indicated by a dotted red line labeled by its slope, the temperature factor B_{image}. Additional contrast lost due to imperfect computations gives a line with slope $B_{overall}$, which is the sum of temperature factors B_{image} and $B_{computation}$. The resolution limit is indicated where the structure factor curve equals the noise level, which in this example occurs at 10^6 particles for $B_{overall}$, but at 10^5 particles if $B_{computation}$ =0.
(Rosenthal and Henderson 2003):

3.3.2.2 Maximum likelihood implementation

The maximum-likelihood method provides a powerful approach to align a large number of very noisy electron-microscope projections with the ultimate goal .to deduce the three-dimensional (3D) structure of the particles that were imaged. It is implemented into at least two popular commonly used SPA software relion (Scheres 2012) and cryoSPARC (Punjani et al. 2017).

The Maximum-likelihood method is a statistical approach which seeks to maximize a probability function. The aim is to maximize the probability $P(\Theta|\chi)$ that the model Θ is the correct one, given the data χ. To do that one solution is to estimate the probability of observing χ given Θ. This probability is called likelihood and can be defined as $L(\Theta) = P(\chi|\Theta)$. The expectation-maximization algorithm (Dempster, Laird, and Rubin 1977) a general approach to iteratively computation of maximum-likelihood estimates when the observations can be viewed as incomplete data, is the most widely followed approach to this problem.

Expectation-maximization algorithm

The first step to use the expectation-maximization algorithm is to set randomly a set of parameters that will be iteratively tuned to maximize the likelihood. For example for a gaussian mix with two gaussian parameters, the parameters are (i) the probabilities π for each n in data χ to belongs to the first (Cl1) or the second (Cl2) gaussian and, (ii) the parameters of the two Gaussian distributions $\Theta_k(\mu_k;E_k)$. Global parameters can be defined as $\phi_n = (\pi_1, \dots, \pi_g; \Theta_1, \dots, \Theta_g)$. Interestingly, each individual is not attributed to one single class, but in all the classes weighted by a probability, it is a probabilistic approach qualified as soft clustering. For example, individual 1 can have π_1 =0.2 and π_2 =0.8 this means, it will be considered as part of the Cl1 with 20% probability and as part of the Cl2 with 80% probability (Figure 3-27).

The next step is to calculate the likelihood with the formula (for a gaussian mix with two gaussian) (Figure 3-27).

$$L(\Theta) = L(\chi;\phi) = \sum_{i=1}^{n} \log\left(\sum_{k=1}^{g} \pi f(x_i, \Theta_k)\right)$$

Then the Expectation step allows the calculation of the $\pi_{(r+1)}$ conditional probabilities (probability to belong to Cl1 or Cl2) accordingly to $\Theta_{(r)}$ (Figure 3-27).

The subsequent Maximisation step computes new estimated gaussian parameters $\Theta_{(r+1)}$ accordingly to the precedently calculated $\pi_{(r+1)}$ (Figure 3-27).

Finally, we compute once again the likelihood accordingly to $\phi_{n_{(r+1)}} = (\pi_{1(r+1)}, \dots, \pi_{g(r+1)}; \Theta_{1(r+1)}, \dots, \Theta_{g(r+1)})$. If the likelihood converges to the same value we can keep the model, if the likelihood increases we can improve it iteratively with a new cycle (Figure 3-27) (Sigworth et al. 2010; Walker and Redner 1984; Dempster, Laird, and Rubin 1977).

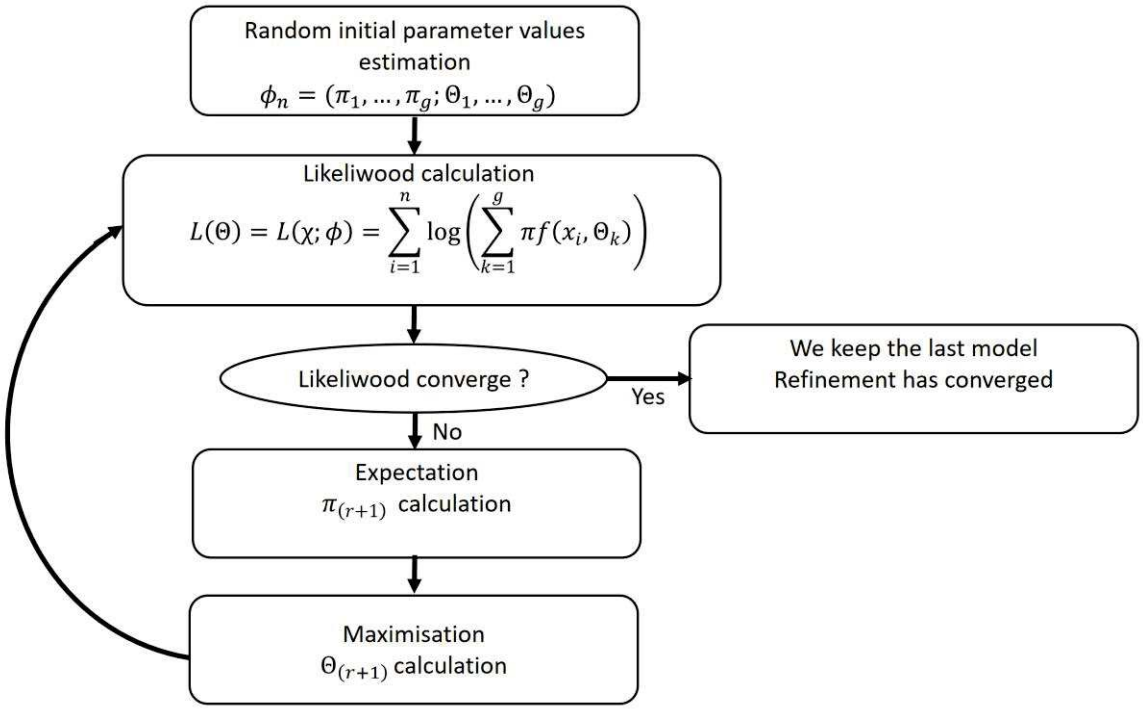

Figure 3-27 Schematic representation of the EM algorithm application

3.3.2.3 2D Classification

2D classification consists of aligning 2D projections of the same object in the same orientation and averaging them in an attempt to obtain well-defined views with increased SNR of a molecule, amenable to quantitative measurements (Figure 3-28). In the SPA workflow, it is a critical step for projections curation and data quality estimation. In the frame of 2D classification using the expectation-maximization algorithm, all projections are first attributed to all classes in all orientations weighted by an equal probability and iteratively classified as precedently described (Sigworth et al. 2010).

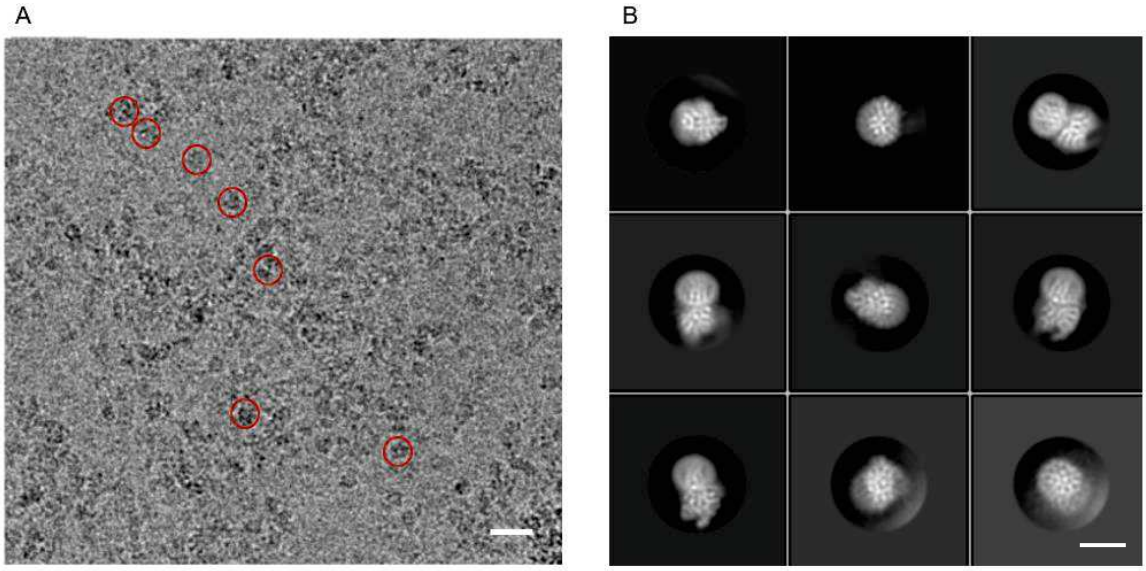

Figure 3-28 Cryo-EM micrograph and 2D classes of the activated AVP-V2R-Gs-Nb35 complex.
Examples of sample particle projections are circled (scale bar: 30 nm). b, Representative reference-free two-dimensional averages show distinct secondary structure features for G protein and GLP-1R embedded in MNG detergent micelle. The diameter of the circular windows is 15 nm.

3.3.2.4 3D Abinitio models and stochastic gradient descent

Traditionally, it was difficult to calculate a good initial *ab-initio* model, and various strategies such as random conical tilt (Radermacher et al., 1987) or the common lines approach (Van Heel, 1987) were employed. Recently, *ab-initio* model generation algorithms have been significantly improved and are no longer as much of a limiting step in the image processing pipeline.

The stochastic gradient descent (SGD) is initialized from a computer-generated random 3D map. SGD iteratively optimizes an objective function by computing approximate gradients and taking steps in the parameter space according to those gradients. This method allows for generating a first model used downstream in the 3D processing (Figure 3-29) (Punjani et al. 2017). The SGD noisy sampling allows the algorithm to widely explore the space of all 3D maps to finally arrive near the correct structure. It can also be executed with more than one class to sort projections in heterogeneous data sets (Punjani et al. 2017).

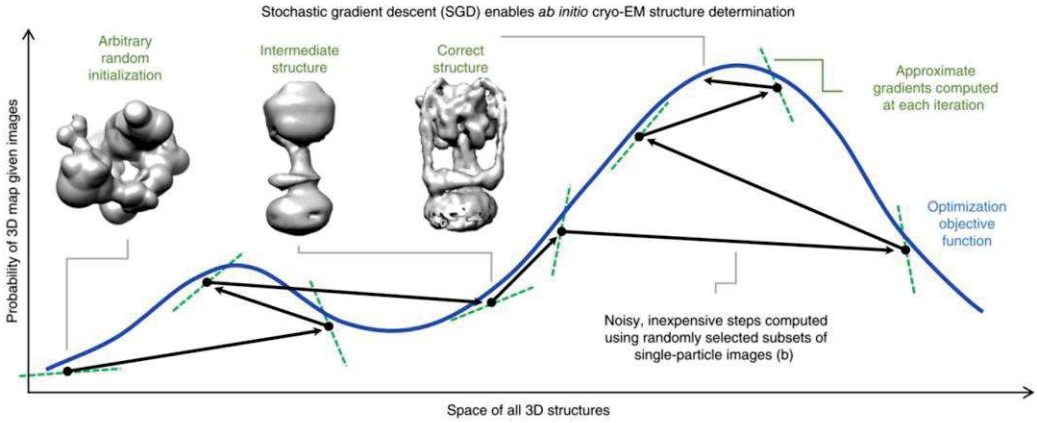

Figure 3-29 Stochastic gradient descent (SGD) algorithm
Stochastic gradient descent (SGD) algorithm enables ab initio structure determination through insensitivity to initialization. An arbitrary computer-generated random initialization is incrementally improved by many noisy steps. Each step is based on the gradient of the approximated objective function obtained by random selection. These approximate gradients do not exactly match the overall optimization objective. (Punjani et al. 2017)

3.3.2.5 3D Classification

3D classification against the initial model can then be employed to curate a data set and to sort conformational heterogeneity in 3D space. this can yield multiple reconstructions corresponding to different conformational or compositional states. For example, for the AVP-V2R-Gs-Nb35 complex data processing, a classification on 877,003 particles with 6 classes discriminated three sub-conformations which were further processed independently (Figure 3-30)

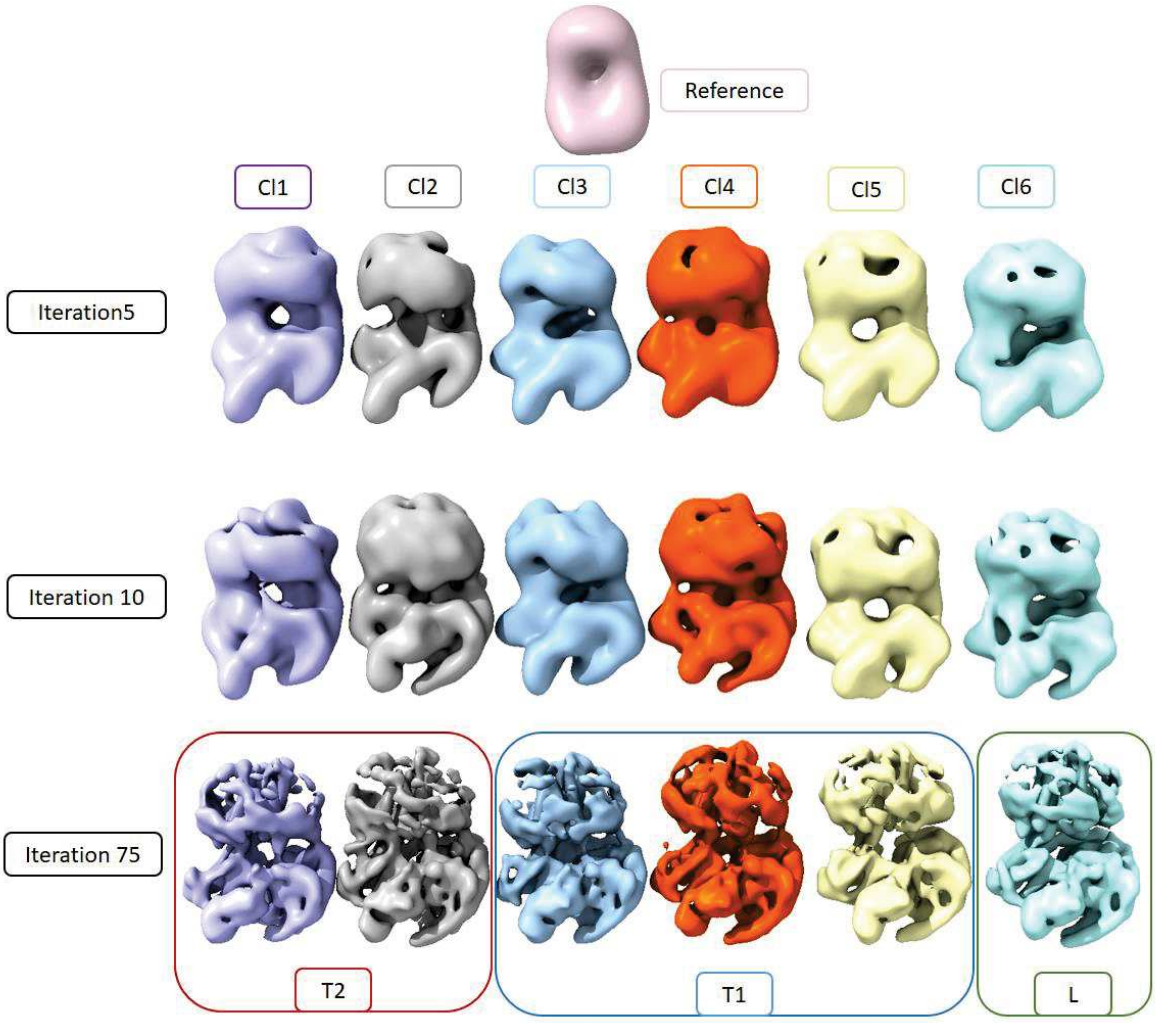

Figure 3-30 3D classification with six classes of the AVP-V2R-Gs-Nb35 complex,
The reference was low-pass filtered at 30Å resolution. The classification allowed to discriminate three conformational substates.

3.3.2.6 3D Refinement

Selected particles after 3D classification are further subjected to 3D refinement against a reference volume, either the previously determined initial model, or a volume resulting from 3D classification. During 3D refinement, the data is split into two independent random halves datasets and refined independently (Scheres and Chen 2012). During refinement, the independent volumes are aligned at low resolution to prevent the two half-maps from diverging too far. This approach is termed "gold-standard refinement" and avoids overfitting and inflated resolution estimations.

3.3.3 Postprocessing

3.3.3.1 CTF refinement, Bayesian polishing, and high order aberrations correction

Postprocessing is a combination of new steps introduced in 2018 that take advantage of the final 3D computed map to improve the CTF estimation and correct optical aberration, magnification anisotropy, and beamtilt (Zivanov et al. 2018; Forsberg et al. 2018).

CTF refinement

To refine the CTF parameters, (defocus and astigmatism). The use of a 3D reference structure allows CTF estimation to exploit both the phases and the amplitudes of the experimental images, instead of having to rely exclusively on their power spectra for per-projection CTF estimation like during conventional CTF estimation (Forsberg et al. 2018).

Correction of (beam-tilt, trefoil, spherical aberration, tetrafoil)

Ultra-high-resolution cryo-EM structures require correcting for electron-optical aberrations and microscope misalignments that result in nuanced "high-order" terms in the CTF. Each of those needs to be estimated from single projection data itself, by refining the corresponding CTF parameters against a high-resolution reference map.

The bayesian polishing

It implements a Gaussian Process regression algorithm for estimating beam-induced motion tracks for individual projections and an improved B-factor estimation algorithm for resolution-dependent weighting of individual movie frames (Forsberg et al. 2018).

Iterative use of these recent features allows to improve the CTF and motion image parameters estimation and to correct optical aberration, magnification anisotropy, and beamtilt leading to an improved map quality and resolution for the final 3D reconstruction.

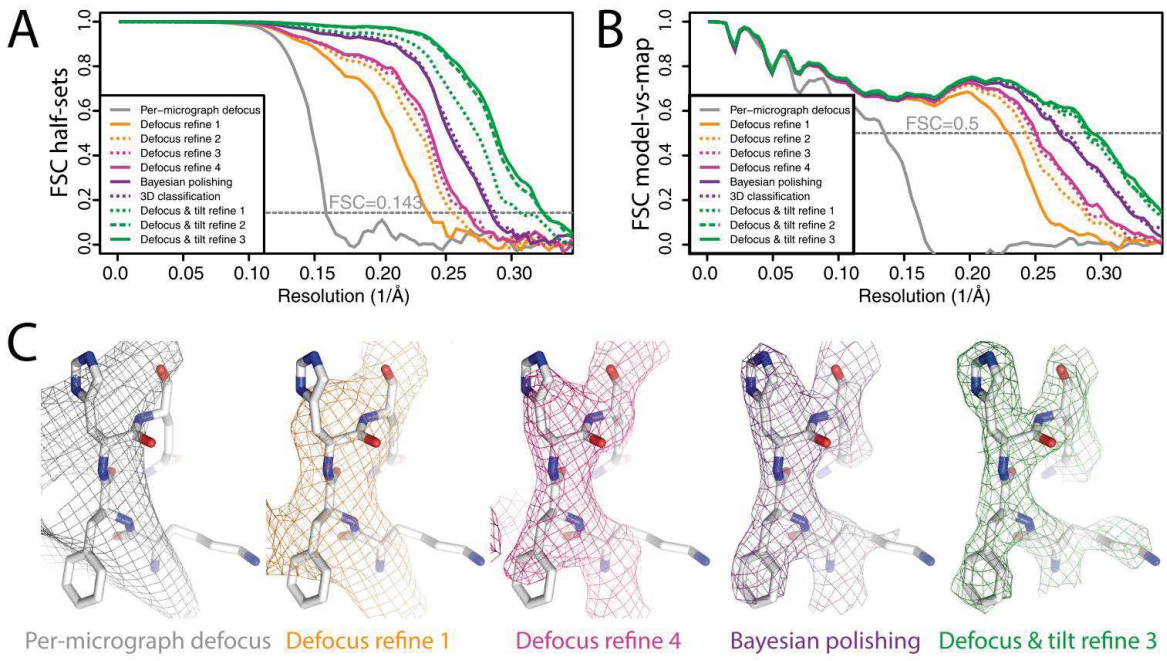

Figure 3-31 Postprocessing cryo-EM map improvement
Per-projection defocus correction (A) FSC curves between independently refined half-maps for the different stages of processing as explained in the main text. (B) As in A, but FSC curves are between the cryo-EM maps and the corresponding atomic model (PDB-4FNK) (Ekiert et al., 2012). (C) Representative density features for some of the maps for which FSC curves are shown in A and B.From (Forsberg et al. 2018)

3.3.3.2 Map Resolution estimation

The commonly accepted procedure for resolution estimation in cryo-EM is the Fourier shell correlation (FSC), which measures the correlation of Fourier coefficients in resolution shells between independent map reconstructions (Saxton and Baumeister 1982). The map resolution is currently a specific cut-off of the FSC curve. By convention, the cut-off value is 0.143 as determined by Henderson and co-workers (Rosenthal and Henderson 2003). Nonetheless, the cutoff choice is a point of contention within the EM community.

3.3.3.3 Density map sharpening

Once the cryo-EM map has been calculated, and the resolution estimated, low-pass filtering at its resolution cut-off and a sharpening process is usually performed on the 3D volume (Rosenthal and Henderson 2003). It allows to enhance map visualization and has proven very important in the key task of structural modeling.

Indeed, High-resolution contrast in cryo-EM maps is attenuated by a resolution-dependent amplitude gaussian falloff induce by optical image properties and sample heterogeneity (Figure 3-26). Compensation is achieved by sharpening with a uniform map B-factor, which partially

restores contrast loss in cryo-EM maps (Rosenthal and Henderson 2003). Moreover, to better restore the high resolution signal new tools allows to sharpen maps locally according to the local resolution, and in a more optimal way (Terwilliger et al. 2018; Kaur et al. 2021; Jakobi, Wilmanns, and Sachse 2017).

3.3.4 New tool to probe continuous dynamic systems

Classical SPA is perfectly suited to process data of homogeneous samples with a limited number of rigid conformation. However, biologic systems can be dynamic and can experience a continuum of sub-conformation. This potential flexibility may raise difficulty for structure determination. Commonly, it is handled through efforts during molecular biology (thermostabilization, fusion modules addition) and biochemistry (complexation with stabilizing Nbs and ScFvs) to favor and constrain one conformation of the system. Nonetheless, this raises the question of the physiological relevance of these systems and we can hypothesize that the study of the dynamic itself might improve our understanding of biological processes at the molecular scale.

New tools recently emerged to tackle such flexible systems, such as ‘multibody refinement’ in Relion (Nakane et al. 2018) or ‘3D-variability analysis (3Dvar)’ in Cryosparc (Punjani and Fleet 2021) or CryoDRGN (Zhong et al. 2020). Since multi-body refinement probe flexibility between a defined number of rigid bodies, 3Dvar and CryoDRGN can probe detailed molecular motions at the scale of α-helices with multivariate statistical analysis and neural network-based approaches respectively.

3.4 Preparation of biological samples

3.4.1 Protein expression and purification

3.4.1.1 V2R expression

Due to the degeneracy of the genetic code, most amino acids are specified by more than one codon (synonymous codons). Synonymous codons are not used at equal frequencies, their relative frequency varying with both the gene and the organism (Gribskov, Devereux, and Burgess 1984). Consequently, sequences need to be optimized for an optimal expression. The V2R sequence was optimized with GENEius (Eurofins proprietary software) for expression in insect Sf9 (a clonal isolate of *Spodoptera frugiperda* Sf21 cells) cells.

The optimized sequence of the human V2R was cloned into a pFastBac1 vector (Invitrogen) adapted for insect Sf9 cells infection using a baculovirus cell expression system (Figure 3-32 A).

Construct for Gs protein coupling:

To facilitate expression and purification of the V2R construct for cryo-EM, the hemagglutinin signal peptide (MKTIIALSYIFCLVFA) followed by a Flag tag (DYKDDDDA) was added at the N terminus, and a Twin-Strep-tag (WSHPQFEKGGGSGGGSGGGSWSHPQFEK) was inserted at the C terminus. In addition, N22 was substituted with a glutamine residue to avoid *N*-glycosylation, and C358 was mutated into an alanine to eliminate potential intermolecular disulfide bridges during solubilization and purification. A Tobacco Etch Virus protease cleavage site (following the Flag tag) and two Human Rhinovirus 3C protease cleavage sites (HRV3C) (one inserted in the N terminus between D30 and T31 and the other inserted in the C terminus between G345 and Q354 and replacing R346-TPPSLG-P353) were also added to remove N and C termini and facilitate structure determination. M1L2 residues were replaced by AS residues, and LE residues were added before the Twin-Strep-tag, during subcloning (introduction of Nhe I and Xho I restriction sites, respectively) (Figure 3-33A).

Construct for Arrestin protein coupling:

The hemagglutinin signal peptide (MKTIIALSYIFCLVFA), a Flag tag (DYKDDDDA), a Twin-Strep-tag (WSHPQFEKGGGSGGGSGGGSWSHPQFEK), a (HRV3C) protease cleavage site, and an additional Flag tag were at the N-terminus of the receptor. N22 was substituted with a glutamine residue to avoid *N*-glycosylation (Figure 3-33B). The whole C terminus was conserved intact as it is crucial for arrestin interaction. M1L2 residues of the wild-type V2R sequence were deleted in the N-terminus of this construct.

3.4.1.1.1 Infection of Sf9 cells using the different V2R constructs:

Sequence modifications did not affect the receptor-ligand binding or function. The V2R was expressed in Sf9 insect cells using the Bac-to-Bac baculovirus expression system (Thermo Fisher Scientific) according to the manufacturer's instructions. Insect cells were grown in suspension in EX-CELL 420 medium (Sigma-Aldrich) to a density of 4×10^6 cells/ml and infected with the recombinant baculovirus at a multiplicity of infection of 2 to 3. The culture medium was supplemented with the V2R pharmacochaperone antagonist TVP (Sigma-Aldrich) at 1 µM to increase the receptor expression levels (J. P. Morello, Bouvier, et al. 2000; Jean-Alphonse et al. 2009). The cells were infected for 48 to 54 hours at 28°C, and expression of the

V2R was checked by immunofluorescence using an anti-Flag M1 antibody coupled to Alexa Fluor 488. Cells were then harvested by centrifugation (two steps for 20 min at 3,000*g*), and pellets were stored at -80°C until use.

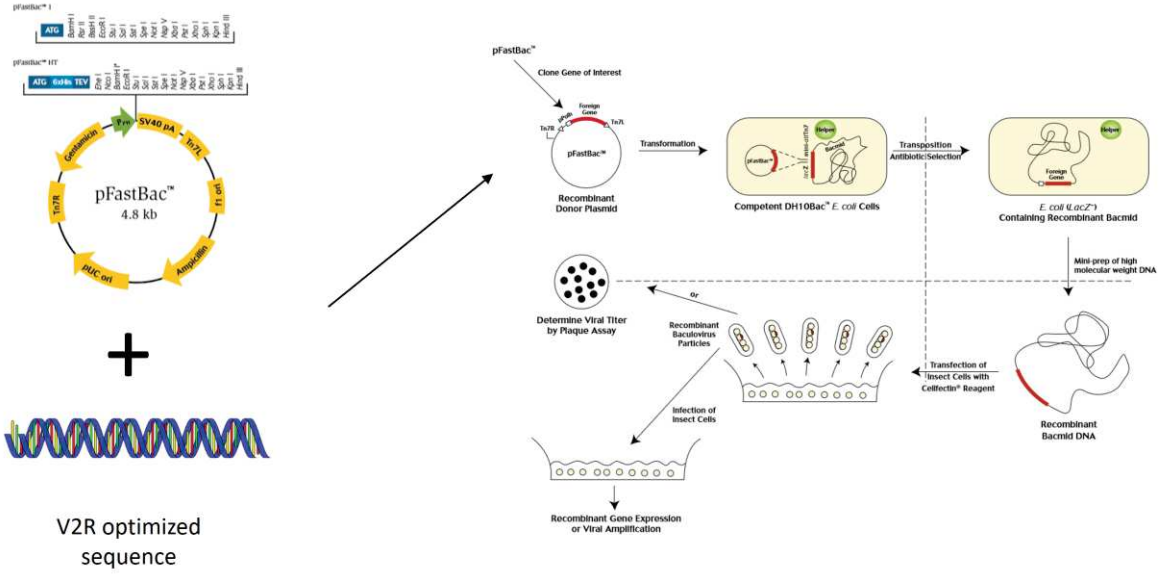

Figure 3-32 V2R Expression
After sequence optimization the V2R gene is inserted in a pFastBac (introduction of Nhe I and Xho I restriction sites).The V2R is then producesd in Sf9 cells according to the protocol provided by the manufacturer.

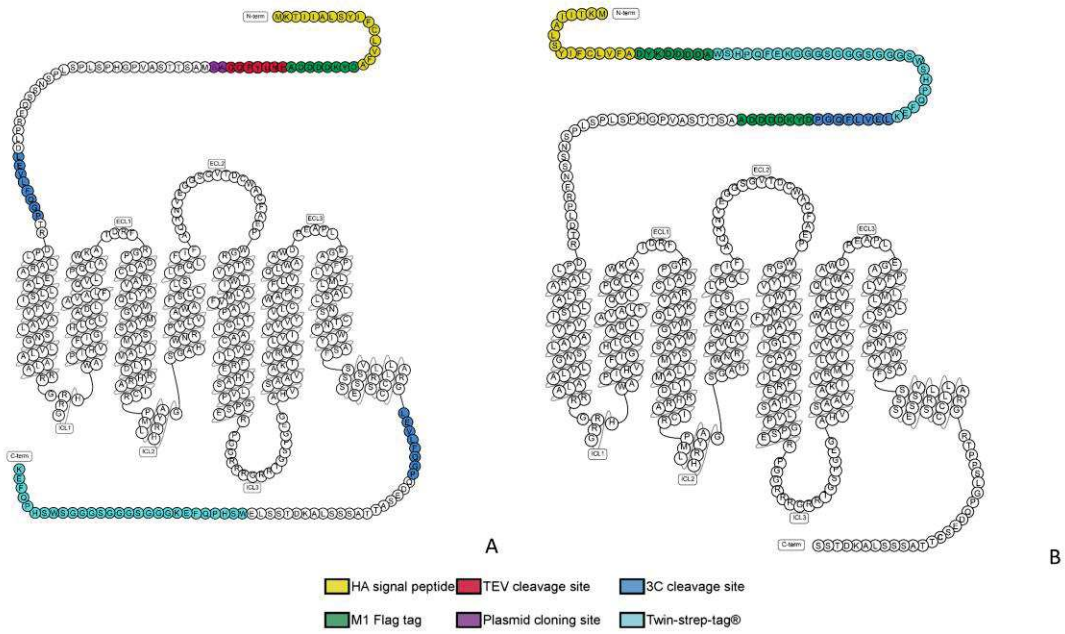

Figure 3-33 snake plots of the two constructs used to in the V2R-Gs and V2R-βarr complexes
Modified snake plots from https://gpcrdb.org of the engineered V2R. A) V2R construct used for cryo-EM structure determination of the V2R-Gs complex (left). HA, hemagglutinin signal peptide; TEV protease, tobacco etch virus protease; 3C, human rhinovirus 3C protease; plasmid cloning sites are Nhe1 and Xho1 restriction sites. B) V2R construct used for cryo-EM structure determination of the V2R-βarrestin1 (right). HA, Flag tags, Twin-Strep-tag, HRV3C protease cleavage site, as in the previous construct.

3.4.1.2 V2R Purification

3.4.1.2.1 Solubilization and first affinity chromatography (Anti-strep Streptactin column):

The cell pellets were thawed and lysed by osmotic shock in 10 mM tris-HCl (pH 8), 1 mM EDTA buffer containing iodoacetamide (2 mg/ml), 1 µM TVP, and protease inhibitors [leupeptine (5 µg/ml), benzamidine (10 µg/ml), and phenylmethylsulfonyl fluoride (PMSF) (10 µg/ml)]. After centrifugation (15 min at 38,400*g*), the pellet containing crude membranes was solubilized using a glass dounce tissue grinder (15 and 20 strokes using A and B pestles, respectively) in a solubilization buffer containing 20 mM tris-HCl (pH 8), 500 mM NaCl, 0.5% (w/v) *n*-dodecyl-β-d-maltopyranoside (DDM, Anatrace), 0.2% (w/v) sodium cholate (Sigma-Aldrich), 0.03% (w/v) cholesteryl hemisuccinate (CHS, Sigma-Aldrich), 20% glycerol, iodoacetamide (2 mg/ml), biotin BioLock (0.75 ml/liter, IBA), 1 µM TVP, and protease inhibitors. The extraction mixture was stirred for 1 hour at 4°C and centrifuged (20 min at 38,400*g*). The cleared supernatant was poured onto an equilibrated Strep-Tactin resin (IBA) for a first affinity purification step. After 2 hours of incubation at 4°C under stirring, the resin was washed three times with 10 column volume (CV) of a buffer containing 20 mM tris-HCl

(pH 8), 500 mM NaCl, 0.1% (w/v) DDM, 0.02% (w/v) sodium cholate, 0.03% (w/v) CHS, and 1 µM TVP. The bound receptor was eluted in the same buffer supplemented with 2.5 mM desthiobiotin (IBA).

3.4.1.2.2 Second affinity purification for AVP-V2R-Gs complex:

The eluate was supplemented with 2 mM $CaCl_2$ and loaded onto a M1 anti-Flag affinity resin (Sigma-Aldrich). The resin was washed with 10 CV of two successive buffers containing 20 mM Hepes (pH 7.5), 100 mM NaCl, 0.1% DDM, 0.01% CHS, 10 µM AVP, and 2 mM $CaCl_2$ and then 20 mM Hepes (pH 7.5), 100 mM NaCl, 0.025% DDM, 0.005% CHS, 10 µM AVP, and 2 mM $CaCl_2$, respectively. The receptor was eluted from the Flag resin using a buffer containing 20 mM Hepes (pH 7.5), 100 mM NaCl, 0.025% DDM, 0.005% CHS, 10 µM AVP, 2 mM EDTA, and Flag peptide (200 µg/ml) (Covalab).

After concentration using a 50-kDa molecular weight cutoff (MWCO) concentrator (Millipore), the V2R was purified by SEC using a Superdex 200 (10/300 column) connected to an ÄKTA purifier system (GE Healthcare). Fractions corresponding to the pure monomeric receptor were pooled (~2 ml) and concentrated to 50 to 100 µM with an excess of AVP (200 µM).

3.4.1.2.3 Second affinity purification for AVP-V2R-Arrestin2 complex:

3C protease was added for overnight cleavage. After digestion, the eluate was loaded onto a M2 anti-Flag affinity resin (Sigma-Aldrich). After loading, the DDM detergent was then gradually exchanged with Lauryl Maltose Neopentyl Glycol (LMNG, Anatrace). The LMNG concentration was then decreased gradually from 0.5 to 0.02%. The V2R was eluted in 20 mM Hepes (pH 7.5), 100 mM NaCl, 0.02% LMNG, 0.002% CHS, 10 µM AVP, and Flag peptide (0.4 mg/ml).

After concentration using a 50-kDa molecular weight cutoff (MWCO) concentrator (Millipore), the V2R was purified by SEC using a Superdex 200 (10/300 column) connected to an ÄKTA purifier system (GE Healthcare). Fractions corresponding to the pure monomeric receptor were pooled (~2 ml) and concentrated to 50 to 100 µM with an excess of AVP (200 µM).

3.4.1.3 G_s expression and purification

Human $G\alpha_s$, $G\beta_1$ with an N-terminal Twin-Strep-tag, and $G\gamma_2$ were all expressed in Sf9 insect cells grown in EX-CELL 420 medium (Sigma-Aldrich). A recombinant baculovirus for $G\alpha_s$ subunit was prepared using the BestBac (Expression Systems) strategy, whereas a baculovirus for $G\beta_1$ and $G\gamma_2$ was prepared using the Bac-to-Bac system. $G\beta_1$ and $G\gamma_2$ were cloned in tandem into the pFastBac Dual vector (Thermo Fisher Scientific). Sf9 cells, at a density of 4×10^6

cells/ml, were coinfected with both viruses at a 1:2 $G\alpha_s$:$G\beta_1\gamma_2$ ratio for 72 hours at 28°C. Cells were harvested and pellets were stored at -80°C.

Coinfected Sf9 cell pellets were thawed and lysed in a buffer containing 10 mM tris-HCl (pH 7.4), 1 mM EDTA, 5 mM β-mercaptoethanol, 10 µM guanosine diphosphate (GDP), and protease inhibitors [leupeptine (5 µg/ml), benzamidine (10 µg/ml), and PMSF (10 µg/ml)]. Lysed cells were centrifuged (20 min at 38,400*g*). The pellets containing the crude membranes were homogenized using a glass dounce tissue grinder (20 strokes with tight B pestle) in solubilization buffer containing 20 mM Hepes (pH 7.5), 100 mM NaCl, 1% DDM, 5 mM $MgCl_2$ supplemented with 5 mM β-mercaptoethanol, 10 µM GDP, biotin BioLock (0.75 ml/liter), and protease inhibitors. The mixture was stirred for 40 min at 4°C and centrifuged (20 min at 38,400*g*). The supernatant was loaded onto a Strep-Tactin affinity resin equilibrated with the same buffer. The resin was washed three times, first with 5 CV of solubilization buffer, then with 5 CV of solubilization buffer supplemented with 100 µM tris(2-carboxyethyl)phosphine (TCEP) (instead of β-mercaptoethanol), and last with 10 CV of wash buffer containing 20 mM Hepes (pH 7.5), 50 mM NaCl, 0.1% DDM, 1 mM $MgCl_2$, 100 µM TCEP, and 10 µM GDP. The G_s heterotrimer protein was eluted in the same buffer supplemented with 2.5 mM desthiobiotin. After treatment with antarctic phosphatase (5 U; NEB Inc.) for 30 min at 4°C, the G_s protein was concentrated to 10 mg/ml using 50-kDa MWCO concentrators. Twenty percent of glycerol was added to the sample, and aliquots were flash-frozen in liquid nitrogen before storage at -80°C.

3.4.1.4 βarrestin1 (arrestin2) expression and purification

βarr1(ΔCT) truncated at residue 382 was used (Kovoor et al. 1999b). It was prepared as follows. BL21(DE3) competent E. coli cells (ThermoFisher Scientific) were transformed and large-scale cultures were grown in LB + kanamicin at 37 °C (170rpm) until an optical density (OD600) at 0.6 U was reached. Cells were either induced at 37 °C by 0.025mM IPTG and collected 5h post-induction or induced at 20 °C by 0.025mM IPTG and collected 10-12 h post-induction. Cells were collected by centrifugation (two steps for 20 min at 3,000*g*), and pellets were stored at -80°C until use. Cells were resuspended in lysis buffer (20 mM Tris-HCl (pH 8), 1 mM EDTA, 200 mM NaCl, 1 mM β-mercaptoethanol) supplemented with protease inhibitors [leupeptine (5 µg/ml), benzamidine (10 µg/ml), and PMSF (10 µg/ml)]. Cells were lysed by sonication and the lysate was supplemented with $MgCl_2$ (5mM final) and Benzonase (highly active nuclease that degrades DNA and RNA). After centrifugation (20 min, 4°C, 38,400g), the supernatant was supplemented with biotin BioLock (0.75 ml/liter) and loaded to Strep-Tactin affinity resin

at 4°C. The resin was washed with 20 column volumes of wash buffer (20 mM Tris pH, 200 mM NaCl, 100µM TCEP). The protein was then eluted with 5 column volumes of wash buffer supplemented with 2.5 mM desthiobiotin (IBA). Subsequently, it was subjected to a superdex 200 Superdex 200 (10/300 column) with a buffer containing 20 mM Hepes (pH 7.5), 200 mM NaCl and 100µM TCEP. The fractions corresponding to the complex were collected, concentrated to approximately 11 mg/ml using a 10-kDa MWCO concentrator (Millipore). Aliquots were stored at -80°C until use.

3.4.1.5 Nb35 expression and purification

The production and purification of Nb35 were performed following a protocol established by Kobilka and co-workers (Sŏren G.F. Rasmussen et al. 2011). Nb35 having a C-terminal 6His-tag was expressed in the periplasm of *Escherichia coli* strain BL21 following induction with 1 mM isopropyl-β-d-thiogalactopyranoside. Cultures were grown to an optical density at 600 nm of 0.6 at 37°C in LB medium containing 0.1% glucose and ampicillin (100 µg/ml). Induced cultures were grown overnight at 25°C. Cells were harvested by centrifugation and lysed in ice-cold buffer 50 mM tris-HCl (pH 8), 125 mM sucrose, and 2 mM EDTA. The lysate was centrifuged to remove cell debris, and Nb35 was purified by nickel affinity chromatography. Eluate was concentrated to 5 mg/ml and loaded onto a Superdex 200 (16/600 column, GE Healthcare) at a 1 ml/min flowrate. Fractions containing the monodisperse peak of Nb35 were pooled and dialyzed overnight against a buffer containing 10 mM Hepes (pH 7.5) and 100 mM NaCl at room temperature (RT). The dialyzed sample was concentrated to approximately 100 mg/ml using a 10-kDa MWCO concentrator (Millipore). Aliquots were stored at -80°C until use.

3.4.1.6 ScFv30 expression and purification

The production and purification ScFv30 was performed as follows. ScFv30 having a C-terminal Strep-Tactin tag were expressed in *Drosophila* S2 cells (Schneider). Cells were harvested by centrifugation, protease inhibitors [leupeptine (5 µg/ml), benzamidine (10 µg/ml), and phenylmethylsulfonyl fluoride (PMSF) (10 µg/ml)] were added to the supernatant. The ScFv30 was purified by Strep-Tactin affinity chromatography. The eluate was concentrated at 5-10ml and dialyzed 2 hours to remove the desthiobiotin in a buffer containing 20mM HEPES, 100mM NaCl. The dialyzed sample was concentrated to approximately 100 mg/ml using a 10-kDa MWCO concentrator (Millipore). Aliquots were stored at -80°C until use.

3.4.1.7 Purification of the AVP-V2R-G_s-Nb35 complex

Formation of a stable complex was performed by mixing the purified V2R with 1.2 molar excess of purified G_s heterotrimer, 250 µM AVP, and 2.5 mM $MgCl_2$ (Figure 3-34 A). The coupling reaction was allowed to proceed at RT for 45 min and was followed by the addition of apyrase (0.0125 U; NEB Inc.) to hydrolyze residual GDP and maintain the high-affinity nucleotide-free state of G_s. Fifteen minutes later, Nb35 was added at a twofold molar excess compared to G_s. After 15 more minutes at RT, the mix was incubated overnight at 4°C. In most reaction mixtures, the final concentration of V2R was 20 to 30 µM, that of G_s 30 to 40 µM, and the one of Nb35 around 80 µM. To remove excess of G protein heterotrimer and Nb35, the complex AVP-V2R-G_s-Nb35 was purified by an M1 anti-Flag affinity chromatography. After loading, the DDM detergent was then gradually exchanged with Lauryl Maltose Neopentyl Glycol (LMNG, Anatrace). The LMNG concentration was then decreased gradually from 0.5 to 0.01%. The complex and the unbound V2R were eluted in 20 mM Hepes (pH 7.5), 100 mM NaCl, 0.01% LMNG, 0.002% CHS, 2 mM EDTA, 10 µM AVP, and Flag peptide (0.2 mg/ml). The eluted AVP-V2R-G_s-Nb35 complex was separated from unbound V2R by SEC on a Superdex 200 (10/300 column) with a buffer containing 20 mM Hepes (pH 7.5), 100 mM NaCl, 0.002% LMNG, 0.0025% glyco-diosgenin (GDN, Anatrace), 0.002% CHS, and 10 µM AVP. The fractions corresponding to the complex were collected, concentrated with a 50-kDa MWCO concentrator, and subjected to a second SEC on a Superose 6 (10/300 GL, GE Healthcare) with a buffer containing 20 mM Hepes (pH 7.5), 100 mM NaCl, 0.0011% LMNG, 0.001% GDN, 0.002% CHS, and 10 µM AVP. Peak fractions were pooled and concentrated using a 50-kDa MWCO concentrator to concentrations ranging from ~1 to ~4 mg/ml for cryo-EM studies. The amphipol A8-35 (Anatrace) was added at 0.001% to help in the dispersion of the particles for cryo-EM grid preparation.

3.4.1.8 Purification of the AVP-V2R-Arr-ScFv30 complex

Purified V2R was mixed with equimolar PIP2, an excess of βarr1 (2:1) and an excess of ScFv30 (2:1) as well as 250mM AVP and 2.5 mM $MgCl_2$. The coupling reaction was allowed to proceed at room temperature for 2 h. To remove excess of βarr1 and ScFv30, the complex AVP-V2R-Arr-ScFv30 was purified by an M2 anti-Flag affinity chromatography. The complex was loaded three times on the column, the resin was washed three times with 10 (CV) of wash buffer containing 20 mM Hepes (pH 7.5), 100 mM NaCl, 0.02% CHS; 0.02% LMNG, 10µM AVP. The protein was then eluted with 5 column volumes of wash buffer supplemented with Flag

peptide (400 μg/ml). The complex was then loaded to Strep-Tactin affinity resin. The resin was washed with 10 column volumes of wash buffer (20 mM Hepes (pH 7.5), 100 mM NaCl, 0.002% LMNG, 0.002% glyco-diosgenin (GDN, Anatrace), 0.002% CHS, and 10 μM AVP). The protein was then eluted with 5 column volumes of wash buffer complemented with Desthiobiotine. The fractions corresponding to the complex were collected, concentrated with a 50-kDa MWCO concentrator, and subjected to a SEC Superose 6 (10/300 GL, GE Healthcare) equilibrated with a buffer containing 20 mM Hepes (pH 7.5), 100 mM NaCl, 0.0011% LMNG, 0.001% GDN, 0.002% CHS, and 10 μM AVP. Peak fractions were pooled and concentrated using a 50-kDa MWCO concentrator to concentrations of 2.7mg/ml for cryo-EM studies.

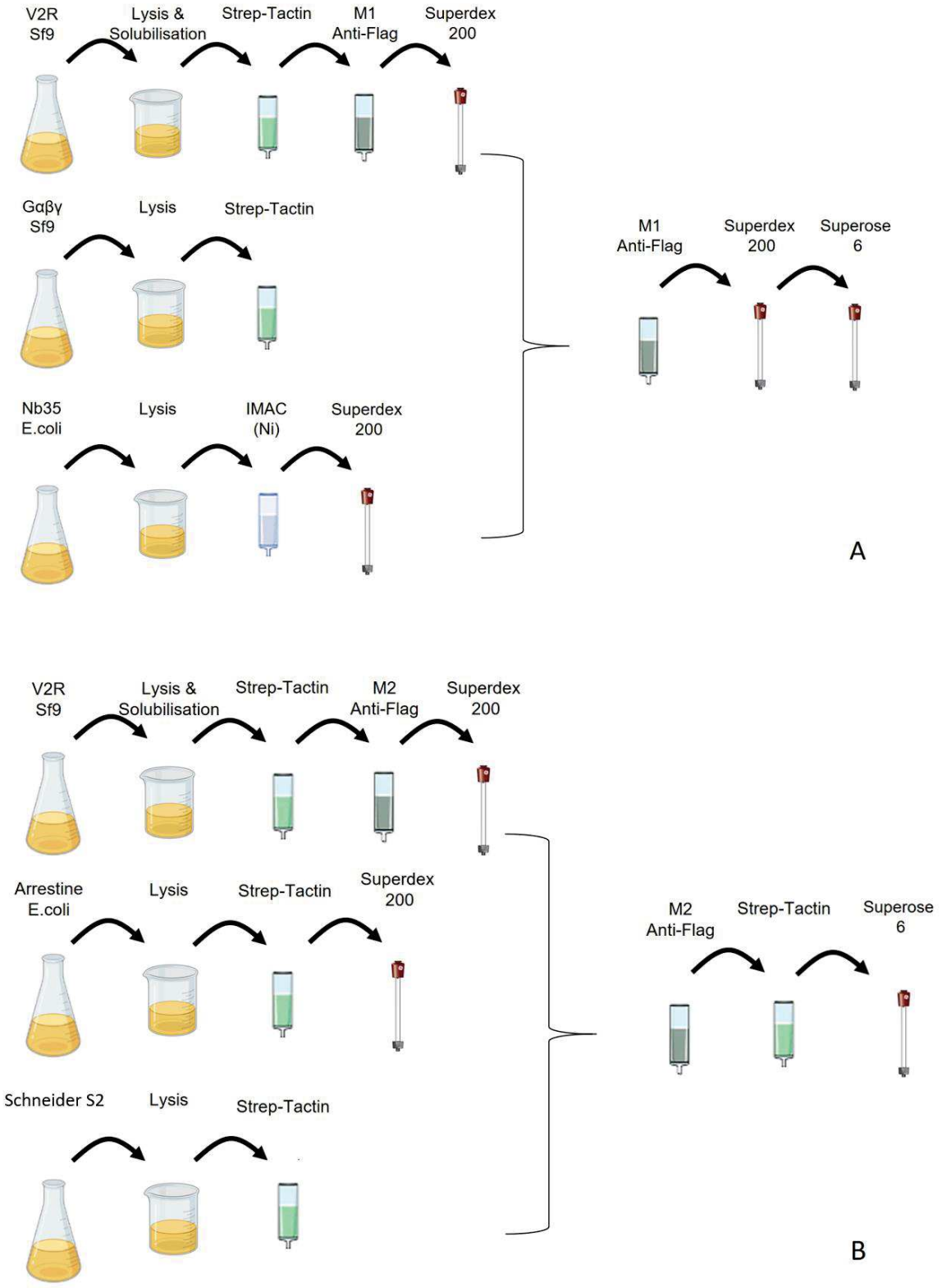

Figure 3-34 Schematic representation of the purification protocols
A). AVP-V2R-Gs-Nb35 purification protocol. B. AVP-V2R-βarr-ScFv30 purification protocol.

3.5 Negative stain microscopy observations

Before preparing cryo-EM grids, we first checked the quality and the homogeneity of the AVP-V2R-G_s-Nb35 and AVP-V2R-βArr1-ScFv30 samples by NS-EM. Three microliters of each complex at 0.04 mg/ml were applied for 2 min on glow-discharged carbon-coated grids and then negatively stained with 1% uranyl acetate or uranyl formate 0.75% for 1 min. Observation of EM grids was carried out on a JEOL 2200FS FEG operating at 200 kV under low-dose conditions (total dose of 20 electrons/$Å^2$) in the zero–energy loss mode with a slit width of 20 eV. Images were recorded on a 4K × 4K slow-scan charge-coupled device camera (Gatan Inc.) at a nominal magnification of ×50,000 with defocus ranging from 0.5 to 1.5 µm. Magnifications were calibrated from cryo-images of tobacco mosaic viruses.

3.5.1 AVP-V2R-G_s-Nb35 complex

In total, 37 micrographs were recorded, allowing us to pick 22,791 particles using e2boxer from Eman2 package (Tang et al. 2007). Further processing was performed with Relion 2.0 (Kimanius et al. 2016; Fernandez-Leiro and Scheres 2016). The particles were subjected to a 2D classification included to get rid of free micelles and dissociated components of the complex. From 2D classes, 14,545 particles corresponding to the AVP-V2R-G_s-Nb35 complexes were selected, representing 63% of all particles. This selection was used to calculate an ab initio low-resolution model. The sample was also subjected to NS-EM analysis after 5 days. At this point, after particle picking and 2D classification, 35% of particles were representing the complex. The fresh sample was also mixed with 100 µM GTPγS and 10 µM SR121463 V2R antagonist and visualized in negative stain to observe complete dissociation.

3.5.2 AVP-V2R-βArr1-ScFv30 complex

In total, 55 micrographs were recorded, allowing us to pick 97,182 particles using e2boxer from Eman2 package (Tang et al. 2007). Further processing was performed with Relion 3.1. The particles were subjected to a 2D classification included to get rid of free micelles and dissociated components of the complex. From 2D classes, 65,090 particles corresponding to the AVP-V2R-βArr1-ScFv30 complexes were selected, representing 67% of all particles.

3.6 Data acquisition for cryo-EM

3.6.1 AVP-V2R-G_s-Nb35 complex

In this study, two datasets have been recorded from two different preparations of AVP-V2R-G_s-Nb35. For the first dataset acquisition, 3 µl of purified AVP-V2R-G_s-Nb35 at a concentration of 0.75 mg/ml were applied on glow-discharged Quantifoil R 1.2/1.3 300-mesh copper holey carbon grids (Quantifoil Micro Tools GmbH, Germany), blotted for 4.5 s, and then flash-frozen in liquid ethane using the semi-automated plunge-freezing device Vitrobot Mark IV (Thermo Fisher Scientific) maintained at 100% relative humidity and 4°C. For the second dataset acquisition, cryo-EM grids were prepared as previously, but the purified V2R-G_s-Nb35 complex was at a concentration of 4 mg/ml, and the cryo-EM grids were prepared using an EM GP2 (Leica Microsystems) plunge freezer with a 4 s blotting time (100% humidity and 4°C).

Images were collected in two independent sessions on a TEI Titan Krios (Thermo Fisher Scientific) at the European Molecular Biology Laboratory (EMBL) of Heidelberg (Germany) at 300 keV through a Gatan Quantum 967 LS energy filter using a 20-eV slit width in zero-loss mode and equipped with a K2 Summit (Gatan Inc.) direct electron detector configured in counting mode. Movies were recorded at a nominal energy-filtered transmission electron microscope magnification of ×165,000 corresponding to a 0.81 Å calibrated pixel size. The movies were collected in 40 frames in defocus range between -0.8 and -2.2 µm with a total dose of 50.19 $e^-/Å^2$ (first dataset) and 41.19 $e^-/Å^2$ (second dataset). Data collection was fully automated using SerialEM (Mastronarde 2005).

3.6.2 AVP-V2R-βArr1-ScFv30 complex

For AVP-V2R-βarr1-ScFv30 cryoEM investigation, 3µl samples were applied on glow-discharged Quantifoil R 1.2/1.3 300-mesh UltrAufoil grids (Quantifoil Micro Tools GmbH, Germany), blotted for 3.5 s, and then flash-frozen in liquid ethane using the semi-automated EM GP2 (Leica Microsystems) plunge freezer (100% humidity and 4°C). Images were collected in one session on a TEI Titan Krios (Thermo Fisher Scientific) at the European Molecular Biology Laboratory (EMBL) of Heidelberg (Germany) at 300 keV through a Gatan Quantum 967 LS energy filter using a 20-eV slit width in zero-loss mode and equipped with a K3 Summit (Gatan Inc.) direct electron detector configured in counting mode. Movies were recorded at a nominal energy-filtered transmission electron microscope magnification of

×130,000 corresponding to a 0.64 Å calibrated pixel size. The movies were collected in 40 frames in defocus range between -1 and -2 µm with a total dose of 52.63 $e^-/Å^2$. Data collection was fully automated using SerialEM, resulting in 14,080 Movies.

3.7 Cryo-EM data processing

3.7.1 AVP-V2R-G_s-Nb35 complex

All data processing operations were performed with Relion-3.0.7 (Forsberg et al. 2018) unless otherwise specified. In total, 17,290 movies of the AVP-V2R-G_s-Nb35 sample at 0.75 mg/ml were collected. Dose-fractionated image stacks were subjected to beam-induced motion correction and dose weighting using Motioncorr's own implementation. Gctf was used to determine the contrast transfer function (CTF) parameters (Kai Zhang 2016) from non–dose-weighted images. After sorting, micrographs with maximum estimated resolution beyond 5 Å were discarded. Particle picking was carried out using Gautomatch [K. Zhang, Medical Research Council Laboratory of Molecular Biology (www.mrc-lmb.cam.ac.uk/kzhang/)], allowing us to pick out 2,291,432 particles. Particles were extracted in a box size of 240 Å, downscaled to 4 Å per pixel, and subjected to reference-free 2D classifications to discard false-positive particles or particles categorized in poorly defined classes. A subset of 1,109,475 particles was selected for further processing. This particle set was subjected to a 3D classification with four classes using the 30-Å low-pass filtered calcitonin receptor map as reference (Y. L. Liang et al. 2017). Particles from the two classes representing 27% of total particles and showing a complete AVP-V2R-G_s-Nb35 complex were selected, reextracted with a pixel size of 1.62 Å, and subjected to a 3D refinement. This subset of 307,125 particles yielded a map with a global resolution [Fourier shell correlation (FSC) = 0.143] of 4.8-Å resolution. Particles were then subjected to a focused 3D classification without angular and translational alignments with a mask including the complex minus $G\alpha_s$AH ($G\alpha_s$ α-helical domain). The best class corresponding to 150,000 particles was reextracted without binning and submitted to a 3D refinement, allowing us to obtain a map at 4.4-Å resolution. All further processing including signal subtraction, using different types of masks, CTF refinement, and polishing did not improve the resolution of the map.

In total, 8490 movies of the AVP-V2R-G_s-Nb35 sample at 4.0 mg/ml were recorded. The image processing steps were the same as previously described, except that the picking was performed using boxnet from Warp software package (Tegunov and Cramer 2018) allowing us to extract 1,214,575 particles. After a 2D classification to clean the dataset, a subset of 917,990 particles

was subjected to two successive rounds of 3D classification. A subset of 150,000 particles was used for further 3D refinements, yielding a final map at 4.4-Å resolution.

Both cleaned datasets were merged, corresponding to 1,109,475 particles from dataset 1 and 917,990 particles from dataset 2. Particles were subjected to 3D classification with three classes. One class displayed the expected structural features of the AVP-V2R-G_s-Nb35 complex corresponding to 877,003 particles and was selected for a new round of 3D classification with six classes. This classification revealed a structural variability in the ligand location and at the interface between the receptor and the G_s protein. Three subsets of particles were selected (L, T1, and T2 states), reextracted with a pixel size of 1.62 or 0.81 Å, and subjected to 3D refinements, yielding maps at 4.5, 4.7, and 5.5 Å, respectively. New rounds of 3D refinements were performed by applying a mask to exclude both the micelle and the $G\alpha_sAH$, yielding maps at 4.23, 4.4, and 4.7 Å. CTF refinement and polishing steps were applied on the three subsets of particles, allowing us to improve the resolution of the best map to 4.17 Å (FSC = 0.143). The T1 map (1.62 Å per pixel) was resampled at 0.81 Å per pixel for visualization purposes. Final refinements were processed with the option of masking individual particles with zero turned off. All our attempts to refine our final subsets in cisTEM (T. Grant, Rohou, and Grigorieff Nikolaus 2018) and cryoSPARC (Punjani et al. 2017) using nonuniform refinement did not improve the resolution of final maps.

To investigate the conformational dynamics of the signaling complex, multibody refinement was performed on 877,003 particles, with two bodies corresponding to AVP-V2R and G_s-Nb35. Local resolution was estimated with the Bsoft 2.0.3 package (Heymann 2017). Map sharpening was reevaluated with Phenix autosharpen tool (Terwilliger et al. 2018). Phenix resolve_cryoEM tool (Terwilliger et al. 2020) was used to improve the map interpretability and allowed to increase the estimated resolution to 4.04, 4.13, and 4.5 Å for L, T1, and T2 states, respectively (Figure 3-35).

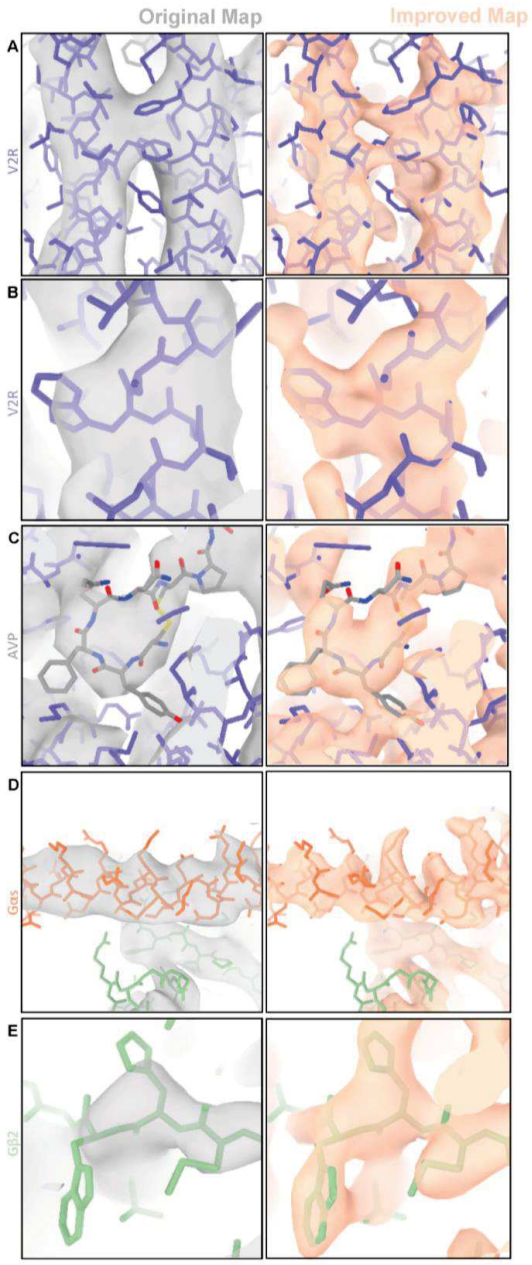

Figure 3-35 Improvement of the L density map using cryoresolve
In all panels, the density map and the corresponding final all-atom 3D model are superimposed. The improved map (right) is compared to the original map (left). V2R is depicted in purple, AVP in grey, Gαs subunit in orange and Gβ2 subunit in green. Increase in the visibility of several different regions of the AVP-V2R-Gs-Nb35 complex is shown: for instance contacts between F214 and F287 in V2R TM5 and 6 (A), W164 in V2R TM4 (B), AVP (C), N-terminal α helix of Gαs subunit (D) and H62-W63 in Gβ2 subunit (E).

3.7.2 AVP-V2R-βArr1-ScFv30 complex

Video frames were aligned using MotionCorr relion own implementation (relion 3.1.2) with 7 by 5 patches, with a B-factor of 150 and a binning factor 2, resulting in motion-corrected

micrographs with 1.28 Å pixel size. Contrast transfer function (CTF) estimations were performed using GCTF. The micrographs with a maximal resolution estimation worse than 7Å were discarded, resulting in 13,566 micrographs. A first picking was performed using boxnet from Warp software package (Tegunov and Cramer 2018) allowing to extract 3,610,370 particles which were transferred into Relion 3.1.2. Successive 2D classifications yielded a total of 1,169,437 particles. Those particle coordinates were used as references to train a model with Topaz (Bepler et al. 2019), a positive-unlabeled convolutional neural network for particle picking. It resulted in the picking of 4,595,394 particles. Those particles were transferred into Relion 3.1.2 and subjected to 2D classification. Best particles from boxnet and Topaz were merged and duplicate removed yielding 3,721,020 particles. Successive 2D classifications yielded a total of 729,335 projections. Successive rounds of CryoSPARC v.3.2.0 2D classification and ab initio (using two models) were then performed to further refine the particle stack to 27.637 particles which yielded an overall resolution of 4.75 Å after three-dimensional non-uniform refinement. The particle stack was transferred into relion for micelle-V2R signal subtraction and particles box were recentered and resized according to the βArr1-ScFv30 complex. Substracted particles were subjected to a local refinement yielding a density map with an overall resolution of 4.35Å. Attempts to align the complex with micelle subtraction yielded density maps with similar apparent quality and overall resolution than without subtraction ($r \approx$ 4.8-5 Å). Attempts to align the V2R alone were unsuccessful.

3.8 Model building and refinement

3.8.1 AVP-V2R-G_s-Nb35 complex

3.8.1.1 Receptor and AVP initial models.

The V2R was built by comparative modeling, using the MODELLER software (Webb and Sali 2017) and the x-ray structure of the δ-opioid receptor at 3.4-Å resolution (PDB code 4EJ4) as a template (Granier et al. 2012), sharing a sequence similarity of about 44% with the V2R (on the modeled region). Because modeling loops or terminal regions is a very challenging task and their dynamical behavior is very poorly described in Coarse-grained (CG) simulations, N and C termini of the receptor (residues 1 to 35 and 335 to 371, respectively) and part of the ICL3 loop (residues 237 to 262) were lacking in the used template. Thus, only residues 36 to 236 and 263 to 334 were modeled. Five hundred models were generated, and the one sharing the best objective function score was further selected as a starting point for the simulations. The

disulfide bridge conserved among the class A GPCRs was included between residues 112 and 192 of the V2R.

The AVP peptide (NH_3^+-CYFQNCPRG-$CONH_2$) was built from its X-ray structure available in the PDB (code 1JK4; 2.3-Å resolution) (Figure 3-36), which describes the six-residue cycle of the peptide in interaction with neurophysin (C. K. Wu et al. 2001). This structure shows a cycle conformation equivalent to that one found in bound (PDB code 1NPO) and unbound related peptide OT (PDB code 1XY2) (Rose et al. 1996; C. K. Wu et al. 2001). It was thus preferred to the one describing the trypsin-vasopressin complex (PDB code 1YF4) (Ibrahim and Pattabhi 2005) harboring a completely different conformation of the cycle. The three last residues of the peptide ($_7$-PRG-$_9$) were also built with the OT structure templates.

The obtained initial models of both receptor and peptide were then converted to a CG representation using the MARTINI force field (version 2.2; Elnedyn) (Marrink et al. 2007) (Figure 3-36 C). Using such a model, residues (backbone beads) closer than 9.0 Å are bound by a spring, displaying a force constant of 500 kJ/mol per nm^2 (default value from the Elnedyn force field). Such a link is meant to maintain both the secondary and the tertiary structures of the polypeptides. For the peptide, only the springs involving two residues of the cycle were conserved for further calculations, the three last residues being free to move. The standard elastic network of the receptor was not modified and allowed the latter to open or close freely as no spring was bridging the extracellular loops (Figure 3-36 E).

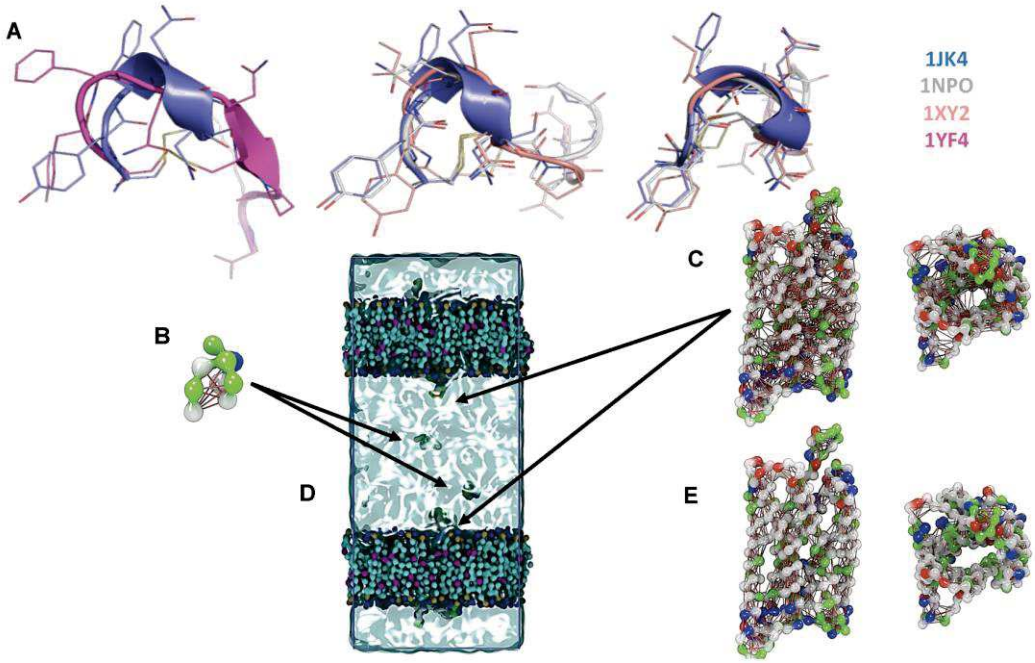

Figure 3-36 Coarse grain-REMD molecular dynamics approach
A) Structural alignment of the two X-ray structures available for AVP (PDB codes: 1JK4 and 1YF4). The 1JK4 structure which describes the 6-residue cycle of AVP was preferred to the 1YF4 structure corresponding to the full-length peptide because it displays a cycle conformation equivalent to that found in the unbound and bound oxytocin peptide analog (1XY2 and 1NPO). B) Schematic representation of the internal elastic networks used for the peptide AVP. C) Schematic representation of the internal elastic network used for V2R (side and extracellular view). D) The full system used for the CG-REMD simulations included 2 receptors and 2 ligands to create an artificial extracellular compartment and improve the conformational sampling of the AVP:V2R complex.E) Modified elastic network of the receptor used for the fit of the obtained CG models into the cryo-EM density maps. (Bous et al. 2021)

3.8.1.2 Molecular dynamics simulations.

The receptor was inserted in a 100 Å–by–100 Å lipid bilayer exclusively composed of 1-palmitoyl-2-oleoyl-sn-glycerol-3-phosphocholine (POPC). To avoid the exploration by the peptide of the intracellular side of the membrane during molecular dynamics (because of periodic boundary conditions), the system was duplicated/rotated along the *z*-axis (the two extracellular sides of the receptors were facing each other) to create an extracellular compartment. Two copies of the peptide were added to increase the interaction sampling with a 1:1 ratio. In the last step, water and chloride counterions were added to neutralize the system (Figure 3-36 D). The fully solvated system included 20,004 beads. After 10,000 steps of energy minimization using the conjugate gradient algorithm, the system was further equilibrated at 51 different temperatures (in the range 300:450 K by steps of 3 K) in the NVT (constant particle number, volume, and temperature) ensemble, using an integration step of 20 fs and for 5 ns. The final production step was performed in the NPT (constant particle number, pressure, and

temperature) ensemble, using an integration step of 20 fs, and was stopped after 20 μs. During production, REMD was used to improve the sampling of all possible configurations of the peptide:receptor complex. The potential energy difference of adjacent replicas was computed every 1000 steps (20 ps), and their coordinates were exchanged according to a Boltzmann criterion. With the used parameters, the probability of exchange between adjacent replica was in the range 0.11 (300 K):0.23(450 K). Three independent CG-REMD simulations were run to verify the convergence of the obtained models, together representing a cumulated sampling time of ~3 ms. For each of these simulations, a clustering was performed on all conformations of the peptide:receptor complex obtained at the lowest temperature (300 K). To do so, we first concatenated the data corresponding to the four possible complexes (peptide1-receptor1, peptide1-receptor2, peptide2-receptor1, and peptide2-receptor2). For that step, only the conformations displaying at least one peptide:receptor contact were kept (a contact was defined using a cutoff distance of 7 Å). For clustering, we used the algorithm (Daura et al. 1998) with an RMSD cutoff of 3.0 Å. The RMSD was computed only on the backbone beads of the peptide's residues 1 to 6 after structural fit onto those of the V2R. The two cysteine side-chain beads were also included for RMSD calculations (Figure 3-37). All simulations and analyzes were performed with the GROMACS software (version 5) (Abraham et al. 2015). Figures were produced with Visual Molecular Dynamics (Humphrey, Dalke, and Schulten 1996).

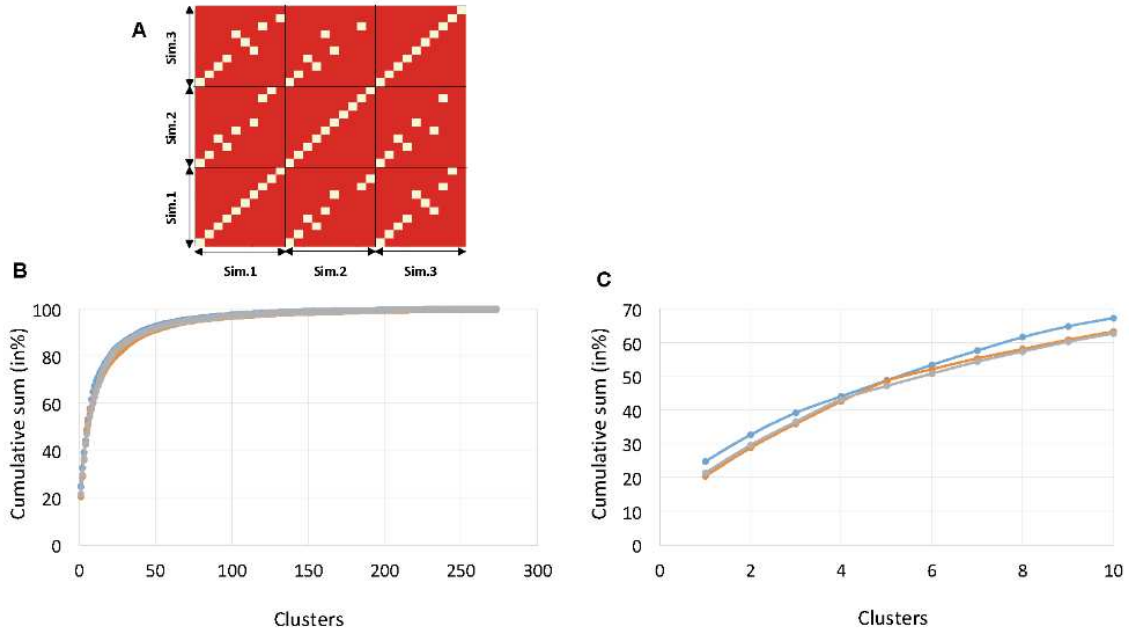

Figure 3-37 CG-REMD simulations
A) Cross-RMSD matrix of the ten most populated clusters resulting from the 3 independent CG-REMD simulations and showing that the same models were systematically retrieved (white squares correspond to RMSD < 3Å). B and C) Analyse of the populations of all the obtained clusters in terms of cumulative sums showing that the ten first clusters together represent more than 60% of the whole conformations. Data from the 3 independent simulations are reported in blue, orange, and grey, respectively.

3.8.1.3 Refinement of the obtained CG models in the cryo-EM maps.

The CDMD method (Igaev et al. 2019) was used to refine the most populated clusters obtained in CG-REMD using the L-state cryo-EM map of the AVP-V2-G_s-Nb35 complex. The principle of the method is to use an accurate force field and thermodynamic sampling to improve the real-space correlation between the modeled structure and the cryo-EM maps. Before this refinement step, the G_s heterotrimer and the Nb35 were modeled using the structure of the β_2AR-G_s-Nb35 complex (Sŏren G.F. Rasmussen et al. 2011) as a reference. The MARTINI force field restrained the internal conformations of the different partners with an internal elastic network. To increase significantly the conformational plasticity of the receptor and explore new conformations specific to the V2R, we modified its default elastic network. We automatically deleted the "long-range" springs involving two beads whose indexes differ by at least 15. This contributed to delete all interhelix springs. The standard elastic network was conserved for all other partners including the AVP peptide, the G protein, and the Nb35. No interchain springs were included for the G protein. After the conversion of G_s and Nb35 into the CG model, the two proteins were placed at a rational position in respect to the V2R using the β_2AR-G_s-Nb35

complex (Sŏren G.F. Rasmussen et al. 2011). The full system was inserted in a larger membrane (150 Å by 150 Å) and solvated on each side for further calculations.

The fit in each cryo-EM map was performed in four successive steps. First, a quick energy minimization (2000 steps of conjugate gradient) was performed on the full system without taking the map into account. This step was dedicated to the removal of bad contacts resulting from the addition of G_s and Nb35 proteins. Then, the second step consisted in a first equilibration of 5 ns (10-fs time step; NVT; 300 K) performed with CDMD and using a constant targeted low resolution of 5 Å together with a strength constant of 10,000 kJ/mol for the map potential. This bias was applied only to the backbone beads of the system. This step was useful to quickly optimize the alignment of the system with the targeted map. During this second step, an additional force of 50,000 kJ/mol per nm^2 was added to keep the distance between the two centers of masses (COMs) of both the peptide and surrounding residues of the receptor close to its initial value. This force prevented a quick motion of the AVP peptide in the first steps of the simulation that resulted from large forces applying to the receptor. For the subsequent steps of the fitting procedure, this additional force on COMs was removed. During the step 3 (30 ns), the same molecular dynamics parameters were used but with a gradual increase in both the resolution (from 5 to 3 Å) and the strength constant (from 10,000 to 50,000 kJ/mol), over a period of 25 ns. During the last 5 ns, these values were kept constant. This step was the key step allowing the whole system to adapt and fit to the maps. Last, the last step (10 ns) consisted in keeping the resolution and the strength constant at their reached values (3 Å; 50,000 kJ/mol), but this time applying the force only to the backbone and side-chain beads of the peptide. All the other backbone beads of the system were restrained in positions during this step with a force constant of 5000 kJ/mol. This step was useful to refine the position of the peptide in the density, especially of its side chains (Figure 3-39). For every step of the fitting procedure, the fit of each cluster was performed five times to verify the convergence of the obtained models (Figure 3-38).

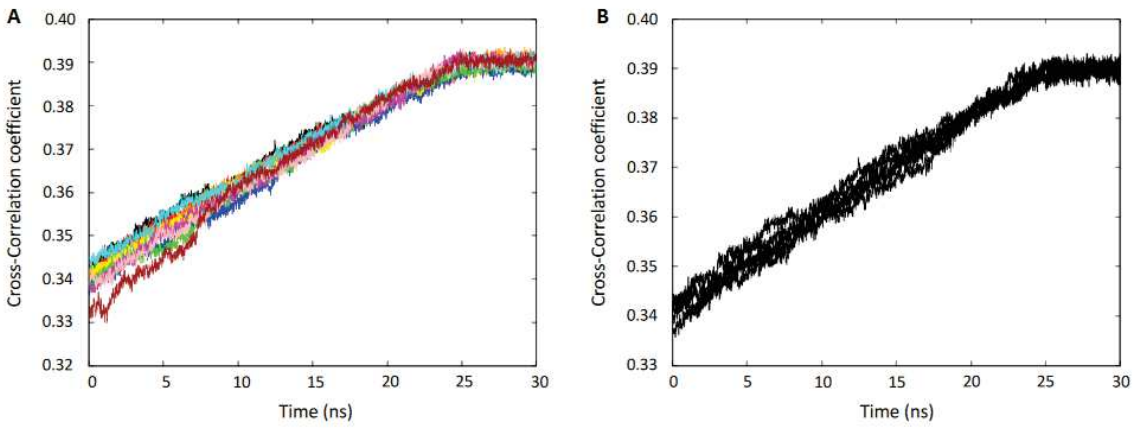

Figure 3-38 Typical curves of cross-correlation coefficients as a function of time for each CDMD simulation
A) and B) Cross-correlation coefficients values computed between the experimental and the simulated maps along CDMD simulations starting from the 10 most observed orientations of AVP in its receptor. In A), we reported one representative cross-correlation coefficients curve for each cluster whereas in B), the five curves obtained for the same cluster are depicted (five independent replicas). In each case, it shows a small variability of the obtained values and the convergence of the models at the end of the protocol. These curves were extracted from the main step 3 of fitting procedure.

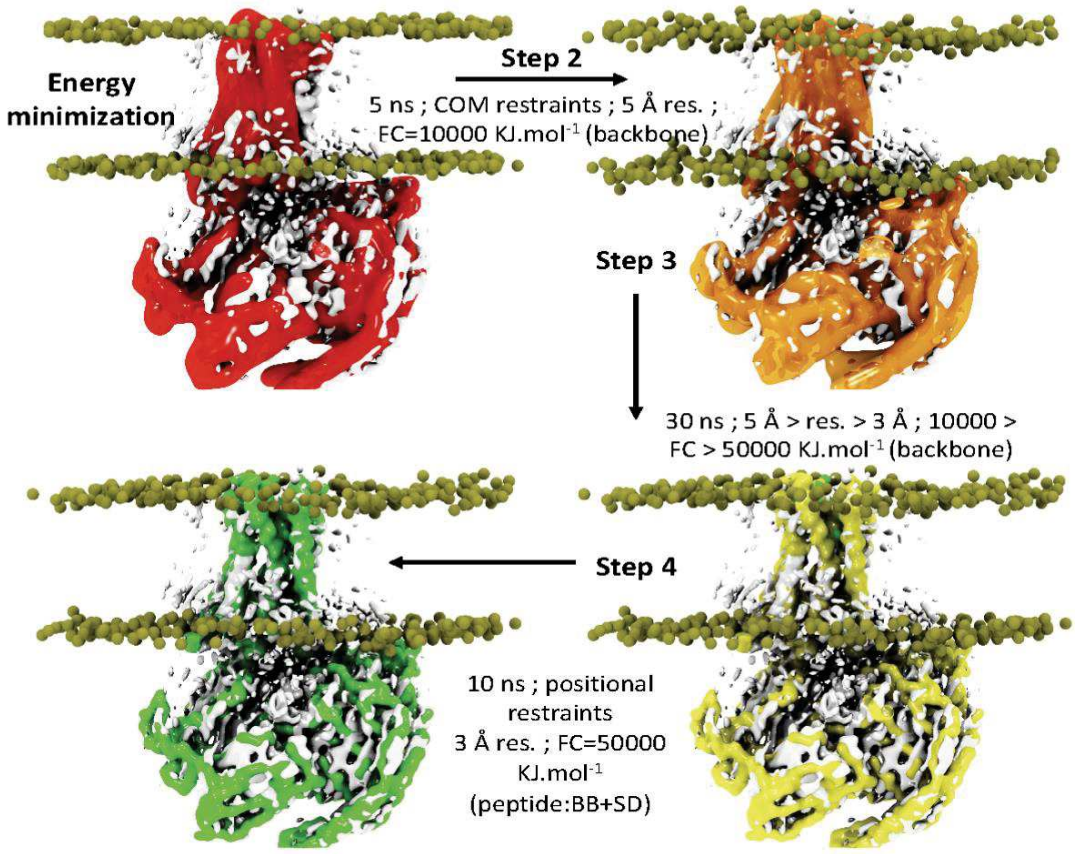

Figure 3-39 Summary of the successive steps employing the CDMD method to fit the models
They result from the CG-REMD simulations into the cryo-EM maps. .(Bous et al. 2021)

3.8.1.4 All-atom refinement of the models in the maps

The CG models obtained from the fitting procedure were back-mapped to a full-atom representation. We used the standard "initram" procedure provided by the developers of MARTINI (Best et al. 2012) with subtle changes. These changes concerned restrains on ω angles and Cα positions for all chains (V2R, G_s, and Nb35) to keep ω angles in trans conformation and to avoid large backbone motions, which inevitably would lead to models out of cryo-EM maps. Those restrains were added during the minimization and the MDSs inherent to the default initram procedure. In practice, the initram procedure was as follows: (i) after the very raw guess of atomic positions, from CG beads, performed by the initram script, (ii) the Charmm36 force field (Best et al. 2012) was used for 10,000 steps of steepest descent, disabling the nonbonded terms, (iii) followed by 5000 steps of steepest descent including all terms of the force field, and last, (iv) 300 steps of molecular dynamics were performed. Except the number of steps, the parameters for minimization and MDSs were set as default from the initram procedure. Minimization and MDSs were performed using the GROMACS package(Abraham et al. 2015).

As a final step, iterative manual adjustments were carried out in Coot (Emsley and Cowtan 2004) and real-space refinement using Phenix programs (Afonine et al. 2010). The model statistics were validated using MolProbity (Chen et al. 2010).

3.8.1.5 Classical all-atom MDSs

Following procedures previously described (Vasiliauskaité-Brooks et al. 2018), the L-state cryo-EM structure was subjected to MDSs. The system was set up using the CHARMM-GUI micelle builder(E. L. Wu et al. 2015). The protein complex was inserted into a hydrated, equilibrated micelle composed of 60 molecules of LMNG after addition of missing protein loops in Coot. A total of 495 sodium and 511 chloride ions were added to neutralize the system, reaching a final concentration of approximately 150 mM. MDSs were performed in GROMACS 2020 using the CHARMM36m force field and the CHARMM TIP3P water model. The input systems were subjected to energy minimization, equilibration, and production simulation using the GROMACS input scripts generated by CHARMM-GUI (J. Lee et al. 2016). Briefly, the system was energy minimized using 5000 steps of steepest descent, followed by 375 ps of equilibration. NVT and NPT equilibrations were followed by NPT production runs. The van der Waals interactions were smoothly switched off at 10 to 12 Å by a force-switching function (Steinbach and Brooks 1994), whereas the long-range electrostatic interactions were calculated using the particle mesh Ewald method (Essmann et al. 1995). The

temperature and pressure were held at 310.15 K and 1 bar, respectively. The assembled system was equilibrated by the well-established protocol in Micelle Builder, in which various restraints were applied to the protein, detergents, and water molecules, and the restraint forces were gradually reduced during this process. During production simulations, an NPT ensemble was used with isotropic pressure coupling via the Parrinello-Rahman barostat method, while the Nose-Hoover thermostat was used to maintain a temperature of 310.15 K. A leapfrog integration scheme was used, all bonds were constrained, and hydrogen mass repartitioning was applied(Balusek et al. 2019), allowing for a time step of 4 ps to be used during NPT equilibration and production MDSs. We performed 10 independent production runs starting from the highest-resolution L state model, for a total simulation time of ~2.6 μs. Production runs were subsequently pooled together, and the resulting trajectory was analyzed using GROMACS tools to yield principal components. The analysis was performed on the subset of Cα atoms common to the simulated and experimental structures using 1 frame/ns of trajectory. The experimental L, T1, and T2 states were included in the analysis for comparison.

3.8.1.6 AVP-V2R-βArr1-ScFv30 complex

A starting model was built using V2R-AVP (7KH0) at 2.8Å resolution, V2R-Cter (6U1N) at 4 Å resolution, ScFv30 adapted from Fab30 (4JQI) at 2.6Å resolution, and βarr1 finger loop was adapted from the PDB (6UP7) at 4.2Å resolution, and the PDB (4JQI) at 2.6Å resolution was used for the rest of the βarr1. The starting model was manually adjusted in Coot (Emsley and Cowtan 2004) and the fit was improved using Flex-EM (Joseph et al. 2016; Topf et al. 2008). Flex-EM was first used on the AVP-V2R-βarr1-Scfv30 map with Flex-EM automatic rigid-body domains determination. Model refinement was then carried out with Flex-EM in the βarr1-Scfv density map obtained with local refinement. Rigid body restraints were applied on AVP-V2R which are not represented in this density map.

3.9 NMR data analysis

Saturation transfer difference (STD) NMR has emerged as a powerful ligand-based NMR technique for the study of protein-ligand interactions. The success of this technique focused on the signals of the ligand is a consequence of its robustness (Viegas et al. 2011) (Figure 3-40).

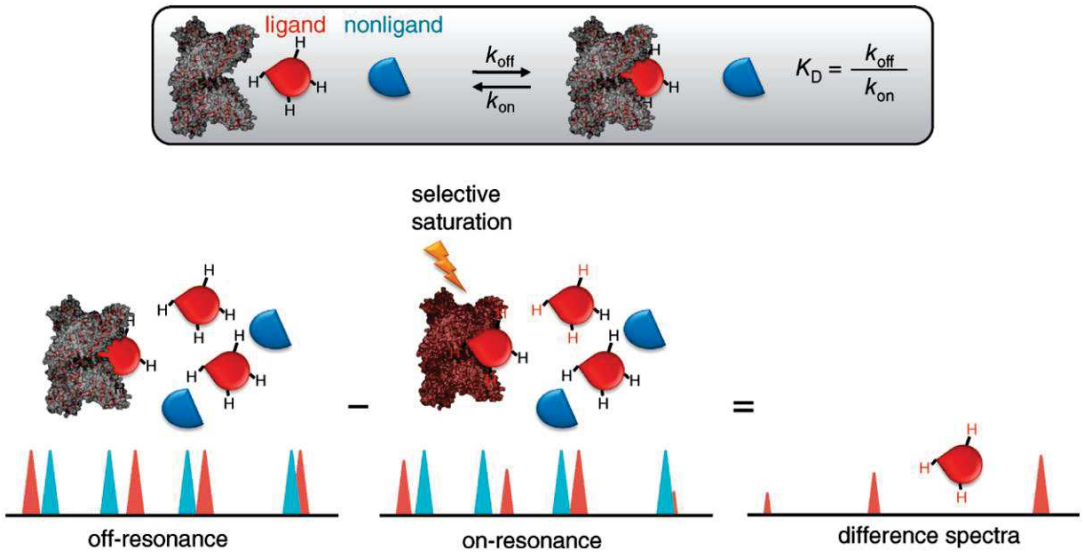

Figure 3-40 Schema of the STD-NMR experiment
The exchange between free and bound ligand allows intermolecular transfer of magnetization from the receptor to the bound small molecule (Viegas et al. 2011)

The purified V2R was prepared either in neutral amphipol (Rahmeh et al. 2012; Bazzacco et al. 2012) or in LMNG detergent. In both cases, the V2R was expressed in Sf9 insect cells and purified as described above, except it was cleaved overnight at 4°C using the HRV3C protease at a 1:20 weight ratio (HRV3C:V2R) before concentration and purification by SEC.

1D STD NMR spectra (Mayer and Meyer 1999) were recorded either on a mixture of AVP with V2R (400:2 µM) or on AVP. Selective methyl resonance saturation was achieved by equally spaced 60-ms Gaussian 180° pulses separated by 1-ms delay at 0 parts per million (ppm) (-50 ppm for reference spectra) at 274 and 283 K. An irradiation test was performed on a free peptide sample (400 µM) to verify that only V2R resonances were irradiated. Subtraction of free induction decay with on- and off-resonance protein saturation was achieved by phase cycling. A relaxation delay of 2.6 s (Aq and D1) and 128 dummy scans were used to reduce subtraction artifacts. Investigation of the time dependence of the saturation transfer from 0.5 to 4 s with equally spaced 50-ms Gaussian-shaped pulses (separated by a 1-ms delay) showed that 2 s was needed for efficient transfer of saturation from V2R to the AVP. A T1ρ filter of 30 ms was applied to eliminate background resonances of V2R. The transient number was typically 4000. To determine the specificity of STD signals, similar samples were prepared with the antagonist TVP as a competitor, using 3 µM V2R, 80 µM AVP, and 550 µM TVP. The STD effect was then calculated as $(I_0 - I_{sat})/I_0$, where I_0 and I_{sat} are the intensities of one signal in the reference NMR spectrum and in the on-resonance spectrum, respectively.

We discriminated the different molecular models issued from CG-REMD simulations by comparing the experimental STD values and the expected simulated STD from model structures. Back calculation of STD intensities were calculated with the 3.8 version of CORCEMA-ST software (Krishna and Jayalakshmi 2008). An order parameter value of 0.85 for methyl groups and a Kon value of a 10^8 s^{-1} were used. The correlation times were set to 0.5 and 40 ns for the free and bound states, respectively. Calculations with different correlation time values exploring the 0.2 to 2 ns and 10 to 30 ns for the free and bound forms, respectively, showed that the simulated profiles, as well as, in particular, the correlation coefficient between calculated and experimental values, were much more dependent on the template model than on the correlation time values. Coefficient correlations between simulated and experimental values were calculated for the whole peptide (residues 1 to 9). Mean correlations factors R_{1-9} were calculated for five representative structures of each cluster.

3.10 V2R binding assays

V2R binding studies using TagLite assays (Cisbio Bioassays, Codolet, France) based on time-resolved fluorescence resonance energy transfer (FRET) measurements were previously described (Loison et al. 2012; Zwier et al. 2010) (Figure 3-41).

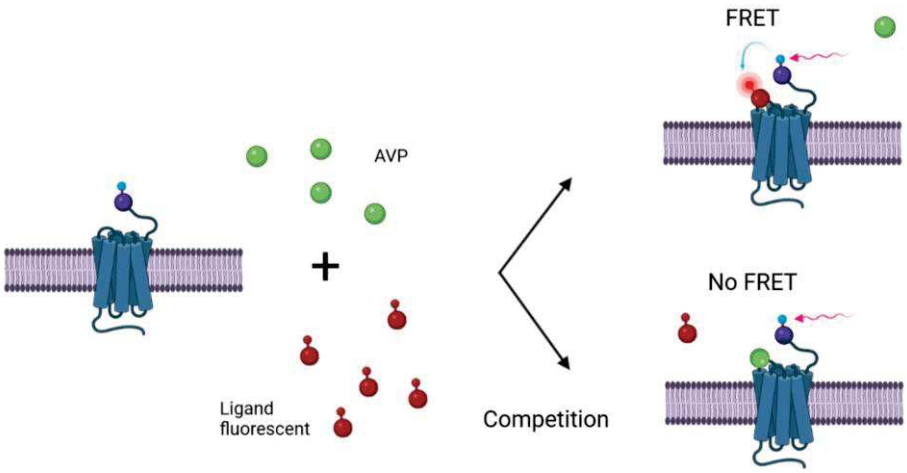

Figure 3-41 Schematic representation of time-resolved FRET binding competition assays. Made from (https://app.biorender.com)

Briefly, HEK cells were plated in white-walled, flat-bottom, 96-well plates (Greiner CELLSTAR plate, Sigma-Aldrich) in Dulbecco's minimum essential medium (DMEM) containing 10% fetal bovine serum (Lonza), 1% nonessential amino acids, and penicillin/streptomycin (GIBCO) at 15,000 cells per well. Cells were transfected 24 hours later with a plasmid coding for the V2R version used in cryo-EM studies fused at its N terminus to

the SNAP-tag (SNAP-V2R) (Cisbio Bioassays, Codolet, France). Transfections were performed with X-tremeGENE 360 (Sigma-Aldrich), according to the manufacturer's recommendations: 10 µl of a premix containing DMEM X-tremeGENE 360 (0.3 µl per well), SNAP-V2 coding plasmid (30 ng per well), and noncoding plasmid (70 ng per well) were added to the culture medium. After a 48-hour culture period, cells were rinsed once with Tag-lite medium (Cisbio Bioassays, Codolet, France) and incubated in the presence of Tag-lite medium containing 100 nM benzylguanine-Lumi4-Tb for at least 60 min at 37°C. Cells were then washed four times. For saturation studies, cells were incubated for at least 4 hours at 4°C in the presence of benzazepine-red nonpeptide vasopressin antagonist (BZ-DY647, Cisbio Bioassays, Codolet, France) at various concentrations ranging from 1×10^{-10} to 1×10^{-7} M. Nonspecific binding was determined in the presence of 10 µM vasopressin. For competition studies, cells were incubated for at least 4 hours at 4°C with benzazepine-red ligand (5 nM) and increasing concentrations of vasopressin ranging from 1×10^{-11} to 3.16×10^{-6} M. Fluorescent signals were measured at 620 nm (fluorescence of the donor) and at 665 nM (FRET signal) on a PHERAstar (BMG LABTECH, Champigny s/Marne, France). Results were expressed as the 665/620 ratio [10,000 × (665/620)]. A specific variation of the FRET ratio was plotted as a function of benzazepine-red concentration (saturation experiments) or competitor concentration (competition experiment). All binding data were analyzed with GraphPad 8.3.0 (GraphPad Software Inc.) using the one site-specific binding equation. All results are expressed as the means ± SEM of at least three independent experiments performed in triplicate. K_i values were calculated from median inhibitory concentration values with the Cheng-Prusoff equation.

3.11 cAMP accumulation assays

Cyclic adenosine monophosphate (cAMP) is an important intracellular second messenger in GPCR signal transduction. Agonist activation of GPCRs that couple to the Gαs protein leads to increased production of intracellular cAMP levels. HTRF cAMP kit from Cisbio, can be used to measure intracellular cAMP levels. It's based on recognition of a fluorescent acceptor labeled cAMP by a fluorescent donor labeled anti-cAMP leads to energy transfer signal through Förster resonance energy transfer (FRET). Competition from endogenous cAMP for the antibody results in reduced energy transfer signal. Loss-of-signal measurement: the level of cellular cAMP is inversely related to the signal (Figure 3-42) (T. Wang et al. 2004).

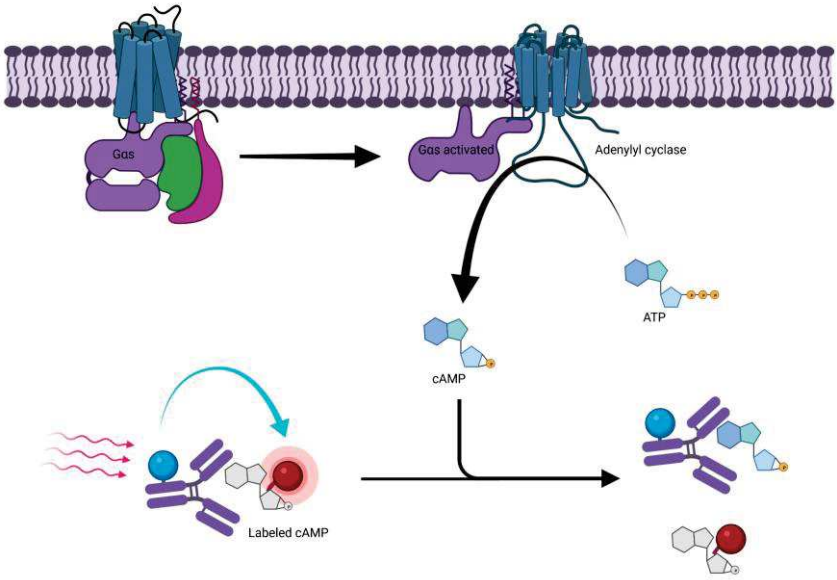

Figure 3-42 Shematic representation of Gs coupled cAMP accumulation assays.
Made from (https://app.biorender.com)

As for V2R binding studies, V2R functional studies based on time-resolved FRET measurements were described previously (Tenenbaum et al. 2009; Jean-Alphonse et al. 2009). Briefly, Chinese hamster ovary cells were plated in six-well plates (Falcon) at 350,000 cells per well and transfected 24 hours later with jetPEI (Ozyme) with a pRK5 plasmid coding for the version of the V2R used in the cryo-EM studies. A mix of isotonic NaCl solution (200 µl per well) containing jetPEI (2 µl per well), V2R coding plasmid (1 ng per well), and noncoding plasmid (3000 ng per well) was added to the culture medium (2 ml). Twenty-four hours later, cells were harvested with trypsin and cultured in white-walled, flat-bottom, 96-well plates (Greiner CELLSTAR plate, Sigma-Aldrich) at a density of 30,000 cells per well in DMEM containing 10% fetal bovine serum (Lonza), 1% nonessential amino acids, and penicillin/streptomycin (GIBCO). After a 24-hour culture period, cells were treated for 30 min at 37°C in the cAMP buffer with or without increasing AVP concentrations (3.16×10^{-12} to 10^{-6} M) in the presence of 0.1 mM RO201724, a phosphodiesterase inhibitor (Sigma-Aldrich). The accumulated cAMP was quantified using the cAMP Dynamic 2 Kit (Cisbio Bioassays, Codolet, France) according to the manufacturer's protocol. Fluorescent signals were measured at 620 and 665 nm on a Spark 20M multimode microplate reader (Tecan). Data were plotted as the FRET ratio [10,000 × (665/620)] as a function of AVP concentration [log(AVP)]. Data were analyzed with GraphPad Prism using the "dose-response stimulation" subroutine. Median effective concentrations were determined using the log(agonist) versus response variable slope

(four parameters) fit procedure. Experiments were repeated at least three times on different cultures, each condition in triplicate. Data are presented as means ± SEM.

3.12 β-arrestin recruitment assays

Upon GPCR activation, β-arrestins are recruited to initiate desensitization and clathrin-mediated receptor internalization processes, leading also to the arrest of G protein-dependent signaling pathways. To this end, release of the C-terminal domain of β-arrestins is a crucial step, allowing binding of AP2 to β-arrestins. This interaction can be measured using HTRF® technology (CisBio PerkinElmer Inc.) based on the use of two specific antibodies, one directed against β-arrestin2, the second one specific for AP2. In this assay (βArr2 recruitment kit, CisBio PerkinElmer), the AP2 antibody is labeled with an Europium cryptate fluorescent donor, and that against βArr2 is labeled with a d2 fluorescent acceptor, their proximity being detected by FRET signals. The specific signal modulates positively in proportion to the recruitment of β-arrestin2 by interacting with AP2 (Figure 3-43).

Briefly, HEK cells -were plated at a seeding density of $2.5x10^4$ cells per well in a white-walled 96-well plates (CELLSTAR plate, Sigma-Aldrich) precoated with poly-L-ornithine for 24 hours, in Dulbecco's minimum essential medium (DMEM) (Sigma-Aldrich) complemented with 10% fetal bovine serum (FBS) (Lonza), 1% non-essential amino acids (GIBCO), and 1% penicillin-streptomycin antibiotics solution (GIBCO). To produce the V2 receptor, the cells were transfected with 10 ng of the pRK5-Flag-Snap-V2R plasmid (coding for the cleaved V2R construct used in cryo-EM studies) using X-trem gene 360 (Sigma-Aldrich), according to the manufacturer's recommendations. After a 24-hour culture, cells were rinsed one time with DMEM-free and incubated 2 hours at room temperature (RT) with 100 ul per well of stimulation buffer (βArr2 recruitment kit, CISBIO) containing various concentrations of the ligand AVP ranging from 10^{-7}M to 10^{-12}M). The media was then replaced by 30 ul per well of Stabilization buffer (βArr2 recruitment kit, CISBIO) for 15 min at RT. The cells were then washed three times with 100 ul per well of wash buffer (βArr2 recruitment kit, CISBIO) before adding 100 ul per well of a pre-mix of Eu cryptate and d2 antibodies in detection buffer (βArr2 recruitment kit, CISBIO). Following overnight incubation at RT, 80 ul of media were removed from each well before reading the 96-well plates on a PHERAstar (Labtech) by measuring the signals of the donor (Europium cryptate-labeled AP2 antibody) at a wavelength of 620 nm and the acceptor at 665 nm (d2-labeled βArr2). Finally, the results were expressed as the FRET 665/620 ratio and plotted using GraphPad 9.1.1 (GraphPad Prism software inc.). Experiments

were repeated at least three times on different cultures, each condition in triplicate. Data are presented as means ± SEM.

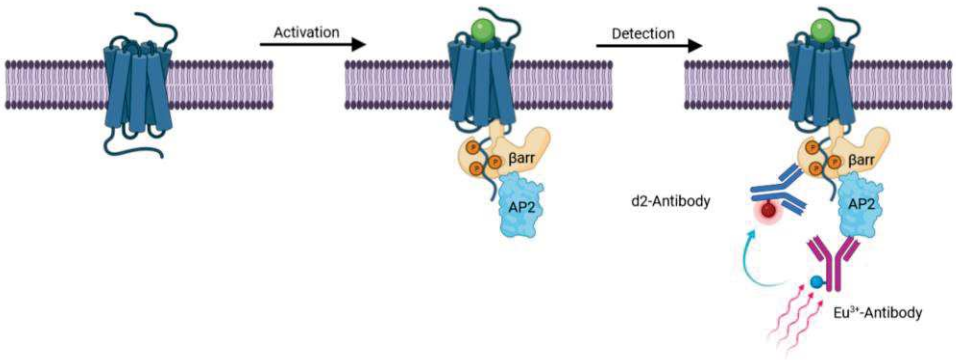

Figure 3-43 Schematic representation of βarr recruitment assays.
Made from (https://app.biorender.com)

3.13 Liquid chromatography–tandem mass spectrometry

The purified proteins were digested using micro S-Trap columns (https://protifi.com/, Huntington NY) following the supplier's protocol. Briefly, after reduction (20 mM DTT 10 min 95 ° C) and alkylation (40 mM IAA 30 min in the dark), the proteins were digested using 3 µg of trypsin (Promega, Gold) for 1 hour at 47 ° C.

The peptides obtained were analyzed using nano-throughput HPLC (Ultimate 3000-RSLC, Thermo Scientific) coupled to a mass spectrometer (Qexactive-HF, Thermo Scientific) equipped with a nanospray source. The pre-concentration of the samples was carried out

in-line on a pre-column (0.3 mm × 10 mm, Pepmap®, Thermo Scientific) and separation of the peptides on a column (0.075 mm × 500 mm, reverse phase C18, Pepmap®, Dionex) following a gradient from 2 to 25% buffer B (0.1% AF in 80% ACN) for 100 min at a flow rate 300 nl / min, then 25 to 40% in 20 min and finally 40 to 90% in 3 minutes.

The spectra are acquired in mode: "data-dependent acquisition" (dynamic exclusion of 20 seconds). The LC-MS / MS analysis cycle is therefore composed of several phases, a "Full scan MS ”with analysis in the orbitrap at 60,000 resolution followed by MS / MS analyzes in HCD, for the 12 most abundant precursors at a resolution of 30,000.

The spectra were then compared to a database for identification. We used the sequence of the V2R construct as well as the Uniprot entries (https://www.uniprot.org/) for Spodoptera

frugiperda and Autographa californica nuclear polyhedrosis virus as well as a base containing 250 classical contaminants. For this analysis, we used MaxQuant software (v 1.6.10.43) with standard parameters.

Receptor peptidic signals intensity were extracted using Skyline (2.1.0.31) with the option « Use high-selectivity extraction ».

4 Structure of the AVP-V2R-G_s-Nb35 complex

4.1 Biochemistry of the V2R and of the signaling complex

Significant efforts were dedicated to develop the AVP-V2R-G_s-Nb35 complex purification based on the work and experience of Dr. Bernard Mouillac, Dr. Sébastien Granier, Hélène Orcel and coworkers focused on V2R biochemistry. The complete purification approach is reported in the Materials and Methods chapter. Briefly, to improve the expression of the human V2R and facilitate its purification, we constructed a receptor version with a hemagglutinin signal peptide followed by a flag tag at its N terminus, and a twin strep tag at its C terminus (Figure 3-33 A). In addition, N22 was substituted with a glutamine residue to avoid *N*-glycosylation, and C358 was mutated into an alanine to eliminate the possibility of intermolecular disulfide bridges. Apart from receptor engineering designed uniquely for expression and purification purposes and unlike many of the recently published GPCR structures, we did not modify the receptor sequence (the V2R is wild-type from T31 to G345). We aimed at avoiding possible artifacts and irrelevant information due to the introduction of mutations in the transmembrane (TM) core domain of the receptor, even if this was at the expense of lower-resolution cryo-EM data. Following infection of Sf9 cells with the V2R recombinant baculovirus, the receptor was purified through an orthogonal chromatography procedure (Figure 3-34 A). It was then mixed with the purified heterotrimeric G_s protein and the Nb35 in the presence of an excess of AVP. The purified complex displayed a monodisperse peak on size exclusion chromatography (SEC)(Figure 4-1 A; B) and SDS gel analyses confirmed the presence of all components in the complex (Figure 4-1 C).

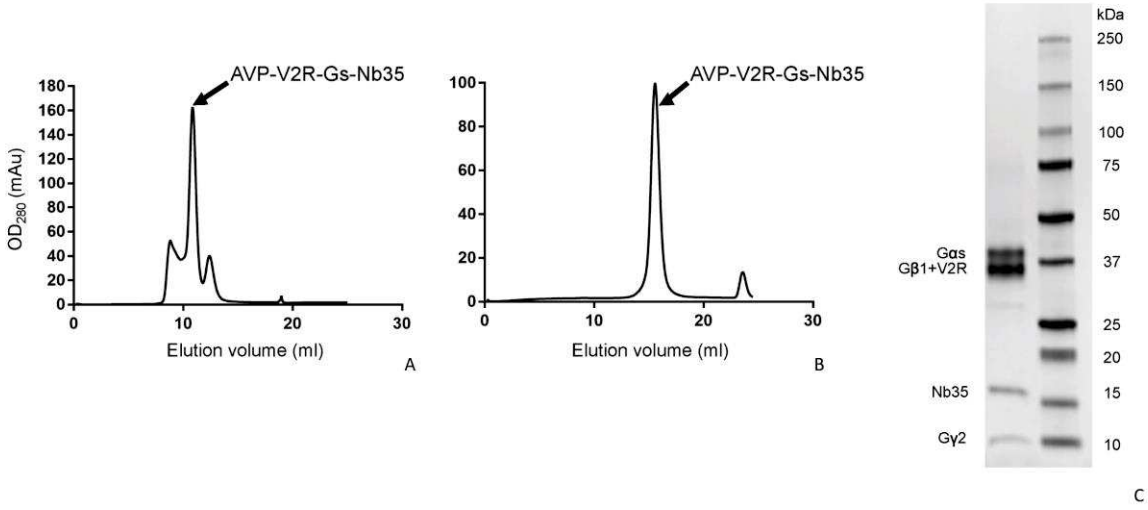

Figure 4-1 chromatograms and SDS-PAGE of the AVP-V2R-Gs-Nb35
A) and B) Representative chromatograms of the AVP-V2R-Gs-Nb35 complex using Superdex200 (first of the two successive SEC (see method and figure 3-34)), and Superose6 (second of the two successive SEC) respectively, show a monodisperse peak. Fractions containing the sample were combined and concentrated for the preparation of cryo-EM grids. C) SDS-PAGE of peak fraction from the Superose6 step. Coomassie blue staining of proteins confirmed that the complex is made of Gαs, V2R, Gβ1, Nb35, and Gγ2 (AVP is not visible).

4.2 Pharmacology of the V2R

The pharmacological properties of the engineered V2R were verified in human embryonic kidney (HEK) mammalian cells (Figure 4-2). The cryo-EM version of the V2R bound a fluorescent nonpeptide antagonist and AVP with high affinity [dissociation constant (K_d) and inhibition constant (K_i) = 2.27 ± 0.24 nM (n = 3) and 1.12 ± 0.5 nM (n = 3), respectively], close to the values determined for a wild-type V2R (Loison et al. 2012). Moreover, the receptor was proven to be functional as it was able to stimulate cAMP accumulation upon AVP binding [K_{act} = 2.05 ± 0.11 nM (n = 4), similar to the wild-type V2R in transfected cells (Ala et al. 1998).

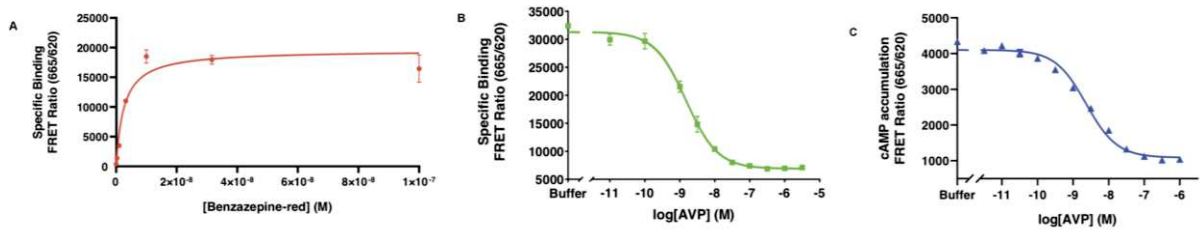

Figure 4-2 Pharmacological and functional properties of the cryo-EM V2R construct
A) Binding of the benzazepine-red fluorescent antagonist to the V2R construct measured by FRET (see Methods). Specific binding of BZ-Red from a typical saturation assay is shown as FRET ratio (665nm/620 nm). The experiment was repeated 3 times each point measured in triplicate. Each value is presented as mean ± SEM. B) Binding of AVP to the V2R construct is illustrated as FRET ratio (665nm/620nm). Specific binding of benzazepine-red is shown. The fluorescent antagonist was used at 5 nM with or without increasing concentrations of AVP. A typical competition curve is shown and was repeated at least 3 times each point in triplicate. Each value is presented as mean ± SEM. C) Capacity of the V2R construct to functionally activate adenylyl cyclase measured by FRET (see Methods). The cAMP accumulation is shown as FRET ratio (665nm/620nm) and measured in the presence of increasing concentrations of AVP. A typical experiment is shown, was repeated at least 3 times, each point in triplicate. Each value is presented as mean ± SEM.

4.3 Negative stain EM of the AVP-V2R-Gs-Nb35 particles

The complex was first characterized using negative stain electron microscopy (NS-EM), before the preparation of vitrified samples onto Quantifoil grids for cryo-EM single-particle analysis.

Images of the complex, first recorded in NS-EM revealed a homogeneous distribution of the particles, as observed from two-dimensional (2D) class averages (Figure 4-3 A B). More than 60% of the particles correspond to the complex. Reconstruction at 20 Å clearly showed the micelle of detergent and the G protein–Nb35 components (Figure 4-3 C). Fitting the 3D model of the crystal structure of the β_2-adrenergic receptor (β_2AR)–G_s-Nb35 complex (Sŏren G.F. Rasmussen et al. 2011) in this low-resolution reconstruction map confirms that V2R-G_s-Nb35 displays typical structural features of a TM signaling GPCR complex (Figure 4-3 D). To assess the sample stability over time, we kept the sample at 4°C for 5 days and carried out an NS-EM analysis. Despite complex dissociation, there was still 35% of the particles corresponding to the complex (Figure 4-3 E). Moreover, the addition of the specific V2R nonpeptide antagonist SR121463 (Serradeil-Le Gal et al. 1996) and guanosine 5′-O-(3-thiotriphosphate) (GTPγS) to the purified complex led to the dissociation of the different components, confirming the functionality of the signaling particle (Figure 4-3 F).

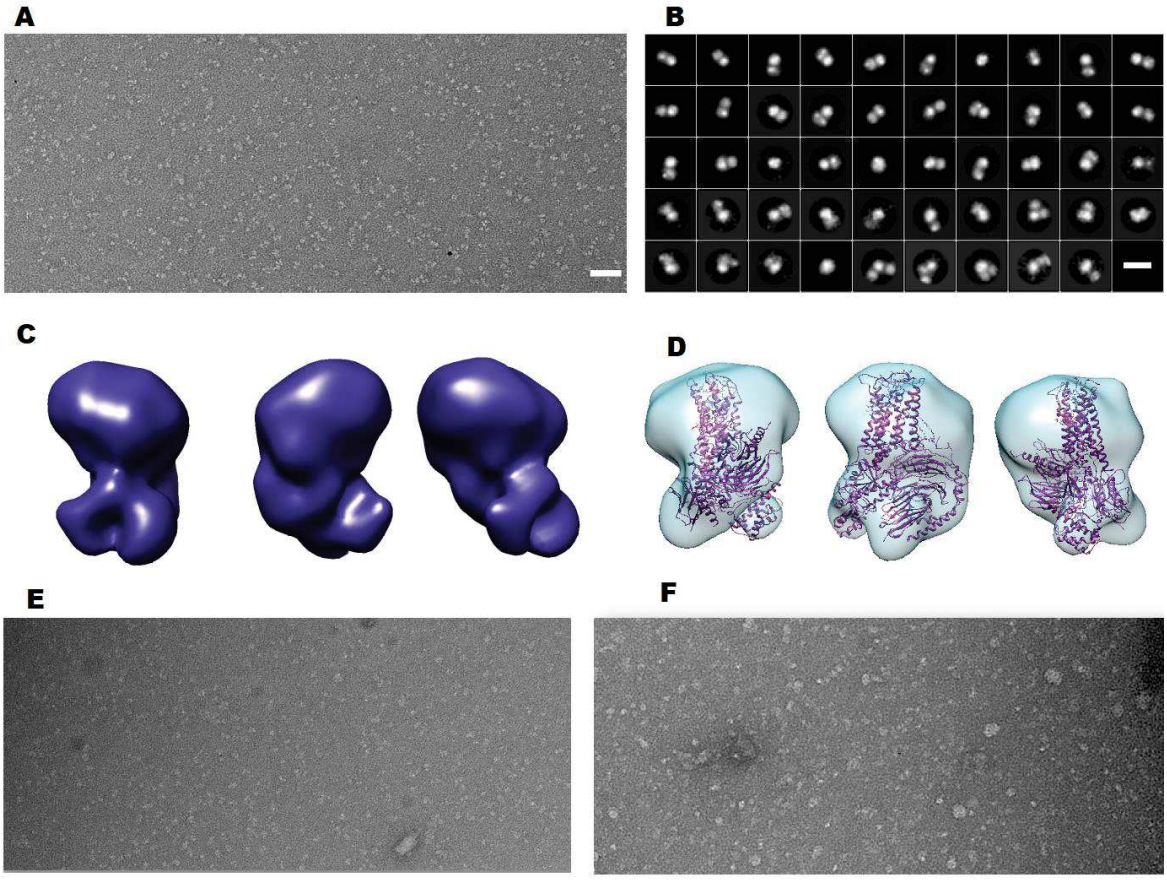

Figure 4-3 Negative stain electron microscopy characterization of the AVP-V2R-Gs-Nb35 complex
A) Representative micrograph of the purified sample of the complex isolated from the Superose6 SEC peak (scale bar, 54 nm). B) 2D most representative class averages showing different orientations. (scale bar, 18 nm). C) Density map of the AVP-V2R-Gs-Nb35 complex (contour level set to 0.115), and D) fitting of the 3D model of the crystal structure of β2AR-Gs-Nb35 complex in this low-resolution map. E) Representative micrograph of the purified sample of the complex isolated from the Superose 6 SEC peak after 5 days at 4°C (scale bar, 54 nm). F) Representative micrograph of AVP-V2R-Gs-Nb35 complex dissociated using an excess of 10 μM SR121463 (selective nonpeptide antagonist of the V2R) and 100 μM GTPγS (scale bar, 43 nm).

4.4 Cryo-EM and model building

After validation of cryo-EM grid sample vitrification, a total number of 25,770 movies were recorded, with 3.5 million particles picked and sorted out for further data processing (Figure 4-4). After 3D classification of projections and 3D refinement, we identified three different conformational states of the complex, referred to as loose (L), tight-1 (T1), and tight-2 (T2). Reconstruction of each state was at 4.2, 4.5, and 4.7 Å, with a distribution of 16, 48, and 36%, respectively (Figure 4-4), the local resolution varying from 3.2 to 6.4 Å (Figure 4-5) Using the recent algorithm developed to enhance cryo-EM maps by density modification (Terwilliger et al. 2020), the resolution of density maps was improved to 4.0 Å (L state), 4.1 Å (T1 state), and

4.5 Å (T2 state), respectively (Table 2, and Figure 4-4). This step enhanced the visibility of many details for some V2R TM regions (Figure 3-35 A), for the hormone AVP (Figure 3-35 B), for the $G\alpha_s$ subunit (Figure 3-35 C), and for $G\beta_2$ subunit (Figure 3-35 D). The maps mainly differ in the angle of G_s-Nb35 with the receptor 7TM and may reflect an inherent high flexibility of the complex (Figure 4-6 Figure 4-9). A conformational heterogeneity analysis using multibody refinement revealed that more than 78% of the variance is accounted for by the four first eigenvectors related to rotations and translations between AVP-V2R and G_s-Nb35. The 4.5-Å map of the T2 state was not well enough resolved to build a reliable model at the atomic level, but a model was constructed based on the open state and was refined with Phenix realspace with secondary structure constraints to be interpreted at the secondary structure level.

Table 2

	AVP-V2R-$G\alpha_s\beta_1\gamma_2$-Nb35 (L state) (EMD-12128) (PDB code 7BB6)	AVP-V2R-$G\alpha_s\beta_1\gamma_2$-Nb35 (T state) (EMD-12129) (PDB code 7BB7)
Data collection and processing		
Magnification	165,000	165,000
Voltage (kV)	300	300
Electron exposure ($e^-/Å^2$)	50.19*/41.19†	50.19*/41.19†
Defocus range (μm)	−0.8 to −2.2	−0.8 to −2.2
Pixel size (Å)	0.81	0.81
Symmetry imposed	C1	C1
Initial particle images (no.)	3,566,007	3,566,007
Final particle images (no.)	147,524	420,953
Map resolution (Å)	4.2	4.4
FSC threshold	0.143	0.143
Map resolution range (Å)	3.2–5.6	3.8–6
Refinement		
Model resolution (Å)	4.2	4.4
FSC threshold	0.5	0.5
Model resolution range (Å)	3.2–5.6	3.8–6
Map improved resolution (Å) (cryoresolve)	4.0	4.1
Map sharpening *B* factor ($Å^2$)	−141.6	−75
Model composition		
Nonhydrogen atoms	7955	8040
Protein residues	1017	1022
Ligands	0	0
B factors ($Å^2$)		
Protein	87.61	72.14
Ligand	163.31	106.00
RMSD		
Bond lengths (Å)	0.007	0.007
Bond angles (°)	0.947	1.027
Validation		
MolProbity score	2.55	2.81
Clashscore	28.39	37.36
Poor rotamers (%)	0	0
Ramachandran plot		
Favored (%)	87.46	78.74
Allowed (%)	12.54	21.26
Disallowed (%)	0	0

*Dataset 1. †Dataset 2.

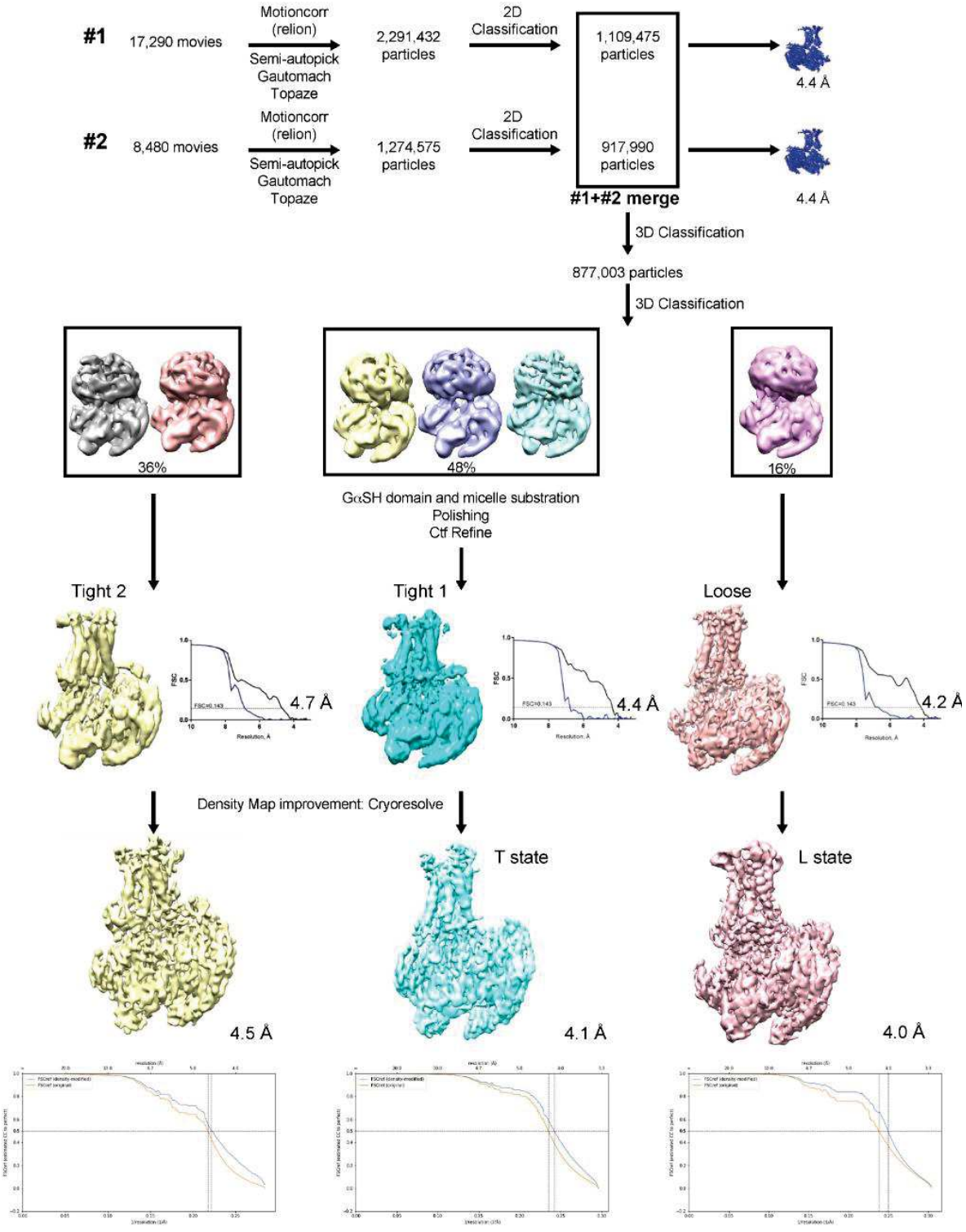

Figure 4-4 Flowchart of the single-particle analysis of the AVP-V2R-Gs-Nb35 complex
The two datasets processed separately Merging of the two sets, substates determination, and high-resolution reconstructions. Density map improvement with cryoresolve as a final step.

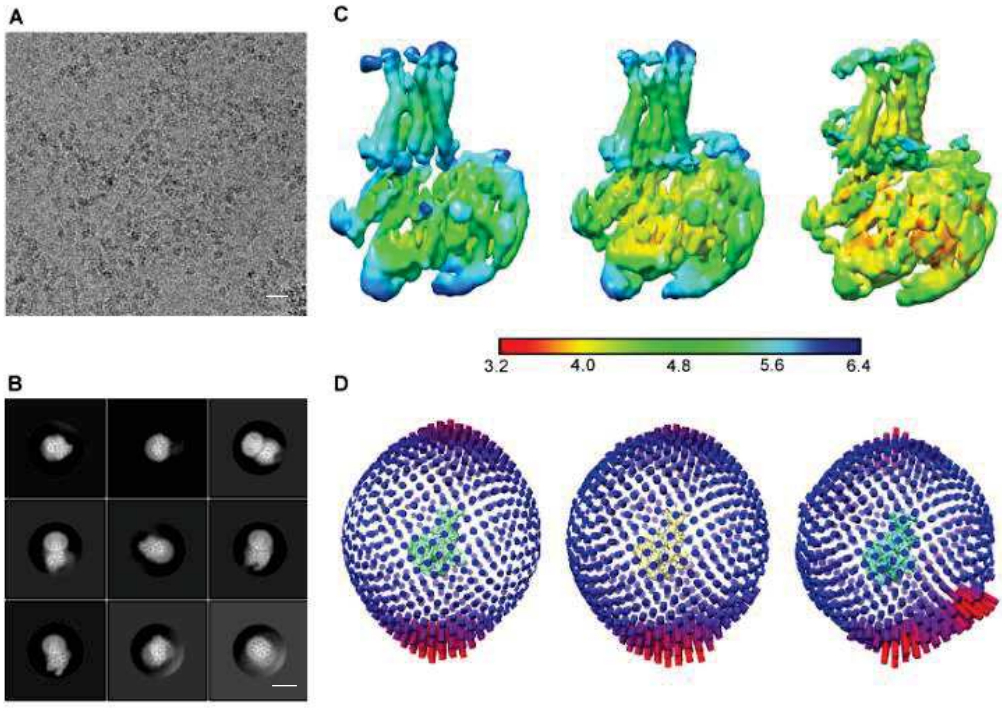

Figure 4-5 Cryo-EM characterization of the AVP-V2R-Gs-Nb35 complex.
A) Representative micrograph of the AVP-V2R-Gs-Nb35 protein complex (scale bar, 30 nm). B) Representative 2D class averages showing distinct secondary structure features (including the V2R TM regions embedded in the detergent micelle) and different orientations of the AVP-V2R-Gs-Nb35 complex (scale bar, 5 nm). C) Local resolution estimation computed with blocres from bsoft program; Tight-2, Tight-1, and Loose particle density maps are shown, respectively. D) Euler angle distribution of particles from the final reconstructions for Tight-2, Tight-1, and Lose populations.

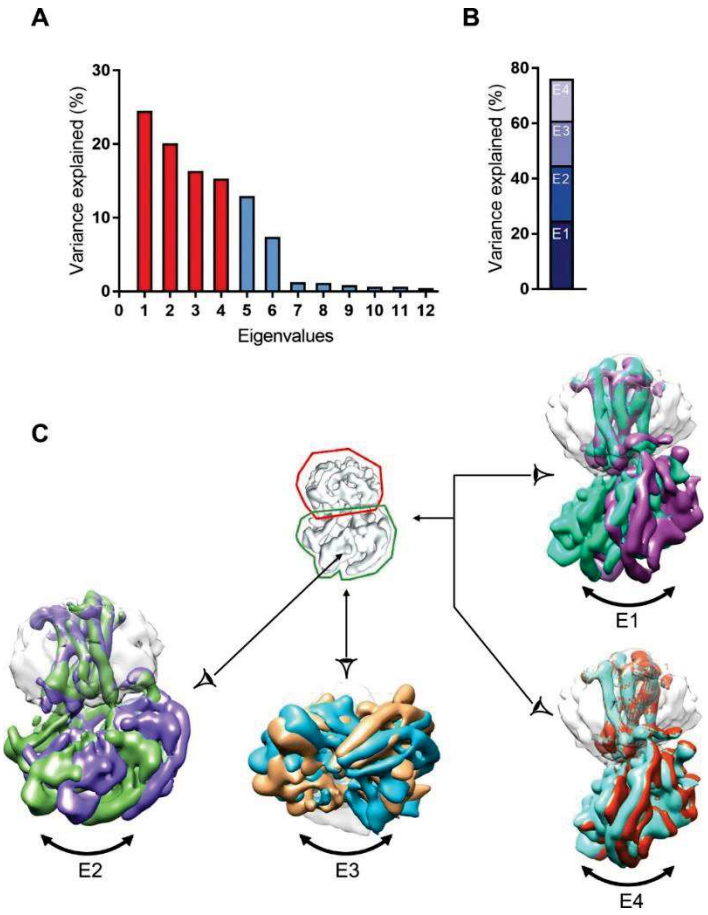

Figure 4-6 Flexibility in the AVP-V2R-Gs-Nb35 complex
A) The contribution of each of the 12 eigenvectors (numbered along *x*-axis) to the variance of the overall final map is illustrated. B) Eigenvectors 1 to 4 correspond to 78% of the variance. C) Mask used for multibody refinement is shown in the middle, detergent micelle and V2R are surrounded by a red line, and G_s and Nb35 are surrounded by a green line. Maps corresponding to the four first vectors are illustrated, showing swing-like motion and tilting of G_s-Nb35 with respect to AVP-V2R. E4 is part of E1.

Because we could not unambiguously build the AVP in the calculated maps, we designed an original hybrid strategy based on a combination of cryo-EM maps, computational molecular dynamics simulations (MDSs), and experimental saturation transfer difference (STD) nuclear magnetic resonance (NMR) (Figure 4-8). First, the conformational sampling of the peptide-receptor complex was improved using the unbiased coarse-grained (CG) method coupled to replica exchange molecular dynamics (REMD) simulation protocol (Figure 4-8B Figure 3-37). This protocol was previously successfully used to predict the binding modes of peptides in the class A GPCRs neurotensin receptor type 1 (NTSR1), C-X-C chemokine receptor type 4 (CXCR4), and growth hormone secretagogue receptor (GHSR)(Delort et al. 2017; Ferré et al. 2019). Three independent CG-REMD simulations were run, together representing about 3 ms

of cumulated simulation time (Figure 3-37). Each of the three simulations led to, respectively, 288, 306, and 302 clusters of peptide:receptor conformations. The first 10 most populated clusters (Figure 4-8) were identically retrieved among the three independent simulations, as shown by the root mean square deviation (RMSD) matrix (Figure 3-37) and represented more than 60% of the whole explored conformations. After addition of the G_s heterotrimer and Nb35 proteins, refinement of each of these clusters was performed in the L cryo-EM density map (Figure 4-8C). At this step, we used the correlation-driven molecular dynamics (CDMD) method (Igaev et al. 2019) while keeping advantage of using a CG representation for sampling speed and better agreement with the resolution of the maps (Figure 3-38). Fitting of each cluster was repeated five times. Typical curves of cross-correlation coefficients as a function of time for each CDMD show that the used protocol reached a "plateau" in each case, indicating the convergence of the fit for all clusters (Figure 3-38). Small variability of the position of the peptide among the five obtained models for clusters 2 and 5 (mean RMSD of 3.0 and 2.2 Å, respectively) and in a lower manner for the clusters 6 and 8 (mean RMSD of 3.2 and 3.6 Å, respectively) was seen (Figure 4-8 DE). The higher values obtained for the other clusters (in the range 4.8 to 8.7 Å) were explained by the upper starting position of the peptide in the pocket, finding more easily the density located at the surface of the receptor during the fitting procedure (Figure 4-8 E). Last, the CG models obtained from the fitting procedure were back-mapped to an all-atom (AA) representation. Minimization, MDSs, iterative manual adjustment, and real-space refinement were carried out to finalize AVP docking.

The AVP binding modes were further cross-validated using experimental STD NMR spectroscopy, which can efficiently monitor the binding and map the contact surface of a given ligand with its cognate GPCR (Assadi-Porter et al. 2008; Bartoschek et al. 2010). 1D STD spectra were thus recorded either on a mixture of AVP with V2R or on AVP alone (Figure 4-7). Intense STD signals were only observed in the presence of V2R, mostly for the aromatic protons of Y2 and F3 residues of AVP (Figure 4-8 E). The addition of the orthosteric antagonist tolvaptan (TVP) significantly attenuated the STD signals, demonstrating specific binding of AVP to the V2R orthosteric site (Figure 4-7 B). Calculation of normalized STD effects as STD intensities=(Io-Isat/Io)showed that the most intense effects were observed for the N-terminal cyclic part of AVP, with a strong involvement of the aromatic side chains of Y2 and F3 (and to a lesser extend C1), whereas the residues in the C-terminal tripeptide (P7, R8, and G9 amide) were less affected upon V2R binding (Figure 4-8 D). In addition, we compared these experimental STD values to the expected STD values from AA models issued from MDSs and

subsequently refined with the density maps. As explained in Materials and Methods, coefficient correlations between simulated and experimental STD values were calculated for the whole peptide (R_{1-9}). Cluster 5 fitted on L density map appeared as the best cluster fitting to experimental STD values (Figure 4-8 E).

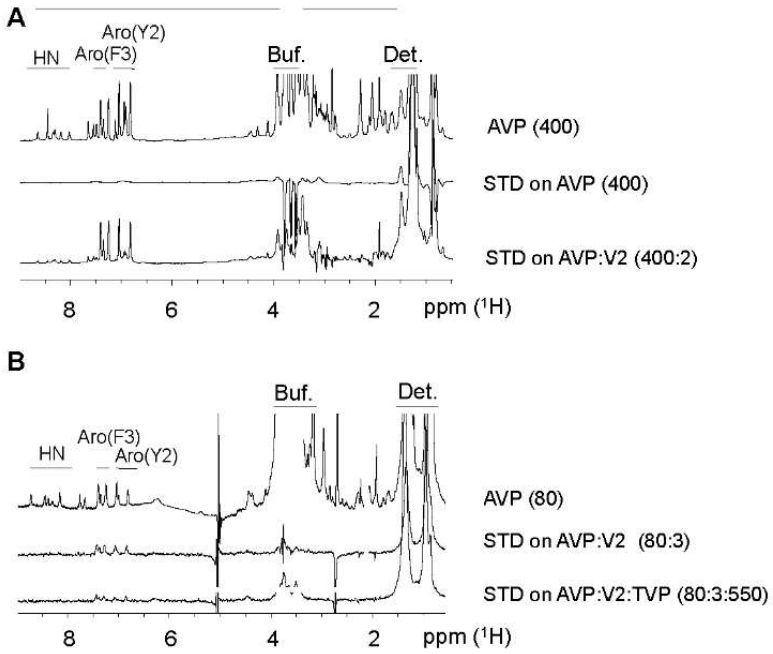

Figure 4-7 Mapping of AVP interaction surfaces by STD NMR experiments.
A)and B) Comparison of standard 1D proton spectrum (AVP 400 µM) with STD experiments on (A) 400µM AVP and 400 µM AVP binding to 2 µM V2R and (B) 80 µM AVP binding to 3 µM V2R in absence/presence of 550 µM TVP (tolvaptan). Buffer resonance (Bis-Tris) and detergent resonance are labelled buf and det, respectively.

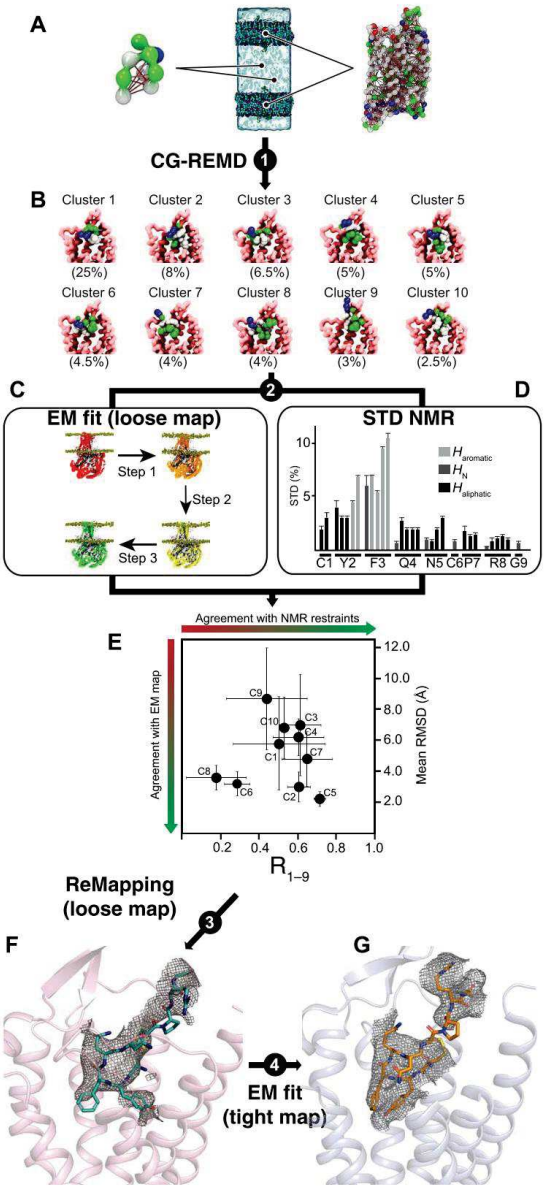

Figure 4-8 Overview of the hybrid strategy: A combination of cryo-EM, computation- al, and NMR

A) Schematic representation of the unbiased CG ab initio approach. The internal elastic networks used for both AVP (left) and V2R (right) are shown. The full system (center) used for the CG-REMD simulations included two receptors and two peptides. B) Ten most populated clusters (67.5% of the whole conformations) obtained for the AVP-V2R complex after three independent CG-REMD simulations. C) Schematic representation of the successive steps using the CDMD method to fit the models resulting from the CG-REMD simulations into the L cryo-EM map. D) Mapping AVP contact surface by experimental STD NMR. The STD effect profile (in percentage) is shown as a function of AVP protons [aliphatic, N (backbone), and aromatic]. E) Cross-correlation between computational and STD NMR. Variability of the position of AVP was calculated as mean RMSD values (in angstroms) after cross-comparison of five models resulting from the fitting procedure of each of the 10 clusters in the L density map. Cluster 5 showed the smaller variability (2.2 Å). Experimental STD values were compared to the expected STD values from all-atom models issued from MDSs, and correlation coefficients were calculated for the whole peptide (R1–9). Cluster 5 appeared as the best cluster fitting to experimental STD values. F) Building of the final L structure based on remapping cluster 5 into the L density map. G) On the basis of the L structure, the T structure was built to match the T density map.

On the basis of this approach, the L and T models were then built in a more conventional manner to match the density maps as closely as possible (Figure 4-8 E F, and Table 2). In the final models, the 7TM and helix 8 of the V2R were reconstructed in both structures. Intracellular loop 1 (ICL1) was well defined in the maps, as well as the contacts between V2R and the G_s protein. The α-helical domain of $G\alpha_s$ subunit signal was subtracted during single-particle analysis for high-resolution map refinement. ICL2, ICL3, and the C terminus of V2R were not seen in the density maps and were not constructed in the final models.

4.5 The overall architecture of the ternary complex and dynamic of the system

Because of its poor resolution, the T2 state was not interpretable at the atomic level, but it is interesting to compare its overall architecture to the T1 and L states. Both L and T AVP-V2-G_s ternary complexes present a typical GPCR–G protein architecture with the receptor 7TM helix bundle engaging the peptide agonist on the extracellular side and the $G\alpha_s$ C-terminal domain (α_5 helix) on the intracellular side (Figure 4-9 A-D). However, the L, T1 and T2 states present large structural differences most notably in the position of the G protein heterotrimer relative to V2R. The α_5 helix interacts most tightly in the T2 state, intermediately in the T1 state, and more superficially in the L state, inducing a translation of the whole G_s heterotrimer. In particular, the α_5 helix and the Ras-like domain of $G\alpha_s$ are translated from 4 and 5 Å between the L and T1 or T2, respectively. These movements position the α*N* helix 5 Å closer to the receptor in the T states in comparison to the L state. Those Gα movements are also accompanied by a 7-Å translation of the Gβ N-terminal helix, a translation of the γ subunit of 6 Å (T1-L), and a translation of Nb35 of 7 Å (T1-L). T1 and T2 states are similar nonetheless, T2 state displaying a tighter interaction. (Figure 4-9 F)

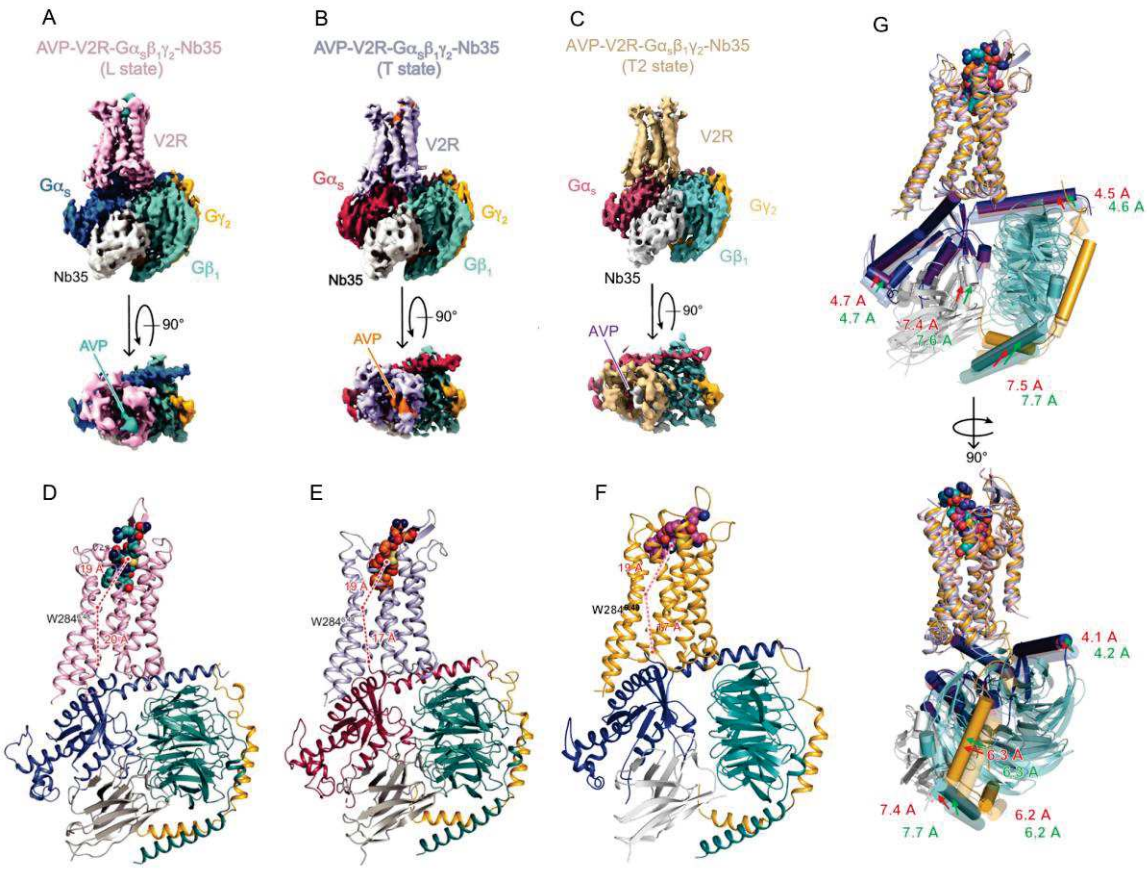

Figure 4-9 Structures of AVP-V2R-Gs-Nb35 complexes in L, T1 and T2 conformations
Structures of AVP-V2R-G_s-Nb35 complexes in L, T1, and T2 conformations. A) An Orthogonal view of the cryo-EM density maps of the L state of the AVP-V2R-G_s-Nb35 complex and (**D**) corresponding model as ribbon representation. V2R is colored in pink, $G\alpha_s$ in dark blue, $G\beta_1$ in turquoise, $G\gamma_2$ in yellow, Nb35 in gray, and AVP in cyan. In (B), the distances between $W284^{6.48}$ (at its Cα carbon) and the AVP center of mass (COM) and between $W284^{6.48}$ and the C-terminal end of α_5 helix of G_s (at the Cα carbon of the free carboxylic acid) are shown. (**B** and **E**) Corresponding map and model for the T state. V2R is colored in blue-gray, $G\alpha_s$ in raspberry, $G\beta_1$ in turquoise, $G\gamma_2$ in yellow, Nb35 in gray, and AVP in orange. In (E), distances are measured as in (D). (**C** and **F**) Corresponding map and model for the T2 state. V2R is colored in yellow, $G\alpha_s$ in light raspberry, $G\beta_1$ in turquoise, $G\gamma_2$ in yellow, Nb35 in gray, and AVP in grey. In (F), distances are measured as in (B). (**G**) L and T1 and T2 models are aligned on the V2R chains, and rotations/translations are shown by measuring displacement (in angstroms) of $G\alpha_s$, $G\beta_1$, $G\gamma_2$, and Nb35. (red arrows, L to T1 displacement, and green arrows L to T2 displacements).

The presence of several conformational states and the multibody refinement analysis (Figure 4-6) reflect the dynamics of V2-G_s complex formation. Those differences are less pronounced than the ones recently described for the neurotensin receptor NTSR1-G_{i1} complexes (Kato et al. 2019), they further indicate that GPCR–G protein coupling is a dynamic process in which the G protein may explore different sets of conformations. The cryo-EM experimental structures might represent discrete conformational states from a continuum of dynamic conformational distribution which can not be efficiently probed by SPA and Cryo-EM. Because

of its poor resolution, the T2 state was not interpretable at the atomic level. Therefore, only the L and T1 structures, referred to as L and T states, were used for further analysis.

4.6 Comparison with V2R active high-resolution structures and OTR-inactive structure coupled to retosiban

Concomitantly to our publication, two other active structures of the AVP-V2R-Gs complex were published (F. Zhou et al. 2021; L. Wang et al. 2021). Interestingly, in both cases, the authors used a short form of Gs modified by replacing the N-terminal segment with N-terminal residues of human Gαi1. These chimeric Gs were capable of binding to scFv16, which stabilizes these active GPCR conformations. This modification, together with another protein engineering (NanoBiT tethering strategy (Figure 4-10) (F. Zhou et al. 2021)), probably explains not only a better resolution in both studies (2.6 Å and 2.8 Å) but also why flexibility and dynamics of the signaling complex were not addressed (L. Wang et al. 2021)(F. Zhou et al. 2021). Hence, the different structures are complementary and help to have a complete view of this signaling system.

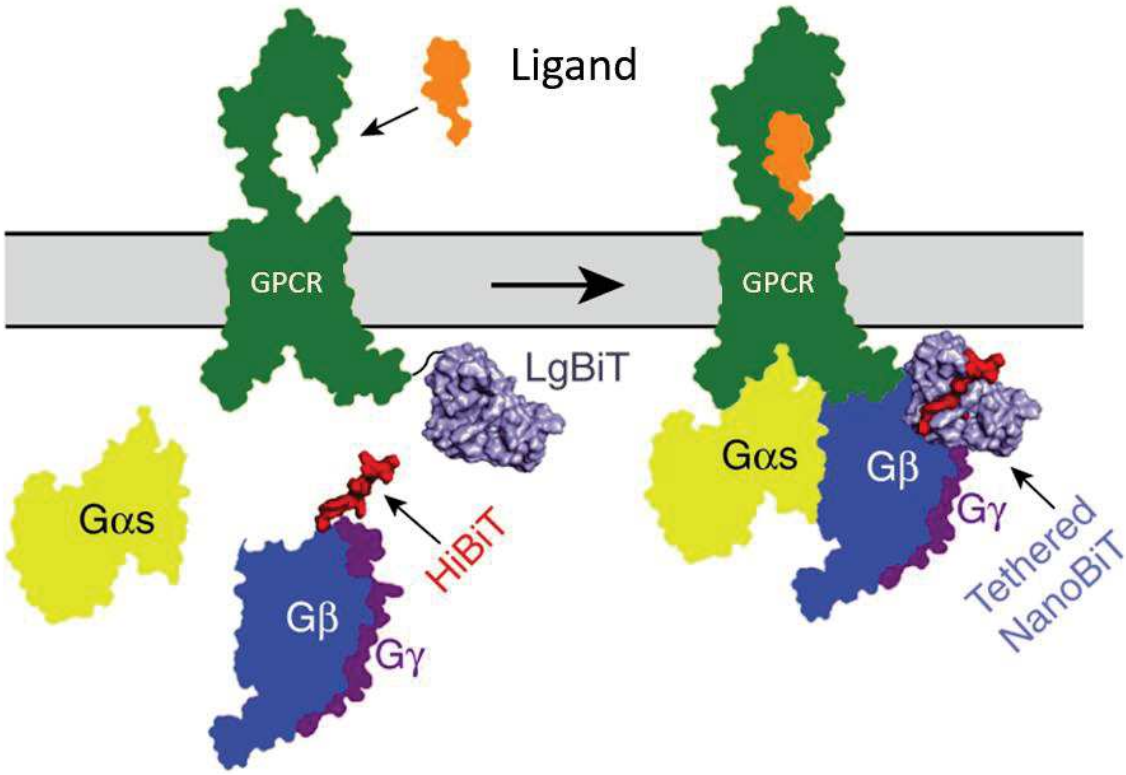

Figure 4-10 Schematic diagram of the NanoBiT aided assembly of a GPCR–Gs complex
Ligand is colored in orange, the GPCR in green, Gαs in yellow, Gβ in blue, Gγ in purple, LgBiT in light blue, and HiBiT in red. Adapted from (Duan et al. 2020)

4.6.1 AVP binding pocket within V2R and comparison with oxytocin antagonist binding in OTR

The overall positioning of AVP in the orthosteric binding pocket is comparable in the three studies focused on the V2R active form, in terms of AVP depth and orientation (Figure 4-11). This demonstrates that our hybrid approach allowed us to build convincing models of AVP binding poses in both L and T structures. There is more flexibility related to the C-terminal tripeptide of AVP which appears to interact sequentially with variable clusters of residues in the receptor either at the top of the TM1, the ECL1, or the ECL2. The final calculated structures present a central position of AVP in the orthosteric pocket of the V2R along the axis of the helical bundle (Figure 4-11; Figure 4-12). The extracellular domains of the V2R are widely opened in both L and T conformations, a feature consistent with the accommodation of a cyclic peptide such as AVP and with the three other AVP/OT receptors structures (the two other active structures of V2R and the inactive one of the OTR) reported to date (Figure 4-12). In the L and

T structures, AVP contacts residues from both TM helices and extracellular loops (Figure 4-11 and Figure 4-12) in agreement with what was originally proposed based on pharmacological data (Mouillac et al. 1995). Consistent with its amphipathic nature, AVP interacts with two chemically distinct interfaces in a 15-Å-deep binding pocket to form both polar and hydrophobic contacts (Figure 4-11 B; C). While AVP conformations occupy a central position in both the L and T binding clefts, interesting changes are observed because of a translation of the Y2 residue side chain (contacts changing from TM7 to TM3). On this aspect, the L state is more comparable to the high-resolution model (PDB ID:7KH0). On the opposite, the C-terminal tripeptide of AVP from the T form is similar to that in 7KH0, and the L form displays an inversion in R8 and G9-NH_2 positions (Figure 4-11 D). In our structure, the C-terminal tripeptide mainly interacts with the top of the TM1, and the ECL2 like in 7KH0. The other high-resolution structure (PDB ID: 7DW9 not released) shows an interaction between D103 (ECL1) and the AVP G9-NH_2 position.

The cyclic part of AVP (C1 to C6) and the P7 are buried into the cleft defined by the seven-helix bundle of V2R, leaving only R8 residue and C-terminal glycinamide exposed to the solvent (Figure 4-12). In all V2R structures, the C1-Y2-F3 hydrophobic motif of AVP binds deeper in the binding site, creating key contacts with the receptor (Figure 4-11 Figure 4-12), in agreement with STD spectroscopy data (Figure 4-8).

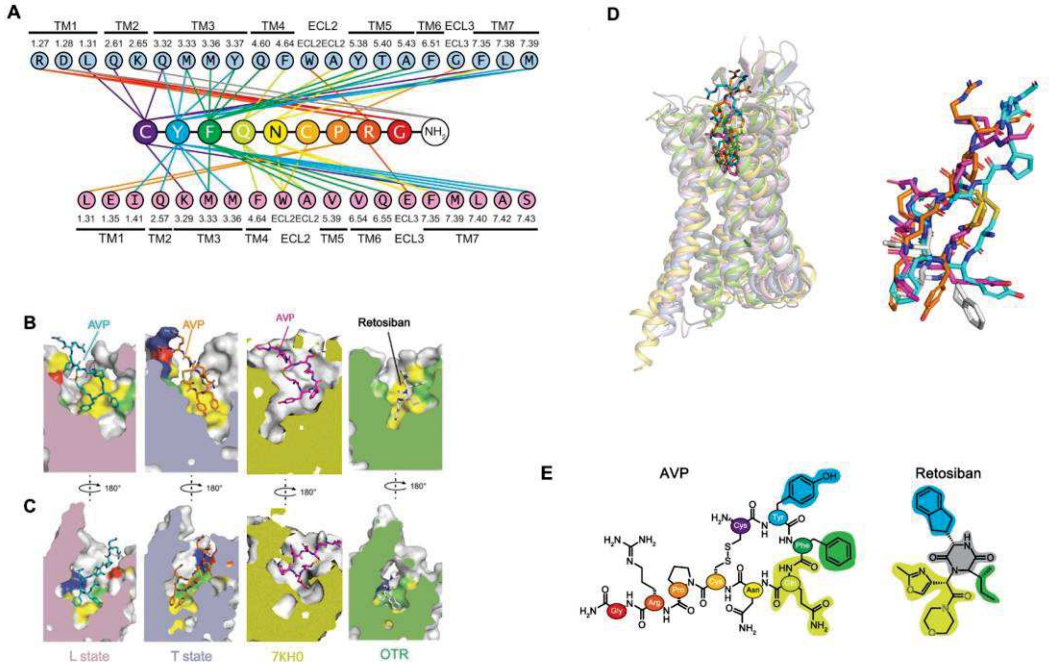

Figure 4-11 AVP-binding site of the V2R, comparison with retosiban-binding site in OTR.
A) Direct contacts between AVP and V2R in L and T structures. Interactions (within a maximum of 5 Å in distance) are shown between each AVP residue (and the C-terminal amide) with V2R residues in the L structure (pink) and in the T structure (blue). All TM helices, extracellular loop 2 (ECL2), and ECL3 interact with the hormone AVP. V2R residues are labeled according to the Ballesteros-Weinstein numbering. Each residue from AVP is colored differently for clarity. **B)** Side views of the binding pocket in the L and T structures and in the inactive structure of OTR. AVP binding modes in the L (pink) and T (light blue) structures are compared to that of the small-molecule antagonist retosiban in the OTR structure (green), all viewed from TM3. Residues from receptors that interact with AVP or retosiban are depicted in different colors: yellow for hydrophobic, green for polar, and red and dark blue for negatively and positively charged, respectively. **C)** Side views of the binding pockets after a 180° rotation. AVP and retosiban are viewed from TM6. The same color code is used. **D)** Superimposition of AVP and retosiban. The peptide agonist and the nonpeptide antagonist are superimposed after alignment of V2R and OTR structures. The most hydrophobic parts of both ligands superimpose at the bottom of the orthosteric binding pocket. **E)** Structure comparison of AVP and retosiban. AVP is shown using the same color code in A, (Purple AVP from 7KH0). The retosiban indanyl moiety, the *sec*-butyl group, and the oxazol-morpholine amide moiety superimpose with AVP Y2, F3, and Q4, respectively. The retosiban 2,5-diketopiperazine core is positioned between AVP Y2 and F3.

In the 7DW9 structure, C1 is proposed to interact with Q96$^{2.61}$, K116$^{3.29}$, Q119$^{3.32}$ of V2R forming a stabilizing H-bond network (F. Zhou et al. 2021), Contacts with Q96$^{2.61}$, K116$^{3.29}$ are present in the L state but not in the T state. Indeed, in the T state, C1 interacts with Q119$^{3.32}$. Y2 also forms hydrophobic interactions with V2R residues M311$^{7.39}$ and L312$^{7.40}$ in L and T states as proposed in the 7KH0 structure (L. Wang et al. 2021). Nonetheless, the specific Y2 interaction with the main chain oxygen of L312$^{7.40}$ is not seen in our structures. Indeed, the TM7

is slightly rotated in T and L states relatively to 7KH0, because of the difficulty of model building with a limited resolution (L. Wang et al. 2021).

V2R and OTR belong to the same subfamily of peptide class A GPCRs and share a common orthosteric binding site (Mouillac et al. 1995; Hibert, Hoflack, and Trumpp-Kallmeyer 1999). Although V2R and OTR (PDB ID:6TPK) structures (Waltenspühl et al. 2020) represent different GPCR conformations (active agonist-bound V2R versus inactive antagonist-bound OTR), it is interesting to compare the complete set of residues involved in the binding of the natural hormone AVP with the ones involved in retosiban binding to gain insights into ligand binding and efficacy in this receptor family (Figure 4-11; Figure 4-12). Many OTR residues involved in the binding of retosiban are conserved among AVP/OTRs and also interact with AVP in the V2R. The conserved $W^{6.48}$ and $F^{6.51}$ (Ballesteros-Weinstein numbering) in AVP/OTRs interact with the highly hydrophobic indanyl moiety of retosiban in the crystal structure of inactive OTR. AVP also makes contact with $F^{6.51}$ through its Y2 and F3 and form a hydrophobic cluster with $M120^{3.33}$, $M123^{3.36}$, $F287^{6.51,}$ and $F288^{6.52}$ in all V2R structures but AVP is not in direct contact with $W284^{6.48}$ in the V2R, probably because it is too bulky to bind deeper in the pocket. This is consistent with the fact that F287V, was shown to affect AVP binding. (Makita et al. 2020) and mutations of M123R/K were identified as cNDI-causing mutations (Sasaki et al. 2013). These data confirm that hydrophobic small-molecule nonpeptide antagonists and AVP partially superimpose at the bottom of the orthosteric binding pocket of AVP/OTRs (Macion-Dazard et al. 2006; Ala et al. 1998; Tahtaoui et al. 2003).

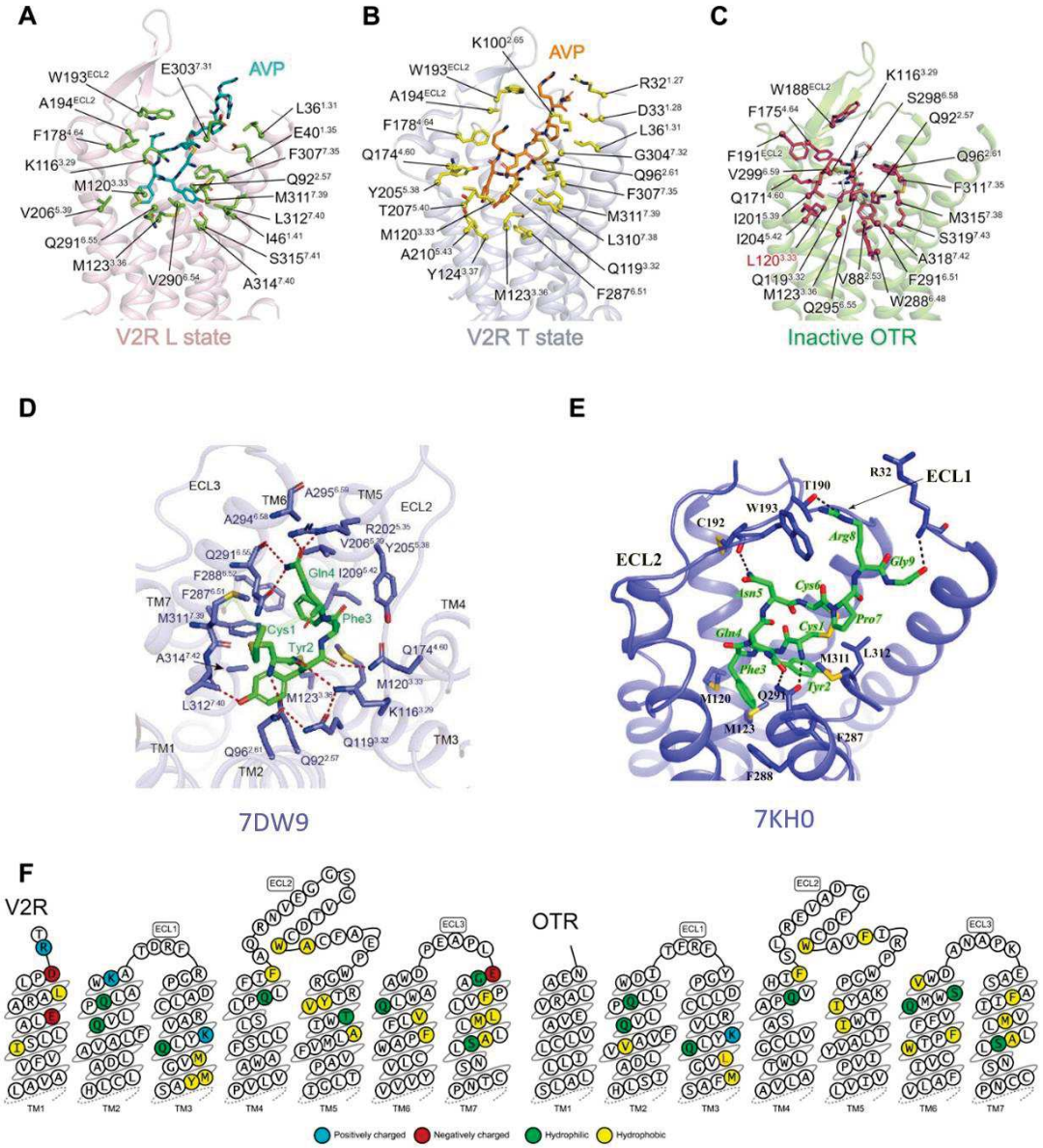

Figure 4-12 V2R and OTR binding pockets: Binding of AVP versus retosiban.
AVP binding poses are viewed from the side of the V2R helix bundle in L (A) or T (B) state and are compared with that of retosiban (in white sticks) in OTR (C). Receptor residues directly interacting with the ligands (at a maximum of 5 Å in distance) are indicated (Ballesteros-Weinstein numbering). In the OTR, L120$^{3.33}$ (highlighted in red) is a mutation introduced in the sequence to increase thermostability and facilitate crystallogenesis (V120L). D) AVP binding poses are viewed from the side of the V2R helix bundle PDB ID 7DW9 (F. Zhou et al. 2021). E) AVP binding poses are viewed from the side of the V2R helix bundle PDB ID 7KH0 (L. Wang et al. 2021). F) Residues of V2R and OTR involved in the binding of ligands are shown in receptor snake-like plot representations (https://gpcrdb.org).

4.7 Activation of the V2R and comparison with other class A GPCRs

4.7.1 Main activation conformational features

V2R reveals key structural features of the activation process by comparison with the OTR inactive structure (Figure 4-13). Moreover, to get a more general view of V2R activation, it is also important to look at the canonical conformational changes of TMs and of conserved motifs involved in other ligand-activated GPCRs of class A (Filipek 2019; Deupi 2014). Thus, compared to other active GPCR structures, to the inactive antagonist-bound OTR structure, and to the high-resolution active V2R structure (PDB 7KH0) (Figure 4-13 A), the L and T structures of V2R present all the features of active conformations, i.e., a large-scale displacement of TM6 (Figure 4-13 A to E), an inward movement of the TM7, a rearrangement of the $P^{5.50}$-$S^{3.40}$-$Y^{6.44}$ transmission switch, equivalent to the PIF motif in other GPCRs (Figure 4-13 C), a rotation of the conserved $NPxxY^{7.53}$ motif (Figure 4-13 D), and a broken $D136^{3.49}$-$R137^{3.50}$ ionic lock (Figure 4-13 E).

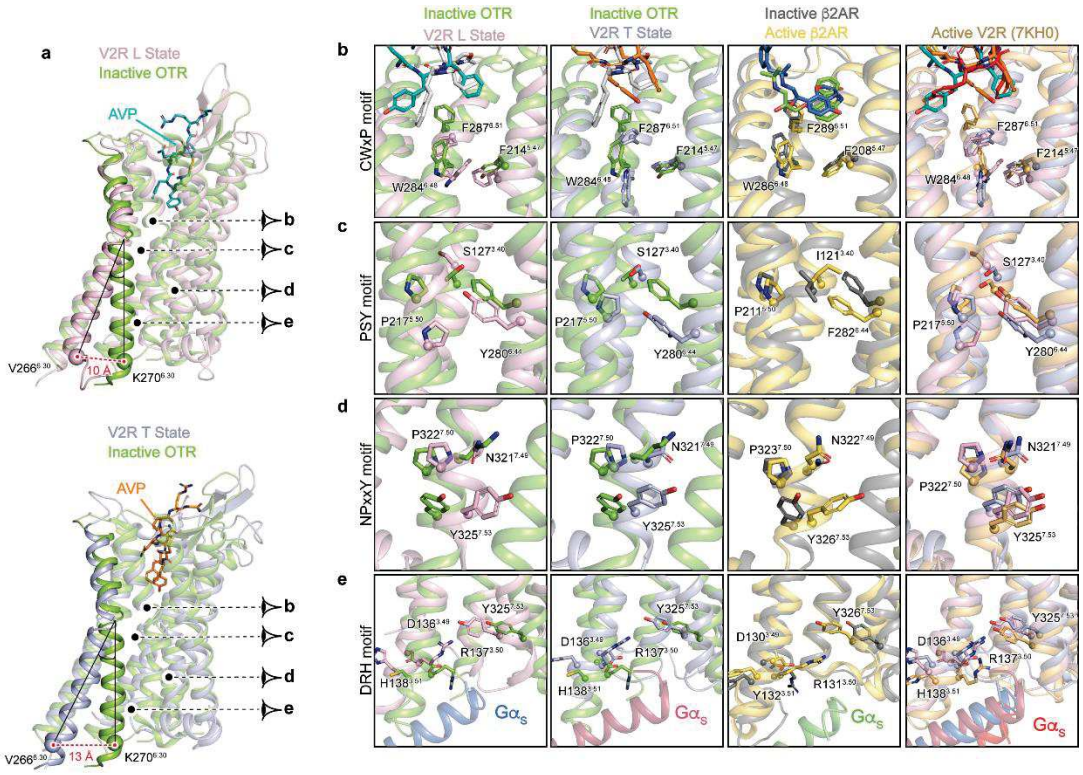

Figure 4-13 Active conformations of L and T V2R states comparison with inactive structure of OTR, active/inactive structures of β_2AR, and active V2R in 7KH0
(**A**) Large-scale displacement of TM6. The V2R L (pink) and T (blue-gray) active structures are aligned onto that of the inactive OTR (green) structure. Residue 6.30 (Ballesteros-Weinstein numbering) is chosen as a reference (V266 in V2R and K270 in OTR) for measuring the outward movement of TM6: 10 and 13 Å between OTR and V2R in the L and T states, respectively. Activation of molecular switches along the helix bundle of the V2R is viewed in (B) to (E). For comparison, rearrangements of those corresponding motifs in the β_2AR are depicted. (**B**) Rotameric toggle switch in the conserved CWxP motif. Position of $W^{6.48}$, $F^{6.51}$, and $F^{5.47}$ (284, 287, and 214 in V2R) are shown. (**C**) Rearrangement of the PSY transmission switch. The $P^{5.50}$-$S^{3.40}$-$Y^{6.44}$ motif (217, 127, and 280 in V2R) is equivalent to the PIF motif in other GPCRs. (**D**) Rotation of the NPxxY conserved motif in TM7. The conserved $Y^{7.53}$ (position 325 in V2R) is shown. (**E**) Breaking of the conserved ionic lock in TM3. Upon activation of V2R, the ionic bond between $D136^{3.49}$ and $R137^{3.50}$ is broken, and $R137^{3.50}$ projects to $Y325^{7.53}$.

By comparing the structures of the inactive antagonist-bound OTR with the active agonist-bound V2R, it appears that contacts between $M123^{3.36}$ and $F287^{6.51}$-$W284^{6.48}$ motif (all in contact with Y2 of AVP) undergo large conformational rearrangements (Figure 4-13), as it was demonstrated in other class A GPCRs (review here (Q. Zhou et al. 2019)).

In the PSY motif, AVP binding is proposed to triggers a rotation of $Y280^{6.44}$ relative to the inactive OTR, subsequently forming a featured H-bond between $Y280^{6.44}$/$S127^{3.40}$ probably stabilizing the active conformation of the receptor.

4.7.2 Mutations in the V2R and structural hypothesis towards their role in activation

As indicated above, The V2R R137$^{3.50}$ participates in the ionic lock motif involved in the balance of active versus inactive states of class A GPCRs (Filipek 2019). In the inactive structure of OTR, D136$^{3.49}$ and R137$^{3.50}$ interact with each other through this ionic lock (the distance between the two charged groups is 3 Å; Figure 4-14A). For comparison, this salt bridge is broken in the L and T active conformations of the V2R-G_s complex (Figure 4-13E Figure 4-14 B). In that case, the distance between the two charges is 10 Å in the L state and 8 Å in the T state. The observed constitutive activity toward G_s coupling for the missense mutations C137$^{3.50}$ or L137$^{3.50}$ responsible for NSIAD (Feldman et al. 2005; Tenenbaum et al. 2009; Rochdi et al. 2010) can thus be explained from a structural point of view since these hydrophobic residues are not able to form such an ionic lock to stabilize the inactive state (Figure 4-14C). On the contrary, the mutant H137$^{3.50}$ causing cNDI (Bernier et al. 2004; Barak et al. 2001) might still be able to maintain the balance between active and inactive states of the V2R through its partial positive charge (Figure 4-14C). Its loss of function rather reflects the loss of accessibility to AVP due to the constitutive internalization (Bernier et al. 2004; Barak et al. 2001; Rochdi et al. 2010).

In the same line, I130$^{3.43}$ mutation can induce either a loss of function when substituted into F130$^{3.43}$ (cDNI) (Robben, Knoers, and Deen 2005), or a gain of function of V2R if changed into N130$^{3.43}$ (NSIAD) (Erdélyi et al. 2015). Interestingly, in the inactive state of OTR, the L130$^{3.43}$ makes a hydrophobic cluster with I280$^{6.40}$ and L281$^{6.41}$. We can hypothesize then, that the same contact is present in V2R between I130$^{3.43}$ and I276$^{6.40}$ and V277$^{6.41}$. Activation could break this contact by TM6 large outward movement. In this condition, N130$^{3.43}$, a polar residue, can not stabilize the inactive state explaining the gain of function of this mutant I130N. The F130$^{3.43}$ mutant would at the opposite still be able to make hydrophobic contacts. However, it is mainly expressed in the endoplasmic reticulum (ER) as an immature protein and consequently never reaches the cell surface membrane (Robben, Knoers, and Deen 2005).

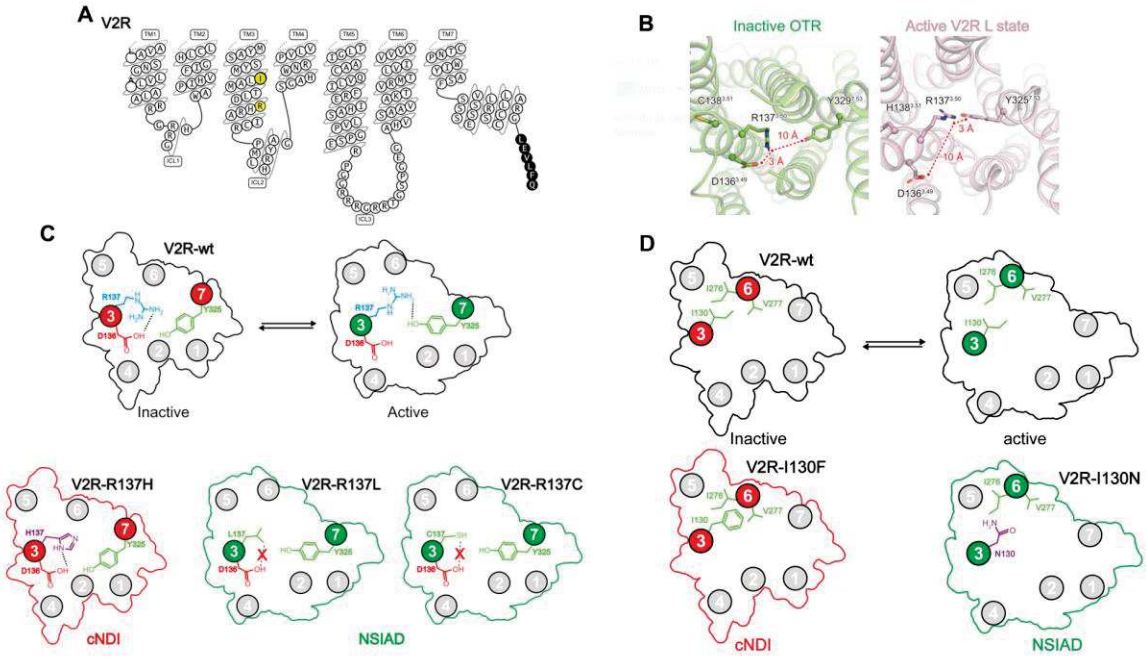

Figure 4-14 Structural insights into V2R mutations associated with cNDI or NSIAD.
(**A**) Modified snake plot of the human V2R construct used in the study (https://gpcrdb.org). The R137$^{3.50}$ residue involved in the ionic lock motif with D136$^{3.49}$ is highlighted in yellow. The mutation of this residue into a histidine or a cysteine/leucine is responsible for two genetic diseases, cNDI and NSIAD, respectively. Part of the human rhinovirus 3C (HRV3C) protease cleavage site introduced in the C-terminal end is indicated in black. (**B**) Ionic lock motif in the inactive structure of OTR (left) and in the active V2R L state structure (right). In the inactive OTR, the distance between positively charged R137$^{3.50}$ and negatively charged D136$^{3.49}$ is 3 Å (locked confirmation), whereas it is 10 Å in the active V2R (open conformation). In the active V2R L state, R137$^{3.50}$ directly contacts Y325$^{7.53}$, an interaction that is not seen in the inactive OTR. (**C**) Schematic representation of R137$^{3.50}$ mutations responsible for either cNDI or NSIAD. In the top, equilibrium between inactive and active conformations of the wild-type V2R (V2R-wt) and the ionic lock motif are illustrated. Bottom: Mutations of R137$^{3.50}$ that induce cNDI (V2R-R137H) or NSIAD (V2R-R137L and V2R-R137C) are compared. Breakage of the R137$^{3.50}$-D136$^{3.49}$ ionic lock is shown in the R137C and R137L mutants. TM3 and TM7 are depicted in red in the V2R-R137H mutant, whereas they are shown in green in the constitutively active mutants V2R-R137L/C. (**D**) Schematic representation of I130$^{3.43}$ mutations responsible for either cNDI or NSIAD. In the top, equilibrium between inactive and active conformations of the wild-type V2R (V2R-wt) and the hydrophobic interaction between I130$^{3.43}$ (TM3) with I276$^{6.40}$ and V277$^{6.41}$ are illustrated. Bottom: Mutations of I130$^{3.43}$ that induce cNDI (V2R-I130F) or NSIAD (V2R-I130N) are compared. Breakage of the hydrophobic interaction is shown in the I130N mutants. TM3 and TM6 are depicted in red in the V2R-I130F mutant, whereas they are shown in green in the constitutively active mutants V2R-I130N.

4.8 V2R-Gs interactions

The cryo-EM maps of the ternary complex establish the structural details of V2R-Gs coupling. As anticipated from the conserved mechanism of GPCR–G protein coupling (Weis and Kobilka 2018; Hilger, Masureel, and Kobilka 2018), both the L and T conformations show a similar overall architecture of the complex interface with the engagement of the Gαs C-terminal α5

helix in the core of the 7TM (Figure 4-15 D, I). However, there are some interesting differences between the V2R active conformations and other GPCR-Gs complex structures. ICL1 residues G69 H70 interact with GαN helix residues R38 Q35 and Q31. In the L state, Q35 interact with GαN helix residue W71. This is an original feature of V2R-Gs interface. Notably, in both the L and T structures, the V2R ICL1 makes many direct contacts with the Gβ subunit. These contacts are not present in 7KH0, this is consistent with the fact that the miniGs chimera adopts a slightly different orientation relative to the receptor and consequently induces fewer interactions between the G protein and the complex. In the T state, ICL1 residues L62-A63-R64-R65-G66 interact with Gβ R52, D312-N313, and D333-F335. In the L state, ICL1 residues R65-G66-R67-R68 interact with Gα R52, D312, and D333. These contacts between V2R and G are much more numerous than in the class A GPCR β2AR- or adenosine A2A receptor (A2AR)-Gs complexes (Rasmussen et al. 2011; Hilger, Masureel, and Kobilka 2018). Moreover, in the T conformation, there are some additional contacts between V2R ICL1 (R67-G69-H70) with the N-terminal α helix of Gαs (Q31, Q35, and R38), resulting in a more compact interaction Figure 4-15. In the L state, V2R (W71) and N-terminal α helix of Gαs (Q35 and R38) contacts are more limited. Contacts between the N-terminal α helix of Gαs with GPCRs have only been seen in glucagon-like peptide-1 receptor (GLP1R) and calcitonin receptor (CTR) class B GPCR complexes (Y.L. Liang et al. 2018; Y. L. Liang et al. 2017), not in class A GPCR–G protein complexes.

In contrast to what was observed for the β_2AR (Sŏren G.F. Rasmussen et al. 2011) and the mu-opioid receptor (μOR) (Koehl et al. 2018), the Gαs C-terminal α5 helix appears to extend helix 8 (H8) of the V2R, lying almost parallel to the membrane plane (Figure 4-15 C, H). Interestingly, this feature is not shared by the V2R active conformation coupled with the miniG_s-G_iα chimera, this might be because the engineered G protein stabilizes the complex in a slightly different conformation than the one adopted by the more physiological G_sα protein.

In addition, compared to the β_2AR, the C terminus of Gαs is interacting deeper in the V2R 7TM core, making direct contact with the residues of V2R that are part or in close proximity of the conserved NPxxY (TM7) and DRH (TM3) activation motifs (Figure 4-15 E, J). In this respect, the V2-Gs interaction resembles more the interaction seen in the μOR-Gi complex (Figure 4-15 K, M). The V2R TM7-H8 hinge region also makes a strong contact with the Gαs ELL motif, particularly through hydrophobic contacts with the F328$^{7.56}$ side chain (Figure 4-15 D, I). The T and L conformations differ here in the position of the Gαs L394 side chain originating from a distinct F328$^{7.56}$ side-chain conformation (pointing toward I78$^{2.43}$ of the receptor in the T

structure or toward Gαs L394 in the L structure) (Figure 4-15 D, I). Most notably in the T state, the side chain of R137$^{3.50}$, which is part of the ionic lock motif, forms an ionic interaction with the free carboxylic acid function of the Gαs C terminus (Figure 4-15), a direct contact that was not observed before between a GPCR and a G protein of any family (Gs, Gi, Go, or Gq) (14, 15, 46). Moreover, in the L state, the density map suggests that the R137$^{3.50}$ side chain could adopt two conformations, one forming a similar ionic interaction with the carboxylic acid of Gαs L394 main chain and the other one pointing toward the Y325$^{7.53}$ from the NPxxY motif (Figure 4-15).

This atypical orientation of the wavy-hook is not reported in the two high-resolution V2R active structures (7KH0 and 7DW9). It can be a feature of the V2R-Gs compact interaction, nonetheless, because of the limited resolution, this orientation of the wavy hook can be artefactual and need to be confirmed with other experiments.

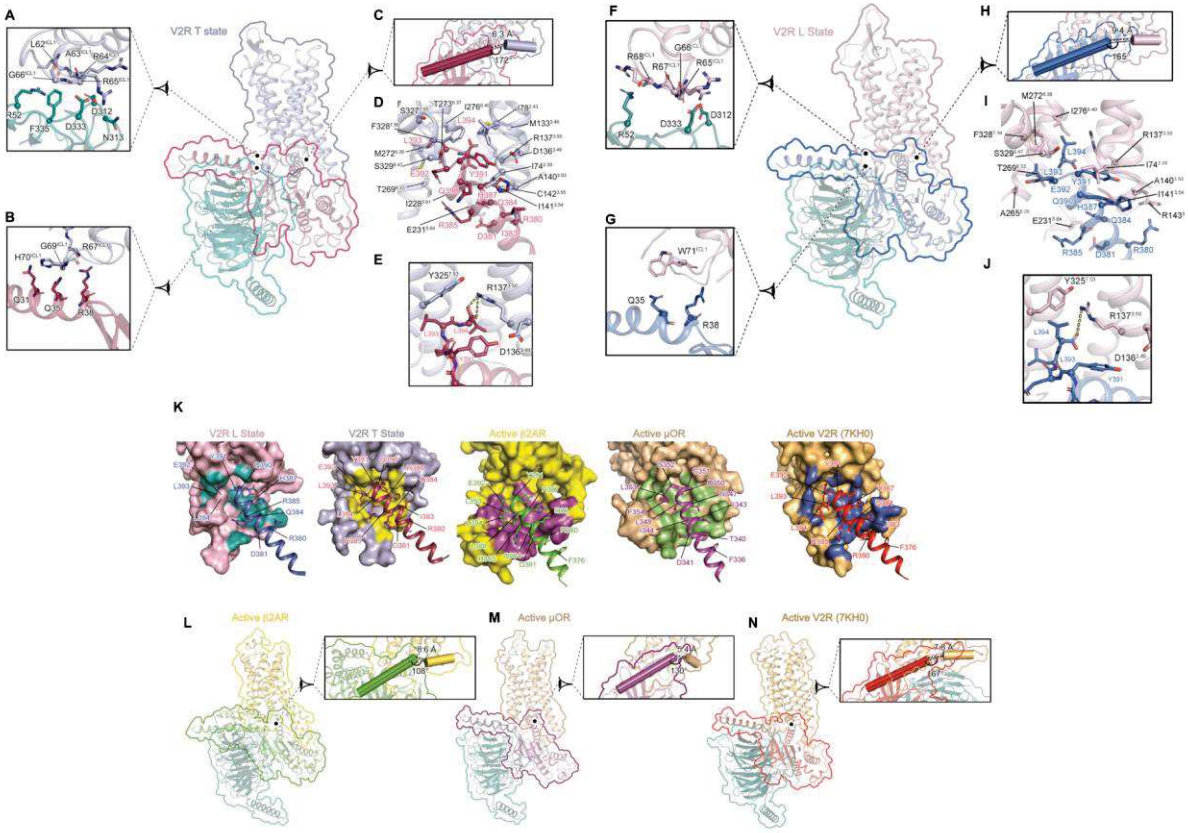

Figure 4-15 The interface of the V2R L and V2R T states with Gs
Interactions between V2R and Gs heterotrimer are shown. Specific interfaces are depicted, and residues in close proximity (within a maximal 3.9 Å distance) are highlighted (A, F) Interaction of V2R ICL1 with Gβ subunit. (B, G) Interaction of V2R ICL1 with N-terminal helix of Gα subunit. (C, H) Positioning of C-terminal h5 helix of Gα subunit relative to V2R helix 8. The distance between Gα and helix 8 is indicated. Angle between these two domains is shown. (D, I) Interacting residues between the C-terminal h5 helix of Gα subunit and V2R. (E, J) Zoom on an ionic bridge between the C-terminal free carboxylic moiety of h5 helix of Gα subunit and V2R R137$^{3.50}$. K) Comparison of class A GPCR-Gα protein interfaces and V2R structure (7KH0). The V2R-Gαs interfaces of L and T states are compared to those of the β2AR-Gαs and μOR-Gαi complexes. The h5 helix of the Gα subunit is shown for each complex with its residues indicated. The residues of receptors in contact with the Gα C-terminal are colored. L, M, N) Position of the C-terminal h5 helix of Gα subunit relative to receptor helix 8 in active β2AR-Gs, μOR-Gi and V2R structure (7KH0) complexes, respectively. Distances and angles between these domains are indicated as in panel C.

4.9 Discussion

In this study, we identified three different states and solved two structures of the AVP hormone–bound V2R in complex with the G_s protein. They reveal distinct agonist and G protein binding modes and a more compact architecture compared to other class A GPCR–G protein complexes. Interestingly two recently published high-resolution structures with the active V2R coupled to a miniG_s-G_iα chimera and stabilized with ScFv16 and Nb35 (F. Zhou et al. 2021; L. Wang et al. 2021) do not share this architecture and adopt a more loose conformation, similar to the ones precedently described for Class A GPCRs. Although this work provides structural insights into

the mechanisms of G protein activation by V2R, additional data are needed to determine whether the different conformations represent distinct intermediates along the signaling activation pathway. However, their identification using single-particle analysis and all-atom MDSs reports high intrinsic flexibility, in agreement with the concept that GPCRs can explore a wide range of conformations, adapting their shape in response to different ligands and/or intracellular signaling partners (Manglik and Kobilka 2014). We also consider that the characterization of three different populations of the AVP-V2R-G_s complex was made possible because of using native receptor (the V2R is wild-type from T31 to G345) and Gs protein, which were not engineered with thermostabilizing mutations or fusion partners although it's detrimental for the resolution.

Despite their various physiological roles, the cyclic peptides AVP and OT share a common receptor family. The V1aR, V1bR, V2R, and OTR display a common binding pocket that accommodates peptide and nonpeptide orthosteric agonists and antagonist ligands (Mouillac et al. 1995; Hibert, Hoflack, and Trumpp-Kallmeyer 1999). Although V2R and OTR (Mouillac et al. 1995) structures represent different GPCR conformations (active agonist-bound V2R versus inactive antagonist-bound OTR), it is not unexpected to see that many residues involved in the binding of AVP (natural cyclic peptide agonist) are conserved among AVP/OTRs and also interact with retosiban (small nonpeptide antagonist) in the OTR. These data confirm that specific binding sites for nonpeptide antagonists and for AVP/OT peptides overlap at the bottom of the receptor binding pocket (Macion-Dazard et al. 2006; Ala et al. 1998; Tahtaoui et al. 2003). Moreover, these are the most hydrophobic parts of AVP and retosiban that superimpose (AVP Y2 and F3 residues versus retosiban indanyl and *sec*-butyl moieties) in the binding pocket. The main pharmacophore responsible for activating V2R seems also to be the Y2-F3 AVP side chains (the message, i.e., efficacy), while the rest of the peptide rather seems to be responsible for the address (selectivity). In agreement, we demonstrated that the presence of the AVP F3 residue (L3 residue for OT) is responsible for partial agonist activity of AVP to the human OTR, whereas AVP hormone is a full agonist on V1aR (Bice Chini et al. 1996), V1bR, and V2R. In addition, modification of residues at position 4 (glutamine for AVP and OT) and 8 (arginine for AVP and isoleucine for OT) has been shown to control the selectivity of AVP analogs toward the different receptor subtypes in the AVP/OTR family (B. Chini et al. 1995; Rodrigo et al. 2007). The deep position of AVP and contacts found in the L and T states are in agreement with the ones found in the high-resolution structures (F. Zhou et al. 2021; L. Wang et al. 2021). We didn't observe the interaction between Y2 and the main chain oxygen

of L312$^{7.40}$ which was proposed to induce a distortion of the TM7 helix. This distorted TM7 conformation, nonetheless observed in the T and L states, is characteristic of active Class A GPCRs (Weis and Kobilka 2018).

The significance of our study also lies in the clinical relevance of the AVP receptor family, particularly for two rare X-linked genetic diseases involving mutations in the V2R, cNDI (J.-P. Morello and Bichet 2001), and NSIAD (Feldman et al. 2005). Our work provides a structural explanation of how those mutations can possibly affect the level of V2R activity and G_s protein coupling. These two pathologies are associated with V2R loss of function or constitutive activity, respectively. Substitution of R137$^{3.50}$ of the V2R for histidine (H137$^{3.50}$) leads to cNDI (Bernier et al. 2004; Barak et al. 2001), whereas substitution of the same residue to cysteine or leucine (C/L137$^{3.50}$) causes NSIAD (Nawal et al. 2019; Tenenbaum et al. 2009; Rochdi et al. 2010). Paradoxically, the three mutant receptors were shown to share common features, such as constitutive arrestin recruitment and endocytosis, resistance to AVP-stimulated cAMP accumulation and MAP kinase activation, and marked decrease in receptor cell surface expression (Tenenbaum et al. 2009; Rochdi et al. 2010; Bernier et al. 2004; Barak et al. 2001). The unique difference observed between the H137$^{3.50}$ mutant and the C/L137$^{3.50}$ mutants resides in their basal constitutive activity toward the cAMP pathway (Nawal et al. 2019). C/L137$^{3.50}$ gain-of-function mutants promote a significantly higher basal cAMP level as compared to the wild-type V2R or the H137$^{3.50}$ loss-of-function mutant. In the present study, we proposed that the two hydrophobic cysteine or leucine residues are not able to form an ionic lock with D136$^{3.49}$ to stabilize the inactive state, explaining their constitutive activity. That is, the conformation of these mutants may be comparable to that of active V2R in the L and T states of the AVP-V2R-G_s signaling complex, at least considering a broken D136$^{3.49}$-C/L137$^{3.50}$ ionic lock.

Similarly, I130$^{3.43}$ substitution for a phenylalanine F130$^{3.43}$ induces a loss of function responsible for cDNI. The same residue mutated in N130$^{3.43}$ induces a gain of function and a constitutively active receptor. In the inactive OT receptor structure, the residue in position 3.43, L130$^{3.43}$, displays hydrophobic contacts with the TM6 I280$^{6.40}$ (I276$^{6.40}$ in V2R) residue. We proposed that I130$^{3.43}$ interact with I276$^{6.40}$ to maintain V2R in an inactive conformation. The mutation N130$^{3.43}$ might induce a constitutive outward TM6 position and therefore, a constitutively active receptor. I130N mutation results in constitutive activity of the V2R with constitutive cyclic adenosine monophosphate (cAMP) generation in HEK293 cells. In contrast to R137(C/L), I130N mutant displays a biased profile preferring Gs to βarrestin coupling (Erdélyi et al. 2015). Confocal laser-scanning microscopic analysis experiments demonstrated

a nearly complete localization of the I130F V2R in the endoplasmic reticulum. Further analysis demonstrates that only 7.3% of this mutant are expressed in the mature form and might be addressed to the cytoplasmic membrane but this is not sufficient to provide an appropriate antidiuretic response (Robben, Knoers, and Deen 2005).

We provided here a unique evaluation of these loss- and gain-of-function V2R mutations.

A patient bearing the V2R H137$^{3.50}$ mutation was shown to increase his urine osmolality after short-term therapeutic treatment with the V1a antagonist SR49059 (Bernier et al. 2006). A structural knowledge about this ligand rescue is clinically important since this mutation is recurrent in independent cNDI families and also presents a phenotypic variability(Kalenga et al. 2002). SR49059 antagonist is used as a pharmacological chaperone. This lipophilic nonpeptide antagonist able to cross biological membranes is selective for the V1aR subtype but still displays a measurable affinity for V2R. This ligand, which is a competitive analog of AVP, is able to rescue the function of endoplasmic reticulum (ER)–trapped mutants of the V2R responsible for cNDI (J. P. Morello, Bouvier, et al. 2000). Upon binding to the orthosteric site of the V2R mutants, SR49059 triggers targeting and stabilization of the mutated receptors to the plasma membrane of receptor-expressing cells, including R137H V2R. This mutant combines most of the properties of the wild-type receptor but is constitutively internalized (Kalenga et al. 2002; Rochdi et al. 2010), leading to a reduced cell surface expression, thus explaining a cNDI phenotype. Treatment of the patient with the pharmacological chaperone probably allows us to stabilize the R137H mutant at the plasma membrane where it is displaced by endogenous circulating AVP hormone, eliciting an antidiuretic response (increase in the osmolality of urine from 150 to 300 mOsm/kg).

The use of cell-permeable pharmacological chaperones for rescuing function of misfolded V2R mutants responsible for cNDI is a very attractive therapeutic avenue, in particular, regarding those that are trapped in the ER but, otherwise, are functional once they are targeted to the cell plasma membrane (see above for the V2R H137$^{3.50}$ and F130$^{3.43}$ mutation). It is thus tempting to interpret clinical observations (or in vitro pharmacological and cellular data) based on the present structures of the V2R. The importance of the structural data to help in understanding mutations is discussed here with three examples of cNDI loss-of-function mutations that can be rescued using pharmacological chaperones using the V2R-selective nonpeptide antagonist TVP, which is now used in thousands of patients with autosomal polycystic kidney disease with a reasonable safety profile (V. E. Torres et al. 2021). The V88M mutation is responsible for a mild phenotype, which is moderate polyuria and some degree of increased urine osmolality

following treatment with desmopressin, an analog of AVP (Bockenhauer et al. 2010). Both the expression level and the hormone binding affinity are affected by this mutation. Structurally, V88$^{2.53}$ makes direct contact with M123$^{3.36}$, which belongs to the AVP-binding site. We hypothesize that V88M induces a local destabilization by a steric clash with M123, leading to the decreased AVP binding affinity observed in in vitro pharmacological experiments but to a substantial increase in urinary concentration after desmopressin treatment in vivo. The M272R mutation is responsible for a severe phenotype with polyuria and no response to desmopressin treatment (Prosperi et al. 2020). In Madin-Darby canine kidney cells, this mutant is trapped in the ER and is not accessible to AVP but can be rescued using the pharmacological chaperone TVP. Once it is at the cell surface, it can respond to desmopressin. M272$^{6.36}$ is located at the bottom of TM6, a highly flexible region that moves outward the V2 core upon activation. Based on the positioning of the corresponding conserved M276$^{6.36}$ in the inactive structure of the related OTR (*28*), M272$^{6.36}$ in the V2R is surrounded by an aromatic/hydrophobic residue cluster, made of I74$^{2.39}$, I78$^{2.43}$, V275$^{6.39}$, I276$^{6.40}$, Y325$^{7.53}$, and F328$^{7.56}$. Mutation of M272 into a positively charged arginine probably destabilizes this domain, induces misfolding of the receptor, and results in ER retention. TVP can rescue the receptor to the cell surface probably by stabilizing its well folded structure.

5 Structure of the AVP-V2R-βarrestin1-ScFv30 complex

5.1 Biochemistry of the V2R and of the signaling complex

Based on our expertise in GPCR signaling, we designed a new V2R construct with a wild-type C-terminal domain since it has been shown to play a critical role in GPCR coupling to βarrestin (Figure 3-33 B) (Perkovska et al. 2018; Kocan et al. 2009). Also, we used a βarrestin1 construct truncated after residue 382 (βarr1ΔCT) which was demonstrated to bind to agonist-activated β2AR in a phosphorylation-independent manner in an *in vitro* reconstituted system and also in living Xenopus oocytes (Kovoor et al. 1999a). Nonetheless, GPCR phosphorylation is a critical parameter to obtain a stable complex with βarr1ΔCT *in-vitro* (W. Huang et al. 2020). Moreover, we stabilized the complex by the addition of an antibody fragment, ScFv30, known to stabilize the β2AR-βarrestin1complex or a chimeric β2V2R-βarrestin1complex in their active state (Shukla et al. 2015).

The receptor was expressed in Sf9 cells using a recombinant baculovirus, extracted from the cell membranes, and purified. The βarr1ΔCT was produced in E. coli and the antibody fragment ScFv30 in S2 Schneider insect cells. The three proteins were mixed using a 1:2:2 ratio (V2R:βarr1ΔCT:ScFv30) in the presence of $MgCl_2$ 2.5 µM and AVP 250 µM and incubated 2 hours at 20°C. (Figure 3-34 B). The purified complex displayed a monodisperse peak using size exclusion chromatography (SEC) and SDS gel analyses confirming the presence of all components of the complex (Figure 5-1). For simplicity, βarr1ΔCT will thus be referred as βarr1.

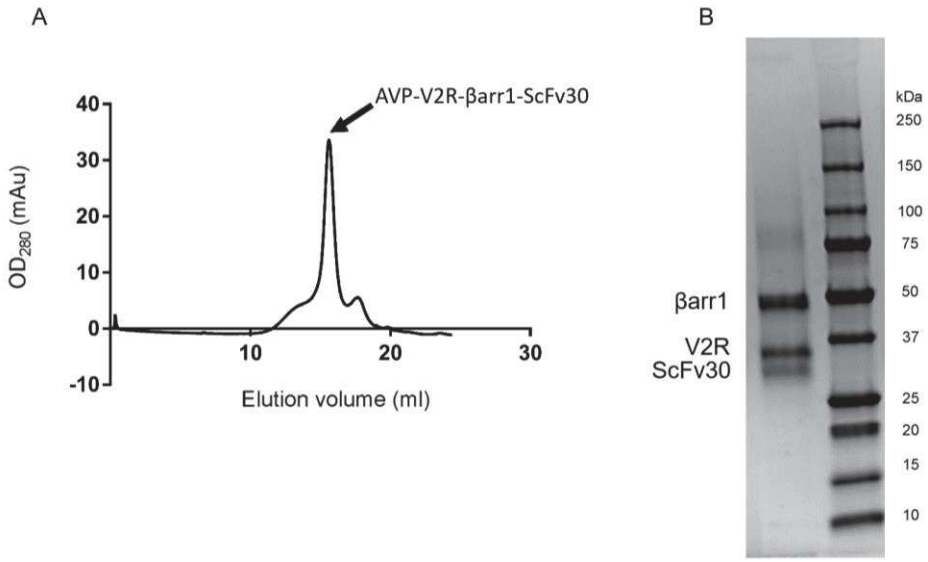

Figure 5-1 SEC chromatogram and SDS-PAGE of the AVP-V2R- βarr1-ScFv30 complex
A) Representative chromatogram of the AVP-V2R-βarr1-ScFv30 complex using a Superose6 column. The stable complex is shown as a monodisperse peak. Fractions containing the sample were combined and concentrated for the preparation of cryo-EM grids. B) SDS-PAGE of peak fraction from the Superose6 step. Coomassie blue staining of proteins confirmed that the complex is made of βarr1, V2R, ScFv30 (AVP is not visible).

5.2 Pharmacology of the "arrestin-dedicated" V2R construct

The binding properties of the engineered V2R were investigated in human embryonic kidney (HEK) mammalian cells, as also presented in the previous chapter (Figure 5-2). The cryo-EM version of the V2R dedicated to βarr1 coupling (Figure 3-33 B) bound a fluorescent nonpeptide antagonist and AVP with high affinity [dissociation constant (K_d) = 4.22 ± 1.21 nM (n = 3) and inhibition constant (K_i) = 3.17 ± 0.97 nM (n = 3), respectively], close to the values determined for a wild-type V2R (Loison et al. 2012). The capacity of this engineered V2R to bind arrestins was measured in HEK cells using a FRET-based assay (PerkinElmer Cisbio, see Materials and Methods). It was proven to be functional regarding arrestin recruitment [K_{act} = 2.02 ± 0.28 nM (n = 4).

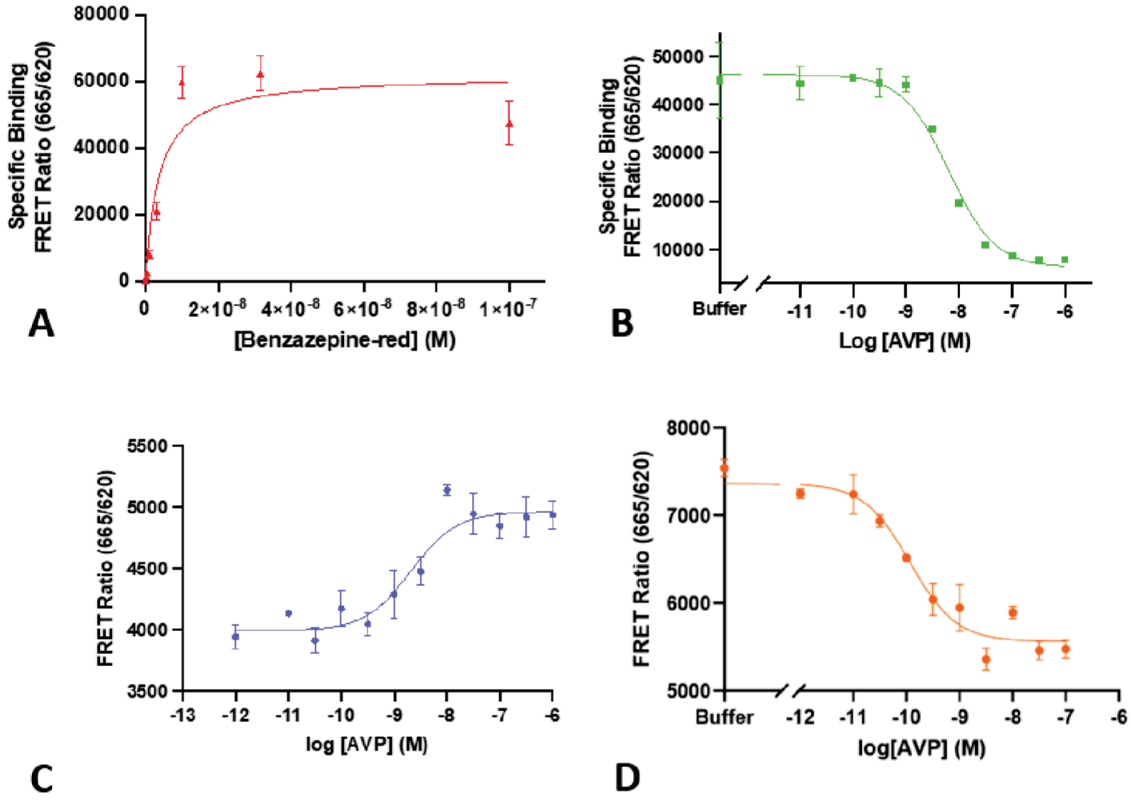

Figure 5-2 Pharmacological and functional properties of the arrestin-dedicated V2R construct.
A) Binding of the benzazepine-red fluorescent antagonist to the V2R construct measured by FRET (see Methods). Specific binding of Benzazepin-red from a typical saturation assay is shown as FRET ratio (665nm/620 nm x 10,000). The experiment was repeated 3 times, each point measured in triplicate. Each value is presented as mean ± SEM. **B**) Binding of AVP to the V2R construct is illustrated as FRET ratio (665nm/620nm x 10,000). Specific binding of benzazepine-red is shown. The fluorescent antagonist was used at 3 nM with or without increasing concentrations of AVP. A typical competition curve is shown and was repeated at least 3 times with each point in triplicate. Each value is presented as mean ± SEM. **C**) Capacity of the engineered V2R construct to recruit the βarrestin2 measured by FRET (see Methods). The recruitment of βarrestin is shown as FRET ratio (665nm/620nm x 10,000) and measured in the presence of increasing concentrations of AVP. A typical experiment is shown, was repeated at least 3 times, each point in triplicate. Each value is presented as mean ± SEM. D) Capacity of the V2R construct to functionally activate adenylyl cyclase measured by FRET (see Methods). The cAMP accumulation is shown as FRET ratio (665nm/620nm) and measured in the presence of increasing concentrations of AVP. A typical experiment is shown, was repeated at least 3 times, each point in triplicate. Each value is presented as mean ± SEM.

5.3 Negative Stain Electron Microscopy

The complex was first characterized using NS-EM. Samples were prepared using uranyl acetate 1% or uranyl formate 0.75%. Images of AVP-V2R-βarr1-ScFv30 complexes were visually similar in terms of complex proportion but uranyl formate 2D classes display better quality.

Images of negatively stained complexes revealed a homogeneous distribution of particles exhibiting a bilobed shape, as observed from two-dimensional (2D) class averages. The globular domain corresponds to the V2R surrounded by detergent whereas the weak domain presenting irregular shapes corresponds to βarr1-ScFv30. From 2D class averages, we estimated that approximately 70% of particles correspond to the entire complex (Figure 5-3).

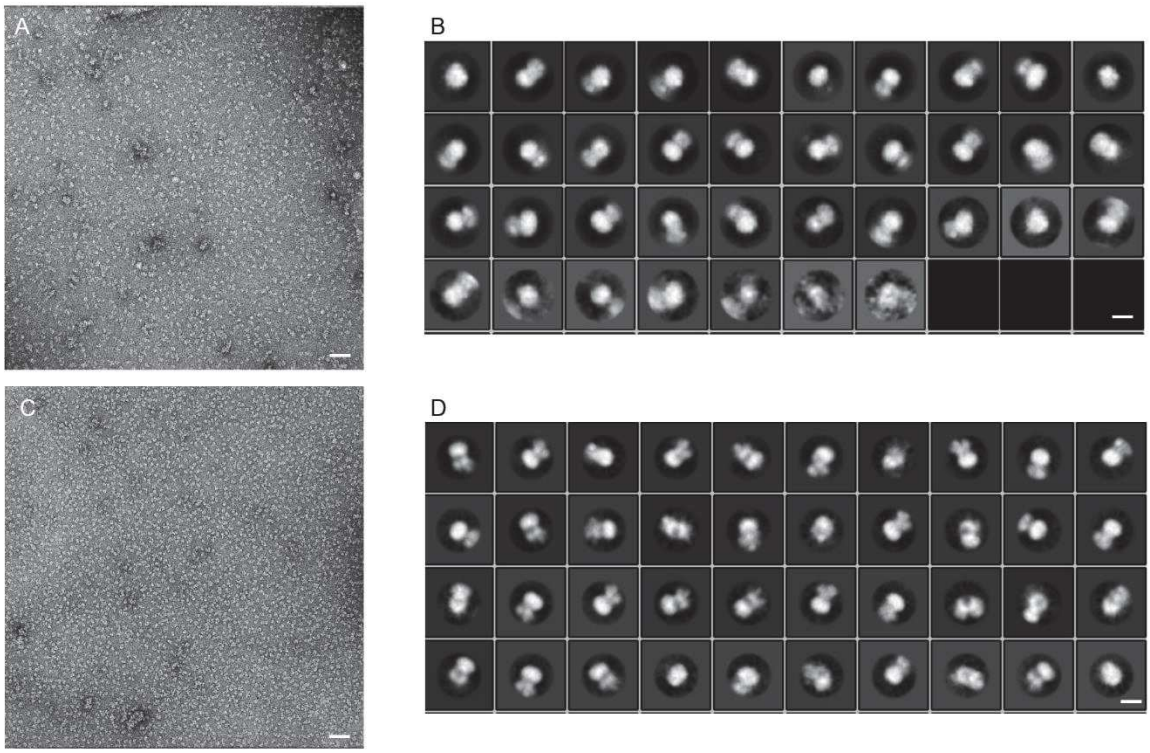

Figure 5-3 Negative stain electron microscopy characterization of the AVP-V2R-βarr1-ScFv30 complex
Representative micrographs of the purified sample of the complex isolated from the Superose6 SEC peak are shown in A (1% uranyl acetate) and C (0.75% uranyl formate). For both micrographs, the scale bar is 65 nm. B and D, extracted 2D most representative class averages showing different orientations (scale bar, 12 nm).

5.4 Cryo-EM of the AVP-V2R-βarr1-ScFv30 complex

After cryo-EM grid sample vitrification using the Leika GP2, 14,080 movies were recorded on a TEI Titan Krios at the European Molecular Biology Laboratory (EMBL) of Heidelberg (Germany) at 300 keV through a Gatan Quantum 967 LS energy filter using a 20-eV slit width in zero-loss mode and equipped with a K3 Summit (Gatan Inc.) direct electron detector configured in counting mode. Movies were recorded at a nominal magnification of ×130,000 corresponding to a 0.64 Å calibrated pixel size. 14,080 movies were collected in 40 frames in defocus range between -1 and -2 µm with a total dose of 52.63 $e^-/Å^2$ in a fully automated manner using SerialEM. Data were preprocessed using Warp (Tegunov and Cramer 2018). Particle

picking performed in Warp uses BoxNet**,** a deep convolutional neural network that allowed to select 3,610,370 particles. After 2D curation in relion3.1, particles (1,169,437) were used as references to train Topaz, a positive-unlabeled convolutional neural network for particle picking (Bepler et al. 2019). Topaz selected 4,595,394 particles, that were exported in relion and pared down through 2D classification. The best particles from BoxNet and Topaz were merged and duplicates were removed. The particles were then iteratively curated through 2D classification on user-defined subsets based on projections orientation. At the end, best 2D class averages displaying various orientations of the AVP-βarr1-ScFv30 complex were ultimately merged representing 729,335 particles. Further iterative 3D classification and refinement in relion resulted in poor quality maps with low-resolution ≃ 12Å. The particles (729,335) were then exported in cryosparc v3.2, and successive rounds of ab-initio refinement (using two models) were performed. A final set of 27,682 particles was refined giving a convincing first model. The best set of particles and model were then processed using the new non-uniform refinement procedure. This resulted in a 4.75 Å map from the 27,682 particles. Postprocessing did not improve the resolution of the map and the overall quality of the density. The map was then sharpened using the autosharpen tool in phenix. Iterative refinement focused on arrestin yielded an improved map with an overall resolution of 4.35 Å with significantly better densities, notably in the area of the V2R C-terminal domain (Figure 5-4).

5.5 Model Building

A starting model was built using V2R-AVP (7KH0) at 2.8Å resolution, V2R-Cter (6U1N) at 4 Å resolution, ScFv30 adapted from Fab30 (4JQI) at 2.6Å resolution, and βarr1 finger loop was adapted from the PDB (6UP7) at 4.2Å resolution for and the PDB (4JQI) at 2.6Å resolution was used for the rest of the βarr1. The starting model was manually adjusted in Coot (Emsley and Cowtan 2004) and the fit was improved using Flex-EM (Joseph et al. 2016; Topf et al. 2008), a software dedicated to the fit of atomic models in intermediate-to-low resolution density maps. Flex-EM was first used on the AVP-V2R-βarr1-Scfv30 map with Flex-EM automatic rigid-body domains determination. Model refinement was then carried out with Flex-EM in the βarr1-Scfv density map obtained with local refinement. Rigid body restraints were applied on AVP-V2R which are not represented in this density map.

Currently, the model is still under construction, nonetheless, the main features of the AVP-V2R-βarr1-ScFv30 complex can be discussed on its base but the subsequent analysis will be validated by careful comparison between the model and the density map.

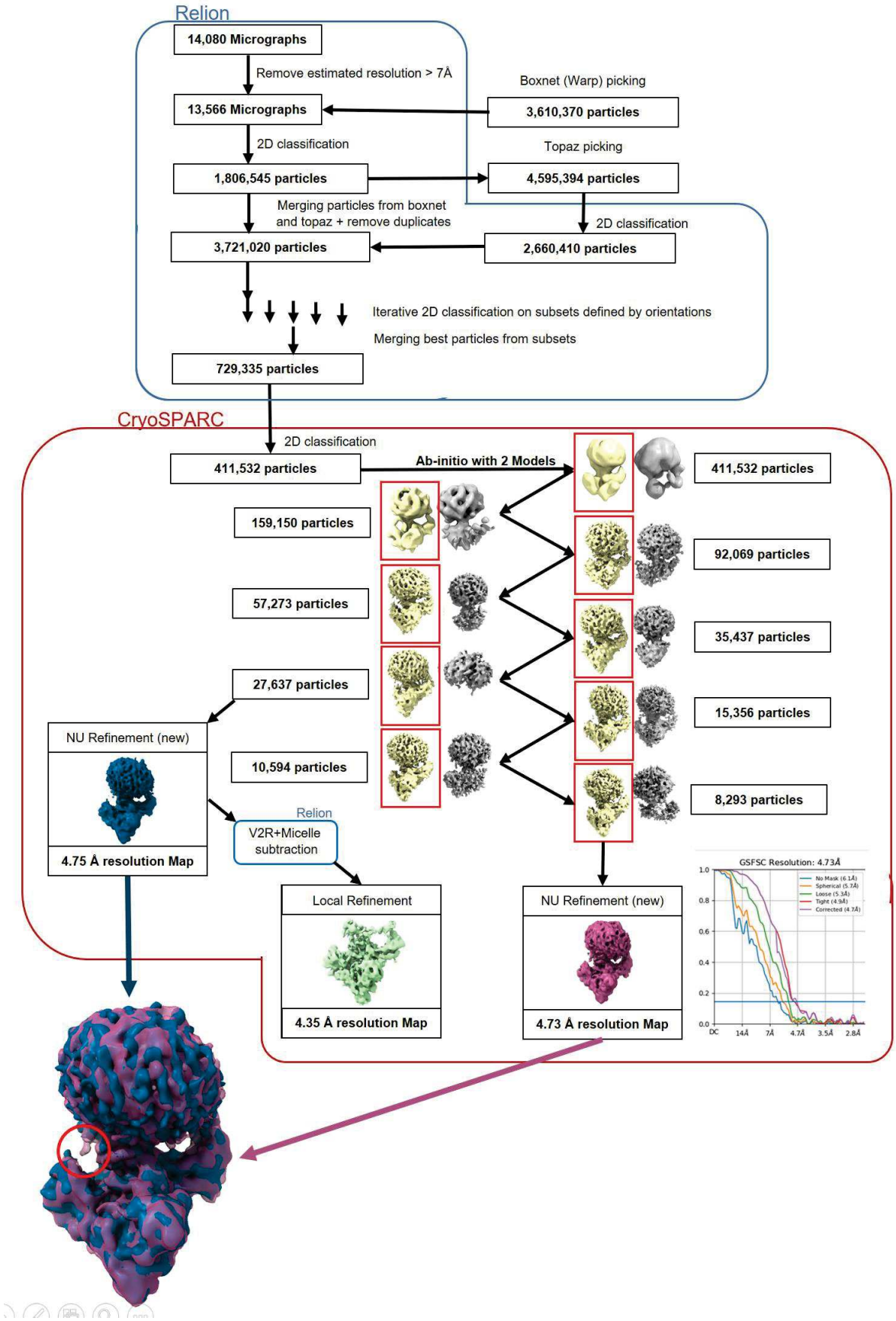

Figure 5-4 Flowchart of the V2R-Arr single particle analysis

5.6 The overall architecture of the ternary complex

As previously reported (Shukla et al. 2015; Cahill et al. 2017), β-arrestins can bind to GPCRs in multiple conformational states, including a core engagement state, and a tail-engagement state whose interaction with arrestin is exclusively mediated by the receptor C-terminal tail (Nguyen et al. 2019). Furthermore, even within the core conformation, there is a strong heterogeneity in terms of GPCR βarr binding with significant differences located in the finger loop which engages the GPCRs. There are mainly two conformational tendencies reported so far. One which is seen in rhodopsin-Arr1complex (Y. Kang et al. 2015) and also reported for the M2R-βarr1 and the β_1AR-βarr1 complexes (Staus et al. 2020a; Y. Lee, Warne, Nehmé, et al. 2020) (Figure 5-5 C) and one with a rotation of approximatively 80° of βarr1 parallel to the membrane plane in comparison to Arr1 in rhodopsin-Arr1 complex (Figure 5-5 C). This is the case for βarr1 in NTSR1-βarr1 complexes (Yin, Li, Jin, Yin, de Waal, et al. 2019; W. Huang et al. 2020) (Figure 5-5 C).

The structure of AVP-V2R bound to βarr1 reveals an overall assembly with a different arrestin orientation compared to what was precedently reported. It corresponds to an intermediate arrestin position relative to that in the β_1AR-βarr1 and NTSR1-βarr1 complexes (Figure 5-5 C). The AVP-V2R-βarr1-ScFv30 also displays a strong tilt in the membrane plane which is comparable to the one reported for the NTSIR-βarr1 complex (W. Huang et al. 2020) (Figure 5-5 B). In this configuration, the ICL1 is at the proximity of the middle loop of βarr1, and ICL2-3 of V2R seem to interact with the N-lobe of the βarr1.

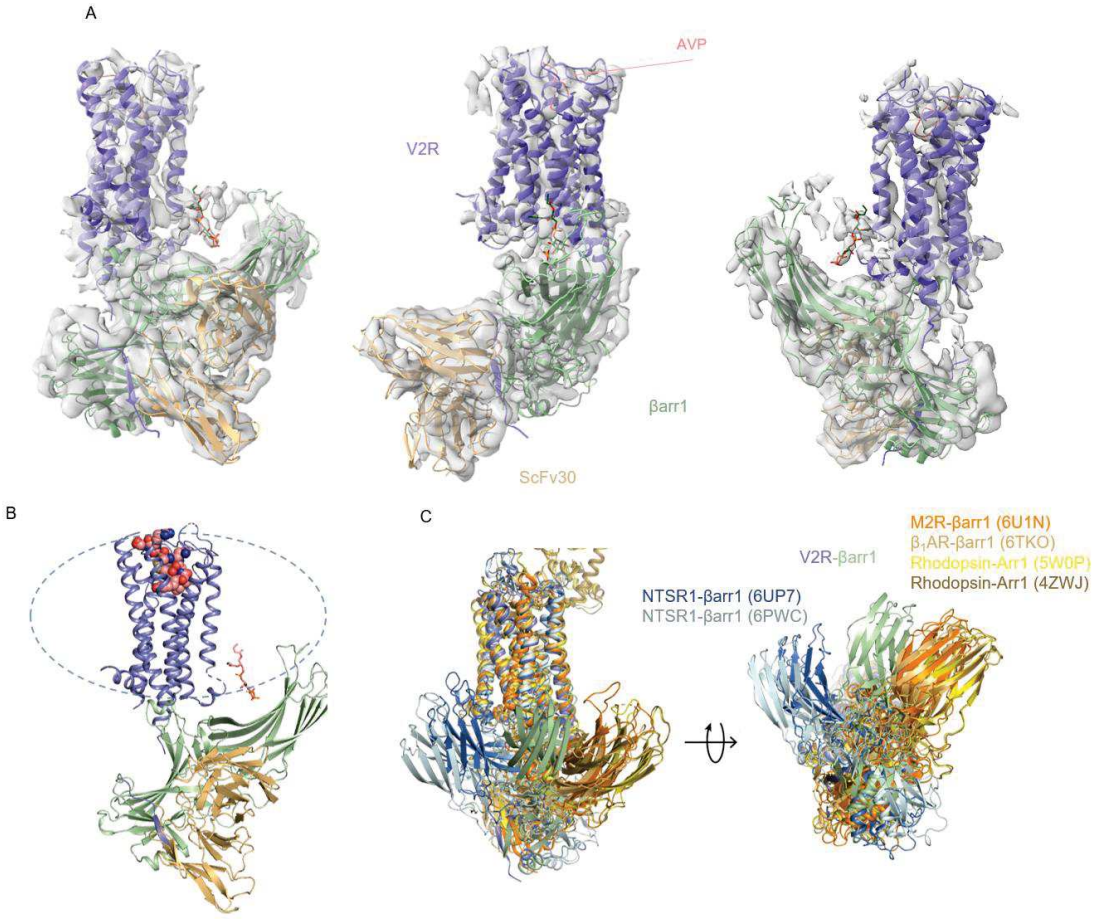

Figure 5-5 The AVP-V2R-βarr1-ScFv30 cryoEM structure
A) AVP-V2R-βarr1-ScFv30 model fitted in the cryo-EM density map. B) AVP-V2R-βarr1-ScFv30 model with a schematic representation of the detergent micelle: the βarr1 displays a strong tilt toward the micelle. C) Superposition of V2R with rhodopsin (5W0P; 4ZWJ) M2R (6U1N), β1AR (6TKO) and NTSR1 (6UP7; 6PWC) in the corresponding complex structures. The βarr1 displays an atypical orientation compared to the other GPCR-arrestin complex structures reported so far.

5.7 AVP binding and V2R activation, comparison with the other V2R active states

At the secondary structure scale, the V2R displays an active conformation similar to the one described for the V2R-Gs complexes (PDB entries: 7BB7, 7BB6, 7KH0). Because of the limited resolution, the active conformation of V2R (7KH0) was fitted as a rigid body into the density map. The model fits nicely (Figure 5-6B), the TMs adopt the same orientation with a similar TM6 outward displacement and TM7 inward motion when compared to the inactive OTR structure (Figure 5-6B). The ICL2 loop was manually adjusted in Coot since the map displays a clear density contacting the N-lobe of βarr1, which was not properly fitted using the receptor (7KH0) model (Figure 5-7B). The hormone AVP adopts the same overall position in

the binding pocket of the V2R as in the AVP-V2R-Gs complexes (PDB entries: 7BB7, 7BB6, 7KH0) (Figure 5-6A). However, the medium resolution is not sufficient to distinguish differences in AVP contacts and orientation between the different AVP-bound V2R-Gs complexes.

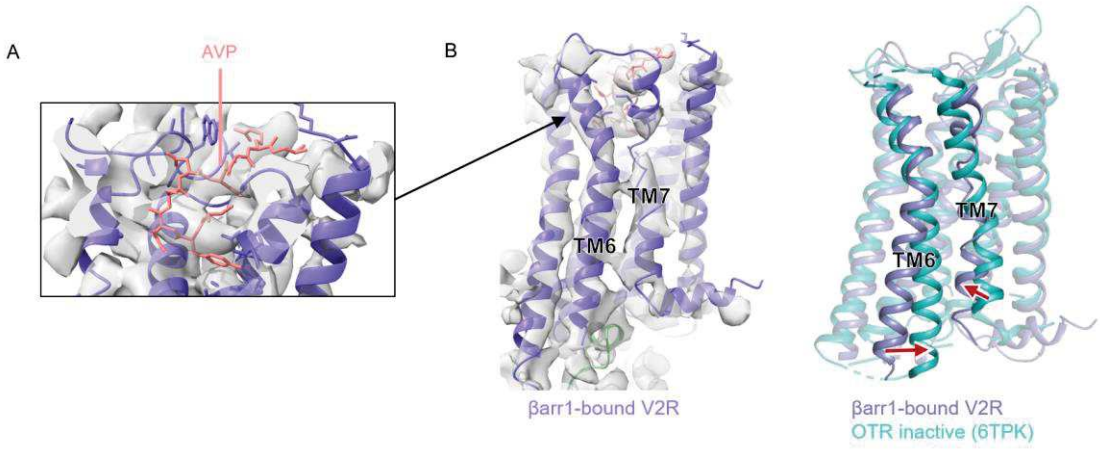

Figure 5-6 AVP-binding site of the V2R and V2R active conformation
A) Cryo-EM density and model for AVP in the V2R seven-transmembrane bundle, the overall position and size are similar to what was observed for the AVP-V2R-Gs protein complexes. B) Cryo-EM density map and model of V2R. Compared with the inactive OTR, V2R displays the hallmarks of activation such as TM6 outward and TM7 inward motions, as precedently reported.

5.8 V2R-βarr1 Interface

The EM map allowed clear determination of the position and orientation of V2R, βarr1, and ScFv30. The βarr1 engages the receptor with an atypical orientation. Indeed, with respect to NTSR1-βarr1 complexes (Yin, Li, Jin, Yin, de Waal, et al. 2019; W. Huang et al. 2020), the βarr1 coupled to V2R displays a rotation of about 50° parallel to the membrane plane (Figure 5-7 A) and a strong tilt, toward the membrane plane comparable to that one described for the NTSR1-βarr1(Figure 5-7 B) (W. Huang et al. 2020). This strong tilt allows for the interaction of the hydrophobic C-edge loops of the βarr1 with the detergent micelle (Figure 5-7 B). In this configuration, the finger loop of βarr1 located between D67 and T74 appears to have a similar conformation to that one described in the NTSR1-βarr1 complex (W. Huang et al. 2020), contacting the TM4 and the TM6 of V2R. βarr1 is near or in contact with the three V2R intracellular loops ICLs1-3. The middle loop is in the vicinity of the V2R ICL1 (Figure 5-7 C) but the density of the EM map is not sufficient to unambiguously fit the loop. Interestingly, both the ICL2 and ICL3 make direct contacts with the N-lobe of βarr1 (Figure 5-7 D).

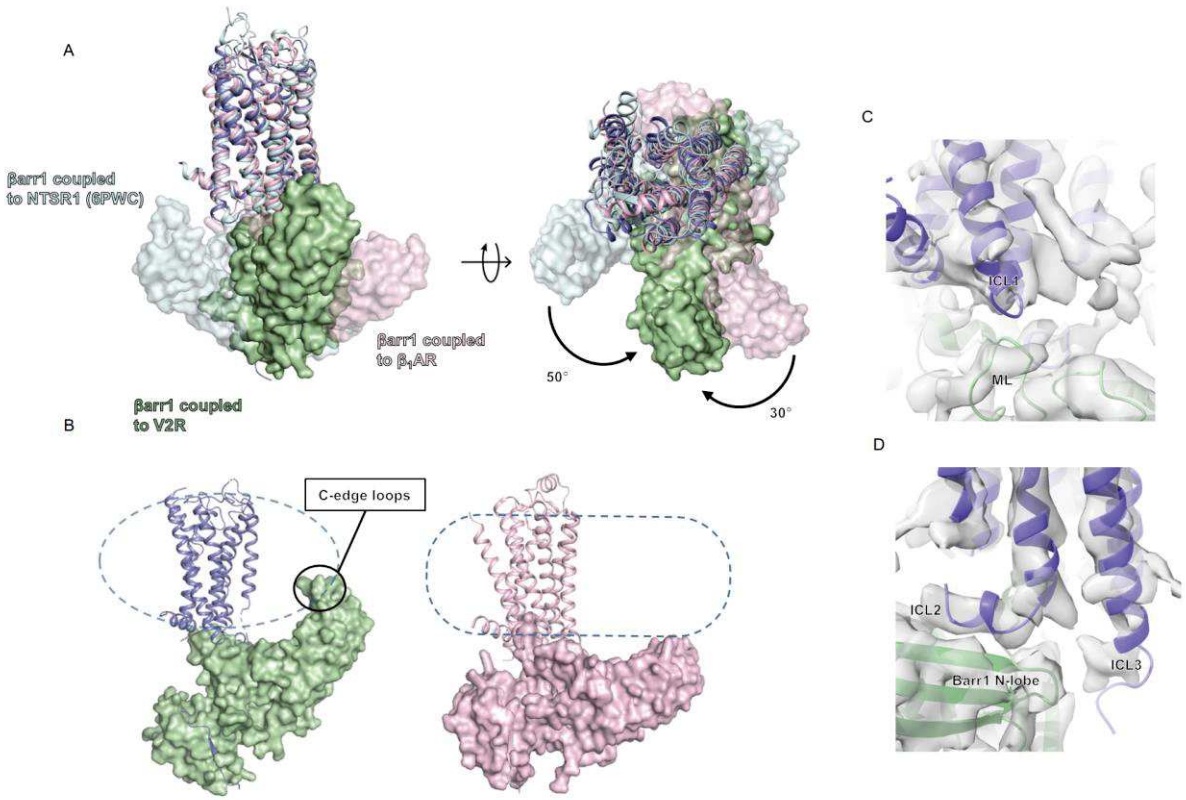

Figure 5-7 V2R-βarr1 Interface
A) Superposition of V2R with β_1AR (6TKO) and NTSR1 (6PWC), The βarr1 displays a rotation of 50° compared to the βarr1 in the NTSR1-βarr1 and a 30° rotation compared to the βarr1 in the β_1AR-βarr1. B) Comparison between the β_1AR-βarr1 and V2R-βarr1 tilt with schematic representation of the micelle and nanodisc used respectively for the purification. C) Snapshot of map versus model for ICL1 and βarr1middle loop proximity. D) Snapshot of map versus model for ICL2-3 and the βarr1 N-lobe contact.

5.8.1 The V2R C-tail–βarr1 interface: focus on phosphorylated residues

To gain further insight into which serine and threonine residues of the V2R are phosphorylated upon AVP receptor stimulation or not, a liquid chromatography-tandem mass spectrometry (LC-MS/MS) was performed (IGF Functional Proteomics Platform (https://www.fpp.cnrs.fr/en)) either on the unstimulated V2R sample, on the AVP-stimulated V2R sample (30 minutes before Sf9 cells harvesting), or on the sample prepared from cells coexpressing V2R and GRK2. Indeed, the GRK2 kinase was precedently used to phosphorylate GPCR C-terminal domain with success (Nguyen et al. 2019). The results revealed that there are no significant differences between the three conditions. In addition, they also show that three residues in the ICL3 are phosphorylated, namely S241, T253, S255. In the C-terminal domain, 6 residues are fully phosphorylated (T347, S350, S357, T359, S362, S364) and two residues (T360 and T363) are partially phosphorylated (Figure 5-8 B). The three terminal residues

(T369, S370, S371) might also be phosphorylated but results are not significant because of their location in the sequence.

The V2R C-terminal tail backbone and 6 potentially phosphorylated residues can be unambiguously fitted in the AVP-V2R-βarr1-ScFv30 density map (map obtained from the local refinement (Figure 5-4)) (Figure 5-8 A). The V2R C-terminal domain contacts the βarr1 N-domain similarly to what was described for M2R-βarr1–Fab30 and βarr1–Fab30–V2Rpp complexes (Shukla et al. 2013; Staus et al. 2020a) (Figure 5-9 B). The phosphorylated serines and threonines are involved in binding to the positively charged residues on the surface of the arrestin N-domain, namely R7, K10, K11, R25, K107 (Figure 5-9 A). The position of the C-terminal V2R-6P segment in the cryo-EM structure of V2R-βarr1 is also almost identical to its position in the structure of the β_1AR-βarr1 (Y. Lee, Warne, Nehmé, et al. 2020) complex with the exception of the T359 which does not make contact with the βarr1 since it contacts the tip of the lariat loop in the β_1AR-βarr1 (Figure 5-9 B).- This similarity is consistent with the fact that in the M2R-βarr1–Fab30 and β_1AR-βarr1-Fab30 studies, the V2R C-terminal sequence is used instead of the natural C-terminal domain of those receptors to stabilize the GPCR-βarr1 interaction. The strong V2R C-terminal domain phosphorylation observed in LC-MS/MS is in agreement with the cryo-EM data.

A

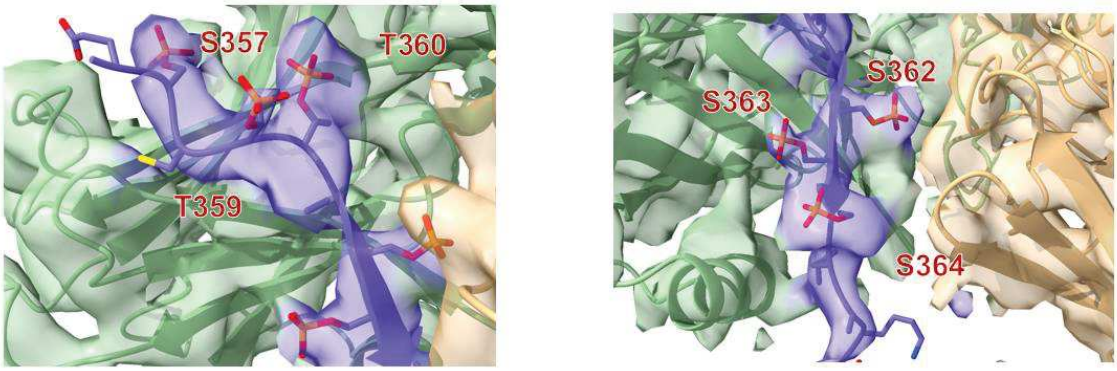

B

ICL3	S241	1
	T253	0,777545
	S255	0,999585
C-terminal domain	T347	1
	S350	1
	S357	0,999628
	T359	0,827258
	T360	0,668135
	S362	0,818253
	S363	0,445135
	S364	0,935601
Last portion of C-terminal domain	T369	0,274826
	S370	0,726508
	S371	0,55482

C

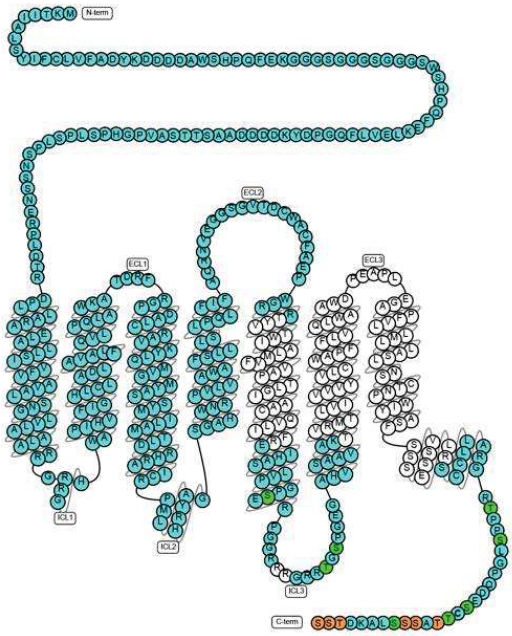

Figure 5-8 V2R C-terminal domain phosphorylation
Localization probabilities of potential sites of phosphorylation on the V2R ICL3 and C-terminal domain assessed by LC-MS/MS after a trypsin digestion.
A) Cryo-EM density from arrestin-focalized local refinement, for the six phosphorylated residues on the V2 C-terminal domain. B) Table of probabilities. C) V2R snake representation with phosphorylated positions. Residues phosphorylated with a probability higher than 75 % are represented in green and residues with a smaller probability of phosphorylation are represented in orange. The amino acids significantly probed by LC-MS/MS are represented in blue. Residues were phosphorylated in all conditions tested without significant difference: unstimulated V2R, AVP-stimulated V2R or AVP-stimulated V2R when coexpressed with GRK2.

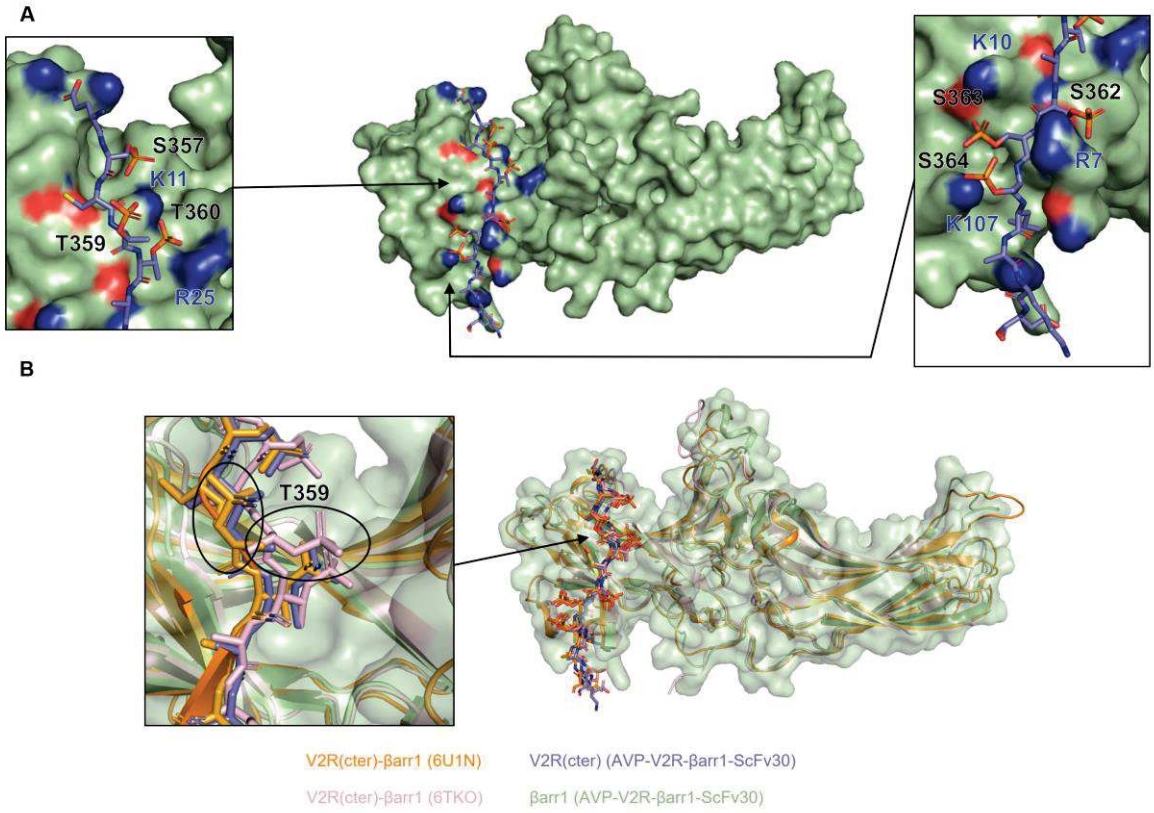

Figure 5-9 V2R C-terminal domain-βarr1 interface
A) The interface between a C-terminal domain of V2R and the positively charged N-domain residues of βarr1 is shown. B) Superposition of the βarr1 and C-terminal domain of the V2R in V2R-βarr1-ScFv30, M2R-βarr1-Fab30, β_1AR-βarr1-Fab30.

5.8.2 Involvement of diC8-PtdIns$_{(4,5)}$P$_2$ in the V2R-βarr1 interface

As precedently evoked, βarr1 is strongly tilted toward the membrane in the AVP-V2R-βarr1-ScFv30 complex. Taking into account this observation, AVP-V2R-βarr1-ScFv30 is similar to the NTSR1–βarr1 complex (W. Huang et al. 2020). Huang and coworkers hypothesized that this tilted orientation might be dependent on two factors, the relative curvature of the micelle as compared to a plane membrane and the presence of diC8-PtdIns$_{(4,5)}$P$_2$, bridging the membrane surface of TM1 and TM4 with the top of the C-lobe of arrestin. Based on this hypothesis, they confirmed the presence of diC8-PtdIns$_{(4,5)}$P$_2$ in the NTSR1–βarr1 complex by mass spectrometry and fluorescence microscopy experiments. In the AVP-V2R-βarr1-ScFv30 purification protocol, we added the diC8-PtdIns$_{(4,5)}$P$_2$ during complex formation since it was described to improve complex stability. Interestingly, the cryo-EM map of the V2R-βarr1 complex displays a density protruding out of the micelle located at the hypothetical diC8-PtdIns$_{(4,5)}$P$_2$ binding site (Figure 5-10 A, C). It is thus tempting to speculate that the diC8-PtdIns$_{(4,5)}$P$_2$ is indeed present in the AVP-V2R-βarr1-ScFv30 complex. According to this

hypothesis, the PtdIns$_{(4,5)}$P$_2$ might bridge the TM4 of the V2R with the βarr1 C-lobe. Nonetheless, the overall architecture of the receptor does not accommodate contacts between the diC8-PtdIns$_{(4,5)}$P$_2$ with its TM1 and TM2 regions. This might result in a weaker interaction than the one observed in the NTSR1 complex (W. Huang et al. 2020). Complementary experiments would be necessary to confirm the presence of diC8-PtdIns$_{(4,5)}$P$_2$ in the purified complex.

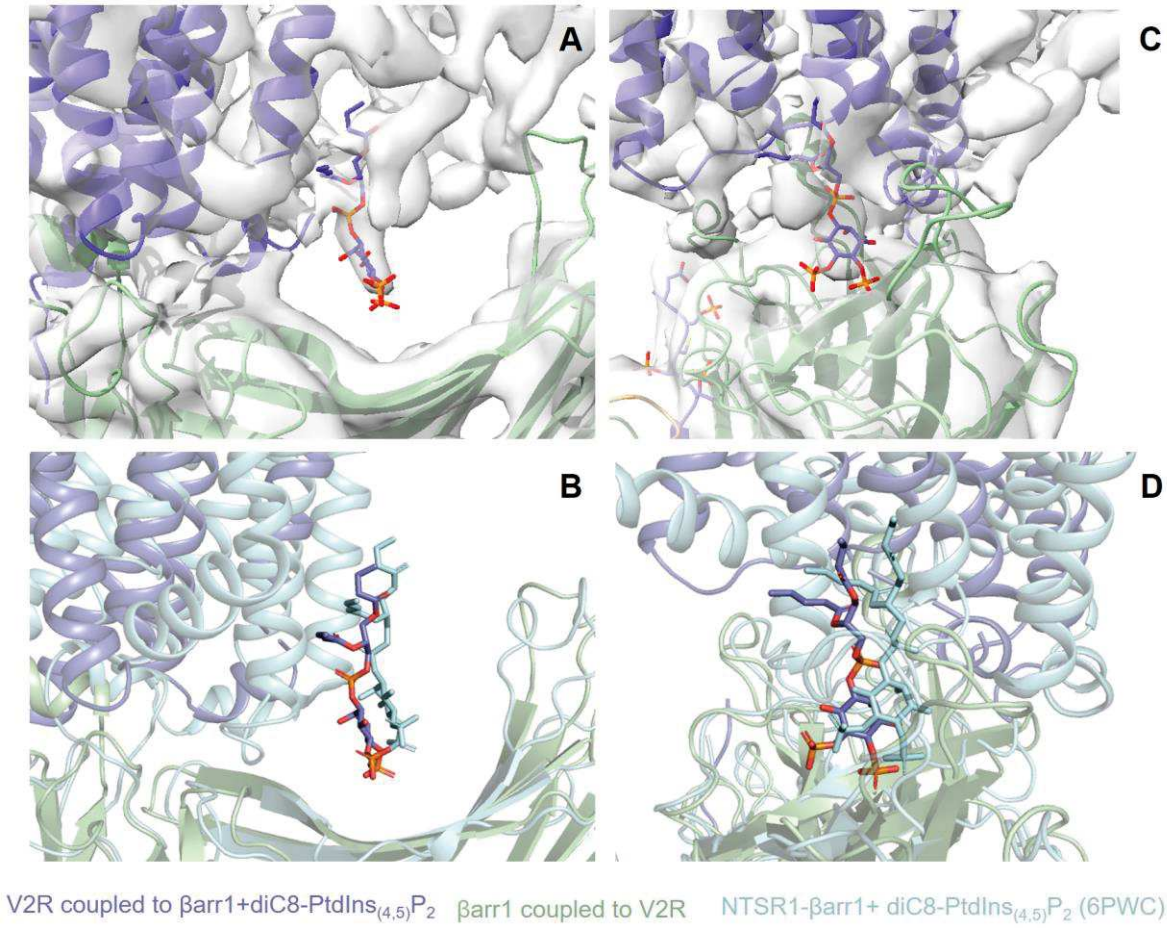

Figure 5-10 diC8-PtdIns$_{(4,5)}$P$_2$ interface
A, C) Snapshots of map versus model for the diC8-PtdIns$_{(4,5)}$P$_2$ which might be in contact with the V2R TM4 and the Top of the C-lobe of the βarr1. B, D) Superposition of the βarr1 of the V2R-βarr1-ScFv30, NTSR1-βarr1-Fab30. It seems that the diC8-PtdIns$_{(4,5)}$P$_2$ adopt the same overall position.

5.9 The βarr1 active conformation

The βarr1 bound to the V2R displays the hallmarks of arrestin activation (Scheerer and Sommer 2017). Compared to the inactive crystal structure of βarr1 (PDB:1G4M) (Han et al. 2001), we observed conformational changes comparable to the ones observed in the M2R-βarr1, the

β_1AR-βarr1, and NTSR1-βarr1 complexes (Y. Lee, Warne, Nehmé, et al. 2020; Staus et al. 2020a; W. Huang et al. 2020; Yin, Li, Jin, Yin, de Waal, et al. 2019). First, we observed a rotation of approximately 13° between the N and C lobes with respect to what is observed in inactive βarr1. This is smaller than the twist of approximately 22° that is observed in the structures of V2Rpp–βarr1 and Rho–Arr1, but comparable to the one observed in M2R-βarr1, β_1AR -βarr1, and NTSR1-βarr1 complexes. Also, the finger loop, gate loop, and lariat loops, which are essential in receptor coupling, form a "central crest" which is a signature of an active-state conformation (Figure 5-11).

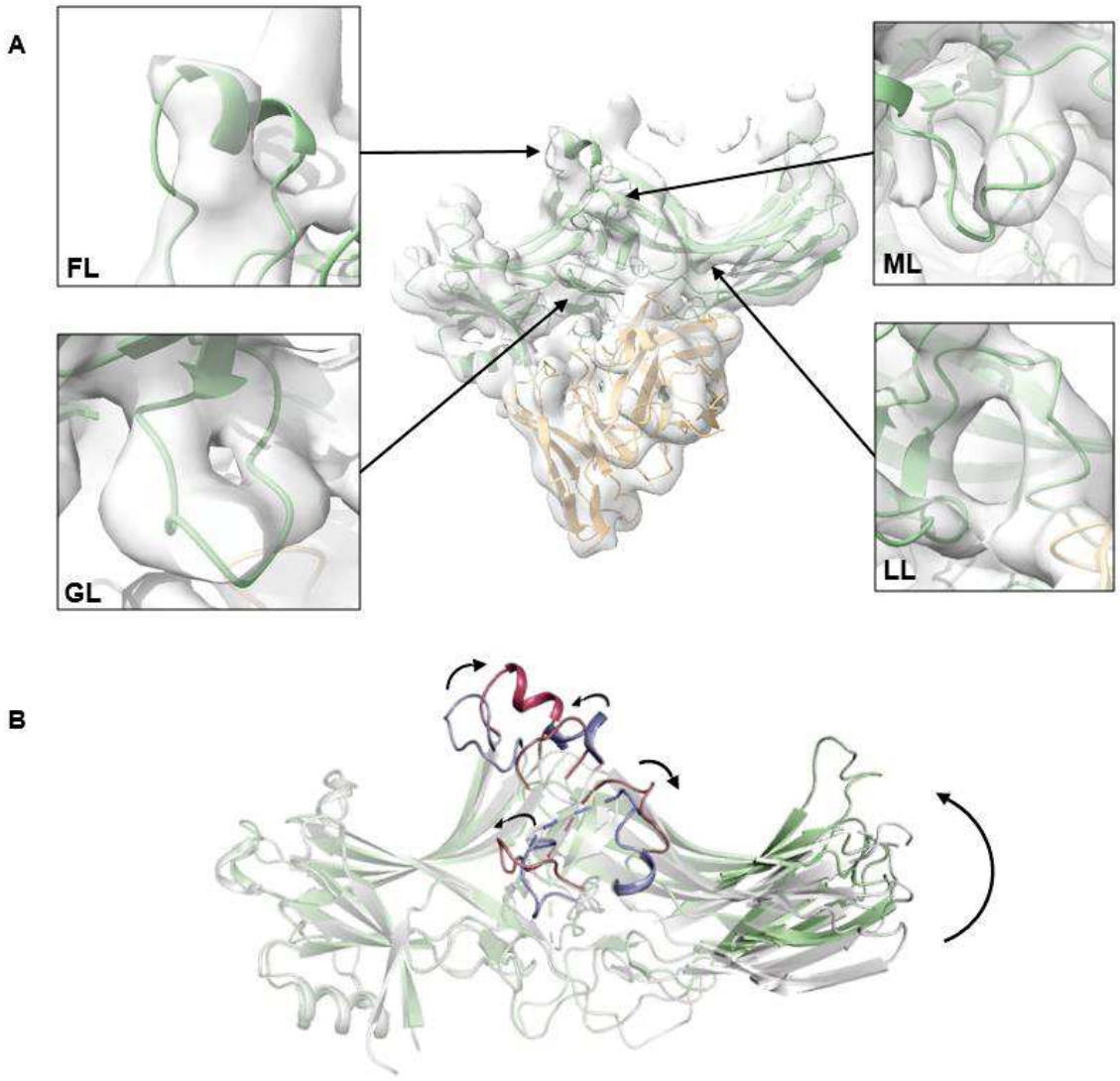

Figure 5-11 βarr1 in its active conformation
A) Snapshots of the AVP-V2R-βarr1-ScFv30 map versus model for the loops: finger loop (FL); middle loop(ML), lariat loop (LL), and gate loop(GL). B) Superposition of βarr1 in the inactive state (grey, PDB: 1G4M and in the receptor-bound active state (green, AVP-V2R-βarr1-ScFv30). Arrows indicate movements of C-lobe and of the different loops (in pink and purple).

5.10 Discussion

In this study, we determined the structure of the AVP-bound V2R in complex with the βarr1. It reveals an atypical overall architecture, as compared to that of GPCR-arrestin complexes already published. Indeed the V2R-βarr1 interface differs from GPCR-βarr1 complexes precedently described (Y. Lee, Warne, Nehmé, et al. 2020; Staus et al. 2020a; W. Huang et al. 2020; Yin, Li, Jin, Yin, de Waal, et al. 2019) and that of rhodopsin-Arr1 (Y. Kang et al. 2015; X. E. Zhou et al. 2017). In the AVP-V2R-βarr1 complex, the βarr1 orientation accommodates more contact with the receptor loops than what is usually observed. More precisely, the βarr1 middle loop seems to make a contact with the V2R ICL1 and the cryo-EM density strongly suggests contacts between the V2R ICL2 and ICL3 with the βarr1 N-lobe. Consistently with the overall architecture of the complex, the ICL3 forms a large interface with the N-domain of β-arrestin as already reported by disulfide cross-linking for the NTSR1-βarr1 complex (Yin, Li, Jin, Yin, de Waal, et al. 2019). In this context, the three phosphorylated residues identified in the ICL3 namely pS241, pT253, and pS255 might play a role in stabilizing arrestins binding. Unfortunately, the whole loop is not entirely visible in the density map certainly due to its size and flexibility. This will be investigated further through biochemistry and molecular dynamics analysis.

Interestingly, the β_1AR and M2R appear to interact with βarr1 through the ICLs 1 and 2 but there is no evidence of interaction through ICL3. At the opposite, NTSR1 overall architecture allows ICL3 and ICL1 to contact βarr1 but not ICL2. The V2R ICLs interaction with the βarr1 accommodated by its atypical conformation might be a key factor responsible for the strong and long-lasting interaction displayed by the V2R, potentially explaining its classification as a prototypic class B arrestin binder. Indeed GPCRs can be sorted into two classes in terms of arrestin binding: the class A where receptors form transient and rapidly dissociating complexes with arrestin, and resensitize rapidly, and the class B where receptors form long-lived complexes with arrestins that remain stable through their internalization via clathrin-coated pits and resensitize slowly (Lefkowitz, Rajagopal, and Whalen 2006).

The finger loop plays a pivotal role in the formation of a fully engaged arrestin–receptor complex (core conformation) since it represents the main interaction region between the GPCR TM bundle and the βarr1 (Shukla et al. 2015). Interestingly, in the V2R-bound βarr1 complex, the finger loop looks to adopt a conformation more similar to the one described for the NTSR1-βarr1 complex than to the one in the β1AR-βarr1 complex structure. Indeed, the finger loop of

the β1AR-βarr1 complex inserts into a narrow cleft at the intracellular surface and dives deeply into the TM-core. On the opposite, in the NTSR1–βarr1 complex, the finger loop adopts a helical structure which is also seen for rhodopsin-Arr1 complex (Szczepek et al. 2014). In the AVP-V2R-βarr1 complex, the finger loop occupies a similar position to that of the α5-helix of the Ras domain of the Gs protein in AVP-V2R-Gs complexes (PDB entries 7BB7 and 7BB6), but the helix adopts a different orientation. Thus, it is tempting to hypothesize that the conformation adopted by the βarr1 finger loop and its molecular contacts with GPCRs are also determinant factors responsible for classification of GPCRs into classes A and B in terms of arrestin binding.

Based on the density map of the AVP-V2R- βarr1 complex, the V2R also contacts the βarr1 through its C-terminal domain. Interestingly, using an LC-MS/MS approach dedicated to the identification of phosphorylated residues, we demonstrated that purified V2R extracted from Sf9 cells displays a strong constitutive phosphorylation pattern without any need for AVP stimulation. It was recently demonstrated that GPCR-βarr1 binding and activation depend on the spatial arrangement of phosphates (Latorraca et al. 2020). Phosphorylation of the V2R C-terminus T347 and S350 residues were proposed to have a functional role in the equilibrium between the core and the hanging conformations (He et al. 2021). Based on the LC-MS/MS approach, those two residues are strongly phosphorylated in V2R, but not seen in the density map of the complex. However, pS357, pT359, pT360, pS362, pS363, and pS364, which are visible in the density map, were also proposed to play a role in activation. The position of the V2R C-terminal segment in the cryo-EM structure of the V2R-βarr1 complex is almost identical to that of the peptide in the cryo-EM structure of the β1AR (fused to a V2R C-terminus containing 6 phosphorylated residues)–βarr1complex (Y. Lee, Warne, Nehmé, et al. 2020) and in the crystal structure of the V2Rpp(phosphorylated V2R peptide)–βarr1–Fab30 complex (Shukla et al. 2013). Unlike the finger loop which displays great plasticity in binding, the GPCR C-terminal domain interacts with the βarr1 N-lobe similarly among variable structures. This is partially explained by the use of GPCR chimeras containing a V2Rpp C-terminal domain in most of the studies. Nonetheless, in the NTSR1-βarr1 structures, the wild-type C-terminal domain is conserved and also adopts an overall equivalent conformation (Yin, Li, Jin, Yin, de Waal, et al. 2019; W. Huang et al. 2020). This interaction is critical for GPCR-arrestin binding (X. E. Zhou et al. 2017). It has also been demonstrated that each single phosphorylation depletion directly alters the affinity of V2R phosphorylated peptides with βarrestin-1, and the stability of the complexes after their formation (He et al. 2021).

In the AVP-V2R-βarr1-ScFv30, the βarr1 is strongly tilted towards the membrane similarly to to what has been observed in the NTSR1-βarr1 complex (W. Huang et al. 2020). This is probably because of the micelle curvature and the presence of diC8-$PtdIns_{(4,5)}P_2$. Although even if the density map resolution of the V2R-βarr1 complex is limited, we observed that diC8-$PtdIns_{(4,5)}P_2$ contact arrestin through its $PtdIns_{(4,5)}P_2$ high-affinity binding site located on the top of the C-lobe (W. Huang et al. 2020) and the V2R through interactions with the TM4. This might strengthen the complex interaction and stability (D. S. Kang et al. 2009).

$PtdIns_{(4,5)}P_2$ play a pivotal rôle in membrane protein internalization (Antonescu et al. 2011). Indeed, it regulates clathrin coated vesicles initiation, stabilization, and size. It was also demonstrated to regulate cargo loading during clathrin-coated pits initiation and might play a rôle in arrestin-bound GPCR trafficking and internalization. On this basis, it is of interest to probe more extensively how important it is for GPCR-mediated arrestin recruitment since the first structural data seems to suggest that it is not only a major component of endocytosis but also involved in downstream GPCR-arrestin binding.

6 Conclusions and perspectives

6.1 General conclusion

This thesis consists of two main results dedicated to better understand the molecular mechanisms which govern AVP V2 receptor functions.

6.1.1 Characterization of AVP-V2R-Gs-Nb35 protein complex

In the first part, the study of the structures of the active V2R coupled to the Gs protein (Bous et al. 2021), highlighted interesting structural features. In the frame of this project, two high-resolution structures of AVP-bound active V2R in complex with a miniG_s-$G_i\alpha$ chimera were also published (L. Wang et al. 2021; F. Zhou et al. 2021). V2R actives structures coupled to Gs and miniG_s-$G_i\alpha$ chimera provide valuable insights on AVP-V2R interactions and confirm what was precedently proposed by a combination of site-directed mutagenesis, molecular modeling, and photolabelling with ligand structure-activity relationships. Consistently with its amphipathic nature, AVP interacts with two chemically distinct interfaces in a 15-Å-deep binding pocket to form both polar and hydrophobic contacts. Since OTR is a close phylogenetic GPCR of V2R with a 47% sequence identity in the 7TM domains it is interesting to compare its inactive conformation recently released (Waltenspühl et al. 2020). As proposed precedently, the cyclic peptide and nonpeptidic antagonist share a common orthosteric binding site and partially overlap (Mouillac et al. 1995; Hibert, Hoflack, and Trumpp-Kallmeyer 1999). As expected, the V2R in complex with both Gs and miniG_s-$G_i\alpha$ chimera display activation hallmarks such as TM6 outward movement, TM7 inward movement, and an active conformation of the ionic lock, as compared to the inactive OTR.

Multiple missense mutations of the V2R are responsible for two rare genetic diseases: 1/ the cNDI associated with loss-of-function mutations leading people suffering from this pathology to be unable to concentrate their urine, and 2/ the NSIAD linked to constitutive active mutations and characterized by water loading and hyponatremia. Our structural input is very useful to interpret on a rational basis the links between these mutations and their pharmacological/clinical consequences. For instance, we propose an hypothesis to explain why mutants of the amino-acid residues arginine 137 into a leucine or cysteine (R137L or R137C), and isoleucine 130 into an asparagine (I137N), give rise to constitutive activity responsible for NSIAD. Hypotheses are proposed to explain structural consequences of mutations V88M (valine mutated into

methionine) or M272R (methionine mutated into arginine) that are responsible for V2R loss-of-function. In the same line, the mutant R137H displays constitutive internalization responsible for a cDNI phenotype. Nonetheless, according to the structures, it might still be able to maintain the ionic lock. Also, A patient bearing the V2R H137$^{3.50}$ mutation was shown to increase his urine osmolality after short-term therapeutic treatment with the V1a antagonist SR49059. Based on these data, we hypothesized that treatment of the patient with the pharmacological chaperone probably allows to stabilize the R137H mutant at the plasma membrane where it is displaced by endogenous circulating AVP hormone, eliciting an antidiuretic response. In the future, it would be interesting to extend our hypotheses established for certain mutants to a whole wider range of mutations (Figure 6-1).

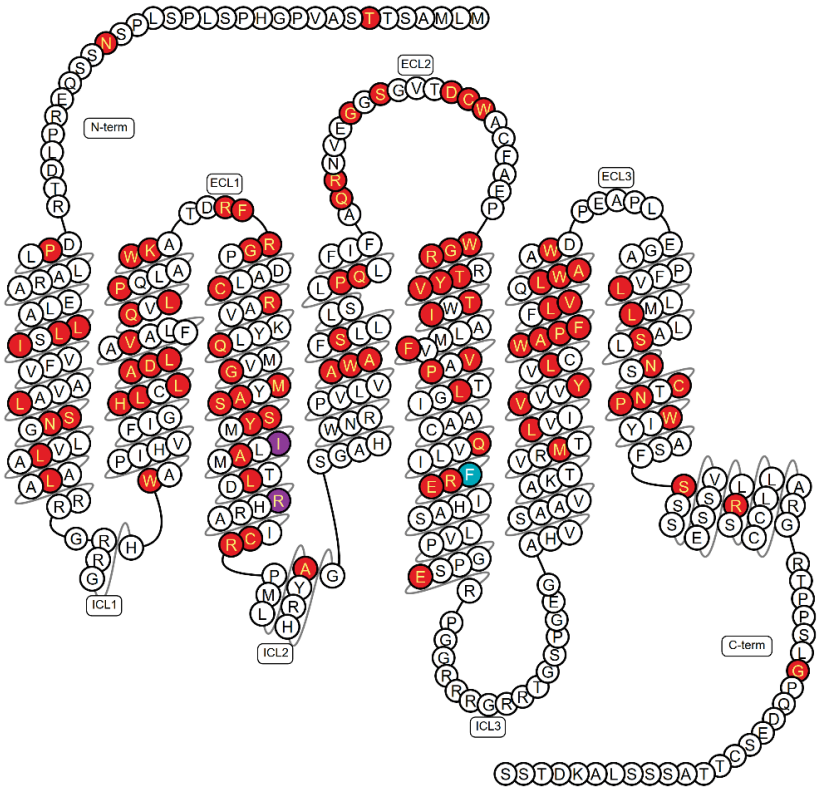

Figure 6-1 V2R snake plot highlighting mutants associated to cDNI and NSIAD
Red: mutated residues associated with a V2R loss of function. Blue: mutated residues associated with a V2R gain of function. Purple: Mutated residue associated with either a loss or a gain of function

Interestingly, V2R coupling to Gs and miniG_s-$G_i\alpha$ chimera is significantly different, with a strong dynamic, and a tighter interaction between the receptor and the Gs protein trimer in the AVP-V2R-Gs complex, and a less flexible complex and shallower Gs interaction with the AVP-

V2R-miniG_s-$G_i\alpha$ complexes. MiniG_s-$G_i\alpha$ allows reaching a significantly higher resolution, necessary to assign amino-acid side chain positions without ambiguity. Nonetheless, the AVP-V2R-Gs complex represents a more physiological system. This illustrates the need for multiple complementary studies which, combined together, depict a more realistic view of the system. The high-resolution structures will also be useful to accurately interpret the consequences of natural mutations from a structural point of view.

6.1.2 Characterization of AVP-V2R-βarr1-ScFv30 protein complex

In the second part, we describe the active structure of the V2R coupled to the βarrestin1, for which we were able to obtain data with a medium range resolution, limiting the interpretation to the secondary structure level. The vasopressin V2 receptor displays active features, similar to those observed in the G protein-coupled V2R structures with an overall similar position of AVP in the binding pocket. Hallmarks of ClassA GPCR activation are well characterized, such as a large TM6 outward movement, a TM7 inward movement, or a broken ionic lock.

Compared to the precedently published structures of GPCR-arrestin complexes, the overall structure of βarr1-coupled to V2R is more similar to that of the β_1AR-βarr1, the M2R-βarr1 (Staus et al. 2020a; Y. Lee, Warne, Nehmé, et al. 2020), and the rhodopsin-Arr1 (X. E. Zhou et al. 2017; Y. Kang et al. 2015) than to the structure of the NTSR1-βarr1 complex (Yin, Li, Jin, Yin, de Waal, et al. 2019; W. Huang et al. 2020). Nonetheless, it displays significant differences with all the structures precedently cited. For instance, the orientation of βarr1 in the V2R complex compared to that of βarr1 coupled to β_1AR, differs by approximately 30° perpendicularly to the membrane plane, and by a 10° rotation towards the membrane.

The βarr1 contains the conformational hallmarks of arrestin activation such as a rotation of the C-lobe relative to the N-lobe of around 13° and an active conformation of the gate loop, lariat loop, and middle loop. The top finger loop is not clearly defined in the density but the base of the loop looks to adopt a similar conformation to the one bound to NTSR1. Interestingly, we can see a clear density located in the PIP2 high-affinity binding site of the βarr1 C-lobe which might be occupied by the PIP2 analog used in our study to stabilize the complex. In the biological context, PIP2 plays a central role in clathrin-coated vesicles (CCV) formation and might be a key component in the regulation of GPCR-Arr complexes addressing to CCVs and in their internalization. The AVP-V2R-βarr1-ScFv30 highlights the plasticity and diversity of interactions notably at the receptor/arrestin interface.

Despite these new structures, our comprehension of V2R molecular mechanisms remains incomplete. The next paragraphs open perspectives of interest to acquire a better understanding of this major signaling system.

6.1.3 Optimization of V2R-β arrestin coupling

Our new AVP-V2R-βarr1 structure gives valuable information at the secondary structural scale. It is notably interesting to compare it with other GPCR-βarr1 structures since there is great variability between the few structures already investigated (Yin, Li, Jin, Yin, Waal, et al. 2019; Staus et al. 2020a; Y. Lee, Warne, Nehmé, et al. 2020; W. Huang et al. 2020). Nonetheless, because of the limited resolution, these data are not suited for analysis at the atomic scale, necessary to determine precise insights in AVP binding, V2R-βarr1 interface, or βarr1 activation. From this perspective, significant efforts need to be done to remove flexibility by optimizing protein constructs and biochemistry. In this context, we will currently explore promising optimization.

6.1.3.1 Nanobody32 stabilization of the AVP-V2R- βArr1 complex

As precedently described, GPCR-βarr complexes are highly dynamic systems (W. Huang et al. 2020; Staus et al. 2020a). In *in-vitro* conditions using detergent-embedded GPCRs, two main binding modes between GPCRs and βarrestins are observed (Shukla et al. 2015). The "hanging form" where the βarr interacts exclusively with the GPCR C-terminal extremity and the "core form" involving an interaction between the βarr finger loop with the GPCR cytoplasmic domains (Shukla et al. 2015). Since heterogeneity is a critical limitation for high-resolution cryo-EM, we will use the Nanobody32 (Nb32) shown to bind to and stabilize active βarr1 that predominantly complexes with chimeric β2-V2R in the core conformation (Cahill et al. 2017), to limit the heterogeneity of the AVP-V2R- βarr1 complex. It will be used in combination with the ScFv30 since both conformation-stabilizing antibody fragments target distinct binding sites in βarrestins (Cahill et al. 2017).

6.1.3.2 V2R-embedded in nanodiscs

Phospholipids have an important role in the binding of arrestins to GPCRs (Sommer, Smith, and Farrens 2006; Bayburt et al. 2011). The C edge loop interface with the phospholipid membrane is in agreement with the strong lipid dependence of arrestin–rhodopsin complex formation (Ostermaier et al. 2014). This was confirmed by molecular dynamics simulations and site-directed fluorescence spectroscopy on the 344-loop and 197-loop (Peterhans et al. 2016; Ostermaier et al. 2014; Lally et al. 2017; Sommer, Hofmann, and Heck 2012).

Recent cryo-EM structures of GPCR-βarr complexes (Staus et al. 2020b; Y. Lee, Warne, Nehmé, et al. 2020; W. Huang et al. 2020) confirm the role of lipid bilayer for GPCR-βarr binding. Indeed, M2R-βarr1 and β_1AR-βarr1 structures were investigated in nanodiscs and both structures display strong contacts between the C-edge domain and the lipids in the nanodisc. The micelle relative curvature in comparison with plane membrane or nanodisc leads to the loss of this interaction with a 'rocking' βarr relative to the receptor or to a stronger arrestin tilt to accommodate the interaction. Consequently, the AVP-V2R-βarr1 in nanodisc condition might be less dynamic with predominantly core conformation and a more biologically relevant conformation than the one in micelle condition. (Figure 6-2).

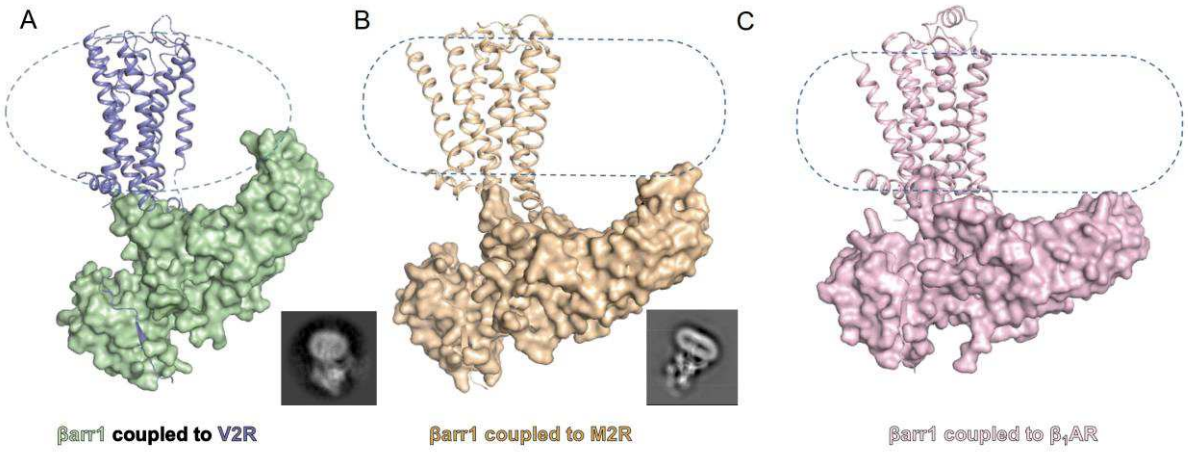

Figure 6-2 βarr1 in variable GPCRs-βarr1 complexes
Tilt of βarr1 in variable GPCRs-βarr1 complexes, either purified in nanodiscs or detergent micelles. A)V2R-βarr1 model with a schematic representation of the micelle and a 2D class average micrograph. B) M2R-βarr1 model with a schematic representation of the nanodisc and a 2D class average micrograph. C) β1AR-βarr1 model with a schematic representation of the nanodisc. βarr1 needs to display a stronger tilt to accommodate interaction with the micelle than with the nanodiscs lipids.

6.1.3.3 Conclusion

These two optimization strategies should be critical to reduce sample flexibility and favor the core conformation. If this is not sufficient to reach a high resolution, other options such as thermostabilizing mutations of V2R or βarr1 (Y. Lee, Warne, Nehmé, et al. 2020), crosslinking between complex subcomponents (W. Huang et al. 2020) will be investigated further.

6.2 Determination of the V2R inactive conformation: the mambaquaretin1 challenge

A clear understanding of the conformational changes responsible for V2R transition requires to compare structures in both active and inactive states. Unfortunately, despite extended efforts, the V2R inactive state has been reluctant to crystallogenesis up to now. Moreover, because of the limit of size and the micelle surrounding the receptor, it is quite difficult to investigate the inactive structure of V2R by cryo-EM when bound to a small non-peptidic antagonist such as tolvaptan. The green mamba snake (Figure 6-3A) mambaquaretin toxin (MQ1) is a small peptide (6.56 kDa) belonging to the Kunitz peptide family recently described as a full antagonist of V2R (Figure 6-3 B, C). This rigid peptide fully antagonizes cAMP signal, arrestin recruitment, and MAP kinase phosphorylation associated to V2R activation with a nanomolar affinity (Figure 6-3 D-K) (Ciolek et al. 2017). It represents a promising perspective for cryo-EM V2R inactive state investigation as it protrudes out of the micelle allowing to align particles during single particle analysis processing. The small size of the MQ1-V2R is however hardly compatible with cryo-EM (53 kDa particle + MNG micelle). Nonetheless recently, the first structure of a GPCR in “apo” state was resolved despite the limitation in size (Josephs et al. 2021). In addition, just one structure of animal toxin in complex with GPCR (Maeda et al. 2020) has been solved so far, probably because the ligand-receptor interactions are not stable enough. In the case of MQ1-V2R, it will be essential to face two challenges, obtaining a stable V2R-MQ1 complex and artificially increasing its size.

To address these challenges, different strategies can be developed. One might either create a covalent bond between MQ1 and V2R, derivatize the MQ1, modify the V2R by introducing T4L of GFP fusion modules at different positions, add specific anti-V2 nanobodies (15 kDa each, supplied by Theranyx, Marseille) and perform in parallel LCP crystallography trials of the MQ1-V2 complex as the amount of V2R and MQ1 is no more a limitation.

Regarding the covalent bond to lock the MQ1-V2R complex, cysteine residues can be introduced in identified 15 MQ1 positions and 8 V2R positions (mainly in extracellular loops 2 and 3) and classical cross-reactions performed. If needed, bifunctional cross-linker reagents can also be used. Briefly, homo (like di(N-succinimidyl) glutarate or glutaraldehyde agents) or hetero (like bromoacetic acid N-hydroxysuccinimide ester or others) cross-linker reagents can be added to create stable bridges between the two partners. A photoreactive cross-linker such as benzoylphenylalanine may also be easily introduced in MQ1 during its chemical synthesis

and would display a high yield of crosslinking with methionines that could be incorporated in the V2R.

As precedently evoked, the small size of the MQ1-V2R particle is highly challenging in terms of cryo-EM micrograph acquisition and image processing. To circumvent these difficulties, the size of MQ1-V2R complex will be increased. V2R or the MQ1 can be modified by introducing T4L of GFP fusion modules or the thermostabilized apocytochrome b562RIL as a fusion partner at different positions such as the ICL3 or the C-terminal domain in the receptor and in the N-terminal region for the toxin (E. Chun et al. 2013).

In addition, LCP crystallography trials of the MQ1-V2R can be envisaged as the amount of V2R and MQ1 is not a limitation.

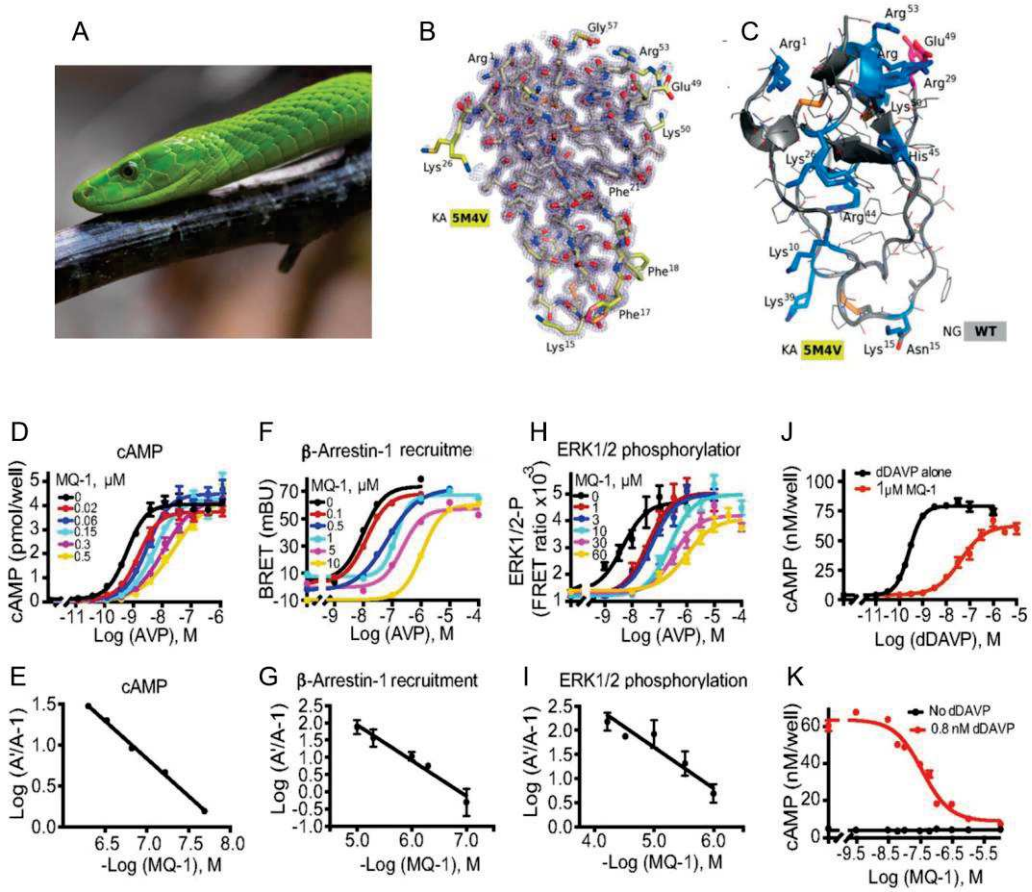

Figure 6-3 V2R antagonist activity and structure of mambaquaretin-1 (MQ-1)
A) Green mamba (https://www.stocklib.fr). B) X-ray structure of mambaquaretin-1 KA variant in stick representation colored according to B value (light blue to red). C) Cartoon representation of mambaquaretin-1 and the KA variant showing the preponderance of positively charged residues. V2R antagonist activity of mambaquaretin-1 (MQ1). (*D*, F, and H) Competitive inhibition of AVP-induced (D) cAMP production in stable CHO-hV2R cell line, (F) β-arrestin-1 recruitment by BRET-β-arrestin-1–YFP, and hV2R-Rluc tsA transfected cell line, and (H) MAP kinase phosphorylation on hV2R tsA transfected cell line. (E, G, and I) Corresponding Arunlakshana–Schild plots. (J) Antagonistic effect of mambaquaretin-1 on cAMP production in dDAVP-stimulated renal KC3AC1 cells. (K) Effect of increasing concentrations of mambaquaretin-1 on cAMP production in the absence or in the presence of 0.8 nM of dDAVP in renal KC3AC1 cell line. All panels are representative of at least three independent experiments and Schild representations are plotted as mean ± SEM. mBU, milliBRET unit. Adapted from (Ciolek et al. 2017)

6.3 Determination of the V2R active conformation in the presence of a Gs-biased agonist

GPCR ligands often display biased signaling. The few released structures of GPCRs coupled to biased agonists provide an interesting insight into structural differences dependent on the biased activation. For example, GLP1 receptor, coupled to the G protein-biased peptide exendin-P5 (Y. L. Liang et al. 2018b) displays key differences in the conformation of ECL3 and the top of TM1 of the receptor, as compared to the physiological ligand GLP-1-bound conformation. Also, a

structural investigation of the V2R active conformation induced by a biased agonist such as the MCF14 (Jean-Alphonse et al. 2009) which prefers the Gs activation pathway to the βarr1 pathway will be of great interest for the overall comprehension of V2R activation and future therapeutic applications. From that perspective, we took advantage of the precedently optimized protocol for the preparation of the AVP-V2R-Gs-Nb35 complex to purify an MCF14-V2R-Gs-Nb35 (Figure 6-4). In the preliminary purifications, the complex appeared to be unstable in comparison with the AVP-bound complex. So far we have failed to improve the proportion of complex during complex formation and to stabilize it (Figure 6-4 A). Nonetheless, we were able to purify a small quantity of complex (Figure 6-4 B; C). Regarding the quantity of sample loaded on the SDS-PAGE gel, the Gγ subunit is hardly visible. Also, the Nb35 seems to be missing, this assumption needs to be validated by western blot analysis in future purifications. A preliminary cryo-EM analysis (Figure 6-5) on this sample yielded a low-resolution density map (resolution=12Å). Interestingly, the map seems to indicate significant structural differences in comparison to the AVP-bound form in terms of relative position between the Gα and Gβγ subunits. Furthermore, the map doesn't display density corresponding to the Nb35 in agreement with the biochemistry characterization. This Gs protein trimer conformation might prevent the binding of the Nb35. This phenomenon fits well with the concept that GPCR complexes may have multiple active conformations with variable characteristics (Wei et al. 2003; Y. L. Liang et al. 2018b). This hypothesis based on preliminary results needs to be considered with caution and confirmed with complementary biochemical and structural analysis. A high-resolution structure of this complex will be of great interest for further understanding of V2R active states and biased agonism in general.

It will also be interesting to elucidate the structure of constitutively active mutants responsible for NSIAD I130N, R137L/C or F229V and to compare them. Indeed, unlike R137L/C which is constitutively internalized, I130N and F229V both share the characteristic property of the lack of basal β-arrestin2 binding. These two missense mutations can be considered as biased V2R conformations, as the G-protein-dependent pathway can be selectively activated (Erdélyi et al. 2015).

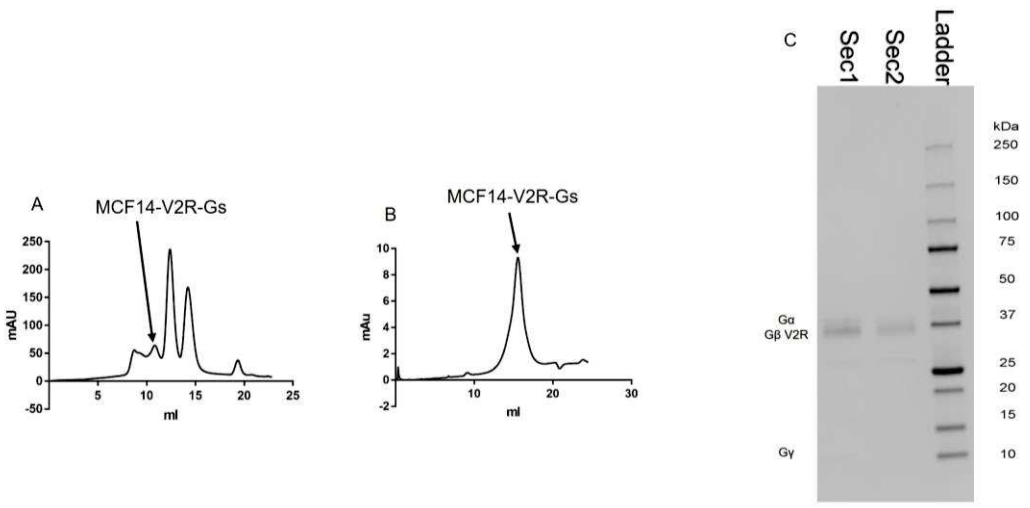

Figure 6-4 chromatograms and SDS-PAGE of the MCF14-V2R-Gs-Nb35 complex
A) Representative chromatogram of the MCF14-V2R-Gs-Nb35 complex using Superdex200 SEC, (first of the two succesive SEC). B) Superose6 SEC chromatogram show a monodisperse peak (second of the two succesive SEC). Fractions containing the sample were combined and concentrated for preparation of cryo-EM grids. C) SDS-PAGE of peak fraction from the Superose6 step. Coomassie blue staining of proteins confirmed that the complex is made of Gαs, V2R, Gβ1 and Gγ2 (MCF and Nb35 are not visible).

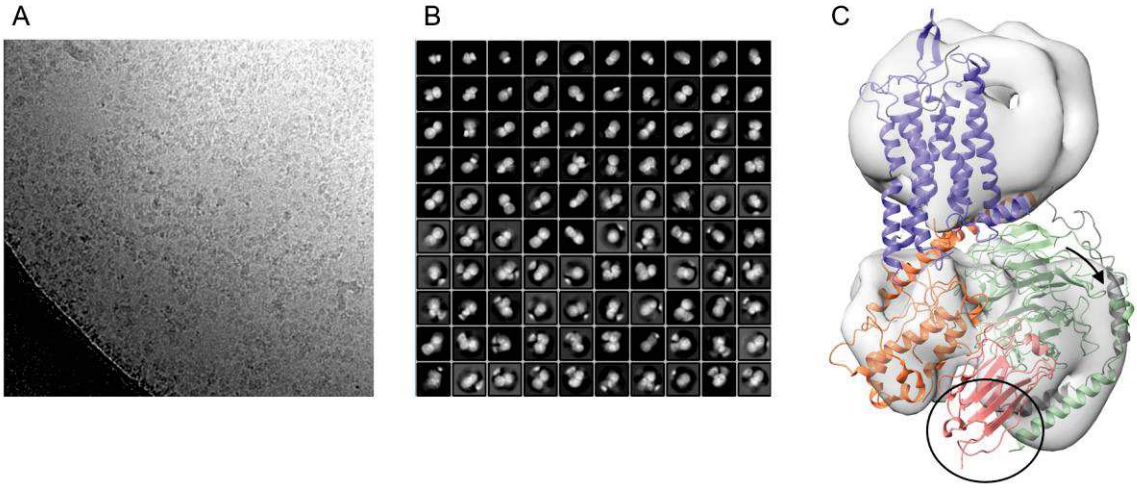

Figure 6-5 Cryo-EM preliminary analysis of the MCF14-V2R-Gs-Nb35 complex
A) Representative micrograph of the MCF14-V2R-Gs-Nb35 protein complex. B) Representative 2D class averages displaying low resolution features (micelle and Gs protein). C) Density map of the MCF14-V2R-Gs-Nb35 complex (contour level set to 0.0494) and fitting of the 3D model of the cryo-EM structure of AVP-V2R-Gs-Nb35 complex (L or T state) in this low resolution map. As shown, the Nb35 present in the AVP-V2R-Gs-Nb35 complex seems to be absent in the biased agonist-V2R-Gs complex (black circle). The arrow indicates that Gs protein is not tightly in interaction with V2R, as in the full agonist AVP complex.

To conclude, the solving of V2R structures in active and inactive conformations is a necessary step to complete our understanding of V2R activation mechanism, and thus will greatly favor

the drug design of therapeutic molecules. The search for molecules without adverse effects is also an important prospect, and in this sense structures with biased ligands should help to select more efficient, more selective molecules.

7 Bibliography

Aashish Manglik, Tae Hun Kim, Matthieu Masureel, Christian Altenbach, Zhongyu Yang, Daniel Hilger, . T, Michael Lerch, et al. 2016. “Structural Insights into the Dynamic Process of B2-Adrenergic Receptor Signaling.” *Physiology & Behavior* 176 (12): 139–48. https://doi.org/10.1016/j.cell.2015.04.043.Structural.

Abraham, Mark James, Teemu Murtola, Roland Schulz, Szilárd Páll, Jeremy C. Smith, Berk Hess, and Erik Lindah. 2015. “Gromacs: High Performance Molecular Simulations through Multi-Level Parallelism from Laptops to Supercomputers.” *SoftwareX* 1–2: 19–25. https://doi.org/10.1016/j.softx.2015.06.001.

Acher, Roger, and Jacqueline Chauvet. 1954. “LA STRUCTURE DE LA VASOPRESSINE DE BOEUF” 14.

Adrian, Marc, Jacques Dubochet, Jean Lepault, and Alasdair W. McDowall. 1984. “Cryo-Electron Microscopy of Viruses.” *Nature* 308 (5954): 32–36. https://doi.org/10.1038/308032a0.

Afonine, Pavel V., Marat Mustyakimov, Ralf W. Grosse-Kunstleve, Nigel W. Moriarty, Paul Langan, and Paul D. Adams. 2010. “Joint X-Ray and Neutron Refinement with Phenix.Refine.” *Acta Crystallographica Section D: Biological Crystallography* 66 (11): 1153–63. https://doi.org/10.1107/S0907444910026582.

Ala, Youssef, Denis Morin, Bernard Mouillac, Nancy Sabatier, Rosa Vargas, Nathalie Cotte, Michèle Déchaux, et al. 1998. “Functional Studies of Twelve Mutant V2 Vasopressin Receptors Related to Nephrogenic Diabetes Insipidus: Molecular Basis of a Mild Clinical Phenotype.” *Journal of the American Society of Nephrology* 9 (10): 1861–72. https://doi.org/10.1681/asn.v9101861.

Alexander, Stephen P.H., Arthur Christopoulos, Anthony P. Davenport, Eamonn Kelly, Alistair Mathie, John A. Peters, Emma L. Veale, et al. 2019. “THE CONCISE GUIDE TO PHARMACOLOGY 2019/20: G Protein-Coupled Receptors.” *British Journal of Pharmacology* 176 (S1): S21–141. https://doi.org/10.1111/bph.14748.

Alonso, Gérard, Evelyne Galibert, Véra Boulay, Anne Guillou, Alexandra Jean, Valérie Compan, and Gilles Guillon. 2009. “Sustained Elevated Levels of Circulating Vasopressin

Selectively Stimulate the Proliferation of Kidney Tubular Cells via the Activation of V2 Receptors." *Endocrinology* 150 (1): 239–50. https://doi.org/10.1210/en.2008-0068.

Alonso, Hernan, and Anna Roujeinikova. 2012. "Characterization and Two-Dimensional Crystallization of Membrane Component AlkB of the Medium-Chain Alkane Hydroxylase System from Pseudomonas Putida GPo1." *Applied and Environmental Microbiology* 78 (22): 7946–53. https://doi.org/10.1128/AEM.02053-12.

Antonescu, Costin N., François Aguet, Gaudenz Danuser, and Sandra L. Schmid. 2011. "Phosphatidylinositol-(4,5)-Bisphosphate Regulates Clathrin-Coated Pit Initiation, Stabilization, and Size." *Molecular Biology of the Cell* 22 (14): 2588–2600. https://doi.org/10.1091/mbc.E11-04-0362.

Arima, Hiroshi, Kunikazu Kondo, Takashi Murase, Hisashi Yokoi, Yasumasa Iwasaki, Hidehiko Saito, and Yutaka Oiso. 1998. "Regulation of Vasopressin Synthesis and Release by Area Postrema in Rats." *Endocrinology* 139 (4): 1481–86. https://doi.org/10.1210/endo.139.4.5873.

Assadi-Porter, Fariba, Marco Tonelli, Emeline Maillet, Hallenga Klaas, Benard Outhiriaradjou, Max Marianna, and Markley John. 2008. "Direct NMR Detection of the Binding of Functional Ligands to the Human Sweet Receptor, a Heterodimeric Family 3 GPCR." *J Am Chem Soc* 23 (1): 1–7. https://doi.org/10.1021/ja8016939.Direct.

Attwood, T. K., and J. B.C. Findlay. 1994. "Fingerprinting G-Protein-Coupled Receptors." *Protein Engineering, Design and Selection* 7 (2): 195–203. https://doi.org/10.1093/protein/7.2.195.

Audet, Martin, and Raymond C. Stevens. 2019. "Emerging Structural Biology of Lipid G Protein-Coupled Receptors." *Protein Science* 28 (2): 292–304. https://doi.org/10.1002/pro.3509.

Baldwin, Philip R., Yong Zi Tan, Edward T. Eng, William J. Rice, Alex J. Noble, Carl J. Negro, Michael A. Cianfrocco, Clinton S. Potter, and Bridget Carragher. 2018. "Big Data in CryoEM: Automated Collection, Processing and Accessibility of EM Data." *Current Opinion in Microbiology* 43 (Ccd): 1–8. https://doi.org/10.1016/j.mib.2017.10.005.

Ballesteros, Juan A, and Harel Weinstein. 1994. "Integrated Methods for the Construction of Three-Dimensional Models and Computational Probing of Structure-Function Relations in G Protein-Coupled Receptors." *Pharmacological Reviews* 46 (2): 121–36.

Balusek, Curtis, Hyea Hwang, Chun Hon Lau, Karl Lundquist, Anthony Hazel, Anna Pavlova, Diane L. Lynch, Patricia H. Reggio, Yi Wang, and James C. Gumbart. 2019. "Accelerating Membrane Simulations with Hydrogen Mass Repartitioning." *Journal of Chemical Theory and Computation* 15 (8): 4673–86. https://doi.org/10.1021/acs.jctc.9b00160.

Barak, Larry S., Robert H. Oakley, Stéphane A. Laporte, and Marc G. Caron. 2001. "Constitutive Arrestin-Mediated Desensitization of a Human Vasopressin Receptor Mutant Associated with Nephrogenic Diabetes Insipidus." *Proceedings of the National Academy of Sciences of the United States of America* 98 (1): 93–98. https://doi.org/10.1073/pnas.98.1.93.

Bartoschek, Stefan, Thomas Klabunde, Elisabeth Defossa, Viktoria Dietrich, Siegfried Stengelin, Christian Griesinger, Teresa Carlomagno, Ingo Focken, and K. Ulrich Wendt. 2010. "Drug Design for G-Protein-Coupled Receptors by a Ligand-Based NMR Method." *Angewandte Chemie - International Edition* 49 (8): 1426–29. https://doi.org/10.1002/anie.200905102.

Bayburt, Timothy H., Sergey A. Vishnivetskiy, Mark A. McLean, Takefumi Morizumi, Chih Chin Huang, John J.G. Tesmer, Oliver P. Ernst, Stephen G. Sligar, and Vsevolod V. Gurevich. 2011. "Monomeric Rhodopsin Is Sufficient for Normal Rhodopsin Kinase (GRK1) Phosphorylation and Arrestin-1 Binding." *Journal of Biological Chemistry* 286 (2): 1420–28. https://doi.org/10.1074/jbc.M110.151043.

Bazzacco, Paola, Emmanuelle Billon-Denis, K. Shivaji Sharma, Laurent J. Catoire, Sophie Mary, Christel Le Bon, Elodie Point, et al. 2012. "Nonionic Homopolymeric Amphipols: Application to Membrane Protein Folding, Cell-Free Synthesis, and Solution Nuclear Magnetic Resonance." *Biochemistry* 51 (7): 1416–30. https://doi.org/10.1021/bi201862v.

Bellot, Gaëtan, Sébastien Granier, William Bourguet, René Seyer, Rita Rahmeh, Bernard Mouillac, Robert Pascal, Christiane Mendre, and Hélène Déméné. 2009. "Structure of the Third Intracellular Loop of the Vasopressin V2 Receptor and Conformational Changes upon Binding to GC1qR." *Journal of Molecular Biology* 388 (3): 491–507. https://doi.org/10.1016/j.jmb.2009.02.065.

Benovic, J. L., R. H. Strasser, M. G. Caron, and R. J. Lefkowitz. 1986. "β-Adrenergic Receptor Kinase: Identification of a Novel Protein Kinase That Phosphorylates the Agonist-Occupied Form of the Receptor." *Proceedings of the National Academy of Sciences of the*

United States of America 83 (9): 2797–2801. https://doi.org/10.1073/pnas.83.9.2797.

Benovic, Jeffrey L, Antonio Deblasi, W Carl Stone, Marc G Caron, and Robert J Lefkowitz. 1989. "Beta-Adrenergic Receptor Kinase: Primary Structure Delineates a Multigene Family." *Science*.

Bepler, Tristan, Andrew Morin, Micah Rapp, Julia Brasch, Lawrence Shapiro, Alex J. Noble, and Bonnie Berger. 2019. "Positive-Unlabeled Convolutional Neural Networks for Particle Picking in Cryo-Electron Micrographs." *Nature Methods* 16 (11): 1153–60. https://doi.org/10.1038/s41592-019-0575-8.

Berde, B., and R.A. Boissonnas. 1968. "Basic Pharmacological Properties of Synthetic Analogues and Homologues of the Neuro-Hypophysial Hormones." *Handbook of Experimental Pharmacology* 23: 802.

Bergmann, Carsten, Lisa M Guay-woodford, Peter C Harris, Shigeo Horie, J Dorien, M Peters, Vicente E Torres, Translational Science, and Mayo Clinic. 2019. "Nat Rev Dis Primers." 4 (1): 1–58. https://doi.org/10.1038/s41572-018-0047-y.Polycystic.

Bernier, Virginie, Monique Lagacé, Michèle Lonergan, Marie Françoise Arthus, Daniel G. Bichet, and Michel Bouvier. 2004. "Functional Rescue of the Constitutively Internalized V2 Vasopressin Receptor Mutant R137H by the Pharmacological Chaperone Action of SR49059." *Molecular Endocrinology* 18 (8): 2074–84. https://doi.org/10.1210/me.2004-0080.

Bernier, Virginie, Jean Pierre Morello, Alexandro Zarruk, Nicolas Debrand, Ali Salahpour, Michèle Lonergan, Marie Françoise Arthus, et al. 2006. "Pharmacologic Chaperones as a Potential Treatment for X-Linked Nephrogenic Diabetes Insipidus." *Journal of the American Society of Nephrology* 17 (1): 232–43. https://doi.org/10.1681/ASN.2005080854.

Berridge, Michael J., and Robin F. Irvine. 1984. "Inositol Trisphosphate, a Novel Second Messenger in Cellular Signal Transduction." *Nature* 312 (5992): 315–21. https://doi.org/10.1038/312315a0.

Best, Robert B., Xiao Zhu, Jihyun Shim, Pedro E.M. Lopes, Jeetain Mittal, Michael Feig, and Alexander D. MacKerell. 2012. "Optimization of the Additive CHARMM All-Atom Protein Force Field Targeting Improved Sampling of the Backbone φ, ψ and Side-Chain X1 and X2 Dihedral Angles." *Journal of Chemical Theory and Computation* 8 (9): 3257–

73. https://doi.org/10.1021/ct300400x.

Bhella, David. 2019. “Cryo-Electron Microscopy: An Introduction to the Technique, and Considerations When Working to Establish a National Facility.” *Biophysical Reviews* 11 (4): 515–19. https://doi.org/10.1007/s12551-019-00571-w.

Bichet, Daniel G. 1996. “Vasopressin Receptors in Health and Disease.” *Kidney International* 49 (6): 1706–11. https://doi.org/10.1038/ki.1996.252.

Bichet, Daniel G., and Detlef Bockenhauer. 2016. “Genetic Forms of Nephrogenic Diabetes Insipidus (NDI): Vasopressin Receptor Defect (X-Linked) and Aquaporin Defect (Autosomal Recessive and Dominant).” *Best Practice and Research: Clinical Endocrinology and Metabolism* 30 (2): 263–76. https://doi.org/10.1016/j.beem.2016.02.010.

Bijlsma, U.G., J.H Burn, and J.H. Gaddum. 1928. “A Comparison of the Oxytocic, Pressor and Antidiuretic Activities of Commercial SampIes of Pituitary Extract.” *Quart. J. Pharm. Allied Sci*.

Bissantz, Caterina, Antoine Logean, and Didier Rognan. 2004a. “High-Throughput Modeling of Human g-Protein Coupled Receptors: Amino Acid Sequence Alignment, Three-Dimensional Model Building, and Receptor Library Screening.” *Journal of Chemical Information and Computer Sciences* 44 (3): 1162–76. https://doi.org/10.1021/ci034181a.

———. 2004b. “High-Throughput Modeling of Human g-Protein Coupled Receptors: Amino Acid Sequence Alignment, Three-Dimensional Model Building, and Receptor Library Screening.” *Journal of Chemical Information and Computer Sciences* 44 (3): 1162–76. https://doi.org/10.1021/ci034181a.

Bockaert, J., C. Roy, R. Rajerison, and S. Jard. 1973. “Specific Binding of [3H]Lysine Vasopressin to Pig Kidney Plasma Membranes. Relationship of Receptor Occupancy to Adenylate Cyclase Activation.” *Journal of Biological Chemistry* 248 (17): 5922–31. https://doi.org/10.1016/S0021-9258(19)43489-3.

Bockaert, J, C Roy, R Rajerison, and S Jard. 1973. “Specific Binding of [3H]Lysine-Vasopressin to Pig Kidney Plasma Membranes.” *J. Biol. Chem.* 248 (17): 5922–31. files/435/J. Biol. Chem.-1973-Bockaert-5922-31.pdf.

Bockaert, Joël, and Jean Philippe Pin. 1999. “Molecular Tinkering of G Protein-Coupled

Receptors: An Evolutionary Success." *EMBO Journal* 18 (7): 1723–29. https://doi.org/10.1093/emboj/18.7.1723.

Bockenhauer, Detlef, and Daniel G. Bichet. 2015. "Pathophysiology, Diagnosis and Management of Nephrogenic Diabetes Insipidus." *Nature Reviews Nephrology* 11 (10): 576–88. https://doi.org/10.1038/nrneph.2015.89.

Bockenhauer, Detlef, Eric Carpentier, Driss Rochdi, W. Van'T Hoff, Billy Breton, Virginie Bernier, Michel Bouvier, and Daniel G. Bichet. 2010. "Vasopressin Type 2 Receptor V88M Mutation: Molecular Basis of Partial and Complete Nephrogenic Diabetes Insipidus." *Nephron - Physiology* 114 (1). https://doi.org/10.1159/000245059.

Booth, Christopher. 2019. "Key Concepts in Detecting Electrons." *S 2 C 2 Workshop*.

Bortolato, Andrea, Andrew S. Doré, Kaspar Hollenstein, Benjamin G. Tehan, Jonathan S. Mason, and Fiona H. Marshall. 2014. "Structure of Class B GPCRs: New Horizons for Drug Discovery." *British Journal of Pharmacology* 171 (13): 3132–45. https://doi.org/10.1111/bph.12689.

Bous, Julien, Hélène Orcel, Nicolas Floquet, Cédric Leyrat, Joséphine Lai-Kee-Him, Gérald Gaibelet, Aurélie Ancelin, et al. 2021. "Structure of the Antidiuretic Hormone Vasopressin Receptor Signalling Complex." *Science Advances* in press (May): 1–19.

Brenner, S, and R W Horne. 1959. "A Negative Staining Method for High Resolution Electron Microscopy of Viruses." *Biochim Biophys Acta*.

Breton, Christophe, Hichem Chellil, Majida Kabbaj-Benmansour, Eric Carnazzi, René Seyer, Sylvie Phalipou, Denis Morin, et al. 2001. "Direct Identification of Human Oxytocin Receptor-Binding Domains Using a Photoactivatable Cyclic Peptide Antagonist: Comparison with the Human V 1a Vasopressin Receptor." *Journal of Biological Chemistry* 276 (29): 26931–41. https://doi.org/10.1074/jbc.M102073200.

Brilot, Axel F., James Z. Chen, Anchi Cheng, Junhua Pand, Stephen C. Harrison, Clinton S. Potter, Bridget Carragher, Richard Henderson, and Nikolaus Grigorieff. 2012. "Beam-Induced Motion of Vitrified Specimen on Holey Carbon Film." *J Struct Biol* 177 (3): 630–37. https://doi.org/10.1016/j.jsb.2012.02.003.Beam-Induced.

Brown, E, DL Clarke, V Roux, and GH Sherman. 1963. "The Stimulation of Adenosine 3,5-Monophosphate Production by Antidiuretic Factors" 238 (2).

Brunn, Fritz. 1921. “Beitrag Zur Kenntnis Der Wirkung Des Strychnins Auf Den Gesichtssinn.” *Skandinavisches Archiv Für Physiologie* 47 (1): 121–26. https://doi.org/10.1111/j.1748-1716.1926.tb00152.x.

Burt, D J. 1974. “Basic Operation of the Charge Coupled Device.” *GEC Hirst Research Centre*, no. Ccd.

Butlen, Dniel, Gilles Guillon, Rabary. Rajerison, Serge Jard, Wilbur Sawyer, and Maurice Manning. 1978. “Structural Requirements for Activation of Vasopressin-Sensitive Adenylate Cyclase, Hormone Binding, and Antidiuretic Actions: Effects of Highly Potent Analogues and Competitive Inhibitors.” *Molecular Pharmacology* 14 (6): 1006–17.

Cabrera-Vera, Theresa M., Jurgen Vanhauwe, Tarita O. Thomas, Martina Medkova, Anita Preininger, Maria R. Mazzoni, and Heidi E. Hamm. 2003. “Insights into G Protein Structure, Function, and Regulation.” *Endocrine Reviews* 24 (6): 765–81. https://doi.org/10.1210/er.2000-0026.

Cahill, Thomas J., Alex R.B. Thomsen, Jeffrey T. Tarrasch, Bianca Plouffe, Anthony H. Nguyen, Fan Yang, Li Yin Huang, et al. 2017. “Distinct Conformations of GPCR-β-Arrestin Complexes Mediate Desensitization, Signaling, and Endocytosis.” *Proceedings of the National Academy of Sciences of the United States of America* 114 (10): 2562–67. https://doi.org/10.1073/pnas.1701529114.

Carpentier, Eric, Larry A. Greenbaum, Driss Rochdi, Ravinder Abrol, William A. Goddard, Daniel G. Bichet, and Michel Bouvier. 2012. “Identification and Characterization of an Activating F229V Substitution in the V2 Vasopressin Receptor in an Infant with NSIAD.” *Journal of the American Society of Nephrology* 23 (10): 1635–40. https://doi.org/10.1681/ASN.2012010077.

Celver, Jeremy, Sergey A. Vishnivetskiy, Charles Chavkin, and Vsevolod V. Gurevich. 2002. “Conservation of the Phosphate-Sensitive Elements in the Arrestin Family of Proteins.” *Journal of Biological Chemistry* 277 (11): 9043–48. https://doi.org/10.1074/jbc.M107400200.

Charest, Pascale G., Geneviève Oligny-Longpré, Hélène Bonin, Mounia Azzi, and Michel Bouvier. 2007. “The V2 Vasopressin Receptor Stimulates ERK1/2 Activity Independently of Heterotrimeric G Protein Signalling.” *Cellular Signalling* 19 (1): 32–41. https://doi.org/10.1016/j.cellsig.2006.05.020.

Chase, L. R., and G. D. Aurbach. 1968. “Renal Adenyl Cyclase: Anatomically Separate Sites for Parathyroid Hormone and Vasopressin.” *Science* 159 (3814): 545–47. https://doi.org/10.1126/science.159.3814.545.

Chen, Vincent B., W. Bryan Arendall, Jeffrey J. Headd, Daniel A. Keedy, Robert M. Immormino, Gary J. Kapral, Laura W. Murray, Jane S. Richardson, and David C. Richardson. 2010. “MolProbity: All-Atom Structure Validation for Macromolecular Crystallography.” *Acta Crystallographica Section D: Biological Crystallography* 66 (1): 12–21. https://doi.org/10.1107/S0907444909042073.

Chini, B., B. Mouillac, Y. Ala, M.N. Balestre, S. Trumpp-Kallmeyer, J. Hoflack, J. Elands, M. Hibert, M. Manning, and S. Jard. 1995. “Tyr115 Is the Key Residue for Determining Agonist Selectivity in the V1a Vasopressin Receptor.” *The EMBO Journal* 14 (10): 2176–82. https://doi.org/10.1002/j.1460-2075.1995.tb07211.x.

Chini, Bice, Bernard Mouillac, Marie Noëlle Balestre, Susanne Trumpp-Kallmeyer, Jan Hoflack, Marcel Hibert, Maria Andriolo, Sandrine Pupier, Serge Jard, and Claude Barberis. 1996. “Two Aromatic Residues Regulate the Response of the Human Oxytocin Receptor to the Partial Agonist Arginine Vasopressin.” *FEBS Letters* 397 (2–3): 201–6. https://doi.org/10.1016/S0014-5793(96)01135-0.

Chun, Eugene, Aaron A. Thompson, Wei Liu, Christopher B. Roth, Mark T. Griffith, Vsevolod Katritch, Joshua Kunken, et al. 2013. “Fusion Partner Toolchest for the Stabilization and Crystallization of G Protein-Coupled Receptors.” *Promotional Culture: Advertising, Ideology and Symbolic Expression* 20 (6): 22–47. https://doi.org/10.1016/j.str.2012.04.010.Fusion.

Chun, Lei, Wen Hua Zhang, and Jian Feng Liu. 2012. “Structure and Ligand Recognition of Class C GPCRs.” *Acta Pharmacologica Sinica* 33 (3): 312–23. https://doi.org/10.1038/aps.2011.186.

Ciolek, Justyna, Helen Reinfrank, Loic Quinton, Say Viengchareun, Enrico A. Stura, Laura Vera, Sabrina Sigismeau, et al. 2017. “Green Mamba Peptide Targets Type-2 Vasopressin Receptor against Polycystic Kidney Disease.” *Proceedings of the National Academy of Sciences of the United States of America* 114 (27): 7154–59. https://doi.org/10.1073/pnas.1620454114.

Clapham, David, and Eva Neer. 1997. “G PROTEIN Bγ SUBUNITS,” 1–3.

https://doi.org/10.1007/978-3-319-28845-1_5107-1.

Colliex, Christian. 2008. *La Microscopie Electronique*.

Cong, Xiaojing, Sébastien Fiorucci, and Jérôme Golebiowski. 2018. "Activation Dynamics of the Neurotensin G Protein-Coupled Receptor 1." *Journal of Chemical Theory and Computation* 14 (8): 4467–73. https://doi.org/10.1021/acs.jctc.8b00216.

Costa, Tiago R.D., Athanasios Ignatiou, and Elena V. Orlova. 2017. *Structural Analysis of Protein Complexes by Cryo Electron Microscopy*. *Methods in Molecular Biology*. Vol. 1615. https://doi.org/10.1007/978-1-4939-7033-9_28.

Cotte, Nathalie, Marie Noëlle Balestre, André Aumelas, Eve Mahé, Sylvie Phalipou, Denis Morin, Marcel Hibert, et al. 2000. "Conserved Aromatic Residues in the Transmembrane Region VI of the V(1a) Vasopressin Receptor Differentiate Agonist vs. Antagonist Ligand Binding." *European Journal of Biochemistry* 267 (13): 4253–63. https://doi.org/10.1046/j.1432-1033.2000.01472.x.

Cotte, Nathalie, Marie Noëlle Balestre, Sylvie Phalipou, Marcel Hibert, Maurice Manning, Claude Barberis, and Bernard Mouillac. 1998. "Identification of Residues Responsible for the Selective Binding of Peptide Antagonists and Agonists in the V2 Vasopressin Receptor." *Journal of Biological Chemistry* 273 (45): 29462–68. https://doi.org/10.1074/jbc.273.45.29462.

Cowley, Allen W., William C. Cushman, Edmond W. Quillen, Meredith M. Skelton, and Herbert G. Langford. 1981. "Vasopressin Elevation in Essential Hypertension and Increased Responsiveness to Sodium Intake." *Hypertension* 3 (3): 93–100. https://doi.org/10.1161/01.hyp.3.3_pt_2.i93.

dal Maso, Emma, Alisa Glukhova, Yue Zhu, Javier Garcia-Nafria, Christopher G. Tate, Silvia Atanasio, Christopher A. Reynolds, et al. 2019. "The Molecular Control of Calcitonin Receptor Signaling." *ACS Pharmacology & Translational Science* 2 (1): 31–51. https://doi.org/10.1021/acsptsci.8b00056.

Dalgaard, O Z. 1957. "Bilateral Polycystic Disease of the Kidneys; a Follow-up of Two Hundred and Eighty-Four Patients and Their Families." *Acta Medica Scandinavica*.

Danev, Radostin, Matthew Belousoff, Yi-lynn Liang, Xin Zhang, Denise Wootten, and Patrick M Sexton. 2020. "Routine Sub-2 . 5 Å Cryo-EM Structure Determination of B-Family G

Protein- Coupled Receptors."

Danev, Radostin, Haruaki Yanagisawa, and Masahide Kikkawa. 2021. "Cryo-EM Performance Testing of Hardware and Data Acquisition Strategies." *Microscopy*, no. May: 1–11. https://doi.org/10.1093/jmicro/dfab016.

Daura, Xavier, Bernhard Jaun, Dieter Seebach, Wilfred F. Van Gunsteren, and Alan E. Mark. 1998. "Reversible Peptide Folding in Solution by Molecular Dynamics Simulation." *Journal of Molecular Biology* 280 (5): 925–32. https://doi.org/10.1006/jmbi.1998.1885.

Davies, F, G A Coles, P S Harper, A J Williams, C Evans, and D Cochlin. 1991. "Polycystic Kidney Disease Re-Evaluated: A Population-Based Study." *Quarterly Journal of Medicine* 79.

Davisson, C. J., and L. H. Germer. 1928. "Reflection and Refraction of Electrons by a Crystal of Nickel." *Proceedings of the National Academy of Sciences* 14 (8): 619–27. https://doi.org/10.1073/pnas.14.8.619.

Decaux, Guy, Frédéric Vandergheynst, Yasmina Bouko, Jasmine Parma, Gilbert Vassart, and Catheline Vilain. 2007. "Nephrogenic Syndrome of Inappropriate Antidiuresis in Adults: High Phenotypic Variability in Men and Women from a Large Pedigree." *Journal of the American Society of Nephrology* 18 (2): 606–12. https://doi.org/10.1681/ASN.2006090987.

Delort, Bartholomé, Pedro Renault, Landry Charlier, Florent Raussin, Jean Martinez, and Nicolas Floquet. 2017. "Coarse-Grained Prediction of Peptide Binding to G-Protein Coupled Receptors." *Journal of Chemical Information and Modeling* 57 (3): 562–71. https://doi.org/10.1021/acs.jcim.6b00503.

Dempster, A. P., N. M. Laird, and D. B. Rubin. 1977. " Maximum Likelihood from Incomplete Data Via the EM Algorithm ." *Journal of the Royal Statistical Society: Series B (Methodological)* 39 (1): 1–22. https://doi.org/10.1111/j.2517-6161.1977.tb01600.x.

den-Ouweland, Ans M.W. van, Jos C.F.M. Dreesen, Marian Verdijk, Nine V.A.M. Knoers, Leo A.H. Monnens, Mariano Rocchi, and Bernard A. Van-Oost. 1992. "Mutations in the Vasopressin Type 2 Receptor Gene (AVPR2) Associated with Nephrogenic Diabetes Insipidus." *Nature Genetics* 2 (2): 99–102. https://doi.org/10.1038/ng1092-99.

Deupi, Xavier. 2014. "Relevance of Rhodopsin Studies for GPCR Activation." *Biochimica et*

Biophysica Acta - Bioenergetics 1837 (5): 674–82. https://doi.org/10.1016/j.bbabio.2013.09.002.

DeWire, Scott M., Seungkirl Ahn, Robert J. Lefkowitz, and Sudha K. Shenoy. 2007. "β-Arrestins and Cell Signaling." *Annual Review of Physiology* 69: 483–510. https://doi.org/10.1146/annurev.physiol.69.022405.154749.

Dicker, B Y S E, Christine Tyler, S E Dicker, and Christine Tyler. 1952. "AND OXYTOCIC HORMONES IN THE PITUITARY GLAND OF DOGS AND PUPPIES From the Department of Pharmacology , University College , London Vasopressor and Oxytocic Hormones in the Pituitary Gland of Dogs ' Foetuses , Adult Dogs," no. 1948: 141–45.

Dong, Maoqing, Giuseppe Deganutti, Sarah J. Piper, Yi Lynn Liang, Maryam Khoshouei, Matthew J. Belousoff, Kaleeckal G. Harikumar, et al. 2020. "Structure and Dynamics of the Active Gs-Coupled Human Secretin Receptor." *Nature Communications* 11 (1): 1–17. https://doi.org/10.1038/s41467-020-17791-4.

Dorsam, Robert T., and J. Silvio Gutkind. 2007. "G-Protein-Coupled Receptors and Cancer." *Nature Reviews Cancer* 7 (2): 79–94. https://doi.org/10.1038/nrc2069.

Dousa, Thomas, Oscar Hechter, Irving L. Schwartz, and Roderich Walter. 1971. "Neurohypophyseal Hormone-Responsive Adenylate Cyclase from Mammalian Kidney" 68 (8): 1693–97.

Downes, G. B., and N. Gautam. 1999. "The G Protein Subunit Gene Families." *Genomics* 62 (3): 544–52. https://doi.org/10.1006/geno.1999.5992.

Duan, Jia, Dan dan Shen, X. Edward Zhou, Peng Bi, Qiu feng Liu, Yang xia Tan, You wen Zhuang, et al. 2020. "Cryo-EM Structure of an Activated VIP1 Receptor-G Protein Complex Revealed by a NanoBiT Tethering Strategy." *Nature Communications* 11 (1): 1–10. https://doi.org/10.1038/s41467-020-17933-8.

Dubochet, J., J. Lepault, R. Freeman, J. A. Berriman, and J. ???C Homo. 1982. "Electron Microscopy of Frozen Water and Aqueous Solutions." *Journal of Microscopy* 128 (3): 219–37. https://doi.org/10.1111/j.1365-2818.1982.tb04625.x.

Dutta, Somnath, Yan Zhang, Rasmus Fonseca, Tong Sun Kobilka, Antoine Koehl, Bingfa Sun, Brian K. Kobilka, et al. 2019. "Structural Insights into the Activation of Metabotropic Glutamate Receptors." *Nature* 566 (7742): 79–84. https://doi.org/10.1038/s41586-019-

0881-4.

Ecelbarger, Carolyn A., Chung Lin Chou, Stephen J. Lolait, Mark A. Knepper, and Susan R. Digiovanni. 1996. “Evidence for Dual Signaling Pathways for V2 Vasopressin Receptor in Rat Inner Medullary Collecting Duct.” *American Journal of Physiology* 270 (4 PART 2): 623–33. https://doi.org/10.1152/ajprenal.1996.270.4.f623.

Ellison, D. H., H. Velazquez, and F. S. Wright. 1987. “Thiazide-Sensitive Sodium Chloride Cotransport in Early Distal Tubule.” *American Journal of Physiology - Renal Fluid and Electrolyte Physiology* 253 (3 (22/3)). https://doi.org/10.1152/ajprenal.1987.253.3.f546.

Emsley, Paul, and Kevin Cowtan. 2004. “Coot: Model-Building Tools for Molecular Graphics.” *Acta Crystallographica Section D: Biological Crystallography* 60 (12 I): 2126–32. https://doi.org/10.1107/S0907444904019158.

Erdélyi, László S., W. Alexander Mann, Deborah J. Morris-Rosendahl, Ute Groß, Mato Nagel, Péter Várnai, András Balla, and László Hunyady. 2015. “Mutation in the V2 Vasopressin Receptor Gene, AVPR2, Causes Nephrogenic Syndrome of Inappropriate Diuresis.” *Kidney International* 88 (5): 1070–78. https://doi.org/10.1038/ki.2015.181.

Erickson, H P, and A Klug. 1970. “The Fourier Transform of an Electron Micrograph: Effects of Defocussing and Aberrations, and Implications for the Use of Underfocus Contrast Enhancement.” *Philosophical Transactions of the Royal Society of London B* 261 (11): 105–18. http://onlinelibrary.wiley.com/doi/10.1002/bbpc.19700741109/abstract%5Cnpapers2://publication/uuid/A72FFE07-1944-4E9C-8D1F-27B23A9B966A.

Erlandson, Sarah C., Conor McMahon, and Andrew C. Kruse. 2018. “Structural Basis for G Protein-Coupled Receptor Signaling.” *Annual Review of Biophysics* 47 (February): 1–18. https://doi.org/10.1146/annurev-biophys-070317-032931.

Erlenbach, Isolde, and Jürgen Wess. 1998. “Molecular Basis of V2 Vasopressin Receptor/G(s) Coupling Selectivity.” *Journal of Biological Chemistry* 273 (41): 26549–58. https://doi.org/10.1074/jbc.273.41.26549.

Essmann, Ulrich, Lalith Perera, Max L. Berkowitz, Tom Darden, Hsing Lee, and Lee G. Pedersen. 1995. “A Smooth Particle Mesh Ewald Method.” *The Journal of Chemical Physics* 103 (19): 8577–93. https://doi.org/10.1063/1.470117.

Farah, A, H Herken, and A D Welch. 1968. *Handbook of Experimental Pharmacology*. *Pathology - Research and Practice*. Vol. 163. https://doi.org/10.1016/s0344-0338(78)80122-8.

Feldman, Brian J., Stephen M. Rosenthal, Gabriel A. Vargas, Gabriel A. Vargas, Raymond G. Fenwick, Eric A. Huang, Mina Matsuda-Abedini, et al. 2005. "Nephrogenic Syndrome of Inappropriate Antidiuresis." *N Engl J Med*. https://doi.org/10.1056/NEJMoa042743.Nephrogenic.

Fernandez-Leiro, Rafael, and Sjors H.W. Scheres. 2016. "Unravelling Biological Macromolecules with Cryo-Electron Microscopy." *Nature* 537 (7620): 339–46. https://doi.org/10.1038/nature19948.

Ferré, Guillaume, Maxime Louet, Oliver Saurel, Bartholomé Delort, Georges Czaplicki, Céline M'Kadmi, Marjorie Damian, et al. 2019. "Structure and Dynamics of G Protein-Coupled Receptor-Bound Ghrelin Reveal the Critical Role of the Octanoyl Chain." *Proceedings of the National Academy of Sciences of the United States of America* 116 (35): 17525–30. https://doi.org/10.1073/pnas.1905105116.

Filipek, Slawomir. 2019. "Molecular Switches in GPCRs." *Current Opinion in Structural Biology* 55 (iv): 114–20. https://doi.org/10.1016/j.sbi.2019.03.017.

Fitzsimons, J T. 2021. "Angiotensin , Thirst , and Sodium Appetite." *PHYSIOLOGICAL REVIEWS* 78 (3).

Flouret, George, Shigeyuki Terada, Frances Yang, Satoe Hase Nakagawa, Tatsuo Nakahara, and Oscar Hechter. 1977. "Iodinated Neurohypophyseal Hormones as Potential Ligands for Receptor Binding and Intermediates in Synthesis of Tritiated Hormones." *Biochemistry* 16 (10): 2119–24. https://doi.org/10.1021/bi00629a011.

Ford, Carolyn E., Nikolai P. Skiba, Hyunsu Bae, Yehia Daaka, Eitan Reuveny, Lee R. Shekter, Ramon Rosal, et al. 1998. "Molecular Basis for Interactions of G Protein Bγ Subunits with Effectors." *Science* 280 (5367): 1271–74. https://doi.org/10.1126/science.280.5367.1271.

Forsberg, O, Dari Kimanius, Jasenko Zivanov, and Takanori Nakane. 2018. "New Tools for Automated High-Resolution Cryo-EM Structure Determination In," 1–22.

Fredriksson, Robert, Malin C. Lagerström, Lars Gustav Lundin, and Helgi B. Schiöth. 2003. "The G-Protein-Coupled Receptors in the Human Genome Form Five Main Families.

Phylogenetic Analysis, Paralogon Groups, and Fingerprints." *Molecular Pharmacology* 63 (6): 1256–72. https://doi.org/10.1124/mol.63.6.1256.

Fredriksson, Robert, and Helgi B. Schiöth. 2005. "The Repertoire of G-Protein-Coupled Receptors in Fully Sequenced Genomes." *Molecular Pharmacology* 67 (5): 1414–25. https://doi.org/10.1124/mol.104.009001.

Fushimi, Kiyohide, Sei Sasaki, and Fumiaki Marumo. 1997. "Phosphorylation of Serine 256 Is Required for CAMP-Dependent Regulatory Exocytosis of the Aquaporin-2 Water Channel." *Journal of Biological Chemistry* 272 (23): 14800–804. https://doi.org/10.1074/jbc.272.23.14800.

Gal, C Serradeil-le, J Wagnon, C Garcia, C Lacour, P Guiraudou, B Christophe, G Villanova, et al. 1993. "Biochemical and Pharmacological Properties of SR 49059 , a New , Potent , Nonpeptide Antagonist of Rat and Human Vasopressin Via Receptors" 92 (July): 224–31.

Garcha, Amarinder S., and Apurv Khanna. 2011. "Review of Tolvaptan in the Treatment of Hyponatremia." *Clinical Medicine Insights: Therapeutics* 3: 315–25. https://doi.org/10.4137/CMT.S4884.

García-Nafría, Javier, and Christopher G. Tate. 2019a. "Cryo-EM Structures of GPCRs Coupled to G s , G i and G O." *Molecular and Cellular Endocrinology* 488: 1–13. https://doi.org/10.1016/j.mce.2019.02.006.

———. 2019b. "Cryo-EM Structures of GPCRs Coupled to G s , G i and G O." *Molecular and Cellular Endocrinology* 488 (March): 1–13. https://doi.org/10.1016/j.mce.2019.02.006.

Garcia Iglesias, Carmen, Vicente E. Torres, Kenneth P. Offord, Keith E. Holley, C. Mary Beard, and Leonard T. Kurland. 1983. "Epidemiology of Adult Polycystic Kidney Disease, Olmsted County, Minnesota: 1935–1980." *American Journal of Kidney Diseases* 2 (6): 630–39. https://doi.org/10.1016/S0272-6386(83)80044-4.

García Reyes, Luis Enrique. 1983. "Stimulation and Inhibition of Adenylyl Cyclases Mediated by Distinct Regulatory Proteins." *Journal of Chemical Information and Modeling* 53 (9): 1689–99.

Gattone, Vincent H., Robin L. Maser, Chunqiao Tian, Joshua M. Rosenberg, and Michael G. Branden. 1999. "Developmental Expression of Urine Concentration-Associated Genes and Their Altered Expression in Murine Infantile-Type Polycystic Kidney Disease."

Developmental Genetics 24 (3–4): 309–18. https://doi.org/10.1002/(SICI)1520-6408(1999)24:3/4<309::AID-DVG14>3.0.CO;2-5.

Gattone, Vincent H., Xiaofang Wang, Peter C. Harris, and Vicente E. Torres. 2003. "Inhibition of Renal Cystic Disease Development and Progression by a Vasopressin V2 Receptor Antagonist." *Nature Medicine* 9 (10): 1323–26. https://doi.org/10.1038/nm935.

Gershengorn, Marvin C, and Roman Osman. 2001. "Minireview: Insights into G Protein-Coupled Receptor Function Using Molecular Models*." http://swift.embl-heidelberg.de/.

Ghebrehiwet, Berhane, Yan Ji, Alisa Valentino, Mahalakshmi Ramadass, David Habiel, R Kew, Kinga H Hosszu, Dennis K Galanakis, and Ellinor I B Peerschke. 2021. "Soluble GC1qR Is an Autocrine Signal That Induces B1R Expression on Endothelial Cells." https://doi.org/10.4049/jimmunol.1302031.

Giamarchi, Aurélie, Shuang Feng, Lise Rodat-Despoix, Yaoxian Xu, Ekaterina Bubenshchikova, Linda J. Newby, Jizhe Hao, et al. 2010. "A Polycystin-2 (TRPP2) Dimerization Domain Essential for the Function of Heteromeric Polycystin Complexes." *EMBO Journal* 29 (7): 1176–91. https://doi.org/10.1038/emboj.2010.18.

Gillen, Christopher M., Susan Brill, John A. Payne, and Forbush Bliss III. 1996. "Molecular Cloning and Functional Expression of the K-Cl Cotransporter from Rabbit, Rat, and Human." *Journal of Biological Chemistry*.

Granier, Sébastien, Frédéric Jean-Alphonse, Daniel Bacqueville, Arnaud Monteil, Robert Pascal, Joël Poncet, Gilles Guillon, et al. 2008. "The Multifunctional Protein GC1q-R Interacts Specifically with the I3 Loop Arginine Cluster of the Vasopressin V2 Receptor." *Regulatory Peptides* 148 (1–3): 76–87. https://doi.org/10.1016/j.regpep.2008.01.007.

Granier, Sébastien, Aashish Manglik, Andrew C. Kruse, Tong Sun Kobilka, Foon Sun Thian, William I. Weis, and Brian K. Kobilka. 2012. "Structure of the δ-Opioid Receptor Bound to Naltrindole." *Nature* 485: 400–404. https://doi.org/10.1038/nature11111.Structure.

Grant, M, M Sharma, L Elzinga, S Swan, T Yamaguchi, M Ye, M Grant, A Phillips, and J Kornhaus. 1992. "Cyst Fluid From Human Autosomal Dominant Polycystic Kidneys Promotes Cyst Formation and Expansion by Renal Epithelial Cells In Vitr&'2" 3 (4).

Grant, Timothy, and Nikolaus Grigorieff. 2015. "Measuring the Optimal Exposure for Single Particle Cryo-EM Using a 2.6 Å Reconstruction of Rotavirus VP6." *ELife* 4 (MAY): 1–

19. https://doi.org/10.7554/eLife.06980.

Grant, Timothy, Alexis Rohou, and Grigorieff Nikolaus. 2018. “CisTEM, User-Friendly Software for Single- Particle Image Processing.” *ELife*.

Grantham, J. J., M. Uchic, E. J. Cragoe, J. Kornhaus, J. A. Grantham, V. Donoso, R. Mangoo-Karim, A. Evan, and J. McAteer. 1989. “Chemical Modification of Cell Proliferation and Fluid Secretion in Renal Cysts.” *Kidney International* 35 (6): 1379–89. https://doi.org/10.1038/ki.1989.137.

Granzin, J., U. Wilden, H. W. Choe, J. Labahn, B. Krafft, and G. Buldt. 1998. “X-Ray Crystal Structure of Arrestin from Bovine Rod Outer Segments.” *Nature* 391 (6670): 918–21. https://doi.org/10.1038/36147.

Gray-Keller, Mark P., Peter B. Detwiler, Jeffrey L. Benovic, and Vsevolod V. Gurevich. 1997. “Arrestin with a Single Amino Acid Substitution Quenches Light-Activated Rhodopsin in a Phosphorylation-Independent Fashion.” *Biochemistry* 36 (23): 7058–63. https://doi.org/10.1021/bi963110k.

Gribskov, Michael, John Devereux, and Richard R. Burgess. 1984. “The Codon Preference Plot: Graphic Analysis of Protein Coding Sequences and Prediction of Gene Expression.” *Nucleic Acids Research* 12 (1 PART2): 539–49. https://doi.org/10.1093/nar/12.1Part2.539.

Groot, Theun De, Kyupil Lee, Michiel Langeslag, Qi Xi, Kees Jalink, René J.M. Bindels, and Joost G.J. Hoenderop. 2009. “Parathyroid Hormone Activates TRPV5 via PKA-Dependent Phosphorylation.” *Journal of the American Society of Nephrology* 20 (8): 1693–1704. https://doi.org/10.1681/ASN.2008080873.

Guhl, U. 1961. “Die Antidiuretische Und Pressorische Wirksamkeit von Arginin8 - Vasopressin, Lysin8-Vasopressin Und Phenylalanin2-Lysin8-Vasopressin Beim Menschen.” *Schweiz. Med. Wschr*.

Guillien, Myriam, Albane le Maire, Assia Mouhand, Pau Bernadó, William Bourguet, Jean Louis Banères, and Nathalie Sibille. 2020. *IDPs and Their Complexes in GPCR and Nuclear Receptor Signaling*. *Progress in Molecular Biology and Translational Science*. 1st ed. Vol. 174. Elsevier Inc. https://doi.org/10.1016/bs.pmbts.2020.05.001.

Guillon, Gilles, Daniel Butlen, Bernard Cantau, Tomislav Barth, and Serge Jard. 1982.

"KINETIC AND PHARMACOLOGICAL CHARACTERIZATION OF VASOPRESSIN MEMBRANE RECEPTORS FROM HUMAN KIDNEY MEDULLA: RELATION TO ADENYLATE CYCLASE ACTIVATION" 85: 291–304.

Gurevich, Vsevolod V., and Eugenia V. Gurevich. 2013. "Structural Determinants of Arrestin Functions." *Progress in Molecular Biology and Translational Science* 118: 57–92. https://doi.org/10.1016/B978-0-12-394440-5.00003-6.

Gurevich, Vsevolod V, and Eugenia V Gurevich. 2019. "GPCR Signaling Regulation : The Role of GRKs and Arrestins" 10 (February): 1–11. https://doi.org/10.3389/fphar.2019.00125.

H, Forssman. 1945. "On the Mode of Hered-Itary Transmission in Diabetes Insipidus." *Nordisk Medicin*.

Han, May, Vsevolod V. Gurevich, Sergey A. Vishnivetskiy, Paul B. Sigler, and Carsten Schubert. 2001. "Crystal Structure of β-Arrestin at 1.9 Å: Possible Mechanism of Receptor Binding and Membrane Translocation." *Structure* 9 (9): 869–80. https://doi.org/10.1016/S0969-2126(01)00644-X.

Handler, J. S., R. W. Butcher, E. W. Sutherland, and J. Orloff. 1965. "The Effect of Vasopressin and of Theophylline on the Concentration of Adenosine 3',5'-Phosphate in the Urinary Bladder of the Toad." *Journal of Biological Chemistry* 240 (11): 4524–26.

He, Qing Tao, Peng Xiao, Shen Ming Huang, Ying Li Jia, Zhong Liang Zhu, Jing Yu Lin, Fan Yang, et al. 2021. "Structural Studies of Phosphorylation-Dependent Interactions between the V2R Receptor and Arrestin-2." *Nature Communications* 12 (1): 1–16. https://doi.org/10.1038/s41467-021-22731-x.

Hechter, O., S. Terada, T. Nakahara, and G. Flouret. 1978. "Neurohypophyseal Hormone-Responsive Renal Adenylate Cyclase. II. Relationship between Hormonal Occupancy of Neurohypophyseal Hormone Receptor Sites and Adenylate Cyclase Activation." *Journal of Biological Chemistry* 253 (9): 3219–29. https://doi.org/10.1016/s0021-9258(17)40826-x.

Hechter, O., S. Terada, V. Spitsberg, T. Nakahara, S. H. Nakagawaga, and G. Flouret. 1978. "Neurohypophyseal Hormone-Responsive Renal Adenylate Cyclase. III. Relationship between Affinity and Intrinsic Activity in Neurohypophyseal Hormones and Structural Analogs." *Journal of Biological Chemistry* 253 (9): 3230–37.

https://doi.org/10.1016/s0021-9258(17)40827-1.

Hems, D. A., and P. D. Whitton. 1973. “Stimulation by Vasopressin of Glycogen Breakdown and Gluconeogenesis in the Perfused Rat Liver.” *Biochemical Journal* 136 (3): 705–9. https://doi.org/10.1042/bj1360705.

Heydenreich, Franziska M, Bianca Plouffe, Aurélien Rizk, Dalibor Milić, Joris Zhou, Billy Breton, Christian Le Gouill, Asuka Inoue, Michel Bouvier, and Dmitry B Veprintsev. 2021. “Vasopressin V2 Is a Promiscuous G Protein-Coupled Receptor That Is Biased by Its Peptide Ligands.” *BioRxiv*, 2021.01.28.427950. https://doi.org/10.1101/2021.01.28.427950.

Heymann, J Bernard. 2017. “Guidelines for Using Bsoft for High Resolution Reconstruction and Validation of Biomolecular Structures from Electron Micrographs” 27: 159–71. https://doi.org/10.1002/pro.3293.

Hibert, M., J. Hoflack, and S. Trumpp-Kallmeyer. 1999. “FUNCTIONAL ARCHITECTURE OF VASOPRESSIN/OXYTOCIN RECEPTORS” 19: 589–96.

Hilger, Daniel, Kaavya Krishna Kumar, Hongli Hu, Mie Fabricius Pedersen, S O Brien, Lise Giehm, Christine Jennings, et al. 2021. “Structural Insights into Differences in G Protein Activation by Family A and Family B GPCRs” 369 (6503): 1–40. https://doi.org/10.1126/science.aba3373.Structural.

Hilger, Daniel, Kaavya Krishna Kumar, Hongli Hu, Mie Fabricius Pedersen, Lise Giehm, Jesper Mosolff Mathiesen, Georgios Skiniotis, and Brian K. Kobilka. 2019. “Structural Insights into Ligand Efficacy and Activation of the Glucagon Receptor.” *BioRxiv*, 660837. https://doi.org/10.1101/660837.

Hilger, Daniel, Matthieu Masureel, and Brian K. Kobilka. 2018. “Structure and Dynamics of GPCR Signaling Complexes.” *Nature Structural and Molecular Biology* 25 (1): 4–12. https://doi.org/10.1038/s41594-017-0011-7.

Hirsch, Joel A, Carsten Schubert, Vsevolod V Gurevich, Paul B Sigler, Howard Hughes, and New Haven. 1999. “The 2.8˚ Crystal Structure of Visual Arrestin : The 2 . 8 A A Model for Arrestin ’ s Regulation.” *Cell* 97 (2): 257–69.

Hoffert, Jason D., Jakob Nielsen, Ming Jiun Yu, Trairak Pisitkun, Stephen M. Schleicher, Soren Nielsen, and Mark A. Knepper. 2007. “Dynamics of Aquaporin-2 Serine-261

Phosphorylation in Response to Short-Term Vasopressin Treatment in Collecting Duct." *American Journal of Physiology - Renal Physiology* 292 (2): 691–700. https://doi.org/10.1152/ajprenal.00284.2006.

Hogg, R. J., and J. P. Kokko. 1979. "Renal Countercurrent Multiplication System." *Reviews of Physiology, Biochemistry and Pharmacology* 86: 95–135. https://doi.org/10.1007/bfb0031532.

Hopkins, Andrew L, and Colin R Groom. 2002. "Opinion: The Druggable Genome." *Nature Reviews Drug Discovery* 1 (9): 727–30.

Huang, Pengxiang, Sanduo Zheng, Bradley M. Wierbowski, Youngchang Kim, Daniel Nedelcu, Laura Aravena, Jing Liu, Andrew C. Kruse, and Adrian Salic. 2016. "The Structural Basis of Smoothened Activation in Hedgehog Signaling." *Physiology & Behavior* 176 (1): 139–48. https://doi.org/10.1016/j.cell.2018.04.029.The.

Huang, Weijiao, Matthieu Masureel, Qianhui Qu, John Janetzko, Asuka Inoue, Hideaki E. Kato, Michael J. Robertson, et al. 2020. "Structure of the Neurotensin Receptor 1 in Complex with β-Arrestin 1." *Nature* 579 (7798): 303–8. https://doi.org/10.1038/s41586-020-1953-1.

Humphrey, William, Andrew Dalke, and Klaus Schulten. 1996. "VMD: Visual Molecular Dynamics." *Journal of Molecular Graphics* 14: 33–38. https://doi.org/10.1016/j.carbon.2017.07.012.

Ibrahim, B. Syed, and Vasantha Pattabhi. 2005. "Trypsin Inhibition by a Peptide Hormone: Crystal Structure of Trypsin-Vasopressin Complex." *Journal of Molecular Biology* 348 (5): 1191–98. https://doi.org/10.1016/j.jmb.2005.03.034.

Igaev, Maxim, Carsten Kutzner, Lars V Bock, Andrea C Vaiana, and Helmut Grubmüller. 2019. "Automated Cryo-EM Structure Refinement Using Correlation-Driven Molecular Dynamics." *ELife* 8: 1–33. https://doi.org/10.7554/elife.43542.

Imaizumi, Tsutomu, Seiki Harada, Yoshitaka Hirooka, Hiroyuki Masaki, Michiko Momohara, and Akira Takeshita. 1992. "Effects of OPC-21268, an Orally Effective Vasopressin V1 Receptor Antagonist in Humans." *Hypertension* 20 (1): 54–58. https://doi.org/10.1161/01.HYP.20.1.54.

J, Dubochet, Marc Adrian, Chang J, JC Homo, J Lepault, Alasdair W. McDowall, and P Schulz.

1988. “Cryo-Electron Microscopy of Vitrified Specimens.” *Quaterly Review of Biophysics* 21 (2): 129.

J J Grantham 1 , R Mangoo-Karim, M E Uchic, M Grant, W A Shumate, C H Park, J P Calvet. 1989. “Net Fluid Secretion by Mammalian Renal Epithelial Cells: Stimulation by CAMP in Polarized Cultures Derived from Established Renal Cells and from Normal and Polycystic Kidneys.” *Association of American Physicians*.

Jakobi, Arjen J, Matthias Wilmanns, and Carsten Sachse. 2017. “Model-Based Local Density Sharpening of Cryo-EM Maps.” *ELife* 6: 1–26. https://doi.org/10.7554/elife.27131.

Jard, S, R C Gaillard, G Guillon, J Marie, P Schoenenberg, A F Muller, M Manning, and W H Sawyer. 1986. “Vasopressin Antagonists Allow Demonstration of a Novel Type of Vasopressin Receptor in the Rat Adenohypophysis.” *Molecular Pharmacology* 30 (2): 171–77.

Jean-Alphonse, Frédéric, Sanja Perkovska, Marie Céline Frantz, Thierry Durroux, Catherine Méjean, Denis Morin, Stéphanie Loison, et al. 2009. “Biased Agonist Pharmacochaperones of the AVP V2 Receptor May Treat Congenital Nephrogenic Diabetes Insipidus.” *Journal of the American Society of Nephrology* 20 (10): 2190–2203. https://doi.org/10.1681/ASN.2008121289.

Jiang, Wen, and Wah Chiu. 2001. “Web-Based Simulation for Contrast Transfer Function and Envelope Functions.” *Microscopy and Microanalysis* 7 (4): 329–34. https://doi.org/10.1007/s10005-001-0004-4.

Johnson, Ronald L, Charles L Saxe Iii, Rachel Gollop, Alan R Kimmel, and Peter N Devreotes. 1993. “Identification and Targeted Gene Disruption of CAR3 , a CAMP Receptor Subtype Expressed during Multicellular Stages of Dictyostelium Development,” 273–82.

Joseph, Agnel Praveen, Sony Malhotra, Tom Burnley, Chris Wood, Daniel K. Clare, Martyn Winn, and Maya Topf. 2016. “Refinement of Atomic Models in High Resolution EM Reconstructions Using Flex-EM and Local Assessment.” *Methods* 100: 42–49. https://doi.org/10.1016/j.ymeth.2016.03.007.

Josephs, Tracy M., Matthew J. Belousoff, Yi-Lynn Liang, Sarah J. Piper, Jianjun Cao, Daniel J. Garama, Katie Leach, et al. 2021. “Structure and Dynamics of the CGRP Receptor in Apo and Peptide-Bound Forms.” *Science* 7258 (February): eabf7258. https://www.sciencemag.org/lookup/doi/10.1126/science.abf7258.

Kalenga, Karine, Alexandre Persu, Eric Goffin, Edith Lavenne-Pardonge, Paul J. Van Cangh, Daniel G. Bichet, and Olivier Devuyst. 2002. “Intrafamilial Phenotype Variability in Nephrogenic Diabetes Insipidus.” *American Journal of Kidney Diseases* 39 (4): 737–43. https://doi.org/10.1053/ajkd.2002.31993.

Kang, Dong Soo, Ronald C. Kern, Manojkumar A. Puthenveedu, Mark von Zastrow, John C. Williams, and Jeffrey L. Benovic. 2009. “Structure of an Arrestin2-Clathrin Complex Reveals a Novel Clathrin Binding Domain That Modulates Receptor Trafficking.” *Journal of Biological Chemistry* 284 (43): 29860–72. https://doi.org/10.1074/jbc.M109.023366.

Kang, Yanyong, X. Edward Zhou, Xiang Gao, Yuanzheng He, Wei Liu, Andrii Ishchenko, Anton Barty, et al. 2015. “Crystal Structure of Rhodopsin Bound to Arrestin by Femtosecond X-Ray Laser.” *Nature* 523 (7562): 561–67. https://doi.org/10.1038/nature14656.

Kato, Hideaki E., Yan Zhang, Hongli Hu, Carl Mikael Suomivuori, Francois Marie Ngako Kadji, Junken Aoki, Kaavya Krishna Kumar, et al. 2019. “Conformational Transitions of a Neurotensin Receptor 1–Gi1 Complex.” *Nature* 572 (7767): 80–85. https://doi.org/10.1038/s41586-019-1337-6.

Katritch, Vsevolod, Vadim Cherezov, and Raymond C Stevens. 2012. “Diversity and Modularity of G Protein-Coupled Receptor Structures.” *Trends in Pharmacological Sciences* 33 (1): 17–27. https://doi.org/10.1016/j.tips.2011.09.003.

Kaur, Satinder, Josue Gomez-Blanco, Ahmad A.Z. Khalifa, Swathi Adinarayanan, Ruben Sanchez-Garcia, Daniel Wrapp, Jason S. McLellan, Khanh Huy Bui, and Javier Vargas. 2021. “Local Computational Methods to Improve the Interpretability and Analysis of Cryo-EM Maps.” *Nature Communications* 12 (1). https://doi.org/10.1038/s41467-021-21509-5.

Keppens, Stefaan, Jackie R. Vandenheede, and Henri De Wulf. 1977. “On the Role of Calcium as Second Messenger in Liver for the Hormonally Induced Activation of Glycogen Phosphorylase.” *BBA - General Subjects* 496 (2): 448–57. https://doi.org/10.1016/0304-4165(77)90327-0.

Kestranek, W., E.P Pick, and H Moliter. 1925. “Über Die Wirkungsstärke von Hypophysen-Extrakten, Gemessen an Ihren Antidiuretischen Eigenschaften.” *Biochem. Z.*

Kieferle, Stefanie, Peying Fong, Marcelle Bens, Alain Vandewalle, and Thomas J. Jentsch.

1994. “Two Highly Homologous Members of the ClC Chloride Channel Family in Both Rat and Human Kidney.” *Proceedings of the National Academy of Sciences of the United States of America* 91 (15): 6943–47. https://doi.org/10.1073/pnas.91.15.6943.

Kim, Jin, Young Hee Kim, Jung Ho Cha, C. Craig Tisher, and Kirsten M. Madsen. 1999. “Intercalated Cell Subtypes in Connecting Tubule and Cortical Collecting Duct of Rat and Mouse.” *Journal of the American Society of Nephrology* 10 (1): 1–12.

Kimanius, Dari, Björn O. Forsberg, Sjors H.W. Scheres, and Erik Lindahl. 2016. “Accelerated Cryo-EM Structure Determination with Parallelisation Using GPUS in RELION-2.” *ELife* 5: 1–21. https://doi.org/10.7554/eLife.18722.

Kimura, Tadashi, Osamu Tanizawa, Kensaku Mori, Michael J. Brownstein, and Hiroto Okayama. 1992. “Structure and Expression of a Human Oxytocin Receptor.” *Nature* 359: 710–13. file:///C:/Users/ASUS/Desktop/Rujukan PhD/p21/xiong1993.pdf.

Kinter, L. B., W. F. Huffman, and F. L. Stassen. 1988. “Antagonists of the Antidiuretic Activity of Vasopressin.” *American Journal of Physiology - Renal Fluid and Electrolyte Physiology* 254 (2 (23/2)). https://doi.org/10.1152/ajprenal.1988.254.2.f165.

Kirk, C. J., and D. A. Hems. 1974. “Hepatic Action of Vasopressin: Lack of a Role for Adenosine-3′,5′-Cyclic Monophosphate.” *FEBS Letters* 47 (1): 128–31. https://doi.org/10.1016/0014-5793(74)80441-2.

Kirk, J, Terence R Verrinder, and Douglas A Hems. 1977. “RAPID STIMULATION, BY VASOPRESSIN AND ADRENALINE, OF INORGANIC PHOSPHATE INCORPORATION INTO PHOSPHATIDY L INOSITOL IN ISOLATED HEPATOCYTES” 83 (2).

Kobayashi, Kazuhiro, Wataru Shihoya, Tomohiro Nishizawa, Francois Marie Ngako Kadji, Junken Aoki, Asuka Inoue, and Osamu Nureki. 2020. “Cryo-EM Structure of the Human PAC1 Receptor Coupled to an Engineered Heterotrimeric G Protein.” *Nature Structural and Molecular Biology* 27 (3): 274–80. https://doi.org/10.1038/s41594-020-0386-8.

Kocan, Martina, Heng B. See, Natália G. Sampaio, Karin A. Eidne, Brian J. Feldman, and Kevin D.G. Pfleger. 2009. “Agonist-Independent Interactions between β-Arrestins and Mutant Vasopressin Type II Receptors Associated with Nephrogenic Syndrome of Inappropriate Antidiuresis.” *Molecular Endocrinology* 23 (4): 559–71. https://doi.org/10.1210/me.2008-0321.

Koehl, Antoine, Hongli Hu, Shoji Maeda, Yan Zhang, Qianhui Qu, Joseph M. Paggi, Naomi R. Latorraca, et al. 2018. “Structure of the M-Opioid Receptor–Gi Protein Complex.” *Nature* 558 (7711): 547–52. https://doi.org/10.1038/s41586-018-0219-7.

Kojro, Elzbieta, Peter Eich, Gerald Gimpl, and Falk Fahrenholz. 1993. “Direct Identification of an Extracellular Agonist Binding Site in the Renal V2 Vasopressin Receptor.” *Biochemistry* 32 (49): 13537–44. https://doi.org/10.1021/bi00212a020.

Kolakowski, L F Jr. 1994. “GCRDb: A G-Protein-Coupled Receptor Database.” *Receptors & Channels* 2 (1): 1–7.

Koning, Roman I., Abraham J. Koster, and Thomas H. Sharp. 2018. “Advances in Cryo-Electron Tomography for Biology and Medicine.” *Annals of Anatomy* 217: 82–96. https://doi.org/10.1016/j.aanat.2018.02.004.

Kooistra, Albert J., Stefan Mordalski, Gáspár Pándy-Szekeres, Mauricio Esguerra, Alibek Mamyrbekov, Christian Munk, György M. Keserű, and David E. Gloriam. 2021. “GPCRdb in 2021: Integrating GPCR Sequence, Structure and Function.” *Nucleic Acids Research* 49 (D1): D335–43. https://doi.org/10.1093/nar/gkaa1080.

Korczynska, Magdalena, Mary J. Clark, Celine Valant, Jun Xu, Ee Von Moo, Sabine Albold, Dahlia R. Weiss, et al. 2018. “Structure-Based Discovery of Selective Positive Allosteric Modulators of Antagonists for the M2 Muscarinic Acetylcholine Receptor.” *Proceedings of the National Academy of Sciences of the United States of America* 115 (10): E2419–28. https://doi.org/10.1073/pnas.1718037115.

Kovoor, Abraham, Jeremy Celver, Ravil I. Abdryashitov, Charles Chavkin, and Vsevolod V. Gurevich. 1999a. “Targeted Construction of Phosphorylation-Independent β-Arrestin Mutants with Constitutive Activity in Cells.” *Journal of Biological Chemistry* 274 (11): 6831–34. https://doi.org/10.1074/jbc.274.11.6831.

———. 1999b. “Targeted Construction of Phosphorylation-Independent β-Arrestin Mutants with Constitutive Activity in Cells.” *Journal of Biological Chemistry* 274 (11): 6831–34. https://doi.org/10.1074/jbc.274.11.6831.

Krishna, N. Rama, and V. Jayalakshmi. 2008. “Quantitative Analysis of STD-NMR Spectra of Reversibly Forming Ligand-Receptor Complexes.” *Topics in Current Chemistry* 273 (August 2007): 15–54. https://doi.org/10.1007/128_2007_144.

Krivanek, O. L., and P. E. Mooney. 1993. “Applications of Slow-Scan CCD Cameras in Transmission Electron Microscopy.” *Ultramicroscopy* 49 (1–4): 95–108. https://doi.org/10.1016/0304-3991(93)90216-K.

Kufareva, Irina, Martin Gustavsson, Yi Zheng, Bryan S. Stephens, and Tracy M. Handel. 2017. “What Do Structures Tell Us about Chemokine Receptor Function and Antagonism?” *Annual Review of Biophysics* 46 (110): 175–98. https://doi.org/10.1146/annurev-biophys-051013-022942.

kuhn, Hermann. 1978. “Light-Regulated Binding of Rhodopsin Kinase and Other Proteins to Cattle Photoreceptor Membranes.” *Biochemistry* 17 (21): 4389–95. https://doi.org/10.1021/bi00614a006.

Kuhn, Hermann. 1974. “Light-Dependent Phosphorylation of Rhodopsin in Living Frogs.” *Nature*.

Kühn, Hermann, and William J. Dreyer. 1972. “Light Dependent Phosphorylation of Rhodopsin by ATP.” *FEBS Letters* 20 (1): 1–6. https://doi.org/10.1016/0014-5793(72)80002-4.

Lally, Ciara C.M., Brian Bauer, Jana Selent, and Martha E. Sommer. 2017. “C-Edge Loops of Arrestin Function as a Membrane Anchor.” *Nature Communications* 8: 1–12. https://doi.org/10.1038/ncomms14258.

Landau, Ehud M., and Jürg P. Rosenbusch. 1996. “Lipidic Cubic Phases: A Novel Concept for the Crystallization of Membrane Proteins.” *Proceedings of the National Academy of Sciences of the United States of America* 93 (25): 14532–35. https://doi.org/10.1073/pnas.93.25.14532.

Latorraca, Naomi R., Matthieu Masureel, Scott A. Hollingsworth, Franziska M. Heydenreich, Carl Mikael Suomivuori, Connor Brinton, Raphael J.L. Townshend, Michel Bouvier, Brian K. Kobilka, and Ron O. Dror. 2020. “How GPCR Phosphorylation Patterns Orchestrate Arrestin-Mediated Signaling.” *Cell* 183 (7): 1813-1825.e18. https://doi.org/10.1016/j.cell.2020.11.014.

Lau, Kai, and E James Bourdeau. 1995. “Parathyroid Hormone Action in Calcium Transport in the Distal Nephron.” *Science*.

Lebon, Guillaume, Tony Warne, Patricia C. Edwards, Kirstie Bennett, Christopher J.

Langmead, Andrew G.W. Leslie, and Christopher G. Tate. 2011. “Agonist-Bound Adenosine A2A Receptor Structures Reveal Common Features of GPCR Activation.” *Nature* 474 (7352): 521–26. https://doi.org/10.1038/nature10136.

Lee, Jumin, Xi Cheng, Jason M. Swails, Min Sun Yeom, Peter K. Eastman, Justin A. Lemkul, Shuai Wei, et al. 2016. “CHARMM-GUI Input Generator for NAMD, GROMACS, AMBER, OpenMM, and CHARMM/OpenMM Simulations Using the CHARMM36 Additive Force Field.” *Journal of Chemical Theory and Computation* 12 (1): 405–13. https://doi.org/10.1021/acs.jctc.5b00935.

Lee, Yang, Tony Warne, Rony Nehmé, Shubhi Pandey, Hemlata Dwivedi-agnihotri, Madhu Chaturvedi, Patricia C Edwards, et al. 2020. “Molecular Basis of β -Arrestin Coupling to Formoterol-Bound β 1 - Adrenoceptor” 583 (7818): 862–66. https://doi.org/10.1038/s41586-020-2419-1.Molecular.

Lee, Yang, Tony Warne, Shubhi Pandey, Hemlata Dwivedi-, Patricia C Edwards, Andrew G W Leslie, Arun K Shukla, Christopher G Tate, and Francis Crick Avenue. 2020. “Molecular Determinants of β -Arrestin Coupling to Formoterol-Bound,” no. December 2019.

Lefkowitz, Robert J., Keshava Rajagopal, and Erin J. Whalen. 2006. “New Roles for β-Arrestins in Cell Signaling: Not Just for Seven-Transmembrane Receptors.” *Molecular Cell* 24 (5): 643–52. https://doi.org/10.1016/j.molcel.2006.11.007.

Legros, J J. 2010. “Un Rôle Social et Généreux Pour l ’ Ocytocine Dans l ’ Espèce Humaine ?” XIV.

Li, Xueming, Paul Mooney, Shawn Zheng, Christopher R. Booth, Michael B. Braunfeld, Sander Gubbens, David A. Agard, and Yifan Cheng. 2013. “Electron Counting and Beam-Induced Motion Correction Enable near-Atomic-Resolution Single-Particle Cryo-EM.” *Nature Methods* 10 (6): 584–90. https://doi.org/10.1038/nmeth.2472.

Liang, Tao, Yuan Yuan, Ran Wang, Yanzhi Guo, Menglong Li, Xuemei Pu, and Chuan Li. 2017. “Structural Features and Ligand Selectivity for 10 Intermediates in the Activation Process of B2-Adrenergic Receptor.” *ACS Omega* 2 (12): 8557–67. https://doi.org/10.1021/acsomega.7b01031.

Liang, Yi-lynn, Matthew J Belousoff, Peishen Zhao, Radostin Danev, Patrick M Sexton, Denise Wootten, Yi-lynn Liang, et al. 2020. “Toward a Structural Understanding of Class B

GPCR Peptide Binding and Activation." *Molecular Cell*, 1–13. https://doi.org/10.1016/j.molcel.2020.01.012.

Liang, Yi Lynn, Maryam Khoshouei, Alisa Glukhova, Sebastian G.B. Furness, Peishen Zhao, Lachlan Clydesdale, Cassandra Koole, et al. 2018a. "Phase-Plate Cryo-EM Structure of a Biased Agonistbound Human GLP-1 Receptor-Gs Complex." *Nature* 555 (7694): 121–25. https://doi.org/10.1038/nature25773.

———. 2018b. "Phase-Plate Cryo-EM Structure of a Biased Agonistbound Human GLP-1 Receptor-Gs Complex." *Nature* 555 (7694): 121–25. https://doi.org/10.1038/nature25773.

Liang, Yi Lynn, Maryam Khoshouei, Mazdak Radjainia, Yan Zhang, Alisa Glukhova, Jeffrey Tarrasch, David M. Thal, et al. 2017. "Phase-Plate Cryo-EM Structure of a Class B GPCR-G-Protein Complex." *Nature* 546 (7656): 118–23. https://doi.org/10.1038/nature22327.

Lin, Shuling, Shuo Han, Xiaoqing Cai, Qiuxiang Tan, Kexiu Zhou, Dejian Wang, Xinwei Wang, et al. 2021. "Structures of Gi-Bound Metabotropic Glutamate Receptors MGlu2 and MGlu4." *Nature* 594 (7864): 583–88. https://doi.org/10.1038/s41586-021-03495-2.

Liu, Jie, and Jürgen Wess. 1996. "Different Single Receptor Domains Determine the Distinct G Protein Coupling Profiles of Members of the Vasopressin Receptor Family." *Journal of Biological Chemistry* 271 (15): 8772–78. https://doi.org/10.1074/jbc.271.15.8772.

Liu, Kaiwen, Lijie Wu, Shuguang Yuan, Meng Wu, Yueming Xu, Qianqian Sun, Shu Li, Suwen Zhao, Tian Hua, and Zhi Jie Liu. 2020. "Structural Basis of CXC Chemokine Receptor 2 Activation and Signalling." *Nature* 585 (7823): 135–40. https://doi.org/10.1038/s41586-020-2492-5.

Lohse, Martin J, Jeffrey L Benovic, Juan Codina, Marc G Caron, and Robert J Lefkowitz. 1984. "I-Arrestin : A Protein That Regulates [I-Adrenergic." *Science*, no. 7: 1–4.

Loison, Stéphanie, Martin Cottet, Hélène Orcel, Hélène Adihou, Rita Rahmeh, Laurent Lamarque, Eric Trinquet, et al. 2012. "Selective Fluorescent Nonpeptidic Antagonists for Vasopressin V2 GPCR: Application to Ligand Screening and Oligomerization Assays." *Journal of Medicinal Chemistry* 55 (20): 8588–8602. https://doi.org/10.1021/jm3006146.

Lolait, S. J., O'Carroll, A. M., McBride, O. W., Konig, M., Morel, A., & Brownstein, M. J. 1992. "Cloning and Characterization of a Vasopressin V2 Receptor and Possible Linkto Nephrogenic Diabetes Insipidus." *Nature* 359: 710–13.

Ludtke, Steven J., Philip R. Baldwin, and Wah Chiu. 1999. "EMAN: Semiautomated Software for High-Resolution Single-Particle Reconstructions." *Journal of Structural Biology* 128 (1): 82–97. https://doi.org/10.1006/jsbi.1999.4174.

Macion-Dazard, Rosemarie, Nicholas Callahan, Zhen Xu, Nan Wu, Marc Thibonnier, and Menachem Shoham. 2006. "Mapping the Binding Site of Six Nonpeptide Antagonists to the Human V 2-Renal Vasopressin Receptor." *Journal of Pharmacology and Experimental Therapeutics* 316 (2): 564–71. https://doi.org/10.1124/jpet.105.095554.

Maeda, Shoji, Qianhui Qu, Michael J. Robertson, Georgios Skiniotis, and Brian K. Kobilka. 2019. "Structures of the M1 and M2 Muscarinic Acetylcholine Receptor/G-Protein Complexes." *Science (New York, N.Y.)* 364 (6440): 552–57. https://doi.org/10.1126/science.aaw5188.

Maeda, Shoji, Jun Xu, Francois Marie N. Kadji, Mary J. Clark, Jiawei Zhao, Naotaka Tsutsumi, Junken Aoki, et al. 2020. "Structure and Selectivity Engineering of the M1muscarinic Receptor Toxin Complex." *Science* 369 (6500): 161–67. https://doi.org/10.1126/science.aax2517.

Makita, Noriko, Katsunori Manaka, Junichiro Sato, and Taroh Iiri. 2020. *V2 Vasopressin Receptor Mutations*. *Vitamins and Hormones*. 1st ed. Vol. 113. Elsevier Inc. https://doi.org/10.1016/bs.vh.2019.08.012.

Manglik, Aashish, and Brian Kobilka. 2014. "The Role of Protein Dynamics in GPCR Function: Insights from the B2AR and Rhodopsin." *Curr Opin Cell Biol*. https://doi.org/10.1016/j.ceb.2014.01.008.The.

Manglik, Aashish, Brian K. Kobilka, and Jan Steyaert. 2017. "Nanobodies to Study G Protein-Coupled Receptor Structure and Function." *Annual Review of Pharmacology and Toxicology* 57 (August): 19–37. https://doi.org/10.1146/annurev-pharmtox-010716-104710.

Manglik, Aashish, and Andrew C. Kruse. 2017. "Structural Basis for G Protein-Coupled Receptor Activation." *Physiology & Behavior* 176 (10): 139–48. https://doi.org/10.1021/acs.biochem.7b00747.Summary.

Manning, M., A. Misicka, A. Olma, K. Bankowski, S. Stoev, B. Chini, T. Durroux, B. Mouillac, M. Corbani, and G. Guillon. 2012. "Oxytocin and Vasopressin Agonists and Antagonists as Research Tools and Potential Therapeutics." *Journal of Neuroendocrinology* 24 (4):

609–28. https://doi.org/10.1111/j.1365-2826.2012.02303.x.

Manning, Maurice, and Wilbur H. Sawyer. 1993. “Design, Synthesis and Some Uses of Receptor-Specific Agonists and Antagonists of Vasopressin and Oxytocin.” *Journal of Receptors and Signal Transduction* 13 (1–4): 195–214. https://doi.org/10.3109/10799899309073655.

Manning, Maurice, Stoytcho Stoev, Bice Chini, Thierry Durroux, Bernard Mouillac, and Gilles Guillon. 2008. “Peptide and Non-Peptide Agonists and Antagonists for the Vasopressin and Oxytocin V1a, V1b, V2 and OT Receptors: Research Tools and Potential Therapeutic Agents.” *Progress in Brain Research* 170 (08): 473–512. https://doi.org/10.1016/S0079-6123(08)00437-8.

Manuscript, Author. 2014. “NIH Public Access” 27 (4): 1–19. https://doi.org/10.1037/a0032811.Child.

Mao, Chunyou, Cangsong Shen, Chuntao Li, Dan Dan Shen, Chanjuan Xu, Shenglan Zhang, Rui Zhou, et al. 2020. “Cryo-EM Structures of Inactive and Active GABAB Receptor.” *Cell Research* 30 (7): 564–73. https://doi.org/10.1038/s41422-020-0350-5.

Mariel Birnbaumer, Anita Seibold, Stephanie Gilbert, Masami Ishido, Claude Barberis, Anaid Antaramian, Phillippe Brabet & Walter Rosenthal. 1992. “Molecular Cloning of the Receptor for Human Antidiuretic Hormone.” *Nature* 359: 710–13.

Marrink, Siewert J., H. Jelger Risselada, Serge Yefimov, D. Peter Tieleman, and Alex H. De Vries. 2007. “The MARTINI Force Field: Coarse Grained Model for Biomolecular Simulations.” *Journal of Physical Chemistry B* 111 (27): 7812–24. https://doi.org/10.1021/jp071097f.

Mastronarde, David N. 2005. “Automated Electron Microscope Tomography Using Robust Prediction of Specimen Movements” 152: 36–51. https://doi.org/10.1016/j.jsb.2005.07.007.

Mayer, Moriz, and Bernd Meyer. 1999. “Characterization of Ligand Binding by Saturation Transfer Difference NMR Spectroscopy.” *Angewandte Chemie - International Edition* 38 (12): 1784–88. https://doi.org/10.1002/(SICI)1521-3773(19990614)38:12<1784::AID-ANIE1784>3.0.CO;2-Q.

McMullan, G., S. Chen, R. Henderson, and A. R. Faruqi. 2009. “Detective Quantum Efficiency

of Electron Area Detectors in Electron Microscopy." *Ultramicroscopy* 109 (9): 1126–43. https://doi.org/10.1016/j.ultramic.2009.04.002.

McMullan, G., A. R. Faruqi, and R. Henderson. 2016. *Direct Electron Detectors*. *Methods in Enzymology*. 1st ed. Vol. 579. Elsevier Inc. https://doi.org/10.1016/bs.mie.2016.05.056.

Meneton, Pierre, Johannes Loffing, and David G. Warnock. 2004. "Sodium and Potassium Handling by the Aldosterone-Sensitive Distal Nephron: The Pivotal Role of the Distal and Connecting Tubule." *American Journal of Physiology - Renal Physiology* 287 (4 56-4): 593–601. https://doi.org/10.1152/ajprenal.00454.2003.

Metzger, Thomas G., and David M. Ferguson. 1995. "On the Role of Extracellular Loops of Opioid Receptors in Conferring Ligand Selectivity." *FEBS Letters* 375 (1–2): 1–4. https://doi.org/10.1016/0014-5793(95)01185-H.

Michell, R. H., C. J. Kirk, and M. M. Billah. 1979. "Hormonal Stimulation of Phosphatidylinositol Breakdown, with Particular Reference to the Hepatic Effects of Vasopressin." *Biochemical Society Transactions* 7 (5): 861–65. https://doi.org/10.1042/bst0070861.

Miner, Jeffrey H. 2012. "The Glomerular Basement Membrane Jeffrey." *Exp Cell Res* 318 (9): 973–78. https://doi.org/10.3217/jucs-021-03-0384.

Møller, Thor C., David Moreno-Delgado, Jean-Philippe Pin, and Julie Kniazeff. 2017. "Class C G Protein-Coupled Receptors: Reviving Old Couples with New Partners." *Biophysics Reports* 3 (4–6): 57–63. https://doi.org/10.1007/s41048-017-0036-9.

Morel, Alain, Anne-Marie O'Carroll, Michael J. Brownstein, and Stephen J. Lolaft. 1992. "Molecular Cloning and Expression of a Rat Via Arginine Vasopressin Receptor." *Nature* 359: 710–13. file:///C:/Users/ASUS/Desktop/Rujukan PhD/p21/xiong1993.pdf.

Morel, Francois, and Serge Jard. 1963. " Inhibition of Frog (Rana Esculenta) Antidiuretic Action of Vasotocin by Some Analogues ." *American Journal of Physiology-Legacy Content* 204 (2): 227–32. https://doi.org/10.1152/ajplegacy.1963.204.2.227.

Morello, Jean-Pierre, and Daniel G. Bichet. 2001. "Nephrogenic Diabetes Insipidus." *Pakistan Paediatric Journal* 35 (3): 169–70. https://doi.org/10.5005/jp/books/12074_22.

Morello, Jean Pierre, Michel Bouvier, Ulla E. Petäjä-Repo, and Daniel G. Bichet. 2000. "Pharmacological Chaperones: A New Twist on Receptor Folding." *Trends in*

Pharmacological Sciences 21 (12): 466–69. https://doi.org/10.1016/S0165-6147(00)01575-3.

Morello, Jean Pierre, Ali Salahpour, André Laperrière, Virginie Bernier, Marie Françoise Arthus, Michèle Lonergan, Ulla Petäjä-Repo, et al. 2000. "Pharmacological Chaperones Rescue Cell-Surface Expression and Function of Misfolded V2 Vasopressin Receptor Mutants." *Journal of Clinical Investigation* 105 (7): 887–95. https://doi.org/10.1172/JCI8688.

Morris, A J, and S Scarlata. 1997. "Regulation of Effectors by G-Protein Alpha- and Beta Gamma-Subunits. Recent Insights from Studies of the Phospholipase c-Beta Isoenzymes." *Biochemical Pharmacology* 54 (4): 429–35. http://www.ncbi.nlm.nih.gov/pubmed/9313768.

Mouillac, B., B. Chini, M. N. Balestre, J. Elands, S. Trumpp-Kallmeyer, J. Hoflack, M. Hibert, S. Jard, and C. Barberis. 1995. "The Binding Site of Neuropeptide Vasopressin V1a Receptor. Evidence for a Major Localization within Transmembrane Regions." *Journal of Biological Chemistry* 270 (43): 25771–77. https://doi.org/10.1074/jbc.270.43.25771.

Nakane, Takanori, Dari Kimanius, Erik Lindahl, and Sjors H.W. Scheres. 2018. "Characterisation of Molecular Motions in Cryo-EM Single-Particle Data by Multi-Body Refinement in RELION." *ELife* 7: 1–18. https://doi.org/10.7554/eLife.36861.

Nauli, Surya M., Francis J. Alenghat, Ying Luo, Eric Williams, Peter Vassilev, Xiaogang Li, Andrew E.H. Elia, et al. 2003. "Polycystins 1 and 2 Mediate Mechanosensation in the Primary Cilium of Kidney Cells." *Nature Genetics* 33 (2): 129–37. https://doi.org/10.1038/ng1076.

Nawal, Benabdellah, Hassan Izzedine, Intissar Haddiya, and Yassamine Bentata. 2019. "Nephrogenic Syndrome of Inappropriate Antidiuresis." *Pan African Medical Journal* 32: 1884–90. https://doi.org/10.11604/pamj.2019.32.210.6006.

Nejsum, Lene N., Marina Zelenina, Anita Aperia, Jørgen Frøkiaer, and Søren Nielsen. 2005. "Bidirectional Regulation of AQP2 Trafficking and Recycling: Involvement of AQP2-S256 Phosphorylation." *American Journal of Physiology - Renal Physiology* 288 (5 57-5): 930–38. https://doi.org/10.1152/ajprenal.00291.2004.

Nguyen, Anthony H, Alex R.B. Thomsen, Thomas J. Cahill, Rick Huang, Li Yin Huang, Tara Marcink, Oliver B Clarke, et al. 2019. "Structure of an Endosomal Signaling GPCR–G

Protein–β-Arrestin Megacomplex." *Nature Structural and Molecular Biology* 26 (12): 1123–31. https://doi.org/10.1038/s41594-019-0330-y.

Nishimoto, Goro, Marina Zelenina, Dailin Li, Masato Yasui, Anita Aperia, Søren Nielsen, and Angus C. Nairn. 1999. "Arginine Vasopressin Stimulates Phosphorylation of Aquaporin-2 in Rat Renal Tissue." *American Journal of Physiology - Renal Physiology* 276 (2 45-2). https://doi.org/10.1152/ajprenal.1999.276.2.f254.

"Notice MINIRIN®." 2011.

Okada, Tetsuji, Isolde Le Trong, Brian A. Fox, Craig A. Behnke, Ronald E. Stenkamp, and Krzysztof Palczewski. 2000. "X-Ray Diffraction Analysis of Three-Dimensional Crystals of Bovine Rhodopsin Obtained from Mixed Micelles." *Journal of Structural Biology* 130 (1): 73–80. https://doi.org/10.1006/jsbi.1999.4209.

Oldham, William M., and Heidi E. Hamm. 2008. "Heterotrimeric G Protein Activation by G-Protein-Coupled Receptors." *Nature Reviews Molecular Cell Biology* 9 (1): 60–71. https://doi.org/10.1038/nrm2299.

Oligny-Longpré, Geneviève, Maithé Corbani, Joris Zhou, Mireille Hogue, Gilles Guillon, and Michel Bouvier. 2012. "Engagement of β-Arrestin by Transactivated Insulin-like Growth Factor Receptor Is Needed for V2 Vasopressin Receptor-Stimulated ERK1/2 Activation." *Proceedings of the National Academy of Sciences of the United States of America* 109 (17). https://doi.org/10.1073/pnas.1112422109.

Orloff, J., and J. S. Handler. 1962. "The Similarity of Effects of Vasopressin, Adenosine-3',5'-Phosphate (Cyclic AMP) and Theophylline on the Toad Bladder." *The Journal of Clinical Investigation* 41 (4): 702–9. https://doi.org/10.1172/JCI104528.

Orlova, E. V., and H. R. Saibil. 2011. "Structural Analysis of Macromolecular Assemblies." *Nature Methods* 5 (1): 23. https://doi.org/10.1038/nmeth1160.

Ostermaier, Martin K., Christian Peterhans, Rolf Jaussi, Xavier Deupi, and Jörg Standfuss. 2014. "Functional Map of Arrestin-1 at Single Amino Acid Resolution." *Proceedings of the National Academy of Sciences of the United States of America* 111 (5): 1825–30. https://doi.org/10.1073/pnas.1319402111.

Palczewski, K., T. Kumasaka, T. Hori, C. A. Behnke, H. Motoshima, B. A. Fox, I. Le Trong, et al. 2000. "Crystal Structure of Rhodopsin: A G Protein-Coupled Receptor." *Science* 289

(5480): 739–45. https://doi.org/10.1126/science.289.5480.739.

Pan, Y., Metzenberg, A., Das, S., Jing, B., & Gitschier, J. n.d. “Mutations in the V2vasopressin Receptor Gene Are Associated with X-Linked Nephrogenic Diabetes Insipidus.”

Penczek, P.A., J. Zhu, R. Schröder, and J. Frank. 2018. “Three Dimensional Reconstruction With Contrast Transfer Compensation From Defocus Series” 11 (518): 232–39. https://doi.org/10.1142/9789813234864_0021.

Perkovska, Sanja, Catherine Méjean, Mohammed Akli Ayoub, Juan Li, Floriane Hemery, Maithé Corbani, Nadine Laguette, et al. 2018. “V1b Vasopressin Receptor Trafficking and Signaling: Role of Arrestins, G Proteins and Src Kinase.” *Traffic* 19 (1): 58–82. https://doi.org/10.1111/tra.12535.

Peterhans, Christian, Ciara C.M. Lally, Martin K. Ostermaier, Martha E. Sommer, and Jörg Standfuss. 2016. “Functional Map of Arrestin Binding to Phosphorylated Opsin, with and without Agonist.” *Scientific Reports* 6 (June): 1–15. https://doi.org/10.1038/srep28686.

Phalipou, Sylvie, Nathalie Cotte, Eric Carnazzi, René Seyer, Eve Mahe, Serge Jard, Claude Barberis, and Bernard Mouillac. 1997. “Mapping Peptide-Binding Domains of the Human V1a Vasopressin Receptor with a Photoactivatable Linear Peptide Antagonist.” *Journal of Biological Chemistry* 272 (42): 26936–26544. https://doi.org/10.1074/jbc.272.42.26536.

Phalipou, Sylvie, René Seyer, Nathalie Cotte, Christophe Breton, Claude Barberis, Marcel Hibert, and Bernard Mouillac. 1999. “ Docking of Linear Peptide Antagonists into the Human V 1a Vasopressin Receptor .” *Journal of Biological Chemistry* 274 (33): 23316–27. https://doi.org/10.1074/jbc.274.33.23316.

Pharmacol, Br J. 2000. “Produces Unique Cation-Permeable Currents.” *Nature* 230: 0–4.

Pin, Jean Philippe, Thierry Galvez, and Laurent Prézeau. 2003. “Evolution, Structure, and Activation Mechanism of Family 3/C G-Protein-Coupled Receptors.” *Pharmacology and Therapeutics* 98 (3): 325–54. https://doi.org/10.1016/S0163-7258(03)00038-X.

Postina, Rolf, Elzbieta Kojro, and Falk Fahrenholz. 1996. “Separate Agonist and Peptide Antagonist Binding Sites of the Oxytocin Receptor Defined by Their Transfer into the V2 Vasopressin Receptor.” *Journal of Biological Chemistry* 271 (49): 31593–601. https://doi.org/10.1074/jbc.271.49.31593.

Pradelles, Philippe, Jean Louis Morgat, Pierre Fromageot, Maryse Camier, Dominique Bonne,

Paul Cohen, Jo Bockaert, and Serge Jard. 1972. “Tritium Labelling of 8-Lysine Vasopressin and Its Purification by Affinity Chromatography on Sepharose Bound Neurophysins.” *FEBS Letters* 26 (1): 189–92.

Prosperi, Federica, Yoko Suzumoto, Pierluigi Marzuillo, Vincenzo Costanzo, Sabina Jelen, Anna Iervolino, Stefano Guarino, et al. 2020. “Characterization of Five Novel Vasopressin V2 Receptor Mutants Causing Nephrogenic Diabetes Insipidus Reveals a Role of Tolvaptan for M272R-V2R Mutation.” *Scientific Reports* 10 (1): 1–11. https://doi.org/10.1038/s41598-020-73089-x.

Punjani, Ali, and David J. Fleet. 2021. “3D Variability Analysis: Resolving Continuous Flexibility and Discrete Heterogeneity from Single Particle Cryo-EM.” *Journal of Structural Biology* 213 (2): 1–25. https://doi.org/10.1016/j.jsb.2021.107702.

Punjani, Ali, John L. Rubinstein, David J. Fleet, and Marcus A. Brubaker. 2017. “CryoSPARC: Algorithms for Rapid Unsupervised Cryo-EM Structure Determination.” *Nature Methods* 14 (3): 290–96. https://doi.org/10.1038/nmeth.4169.

Qi, Xiaofeng, Lucas Friedberg, Ryan De Bose-Boyd, Tao Long, and Xiaochun Li. 2020. “Sterols in an Intramolecular Channel of Smoothened Mediate Hedgehog Signaling.” *Nature Chemical Biology* 16 (12): 1368–75. https://doi.org/10.1038/s41589-020-0646-2.

Rahmeh, Rita, Marjorie Damian, Martin Cottet, Hélène Orcel, Christiane Mendre, Thierry Durroux, K. Shivaji Sharma, et al. 2012. “Structural Insights into Biased G Protein-Coupled Receptor Signaling Revealed by Fluorescence Spectroscopy.” *Proceedings of the National Academy of Sciences of the United States of America* 109 (17): 6733–38. https://doi.org/10.1073/pnas.1201093109.

Rajerison, R., J. Marchetti, C. Roy, J. Bockaert, and S. Jard. 1974. “The Vasopressin Sensitive Adenylate Cyclase of the Rat Kidney. Effect of Adrenalectomy and Corticosteroids on Hormonal Receptor Enzyme Coupling.” *Journal of Biological Chemistry* 249 (20): 6390–6400. https://doi.org/10.1016/S0021-9258(19)42170-4.

Rasmussen, Søren G.F., Hee Jung Choi, Juan Jose Fung, Els Pardon, Paola Casarosa, Pil Seok Chae, Brian T. Devree, et al. 2011. “Structure of a Nanobody-Stabilized Active State of the B2 Adrenoceptor.” *Nature* 469 (7329): 175–81. https://doi.org/10.1038/nature09648.

Rasmussen, Sŏren G.F., Brian T. Devree, Yaozhong Zou, Andrew C. Kruse, Ka Young Chung, Tong Sun Kobilka, Foon Sun Thian, et al. 2011. “Crystal Structure of the β 2 Adrenergic

Receptor-Gs Protein Complex." *Nature* 477 (7366): 549–57. https://doi.org/10.1038/nature10361.

Rayleigh. 1879. "Investigations in Optics, with Special Reference to the Spectroscope." *Philosophical Magazine* 8.

Reichold, Markus, Anselm A. Zdebik, Evelyn Lieberer, Markus Rapedius, Katharina Schmidt, Sascha Bandulik, Christina Sterner, et al. 2010. "KCNJ10 Gene Mutations Causing EAST Syndrome (Epilepsy, Ataxia, Sensorineural Deafness, and Tubulopathy) Disrupt Channel Function." *Proceedings of the National Academy of Sciences of the United States of America* 107 (32): 14490–95. https://doi.org/10.1073/pnas.1003072107.

Reimer, Ludwig, and H Kohl. 1997. *Transmission Electron Microscopy: Physics of Image Formation*. http://www.amazon.com/Transmission-Electron-Microscopy-Formation-Microanalysis/dp/3540625682.

Renal Physiology. 2010. *Miller's Anesthesia*. https://doi.org/10.1016/b978-0-443-06959-8.00018-2.

Richard Kitching, A., and Holly L. Hutton. 2016. "The Players: Cells Involved in Glomerular Disease." *Clinical Journal of the American Society of Nephrology* 11 (9): 1664–74. https://doi.org/10.2215/CJN.13791215.

Ring, Aaron M., Aashish Manglik, Andrew C. Kruse, Michael D. Enos, William I. Weis, K. Christopher Garcia, and Brian K. Kobilka. 2013. "Adrenaline-Activated Structure of β 2-Adrenoceptor Stabilized by an Engineered Nanobody." *Nature* 502 (7472): 575–79. https://doi.org/10.1038/nature12572.

Robben, J. H., N. V.A.M. Knoers, and P. M.T. Deen. 2005. "Characterization of Vasopressin V2 Receptor Mutants in Nephrogenic Diabetes Insipidus in a Polarized Cell Model." *American Journal of Physiology - Renal Physiology* 289 (2 58-2): 265–72. https://doi.org/10.1152/ajprenal.00404.2004.

Robertson. 1986. "1986 - Unknown - © 1986 Nature Publishing Group." *Nature*.

Robishaw, Janet D. 2012. "Preferential Assembly of G-Aβγ Complexes Directed by the γ Subunits." *Subcellular Biochemistry* 63 (May): 181–91. https://doi.org/10.1007/978-94-007-4765-4_10.

Robison, G. A., R. W. Butcher, and E. W. Sutherland. 1967. "Adenyl Cyclase As an Adrenergic

Receptor." *Annals of the New York Academy of Sciences* 139 (3): 703–23. https://doi.org/10.1111/j.1749-6632.1967.tb41239.x.

Rochdi, Moulay D., Gabriel A. Vargas, Eric Carpentier, Geneviève Oligny-Longpré, Stanford Chen, Abraham Kovoor, Stephen E. Gitelman, Stephen M. Rosenthal, Mark Von Zastrow, and Michel Bouvier. 2010. "Functional Characterization of Vasopressin Type 2 Receptor Substitutions (R137H/C/L) Leading to Nephrogenic Diabetes Insipidus and Nephrogenic Syndrome of Inappropriate Antidiuresis: Implications for Treatments." *Molecular Pharmacology* 77 (5): 836–45. https://doi.org/10.1124/mol.109.061804.

Rodrigo, Jordi, Ana Pena, Brigitte Murat, Miguel Trueba, Thierry Durroux, Gilles Guillon, and Didier Rognan. 2007. "Mapping the Binding Site of Arginine Vasopressin to V1a and V1b Vasopressin Receptors." *Molecular Endocrinology* 21 (2): 512–23. https://doi.org/10.1210/me.2006-0202.

Rohou, Alexis, and Nikolaus Grigorieff. 2015. "CTFFIND4: Fast and Accurate Defocus Estimation from Electron Micrographs." *Journal of Structural Biology* 192 (2): 216–21. https://doi.org/10.1016/j.jsb.2015.08.008.

Romann Julien. 2022. "L'imagerie Numérique Rapide Par Caméra Haute Vitesse," 47–50.

Rose, John P., Chia-Kuei Wu, Chwan-Deng Hsiao, Esther Breslow, and Bi-Cheng Wang. 1996. "Crystal Structure of the Neurophysin—Oxytocin Complex." *Nature* 3.

Rosenthal, Peter B., and Richard Henderson. 2003. "Optimal Determination of Particle Orientation, Absolute Hand, and Contrast Loss in Single-Particle Electron Cryomicroscopy." *Journal of Molecular Biology* 333 (4): 721–45. https://doi.org/10.1016/j.jmb.2003.07.013.

Saibil, Helen R. 2000. "Saibil2000," 1–8. papers3://publication/uuid/BBD264BB-1F72-477E-AC9B-386655ED8B48.

Sasaki, Sei, Motoko Chiga, Eriko Kikuchi, Tatemitsu Rai, and Shinichi Uchida. 2013. "Hereditary Nephrogenic Diabetes Insipidus in Japanese Patients: Analysis of 78 Families and Report of 22 New Mutations in AVPR2 and AQP2." *Clinical and Experimental Nephrology* 17 (3): 338–44. https://doi.org/10.1007/s10157-012-0726-z.

Sasaki, Sei, and Yumi Noda. 2007. "Aquaporin-2 Protein Dynamics within the Cell." *Current Opinion in Nephrology and Hypertension* 16 (4): 348–52.

https://doi.org/10.1097/MNH.0b013e32818b27bf.

Saxton, W. O., and W. Baumeister. 1982. “The Correlation Averaging of a Regularly Arranged Bacterial Cell Envelope Protein.” *Journal of Microscopy* 127 (2): 127–38. https://doi.org/10.1111/j.1365-2818.1982.tb00405.x.

Schafer, E A. 1895. “University College,” no. 1.

Scheerer, Patrick, and Martha E. Sommer. 2017. “Structural Mechanism of Arrestin Activation.” *Current Opinion in Structural Biology* 45: 160–69. https://doi.org/10.1016/j.sbi.2017.05.001.

Scheres, Sjors H.W., and Shaoxia Chen. 2012. “Prevention of Overfitting in Cryo-EM Structure Determination.” *Nat Methods* 9 (9): 853–854. https://doi.org/10.1038/nmeth.2115.Prevention.

Scheres, Sjors H W. 2012. “RELION: Implementation of a Bayesian Approach to Cryo-EM Structure Determination.” *Journal of Structural Biology* 180 (3): 519–30. https://doi.org/10.1016/j.jsb.2012.09.006.

Schertler, Gebhard F.X., Claudio Villa, and Richard Henderson. 1993. “Projection Structure of Rhodopsin.” *Nature* 362 (6422): 770–72. https://doi.org/10.1038/362770a0.

Schoessler, Conrad T. O. FongIrving L. SchwartzEdwin A. PopenoeLawrence SilverMary Anne. 1959. “ON THE MOLECULAR BONDING OF LYSINE VASOPRESSIN AT ITS RENAL RECEPTOR SITE.” *Journal of the American Chemical Society* 81 (10): 2592–93. https://doi.org/10.1021/ja01519a073.

Schulte, Gunnar. 2020. “Structural Insight into Class F Receptors – What Have We Learnt Regarding Agonist - Induced Activation ?” 126 (March 2019): 17–24. https://doi.org/10.1111/bcpt.13235.

Schultz, S. G. 1981. “Homocellular Regulatory Mechanisms in Sodium-Transporting Epithelia: Avoidance of Extinction by ‘Flush-Through.’” *American Journal of Physiology - Renal Fluid and Electrolyte Physiology* 10 (6): 579–90. https://doi.org/10.1152/ajprenal.1981.241.6.f579.

Schwartz, IL, Howard Rasmussen, Anne Schoessler, Lawrence Silver, and Conrad T Fong. 1960. “RELATION OF CHEMICAL ATTACHMENT TOPHYSIOLOGICAL ACTION OF VASOPRESSIN,” 1288–98.

Schwartz, L, H Rasmussen, and J Rudinger. 1964. “ACTIVITY OF NEUROHYPOPHYSIAL HORMONE ANALOGUES LACKINGA DISULFIDE BRIDGE” 530 (1957): 1044–45.

Sebti, Yeganeh, Soroush Sardari, Hamid Mir Mohammad Sadeghi, Mohammad Hossein Ghahremani, and Giulio Innamorati. 2015. “Study of V2 Vasopressin Receptor Hormone Binding Site Using in Silico Methods.” *Research in Pharmaceutical Sciences* 10 (4): 288–94.

Sena, Diniz M., Xiaojing Cong, Alejandro Giorgetti, Achim Kless, and Paolo Carloni. 2017. “Structural Heterogeneity of the μ-Opioid Receptor’s Conformational Ensemble in the Apo State.” *Scientific Reports* 8 (March): 1–7. https://doi.org/10.1038/srep45761.

Serradeil-Le Gal, Claudine, Colette Lacour, Gérard Valette, Georges Garcia, Loïc Foulon, Gérard Galindo, Lise Bankir, et al. 1996. “Characterization of SR 121463A, a Highly Potent and Selective, Orally Active Vasopressin V2 Receptor Antagonist.” *Journal of Clinical Investigation* 98 (12): 2729–38. https://doi.org/10.1172/JCI119098.

Serrano-Vega, Maria J., Francesca Magnani, Yoko Shibata, and Christopher G. Tate. 2008. “Conformational Thermostabilization of the B1-Adrenergic Receptor in a Detergent-Resistant Form.” *Proceedings of the National Academy of Sciences of the United States of America* 105 (3): 877–82. https://doi.org/10.1073/pnas.0711253105.

Shannon, Claude E. 1949. “Cominunication Theory in the Presence of Noise.” *Proceedings of the IRE* 37 (1): 10–21.

Shukla, Arun K., Aashish Manglik, Andrew C. Kruse, Kunhong Xiao, Rosana I. Reis, Wei Chou Tseng, Dean P. Staus, et al. 2013. “Structure of Active β-Arrestin-1 Bound to a G-Protein-Coupled Receptor Phosphopeptide.” *Nature* 497 (7447): 137–41. https://doi.org/10.1038/nature12120.

Shukla, Arun K, Gerwin H Westfield, Kunhong Xiao, Rosana I Reis, Li-yin Huang, Prachi Tripathi-shukla, Jiang Qian, et al. 2015. “Visualization of Arrestin Recruitment by a G Protein-Coupled Receptor” 512 (7513): 218–22. https://doi.org/10.1038/nature13430.Visualization.

Shumate, Wendy A, James P Calvet, Chan H Park, and Jared J Granthamt. 2017. “Renal Epithelial Fluid Secretion AMP” 3 (14): 2629–32.

Siehler, Sandra. 2009. “Regulation of RhoGEF Proteins by G 12/13-Coupled Receptors.”

British Journal of Pharmacology 158 (1): 41–49. https://doi.org/10.1111/j.1476-5381.2009.00121.x.

Sierra-Fonseca, Jorge A., Manuel Miranda, Siddhartha Das, and Sukla Roychowdhury. 2021. "The Bγ Subunit of Heterotrimeric G Proteins Interacts with Actin Filaments during Neuronal Differentiation." *Biochemical and Biophysical Research Communications* 549: 98–104. https://doi.org/10.1016/j.bbrc.2021.02.095.

Sigworth, Fred J., Peter C. Doerschuk, Jose Maria Carazo, and Sjors H W Scheres. 2010. *An Introduction to Maximum-Likelihood Methods in Cryo-EM*. *Methods in Enzymology*. 1st ed. Vol. 482. Elsevier Inc. https://doi.org/10.1016/S0076-6879(10)82011-7.

Simon, Melvin I, Michael P Strathmann, and Narasimhan Gautam. 1991. "Diversity of g Proteins." *Science (New York, N.Y.)* 252 (1971): 802–8.

Simon, P, J Y Le Goff, K S Ang, C Charasse, P Le Cacheux, and G Cam. 1996. "Epidemiologic Data, Clinical and Prognostic Features of Autosomal Dominant Polycystic Kidney Disease in a French Region." *Nephrologie* 17.

Sommer, Martha E., Klaus Peter Hofmann, and Martin Heck. 2012. "Distinct Loops in Arrestin Differentially Regulate Ligand Binding within the GPCR Opsin." *Nature Communications* 3: 910–95. https://doi.org/10.1038/ncomms2000.

Sommer, Martha E., W. Clay Smith, and David L. Farrens. 2006. "Dynamics of Arrestin-Rhodopsin Interactions: Acidic Phospholipids Enable Binding of Arrestin to Purified Rhodopsin in Detergent." *Journal of Biological Chemistry* 281 (14): 9407–17. https://doi.org/10.1074/jbc.M510037200.

Spanakis, Elias, Edrice Milord, and Claudia Gragnoli. 2008. "AVPR2 Variants and Mutations in Nephrogenic Diabetes Insipidus: Review and Missense Mutation Significance." *Journal of Cellular Physiology* 217 (3): 605–17. https://doi.org/10.1002/jcp.21552.

Spillmann, Martin, Larissa Thurner, Nina Romantini, Mirjam Zimmermann, Benoit Meger, Martin Behe, Maria Waldhoer, Gebhard F.X. Schertler, and Philipp Berger. 2020. "New Insights into Arrestin Recruitment to GPCRs." *International Journal of Molecular Sciences* 21 (14): 1–14. https://doi.org/10.3390/ijms21144949.

Staus, Dean P., Hongli Hu, Michael J. Robertson, Alissa L.W. Kleinhenz, Laura M. Wingler, William D. Capel, Naomi R. Latorraca, Robert J. Lefkowitz, and Georgios Skiniotis.

2020a. “Structure of the M2 Muscarinic Receptor–β-Arrestin Complex in a Lipid Nanodisc.” *Nature* 579 (7798): 297–302. https://doi.org/10.1038/s41586-020-1954-0.

Staus, Dean P., Ryan T. Strachan, Aashish Manglik, Biswaranjan Pani, Alem W. Kahsai, Tae Hun Kim, Laura M. Wingler, et al. 2016. “Allosteric Nanobodies Reveal the Dynamic Range and Diverse Mechanisms of G-Protein-Coupled Receptor Activation.” *Nature* 535 (7612): 448–52. https://doi.org/10.1038/nature18636.

Staus, Dean P, Hongli Hu, Michael J Robertson, Alissa L W Kleinhenz, Laura M Wingler, William D Capel, Naomi R Latorraca, Robert J Lefkowitz, and Georgios Skiniotis. 2020b. “Structure of the M2 Muscarinic Receptor–β-Arrestin Complex in a Lipid Nanodisc.” *Nature*. https://doi.org/10.1038/s41586-020-1954-0.

Steinbach, Peter J., and Bernard R. Brooks. 1994. “New Spherical-cutoff Methods for Long-range Forces in Macromolecular Simulation.” *Journal of Computational Chemistry* 15 (7): 667–83. https://doi.org/10.1002/jcc.540150702.

Streets, Andrew J., Bart E. Wagner, Peter C. Harris, Christopher J. Ward, and Albert C.M. Ong. 2009. “Erratum: Homophilic and Heterophilic Polycystin 1 Interactions Regulate E-Cadherin Recruitment and Junction Assembly in MDCK Cells (Journal of Cell Science Vol. 122 (1410-1417)).” *Journal of Cell Science* 122 (10): 1702. https://doi.org/10.1242/jcs.053603.

Subramanya, Arohan R., and David H. Ellison. 2014. “Distal Convoluted Tubule.” *Clinical Journal of the American Society of Nephrology* 9 (12): 2147–63. https://doi.org/10.2215/CJN.05920613.

Sugimoto, T., M. Saito, S. Mochizuki, Y. Watanabe, S. Hashimoto, and H. Kawashima. 1994. “Molecular Cloning and Functional Expression of a CDNA Encoding the Human V(1b) Vasopressin Receptor.” *Journal of Biological Chemistry* 269 (43): 27088–92. https://doi.org/10.1016/s0021-9258(18)47129-3.

Sutherland, Earl, and T W Rall. 1960. “THE RELATION OF ADENOSINE-3’, 5’-PHOSPHATE AND PHOSPHORYLASE TO THE ACTIONS OF CATECHOLAMINES AND OTHER HORMONES.” *Pharmacological Reviews* 12 (3): 265–99.

Sutton, R. Bryan, Sergey A. Vishnivetskiy, Justin Robert, Susan M. Hanson, Dayanidhi Raman, Barry E. Knox, Masahiro Kono, Javier Navarro, and Vsevolod V. Gurevich. 2005. “Crystal Structure of Cone Arrestin at 2.3 Å: Evolution of Receptor Specificity.” *Journal*

of Molecular Biology 354 (5): 1069–80. https://doi.org/10.1016/j.jmb.2005.10.023.

Suzuki, Nobuchika, Nicole Hajicek, and Tohru Kozasa. 2009. "Regulation and Physiological Functions of G12/13-Mediated Signaling Pathways." *NeuroSignals* 17 (1): 55–70. https://doi.org/10.1159/000186690.

Syrovatkina, Viktoriya, Kamela O. Alegre, Raja Dey, and Xin-Yun Huang. 2016. "Regulation, Signaling and Physiological Functions of G-Proteins." *Physiology & Behavior* 428 (19): 3850–68. https://doi.org/10.1016/j.jmb.2016.08.002.Regulation.

Szczepek, Michal, Florent Beyrière, Klaus Peter Hofmann, Matthias Elgeti, Roman Kazmin, Alexander Rose, Franz J. Bartl, et al. 2014. "Crystal Structure of a Common GPCR-Binding Interface for G Protein and Arrestin." *Nature Communications* 5 (May): 1–8. https://doi.org/10.1038/ncomms5801.

Tahtaoui, Chouaïb, Marie Noëlle Balestre, Philippe Klotz, Didier Rognan, Claude Barberis, Bernard Mouillac, and Marcel Hibert. 2003. "Identification of the Binding Sites of the SR49059 Nonpeptide Antagonist into the V1a Vasopressin Receptor Using Sulfydryl-Reactive Ligands and Cysteine Mutants as Chemical Sensors." *Journal of Biological Chemistry* 278 (41): 40010–19. https://doi.org/10.1074/jbc.M301128200.

Tang, Guang, Liwei Peng, Philip R. Baldwin, Deepinder S. Mann, Wen Jiang, Ian Rees, and Steven J. Ludtke. 2007. "EMAN2: An Extensible Image Processing Suite for Electron Microscopy." *Journal of Structural Biology* 157 (1): 38–46. https://doi.org/10.1016/j.jsb.2006.05.009.

Tate, Christopher G. 2012. "A Crystal Clear Solution for Determining G-Protein-Coupled Receptor Structures." *Trends in Biochemical Sciences* 37 (9): 343–52. https://doi.org/10.1016/j.tibs.2012.06.003.

Tegunov, Dimitry, and Patrick Cramer. 2018. "Real-Time Cryo-EM Data Pre-Processing with Warp." *BioRxiv*. https://doi.org/10.1101/338558.

Tenenbaum, Julie, Mohammed A. Ayoub, Sanja Perkovska, Anne Laure Adra-Delenne, Christiane Mendre, Bruno Ranchin, Giamperro Bricca, et al. 2009. "The Constitutively Active V2 Receptor Mutants Conferring NSIAD Are Weakly Sensitive to Agonist and Antagonist Regulation." *PLoS ONE* 4 (12): 1–6. https://doi.org/10.1371/journal.pone.0008383.

Terrillon, Sonia, Claude Barberis, and Michel Bouvier. 2004. “Heterodimerization of V1a and V2 Vasopressin Receptors Determines the Interaction with β-Arrestin and Their Trafficking Patterns.” *Proceedings of the National Academy of Sciences of the United States of America* 101 (6): 1548–53. https://doi.org/10.1073/pnas.0305322101.

Terrillon, Sonia, Thierry Durroux, Bernard Mouillac, Andreas Breit, Mohammed A. Ayoub, Magali Taulan, Ralf Jockers, Claude Barberis, and Michel Bouvier. 2003. “Oxytocin and Vasopressin V1a and V2 Receptors Form Constitutive Homo- and Heterodimers during Biosynthesis.” *Molecular Endocrinology* 17 (4): 677–91. https://doi.org/10.1210/me.2002-0222.

Terwilliger, Thomas C., Steven J. Ludtke, Randy J. Read, Paul D. Adams, and Pavel V. Afonine5. 2020. “Improvement of Cryo-EM Maps by Density Modification.” *Block Caving – A Viable Alternative?* 21 (1): 1–9. https://doi.org/10.1016/j.solener.2019.02.027.

Terwilliger, Thomas C, Oleg Sobolev, Pavel V Afonine, Paul D Adams, Bioscience Division, Los Alamos, Molecular Biophysics, Integrated Bioimaging Division, and Lawrence Berkeley National. 2018. “Automated Map Sharpening by Maximization of Detail and Connectivity Bioscience Division , Los Alamos National Laboratory , Mail Stop M888 , Los Alamos , NM , Molecular Biophysics and Integrated Bioimaging Division , Lawrence Berkeley National.”

Thibonnier, Marc, Patrick Coles, Doreen M. Conarty, Christine L. Plesnicher, and Menachem Shoham. 2000. “A Molecular Model of Agonist and Nonpeptide Antagonist Binding to the Human V1 Vascular Vasopressin Receptor.” *Journal of Pharmacology and Experimental Therapeutics* 294 (1): 195–203.

Thomson, G. P., and A. Reid. 1927. “Diffraction of Cathode Rays by a Thin Film [1].” *Nature*. https://doi.org/10.1038/119890a0.

Thon, F. 1971. “Phase Contrast Electron Microscopy.” *Microscopy in Material Sciences* 571–625.

Topf, Maya, Keren Lasker, Ben Webb, Haim Wolfson, Wah Chiu, and Andrej Sali. 2008. “Protein Structure Fitting and Refinement Guided by Cryo-EM Density.” *Structure* 16 (2): 295–307. https://doi.org/10.1016/j.str.2007.11.016.

Torres, Vicente, Olivier Devuyst, Arlene B. Chapman, Ron T. Gansevoort, Ronald D. Perrone, John Ouyang, Jaime D. Blais, Frank S. Czerwiec, and Olga Sergeyeva. 2016. “Rationale

and Design of a Clinical Trial Investigating Tolvaptan Safety and Efficacy in Autosomal Dominant Polycystic Kidney Disease." *Physiology & Behavior* 176 (1): 139–48. https://doi.org/10.1159/000456087.Rationale.

Torres, Vicente E., Arlene B. Chapman, Olivier Devuyst, Ron T. Gansevoort, Jared J. Grantham, Eiji Higashihara, Ronald D. Perrone, Holly B. Krasa, John Ouyang, and Frank S. Czerwiec. 2012. "Tolvaptan in Patients with Autosomal Dominant Polycystic Kidney Disease." *New England Journal of Medicine* 367 (25): 2407–18. https://doi.org/10.1056/nejmoa1205511.

Torres, Vicente E., Arlene B. Chapman, Olivier Devuyst, Ron T. Gansevoort, Ronald D. Perrone, Ann Dandurand, John Ouyang, Frank S. Czerwiec, and Jaime D. Blais. 2018. "Multicenter, Open-Label, Extension Trial to Evaluate the Long-Term Efficacy and Safety of Early versus Delayed Treatment with Tolvaptan in Autosomal Dominant Polycystic Kidney Disease: The TEMPO 4:4 Trial." *Nephrology Dialysis Transplantation* 33 (3): 477–89. https://doi.org/10.1093/ndt/gfx043.

Torres, Vicente E., Arlene B. Chapman, Olivier Devuyst, Ron T. Gansevoort, Ronald D. Perrone, Jennifer Lee, Molly E. Hoke, Alvin Estilo, and Olga Sergeyeva. 2021. "Multicenter Study of Long-Term Safety of Tolvaptan in Later-Stage Autosomal Dominant Polycystic Kidney Disease." *Clinical Journal of the American Society of Nephrology* 16 (1): 48–58. https://doi.org/10.2215/CJN.10250620.

Torres, Vicente E., Xiaofang Wang, Qi Qian, Stefan Somlo, Peter C. Harris, and Vincent H. Gattone. 2004. "Effective Treatment of an Orthologous Model of Autosomal Dominant Polycystic Kidney Disease." *Nature Medicine* 10 (4): 363–64. https://doi.org/10.1038/nm1004.

Tsukaguchi, Hiroyasu, Hiroaki Matsubara, Shigeru Taketani, Yasukiyo Mori, Tsutomu Seido, and Mitsuo Inada. 1995. "Rapid Publication" 96 (October): 2043–50.

Ufer, E., R. Postina, V. Gorbulev, and F. Fahrenholz. 1995. "Erratum: An Extracellular Residue Determines the Agonist Specificity of V2 Receptors (FEBS Letters 362 (1995) 19-23)." *FEBS Letters* 369 (2–3): 353.

Umenishi, Fuminori, Takefumi Narikiyo, Alain Vandewalle, and Robert W. Schrier. 2006. "CAMP Regulates Vasopressin-Induced AQP2 Expression via Protein Kinase A-Independent Pathway." *Biochimica et Biophysica Acta - Biomembranes* 1758 (8): 1100–

1105. https://doi.org/10.1016/j.bbamem.2006.06.001.

Vasiliauskaité-Brooks, Ieva, Robert D. Healey, Pascal Rochaix, Julie Saint-Paul, Rémy Sounier, Claire Grison, Thierry Waltrich-Augusto, et al. 2018. "Structure of a Human Intramembrane Ceramidase Explains Enzymatic Dysfunction Found in Leukodystrophy." *Nature Communications* 9 (1): 1–13. https://doi.org/10.1038/s41467-018-07864-w.

Velazhahan, Vaithish, Ning Ma, Gáspár Pándy-Szekeres, Albert J. Kooistra, Yang Lee, David E. Gloriam, Nagarajan Vaidehi, and Christopher G. Tate. 2021. "Structure of the Class D GPCR Ste2 Dimer Coupled to Two G Proteins." *Nature* 589 (7840): 148–53. https://doi.org/10.1038/s41586-020-2994-1.

Velazquez, H., and F. S. Wright. 1986. "Effects of Diuretic Drugs on Na, Cl, and K Transport by Rat Renal Distal Tubule." *American Journal of Physiology - Renal Fluid and Electrolyte Physiology* 250 (6 (19/6)). https://doi.org/10.1152/ajprenal.1986.250.6.f1013.

Venkatakrishnan, A. J., Xavier Deupi, Guillaume Lebon, Christopher G. Tate, Gebhard F. Schertler, and M. Madan Babu. 2013. "Molecular Signatures of G-Protein-Coupled Receptors." *Nature* 494 (7436): 185–94. https://doi.org/10.1038/nature11896.

Viegas, Aldino, João Manso, Franklin L. Nobrega, and Eurico J. Cabrita. 2011. "Saturation-Transfer Difference (STD) NMR: A Simple and Fast Method for Ligand Screening and Characterization of Protein Binding." *Journal of Chemical Education* 88 (7): 990–94. https://doi.org/10.1021/ed101169t.

Vigneau, Vincent Du, Charlotte Ressler, and Stuart Trippet. 1953. "The Sequence of Amino Acids in Oxytocin with a Proposal for the Structure of Oxytocin." *Journal of Chemical Information and Modeling* 53 (9): 1689–99. https://doi.org/10.1017/CBO9781107415324.004.

Vigneaud, Vincent du, Daxe T. Gish, and Panayotis G. Katsoyannis. 1954. "A Synthetic Preparation Possessing Biological Properties Associated with Arginine-Vasopressin." *Journal of the American Chemical Society* 76 (18): 4751–52. https://doi.org/10.1021/ja01647a089.

Vigneaud, Vincent Du, H. Claire Lawler, and Edwin A. Pofenoe. 1953. "Enzymatic Cleavage of Glycinamide From Vasopressin and a Proposed Structure For This Pressor-Antidiuretic Hormone of The Posterior Pituitary." *Journal of the American Chemical Society* 75 (19): 4880–81. https://doi.org/10.1021/ja01115a554.

Vigneaud, Vincent du, Charlotte Resslbr, John M. Swan, Carleton W. Roberts, and Panayotis G. Katsoyannis. 1954. “The Synthesis of Oxytocin.” *Journal of the American Chemical Society* 76 (12): 3115–21. https://doi.org/10.1021/ja01641a004.

Wacker, Daniel, Raymond C. Stevens, and Bryan L. Roth. 2017. “How Ligands Illuminate GPCR Molecular Pharmacology.” *Cell*. Cell Press. https://doi.org/10.1016/j.cell.2017.07.009.

Wacker, Daniel, Chong Wang, Vsevolod Katritch, Gye Won Han, Xi-ping Huang, John D Mccorvy, Yi Jiang, et al. 2014. “NIH Public Access Author Manuscript Science. Author Manuscript; Available in PMC 2014 May 03. Published in Final Edited Form as: Science. 2013 May 3; 340(6132): 615–619. Doi:10.1126/Science.1232808. Structural Features for Functional Selectivity at Seroto” 340 (6132): 615–19. https://doi.org/10.1126/science.1232808.Structural.

Wade, R. H. 1992. “A Brief Look at Imaging and Contrast Transfer.” *Ultramicroscopy* 46 (1–4): 145–56. https://doi.org/10.1016/0304-3991(92)90011-8.

Walker, H F, and R Redner. 1984. “Mixture Densities, Maximum Likelihood and the EM Algorithm” 26 (2): 195–239.

Waltenspühl, Yann, Jendrik Schöppe, Janosch Ehrenmann, Lutz Kummer, and Andreas Plückthun. 2020. “Crystal Structure of the Human Oxytocin Receptor.” *Science Advances* 6 (29): 1–12. https://doi.org/10.1126/sciadv.abb5419.

Walter Rosenthal, Anita Seibold, Anaid Antaramian, Michèle Lonergan, Marie-Francoise Arthus, Geoffrey N. Hendy, Mariel Birnbaumer & Daniel G. Bichet. 1992. “Molecular Identification of the Gene Responsible for Congenital Nephrogenic Diabetes Insipidus.” *Nature* 359: 710–13.

Wang, Chong, Huixian Wu, Tama Evron, Eyal Vardy, Gye Won Han, Xi Ping Huang, Sandy J. Hufeisen, et al. 2014. “Structural Basis for Smoothened Receptor Modulation and Chemoresistance to Anticancer Drugs.” *Nature Communications* 5. https://doi.org/10.1038/ncomms5355.

Wang, Jingjing, Tian Hua, and Zhi Jie Liu. 2020. “Structural Features of Activated GPCR Signaling Complexes.” *Current Opinion in Structural Biology* 63: 82–89. https://doi.org/10.1016/j.sbi.2020.04.008.

Wang, Lei, Jun Xu, Sheng Cao, Dapeng Sun, Heng Liu, Qiuyuan Lu, Zheng Liu, Yang Du, and Cheng Zhang. 2021. "Cryo-EM Structure of the AVP–Vasopressin Receptor 2–Gs Signaling Complex." *Cell Research*, 48–50. https://doi.org/10.1038/s41422-021-00483-z.

Wang, Tao, Zhuyin Li, Mary Ellen Cvijic, Litao Zhang, and Chi Shing Sum. 2004. "Measurement of CAMP for Gαs- and Gαi Protein-Coupled Receptors (GPCRs)." *Assay Guidance Manual*, no. Md: 1–21. http://www.ncbi.nlm.nih.gov/pubmed/29165978.

Wang, Xiaofang, Vincent Gattone, Peter C. Harris, and Vicente E. Torres. 2005. "Effectiveness of Vasopressin V2 Receptor Antagonists OPC-31260 and OPC-41061 on Polycystic Kidney Disease Development in the PCK Rat." *Journal of the American Society of Nephrology* 16 (4): 846–51. https://doi.org/10.1681/ASN.2004121090.

Webb, Benjamin, and Andrej Sali. 2017. "Protein Structure Modeling with MODELLER." *Methods Mol. Biol.* 1654 (39–54).

Wei, Huijun, Seungkirl Ahn, Sudha K. Shenoy, Sadashiva S. Karnik, László Hunyady, Louis M. Luttrell, and Robert J. Lefkowitz. 2003. "Independent β-Arrestin 2 and G Protein-Mediated Pathways for Angiotensin II Activation of Extracellular Signal-Regulated Kinases 1 and 2." *Proceedings of the National Academy of Sciences of the United States of America* 100 (19): 10782–87. https://doi.org/10.1073/pnas.1834556100.

Weis, William I, and Brian K Kobilka. 2018. "The Molecular Basis of G Protein-Coupled Receptor Activation." *Annual Review of Biochemistry*. https://doi.org/10.1146/annurev-biochem-060614-033910.

White, JF, N Noinaj, Y Shibata, J Love, B Kloss, F Xu, J Gvozenovic-Jeremic, et al. 2012. "Structure of the Agonist-Bound Neurotensin Receptor." *Nature* 409 (7421): 508–13. https://doi.org/10.1038/nature11558.Structure.

Wilden, U., S. W. Hall, and H. Kuhn. 1986. "Phosphodiesterase Activation by Photoexcited Rhodopsin Is Quenched When Rhodopsin Is Phosphorylated and Binds the Intrinsic 48-KDa Protein of Rod Outer Segments." *Proceedings of the National Academy of Sciences of the United States of America* 83 (5): 1174–78. https://doi.org/10.1073/pnas.83.5.1174.

Willaime, C. 1987. *Initiation à La Microscopie Electronique Par Transmition*.

Williams, David B., and C. Barry Carter. 1996. *Transmission Electron Microscopes*. *Bull Acad Sci USSR Phys Ser (Columbia Tech Transl)*. Vol. 32.

Wootten, Denise, John Simms, Laurence J. Miller, Arthur Christopoulos, and Patrick M. Sexton. 2013. “Polar Transmembrane Interactions Drive Formation of Ligand-Specific and Signal Pathway-Biased Family B G Protein-Coupled Receptor Conformations.” *Proceedings of the National Academy of Sciences of the United States of America* 110 (13): 5211–16. https://doi.org/10.1073/pnas.1221585110.

Wright, Shane C., Maria Consuelo Alonso Cañizal, Tobias Benkel, Katharina Simon, Christian Le Gouill, Pierre Matricon, Yoon Namkung, et al. 2018. “FZD5 Is a Gαq-Coupled Receptor That Exhibits the Functional Hallmarks of Prototypical GPCRs.” *Science Signaling* 11 (559): 1–15. https://doi.org/10.1126/scisignal.aar5536.

Wu, Chia Kuei, Bing Hu, John P. Rose, Zhi-Jie Liu, Tam L. Nguyen, Changsheng Zheng, Esther Breslow, and Bi-Cheng Wang. 2001. “Structures of an Unliganded Neurophysin and Its Vasopressin Complex: Implications for Binding and Allosteric Mechanisms.” *Protein Science* 10 (9): 1869–80. https://doi.org/10.1110/ps.10601.

Wu, Emilia L, Xi Cheng, Sunhwan Jo, Huan Rui, Kevin C Song, Eder M Dávila-, Yifei Qi, et al. 2015. “CHARMM-GUI Membrane Builder Toward Realistic Biological Membrane Simulations Emilia” 35 (27): 1997–2004. https://doi.org/10.1002/jcc.23702.CHARMM-GUI.

Xing, Changrui, Youwen Zhuang, Ting-Hai Xu, Zhiwei Feng, X. Edward Zhou, Maozi Chen, Lei Wang, et al. 2020. “Cryo-EM Structure of the Human Cannabinoid Receptor CB2-Gi Signaling Complex.” *Cell*, 1–10. https://doi.org/10.1016/j.cell.2020.01.007.

Xu, Zhaojun, Akira Hirasawa, Hitomi Shinoura, and Gozoh Tsujimoto. 1999. “Interaction of the α(1B)-Adrenergic Receptor with GC1q-R, a Multifunctional Protein.” *Journal of Biological Chemistry* 274 (30): 21149–54. https://doi.org/10.1074/jbc.274.30.21149.

Xufan, Tian, Dong Soo Kang, and Jeffrey L. Benovic. 2014. “β-Arrestins and G Protein-Coupled Receptor Trafficking.” *Handbook of Experimental Pharmacology* 219: 1–13. https://doi.org/10.1007/978-3-642-41199-1.

Yamamura, Y, S Nakamura, S Itoh, T Hirano, T Onogawa, T Yamashita, Y Yamada, et al. 1998. “OPC-41061, a Highly Potent Human Vasopressin V2-Receptor Antagonist: Pharmacological Profile and Aquaretic Effect by Single and Multiple Oral Dosing in Rats.” *Journal of Pharmacology and Experimental Therapeutics*.

Yamamura, Yoshitaka, Hidenori Ogawa, Hiroshi Yamashita, Tomihiko Chihara, Hisashi

Miyamoto, Shigeki Nakamura, Toshiyuki Onogawa, et al. 1992. “Characterization of a Novel Aquaretic Agent, OPC-31260, as an Orally Effective, Nonpeptide Vasopressin V2 Receptor Antagonist.” *British Journal of Pharmacology* 105 (4): 787–91. https://doi.org/10.1111/j.1476-5381.1992.tb09058.x.

Yang, Dehua, Qingtong Zhou, Viktorija Labroska, Shanshan Qin, Sanaz Darbalaei, Yiran Wu, Elita Yuliantie, et al. 2021. “G Protein-Coupled Receptors: Structure- and Function-Based Drug Discovery.” *Signal Transduction and Targeted Therapy* 6 (1). https://doi.org/10.1038/s41392-020-00435-w.

Ye, Libin, Ned Van Eps, Marco Zimmer, Oliver P. Ernst, and R. Scott Prosser. 2016. “Activation of the A 2A Adenosine G-Protein-Coupled Receptor by Conformational Selection.” *Nature* 533: 265–68. https://doi.org/10.1038/nature17668.

Yersin, C., P. Bovet, J. P. Wauters, D. F. Schorderet, G. Pescia, and F. Paccaud. 1997. “Frequency and Impact of Autosomal Dominant Polycystic Kidney Disease in the Seychelles (Indian Ocean).” *Nephrology Dialysis Transplantation* 12 (10): 2069–74. https://doi.org/10.1093/ndt/12.10.2069.

Yin, Wanchao, Zhihai Li, Mingliang Jin, Yu-ling Yin, Parker W De Waal, Kuntal Pal, Yanting Yin, et al. 2019. “A Complex Structure of Arrestin-2 Bound to a G Protein-Coupled Receptor.”

Yin, Wanchao, Zhihai Li, Mingliang Jin, Yu Ling Yin, Parker W. de Waal, Kuntal Pal, Yanting Yin, et al. 2019. “A Complex Structure of Arrestin-2 Bound to a G Protein-Coupled Receptor.” *Cell Research* 29 (12): 971–83. https://doi.org/10.1038/s41422-019-0256-2.

Yip, Ka Man, Niels Fischer, Elham Paknia, Ashwin Chari, and Holger Stark. 2020. “Atomic-Resolution Protein Structure Determination by Cryo-EM.” *Nature* 587 (7832): 157–61. https://doi.org/10.1038/s41586-020-2833-4.

Yu, Lingbo, Robert R. Snapp, and Michael Radermacher. 2012. “Projection-Base Volume Alignment.” *Microscopy and Microanalysis* 18 (S2): 66–67. https://doi.org/10.1017/S1431927612002188.

Yuan, Shuguang, Zhenquan Hu, Slawomir Filipek, and Horst Vogel. 2015. “W2466.48 Opens a Gate for a Continuous Intrinsic Water Pathway during Activation of the Adenosine A2A Receptor.” *Angewandte Chemie - International Edition* 54 (2): 556–59. https://doi.org/10.1002/anie.201409679.

Zaoral, M, J Kolc, and F Sorm. 1967. “LXXI.Synthesis of 1-Deamino-8-D-γ-Aminobutyrine Vasopressin, 1-Deami-No-8-D-Lysine Vasopressin, and 1-Deamino-8-D-Arginine Vasopressin.” *Collection of Czechoslovak Chemical Communications*.

Zhan, Xuanzhi, Luis E. Gimenez, Vsevolod V. Gurevich, and Benjamin W. Spiller. 2011. “Crystal Structure of Arrestin-3 Reveals the Basis of the Difference in Receptor Binding between Two Non-Visual Subtypes.” *Journal of Molecular Biology* 406 (3): 467–78. https://doi.org/10.1016/j.jmb.2010.12.034.

Zhang, Kai. 2016. “Gctf: Real-Time CTF Determination and Correction.” *Journal of Structural Biology* 193 (1): 1–12. https://doi.org/10.1016/j.jsb.2015.11.003.

Zhang, Kaiming, Grigore D. Pintilie, Shanshan Li, Michael F. Schmid, and Wah Chiu. 2020. *Resolving Individual Atoms of Protein Complex by Cryo-Electron Microscopy*. *Cell Research*. Vol. 30. https://doi.org/10.1038/s41422-020-00432-2.

Zhang, Xin, Matthew J. Belousoff, Peishen Zhao, Albert J. Kooistra, Tin T. Truong, Sheng Yu Ang, Christina Rye Underwood, Thomas Egebjerg, Petr Šenel, Gregory D. Stewart, Yi Lynn Liang, Alisa Glukhova, Hari Venugopal, Arthur Christopoulos, Sebastian G.B. Furness, et al. 2020. “Differential GLP-1R Binding and Activation by Peptide and Non-Peptide Agonists.” *Molecular Cell* 80 (3): 485-500.e7. https://doi.org/10.1016/j.molcel.2020.09.020.

Zhang, Xin, Matthew J Belousoff, Peishen Zhao, Albert J Kooistra, Tin T Truong, Yu Ang, Christina Rye Underwood, Thomas Egebjerg, Petr Šenel, Gregory D Stewart, Lynn Liang, Alisa Glukhova, Hari Venugopal, Arthur Christopoulos, G B Sebastian, et al. 2020. “Differential GLP-1R Binding and Activation by Peptide and Non-Peptide Agonists.”

Zheng, Shawn Q., Eugene Palovcak, Jean Paul Armache, Kliment A. Verba, Yifan Cheng, and David A. Agard. 2017. “MotionCor2: Anisotropic Correction of Beam-Induced Motion for Improved Cryo-Electron Microscopy.” *Nature Methods* 14 (4): 331–32. https://doi.org/10.1038/nmeth.4193.

Zhong, Ellen D., Tristan Bepler, Bonnie Berger, and Joseph H. Davis. 2020. “Title: CryoDRGN: Reconstruction of Heterogeneous Structures from Cryo-Electron Micrographs Using Neural Networks Authors:” *Nature Methods*.

Zhou, Fulai, Chenyu Ye, Xiaomin Ma, Wanchao Yin, Tristan I. Croll, Qingtong Zhou, Xinheng He, et al. 2021. “Molecular Basis of Ligand Recognition and Activation of Human V2

Vasopressin Receptor." *Cell Research*, 10–12. https://doi.org/10.1038/s41422-021-00480-2.

Zhou, Qingtong, Dehua Yang, Meng Wu, Yu Guo, Wanjing Guo, Li Zhong, Xiaoqing Cai, et al. 2019. "Common Activation Mechanism of Class a GPCRs." *ELife* 8: 1–31. https://doi.org/10.7554/eLife.50279.

Zhou, X. Edward, Yuanzheng He, Parker W. de Waal, Xiang Gao, Yanyong Kang, Ned Van Eps, Yanting Yin, et al. 2017. "Identification of Phosphorylation Codes for Arrestin Recruitment by G Protein-Coupled Receptors." *Cell* 170 (3): 457-469.e13. https://doi.org/10.1016/j.cell.2017.07.002.

Zhu, X, S Gilbert, M Birnbaumer, and L Birnbaumer. 1994. "Dual Signaling Potential Is Common among Gs-Coupled Receptors and Dependent on Receptor Density." *Molecular Pharmacology* 46: 460–69.

Zivanov, Jasenko, Takanori Nakane, Bjorn Forsbeg, Dari Kimanius, Wim J.H. Hagen, Erik Lindhal, and Sjors H.W. Scheres. 2018. "RELION-3 : New Tools for Automated High-Resolution Cryo-EM Structure Determination." *BioRxiv*, 1–38. https://doi.org/10.1101/421123.

Zwier, Jurriaan M., Thomas Roux, Martin Cottet, Thierry Durroux, Stephanie Douzon, Sara Bdioui, Nathalie Gregor, et al. 2010. "A Fluorescent Ligand-Binding Alternative Using Tag-Lite Technology." *Journal of Biomolecular Screening* 15 (10): 1248–59. https://doi.org/10.1177/1087057110384611.

SCIENCE ADVANCES | RESEARCH ARTICLE

STRUCTURAL BIOLOGY

Cryo–electron microscopy structure of the antidiuretic hormone arginine-vasopressin V2 receptor signaling complex

Julien Bous[1,2], Hélène Orcel[1], Nicolas Floquet[3†], Cédric Leyrat[1†], Joséphine Lai-Kee-Him[2], Gérald Gaibelet[1‡], Aurélie Ancelin[2§], Julie Saint-Paul[1‖], Stefano Trapani[2], Maxime Louet[3], Rémy Sounier[1], Hélène Déméné[2], Sébastien Granier[1]*, Patrick Bron[2]*, Bernard Mouillac[1]*

The antidiuretic hormone arginine-vasopressin (AVP) forms a signaling complex with the V2 receptor (V2R) and the G_s protein, promoting kidney water reabsorption. Molecular mechanisms underlying activation of this critical G protein–coupled receptor (GPCR) signaling system are still unknown. To fill this gap of knowledge, we report here the cryo–electron microscopy structure of the AVP-V2R-G_s complex. Single-particle analysis revealed the presence of three different states. The two best maps were combined with computational and nuclear magnetic resonance spectroscopy constraints to reconstruct two structures of the ternary complex. These structures differ in AVP and G_s binding modes. They reveal an original receptor-G_s interface in which the $G\alpha_s$ subunit penetrates deep into the active V2R. The structures help to explain how V2R R137H or R137L/C variants can lead to two severe genetic diseases. Our study provides important structural insights into the function of this clinically relevant GPCR signaling complex.

INTRODUCTION

The biological actions of arginine-vasopressin (AVP), a cyclic nonapeptide, are mediated through three G protein–coupled receptor (GPCR) subtypes, V1a, V1b, and V2 (*1*). In addition, AVP is able to activate the related oxytocin (OT) receptor (OTR) (*2*). The V2 receptor (V2R) is mainly expressed at the basolateral membrane of principal cells of the kidney collecting ducts and governs the crucial physiological function of body water homeostasis (*3*). Binding of AVP to the V2R increases cyclic adenosine monophosphate (cAMP) intracellular level via coupling to the adenylyl cyclase stimulatory G_s protein, leading to activation of protein kinase A, phosphorylation of aquaporin 2 water channels (*4*), and, ultimately, to water reabsorption and urine concentration. Activation of the V2R also elicits arrestin-dependent pathways such as receptor internalization and mitogen-activated protein (MAP) kinase phosphorylation associated with cell growth and proliferation (*5*, *6*). This GPCR is involved in many water balance disorders (hyponatremia consecutive to congestive heart failure, hypertension, or hepatic cirrhosis) and voiding disorders (incontinence and nocturia) and, hence, constitutes a major therapeutic target (*7*). Moreover, inactivating and constitutively active mutations in the V2R sequence are responsible for two rare X-linked genetic diseases with opposite clinical outcomes: (i) congenital nephrogenic diabetes insipidus (cNDI) characterized by excessive urine voiding (*8*) and (ii) nephrogenic syndrome of inappropriate antidiuresis (NSIAD) characterized by excessive water loading and hyponatremia (*9*). V2R is also a target for treating autosomal dominant polycystic kidney disease, the most frequent Mendelian inherited disorder affecting millions of people worldwide (*10*). This pathology results from increased cell proliferation, apoptosis, and dedifferentiation, in which cAMP- and MAP kinase–dependent signaling pathways are highly activated.

The structural biology of GPCRs has made substantial progress during the past decade with a wealth of information about ligand binding and G protein coupling that shed light on structural and dynamic aspects of their function (*11*, *12*). V2R, similar to many GPCRs, has been refractory to high-resolution structure determination. Cryo–electron microscopy (cryo-EM) has emerged as a powerful method for the determination of challenging membrane protein structures (*13*), particularly when the intrinsic structural dynamics of the target prevents the use of crystallogenesis. A growing list of GPCR–G protein complex structures has thus been determined (*14*, *15*), revealing key molecular mechanisms of agonist binding and G protein (G_i, G_s, G_q, and G_o) coupling to class A and class B GPCRs. Here, we have developed an in vitro purification strategy to reconstitute the GPCR signaling complex comprising the AVP-bound V2R and the heterotrimeric G_s protein stabilized with the nanobody Nb35. Cryo-EM single-particle analysis revealed the presence of three distinct populations of the ternary complex with two best maps at a mean resolution of 4.0 and 4.1 Å. A novel hybrid approach was used to build both corresponding structures. Analyses of the structural features of the distinct conformations provide unprecedented molecular insights into the dynamic process of ternary complex formation between the hormone AVP, the V2R, and the G_s protein.

RESULTS

Determination of the AVP-V2R-G_s-Nb35 complex structure

To improve the expression of the human V2R and facilitate its purification, we constructed a receptor version with a hemagglutinin signal peptide followed by a flag tag at its N terminus and a twin strep tag at its C terminus (fig. S1A). In addition, N22 was substituted

[1]Institut de Génomique Fonctionnelle, Université de Montpellier, CNRS, INSERM, 34094 Montpellier cedex 5, France. [2]Centre de Biochimie Structurale, Université de Montpellier, CNRS, INSERM, 34090 Montpellier, France. [3]Institut des Biomolécules Max Mousseron, Université de Montpellier, CNRS, ENSCM, 34093 Montpellier cedex 5, France.
*Corresponding author. Email: sebastien.granier@igf.cnrs.fr (S.G.); patrick.bron@cbs.cnrs.fr (P.B.); bernard.mouillac@igf.cnrs.fr (B.M.)
†These authors contributed equally to this work.
‡Present address: AB Science, 13288 Marseille cedex 9, France.
§Present address: Laboratoire CiTCoM, CNRS UMR8038, Faculté de Pharmacie, Université Paris Descartes, 75006 Paris, France.
‖Present address: iMAb, Institut de Recherche en Cancérologie de Montpellier, 34298 Montpellier cedex 5, France.

with a glutamine residue to avoid *N*-glycosylation, and C358 was mutated into an alanine to eliminate the possibility of intermolecular disulfide bridges. Apart from receptor engineering designed uniquely for expression and purification purpose and unlike many of the recently published GPCR structures, we did not modify the receptor sequence (the V2R is a wild-type from T31 to G345). Our aim was to avoid possible artifacts and irrelevant information due to the introduction of mutations in the transmembrane (TM) core domain of the receptor, even if this was at the expense of lower-resolution cryo-EM data. Moreover, and before the recombinant expression of the receptor in Sf9 insect cells, the pharmacological properties of the engineered V2R were verified in human embryonic kidney (HEK) mammalian cells (fig. S2, A to C). The cryo-EM version of the V2R bound a fluorescent nonpeptide antagonist and AVP with high affinity [dissociation constant (K_d) and inhibition constant (K_i) = 2.27 ± 0.24 nM (n = 3) and 1.12 ± 0.5 nM (n = 3), respectively], close to the values determined for a wild-type V2R (*16*). Moreover, the receptor was proven to be functional as it was able to stimulate cAMP accumulation upon AVP binding [K_{act} = 2.05 ± 0.11 nM (n = 4), similar to the wild-type V2R in transfected cells (*17*)].

Following infection of Sf9 cells with the V2R recombinant baculovirus, the receptor was purified through an orthogonal chromatography procedure (fig. S1B). It was then mixed with the heterotrimeric G_s protein and the Nb35 in the presence of an excess of AVP. The purified complex displayed a monodisperse peak on size exclusion chromatography (SEC) (fig. S1C), and SDS gel analyses confirmed the presence of all components of the complex [the V2R, the three subunits of the G protein (α_s, β_1, and γ_2), and the Nb35; fig. S1D]. The complex was first characterized using negative stain electron microscopy (NS-EM), before the preparation of vitrified samples onto Quantifoil grids for cryo-EM single-particle analysis.

Images of the complex first recorded in NS-EM revealed a homogeneous distribution of the particles, as observed from two-dimensional (2D) class averages (fig. S3, A and B). More than 60% of the particles correspond to the complex. A reconstruction at 20 Å clearly showed the micelle of detergent and the G protein–Nb35 components. Fitting the 3D model of the crystal structure of the β_2-adrenergic receptor (β_2AR)–G_s-Nb35 complex (*18*) in this low-resolution reconstruction map confirms that V2R-G_s-Nb35 displays typical structural features of a TM signaling GPCR complex (fig. S3C). Moreover, the addition of the specific V2R nonpeptide antagonist SR121463 (*19*) and guanosine 5′-O-(3-thiotriphosphate) (GTPγS) to the purified complex led to the dissociation of the different components (fig. S3D), confirming the functionality of the signaling particle.

After validation of cryo-EM grid sample vitrification, a total number of 25,770 movies were recorded, with 3.5 million particles picked and sorted out for further data processing (figs. S4 and S5). After 3D classification of projections and 3D refinement, we identified three different conformational states of the complex, referred to as loose (L), tight-1 (T1), and tight-2 (T2). Reconstruction of each state was at 4.2, 4.5, and 4.7 Å, with a distribution of 16, 48, and 36%, respectively (fig. S4), the local resolution varying from 3.2 to 6.4 Å (fig. S5C). Using the recent algorithm developed to enhance cryo-EM maps by density modification (*20*), the resolution of density maps were improved to 4.0 Å (L state), 4.1 Å (T1 state), and 4.5 Å (T2 state), respectively (Table 1, and figs. S4 to S6). This step enhanced the visibility of many details for some V2R TM regions (fig. S6, A and B), for the hormone AVP (fig. S6C), for the $G\alpha_s$ subunit (fig. S6D), and for $G\beta_2$ subunit (fig. S6E). The maps mainly differ in the angle of G_s-Nb35 with the receptor 7TM and may reflect an inherent high flexibility of the complex. A conformational heterogeneity analysis using multibody refinement revealed that more than 78% of the variance is accounted for by the four first eigenvectors related to rotations and translations between AVP-V2R and G_s-Nb35 (Fig. 1, A to C, and movie S1). The 4.5-Å map of the T2 state was not well enough resolved to compute a reliable structure. Therefore, only the L and T1 structures, referred to as L and T states, were used for further analysis (Table 1).

Because we could not unambiguously build the AVP in the calculated maps, we designed an original hybrid strategy based on a combination of cryo-EM maps, computational molecular dynamics simulations (MDSs), and experimental saturation transfer difference (STD) nuclear magnetic resonance (NMR) (Fig. 2 and figs. S7 to S10). First, the conformational sampling of the peptide-receptor complex was improved using the unbiased coarse-grained (CG) method coupled to replica exchange molecular dynamics (REMD) simulation protocol (Fig. 2Aand fig. S7). We successfully used this protocol to predict the binding modes of peptides in the class A GPCRs neurotensin receptor type 1 (NTSR1), C-X-C chemokine receptor type 4 (CXCR4), and growth hormone secretagogue receptor (GHSR) (*21*, *22*). Three independent CG-REMD simulations were run, together representing about 3 ms of cumulated simulation time (fig. S8). Each of the three simulations led to, respectively, 288, 306, and 302 clusters of peptide:receptor conformations. The first 10 most populated clusters (Fig. 2B) were identically retrieved among the three independent simulations, as shown by the root mean square deviation (RMSD) matrix (fig. S8) and represented more than 60% of the whole explored conformations. After addition of the G_s heterotrimer and Nb35 proteins, refinement of each of these clusters was performed in the L cryo-EM density map (Fig. 2C). At this step, we used the correlation-driven molecular dynamics (CDMD) method (*23*) while keeping advantage of using a CG representation for sampling speed and better agreement with the resolution of the maps (fig. S9). Fitting of each cluster was repeated five times. Typical curves of cross-correlation coefficients as a function of time for each CDMD show that the used protocol reached a "plateau" in each case, indicating the convergence of the fit for all clusters (fig. S10). Small variability of the position of the peptide among the five obtained models for clusters 2 and 5 (mean RMSD of 3.0 and 2.2 Å, respectively) and in a lower manner for the clusters 6 and 8 (mean RMSD of 3.2 and 3.6 Å, respectively) was seen (Fig. 2, D and E). The higher values obtained for the other clusters (in the range 4.8 to 8.7 Å) were explained by the upper starting position of the peptide in the pocket, finding more easily the density located at the surface of the receptor during the fitting procedure (Fig. 2E). Last, the CG models obtained from the fitting procedure were back-mapped to an all-atom (AA) representation. Minimization, MDSs, iterative manual adjustment, and real-space refinement were carried out to finalize AVP docking.

The AVP binding modes were further cross-validated using experimental STD NMR spectroscopy, which can efficiently monitor the binding and map the contact surface of a given ligand with its cognate GPCR (*24*, *25*). 1D STD spectra were thus recorded either on a mixture of AVP with V2R or on AVP alone (fig. S11, A and B). Intense STD signals were only observed in the presence of V2R, mostly for the aromatic protons of Y2 and F3 residues of AVP (Fig. 2, D and E, and fig. S11). The addition of the orthosteric antagonist tolvaptan (TVP) significantly attenuated the STD signals, demonstrating specific binding of AVP to the V2R orthosteric site

Table 1. Cryo-EM data collection, refinement, and validation statistics. PDB, Protein Data Bank; RMSD, root mean square deviation.

	AVP-V2R-G$\alpha_s\beta_1\gamma_2$-Nb35 (L state) (EMD-12128) (PDB code 7BB6)	AVP-V2R-G$\alpha_s\beta_1\gamma_2$-Nb35 (T state) (EMD-12129) (PDB code 7BB7)
Data collection and processing		
Magnification	165,000	165,000
Voltage (kV)	300	300
Electron exposure (e^-/Å^2)	50.19*/41.19†	50.19*/41.19†
Defocus range (μm)	−0.8 to −2.2	−0.8 to −2.2
Pixel size (Å)	0.81	0.81
Symmetry imposed	C1	C1
Initial particle images (no.)	3,566,007	3,566,007
Final particle images (no.)	147,524	420,953
Map resolution (Å)	4.2	4.4
FSC threshold	0.143	0.143
Map resolution range (Å)	3.2–5.6	3.8–6
Refinement		
Model resolution (Å)	4.2	4.4
FSC threshold	0.5	0.5
Model resolution range (Å)	3.2–5.6	3.8–6
Map improved resolution (Å) (cryoresolve)	4.0	4.1
Map sharpening *B* factor (Å^2)	−141.6	−75
Model composition		
Nonhydrogen atoms	7955	8040
Protein residues	1017	1022
Ligands	0	0
B factors (Å^2)		
Protein	87.61	72.14
Ligand	163.31	106.00
RMSD		
Bond lengths (Å)	0.007	0.007
Bond angles (°)	0.947	1.027
Validation		
MolProbity score	2.55	2.81
Clashscore	28.39	37.36
Poor rotamers (%)	0	0
Ramachandran plot		
Favored (%)	87.46	78.74
Allowed (%)	12.54	21.26
Disallowed (%)	0	0

*Dataset 1. †Dataset 2.

(fig. S11B). Calculation of normalized STD effects as $I_{STD} - I_{ref}/I_{ref}$ showed that the most intense effects were observed for the N-terminal cyclic part of AVP, with a strong involvement of the aromatic side chains of Y2 and F3 (and to a lesser extend C1), whereas the residues in the C-terminal tripeptide (P7, R8, and G9 amide) were less affected upon V2R binding (Fig. 2D). In addition, we compared these experimental STD values to the expected STD values from AA models issued from MDSs and subsequently refined with the density maps.

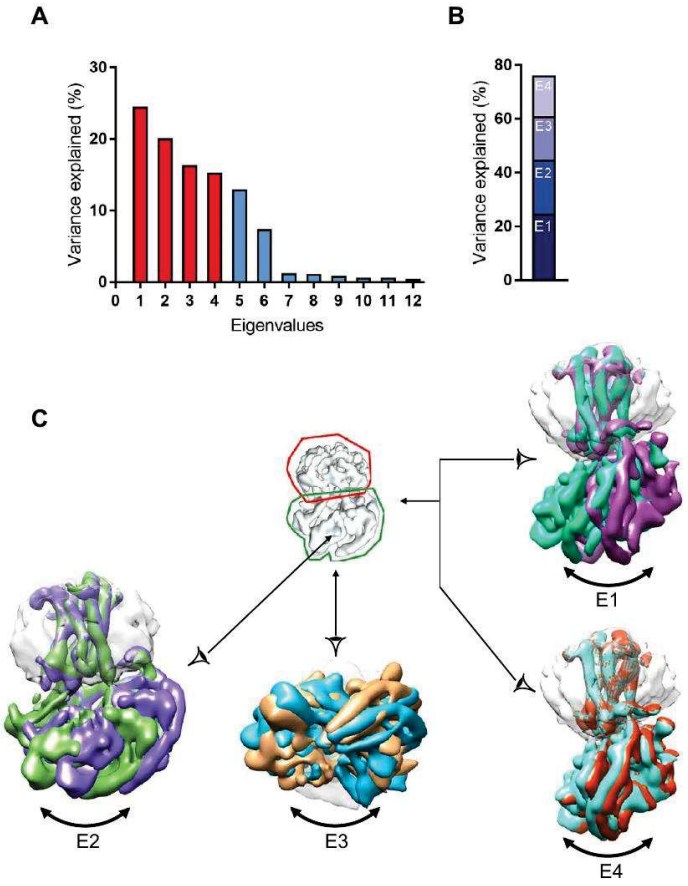

Fig. 1. Flexibility in the AVP-V2R-G_s-Nb35 complex. (**A**) The contribution of each of the 12 eigenvectors (numbered along *x* axis) to the variance of the overall final map is illustrated. (**B**) Eigenvectors 1 to 4 correspond to 78% of the variance. (**C**) Mask used for multibody refinement is shown in the middle, detergent micelle and V2R are surrounded by a red line, and G_s and Nb35 are surrounded by a green line. Maps corresponding to the four first vectors are illustrated, showing swing-like motion and tilting of G_s-Nb35 with respect to AVP-V2R. E4 is part of E1.

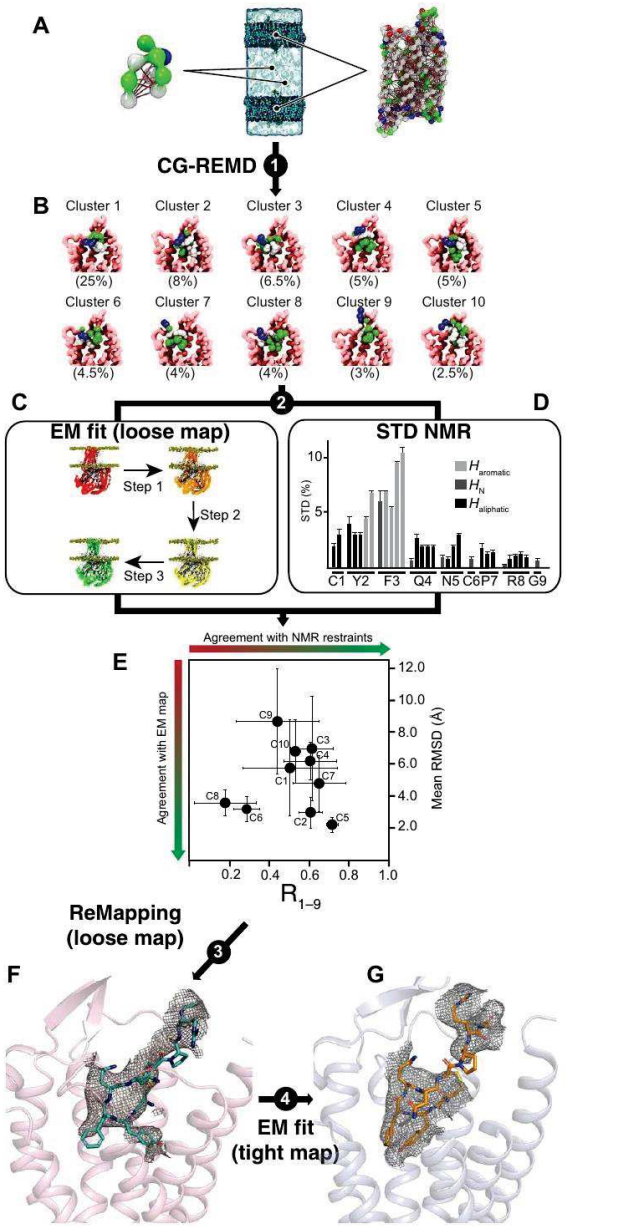

Fig. 2. Overview of the hybrid strategy: A combination of cryo-EM, computational, and NMR. (**A**) Schematic representation of the unbiased CG ab initio approach. The internal elastic networks used for both AVP (left) and V2R (right) are shown. The full system (center) used for the CG-REMD simulations included two receptors and two peptides. (**B**) Ten most populated clusters (67.5% of the whole conformations) obtained for the AVP-V2R complex after three independent CG-REMD simulations. (**C**) Schematic representation of the successive steps using the CDMD method to fit the models resulting from the CG-REMD simulations into the L cryo-EM map. (**D**) Mapping AVP contact surface by experimental STD NMR. The STD effect profile (in percentage) is shown as a function of AVP protons [aliphatic, N (backbone), and aromatic]. (**E**) Cross-correlation between computational and STD NMR. Variability of the position of AVP was calculated as mean RMSD values (in angstroms) after cross-comparison of five models resulting from the fitting procedure of each of the 10 clusters in the L density map. Cluster 5 showed the smaller variability (2.2 Å). Experimental STD values were compared to the expected STD values from all-atom models issued from MDSs, and correlation coefficients were calculated for the whole peptide (R_{1-9}). Cluster 5 appeared as the best cluster fitting to experimental STD values. (**F**) Building of the final L structure based on remapping cluster 5 into the L density map. (**G**) On the basis of the L structure, the T structure was built to match the T density map.

As explained in Materials and Methods, coefficient correlations between simulated and experimental STD values were calculated for the whole peptide (R_{1-9}). Cluster 5 fitted on L density map appeared as the best cluster fitting to experimental STD values (Fig. 2E).

On the basis of this approach, the L and T models were then built in a more conventional manner to match the density maps as closely as possible (Fig. 2, E and F, and Table 1). In the final models, side chains of most residues are clearly identifiable in the 7TM and helix 8 of the V2R in both structures (fig. S12, A and B). Intracellular loop 1 (ICL1) was well defined in the maps, as well as the contacts between V2R and the G_s protein. The α-helical domain of $G\alpha_s$ subunit was subtracted during single-particle analysis for high-resolution map refinement. ICL2, ICL3, and the C terminus of V2R were not seen in the density maps and were not constructed in the final models.

Overall architecture of the ternary complex

Both L and T AVP-V2-G_s ternary complexes present a typical GPCR–G protein architecture with the receptor 7TM helix bundle engaging the peptide agonist on the extracellular side and the $G\alpha_s$ C-terminal domain (α_5 helix) on the intracellular side (Fig. 3, A to D). However, the L and T states present large structural differences

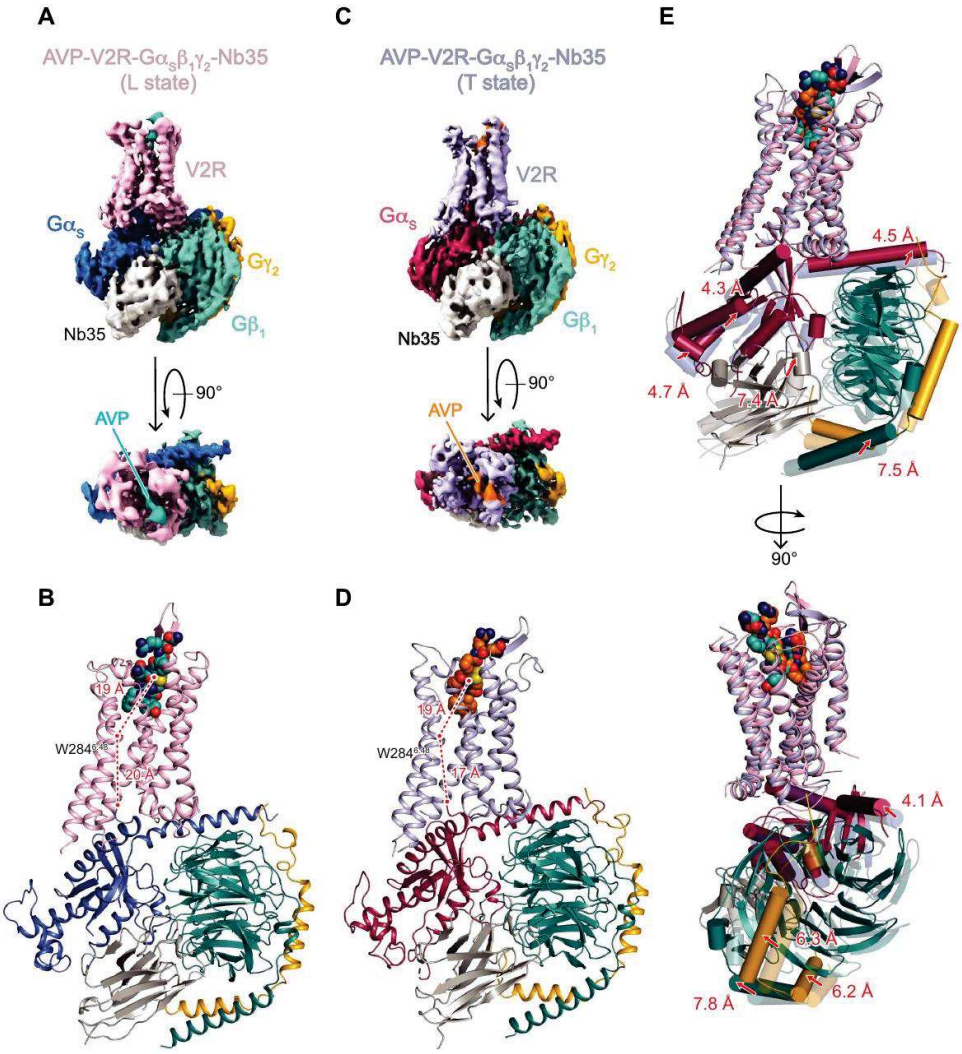

Fig. 3. Structures of AVP-V2R-G_s-Nb35 complexes in L and T conformations. (**A**) Orthogonal views of the cryo-EM density maps of the L state of the AVP-V2R-G_s-Nb35 complex and (**B**) corresponding model as ribbon representation. V2R is colored in pink, $G\alpha_s$ in dark blue, $G\beta_1$ in turquoise, $G\gamma_2$ in yellow, Nb35 in gray, and AVP in cyan. In (B), the distances between $W284^{6.48}$ (at its Cα carbon) and the AVP center of mass (COM) and between $W284^{6.48}$ and the C-terminal end of α_5 helix of G_s (at the Cα carbon of the free carboxylic acid) are shown. (**C** and **D**) Corresponding maps and model for the T state. V2R is colored in blue gray, $G\alpha_s$ in raspberry, $G\beta_1$ in turquoise, $G\gamma_2$ in yellow, Nb35 in gray, and AVP in orange. In (D), distances are measured as in (B). (**E**) L and T models are aligned on the V2R chains, and rotations/translations are shown by measuring displacement (in angstroms) of $G\alpha_s$, $G\beta_1$, $G\gamma_2$, and Nb35.

most notably in the position of the G protein heterotrimer relative to V2R (Fig. 3E). The α_5 helix interacts more tightly in the T state than in the L state (Fig. 3), inducing a translation of the whole G_s heterotrimer (Fig. 3E). In particular, the α_4 helix and the Ras-like domain of $G\alpha_s$ are translated from 4 and 5 Å between the L and T states, respectively. These movements position the α_N helix 5 Å closer to the receptor in the T state in comparison to the L state (Fig. 3E). Those Gα movements are also accompanied by a 7-Å translation of the Gβ N-terminal helix, a translation of the γ subunit of 6 Å and a translation of Nb35 of 7 Å (Fig. 3E).

The presence of several conformational states and the multibody refinement analysis reflect the dynamics of V2-G_s complex formation. From the final L structure model, a principal components analysis obtained from classical MDSs revealed similar dynamics and suggests that the conformations captured by the cryo-EM 3D reconstructions represent averaged states that are part of a much larger conformational ensemble (fig. S13, A to D). Although those differences are less pronounced that the ones recently described for the neurotensin receptor NTSR1-G_{i1} complexes (*26*), they further indicate that GPCR–G protein coupling is a dynamic process in which the G protein may explore different sets of conformations. The cryo-EM experimental structures appear to stem from sparsely populated regions of the conformational landscape of the signaling complex and at the junction between populated regions in principal component 1 space (fig. S13, A to D). The 3D reconstructions obtained from the maximum likelihood classification method (conformationally averaged substates), which select by repeated sifting clusters of homogeneous substates from the initial pool of particles, may not necessarily correspond to global energy minima conformations, highlighting the importance of using complementary

approaches to determining functionally relevant structures such as MDSs and NMR. Similar problems have been documented for other systems (*27*) and remain an area of possible improvement in the field.

AVP binding pocket within V2R and comparison with OTR-binding site

Our hybrid approach allowed us to build convincing models of AVP binding poses in both L and T structures. The final calculated structures present a central position of AVP in the orthosteric pocket of the V2R along the axis of the helical bundle (Figs. 4, A to C, and 5). The extracellular domains of the V2R are widely opened in both L and T conformations, a feature consistent with the accommodation of a cyclic peptide such as AVP (Fig. 5), and in agreement with the recently reported inactive OTR structure (*28*). In the L and T structures, AVP contacts residues from both TM helices and extracellular loops (Figs. 4A and 5, A to F) in agreement with what was originally proposed on the basis of pharmacological data (*29*). Consistent with its amphipathic nature, AVP interacts with two chemically distinct interfaces in a 15-Å-deep binding pocket to form both polar and hydrophobic contacts (Fig. 4, B and C).

While AVP conformations occupy a central position in both the L and T binding clefts, interesting changes are observed because of a translation of the Y2 residue side chain (from TM7 to TM3) and to a movement of the C-terminal tripeptide (inversion in R8 and G9-NH_2 positions) at the V2R surface (Figs. 4, B to D, and 5, A and B). The cyclic part of AVP (C1 to C6) and the P7 are buried into the cleft defined by the seven-helix bundle of V2R, leaving only R8 residue and C-terminal glycinamide exposed to the solvent (Fig. 5). In both the L and T structures, the C1-Y2-F3 hydrophobic motif of AVP binds deeper in the binding site, creating key contacts with the receptor (Figs. 4 and 5), in agreement with STD spectroscopy data (Fig. 2, D and E, and fig. S11).

V2R and OTR belong to the same subfamily of peptide class A GPCRs and share a common orthosteric binding site (*29*, *30*). Although V2R and OTR [Protein Data Bank (PDB) code 6TPK] structures (*28*) represent different GPCR conformations (active agonist-bound V2R versus inactive antagonist-bound OTR), it is interesting to compare the complete set of residues involved in the binding of the natural hormone AVP with the ones involved in retosiban binding to gain insights into ligand binding and efficacy in this receptor family (Figs. 4 and 5). Many OTR residues involved in the binding of retosiban are actually conserved among AVP/OTRs and also interact with AVP in the V2R (Figs. 4 and 5). The conserved $W^{6.48}$ and $F^{6.51}$ (Ballesteros-Weinstein numbering) in AVP/OTRs interact with the highly hydrophobic indanyl moiety of retosiban in the crystal structure of inactive OTR. AVP also makes contact with $F^{6.51}$ through its Y2 but is not in contact with $W^{6.48}$ in the V2R, probably because it is too bulky to bind deeper in the pocket. These data confirm that hydrophobic small-molecule nonpeptide antagonists and AVP partially superimpose at the bottom of the orthosteric binding pocket of AVP/OTRs (Figs. 4 and 5) (*31*–*33*).

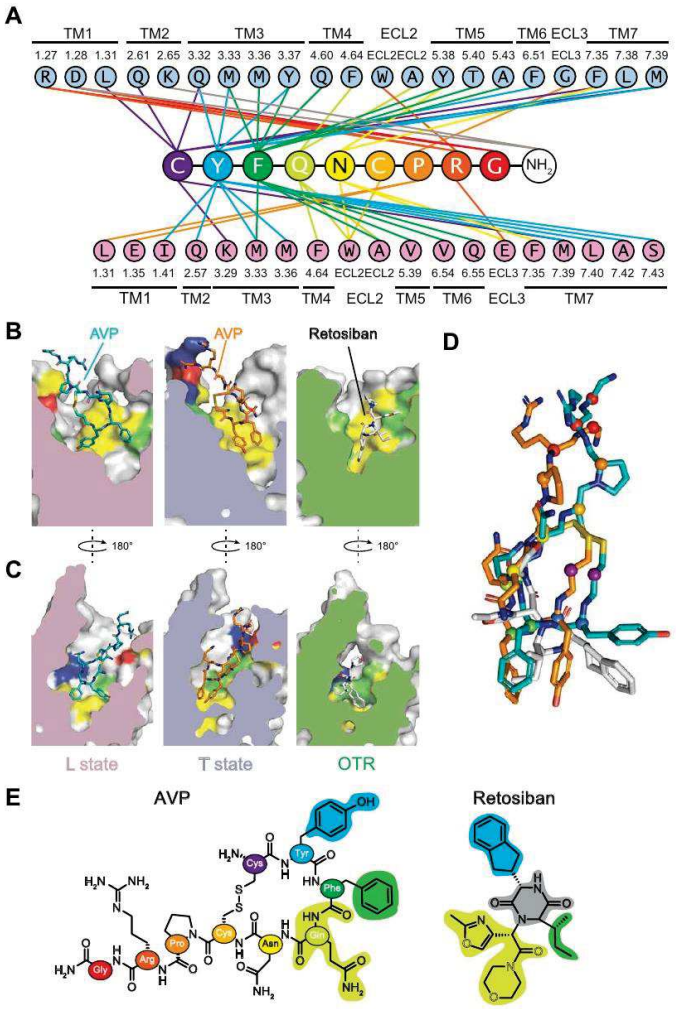

Fig. 4. AVP-binding site of the V2R, comparison with retosiban-binding site in OTR. (**A**) Direct contacts between AVP and V2R in L and T structures. Interactions (within a maximum of 5 Å in distance) are shown between each AVP residue (and the C-terminal amide) with V2R residues in the L structure (pink) and in the T structure (blue). All TM helices, extracellular loop 2 (ECL2), and ECL3 interact with the hormone AVP. V2R residues are labeled according to the Ballesteros-Weinstein numbering. Each residue from AVP is colored differently for clarity. (**B**) Side views of the binding pocket in the L and T structures and in the inactive structure of OTR. AVP binding modes in the L (pink) and T (light blue) structures are compared to that of the small-molecule antagonist retosiban in the OTR structure (green), all viewed from TM3. Residues from receptors that interact with AVP or retosiban are depicted in different colors: yellow for hydrophobic, green for polar, and red and dark blue for negatively and positively charged, respectively. (**C**) Side views of the binding pockets after a 180° rotation. AVP and retosiban are viewed from TM6. The same color code is used. (**D**) Superimposition of AVP and retosiban. The peptide agonist and the nonpeptide antagonist are superimposed after alignment of V2R and OTR structures. The most hydrophobic parts of both ligands superimpose at the bottom of the orthosteric binding pocket. (**E**) Structure comparison of AVP and retosiban. AVP is shown using the same color code in (A). The retosiban indanyl moiety, the *sec*-butyl group, and the oxazol-morpholine amide moiety superimpose with AVP Y2, F3, and Q4, respectively. The retosiban 2,5-diketopiperazine core is positioned between AVP Y2 and F3.

Activation of the V2R and comparison with other class A GPCRs

The active-state structures of the V2R reveal key structural features of the activation process by comparison with the OTR inactive structure (Fig. 6, A to E, and fig. S14, A to C). Moreover, to get a more general view of V2R activation, it was also important to look at the canonical conformational changes of TMs and of conserved motifs involved in other ligand-activated GPCRs of class A (*34*, *35*). Thus, compared to other active GPCR structures and to the inactive antagonist-bound OTR structure (Fig. 6, A to E, and fig. S14, A to C),

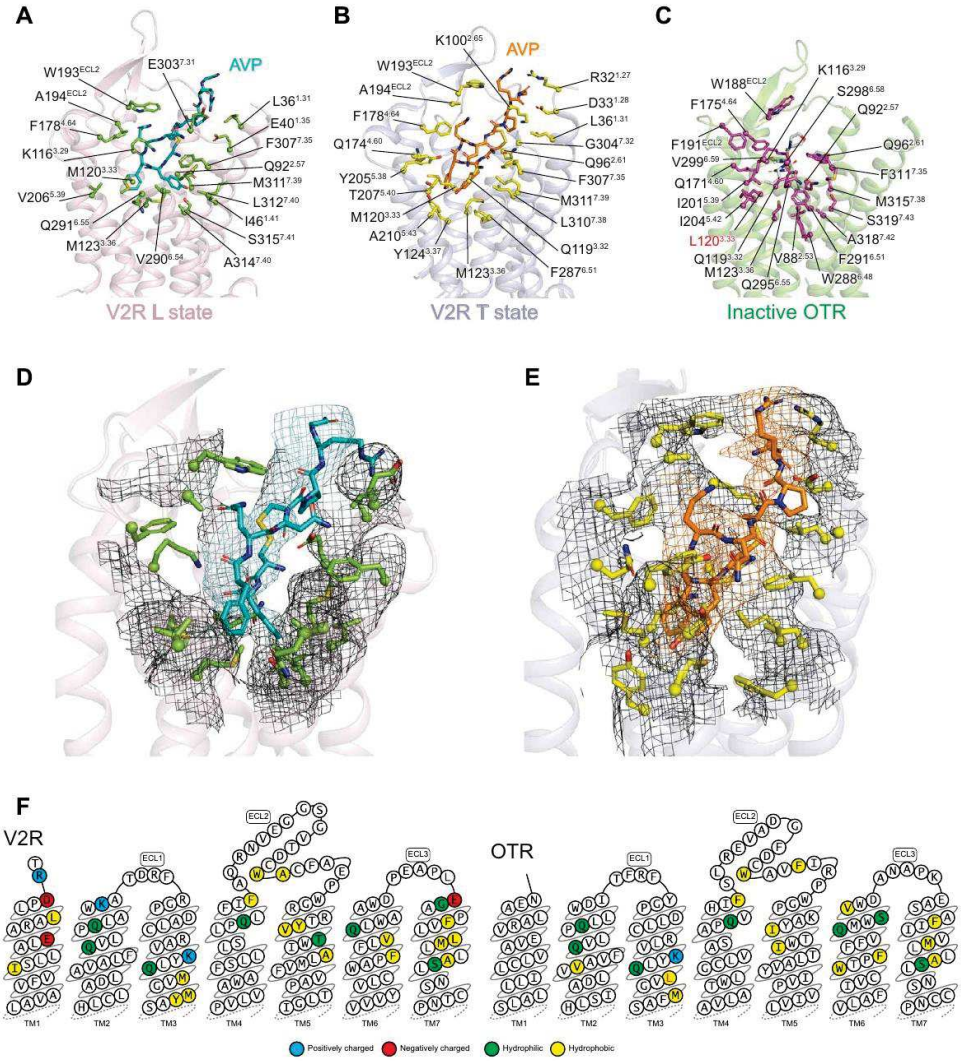

Fig. 5. V2R and OTR binding pockets: Binding of AVP versus retosiban. AVP binding poses are viewed from the side of the V2R helix bundle in L (**A**) or T (**B**) state and are compared with that of retosiban (in white sticks) in OTR (**C**). Receptor residues directly interacting with the ligands (at a maximum of 5 Å in distance) are indicated (Ballesteros-Weinstein numbering). In the OTR, L120$^{3.33}$ (highlighted in red) is a mutation introduced in the sequence to increase thermostability and facilitate crystallogenesis (V120L). Densities of V2R residues in contact with AVP are shown in L (**D**) and T (**E**) states, respectively. (**F**) Residues of V2R and OTR involved in the binding of ligands are shown in receptor snake-like plot representations (https://gpcrdb.org).

the L and T structures of V2R present all the features of active conformations, i.e., a large-scale displacement of TM6 (Fig. 6A); conformational changes of W$^{6.48}$ toggle switch (Fig. 6B); a rearrangement of the P$^{5.50}$-S$^{3.40}$-Y$^{6.44}$ transmission switch, equivalent to the PIF motif in other GPCRs (Fig. 6C); a rotation of the conserved NPxxY$^{7.53}$ motif (Fig. 6D); and a broken D136$^{3.49}$-R137$^{3.50}$ ionic lock (Fig. 6E).

By comparing the structures of the inactive antagonist-bound OTR with the active agonist-bound V2R, it appears that contacts between M123$^{3.36}$ and F287$^{6.51}$-W284$^{6.48}$ motif (all in contact with Y2 of AVP) undergo large conformational rearrangements (Figs. 4 to 6). It is thus tempting to speculate that it is a key motif regulating the activity of this family of receptor.

As indicated above, the V2R R137$^{3.50}$ participates in the ionic lock motif involved in the balance of active versus inactive states of class A GPCRs (*34*). Position of this R137$^{3.50}$ in the V2R snake representation is shown in Fig. 7A. In the inactive structure of OTR (Figs. 6E and Fig. 7B), D136$^{3.49}$ and R137$^{3.50}$ interact with each other through this ionic lock (the distance between the two charged groups is 3 Å; Fig. 7B). For comparison, this salt bridge is broken in the L and T active conformations of the V2R-G$_s$ complex (Figs. 6E and 7B). In that case, the distance between the two charges is 10 Å in the L state (Fig. 7B) and 8 Å in the T state. The observed constitutive activity toward G$_s$ coupling for the missense mutations C137$^{3.50}$ or L137$^{3.50}$ responsible for NSIAD (*9*, *36*, *37*) can thus be explained from a structural point of view since these hydrophobic residues are not able to form such an ionic lock to stabilize the inactive state (Fig. 7C). On the contrary, the mutant H137$^{3.50}$ causing cNDI (*38*, *39*) might still be able to maintain the balance between active and inactive states of the V2R through its partial positive charge (Fig. 7C). Its loss of function rather reflects the loss of accessibility to AVP due to the constitutive internalization (*37*–*39*).

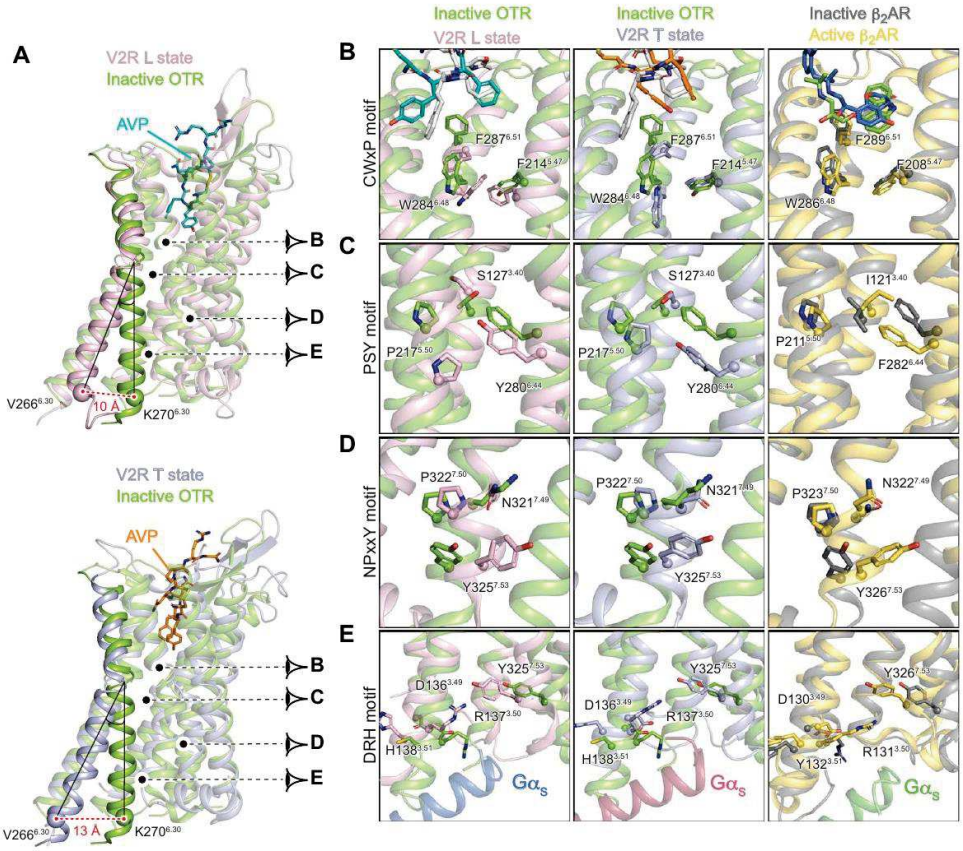

Fig. 6. Active conformations of L and T V2R states, comparison with inactive structure of OTR and active/inactive structures of β_2AR. (**A**) Large-scale displacement of TM6. The V2R L (pink) and T (blue gray) active structures are aligned onto that of the inactive OTR (green) structure. Residue 6.30 (Ballesteros-Weinstein numbering) is chosen as a reference (V266 in V2R and K270 in OTR) for measuring the outward movement of TM6: 10 and 13 Å between OTR and V2R in the L and T states, respectively. Activation of molecular switches along the helix bundle of the V2R is viewed in (B) to (E). For comparison, rearrangements of those corresponding motifs in the β_2AR are depicted. (**B**) Rotameric toggle switch in the conserved CWxP motif. Position of $W^{6.48}$, $F^{6.51}$, and $F^{5.47}$ (284, 287, and 214 in V2R) are shown. (**C**) Rearrangement of the PSY transmission switch. The $P^{5.50}$-$S^{3.40}$-$Y^{6.44}$ motif (217, 127, and 280 in V2R) is equivalent to the PIF motif in other GPCRs. (**D**) Rotation of the NPxxY conserved motif in TM7. The conserved $Y^{7.53}$ (position 325 in V2R) is shown. (**E**) Breaking of the conserved ionic lock in TM3. Upon activation of V2R, the ionic bond between $D136^{3.49}$ and $R137^{3.50}$ is broken, and $R137^{3.50}$ projects to $Y325^{7.53}$.

V2R-G_s interactions

The cryo-EM maps of the ternary complex clearly establish the structural details of V2R-G_s coupling. As anticipated from the conserved mechanism of GPCR–G protein coupling (*40*, *41*), both the L and T conformations show a similar overall architecture of the complex interface with the engagement of the $G\alpha_s$ C-terminal α_5 helix in the core of the 7TM (Fig. 8 and figs. S14, D to F, S15). However, there are some interesting differences compared to other GPCR-G_s complex structures. Notably, in both the L and T structures, the V2R ICL1 makes many direct contacts with the Gβ subunit. In the T state, ICL1 residues L62-A63-R64-R65-G66 interact with Gβ R52, D312-N313, and D333-F335 (Fig. 8A). In the L state, ICL1 residues R65-G66-R67-R68 interact with Gβ R52, D312, and D333 (figs. S14 and S15). These contacts between V2R and Gβ are much more numerous than in the class A GPCR β_2AR- or adenosine A2A receptor (A_{2A}R)-G_s complexes (*18*, *42*). Moreover, in the T conformation, there are some additional contacts between V2R ICL1 (R67-G69-H70) with the N-terminal α helix of $G\alpha_s$ (Q31, Q35, and R38), resulting in a more compact interaction (Fig. 8B). In the L state, V2R (W71) and N-terminal α helix of $G\alpha_s$ (Q35 and R38) contacts are more limited (fig. S15). Contacts between the N-terminal α helix of $G\alpha_s$ with GPCRs have only been seen in glucagon-like peptide-1 receptor (GLP1R) and calcitonin receptor (CTR) class B GPCR complexes (*43*, *44*), not in class A GPCR–G protein complexes.

In contrast to what was observed for the β_2AR (*18*) and the mu-opioid receptor (μOR) (*45*), the $G\alpha_s$ C-terminal α_5 helix appears to extend helix 8 (H8) of the V2R, lying almost parallel to the membrane plane (Fig. 8C and fig. S15, C and F to H). In addition, compared with the β_2AR, the C terminus of $G\alpha_s$ is interacting deeper in the V2R 7TM core, making direct contact with the residues (L and T states, respectively) of V2R that are part or in close proximity to the conserved NPxxY (TM7) and DRH (TM3) activation motifs (Fig. 8, D and E, and fig. S15, D to H). In this respect, the V2-G_s interaction resembles more the interaction seen in the μOR-G_i complex (fig. S15). The V2R TM7-H8 hinge region also makes a strong contact with the $G\alpha_s$ ELL motif, particularly through hydrophobic contacts with the $F328^{7.56}$ side chain (Fig. 8D). The T and L conformations differ here in the position of the $G\alpha_s$ L394 side chain originating from a distinct $F328^{7.56}$ side-chain conformation (pointing toward $I78^{2.43}$ of the receptor in the T structure or toward

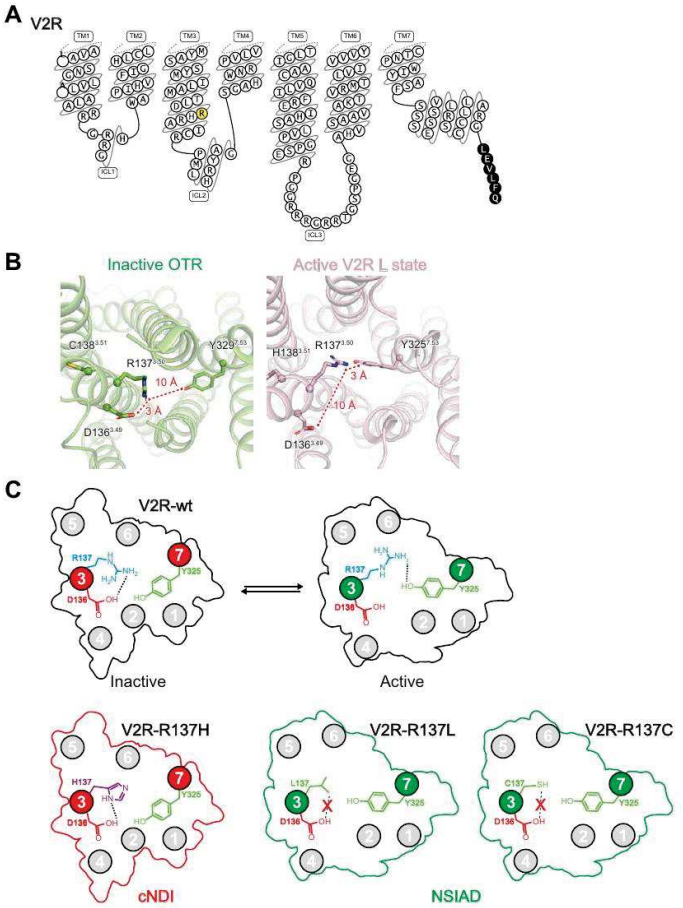

Fig. 7. Structural insights into V2R mutations associated with cNDI or NSIAD. (**A**) Modified snake plot of the human V2R construct used in the study (https://gpcrdb.org). The R137$^{3.50}$ residue involved in the ionic lock motif with D136$^{3.49}$ is highlighted in yellow. The mutation of this residue into a histidine or a cysteine/leucine is responsible for two genetic diseases, cNDI and NSIAD, respectively. Part of the human rhinovirus 3C (HRV3C) protease cleavage site introduced in the C-terminal end is indicated in black. (**B**) Ionic lock motif in the inactive structure of OTR (left) and in the active V2R L state structure (right). In the inactive OTR, the distance between positively charged R137$^{3.50}$ and negatively charged D136$^{3.49}$ is 3 Å (locked conformation), whereas it is 10 Å in the active V2R (open conformation). In the active V2R L state, R137$^{3.50}$ directly contacts Y325$^{7.53}$, an interaction that is not seen in the inactive OTR. (**C**) Schematic representation of R137$^{3.50}$ mutations responsible for either cNDI or NSIAD. In the top, equilibrium between inactive and active conformations of the wild-type V2R (V2R-wt) and the ionic lock motif are illustrated. Bottom: Mutations of R137$^{3.50}$ that induce cNDI (V2R-R137H) or NSIAD (V2R-R137L and V2R-R137C) are compared. Breakage of the R137$^{3.50}$-D136$^{3.49}$ ionic lock is shown in the R137C and R137L mutants. TM3 and TM7 are depicted in red in the V2R-R137H mutant, whereas they are shown in green in the constitutive active mutants V2R-R137L/C.

$G\alpha_s$ L394 in the L structure) (Fig. 8D and fig. S15D). Most notably in the T state, the side chain of R137$^{3.50}$, which is part of the ionic lock motif, forms an ionic interaction with the free carboxylic acid function of the $G\alpha_s$ C terminus (Fig. 8E), a direct contact that was not observed before between a GPCR and a G protein of any family (G_s, G_i, G_o, or G_q) (*14*, *15*, *46*). Moreover, in the L state, the density map suggests that the R137$^{3.50}$ side chain could adopt two conformations, one forming a similar ionic interaction with the carboxylic acid of $G\alpha_s$ L394 main chain and the other one pointing toward the Y325$^{7.53}$ from the NPxxY motif (fig. S15E).

DISCUSSION

In this study, we identified three different states and solved two structures of the AVP hormone–bound V2R in complex with the G_s protein. They reveal distinct agonist and G protein binding modes and a more compact architecture compared to other class A GPCR–G protein complexes. Although this work provides structural insights into the mechanisms of G protein activation by V2R, additional data are needed to determine whether the different conformations represent distinct intermediates along the signaling activation pathway. However, their identification using single-particle analysis and all-atom MDSs reports a high intrinsic flexibility, in agreement with the concept that GPCRs can explore a wide range of conformations, adapting their shape in response to different ligands and/or intracellular signaling partners (*47*). We also consider that the characterization of three different populations of the AVP-V2R-G_s complex was made possible because of using a native receptor (the V2R is a wild-type from T31 to G345), which was not engineered with thermostabilizing mutations or fusion partners.

Despite their various physiological roles, the cyclic peptides AVP and OT share a common receptor family. The V1aR, V1bR, V2R, and OTR display a common binding pocket that accommodates peptide and nonpeptide orthosteric agonists and antagonist ligands (*29*, *30*). Although V2R and OTR (*28*) structures represent different GPCR conformations (active agonist-bound V2R versus inactive antagonist-bound OTR), it is not unexpected to see that many residues involved in the binding of AVP (natural cyclic peptide agonist) are conserved among AVP/OTRs and also interact with retosiban (small nonpeptide antagonist) in the OTR. These data confirm that specific binding sites for nonpeptide antagonists and for AVP/OT peptides overlap at the bottom of the receptor binding pocket (*31*–*33*). Moreover, these are the most hydrophobic parts of AVP and retosiban that superimpose (AVP Y2 and F3 residues versus retosiban indanyl and *sec*-butyl moieties) in the binding pocket. The main pharmacophore responsible for activating V2R seems also to be the Y2-F3 AVP side chains (the message, i.e., efficacy), while the rest of the peptide rather seems to be responsible for the address (selectivity). In agreement, we demonstrated that the presence of the AVP F3 residue (L3 residue for OT) is responsible for partial agonist activity of AVP to the human OTR, whereas AVP hormone is a full agonist on V1aR (*48*), V1bR, and V2R. In addition, modification of residues at position 4 (glutamine for AVP and OT) and 8 (arginine for AVP and isoleucine for OT) has been shown to control selectivity of AVP analogs toward the different receptor subtypes in the AVP/OTR family (*49*).

The significance of our study also lies in the clinical relevance of the AVP receptor family, particularly for two rare X-linked genetic diseases involving mutations in the V2R, cNDI (*8*), and NSIAD (*9*), and our work provides a structural explanation on how those mutations can possibly affect the level of V2R activity and G_s protein coupling. These two pathologies are associated with V2R loss of function or constitutive activity, respectively. Substitution of R137$^{3.50}$ of the V2R for histidine (H137$^{3.50}$) leads to cNDI (*38*, *39*), whereas substitution of the same residue to cysteine or leucine (C/L137$^{3.50}$) causes NSIAD (*9*, *36*, *37*). Paradoxically, the three mutant receptors were shown to share common features, such as constitutive arrestin recruitment and endocytosis, resistance to AVP-stimulated cAMP accumulation and MAP kinase activation, and marked decrease in receptor cell surface expression (*36*–*39*). The unique difference observed between the H137$^{3.50}$ mutant and the C/L137$^{3.50}$ mutants

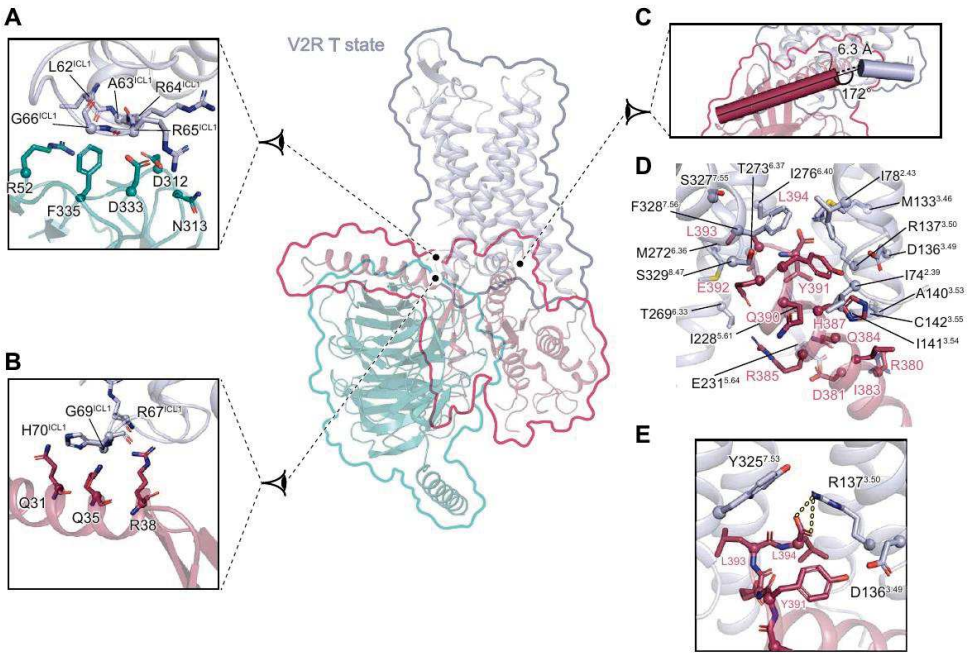

Fig. 8. Interface of the V2R T state with G_s. Interactions between V2R and G_s heterotrimer are shown. Specific interfaces are depicted, and residues in close proximity (within a maximum of 3.9 Å in distance) are highlighted (blue gray for V2R, turquoise for Gβ subunit, and raspberry for Gα subunit). (**A**) Interaction of V2R ICL1 with Gβ subunit. (**B**) Interaction of V2R ICL1 with the N-terminal helix of Gα subunit. (**C**) Position of C-terminal α_5 helix of Gα subunit relative to V2R helix 8. The distance between Gα and helix 8 is indicated. Angle between these two domains is shown. (**D**) Interacting residues between the C-terminal α_5 helix of Gα subunit and V2R. (**E**) Zoom on an ionic bridge between the C-terminal free carboxylic moiety of α_5 helix of Gα subunit and V2R R137$^{3.50}$.

resides in their basal constitutive activity toward the cAMP pathway (*9*). C/L137$^{3.50}$ gain-of-function mutants promote a significant higher basal cAMP level as compared to the wild-type V2R or the H137$^{3.50}$ loss-of-function mutant. In the present study, we proposed that the two hydrophobic cysteine or leucine residues are not able to form an ionic lock with D136$^{3.49}$ to stabilize the inactive state, explaining their constitutive activity. That is, the conformation of these mutants may be comparable to that of active V2R in the L and T states of the AVP-V2R-G_s signaling complex, at least considering a broken D136$^{3.49}$-C/L137$^{3.50}$ ionic lock. We provided here a unique evaluation of these gain-of-function V2R mutations.

A patient bearing the V2R H137$^{3.50}$ mutation was shown to increase his urine osmolality after a short-term therapeutic treatment with the V1a antagonist SR49059 (*50*). A structural knowledge about this ligand rescue is clinically important since this mutation is recurrent in independent cNDI families and also presents a phenotypic variability (*51*). SR49059 antagonist is used as a pharmacological chaperone (*52*). This lipophilic nonpeptide antagonist able to cross biological membranes is selective for V1aR subtype but still displays a measurable affinity for V2R. This ligand, which is a competitive analog of AVP, has been shown to be able to rescue the function of endoplasmic reticulum (ER)–trapped mutants of the V2R responsible for cNDI (*38*). Upon binding to the orthosteric site of the V2R mutants, SR49059 triggers targeting and stabilization of the mutated receptors to the plasma membrane of receptor-expressing cells, including R137H V2R. This mutant combines most of the properties of the wild-type receptor but is constitutively internalized (*37*, *38*), leading to a reduced cell surface expression, thus explaining a cNDI phenotype. Treatment of the patient with the pharmacological chaperone probably allows us to stabilize the R137H mutant at the plasma membrane where it is displaced by endogenous circulating AVP hormone, eliciting an antidiuretic response (increase in the osmolality of urine from 150 to 300 mOsm/kg).

The use of cell-permeable pharmacological chaperones for rescuing function of misfolded V2R mutants responsible for cNDI is a very attractive therapeutic avenue, in particular, regarding those that are trapped in the ER but, otherwise, are functional once they are targeted to the cell plasma membrane (see above for the V2R H137$^{3.50}$ mutation). It is thus tempting to interpret clinical observations (or in vitro pharmacological and cellular data) based on the present structures of the V2R. Importance of the structural data to help in understanding mutations is discussed here with two examples of cNDI loss-of-function mutations that can be rescued using pharmacological chaperones using the V2R-selective nonpeptide antagonist TVP, which is now used in thousands of patients with autosomal polycystic kidney disease with a reasonable safety profile (*53*). The V88M mutation is responsible for a mild phenotype, which is moderate polyuria and some degree of increased urine osmolality following treatment with desmopressin, an analog of AVP (*54*). Both the expression level and the hormone binding affinity are affected by this mutation. Structurally, V88$^{2.53}$ makes a direct contact with M123$^{3.36}$, which belongs to the AVP-binding site. We hypothesize that V88M induces a local destabilization by a steric clash with M123, leading to the decreased AVP binding affinity observed in in vitro pharmacological experiments but to a substantial increase in urinary concentration after desmopressin treatment in vivo. The M272R mutation is responsible for a severe phenotype with polyuria and no response to desmopressin treatment (*55*). In Madin-Darby canine kidney cells, this mutant is trapped in the ER and is not accessible to AVP but can be rescued using the pharmacological

chaperone TVP. Once it is at the cell surface, it is able to respond to desmopressin. M272$^{6.36}$ is located at the bottom of TM6, a highly flexible region that moves outward the V2 core upon activation. On the basis of positioning of the corresponding conserved M276$^{6.36}$ in the inactive structure of the related OTR (*28*), M272$^{6.36}$ in the V2R is surrounded by an aromatic/hydrophobic residue cluster, made of I74$^{2.39}$, I78$^{2.43}$, V275$^{6.39}$, I276$^{6.40}$, Y325$^{7.53}$, and F328$^{7.56}$. Mutation of M272 into a positively charged arginine probably destabilizes this domain, induces misfolding of the receptor, and results in ER retention. TVP can rescue the receptor to the cell surface probably by stabilizing its unfolded structure.

While this manuscript was under review, another structure of AVP-bound V2R in complex with a modified G_s protein was published online (*56*). A major difference between this structure with L and T structures described herein comes from the use of a chimeric G_s/G_i protein in the first study, different from the wild-type G_s. This modification, together with the use of the ScFv16 antibody fragment further stabilizing the complex through interaction with the G_i domain, probably explains not only a better resolution but also why flexibility and dynamics of the signaling complex were not addressed. The use of a physiological G_s protein allowed us to probe the flexibility of the system and to characterize an original V2R-G_s interface. Nonetheless, positioning of AVP in the orthosteric binding pocket and superimposition of AVP with OTR-selective retosiban are comparable in the two studies. Hence, the different structures are complementary, help to have a complete view of this signaling system, and pave the way for future drug development to treat water balance disorders (*7*).

MATERIALS AND METHODS

Data analysis and figure preparation

Figures were created using the PyMOL 2.3.5 Molecular Graphics System (Schrödinger LLC) and the UCSF Chimera X 0.9 package. Data were plotted with GraphPad Prism 8.3.0.

V2R expression and purification

The optimized sequence of the human V2R was cloned into a pFastBac1 vector (Invitrogen) for insect cell expression. To facilitate expression and purification of the V2R construct used for cryo-EM, the hemagglutinin signal peptide (MKTIIALSYIFCLVFA) followed by a Flag tag (DYKDDDDA) was added at the N terminus, and a Twin-Strep-tag (WSHPQFEKGGGSGGGSGGGSWSHPQFEK) was inserted at the C terminus. In addition, N22 was substituted with a glutamine residue to avoid *N*-glycosylation, and C358 mutated into an alanine to eliminate potential intermolecular disulfide bridges during solubilization and purification. A Tobacco Etch Virus (TEV) protease cleavage site (following the Flag tag) and two Human Rhinovirus 3C (HRV3C) protease cleavage sites (one inserted in the N terminus between D30 and T31 and the other inserted in the C terminus between G345 and Q354 and replacing R346-TPPS-LG-P353) were also added to remove N and C termini and facilitate structure determination. M1L2 residues were replaced by AS residues, and LE residues were added before the Twin-Strep-tag, during subcloning (introduction of Nhe I and Xho I restriction sites, respectively). Sequence modifications did not affect the receptor ligand binding or function. The V2R was expressed in Sf9 insect cells using the Bac-to-Bac baculovirus expression system (Thermo Fisher Scientific) according to the manufacturer's instructions. Insect cells were grown in suspension in EX-CELL 420 medium (Sigma-Aldrich) to a density of 4×10^6 cells/ml and infected with the recombinant baculovirus at a multiplicity of infection of 2 to 3. The culture medium was supplemented with the V2R pharmacochaperone antagonist TVP (Sigma-Aldrich) at 1 μM to increase the receptor expression levels (*52*, *57*). The cells were infected for 48 to 54 hours at 28°C, and expression of the V2R was checked by immunofluorescence using an anti-Flag M1 antibody coupled to Alexa Fluor 488. Cells were then harvested by centrifugation (two steps for 20 min at 3000*g*), and pellets were stored at −80°C until use.

The cell pellets were thawed and lysed by osmotic shock in 10 mM tris-HCl (pH 8), 1 mM EDTA buffer containing iodoacetamide (2 mg/ml), 1 μM TVP, and protease inhibitors [leupeptine (5 μg/ml), benzamidine (10 μg/ml), and phenylmethylsulfonyl fluoride (PMSF) (10 μg/ml)]. After centrifugation (15 min at 38,400*g*), the pellet containing crude membranes was solubilized using a glass dounce tissue grinder (15 and 20 strokes using A and B pestles, respectively) in a solubilization buffer containing 20 mM tris-HCl (pH 8), 500 mM NaCl, 0.5% (w/v) *n*-dodecyl-β-D-maltopyranoside (DDM; Anatrace), 0.2% (w/v) sodium cholate (Sigma-Aldrich), 0.03% (w/v) cholesteryl hemisuccinate (CHS; Sigma-Aldrich), 20% glycerol, iodoacetamide (2 mg/ml), biotin BioLock (0.75 ml/liter; IBA), 1 μM TVP, and protease inhibitors. The extraction mixture was stirred for 1 hour at 4°C and centrifuged (20 min at 38,400*g*). The cleared supernatant was poured onto an equilibrated Strep-Tactin resin (IBA) for a first affinity purification step. After 2 hours of incubation at 4°C under stirring, the resin was washed three times with 10 column volume (CV) of a buffer containing 20 mM tris-HCl (pH 8), 500 mM NaCl, 0.1% (w/v) DDM, 0.02% (w/v) sodium cholate, 0.03% (w/v) CHS, and 1 μM TVP. The bound receptor was eluted in the same buffer supplemented with 2.5 mM desthiobiotin (IBA).

The eluate was supplemented with 2 mM $CaCl_2$ and loaded onto a M1 anti-Flag affinity resin (Sigma-Aldrich). The resin was washed with 10 CV of two successive buffers containing 20 mM Hepes (pH 7.5), 100 mM NaCl, 0.1% DDM, 0.01% CHS, 10 μM AVP, and 2 mM $CaCl_2$ and then 20 mM Hepes (pH 7.5), 100 mM NaCl, 0.025% DDM, 0.005% CHS, 10 μM AVP, and 2 mM $CaCl_2$, respectively. The receptor was eluted from the Flag resin using a buffer containing 20 mM Hepes (pH 7.5), 100 mM NaCl, 0.025% DDM, 0.005% CHS, 10 μM AVP, 2 mM EDTA, and Flag peptide (200 μg/ml) (Covalab).

After concentration using a 50-kDa molecular weight cutoff (MWCO) concentrator (Millipore), the V2R was purified by SEC using a Superdex 200 (10/300 column) connected to an ÄKTA purifier system (GE Healthcare). Fractions corresponding to the pure monomeric receptor were pooled (~2 ml) and concentrated to 50 to 100 μM with an excess of AVP (200 μM).

G_s expression and purification

Human $G\alpha_s$, $G\beta_1$ with an N-terminal Twin-Strep-tag, and $G\gamma_2$ were all expressed in Sf9 insect cells grown in EX-CELL 420 medium (Sigma-Aldrich). A recombinant baculovirus for $G\alpha_s$ subunit was prepared using the BestBac (Expression Systems) strategy, whereas a baculovirus for $G\beta_1$ and $G\gamma_2$ was prepared using the Bac-to-Bac system. $G\beta_1$ and $G\gamma_2$ were cloned in tandem into the pFastBac Dual vector (Thermo Fisher Scientific). Sf9 cells, at a density of 4×10^6 cells/ml, were coinfected with both viruses at a 1:2 $G\alpha_s$:$G\beta_1\gamma_2$ ratio for 72 hours at 28°C. Cells were harvested and pellets were stored at −80°C.

Coinfected Sf9 cell pellets were thawed and lysed in a buffer containing 10 mM tris (pH 7.4), 1 mM EDTA, 5 mM β-mercaptoethanol,

10 μM guanosine diphosphate (GDP), and protease inhibitors [leupeptine (5 μg/ml), benzamidine (10 μg/ml), and PMSF (10 μg/ml)]. Lysed cells were centrifuged (20 min at 38,400*g*). The pellets containing the crude membranes were homogenized using a glass dounce tissue grinder (20 strokes with tight B pestle) in solubilization buffer containing 20 mM Hepes (pH 7.5), 100 mM NaCl, 1% DDM, 5 mM $MgCl_2$ supplemented with 5 mM β-mercaptoethanol, 10 μM GDP, biotin BioLock (0.75 ml/liter), and protease inhibitors. The mixture was stirred for 40 min at 4°C and centrifuged (20 min at 38,400*g*). The supernatant was loaded onto a Strep-Tactin affinity resin equilibrated with the same buffer. The resin was washed three times, first with 5 CV of solubilization buffer, then with 5 CV of solubilization buffer supplemented with 100 μM tris(2-carboxyethyl)phosphine (TCEP) (instead of β-mercaptoethanol), and last with 10 CV of wash buffer containing 20 mM Hepes (pH 7.5), 50 mM NaCl, 0.1% DDM, 1 mM $MgCl_2$, 100 μM TCEP, and 10 μM GDP. The G_s heterotrimer protein was eluted in the same buffer supplemented with 2.5 mM desthiobiotin. After a treatment with antarctic phosphatase (5 U; NEB Inc.) for 30 min at 4°C, the G_s protein was concentrated to 10 mg/ml using 50-kDa MWCO concentrators. Twenty percent of glycerol was added to the sample, and aliquots were flash-frozen in liquid nitrogen before storage at −80°C.

Nb35 expression and purification

The production and purification of Nb35 were performed following a protocol established by Kobilka and co-workers (*18*). Nb35 having a C-terminal 6His-tag was expressed in the periplasm of *Escherichia coli* strain BL21 following induction with 1 mM isopropyl-β-D-thiogalactopyranoside. Cultures of 2L were grown to an optical density at 600 nm of 0.6 at 37°C in LB medium containing 0.1% glucose and ampicillin (100 μg/ml). Induced cultures were grown overnight at 25°C. Cells were harvested by centrifugation and lysed in ice-cold buffer [50 mM tris-HCl (pH 8), 125 mM sucrose, and 2 mM EDTA]. Lysate was centrifuged to remove cell debris, and Nb35 was purified by nickel affinity chromatography. Eluate was concentrated to 5 mg/ml and loaded onto a Superdex 200 (16/600 column, GE Healthcare) at a 1 ml/min of flowrate. Fractions containing the monodisperse peak of Nb35 were pooled and dialyzed overnight against a buffer containing 10 mM Hepes (pH 7.5) and 100 mM NaCl at room temperature (RT). The dialyzed sample was concentrated to approximately 100 mg/ml using a 10-kDa MWCO concentrator (Millipore). Aliquots were stored at −80°C until use.

Purification of the AVP-V2R-G_s-Nb35 complex

Formation of a stable complex was performed by mixing the purified V2R with 1.2 molar excess of purified G_s heterotrimer, 250 μM AVP, and 2.5 mM $MgCl_2$ (fig. S1). The coupling reaction was allowed to proceed at RT for 45 min and was followed by addition of apyrase (0.0125 U; NEB Inc.) to hydrolyze residual GDP and maintain the high-affinity nucleotide-free state of G_s. Fifteen minutes later, Nb35 was added at a twofold molar excess compared to G_s. After 15 more minutes at RT, the mix was incubated overnight at 4°C. In most reaction mixtures, the final concentration of V2R was 20 to 30 μM, that of G_s 30 to 40 μM, and the one of Nb35 around 80 μM. To remove excess of G protein heterotrimer and Nb35, the complex AVP-V2R-G_s-Nb35 was purified by a M1 anti-Flag affinity chromatography. After loading, the DDM detergent was then gradually exchanged with Lauryl Maltose Neopentyl Glycol (LMNG; Anatrace). The LMNG concentration was then decreased gradually from 0.5 to 0.01%. The complex and the unbound V2R were eluted in 20 mM Hepes (pH 7.5), 100 mM NaCl, 0.01% LMNG, 0.002% CHS, 2 mM EDTA, 10 μM AVP, and Flag peptide (0.2 mg/ml). The eluted AVP-V2R-G_s-Nb35 complex was separated from unbound V2R by SEC on a Superdex 200 (10/300 column) with a buffer containing 20 mM Hepes (pH 7.5), 100 mM NaCl, 0.002% LMNG, 0.0025% glyco-diosgenin (GDN; Anatrace), 0.002% CHS, and 10 μM AVP. The fractions corresponding to the complex were collected, concentrated with a 50-kDa MWCO concentrator, and subjected to a second SEC on a Superose 6 (10/300 GL, GE Healthcare) with a buffer containing 20 mM Hepes (pH 7.5), 100 mM NaCl, 0.0011% LMNG, 0.001% GDN, 0.002% CHS, and 10 μM AVP. Peak fractions were pooled and concentrated using a 50-kDa MWCO concentrator to concentrations ranging from ~1 to ~4 mg/ml for cryo-EM studies. The amphipol A8-35 (Anatrace) was added at 0.001% to help in the dispersion of the particles for cryo-EM grid preparation.

Negative stain microscopy observations

Before preparing cryo-EM grids, we first checked the quality and the homogeneity of the AVP-V2R-G_s-Nb35 sample by NS-EM. Three microliters of AVP-V2R-G_s-Nb35 complex at 0.04 mg/ml was applied for 2 min on glow-discharged carbon-coated grids and then negatively stained with 1% uranyl acetate for 1 min. Observation of EM grids was carried out on a JEOL 2200FS FEG operating at 200 kV under low-dose conditions (total dose of 20 electrons/$Å^2$) in the zero–energy loss mode with a slit width of 20 eV. Images were recorded on a 4K × 4K slow-scan charge-coupled device camera (Gatan Inc.) at a nominal magnification of ×50,000 with defocus ranging from 0.5 to 1.5 μm. Magnifications were calibrated from cryo-images of tobacco mosaic viruses. In total, 37 micrographs were recorded, allowing us to pick 22,791 particles using e2boxer from Eman2 package (*58*). Further processing was performed with Relion 2.0 (*13*, *59*). The particles were subjected to a 2D classification included to get rid of free micelles and dissociated components of the complex. From 2D classes, 14,545 particles corresponding to the V2R-G_s-Nb35 complexes were selected, representing 63% of all particles. This selection was used to calculate an ab initio low-resolution model. The sample was also subjected to NS-EM analysis after 5 days. At this point, after particle picking and 2D classification, 35% of particles were representing the complex. The fresh sample was also mixed with 100 μM GTPγS and 10 μM SR121463 V2R antagonist and visualized in negative stain to observe complete dissociation.

Cryo-EM sample preparation and image acquisition

In this study, two datasets have been recorded from two different preparations of AVP-V2R-G_s-Nb35. For the first dataset acquisition, 3 μl of purified AVP-V2R-G_s-Nb35 at a concentration of 0.75 mg/ml were applied on glow-discharged Quantifoil R 1.2/1.3 300-mesh copper holey carbon grids (Quantifoil Micro Tools GmbH, Germany), blotted for 4.5 s, and then flash-frozen in liquid ethane using the semiautomated plunge-freezing device Vitrobot Mark IV (Thermo Fisher Scientific) maintained at 100% relative humidity and 4°C. For the second dataset acquisition, cryo-EM grids were prepared as previously, but the purified V2R-G_s-Nb35 complex was at a concentration of 4 mg/ml, and the cryo-EM grids were prepared using an EM GP2 (Leica Microsystems) plunge freezer with a 4 s blotting time (100% humidity and 4°C).

Images were collected in two independent sessions on a TEI Titan Krios (Thermo Fisher Scientific) at the European Molecular Biology Laboratory (EMBL) of Heidelberg (Germany) at 300 keV

through a Gatan Quantum 967 LS energy filter using a 20-eV slit width in zero-loss mode and equipped with a K2 Summit (Gatan Inc.) direct electron detector configured in counting mode. Movies were recorded at a nominal energy-filtered transmission electron microscope magnification of ×165,000 corresponding to a 0.81 Å calibrated pixel size. The movies were collected in 40 frames in defocus range between −0.8 and −2.2 µm with a total dose of 50.19 $e^-/Å^2$ (first dataset) and 41.19 $e^-/Å^2$ (second dataset). Data collection was fully automated using SerialEM (*60*).

Cryo-EM data processing

All data processing operations were performed with Relion-3.0.7 (*61*), unless otherwise specified. In total, 17,290 movies of the AVP-V2R-G_s-Nb35 sample at 0.75 mg/ml were collected. Dose-fractionated image stacks were subjected to beam-induced motion correction and dose weighting using Motioncorr own implementation. Gctf was used to determine the contrast transfer function (CTF) parameters (*62*) from non–dose-weighted images. After sorting, micrographs with maximum estimated resolution beyond 5 Å were discarded. Particle picking was carried out using Gautomatch [K. Zhang, Medical Research Council Laboratory of Molecular Biology (www.mrc-lmb.cam.ac.uk/kzhang/)], allowing us to pick out 2,291,432 particles. Particles were extracted in a box size of 240 Å, downscaled to 4 Å per pixel, and subjected to reference-free 2D classifications to discard false-positive particles or particles categorized in poorly defined classes. A subset of 1,109,475 particles was selected for further processing. This particle set was subjected to a 3D classification with four classes using the 30-Å low-pass filtered calcitonin receptor map as reference (*44*). Particles from the two classes representing 27% of total particles and showing a complete AVP-V2R-G_s-Nb35 complex were selected, reextracted with a pixel size of 1.62 Å, and subjected to a 3D refinement. This subset of 307,125 particles yielded a map with a global resolution [Fourier shell correlation (FSC) = 0.143] of 4.8-Å resolution. Particles were then subjected to a focused 3D classification without angular and translational alignments with a mask including the complex minus $G\alpha_s$AH ($G\alpha_s$ α-helical domain). The best class corresponding to 150,000 particles was reextracted without binning and submitted to a 3D refinement, allowing us to obtain a map at 4.4-Å resolution. All further processing including signal subtraction, using different types of masks, CTF refinement, and polishing did not improved the resolution of the map.

In total, 8490 movies of the AVP-V2R-G_s-Nb35 sample at 4.0 mg/ml were recorded. The image processing steps were the same as previously described, except that the picking was performed using boxnet from Warp software package (*63*), allowing us to extract 1,214,575 particles. After a 2D classification to clean the dataset, a subset of 917,990 particles was subjected to two successive rounds of 3D classification. A subset of 150,000 particles was used for further 3D refinements, yielding a final map at 4.4-Å resolution.

Both cleaned datasets were merged, corresponding to 1,109,475 particles from dataset 1 and 917,990 particles from dataset 2. Particles were subjected to 3D classification with three classes. One class displayed the expected structural features of the AVP-V2R-G_s-Nb35 complex corresponding to 877,003 particles and was selected for a new round of 3D classification with six classes. This classification revealed a structural variability in the ligand location and at the interface between the receptor and the G_s protein. Three subsets of particles were selected (L, T1, and T2 states), reextracted with a pixel size of 1.62 or 0.81 Å, and subjected to 3D refinements, yielding maps at 4.5, 4.7, and 5.5 Å, respectively. New rounds of 3D refinements were performed in applying a mask to exclude both the micelle and the $G\alpha_s$AH, yielding maps at 4.23, 4.4, and 4.7 Å. CTF refinement and polishing steps were applied on the three subsets of particles, allowing us to improve the resolution of the best map to 4.17 Å (FSC = 0.143). The T1 map (1.62 Å per pixel) was resampled at 0.81 Å per pixel for visualization purposes. Final refinements were processed with the option of masking individual particles with zero turned off. All our attempts to refine our final subsets in cisTEM (*64*) and cryoSPARC (*65*) using non-uniform refinement did not improve the resolution of final maps.

To investigate the conformational dynamics of the signaling complex, multibody refinement was performed on 877,003 particles, with two bodies corresponding to AVP-V2R and G_s-Nb35. Local resolution was estimated with the Bsoft 2.0.3 package (*66*, *67*). Map sharpening was reevaluated with Phenix autosharpen tool (*68*). Phenix resolve_cryoEM tool (*20*) was used to improve the map interpretability and allowed to increase the estimated resolution to 4.04, 4.13, and 4.5 Å for L, T1, and T2 states, respectively.

Model building and refinement

Receptor and AVP initial models

The V2R was built by comparative modeling, using the MODELLER software (*69*) and the x-ray structure of the δ-opioid receptor at 3.4-Å resolution (PDB code 4EJ4) as a template (*70*), sharing a sequence similarity of about 44% with the V2R (on the modeled region). Because modeling loops or terminal regions is a very challenging task and their dynamical behavior is very poorly described in CG simulations, N and C termini of the receptor (residues 1 to 35 and 335 to 371, respectively) and part of the ICL3 loop (residues 237 to 262) were lacking in the used template. Thus, only residues 36 to 236 and 263 to 334 were modeled. Five hundred models were generated, and the one sharing the best objective function score was further selected as a starting point for the simulations. The disulfide bridge conserved among the class A GPCRs was included between residues 112 and 192 of the V2R.

The AVP peptide (NH_3^+-CYFQNCPRG-$CONH_2$) was built from its x-ray structure available in the PDB (code 1JK4; 2.3-Å resolution), which describes the six-residue cycle of the peptide in interaction with neurophysin (*71*). This structure shows a cycle conformation equivalent to that found in bound (PDB code 1NPO) and unbound related peptide OT (PDB code 1XY2) (*72*, *73*). It was thus preferred to the one describing the trypsin-vasopressin complex (PDB code 1YF4) (*74*) harboring a completely different conformation of the cycle. The three last residues of the peptide ($_7$-PRG-$_9$) were also built with the OT structure templates.

The obtained initial models of both receptor and peptide were then converted to a CG representation using the MARTINI force field (version 2.2; Elnedyn) (*75*). Using such a model, residues (backbone beads) closer than 9.0 Å are bound by a spring, displaying a force constant of 500 kJ/mol per nm^2 (default value from the Elnedyn force field). Such a link is meant to maintain both the secondary and the tertiary structures of the polypeptides. For the peptide, only the springs involving two residues of the cycle were conserved for further calculations, the three last residues being free to move. The standard elastic network of the receptor was not modified and allowed the latter to open or close freely as no spring was bridging the extracellular loops.

Molecular dynamics simulations

The receptor was inserted in a 100 Å–by–100 Å lipid bilayer exclusively composed of 1-palmitoyl-2-oleoyl-sn-glycero-3-phosphocholine

(POPC). To avoid the exploration by the peptide of the intracellular side of the membrane during molecular dynamics (because of periodic boundary conditions), the system was duplicated/rotated along the *z* axis (the two extracellular sides of the receptors were facing each other) to create an extracellular compartment. Two copies of the peptide were added to increase the interaction sampling with a 1:1 ratio. In a last step, water and chloride counterions were added to neutralize the system. The fully solvated system included 20,004 beads. After 10,000 steps of energy minimization using the conjugate gradient algorithm, the system was further equilibrated at 51 different temperatures (in the range 300:450 K by steps of 3 K) in the NVT (constant particle number, volume, and temperature) ensemble, using an integration step of 20 fs and over a period of 5 ns. The final production step was performed in the NPT (constant particle number, pressure, and temperature) ensemble, using an integration step of 20 fs and was stopped after 20 μs. During production, REMD was used to improve the sampling of all possible configurations of the peptide:receptor complex. The potential energy difference of adjacent replicas was computed every 1000 steps (20 ps), and their coordinates were exchanged according to a Boltzmann criterion. With the used parameters, the probability of exchange between adjacent replica was in the range 0.11 (300 K):0.23(450 K). Three independent CG-REMD simulations were run to verify the convergence of the obtained models, together representing a cumulated sampling time of ~3 ms. For each of these simulations, a clustering was performed on all conformations of the peptide:receptor complex obtained at the lowest temperature (300 K). To do so, we first concatenated the data corresponding to the four possible complexes (peptide1-receptor1, peptide1-receptor2, peptide2-receptor1, and peptide2-receptor2). For that step, only the conformations displaying at least one peptide:receptor contact were kept (a contact was defined using a cutoff distance of 7 Å). For clustering, we used the algorithm of Daura *et al.* (*76*) with an RMSD cutoff of 3.0 Å. The RMSD was computed only on the backbone beads of the peptide's residues 1 to 6 after structural fit onto those of the V2R. The two cysteine side-chain beads were also included for RMSD calculations. All simulations and analyzes were performed with the GROMACS software (version 5) (*77*). Figures were produced with Visual Molecular Dynamics (*78*).

Refinement of the obtained CG models in the cryo-EM maps

The CDMD method (*23*) was used to refine the most populated clusters obtained in CG-REMD using the L-state cryo-EM map of the AVP-V2-G_s-Nb35 complex. The principle of the method is to use an accurate force field and thermodynamic sampling to improve the real-space correlation between the modeled structure and the cryo-EM maps. Before this refinement step, the G_s heterotrimer and the Nb35 were modeled using the structure of the β_2AR-G_s-Nb35 complex (*18*) as a reference. The MARTINI force field restrained the internal conformations of the different partners with an internal elastic network. To increase significantly the conformational plasticity of the receptor and explore new conformations specific to the V2R, we modified its default elastic network. We automatically deleted the "long-range" springs involving two beads whose indexes differ by at least 15. This contributed to delete all interhelix springs. The standard elastic network was conserved for all other partners including the AVP peptide, the G protein, and the Nb35. No interchain springs were included for the G protein. After conversion of G_s and Nb35 into the CG model, the two proteins were placed at a rational position in respect to the V2R using the β_2AR-G_s-Nb35 complex (*18*). The full system was inserted in a larger membrane (150 Å by 150 Å) and solvated on each side for further calculations.

The fit in each cryo-EM map was performed in four successive steps. First, a quick energy minimization (2000 steps of conjugate gradient) was performed on the full system without taking the map into account. This step was dedicated to the removal of bad contacts resulting from the addition of G_s and Nb35 proteins. Then, the second step consisted in a first equilibration of 5 ns (10-fs time step; NVT; 300 K) performed with CDMD and using a constant targeted low resolution of 5 Å together with a strength constant of 10,000 kJ/mol for the map potential. This bias was applied only to the backbone beads of the system. This step was useful to quickly optimize the alignment of the system with the targeted map. During this second step, an additional force of 50,000 kJ/mol per nm^2 was added to keep the distance between the two centers of masses (COMs) of both the peptide and surrounding residues of the receptor close to its initial value. This force prevented a quick motion of the AVP peptide in the first steps of the simulation that resulted from large forces applying to the receptor. For the subsequent steps of the fitting procedure, this additional force on COMs was removed. During the step 3 (30 ns), the same molecular dynamics parameters were used but with a gradual increase in both the resolution (from 5 to 3 Å) and the strength constant (from 10,000 to 50,000 kJ/mol), over a period of 25 ns. During the last 5 ns, these values were kept constant. This step was the key step allowing the whole system to adapt and fit to the maps. Last, the last step (10 ns) consisted in keeping the resolution and the strength constant at their reached values (3 Å; 50,000 kJ/mol), but this time applying the force only to the backbone and side-chain beads of the peptide. All the other backbone beads of the system were restrained in positions during this step with a force constant of 5000 kJ/mol. This step was useful to refine the position of the peptide in the density, especially of its side chains. For every step of the fitting procedure, the fit of each cluster was performed five times to verify the convergence of the obtained models.

All-atom refinement of the models in the maps

The CG models obtained from the fitting procedure were backmapped to a full-atom representation. We used the standard "initram" procedure provided by the developers of MARTINI (*79*) with subtle changes. These changes concerned restrains on ω angles and Cα positions for all chains (V2R, G_s, and Nb35) to keep ω angles in trans conformation and to avoid large backbone motions, which inevitably would lead to models out of cryo-EM maps. Those restrains were added during the minimization and the MDSs inherent to the default initram procedure. In practice, the initram procedure was as follows: (i) After the very raw guess of atomic positions, from CG beads, performed by the initram script, (ii) the Charmm36 force field (*80*) was used for 10,000 steps of steepest descent, disabling the nonbonded terms, (iii) followed by 5000 steps of steepest descent including all terms of the force field, and last, (iv) 300 steps of molecular dynamics were performed. Except the number of steps, the parameters for minimization and MDSs were set as default from the initram procedure. Minimization and MDSs were performed using the GROMACS package (*77*).

As a final step, iterative manual adjustments were carried out in Coot (*81*) and real-space refinement using Phenix programs (*82*). The model statistics were validated using MolProbity (*83*).

Classical all-atom MDSs

Following procedures previously described (*84*), the L-state cryo-EM structure was subjected to MDSs. The system was set up using the CHARMM-GUI micelle builder (*85*). The protein complex was inserted into a hydrated, equilibrated micelle composed of 60 molecules of LMNG after addition of missing protein loops in Coot. A total of 495 sodium and 511 chloride ions were added to neutralize the system, reaching a final concentration of approximately 150 mM. MDSs were performed in GROMACS 2020 using the CHARMM36m force field and the CHARMM TIP3P water model. The input systems were subjected to energy minimization, equilibration, and production simulation using the GROMACS input scripts generated by CHARMM-GUI (*86*). Briefly, the system was energy minimized using 5000 steps of steepest descent, followed by 375 ps of equilibration. NVT and NPT equilibrations were followed by NPT production runs. The van der Waals interactions were smoothly switched off at 10 to 12 Å by a force-switching function (*87*), whereas the long-range electrostatic interactions were calculated using the particle mesh Ewald method (*88*). The temperature and pressure were held at 310.15 K and 1 bar, respectively. The assembled system was equilibrated by the well-established protocol in Micelle Builder, in which various restraints were applied to the protein, detergents, and water molecules, and the restraint forces were gradually reduced during this process. During production simulations, an NPT ensemble was used with isotropic pressure coupling via the Parrinello-Rahman barostat method, while the Nose-Hoover thermostat was used to maintain a temperature of 310.15 K. A leapfrog integration scheme was used, all bonds were constrained, and hydrogen mass repartitioning was applied (*89*), allowing for a time step of 4 ps to be used during NPT equilibration and production MDSs. We performed 10 independent production runs starting from the highest-resolution L state model, for a total simulation time of ~2.6 μs. Production runs were subsequently pooled together, and the resulting trajectory was analyzed using GROMACS tools to yield principal components. The analysis was performed on the subset of Cα atoms common to the simulated and experimental structures using 1 frame/ns of trajectory. The experimental L, T1, and T2 states were included in the analysis for comparison.

NMR data analysis

The purified V2R was prepared either in neutral amphipol (*90*, *91*) or in LMNG detergent. In both cases, the V2R was expressed in Sf9 insect cells and purified as described above, except it was cleaved overnight at 4°C using the HRV3C protease at a 1:20 weight ratio (HRV3C:V2R) before concentration and purification by SEC.

1D STD NMR spectra (*92*) were recorded either on a mixture of AVP with V2R (400:2 μM) or on AVP. Selective methyl resonance saturation was achieved by equally spaced 60-ms Gaussian 180° pulses separated by 1-ms delay at 0 parts per million (ppm) (−50 ppm for reference spectra) at 274 and 283 K. An irradiation test was performed on a free peptide sample (400 μM) to verify that only V2R resonances were irradiated. Subtraction of free induction decay with on- and off-resonance protein saturation was achieved by phase cycling. A relaxation delay of 2.6 s (Aq and D1) and 128 dummy scans were used to reduce subtraction artifacts. Investigation of the time dependence of the saturation transfer from 0.5 to 4 s with equally spaced 50-ms Gaussian-shaped pulses (separated by a 1-ms delay) showed that 2 s was needed for efficient transfer of saturation from V2R to the AVP. A T1ρ filter of 30 ms was applied to eliminate background resonances of V2R. The transient number was typically 4000. To determine the specificity of STD signals, similar samples were prepared with the antagonist TVP as competitor, using 3 μM V2R, 80 μM AVP, and 550 μM TVP. The STD effect was then calculated as $(I_0 - I_{sat})/I_0$, where I_0 and I_{sat} are the intensities of one signal in the reference NMR spectrum and in the on-resonance spectrum, respectively.

We discriminated the different molecular models issued from CG-REMD simulations by comparing the experimental STD values and the expected simulated STD from model structures. Back calculation of STD intensities were calculated with the 3.8 version of CORCEMA-ST software (*93*). An order parameter value of 0.85 for methyl groups and a Kon value of a 10^8 s^{-1} were used. The correlation times were set to 0.5 and 40 ns for the free and bound states, respectively. Calculations with different correlation time values exploring the 0.2 to 2 ns and 10 to 30 ns for the free and bound forms, respectively, showed that the simulated profiles, as well as, in particular, the correlation coefficient between calculated and experimental values, were much more dependent on the template model than on the correlation time values. Coefficient correlations between simulated and experimental values were calculated for the whole peptide (residues 1 to 9). Mean correlations factors R_{1-9} were calculated for five representative structures of each cluster.

Time-resolved fluorescence resonance energy transfer binding assays

V2R binding studies using TagLite assays (Cisbio Bioassays, Codolet, France) based on time-resolved fluorescence resonance energy transfer (FRET) measurements were previously described (*16*, *94*). Briefly, HEK cells were plated in white-walled, flat-bottom, 96-well plates (Greiner CELLSTAR plate, Sigma-Aldrich) in Dulbecco's minimum essential medium (DMEM) containing 10% fetal bovine serum (Lonza), 1% nonessential amino acids, and penicillin/streptomycin (GIBCO) at 15,000 cells per well. Cells were transfected 24 hours later with a plasmid coding for the V2R version used in cryo-EM studies fused at its N terminus to the SNAP-tag (SNAP-V2R) (Cisbio Bioassays, Codolet, France). Transfections were performed with X-tremeGENE 360 (Sigma-Aldrich), according to the manufacturer's recommendations: 10 μl of a premix containing DMEM X-tremeGENE 360 (0.3 μl per well), SNAP-V2 coding plasmid (30 ng per well), and noncoding plasmid (70 ng per well) were added to the culture medium. After a 48-hour culture period, cells were rinsed once with Tag-lite medium (Cisbio Bioassays, Codolet, France) and incubated in the presence of Tag-lite medium containing 100 nM benzylguanine-Lumi4-Tb for at least 60 min at 37°C. Cells were then washed four times. For saturation studies, cells were incubated for at least 4 hours at 4°C in the presence of benzazepine-red nonpeptide vasopressin antagonist (BZ-DY647, Cisbio Bioassays, Codolet, France) at various concentrations ranging from 1×10^{-10} to 1×10^{-7} M. Nonspecific binding was determined in the presence of 10 μM vasopressin. For competition studies, cells were incubated for at least 4 hours at 4°C with benzazepine-red ligand (5 nM) and increasing concentrations of vasopressin ranging from 1×10^{-11} to 3.16×10^{-6} M. Fluorescent signals were measured at 620 nm (fluorescence of the donor) and at 665 nM (FRET signal) on a PHERAstar (BMG LABTECH, Champigny s/Marne, France). Results were expressed as the 665/620 ratio [10,000 × (665/620)]. Specific variation of the FRET ratio was plotted as a function of benzazepine-red concentration (saturation experiments) or competitor concentration

(competition experiment). All binding data were analyzed with GraphPad 8.3.0 (GraphPad Software Inc.) using the one site-specific binding equation. All results are expressed as the means ± SEM of at least three independent experiments performed in triplicate. K_i values were calculated from median inhibitory concentration values with the Cheng-Prusoff equation.

cAMP accumulation assays

As for V2R binding studies, V2R functional studies based on time-resolved FRET measurements were described previously (*36*, *57*). Briefly, Chinese hamster ovary cells were plated in six-well plates (Falcon) at 350,000 cells per well and transfected 24 hours later with jetPEI (Ozyme) with a pRK5 plasmid coding for the version of the V2R used in the cryo-EM studies. A mix of isotonic NaCl solution (200 µl per well) containing jetPEI (2 µl per well), V2R coding plasmid (1 ng per well), and noncoding plasmid (3000 ng per well) was added to the culture medium (2 ml). Twenty-four hours later, cells were harvested with trypsin and cultured in white-walled, flat-bottom, 96-well plates (Greiner CELLSTAR plate, Sigma-Aldrich) at a density of 30,000 cells per well in DMEM containing 10% fetal bovine serum (Lonza), 1% nonessential amino acids, and penicillin/streptomycin (GIBCO). After a 24-hour culture period, cells were treated for 30 min at 37°C in the cAMP buffer with or without increasing AVP concentrations (3.16×10^{-12} to 10^{-6} M) in the presence of 0.1 mM RO201724, a phosphodiesterase inhibitor (Sigma-Aldrich). The accumulated cAMP was quantified using the cAMP Dynamic 2 Kit (Cisbio Bioassays, Codolet, France) according to the manufacturer's protocol. Fluorescent signals were measured at 620 and 665 nm on a Spark 20M multimode microplate reader (Tecan). Data were plotted as the FRET ratio [10,000 × (665/620)] as a function of AVP concentration [log(AVP)]. Data were analyzed with GraphPad Prism using the "dose-response stimulation" subroutine. Median effective concentrations were determined using the log(agonist) versus response variable slope (four parameters) fit procedure. Experiments were repeated at least three times on different cultures, each condition in triplicate. Data are presented as means ± SEM.

SUPPLEMENTARY MATERIALS

Supplementary material for this article is available at http://advances.sciencemag.org/cgi/content/full/7/21/eabg5628/DC1

View/request a protocol for this paper from *Bio-protocol*.

REFERENCES AND NOTES

1. C. Barberis, B. Mouillac, T. Durroux, Structural bases of vasopressin/oxytocin receptor function. *J. Endocrinol.* **156**, 223–229 (1998).
2. C. Barberis, D. Morin, T. Durroux, B. Mouillac, G. Guillon, R. Seyer, M. Hibert, E. Tribollet, M. Manning, Molecular pharmacology of AVP and OT receptors and therapeutic potential. *Drug News Perspect.* **12**, 279–292 (1999).
3. J. H. Robben, N. V. A. M. Knoers, P. M. T. Deen, Regulation of the vasopressin V2 receptor by vasopressin in polarized renal collecting duct cells. *Mol. Biol. Cell* **15**, 5693–5699 (2004).
4. T. A. Treschan, J. Peters, D. C. Warltier, The vasopressin system: Physiology and clinical strategies. *Anesthesiology* **105**, 599–612 (2006).
5. X.-R. Ren, E. Reiter, S. Ahn, J. Kim, W. Chen, R. J. Lefkowitz, Different G protein-coupled receptor kinases govern G protein and β-arrestin-mediated signaling of V2 vasopressin receptor. *Proc. Natl. Acad. Sci. U.S.A.* **102**, 1448–1453 (2005).
6. G. Alonso, E. Galibert, V. Boulay, A. Guillou, A. Jean, V. Compan, G. Guillon, Sustained elevated levels of circulating vasopressin selectively stimulate the proliferation of kidney tubular cells via the activation of V_2 receptors. *Endocrinology* **150**, 239–250 (2009).
7. S. G. Ball, Vasopressin and disorders of water balance: The physiology and pathophysiology of vasopressin. *Ann. Clin. Biochem.* **44**, 417–431 (2007).
8. J.-P. Morello, D. G. Bichet, Nephrogenic diabetes insipidus. *Annu. Rev. Physiol.* **63**, 607–630 (2001).
9. B. J. Feldman, S. M. Rosenthal, G. A. Vargas, R. G. Fenwick, E. A. Huang, M. Matsuda-Abedini, R. H. Lustig, R. S. Mathias, A. A. Portale, W. L. Miller, S. E. Gitelman, Nephrogenic syndrome of inappropriate antidiuresis. *N. Engl. J. Med.* **352**, 1884–1890 (2005).
10. P. C. Harris, V. E. Torres, Polycystic kidney disease. *Annu. Rev. Med.* **60**, 321–337 (2009).
11. X. Edward Zhou, K. Melcher, H. Eric Xu, Structural biology of G protein-coupled receptor signaling complexes. *Protein Sci.* **28**, 487–501 (2019).
12. A. Gusach, I. Maslov, A. Luginina, V. Borshchevskiy, A. Mishin, V. Cherezov, Beyond structure: Emerging approaches to study GPCR dynamics. *Curr. Opin. Struct. Biol.* **63**, 18–25 (2020).
13. R. Fernandez-Leiro, S. H. W. Scheres, Unravelling biological macromolecules with cryo-electron microscopy. *Nature* **537**, 339–346 (2016).
14. B. Carpenter, C. G. Tate, Active state structures of G protein-coupled receptors highlight the similarities and differences in the G protein and arrestin coupling interfaces. *Curr. Opin. Struct. Biol.* **45**, 124–132 (2017).
15. J. García-Nafría, C. G. Tate, Cryo-EM structures of GPCRs coupled to G_s, G_i and G_o. *Mol. Cell. Endocrinol.* **488**, 1–13 (2019).
16. S. Loison, M. Cottet, H. Orcel, H. Adihou, R. Rahmeh, L. Lamarque, E. Trinquet, E. Kellenberger, M. Hibert, T. Durroux, B. Mouillac, D. Bonnet, Selective fluorescent nonpeptidic antagonists for vasopressin V_2GPCR: Application to ligand screening and oligomerization assays. *J. Med. Chem.* **55**, 8588–8602 (2012).
17. Y. Ala, D. Morin, B. Mouillac, N. Sabatier, R. Vargas, N. Cotte, M. Déchaux, C. Antignac, M. F. Arthus, M. Lonergan, M. S. Turner, M. N. Balestre, G. Alonso, M. Hibert, C. Barberis, G. N. Hendy, D. G. Bichet, S. Jard, Functional studies of twelve mutant V2 vasopressin receptors related to nephrogenic diabetes insipidus: Molecular basis of a mild clinical phenotype. *J. Am. Soc. Nephrol.* **9**, 1861–1872 (1998).
18. S. G. F. Rasmussen, B. T. DeVree, Y. Zou, A. C. Kruse, K. Y. Chung, T. S. Kobilka, F. S. Thian, P. S. Chae, E. Pardon, D. Calinski, J. M. Mathiesen, S. T. A. Shah, J. A. Lyons, M. Caffrey, S. H. Gellman, J. Steyaert, G. Skiniotis, W. I. Weis, R. K. Sunahara, B. K. Kobilka, Crystal structure of the β_2 adrenergic receptor-Gs protein complex. *Nature* **477**, 549–555 (2011).
19. C. Serradeil-Le Gal, C. Lacour, G. Valette, G. Garcia, L. Foulon, G. Galindo, L. Bankir, B. Pouzet, G. Guillon, C. Barberis, D. Chicot, S. Jard, P. Vilain, C. Garcia, E. Marty, D. Raufaste, G. Brossard, D. Nisato, J. P. Maffrand, G. Le Fur, Characterization of SR 121463A, a highly potent and selective, orally active vasopressin V2 receptor antagonist. *J. Clin. Invest.* **98**, 2729–2738 (1996).
20. T. C. Terwilliger, S. J. Ludtke, R. J. Read, P. D. Adams, P. V. Afonine, Improvement of cryo-EM maps by density modification. *Nat. Methods* **17**, 923–927 (2020).
21. B. Delort, P. Renault, L. Charlier, F. Raussin, J. Martinez, N. Floquet, Coarse-grained prediction of peptide binding to G-protein coupled receptors. *J. Chem. Inf. Model.* **57**, 562–571 (2017).
22. G. Ferré, M. Louet, O. Saurel, B. Delort, G. Czaplicki, C. M'Kadmi, M. Damian, P. Renault, S. Cantel, L. Gavara, P. Demange, J. Marie, J.-A. Fehrentz, N. Floquet, A. Milon, J.-L. Banères, Structure and dynamics of G protein-coupled receptor–bound ghrelin reveal the critical role of the octanoyl chain. *Proc. Natl. Acad. Sci. U.S.A.* **116**, 17525–17530 (2019).
23. M. Igaev, C. Kutzner, L. V. Bock, A. C. Vaiana, H. Grubmüller, Automated cryo-EM structure refinement using correlation-driven molecular dynamics. *eLife* **8**, e43542 (2019).
24. F. M. Assadi-Porter, M. Tonelli, E. Maillet, K. Hallenga, O. Benard, M. Max, J. L. Markley, Direct NMR detection of the binding of functional ligands to the human sweet receptor, a heterodimeric family 3 GPCR. *J. Am. Chem. Soc.* **130**, 7212–7213 (2008).
25. S. Bartoschek, T. Klabunde, E. Defossa, V. Dietrich, S. Stengelin, C. Griesinger, T. Carlomagno, I. Focken, K. U. Wendt, Drug design for G-protein-coupled receptors by a ligand-based NMR method. *Angew. Chem. Int. Ed. Engl.* **49**, 1426–1429 (2010).
26. H. E. Kato, Y. Zhang, H. Hu, C.-M. Suomivuori, F. M. N. Kadji, J. Aoki, K. Krishna Kumar, R. Fonseca, D. Hilger, W. Huang, N. R. Latorraca, A. Inoue, R. O. Dror, B. K. Kobilka, G. Skiniotis, Conformational transitions of a neurotensin receptor 1–Gi1 complex. *Nature* **572**, 80–85 (2019).
27. A. Dashti, G. Mashayekhi, M. Shekhar, D. B. Hail, S. Salah, P. Schwander, A. D. Georges, A. Singharoy, J. Frank, A. Ourmazd, Retrieving functional pathways of biomolecules from single-particle snapshots. *Nat. Commun.* **11**, 4734 (2020).
28. Y. Waltenspühl, J. Schöppe, J. Ehrenmann, L. Kummer, A. Plückthun, Crystal structure of the human oxytocin receptor. *Sci. Adv.* **6**, eabb5419 (2020).
29. B. Mouillac, B. Chini, M. N. Balestre, J. Elands, S. Trumpp-Kallmeyer, J. Hoflack, M. Hibert, S. Jard, C. Barberis, The binding site of neuropeptide vasopressin V1a receptor. Evidence for a major localization within transmembrane regions. *J. Biol. Chem.* **270**, 25771–25777 (1995).
30. M. Hibert, J. Hoflack, S. Trumpp-Kallmeyer, B. Mouillac, B. Chini, E. Mahé, N. Cotte, S. Jard, M. Manning, C. Barberis, Functional architecture of vasopressin/oxytocin receptors. *J. Recept. Signal Transduct. Res.* **19**, 589–596 (1999).
31. R. Macion-Dazard, N. Callahan, Z. Xu, N. Wu, M. Thibonnier, M. Shoham, Mapping the binding site of six nonpeptide antagonists to the human V_2-renal vasopressin receptor. *J. Pharmacol. Exp. Ther.* **316**, 564–571 (2006).

32. N. Cotte, M.-N. Balestre, A. Aumelas, E. Mahé, S. Phalipou, D. Morin, M. Hibert, M. Manning, T. Durroux, C. Barberis, B. Mouillac, Conserved aromatic residues in the transmembrane region VI of the V_{1a} vasopressin receptor differentiate agonist vs. antagonist ligand binding. *Eur. J. Biochem.* **267**, 4253–4263 (2000).
33. C. Tahtaoui, M.-N. Balestre, P. Klotz, D. Rognan, C. Barberis, B. Mouillac, M. Hibert, Identification of the binding sites of the SR49059 nonpeptide antagonist into the V_{1a} vasopressin receptor using sulfydryl-reactive ligands and cysteine mutants as chemical sensors. *J. Biol. Chem.* **278**, 40010–40019 (2003).
34. S. Filipek, Molecular switches in GPCRs. *Curr. Opin. Struct. Biol.* **55**, 114–120 (2019).
35. X. Deupi, Relevance of rhodopsin studies for GPCR activation. *Biochim. Biophys. Acta* **1837**, 674–682 (2014).
36. J. Tenenbaum, M. A. Ayoub, S. Perkovska, A.-L. Adra-Delenne, C. Mendre, B. Ranchin, G. Bricca, G. Geelen, B. Mouillac, T. Durroux, D. Morin, The constitutively active V2 receptor mutants conferring NSIAD are weakly sensitive to agonist and antagonist regulation. *PLOS ONE* **4**, e8383 (2009).
37. M. D. Rochdi, G. A. Vargas, E. Carpentier, G. Oligny-Longpré, S. Chen, A. Kovoor, S. E. Gitelman, S. M. Rosenthal, M. von Zastrow, M. Bouvier, Functional characterization of vasopressin type 2 receptor substitutions (R137H/C/L) leading to nephrogenic diabetes insipidus and nephrogenic syndrome of inappropriate antidiuresis: Implications for treatments. *Mol. Pharmacol.* **77**, 836–845 (2010).
38. V. Bernier, M. Lagacé, M. Lonergan, M.-F. Arthus, D. G. Bichet, M. Bouvier, Functional rescue of the constitutively internalized V2 vasopressin receptor mutant R137H by the pharmacological chaperone action of SR49059. *Mol. Endocrinol.* **18**, 2074–2084 (2004).
39. L. S. Barak, R. H. Oakley, S. A. Laporte, M. G. Caron, Constitutive arrestin-mediated desensitization of a human vasopressin receptor mutant associated with nephrogenic diabetes insipidus. *Proc. Natl. Acad. Sci. U.S.A.* **98**, 93–98 (2001).
40. W. I. Weis, B. K. Kobilka, The molecular basis of G protein-coupled receptor activation. *Annu. Rev. Biochem.* **87**, 897–919 (2018).
41. D. Hilger, M. Masureel, B. K. Kobilka, Structure and dynamics of GPCR signaling complexes. *Nat. Struct. Mol. Biol.* **25**, 4–12 (2018).
42. J. García-Nafría, Y. Lee, X. Bai, B. Carpenter, C. G. Tate, Cryo-EM structure of the adenosine A_{2A} receptor coupled to an engineered heterotrimeric G protein. *eLife* **7**, e35946 (2018).
43. Y.-L. Liang, M. Khoshouei, G. Deganutti, A. Glukhova, C. Koole, T. S. Peat, M. Radjainia, J. M. Plitzko, W. Baumeister, L. J. Miller, D. L. Hay, A. Christopoulos, C. A. Reynolds, D. Wootten, P. M. Sexton, Cryo-EM structure of the active, G_s-protein complexed, human CGRP receptor. *Nature* **561**, 492–497 (2018).
44. Y.-L. Liang, M. Khoshouei, M. Radjainia, Y. Zhang, A. Glukhova, J. Tarrasch, D. M. Thal, S. G. B. Furness, G. Christopoulos, T. Coudrat, R. Danev, W. Baumeister, L. J. Miller, A. Christopoulos, B. K. Kobilka, D. Wootten, G. Skiniotis, P. M. Sexton, Phase-plate cryo-EM structure of a class B GPCR-G-protein complex. *Nature* **546**, 118–123 (2017).
45. A. Koehl, H. Hu, S. Maeda, Y. Zhang, Q. Qu, J. M. Paggi, N. R. Latorraca, D. Hilger, R. Dawson, H. Matile, G. F. X. Schertler, S. Granier, W. I. Weis, R. O. Dror, A. Manglik, G. Skiniotis, B. K. Kobilka, Structure of the μ-opioid receptor–G_i protein complex. *Nature* **558**, 547–552 (2018).
46. K. Kim, T. Che, O. Panova, J. F. DiBerto, J. Lyu, B. E. Krumm, D. Wacker, M. J. Robertson, A. B. Seven, D. E. Nichols, B. K. Shoichet, G. Skiniotis, B. L. Roth, Structure of a hallucinogen-activated Gq-coupled 5-HT_{2A} serotonin receptor. *Cell* **182**, 1574–1588. e19 (2020).
47. A. Manglik, B. Kobilka, The role of protein dynamics in GPCR function: Insights from the β_2AR and rhodopsin. *Curr. Opin. Cell Biol.* **27**, 136–143 (2014).
48. B. Chini, B. Mouillac, M. N. Balestre, S. Trumpp-Kallmeyer, J. Hoflack, M. Hibert, M. Andriolo, S. Pupier, S. Jard, C. Barberis, Two aromatic residues regulate the response of the human oxytocin receptor to the partial agonist arginine vasopressin. *FEBS Lett.* **397**, 201–206 (1996).
49. M. Manning, A. Misicka, A. Olma, K. Bankowski, S. Stoev, B. Chini, T. Durroux, B. Mouillac, M. Corbani, G. Guillon, Oxytocin and vasopressin agonists and antagonists as research tools and potential therapeutics. *J. Neuroendocrinol.* **24**, 609–628 (2012).
50. V. Bernier, J.-P. Morello, A. Zarruk, N. Debrand, A. Salahpour, M. Lonergan, M.-F. Arthus, A. Laperrière, R. Brouard, M. Bouvier, D. G. Bichet, Pharmacologic chaperones as a potential treatment for X-linked nephrogenic diabetes insipidus. *J. Am. Soc. Nephrol.* **17**, 232–243 (2006).
51. K. Kalenga, A. Persu, E. Goffin, E. Lavenne-Pardonge, P. J. van Cangh, D. G. Bichet, O. Devuyst, Intrafamilial phenotype variability in nephrogenic diabetes insipidus. *Am. J. Kidney Dis.* **39**, 737–743 (2002).
52. J. P. Morello, M. Bouvier, U. E. Petäjä-Repo, D. G. Bichet, Pharmacological chaperones: A new twist on receptor folding. *Trends Pharmacol. Sci.* **21**, 466–469 (2000).
53. V. E. Torres, A. B. Chapman, O. Devuyst, R. T. Gansevoort, R. D. Perrone, J. Lee, M. E. Hoke, A. Estilo, O. Sergeyeva, Multicenter study of long-term safety of tolvaptan in later-stage autosomal dominant polycystic kidney disease. *Clin. J. Am. Soc. Nephrol.* **16**, 48–58 (2021).
54. D. Bockenhauer, E. Carpentier, D. Rochdi, W. van't Hoff, B. Breton, V. Bernier, M. Bouvier, D. G. Bichet, Vasopressin type 2 receptor V88M mutation: Molecular basis of partial and complete nephrogenic diabetes insipidus. *Nephron Physiol.* **114**, p1–p10 (2010).
55. F. Prosperi, Y. Suzumoto, P. Marzuillo, V. Costanzo, S. Jelen, A. Iervolino, S. Guarino, A. La Manna, E. Miraglia Del Giudice, A. F. Perna, M. Zacchia, E. Cordat, G. Capasso, F. Trepiccione, Characterization of five novel vasopressin V2 receptor mutants causing nephrogenic diabetes insipidus reveals a role of tolvaptan for M272R-V2R mutation. *Sci. Rep.* **10**, 16383 (2020).
56. L. Wang, J. Xu, S. Cao, D. Sun, H. Liu, Q. Lu, Z. Liu, Y. Du, C. Zhang, Cryo-EM structure of the AVP-vasopressin receptor 2-G_s signaling complex. *Cell Res.*, (2021); doi:10.1038/s41422-021-00483-z.
57. F. Jean-Alphonse, S. Perkovska, M.-C. Frantz, T. Durroux, C. Méjean, D. Morin, S. Loison, D. Bonnet, M. Hibert, B. Mouillac, C. Mendre, Biased agonist pharmacochaperones of the AVP V2 receptor may treat congenital nephrogenic diabetes insipidus. *J. Am. Soc. Nephrol.* **20**, 2190–2203 (2009).
58. G. Tang, L. Peng, P. R. Baldwin, D. S. Mann, W. Jiang, I. Rees, S. J. Ludtke, EMAN2: An extensible image processing suite for electron microscopy. *J. Struct. Biol.* **157**, 38–46 (2007).
59. D. Kimanius, B. O. Forsberg, S. H. W. Scheres, E. Lindahl, Accelerated cryo-EM structure determination with parallelisation using GPUS in RELION-2. *eLife* **5**, e18722 (2016).
60. D. N. Mastronarde, Automated electron microscope tomography using robust prediction of specimen movements. *J. Struct. Biol.* **152**, 36–51 (2005).
61. J. Zivanov, T. Nakane, B. O. Forsberg, D. Kimanius, W. J. H. Hagen, E. Lindahl, S. H. W. Scheres, New tools for automated high-resolution cryo-EM structure determination in RELION-3. *eLife* **7**, e42166 (2018).
62. K. Zhang, Gctf: Real-time CTF determination and correction. *J. Struct. Biol.* **193**, 1–12 (2016).
63. D. Tegunov, P. Cramer, Real-time cryo-EM data pre-processing with *Warp*. *bioRxiv*, 338558 (2018).
64. T. Grant, A. Rohou, N. Grigorieff, *cis*TEM, user-friendly software for single-particle image processing. *eLife* **7**, e35383 (2018).
65. A. Punjani, J. L. Rubinstein, D. J. Fleet, M. A. Brubaker, CryoSPARC: Algorithms for rapid unsupervised cryo-EM structure determination. *Nat. Methods* **14**, 290–296 (2017).
66. J. B. Heymann, Guidelines for using Bsoft for high resolution reconstruction and validation of biomolecular structures from electron micrographs. *Protein Sci.* **27**, 159–171 (2018).
67. G. Cardone, J. B. Heymann, A. C. Steven, One number does not fit all: Mapping local variations in resolution in cryo-EM reconstructions. *J. Struct. Biol.* **184**, 226–236 (2013).
68. T. C. Terwilliger, O. V. Sobolev, P. V. Afonine, P. D. Adams, Automated map sharpening by maximization of detail and connectivity. *Acta Crystallogr. D Struct. Biol.* **74**, 545–559 (2018).
69. B. Webb, A. Sali, Protein structure modeling with MODELLER. *Methods Mol. Biol.* **1654**, 39–54 (2017).
70. S. Granier, A. Manglik, A. C. Kruse, T. S. Kobilka, F. S. Thian, W. I. Weis, B. K. Kobilka, Structure of the δ-opioid receptor bound to naltrindole. *Nature* **485**, 400–404 (2012).
71. C. K. Wu, B. Hu, J. P. Rose, Z.-J. Liu, T. L. Nguyen, C. Zheng, E. Breslow, B.-C. Wang, Structures of an unliganded neurophysin and its vasopressin complex: Implications for binding and allosteric mechanisms. *Protein Sci.* **10**, 1869–1880 (2001).
72. J. P. Rose, C. Wu, C.-D. Hsiao, E. Breslow, B.-C. Wang, Crystal structure of the neurophysin–oxytocin complex. *Nat. Struct. Biol.* **3**, 163–169 (1996).
73. J. M. Schmidt, O. Ohlenschläger, H. Rüterjans, Z. Grzonka, E. Kojro, I. Pavo, F. Fahrenholz, Conformation of [8-arginine]vasopressin and V1 antagonists in dimethyl sulfoxide solution derived from two-dimensional NMR spectroscopy and molecular dynamics simulation. *Eur. J. Biochem.* **201**, 355–371 (1991).
74. B. S. Ibrahim, V. Pattabhi, Trypsin inhibition by a peptide hormone: Crystal structure of trypsin–vasopressin complex. *J. Mol. Biol.* **348**, 1191–1198 (2005).
75. S. J. Marrink, H. J. Risselada, S. Yefimov, D. P. Tieleman, A. H. De Vries, The MARTINI force field: Coarse grained model for biomolecular simulations. *J. Phys. Chem. B* **111**, 7812–7824 (2007).
76. X. Daura, B. Jaun, D. Seebach, W. F. van Gunsteren, A. E. Mark, Reversible peptide folding in solution by molecular dynamics simulation. *J. Mol. Biol.* **280**, 925–932 (1998).
77. M. J. Abraham, T. Murtola, R. Schulz, S. Páll, J. C. Smith, B. Hess, E. Lindah, Gromacs: High performance molecular simulations through multi-level parallelism from laptops to supercomputers. *SoftwareX.* **1–2**, 19–25 (2015).
78. W. Humphrey, A. Dalke, K. Schulten, VMD: Visual molecular dynamics. *J. Mol. Graph.* **14**, 33–38 (1996).
79. T. A. Wassenaar, K. Pluhackova, R. A. Böckmann, S. J. Marrink, D. P. Tieleman, Going backward: A flexible geometric approach to reverse transformation from coarse grained to atomistic models. *J. Chem. Theory Comput.* **10**, 676–690 (2014).
80. R. B. Best, X. Zhu, J. Shim, P. E. M. Lopes, J. Mittal, M. Feig, A. D. Mackerell Jr., Optimization of the additive CHARMM all-atom protein force field targeting improved sampling of the backbone φ, ψ and side-chain χ_1 and χ_2 dihedral angles. *J. Chem. Theory Comput.* **8**, 3257–3273 (2012).

81. P. Emsley, K. Cowtan, *Coot*: Model-building tools for molecular graphics. *Acta Crystallogr. Sect. D* **60**, 2126–2132 (2004).
82. P. V. Afonine, M. Mustyakimov, R. W. Grosse-Kunstleve, N. W. Moriarty, P. Langan, P. D. Adams, Joint x-ray and neutron refinement with *phenix.refine*. *Acta Crystallogr. Sect. D* **66**, 1153–1163 (2010).
83. V. B. Chen, W. B. Arendall III, J. J. Headd, D. A. Keedy, R. M. Immormino, G. J. Kapral, L. W. Murray, J. S. Richardson, D. C. Richardson, *MolProbity*: All-atom structure validation for macromolecular crystallography. *Acta Crystallogr. Sect. D* **66**, 12–21 (2010).
84. I. Vasiliauskaité-Brooks, R. D. Healey, P. Rochaix, J. Saint-Paul, R. Sounier, C. Grison, T. Waltrich-Augusto, M. Fortier, F. Hoh, E. M. Saied, C. Arenz, S. Basu, C. Leyrat, S. Granier, Structure of a human intramembrane ceramidase explains enzymatic dysfunction found in leukodystrophy. *Nat. Commun.* **9**, 5437 (2018).
85. E. L. Wu, X. Cheng, S. Jo, H. Rui, K. C. Song, E. M. Dávila-Contreras, Y. Qi, J. Lee, V. Monje-Galvan, R. M. Venable, J. B. Klauda, W. Im, CHARMM-GUI Membrane Builder toward realistic biological membrane simulations. *J. Comput. Chem.* **35**, 1997–2004 (2014).
86. J. Lee, X. Cheng, J. M. Swails, M. S. Yeom, P. K. Eastman, J. A. Lemkul, S. Wei, J. Buckner, J. C. Jeong, Y. Qi, S. Jo, V. S. Pande, D. A. Case, C. L. Brooks III, A. D. Mac Kerell Jr., J. B. Klauda, W. Im, CHARMM-GUI input generator for NAMD, GROMACS, AMBER, OpenMM, and CHARMM/OpenMM simulations using the CHARMM36 additive force field. *J. Chem. Theory Comput.* **12**, 405–413 (2016).
87. P. J. Steinbach, B. R. Brooks, New spherical-cutoff methods for long-range forces in macromolecular simulation. *J. Comput. Chem.* **15**, 667–683 (1994).
88. U. Essmann, L. Perera, M. L. Berkowitz, T. Darden, H. Lee, L. G. Pedersen, A smooth particle mesh Ewald method. *J. Chem. Phys.* **103**, 8577–8593 (1995).
89. C. Balusek, H. Hwang, C. H. Lau, K. Lundquist, A. Hazel, A. Pavlova, D. L. Lynch, P. H. Reggio, Y. Wang, J. C. Gumbart, Accelerating membrane simulations with hydrogen mass repartitioning. *J. Chem. Theory Comput.* **15**, 4673–4686 (2019).
90. K. S. Sharma, G. Durand, F. Gabel, P. Bazzacco, C. Le Bon, E. Billon-Denis, L. J. Catoire, J.-L. Popot, C. Ebel, B. Pucci, Non-ionic amphiphilic homopolymers: Synthesis, solution properties, and biochemical validation. *Langmuir* **28**, 4625–4639 (2012).
91. R. Rahmeh, M. Damian, M. Cottet, H. Orcel, C. Mendre, T. Durroux, K. S. Sharma, G. Durand, B. Pucci, E. Trinquet, J. M. Zwier, X. Deupi, P. Bron, J. L. Banères, B. Mouillac, S. Granier, Structural insights into biased G protein-coupled receptor signaling revealed by fluorescence spectroscopy. *Proc. Natl. Acad. Sci. U.S.A.* **109**, 6733–6738 (2012).
92. M. Mayer, B. Meyer, Characterization of ligand binding by saturation transfer difference NMR spectroscopy. *Angew. Chem. Int. Ed.* **38**, 1784–1788 (1999).
93. N. R. Krishna, V. Jayalakshmi, Quantitative analysis of STD-NMR spectra of reversibly forming ligand-receptor complexes. *Top. Curr. Chem.* **273**, 15–54 (2008).
94. J. M. Zwier, T. Roux, M. Cottet, T. Durroux, S. Douzon, S. Bdioui, N. Gregor, E. Bourrier, N. Oueslati, L. Nicolas, N. Tinel, C. Boisseau, P. Yverneau, F. Charrier-Savournin, M. Fink, E. Trinquet, A fluorescent ligand-binding alternative using Tag-lite® technology. *J. Biomol. Screen.* **15**, 1248–1259 (2010).

Acknowledgments: We thank the cryo-EM staff at EMBL of Heidelberg (Germany) and the IGF Arpege platform of Pharmacology. We thank R. Healey for critical reading of the manuscript and A. Sagar for helping in software installation. **Funding:** This work was supported by grants from FRM (grant DEQ20150331736) and ANR (grants ANR-19-CE11-0014 and ANR-17-CE11-0011) and core funding from CNRS, INSERM, ENSCM, and Université de Montpellier. We thank GENCI (Grand Équipement National de Calcul Intensif) and TGCC/IDRIS to have selected us for the "Great Challenge" phases of both the Irène JOLIOT-CURIE and Jean-ZAY supercomputers. The CBS is a member of the French Infrastructure for Integrated Structural Biology (FRISBI) supported by ANR (ANR-10-INBS-05). J.B. was supported by a doctoral fellowship from the Ministère de L'Enseignement Supérieur, de la Recherche et de l'Innovation. **Author contributions:** J.B. purified V2R and AVP-V2R-G_s-Nb35 complexes, screened samples by NS-EM and cryo-EM, prepared grids, collected and processed cryo-EM data, generated the cryo-EM maps, and built some extended data figures. H.O. managed the Sf9 cell culture and baculoviral infections, expressed and purified V2R, purified AVP-V2R-G_s-Nb35 complexes, and prepared grids for cryo-EM. N.F. developed the CG-REMD modeling approach, fitted the models onto the cryo-EM maps, and back-mapped the models to all-atom representation. C.L. built the final models of AVP-V2R-G_s-Nb35 complexes into cryo-EM and performed MDSs. J.L.-K.-H. and A.A. screened samples by NS-EM and prepared grids for cryo-EM. G.G. contributed to the expression and purification of V2R. J.S.-P. expressed and purified G_s protein and Nb35 nanobody. S.T. contributed to processing cryo-EM data for generating cryo-EM maps. M.L. contributed to CG-REMD MD modeling. S.G. established all the initial procedures for the ternary complex purification. R.S. designed G_s constructs, expressed and purified G_s protein, and built most of the figures. H.D. managed STD NMR experiments and generated the STD NMR data. B.M. designed the V2R construct and determined its pharmacological properties with the help of H.O. S.G., P.B., and B.M. wrote the paper with the input from J.B., N.F., and H.D. Last, S.G., P.B., and B.M. supervised the project. **Competing interests:** The authors declare that they have no competing interests. **Data and materials availability:** The cryo-EM density maps for the AVP-V2R-G_s-Nb35 complex have been deposited in the Electron Microscopy Data Bank (EMDB) under accession codes EMD-12128 (L state) and EMD-12129 (T state). The coordinates for the models of AVP-V2R-G_s-Nb35 complex have been deposited in the PDB under accession numbers 7BB6 and 7BB7 (L and T states, respectively). All data needed to evaluate the conclusions in the paper are present in the paper and/or the Supplementary Materials. Additional data related to this paper may be requested from the authors.

Submitted 14 January 2021
Accepted 1 April 2021
Published 21 May 2021
10.1126/sciadv.abg5628

Citation: J. Bous, H. Orcel, N. Floquet, C. Leyrat, J. Lai-Kee-Him, G. Gaibelet, A. Ancelin, J. Saint-Paul, S. Trapani, M. Louet, R. Sounier, H. Déméné, S. Granier, P. Bron, B. Mouillac, Cryo–electron microscopy structure of the antidiuretic hormone arginine-vasopressin V2 receptor signaling complex. *Sci. Adv.* **7**, eabg5628 (2021).

ScienceAdvances

Cryo–electron microscopy structure of the antidiuretic hormone arginine-vasopressin V2 receptor signaling complex

Julien Bous, Hélène Orcel, Nicolas Floquet, Cédric Leyrat, Joséphine Lai-Kee-Him, Gérald Gaibelet, Aurélie Ancelin, Julie Saint-Paul, Stefano Trapani, Maxime Louet, Rémy Sounier, Hélène Déméné, Sébastien Granier, Patrick Bron and Bernard Mouillac

Sci Adv **7** (21), eabg5628.
DOI: 10.1126/sciadv.abg5628

Science Advances (ISSN 2375-2548) is published by the American Association for the Advancement of Science, 1200 New York Avenue NW, Washington, DC 20005. The title *Science Advances* is a registered trademark of AAAS.

Science Advances
AAAS

advances.sciencemag.org/cgi/content/full/7/21/eabg5628/DC1

Supplementary Materials for

Cryo–electron microscopy structure of the antidiuretic hormone arginine-vasopressin V2 receptor signaling complex

Julien Bous, Hélène Orcel, Nicolas Floquet, Cédric Leyrat, Joséphine Lai-Kee-Him, Gérald Gaibelet, Aurélie Ancelin, Julie Saint-Paul, Stefano Trapani, Maxime Louet, Rémy Sounier, Hélène Déméné, Sébastien Granier*, Patrick Bron*, Bernard Mouillac*

*Corresponding author. Email: sebastien.granier@igf.cnrs.fr (S.G.); patrick.bron@cbs.cnrs.fr (P.B.); bernard.mouillac@igf.cnrs.fr (B.M.)

Published 21 May 2021, *Sci. Adv.* **7**, eabg5628 (2021)
DOI: 10.1126/sciadv.abg5628

The PDF file includes:

Other Supplementary Material for this manuscript includes the following:

(available at advances.sciencemag.org/cgi/content/full/7/21/eabg5628/DC1)

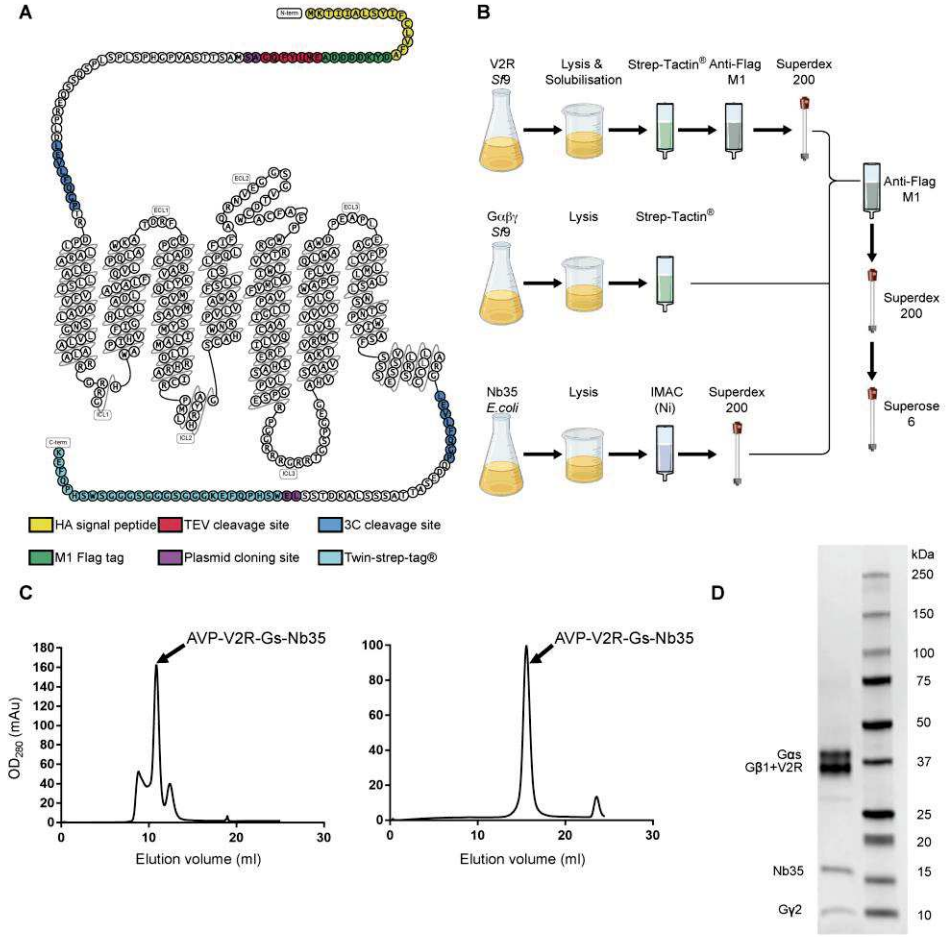

Fig. S1. Overview of AVP-V2R-Gs-Nb35 complex preparation and purification. **A**) Modified snake plot from https://gpcrdb.org of the engineered V2R construct used for cryo-EM structure determination. HA, hemagglutinin signal peptide; TEV protease, tobacco etch virus protease; 3C, human rhinovirus 3C protease; plasmid cloning sites are Nhe1 and Xho1 restriction sites. **B**) Workflow for AVP-V2R-Gs-Nb35 assembly. V2R receptor, Gs heterotrimer and Nb35 were expressed and purified separately, the complex being isolated by a final affinity chromatography and two successive SEC steps. **C**) Representative chromatograms of the AVP-V2R-Gs-Nb35 complex using Superdex200 and Superose6 SEC columns show a monodisperse peak. Fractions containing the sample were combined and concentrated for preparation of cryo-EM grids. **D**) SDS-PAGE of peak fraction from the Superose6 step. Coomassie blue staining of proteins confirmed that the complex is made of Gαs, V2R, Gβ1, Nb35 and Gγ2 (AVP is not visible).

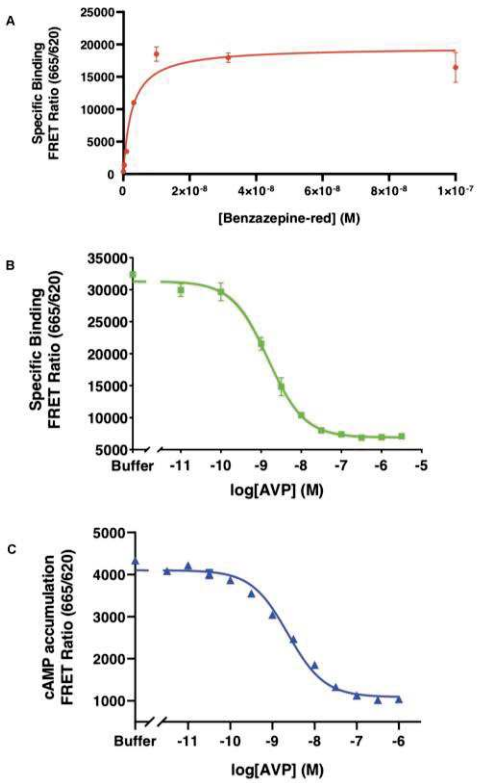

Fig. S2. **Pharmacological and functional properties of the cryo-EM V2R construct. A**) Binding of the benzazepine-red fluorescent antagonist to the V2R construct measured by FRET (see Methods). Specific binding of BZ-Red from a typical saturation assay is shown as FRET ratio (665nm/620 nm). The experiment was repeated 3 times each point measured in triplicate. Each value is presented as mean ± SEM. **B**) Binding of AVP to the V2R construct is illustrated as FRET ratio (665nm/620nm). Specific binding of benzazepine-red is shown. The fluorescent antagonist was used at 5 nM with or without increasing concentrations of AVP. A typical competition curve is shown, and was repeated at least 3 times each point in triplicate. Each value is presented as mean ± SEM. **C**) Capacity of the V2R construct to functionally activate adenylyl cyclase measured by FRET (see Methods). The cAMP accumulation is shown as FRET ratio (665nm/620nm) and measured in the presence of increasing concentrations of AVP. A typical experiment is shown, was repeated at least 3 times, each point in triplicate. Each value is presented as mean ± SEM.

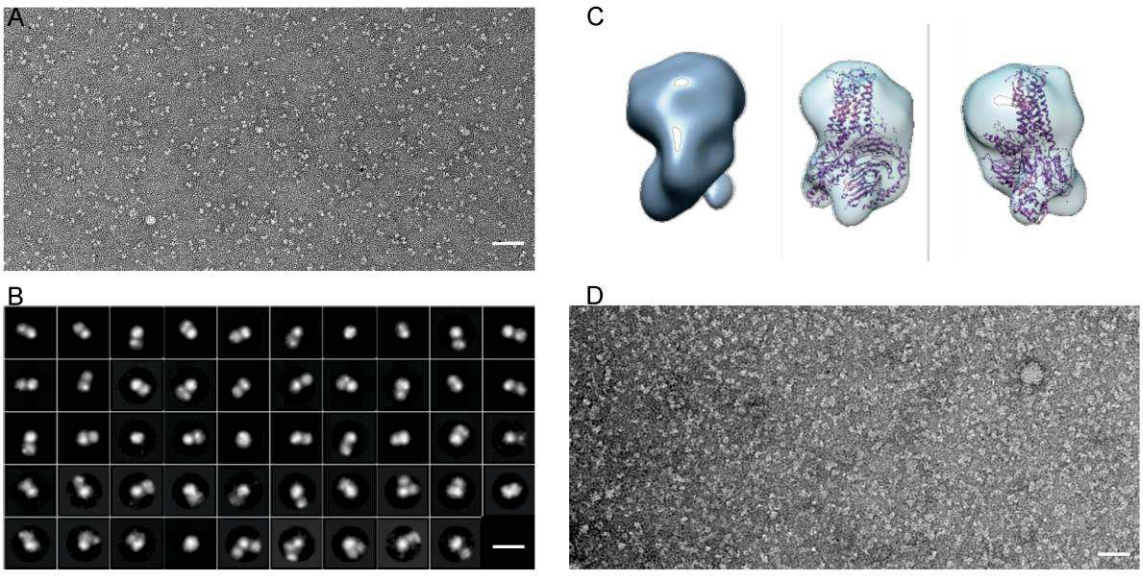

Fig. S3. **Negative stain electron microscopy characterization of the AVP-V2R-Gs-Nb35 complex. A**) Representative micrograph of the purified sample of the complex isolated from the Superose6 SEC peak (scale bar, 54 nm) **B**) 2D most representative class averages showing different orientations. (scale bar, 18 nm). **C**) Density map of the AVP-V2R-Gs-Nb35 complex (contour level set to 0.115), and fitting of the 3D model of the crystal structure of β2ARGs-Nb35 complex in this low resolution map. **D**) Representative micrograph of AVP-V2R-Gs-Nb35 complex dissociated using an excess of 10 μM SR121463 (selective nonpeptide antagonist of the V2R) and 100 μM GTPγS (scale bar, 43 nm).

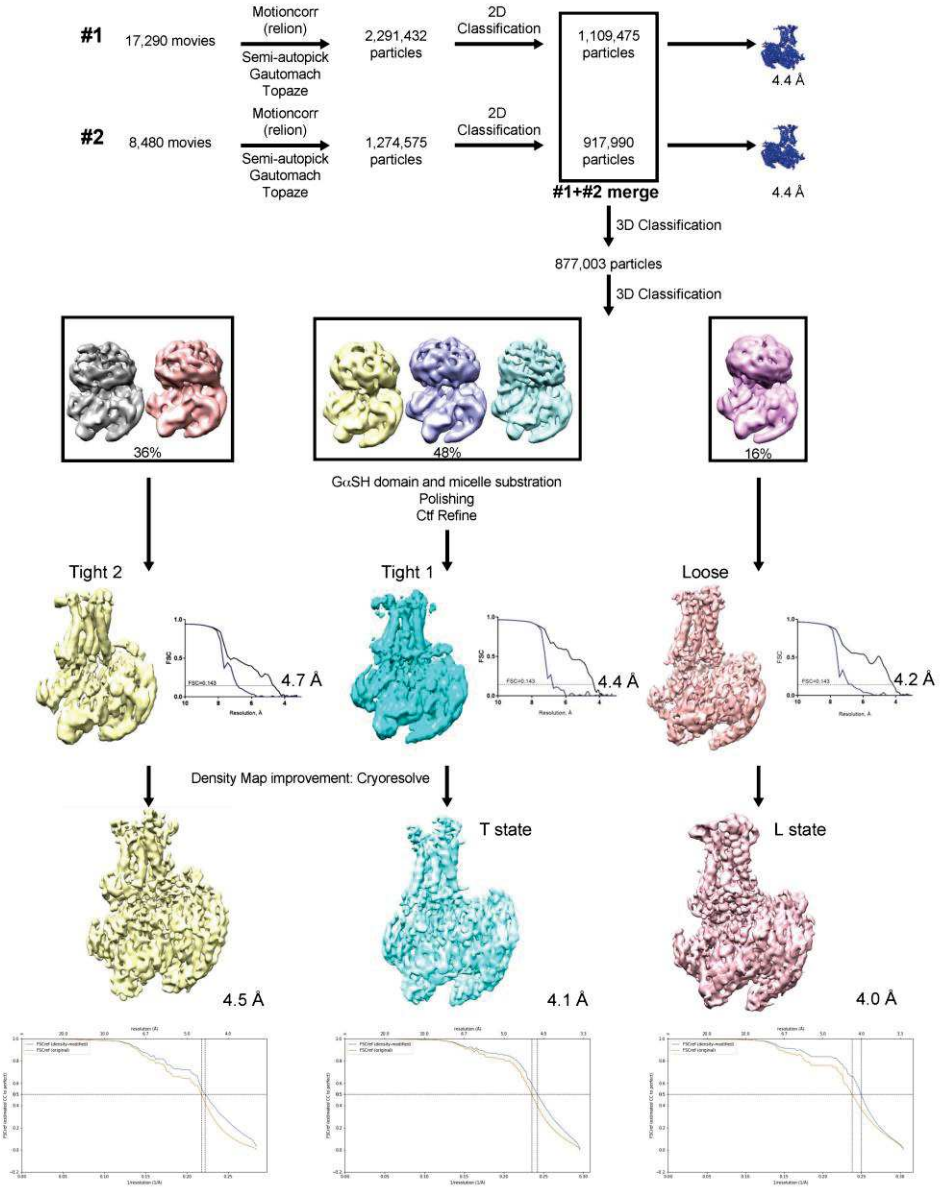

Fig. S4. Cryo-EM workflow. Flowchart of the single particle analysis for the two datasets processed separately. Merging of the two sets, substates determination and high-resolution reconstructions. Density map improvement with cryoresolve as a final step.

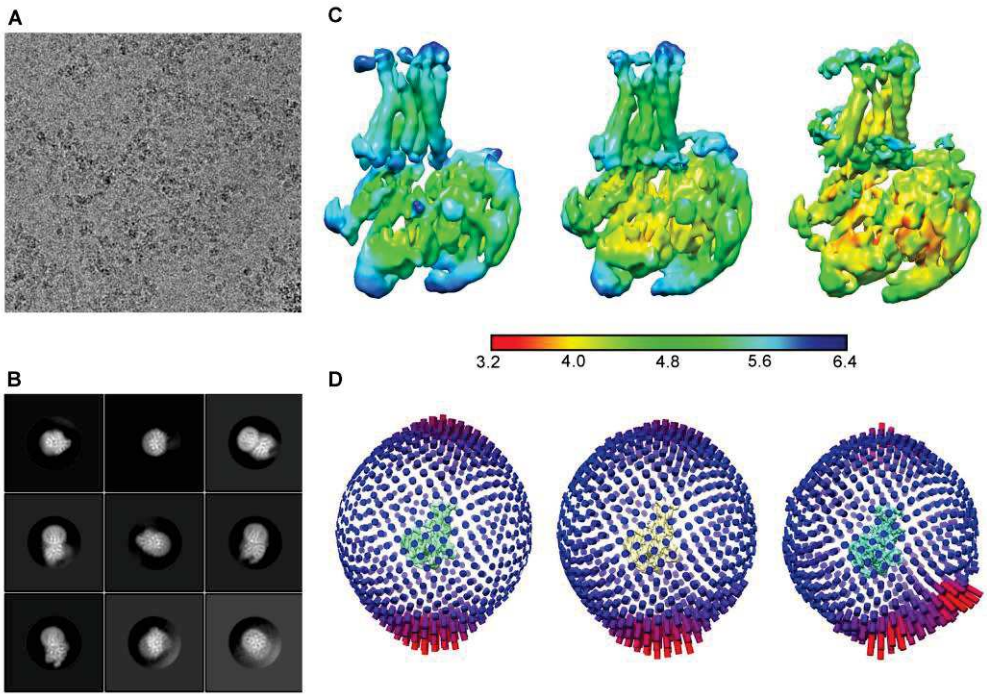

Fig. S5. Cryo-EM characterization of the AVP-V2R-Gs-Nb35 complex. A) Representative micrograph of the AVP-V2R-Gs-Nb35 protein complex (scale bar, 30 nm). **B**) Representative 2D class averages showing distinct secondary structure features (including the V2R TM regions embedded in the detergent micelle) and different orientations of the AVP-V2R-Gs-Nb35 complex (scale bar, 5 nm). **C**) Local resolution estimation computed with blocres from bsoft program; Tight-2, Tight-1 and Loose particle density maps are shown, respectively. **D**) Euler angle distribution of particles from the final reconstructions for Tight-2, Tight-1 and Loose populations.

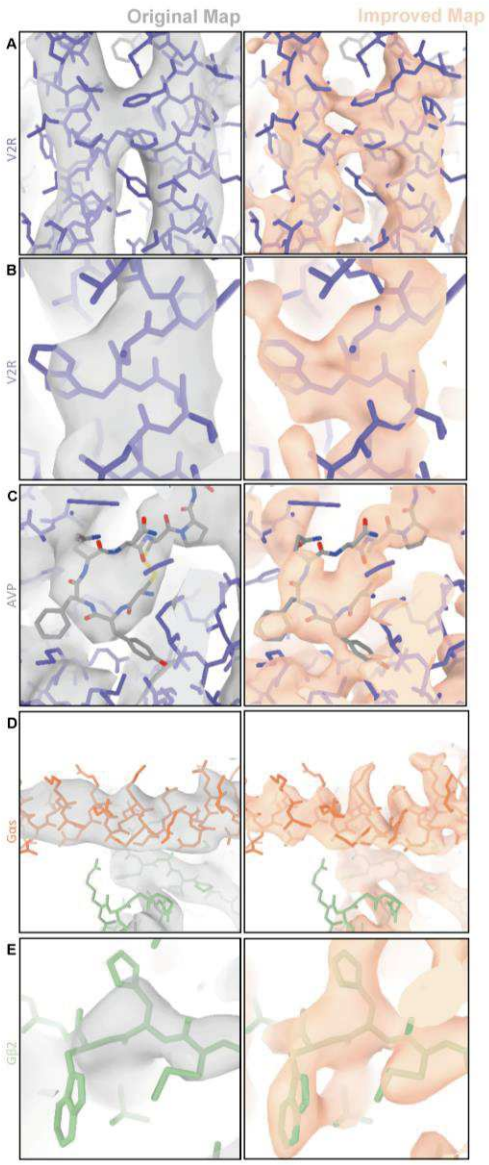

Fig. S6. **Improvement of the L density map using cryoresolve.** In all panels, the density map and the corresponding final all-atom 3D model are superimposed. The improved map (right) is compared to the original map (left). V2R is depicted in purple, AVP in grey, Gαs subunit in orange and Gβ2 subunit in green. Increase in the visibility of several different regions of the AVP-V2R-Gs-Nb35 complex is shown: for instance contacts between F214 and F287 in V2R TM5 and 6 (**A**), W164 in V2R TM4 (**B**), AVP (**C**), N-terminal α helix of Gαs subunit (**D**) and H62-W63 in Gβ2 subunit (**E**).

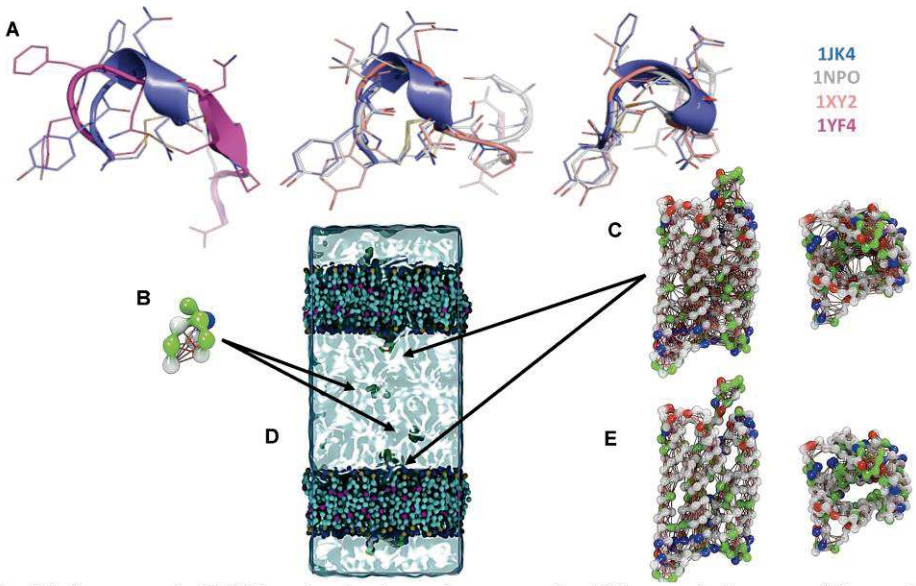

Fig. S7. Coarse grain-REMD molecular dynamics approach. **A**) Structural alignment of the two X-ray structures available for AVP (PDB codes: 1JK4 and 1YF4). The 1JK4 structure which describes the 6-residue cycle of AVP was preferred to the 1YF4 structure corresponding to the full length peptide, because it displays a cycle conformation equivalent to tat found in the unbound and bound oxytocin peptide analog (1XY2 and 1NPO). **B**) Schematic representation of the internal elastic networks used for the peptide AVP. **C**) Schematic representation of the internal elastic network used for V2R (side and extracellular view). **D**) The full system used for the CG-REMD simulations included 2 receptors and 2 ligands in order to create an artificial extracellular compartment and improve the conformational sampling of the AVP:V2R complex. **E**) Modified elastic network of the receptor used for the fit of the obtained CG models into the cryo-EM density maps.

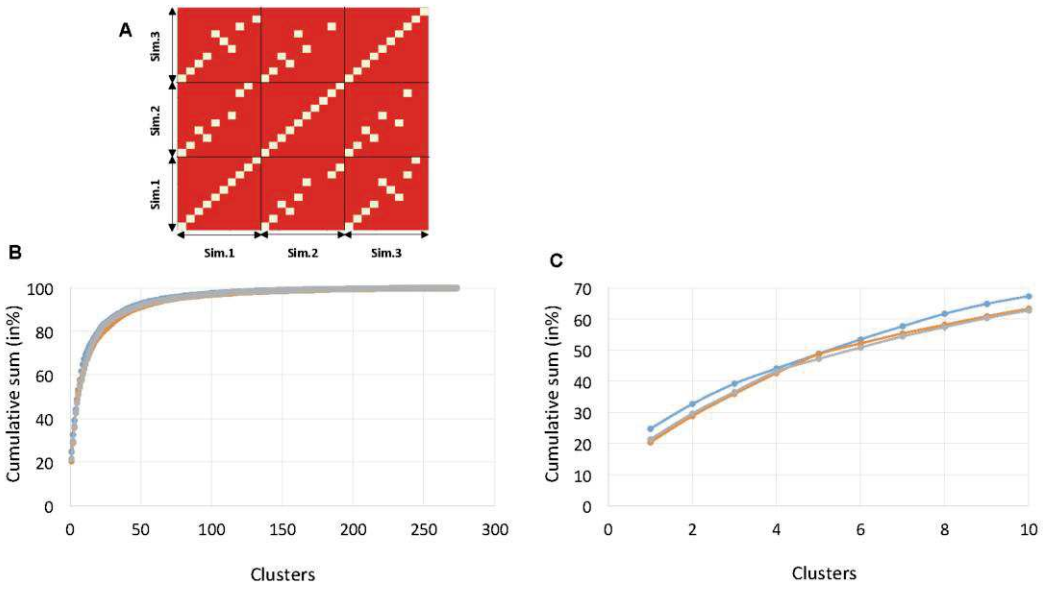

Fig. S8. CG-REMD simulations. A) Cross-RMSD matrix of the ten most populated clusters resuting from the 3 independant CG-REMD simulations and showing that the same models were systematically retrieved (white squares correspond to RMSD < 3Å). **B** and **C**) Analyse of the populations of all the obtained clusters in terms of cumulative sums showing that the ten first clusters together represent more than 60% of the whole conformations. Data from the 3 independent simulations are reported in blue, orange and grey, respectively.

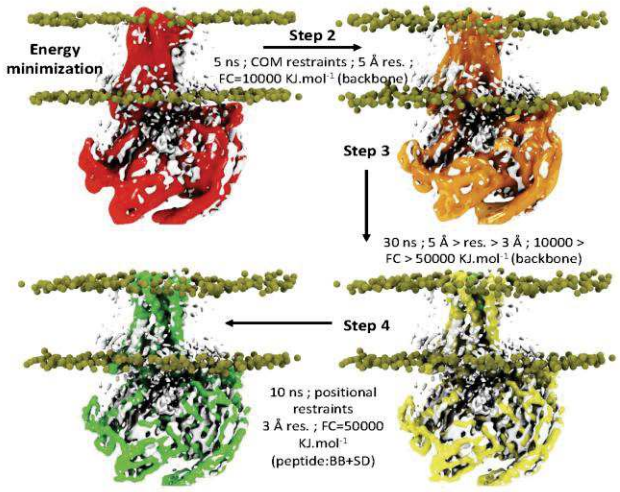

Fig. S9. Summary of the successive steps employing the CDMD method to fit the models. They result from the CG-REMD simulations into the cryo-EM maps.

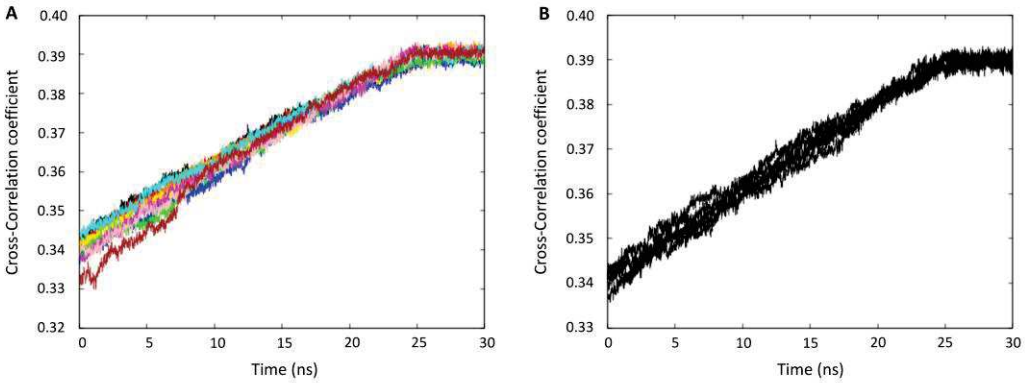

Fig. S10. Typical curves of cross-correlation coefficients as a function of time for each CDMD simulation.
A) and **B**) Cross-correlation coefficients values computed between the experimental and the simulated maps along CDMD simulations starting from the 10 most observed orientations of AVP in its receptor. In **A**), we reported one representative cross-correlation coefficients curve for each cluster whereas in **B**), the five curves obtained for the same cluster are depicted (five independent replicas). In each case, it shows a small variability of the obtained values and the convergence of the models at the end of the protocol. These curves were extracted from the main step 3 of fitting procedure.

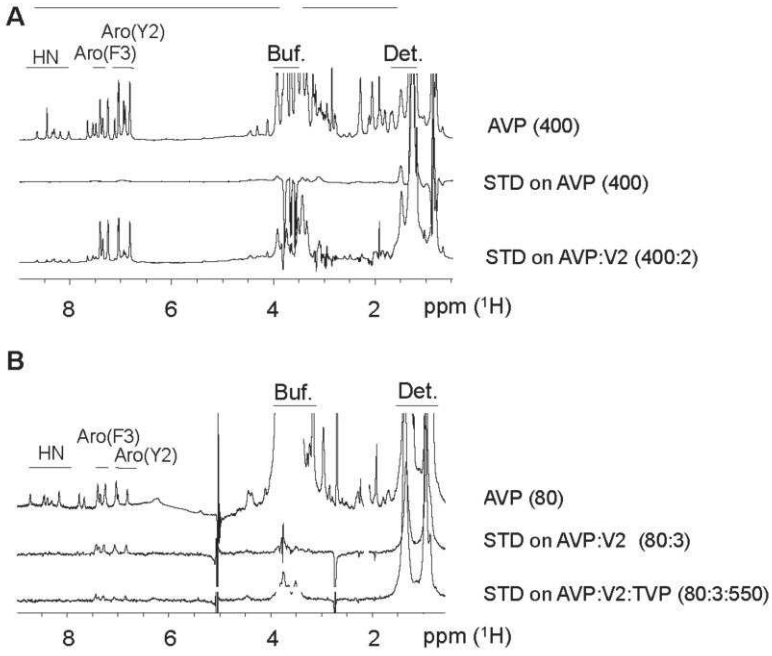

Fig. S11. Mapping of AVP interaction surfaces by STD NMR experiments. A) and **B**) Comparison of standard 1D proton spectrum (AVP 400 μM) with STD experiments on (**A**) 400 μM AVP and 400 μM AVP binding to 2 μM V2R and (**B**) 80 μM AVP binding to 3 μM V2R in absence/presence of 550 μM TVP (tolvaptan). Buffer resonance (Bis-Tris) and detergent resonance are labelled buf and det, respectively.

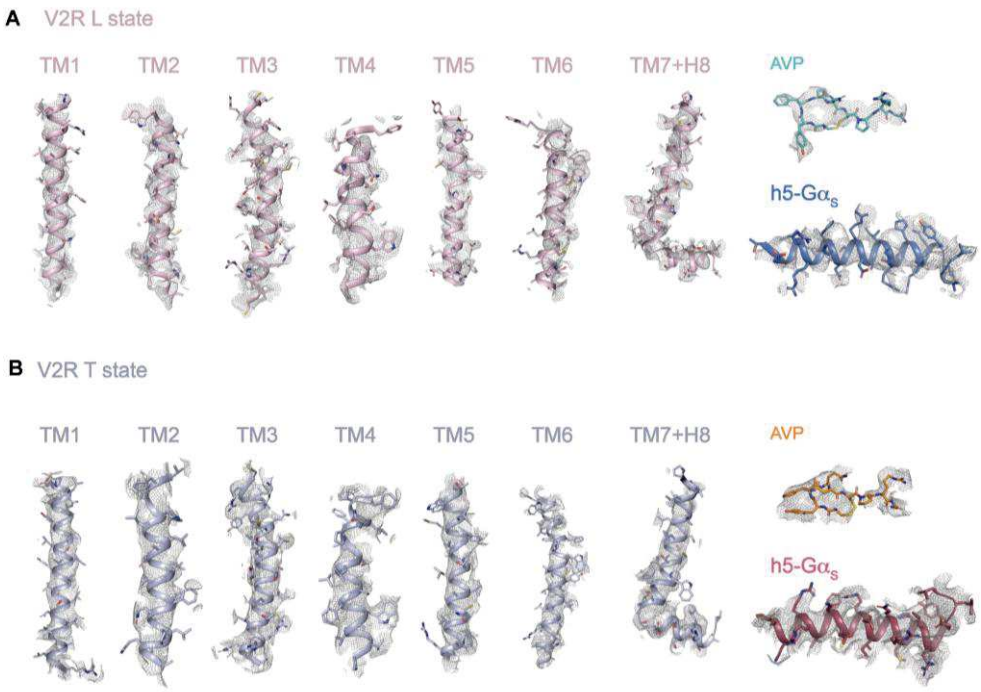

Fig. S12. Cryo-EM map quality for L and T states of the AVP-V2R-Gs-Nb35 complex. a) The density and model for TM helices 1-7 and helix H8 of V2R, α5 helix of Gαs and AVP in Loose (L) state. b) The density and model of corresponding protein domains and AVP in the Tight (T) state.

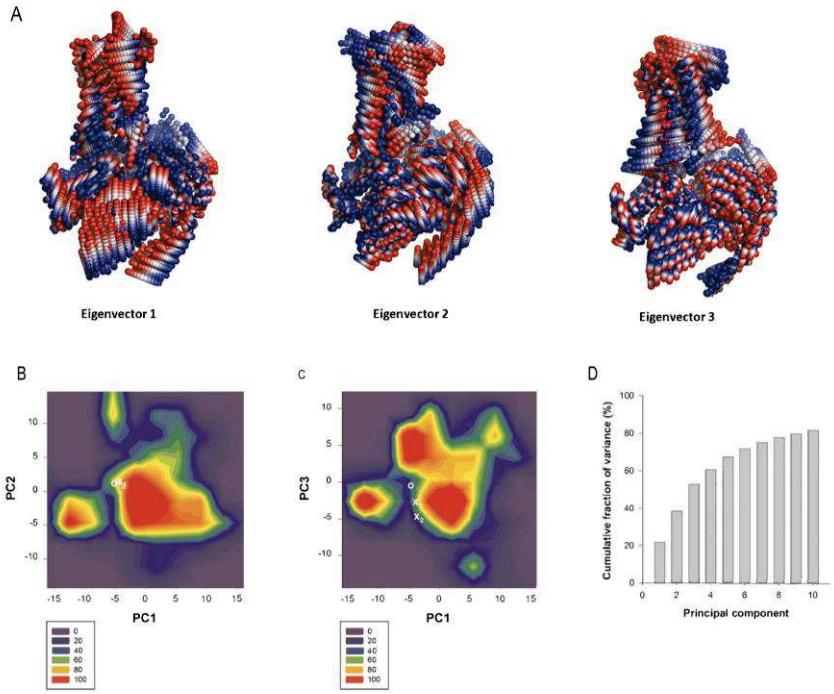

Fig. S13. Principal components analysis (PCA) obtained from molecular dynamics simulations of the L state. **A**) Collective motions of the AVP-V2R-Gs-Nb35 complex captured by PC1, PC2 and PC3. Motions are illustrated as linear interpolations between the extreme projections of the structures onto the PCs. Each cylinder, therefore, describes the path of each Cα atom between the extremes (on a red–white–blue color scale). **B**) and **C**) Conformational landscape of the AVP-V2R-Gs-Nb35 complex in PC space for the MD ensemble. 2D projections of MD trajectories along PC1 and PC2 (B) or PC1 and PC3 (C) were converted into 2D histograms to represent the density of population of each conformational state of the complex. The experimental L, T1 and T2 states are shown in white as (o), (x_1) and (x_2), respectively. **D**) Cumulative fraction of variance captured by the first 10 eigenvectors.

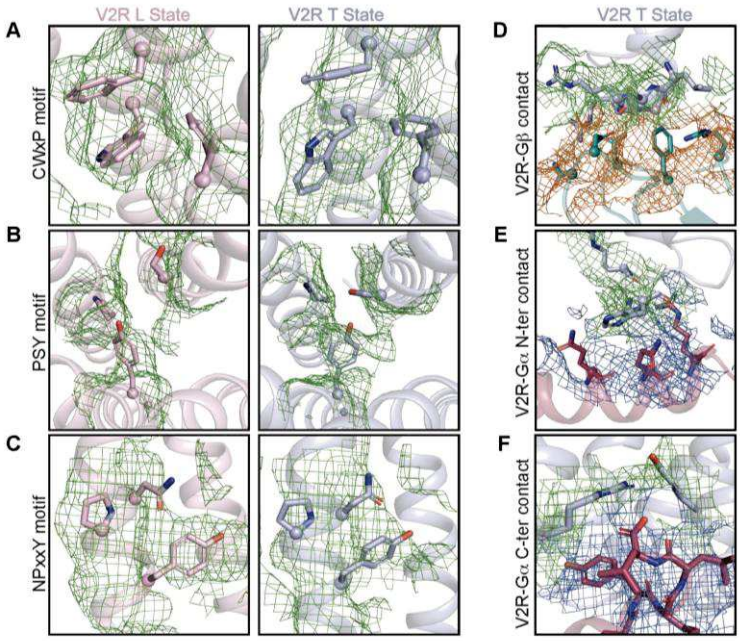

Fig. S14. Activation motifs and coupling interfaces in the AVP-V2R-Gs-Nb35 complex with the details of the cryo-EM maps. In all panels, the 3D models and the corresponding cryo-EM density maps (shown as green, orange or blue mesh) are superimposed. Close-up views of activation motifs in L and T states are shown on the left (**A**, **B**, **C**), whereas V2R-Gs contacts in the T state are shown on the right (**D**, **E**, **F**). The toggle switch CWxP motif including W284$^{6.48}$ (**A**), the PSY transmission motif with P$^{5.50}$-S$^{3.40}$-Y$^{6.44}$ residues (**B**) and the conserved NPxxY motif with Y325$^{7.53}$ (**C**) are highlighted. Different interaction interfaces stabilizing the V2R-Gs complex are depicted: the ICL1 of V2R is in close proximity with the Gβ subunit (**D**) and with the N-terminal helix of Gα subunit (**E**) of Gs protein, the unusual ionic bridge contact of V2R R137$^{3.50}$ side-chain (DRH motif) is in close proximity with the free carboxylic acid function of the C-terminal extremity of Gα subunit of Gs (**F**). The L or T conformation of V2R is depicted in pink or blue grey, respectively. The Gβ subunit is shown in turquoise, and the Gα subunit of Gs is illustrated in raspberry.

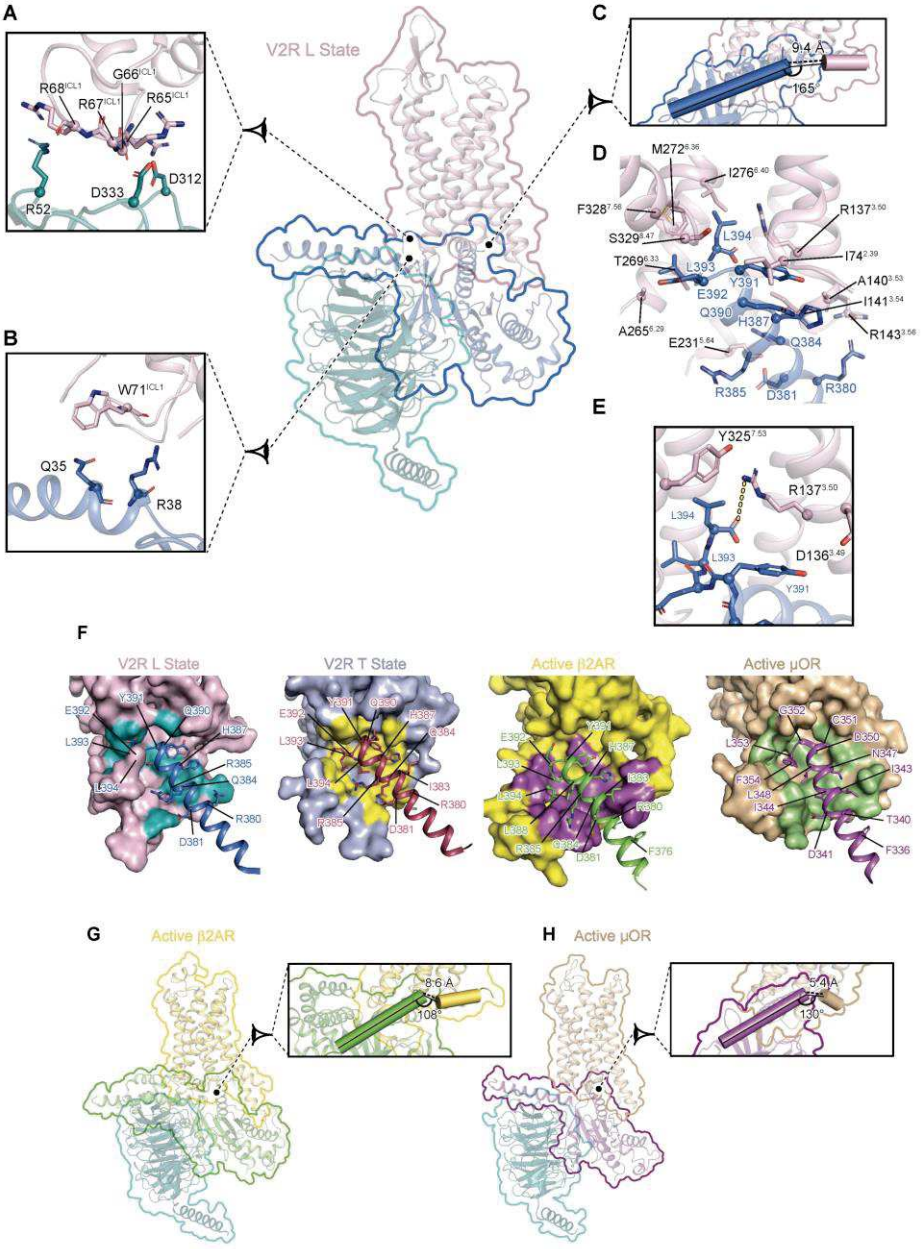

Fig. S15. Interface of the V2R L state with Gs. Interactions between V2R and Gs heterotrimer are shown. Specific interfaces are depicted, and residues in close proximity (within a maximal 3.9 Å distance) are highlighted (pink for V2R, turquoise for Gβ subunit, blue for Gα subunit). **A**) Interaction of V2R icl1 with Gβ subunit. **B**) Interaction of

V2R icl1 with N-terminal helix of Gα subunit. **C**) Positioning of C-terminal h5 helix of Gα subunit relative to V2R helix 8. The distance between Gα and helix 8 is indicated. Angle between these two domains is shown. **D**) Interacting residues between the C-terminal h5 helix of Gα subunit and V2R. **E**) Zoom on an ionic bridge between the C-terminal free carboxylic moiety of h5 helix of Gα subunit and V2R R137$^{3.50}$. **F**) Comparison of class A GPCR-Gα protein interfaces. The V2R-Gαs interfaces of L and T states are compared to those of the β2AR-Gαs and μOR-Gαi complexes. The h5 helix of the Gα subunit is shown for each complex with its residues indicated. The residues of receptors in contact with the Gα C-terminal are coloured. **G**) and **H**) Position of the C-terminal h5 helix of Gα subunit relative to receptor helix 8 in active β2AR-Gs and μOR-Gi complexes, respectively. Distances and angles between these domains are indicated as in panel C.

9 List of contributions:

Julien Bous	Molecular biology; Proteins expression; Biochemistry; Ns-EM and Cryo-EM sample preparation, screening; data processing, Data interpretation and articles redaction
Bernard Mouillac	Molecular biology; Proteins expression; Biochemistry; Pharmacology; Supervision; data interpretation and articles redaction
Patrick Bron	Ns-EM and Cryo-EM supervision; Data interpretation and articles redaction
Hélène Orcel	Molecular biology; Biochemistry; Pharmacology
joséphine lai kee him	Ns-EM and Cryo-EM supervision
Aurélien Fouillen	Molecular biology; Proteins expression; Biochemistry; Ns-EM and Cryo-EM sample preparation, screening; data processing, Data interpretation and articles redaction
Sebastien Granier	Supervision ; Articles redaction Results interpretation and articles redaction
Remy Sounier	Figures Design (V2R-Gs paper)
Nicolas Floquet	Model building; Coarse grain molecular dynamic
Maxime Louet	Model building; Coarse grain molecular dynamic
Hélène Déméné	STD-NMR
Stefano Trapani	Model building
Cedric Leyrat	Model building; Molecular dynamic
Julie Saint-Paul	Proteins purification
Simon Fontanel	Proteins purification

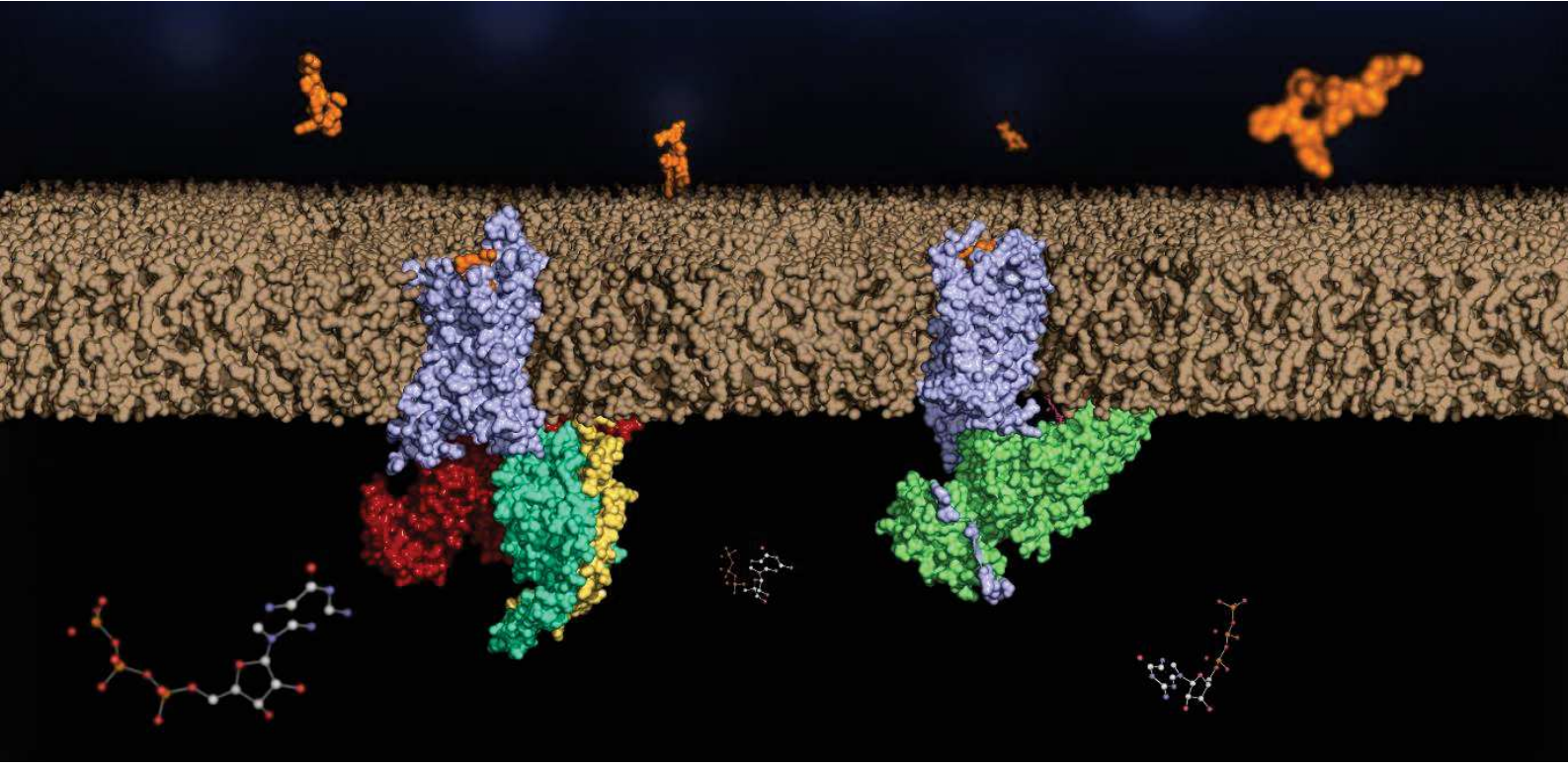

The arginine-vasopressin (AVP) V2 receptor (V2R) is a G protein-coupled receptor that controls body water homeostasis. It is involved in many water balance and urine disorders. Point mutations of its gene are directly responsible for two rare genetic diseases. As such, it is a key therapeutic target. Despite important progress in understanding the molecular basis of its function, it remained for a long time refractory to structure determination. This work is thus focused on the determination of the three-dimensional (3D) V2R structure in complex with its canonical signaling partners Gs protein or β-arrestin1 (βarr1) by cryo-electron microscopy (Cryo-EM). The comparison of the two active states of the V2R at an atomic level is an important step toward the understanding of the molecular mechanisms involved in its activity.

We first successfully determined the AVP-V2R-Gs complex structure by using a combination of single particle analysis (SPA) Cryo-EM, experimental NMR, and molecular dynamic simulations. This structural biology hybrid approach allowed to solve molecular details of AVP binding to V2R and of the interface of the receptor with the Gs protein signaling partner. The structure is in agreement with molecular pharmacology data accumulated over 25 years. The binding pocket is a deep cleft in the center of the seven-helix bundle. The bottom of the orthosteric crevice is mainly composed of hydrophobic residues while the entrance is more hydrophilic. This is consistent with the dual polarity of AVP with the hydrophobic residues (cys1, Tyr2, Phe3, Cys6) oriented toward the bottom of the pocket and polar residues (Gln4, Asn5, and the C-terminal tripeptide Pro7-Arg8-Gly9NH2) interacting with the entrance of the pocket. The active V2R displays hallmarks of receptor activation such as a large outward movement of the transmembrane domain (TM) 6 and inward movement of the TM7 and a break of the Ionic lock involving helices TM3 and TM6 (D/ERY motif). The coupling between the receptor and its Gs signaling partner is significantly tighter compared to what is observed for other class A GPCRs and interestingly, strongly dynamic, allowing us to characterize three conformational sub-states. This study goes further than a simple description of a receptor or a signaling protein complex structure. Indeed, 3D models were interpreted to understand the structural consequences of V2R mutations responsible for two rare genetic diseases. Congenital Nephrogenic Diabetes Insipidus (cNDI) is associated with V2R loss-of-function mutations whereas Nephrogenic Syndrome of Inappropriate Antidiuresis (NSIAD) is associated with V2R constitutively active mutations.

To be able to purify the AVP-V2R-βarr1-ScFv30 complex, we used a truncated version of βArr1(ΔCT) in which the C-terminus is deleted. The complex was then successfully investigated by SPA Cryo-EM. Since there are only a few structures of GPCRs in complex with arrestins, our new structure provides valuable insights of information to understand the coupling specificity of arrestins to GPCRs, and more specifically the coupling of βarr1 to V2R. The AVP displays the same overall position in the binding pocket as in the AVP-V2R-Gs complex, with respect to the limited resolution. The V2R adopts an active conformation similar to the one observed in complex with the Gs protein. The coupling is significantly different compared to the recently published structures. The βarr1 pose is intermediate between the ones reported for the β1-adrenergic receptor (β_1AR-βarr1), the muscarinic M2 receptor (M2R)-βarr1 and to the rhodopsin-Arr1 which adopt a similar overall conformation, and the ones reported for the neurotensin receptor 1 (NTSR1)-βarr1. Nonetheless, βarr1 coupled to V2R comparatively to βarr1 coupled to β_1AR differs by a rotation of approximately 30° parallel to the membrane plane, and displays a strong tilt relatively to the membrane plane. The βarr1 displays an active conformation as expected in this context. In the V2R–βarr1(ΔCT) structure, arrestin is strongly tilted towards the membrane. The strong tilt may be attributed to the interaction of the C-edge with the detergent micelle, as well as to the presence of the phosphatidylinositol-4,5-bisphosphate ($PtdIns_{(4,5)}P_2$) analog used to stabilize the complex during purification. It is of great interest since the $PtdIns_{(4,5)}P_2$ plays a pivotal role in clathrin-coated vesicles (CCVs) formation and might thus be involved in the dynamic of GPCR-Arr complexes recruitment to CCVs or in synergic formation of CCVs with these complexes. This process remains to be clearly established. The V2R coupled to its two canonical signalisation partners shares the same overall architecture and a common overall AVP position in the binding site. The arrestin finger loop seems to occupy a similar position to the α5-helix of the Ras domain of the Gs α subunit into the V2R core but the helices display a different orientation. Structural differences at the atomic level might exist but a AVP-V2R-βarr structure with an improved resolution will be necessary to identify such differences.